materials

Special Issue Reprint

Reaction Mechanism and Properties of Cement-Based Materials (2nd Edition)

Edited by
Weiting Xu

mdpi.com/journal/materials

MDPI

Reaction Mechanism and Properties of Cement-Based Materials (2nd Edition)

Reaction Mechanism and Properties of Cement-Based Materials (2nd Edition)

Guest Editor

Weiting Xu

MDPI

Basel • Beijing • Wuhan • Barcelona • Belgrade • Novi Sad • Cluj • Manchester

Guest Editor
Weiting Xu
School of Materials Science
and Engineering
South China University of
Technology
Guangzhou
China

Editorial Office
MDPI AG
Grosspeteranlage 5
4052 Basel, Switzerland

This is a reprint of the Special Issue, published open access by the journal *Materials* (ISSN 1996-1944), freely accessible at: https://www.mdpi.com/journal/materials/special_issues/MY4JRD5509.

For citation purposes, cite each article independently as indicated on the article page online and as indicated below:

Lastname, A.A.; Lastname, B.B. Article Title. *Journal Name* **Year**, *Volume Number*, Page Range.

ISBN 978-3-7258-5757-9 (Hbk)
ISBN 978-3-7258-5758-6 (PDF)
https://doi.org/10.3390/books978-3-7258-5758-6

© 2025 by the authors. Articles in this book are Open Access and distributed under the Creative Commons Attribution (CC BY) license. The book as a whole is distributed by MDPI under the terms and conditions of the Creative Commons Attribution-NonCommercial-NoDerivs (CC BY-NC-ND) license (https://creativecommons.org/licenses/by-nc-nd/4.0/).

Contents

About the Editor . . . . . **vii**

Preface . . . . . **ix**

Longfei Lu, Guoxiang Yang, Yan Ai, Jingkai Qu, Jinrui Duan, Kun Yang and Wenbin Sun
Cement-Based Grouting Materials Modified with GO/NS Hybrids
Reprinted from: *Materials* **2025**, *18*, 4820, https://doi.org/10.3390/ma18214820 . . . . . **1**

Xinyu Zhang, Wei Li, Xiaojun Huang, Zhixin Wang and Min Deng
Mechanisms for Migration of Alkali in Dolomitic Limestones
Reprinted from: *Materials* **2025**, *18*, 4404, https://doi.org/10.3390/ma18184404 . . . . . **23**

Runze Shang, Dexiang Huang, Wenju Cai, Longlong Niu, Bi Chen, Xinyu Zhang, et al.
Influence of Clinker and Cinder Particle Gradation on the Properties of Blended Cement and Associated Mortars
Reprinted from: *Materials* **2025**, *18*, 2864, https://doi.org/10.3390/ma18122864 . . . . . **45**

Feifei Jiang, Yijiang Xing, Wencong Deng, Qi Wang, Jialei Wang and Zhongyang Mao
Effect of Combined MgO Expansive Agent and Rice Husk Ash on Deformation and Strength of Post-Cast Concrete
Reprinted from: *Materials* **2025**, *18*, 2815, https://doi.org/10.3390/ma18122815 . . . . . **63**

Vanja Đurđevac, Novica Staletović, Lidija Đurđevac Ignjatović, Violeta Jovanović, Nikola Vuković and Vesna Krstić
Application of Flotation Tailings as a Substitute for Cement in Concrete Structures for Environmental Protection and Sustainable Development—Part I: Sulfide Neutralization
Reprinted from: *Materials* **2025**, *18*, 2804, https://doi.org/10.3390/ma18122804 . . . . . **81**

Zhixin Wang, Shaoping Wang, Wei Li, Bing Cao, Xiaojun Huang, Xin Chuai, et al.
Methods for Quantitative Determination of Iron Sulfides in Rocks
Reprinted from: *Materials* **2025**, *18*, 2647, https://doi.org/10.3390/ma18112647 . . . . . **105**

Jiapeng Duan, Yu Zhang, Suwei Xia, Zian Geng and Wenbo Xin
Utilization of Low-Grade Limestone and Solid Waste for the Preparation of High-Belite Portland Cement
Reprinted from: *Materials* **2025**, *18*, 2641, https://doi.org/10.3390/ma18112641 . . . . . **124**

Shanshi Chen, Xinjian Yue and Yongmin Zhou
Influence of Raw Material Fineness on Clinker Burnability and Cement Performance
Reprinted from: *Materials* **2025**, *18*, 2453, https://doi.org/10.3390/ma18112453 . . . . . **140**

Meixin Liu, Yuan Hu, Jing Li, Xiaolin Liu, Huiwen Sun, Yunfei Di, et al
Insights into Hydration Kinetics of Cement Pastes Evaluated by Low-Field Nuclear Magnetic Resonance: Effects of Super-Absorbent Polymer as Internal Curing Agent and Calcium Oxide as Expansive Agent
Reprinted from: *Materials* **2025**, *18*, 836, https://doi.org/10.3390/ma18040836 . . . . . **157**

Jeong-Bae Lee
Redispersible Acrylic Ester Polymers: Effect of Polymer Property Changes Due to Polymerization Method Modification and Functional Additives on the Performance of Polymer Cement Mortar
Reprinted from: *Materials* **2024**, *17*, 5534, https://doi.org/10.3390/ma17225534 . . . . . **172**

Feifei Jiang, Wencong Deng, Qi Wang, Jialei Wang and Zhongyang Mao
Performance Research and Engineering Application of Fiber-Reinforced Lightweight Aggregate Concrete
Reprinted from: *Materials* **2024**, *17*, 5530, https://doi.org/10.3390/ma17225530 . . . . . **192**

Yahya Kaya, Hatice Gizem Şahin, Naz Mardani and Ali Mardani
Influence of Grinding Aids on the Grinding Performance and Rheological Properties of Cementitious Systems
Reprinted from: *Materials* **2024**, *17*, 5328, https://doi.org/10.3390/ma17215328 . . . . . **207**

Jialei Wang, Feifei Jiang, Juan Zhou and Zhongyang Mao
The Synergistic Effect of Limestone Powder and Rice Husk Ash on the Mechanical Properties of Cement-Based Materials
Reprinted from: *Materials* **2024**, *17*, 5058, https://doi.org/10.3390/ma17205058 . . . . . **224**

Zijian Li, Jinjie Li, Weihua Lu and Yongxing Zhang
Research Progress and Application Prospects of Plant Fibers in Geopolymer Concrete: A Review
Reprinted from: *Materials* **2025**, *18*, 2342, https://doi.org/10.3390/ma18102342 . . . . . **244**

About the Editor

Weiting Xu

Weiting Xu is an Associate Professor in the Department of Inorganic Non-metallic Materials, School of Materials Science and Engineering at South China University of Technology. Her research is dedicated to the design of high-performance composite cement-based materials, with a focus on understanding their multiphase reaction mechanisms and comprehensive properties. A significant part of her work involves the hydrophobic, shrinkage-resistant, and toughening modification of geopolymers using organic molecules, and investigating the reaction mechanisms at the organic-inorganic interface. She also employs molecular dynamics simulations to design and study composite cementitious materials. With extensive experience in the field, her work particularly contributes to the design and performance control of low-carbon construction materials.

Preface

Cement is one of the most important building materials in human history, and it is used to build various infrastructures due to its high strength, excellent durability, and relatively low cost. The microstructure of cement-based materials is composed of a cement paste system, stone, porosity, water content, and other components. Among them, the cement paste system, mainly the hydration product of clinker or a reaction precursor, is the most important component of cement-based materials. The microstructure of a reaction product, pores, and the constituent phase, as well as the hardening process of a cement paste system, have crucial influences on the mechanical and physical properties of the resulting materials. The in-depth understanding of the relationship between the microstructure and macroscopic properties of cement-based materials helps to design more efficient and stable cementitious materials for construction. Cement-based materials are multi-phase and multi-scale structures, and each component has a different degree of influence on the overall mechanical and physical properties.

This Reprint of Special Issue focuses on, but is not limited to, the mechanisms of the physicochemical effects on the cracking and toughening properties of cement-based materials on the macroscopic scale, such as gelling components, aggregates, admixtures, fibers, the water–binder ratio, curing system, and environmental effect; the effects of micrometer-scale reinforcement materials on filling, bridging, bonding, and osmotic crystallization in cement-based material systems; the enhancing effects and mechanisms of nano-scale reinforcement materials on the microstructure of hydration products as well as the growth mode and pore structure of hardened paste; and the conjugate toughening effects of cross-scale components on different scales of cement-based materials.

Weiting Xu
Guest Editor

materials

MDPI

Article

Cement-Based Grouting Materials Modified with GO/NS Hybrids

Longfei Lu, Guoxiang Yang *, Yan Ai, Jingkai Qu, Jinrui Duan, Kun Yang and Wenbin Sun

School of Engineering and Technology, China University of Geosciences (Beijing), Beijing 100083, China; 2002230058@email.cugb.edu.cn (L.L.); 3002230012@email.cugb.edu.cn (Y.A.); 3002230036@email.cugb.edu.cn (J.Q.); 3002240053@email.cugb.edu.cn (J.D.); 2002230060@email.cugb.edu.cn (K.Y.); 2002230057@email.cugb.edu.cn (W.S.)
* Correspondence: yanggx@cugb.edu.cn

Abstract: This study systematically investigates the effects of individual and combined incorporation of graphene oxide (GO) and nano-silica sol (NS) on the macroscopic properties and microstructure of cement-based grouting materials, with emphasis on their synergistic mechanisms. A series of macroscopic tests including setting time, fluidity, bleeding rate, and mechanical strength were conducted, complemented by multi-scale microstructural characterization techniques such as scanning electron microscopy (SEM), X-ray diffraction (XRD), mercury intrusion porosimetry (MIP), and Fourier-transform infrared spectroscopy (FTIR). The results demonstrate that both NS and GO effectively reduce setting time and bleeding rate while enhancing mechanical strength; however, NS exhibits a more pronounced adverse effect on fluidity compared to GO. The hybrid system displays a distinct transition from synergy to antagonism: under low-dosage co-incorporation (2 wt% NS + 0.01 wt% GO), the flexural and compressive strengths increased by 13.5% and 45.5%, respectively, relative to the reference group. Microscopic analysis revealed that the synergistic interaction between the pozzolanic effect of NS and the templating effect of GO under this condition optimizes hydrate morphology and pore structure, leading to enhanced performance. Conversely, excessive dosage of either component induces agglomeration, resulting in microstructural deterioration and performance degradation. This study establishes optimal dosage ranges and combination principles for NS and GO in cement-based materials, providing a theoretical foundation for designing high-workability and high-strength cementitious composites.

Keywords: graphene oxide; nano-silica; cement-based grout; mechanical properties; synergistic effect

1. Introduction

Cement-based composites are fundamental materials widely used in modern construction and major engineering projects, including civil infrastructure, hydraulic facilities, and transportation systems [1]. However, their inherent brittleness, low tensile strength, and susceptibility to cracking significantly limit their application potential and service life, particularly in extreme environments and high-performance structures. From a micromechanical perspective, the mechanical properties and durability of cementitious materials are largely governed by the composition and morphological distribution of hydration products, as well as the characteristics of the pore structure [2]. Therefore, controlling the hydration process to optimize microstructure has become a crucial strategy for developing high-performance cement-based materials.

The rapid development of nanotechnology and materials science has introduced the use of nanomaterials as modifiers in cementitious matrices, representing a major research frontier [3–6]. Among these, graphene oxide (GO) and nano-silica (NS) have attracted significant attention due to their unique physicochemical properties and substantial potential for material enhancement [7–9]. GO possesses a distinctive two-dimensional layered structure and exceptional theoretical mechanical strength. Its surface is rich in oxygen-containing functional groups (e.g., hydroxyl, epoxy, and carboxyl groups), which can effectively adsorb cement hydration ions and serve as nucleation sites for hydration products, thereby accelerating hydration [10–12]. Research by Lv et al. [13,14] also indicated that GO can inhibit the propagation of microcracks through a bridging effect, markedly enhancing the material's strength and toughness. Nonetheless, the practical application of GO faces considerable challenges: Zhang et al. [15] observed that its high specific surface area and strong π–π conjugation effects cause GO sheets to agglomerate readily, making uniform dispersion within the cement matrix difficult. This not only reduces its reinforcing efficiency but may also introduce microdefects. Moreover, experimental studies by Li et al. [16] confirmed that incorporating GO negatively affects the rheological properties of fresh paste, resulting in a significant loss of fluidity, which is detrimental to practical workability.

On the other hand, NS consists of colloidal dispersions of nano-sized amorphous silica (SiO_2) particles. Vijayan et al. [17] provided a systematic review of the pozzolanic effect of NS, highlighting its ability to react with calcium hydroxide (CH), a primary hydration product, to form additional calcium silicate hydrate (C–S–H) gel. This process not only refines the microstructure of the interfacial transition zone (ITZ) but also effectively fills nano-scale pores, significantly improving the compactness and durability of the system. However, the use of NS also has limitations: Qing et al. [18] found that the high specific surface area of nano-SiO_2 particles greatly increases water demand, creating a strong dependence on high-range water reducers to maintain adequate workability. Additionally, Ji [19] noted that the pozzolanic reaction rate of NS is relatively slow, resulting in limited early-age strength contribution. Excessive incorporation may lead to particle agglomeration, and unreacted particles may remain as inert fillers, potentially impairing the microstructure.

Notably, recent studies suggest that GO and NS may exhibit theoretical potential for synergistic modification [20–23]. Liu et al. [23] proposed that GO could provide a template for the ordered growth of C–S–H gel, while the gel products resulting from the NS reaction could encapsulate and anchor GO sheets. This synergistic interaction promotes the formation of a denser and tougher three-dimensional network composite structure, potentially overcoming the performance limitations of single-modifier systems. This concept is supported by findings in other composite material systems; for example, Bouibed et al. [22] demonstrated in studies on epoxy resins and coating sealants that GO/SiO_2 hybrids produce a "1 + 1 > 2" synergistic effect, substantially enhancing mechanical strength and corrosion resistance.

Despite considerable progress in single nanomaterial modification, research on GO/NS hybrid systems remains limited [24–27]. Mohammed et al. [26] emphasized that most existing studies focus on the influence of individual materials on final mechanical properties, while systematic investigations into the synergistic variations in key fresh-state properties (e.g., fluidity, stability, and setting time) within composite systems are still lacking. More importantly, from a micromechanical perspective, Li et al. [27] pointed out the scarcity of systematic research on how GO and NS collectively affect the hydration process, product morphology, pore structure evolution, and interface properties. There is a critical need for in-depth studies that reveal the multi-scale "physicochemical" synergistic mechanisms.

Against this background, the present study systematically investigates the individual and synergistic effects of GO and NS on the macroscopic properties and microstructure of cement-based composites. Using PO 42.5 ordinary Portland cement as the base material, experiments were conducted to evaluate the fluidity, bleeding rate, setting time of fresh paste, and the compressive/flexural strength of hardened paste, with varying dosages of GO and NS. Scanning electron microscopy (SEM), X-ray diffraction (XRD), mercury intrusion porosimetry (MIP), and Fourier-transform infrared spectroscopy (FTIR) were employed to analyze the interaction mechanisms and modification effects of GO and NS across four aspects: micromorphology, phase composition, pore structure, and chemical bonding. This research aims to address three fundamental questions: (1) the dose–response relationships for NS and GO individually; (2) the synergy-to-antagonism transition threshold in hybrid systems; and (3) the structure-property relationships between multi-scale structural evolution and macroscopic performance. The findings are expected to provide essential data support for the compound application of nanomaterials in cementitious matrices and offer valuable guidance for designing cement-based materials with high workability, strength, and toughness.

2. Materials and Methods

2.1. Raw Materials

The materials used in this study included Portland cement (P.O 42.5), colloidal nano-silica (NS), an aqueous dispersion of graphene oxide (GO), and a polycarboxylate ether (PCE)-based superplasticizer. All materials were thoroughly characterized to ensure the accuracy and reproducibility of the experimental results.

1. Cement:

Ordinary Portland cement (P·O 42.5 grade) was obtained from Anhui Yicheng Conch Cement Co., Ltd. (Wuhu, China). Its chemical composition, as determined by X-ray fluorescence (XRF) spectroscopy, is presented in Table 1. The fineness of the cement, expressed as the residue on a 45 μm sieve, was measured to be 10.9%.

Table 1. Chemical Composition and Phase Composition of Portland Cement (mass %).

Compound	Content (%)	Phase Name	Approximate Content
CaO	54.36%	C_3S	45–60%
SiO_2	22.31%	C_2S	15–30%
Al_2O_3	9.76%	C_3A	6–12%
SO_3	3.16%	C_4AF	6–8%
Fe_2O_3	3.13%	Gypsum	3–5%
K_2O	1.03%	Additives	5–20%
MgO	1.01%		
TiO_2	0.43%		

2. Nano-silica (NS):

An alkaline colloidal nano-silica solution was supplied by Qingdao Ronghaipolyde Fine Chemical Co., Ltd. (Qingdao, China). The key physical and chemical properties of the NS are summarized in Table 2.

Table 2. Technical specifications of the nano-silica (NS) solution.

Property	Value
SiO_2 content	40.1 wt%
Na_2O	0.22 wt%
pH value	9.6
Average particle size	10 nm
Density(at 25 °C)	1.295 g/cm^3
Appearance	Semi-translucent, milky-white colloid

3. Graphene oxide (GO):

An aqueous graphene oxide dispersion, synthesized via a modified Hummers' method, was provided by Suzhou Tanfeng Technology Co., Ltd. (Suzhou, China). The dispersion had a concentration of 10 mg/mL and a purity exceeding 90%, exhibiting a brownish-yellow to black appearance. The detailed characteristics of the GO nanosheets are listed in Table 3.

Table 3. Physicochemical properties of the graphene oxide (GO) dispersion.

Property	Value
Number of layers	Single-layer
Single-layer ratio	>99.9%
Thickness	~1 nm
Flake diameter	10–50 μm
Oxidation degree	~36%
Specific surface area	50–150 m^2/g

4. Superplasticizer:

A commercial polycarboxylate ether (PCE)-based superplasticizer with a solid content of 20% was used to ensure sufficient workability of the fresh mixtures.

2.2. Sample Preparation

A constant water-to-cement (w/c) ratio of 0.6 was used as the baseline to systematically evaluate the individual and synergistic effects of nano-silica (NS) and graphene oxide (GO) on the properties of cement-based grouting materials. A total of 14 mix designs were formulated, as specified in Table 4. The mixtures were divided into four series:

Series A (Reference): Control group, containing only 0.6 wt% superplasticizer.

Series B (NS-only): Mixes with NS content ranging from 2 wt% to 5 wt%.

Series C (GO-only): Mixes with GO content ranging from 0.01 wt% to 0.04 wt%.

Series D (NS/GO Hybrid): Mixes with combined NS and GO, designed to examine their interaction and potential synergistic effects at various ratios.

The dosages of all additives were calculated based on the mass of cement.

All mixing and sample preparation procedures were performed in a controlled laboratory environment maintained at 25 ± 2 °C. Raw materials were accurately weighed using an electronic balance. A strict mixing sequence was followed: deionized water, the superplasticizer (PCE), the GO dispersion, and the NS colloid were successively introduced into a high-speed slurry mixer (model: SYJ-10, Shandong Luda Testing Instrument Co., Ltd., Taian, China). The mixture was initially homogenized at 400 rpm for 2 min. Cement was then gradually added, and mixing continued at the same speed for an additional 5 min to obtain a homogeneous and stable fresh paste.

Table 4. Mix proportions of the cement-based grouting materials.

Group	w/c	Cement	SP (wt%)	NS (wt%)	GO (wt%)
A0	0.6	100%	0.6	/	/
B2	0.6	100%	0.6	2	/
B3	0.6	100%	0.6	3	/
B4	0.6	100%	0.6	4	/
B5	0.6	100%	0.6	5	/
C01	0.6	100%	/	/	0.01
C02	0.6	100%	/	/	0.02
C03	0.6	100%	/	/	0.03
C04	0.6	100%	/	/	0.04
D2-01	0.6	100%	0.6	2	0.01
D2-02	0.6	100%	0.6%	2	0.02
D2-03	0.6	100%	0.6	2	0.03
D3-01	0.6	100%	0.6	3	0.01
D4-01	0.6	100%	0.6	4	0.01

Note: SP = Superplasticizer; wt% = percentage by mass of cement; The "water" in the water-cement ratio calculation refers to the total amount of water used for mixing, which includes: the added water, the water contained in the nano-silica sol, the water in the graphene oxide dispersion, and the water contained in the water-reducing agent solution.

The resulting grout was cast into pre-assembled molds (40 mm × 40 mm × 160 mm). To minimize air entrapment, the molds were lightly vibrated on a vibrating table each time they were filled to approximately one-third of their height. After casting, the molds were covered and transferred to a standard curing room (20 ± 1 °C, relative humidity ≥ 90%) for 24 h of initial setting. After demolding, the specimens were continuously cured in lime-saturated water until the designated testing ages (3, 7, and 28 days) for subsequent mechanical property tests and microstructural analysis. A flowchart illustrating the sample preparation process is shown in Figure 1.

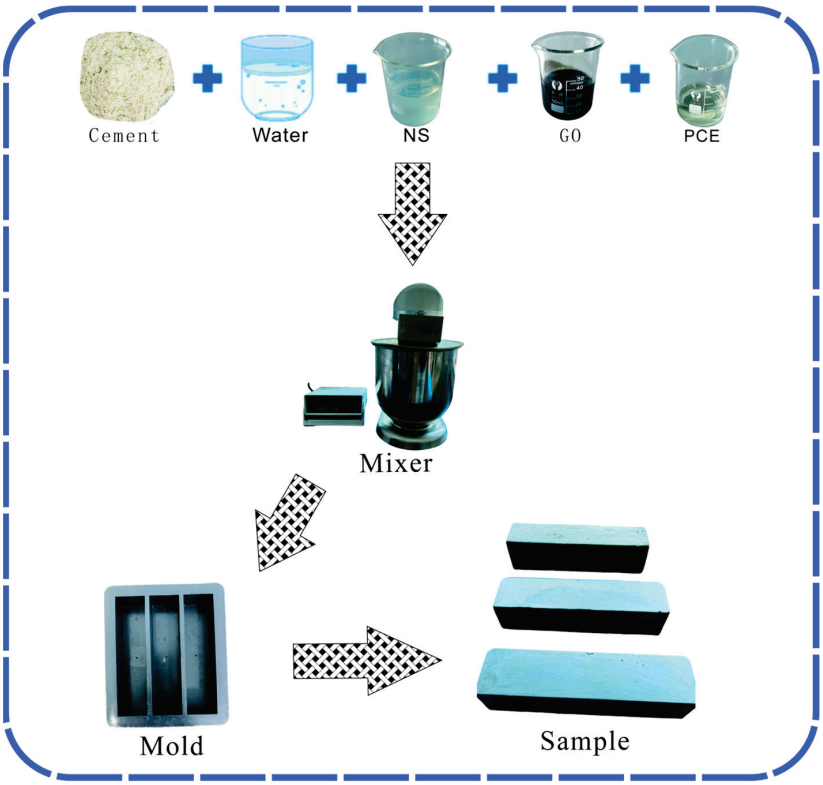

Figure 1. Sample preparation.

2.3. Testing Methods

1. Setting Time

The initial and final setting times of the fresh paste were measured using a Vicat apparatus according to the standard test method [3]. The sample was stored in a constant-temperature chamber (20 ± 1 °C, 90% RH) starting from the time of water addition. The initial setting time was recorded when the penetration depth of the needle reached 4 ± 1 mm above the base plate. The final setting time was defined as the time at which the needle no longer left a visible circular impression on the paste surface.

2. Fluidity (Flowability)

The fluidity of the fresh mixture was evaluated by measuring its flow diameter using the diffusion disc method [28]. Specifically, the freshly mixed paste was poured into a truncated conical mold placed centrally on a flat glass plate. The mold was then lifted vertically, allowing the paste to spread freely. After the flow stabilized, the final diameter was measured along two perpendicular directions. The average of these two values was reported as the flow value, with an accuracy of 1 mm.

3. Bleeding Rate

The stability of the fresh mixture was assessed based on its bleeding rate. A 200 mL graduated cylinder was filled with the freshly prepared grout, sealed, and left undisturbed at room temperature. After 2 h, the volume of water separated and accumulated on the surface (Vw) was recorded. The bleeding rate (BR, in %) was calculated as follows:

$$BR = (Vw/V_0) \times 100\%$$

where V_0 represents the initial volume of the grout sample (200 mL) [29].

4. Mechanical Properties

Prismatic specimens measuring 40 mm × 40 mm × 160 mm were prepared and cured under standard conditions until the designated testing ages. The flexural and compressive strengths were determined using a 305F-2 microcomputer-controlled bending and compression integrated testing machine (Shenzhen Wance Testing Machine Co., Ltd., Shenzhen, China), in accordance with the Chinese National Standard GB/T 17671-2021 [30] (Methods of testing cements—Determination of Strength). The loading rates were set to 50 N/s and 2400 N/s for flexural and compressive tests, respectively. The reported strength values represent the arithmetic average of six individual specimens.

5. Scanning Electron Microscopy (SEM)

Fractured samples were collected at specific ages for microstructural morphology analysis. To arrest hydration, the fragments were immediately immersed in anhydrous ethanol for 48 h and subsequently dried in a vacuum oven at 60 °C. The dried samples were mounted on stubs, and a thin gold layer was sputter-coated onto the fracture surface to enhance conductivity. Microstructural observations were carried out using a scanning electron microscope operated at an accelerating voltage of 15 kV.

6. X-ray Diffraction (XRD)

For phase composition analysis, hydrated samples were ground into fine powder after hydration arrest and drying. The powder was sieved to obtain particles smaller than 80 μm. XRD analysis was performed using an X-ray diffractometer with Cu Kα radiation (λ = 1.5406 Å). The scanning range was set from 5° to 70° (2θ) with a step size of 0.02° and a scanning rate of 4°/min. The resulting diffraction patterns were analyzed using Jade

software (version 6.0) by matching with standard powder diffraction files (PDFs) from the International Centre for Diffraction Data (ICDD).

7. Fourier-Transform Infrared Spectroscopy (FTIR)

Chemical structure and bonding information were obtained via FTIR spectroscopy. Dried sample powder was thoroughly mixed with spectroscopic-grade KBr at a mass ratio of approximately 1:100 and pressed into transparent pellets. Spectra were acquired in the mid-infrared region from 4000 to 400 cm^{-1} with a resolution of 4 cm^{-1}, and each spectrum was averaged over 32 scans to improve the signal-to-noise ratio.

8. Mercury Intrusion Porosimetry (MIP)

Pore structure characteristics, including pore size distribution and total porosity, were determined using MIP. Dried samples of specified size were placed in a penetrometer. Mercury was intruded into the pores under applied pressure, which was gradually increased from 0.5 to 30,000 psi. The pore size distribution was derived from the intrusion data based on the Washburn equation, assuming a mercury surface tension of 485 mN/m and a contact angle of 130°.

3. Results and Discussion

3.1. Fresh State Properties

3.1.1. Setting Time

This study systematically investigated the effects of nano-silica (NS) and graphene oxide (GO) on the setting times of cement paste at a fixed water-to-cement (w/c) ratio of 0.6. A constant dosage of 0.6 wt% polycarboxylate ether (PCE) superplasticizer was used in the NS series. As illustrated in Figure 2, the control group (without NS or GO) exhibited initial and final setting times of 958 min and 1084 min, respectively. The incorporation of NS markedly shortened both setting times in a dose-dependent manner. At NS dosages of 2 wt%, 3 wt%, and 4 wt%, the initial setting time decreased to 665 min, 592 min, and 547 min, while the final setting time was reduced to 795 min, 739 min, and 707 min, respectively. On average, each 1 wt% increase in NS content shortened the initial and final setting times by approximately 102.75 min and 94.25 min, respectively. Similarly, GO also exhibited a significant accelerating effect. With GO dosages of 0.01 wt%, 0.02 wt%, and 0.03 wt%, the initial setting times were recorded as 681 min, 664 min, and 654 min, and the final setting times as 739 min, 723 min, and 711 min, respectively. Notably, even a minimal GO dosage of 0.01 wt% considerably accelerated the setting process. Each 0.01 wt% increase in GO content reduced the initial and final setting times by approximately 26 min and 50 min, respectively. These results confirm that both NS and GO serve as effective setting accelerators, though likely through distinct mechanisms that warrant further microstructural investigation.

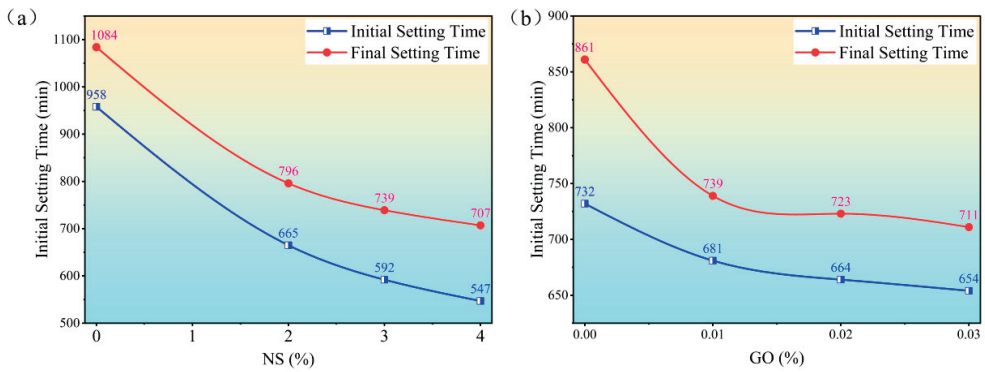

Figure 2. Effect of (**a**) NS and (**b**) GO dosage on the setting time of cement paste.

Figure 3 presents the setting times of the hybrid NS/GO groups. Comparative analysis revealed a clear synergistic effect between NS and GO within the composite system. When 0.01 wt% GO was introduced at constant NS dosages (compare mixes D2-01 vs. B2, D3-01 vs. B3, D4-01 vs. B4), the system exhibited a characteristic delay in initial setting but an acceleration in final setting. Conversely, the addition of 2 wt% NS at constant GO dosages (compare D2-01 vs. C01, D2-02 vs. C02, D2-03 vs. C03) resulted in significantly accelerated initial setting with only minor adjustments to final setting. This indicates that the high reactivity of NS effectively counteracted the potential retardation tendency of GO, ensuring rapid initiation of the setting reaction. These findings suggest that the NS/GO hybrid system modulates the cement setting process across different temporal stages rather than merely combining individual effects. While NS enhances reaction efficiency, GO improves the quality of structural formation. Together, they provide a critical foundation for enhancing the macroscopic properties of the system.

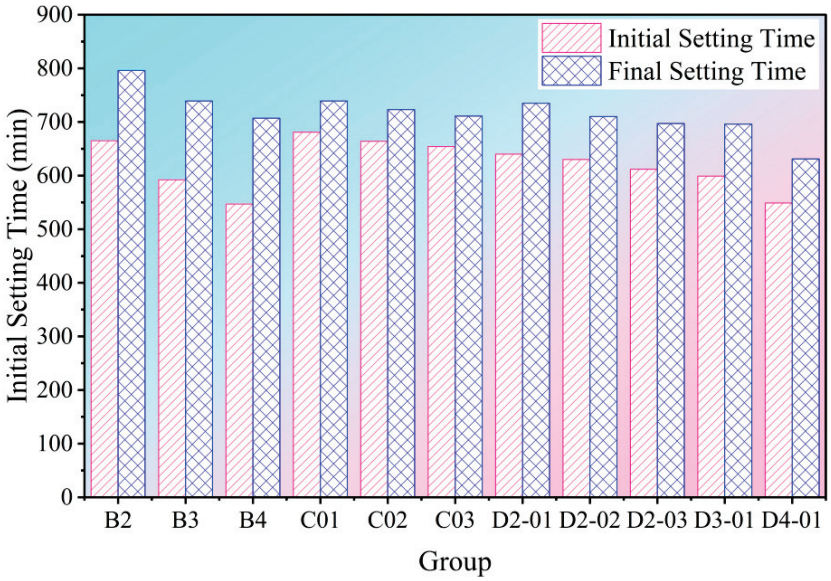

Figure 3. Setting times of each NS/GO group.

3.1.2. Bleeding Rate and Fluidity

The effects of NS and GO on the bleeding rate and fluidity (flow spread) of the cement paste are shown in Figures 4 and 5. The control group with 0.6 wt% PCE (NS baseline) showed a bleeding rate of 5.0% and a fluidity of 343.63 mm, while the group without PCE (GO baseline) exhibited a bleeding rate of 7.5% and a fluidity of 231.69 mm. PCE improves dispersion and fluidity through adsorption and steric hindrance, thereby enhancing stability. Increasing the NS dosage significantly improved stability. At NS dosages of 2 wt%, 3 wt%, and 4 wt%, the bleeding rate decreased to 2.25%, 2.0%, and 1.50%, respectively, demonstrating its strong anti-bleeding capacity. However, this improvement occurred at the expense of fluidity, which dropped to 239.70 mm, 221.46 mm, and 195.00 mm, respectively. On average, each 1 wt% increase in NS content reduced the bleeding rate by 0.875% and the fluidity by 37.16 mm, indicating that NS enhances stability but considerably increases flow resistance. GO incorporation also significantly improved stability, though its adverse effect on fluidity was much less pronounced than that of NS. At GO dosages of 0.01 wt%, 0.02 wt%, and 0.03 wt%, the bleeding rate decreased progressively from 5.25% to 2.50%, while fluidity only slightly decreased from 227.77 mm to 216.10 mm. Each 0.01 wt% increase in GO content reduced the bleeding rate by an average of 1.67% and the fluidity by only 5.2 mm, confirming that GO efficiently enhances stability at very low dosages while maintaining good fluidity.

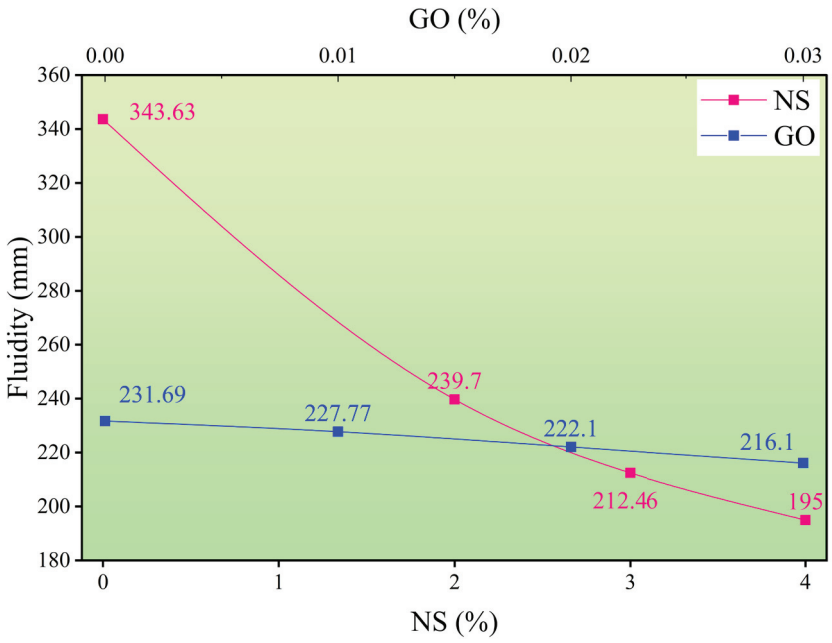

Figure 4. Effect of nano-silica (NS) and graphene oxide (GO) dosage on the fluidity (flow spread) of cement paste.

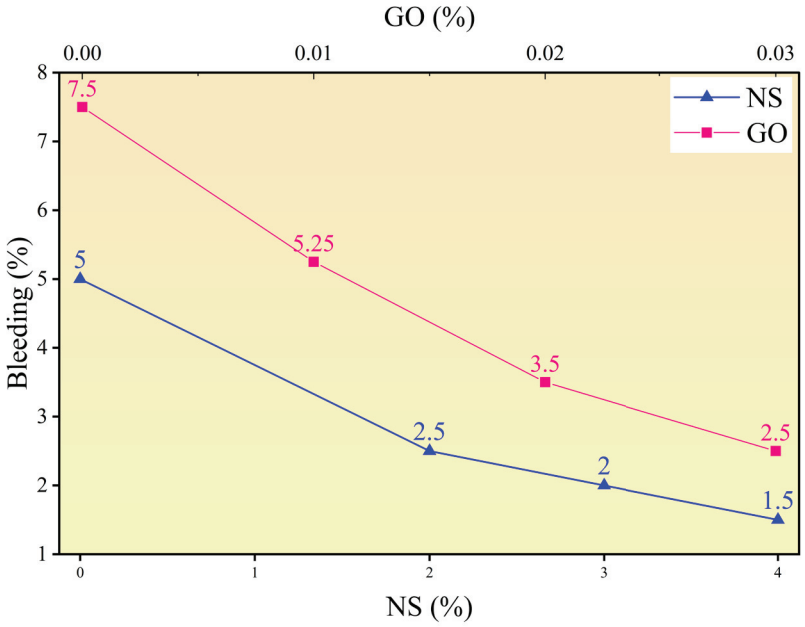

Figure 5. Effect of nano-silica (NS) and graphene oxide (GO) dosage on the bleeding rate of cement paste.

The observed trends in fresh properties align well with the current understanding of cementitious material modification [31,32]. Extensive studies indicate that nanomaterials significantly influence cement hydration and rheological behavior due to their high specific surface area and surface effects [31,32]. The accelerating effect of NS primarily stems from its high pozzolanic reactivity, which enables rapid consumption of $Ca(OH)_2$ to form additional C–S–H gel, while providing abundant nucleation sites for hydration products [33,34], thereby accelerating the dissolution and precipitation of tricalcium silicate (C_3S). In contrast, GO relies more on its unique two-dimensional sheet structure and oxygen-containing functional groups to regulate the setting process by influencing ion migration (e.g., Ca^{2+}), altering solution chemistry, and guiding the ordered crystallization

of hydration products on its surface [35,36]. The systematic data obtained in this study not only corroborate these mechanisms but also, through hybrid experiments, reveal the competitive and synergistic interactions when both materials are present, offering a critical theoretical and experimental basis for the precise design of workability in cementitious materials.

3.2. Mechanical Properties

3.2.1. Effect of NS and GO

As shown in Figures 6 and 7, the effect of nano-silica (NS) content on the compressive and flexural strength of cement stone was investigated under a fixed water-cement ratio of 0.6 and a PCE dosage of 0.6 wt%. The results indicate that the addition of NS significantly improves both the ultimate flexural strength (UFS) and uniaxial compressive strength (UCS). However, this enhancement follows a non-linear trend: strength values peak at around 4 wt% NS, beyond which a "diminishing returns" behavior is observed. This non-monotonic response suggests that the influence of NS is not a simple function of concentration. The initial increase in strength at low to moderate NS contents ($\leq$4 wt%) can be attributed to microstructural refinement driven by physicochemical interactions. In contrast, higher dosages (e.g., 5 wt%) likely induce nanoparticle agglomeration, which disrupts microstructure formation and consequently impairs macroscopic performance. Thus, determining the optimal NS dosage requires balancing its positive effects and potential detrimental impacts.

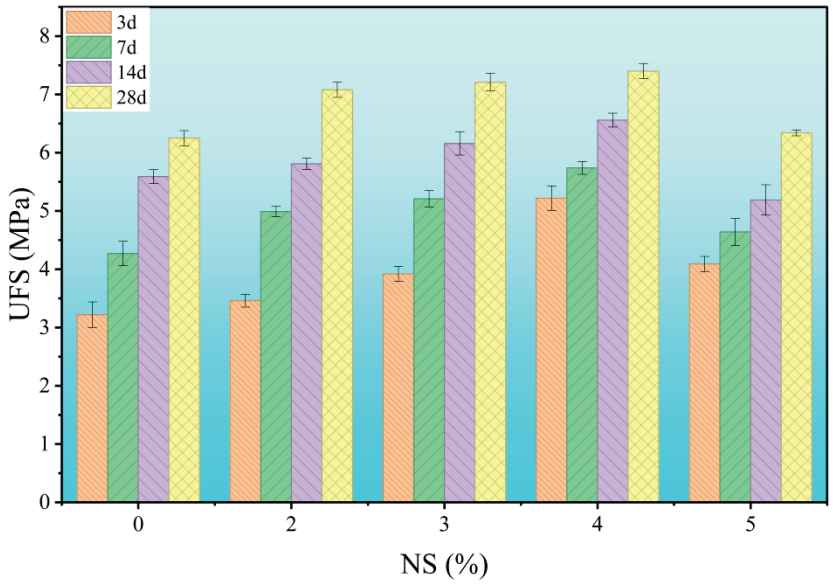

Figure 6. Effect of nano-silica (NS) dosage on the flexural strength of hardened cement paste.

Figures 8 and 9 present the strength results for pastes with different GO dosages (w/c = 0.6). The results demonstrate that even trace amounts of GO significantly enhanced strength, with a particularly pronounced improvement in compressive strength. As the GO dosage increased, both compressive and flexural strengths initially increased and then plateaued, indicating high efficiency of GO at low dosage ranges. The sensitivity of compressive strength to GO dosage suggests its substantial role in improving material compactness. The enhancement in flexural strength implies that GO also improved toughness and deformation resistance. This differential response indicates that GO likely influences compressive and flexural properties through distinct mechanisms.

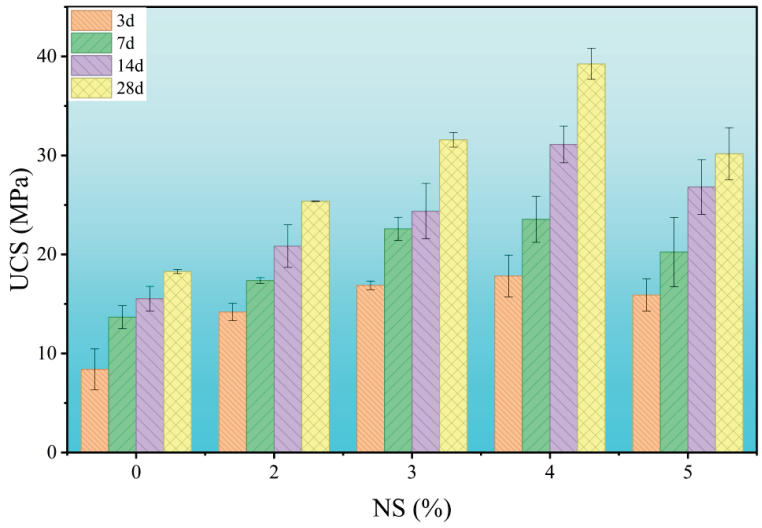

Figure 7. Effect of nano-silica (NS) dosage on the compressive strength of hardened cement paste.

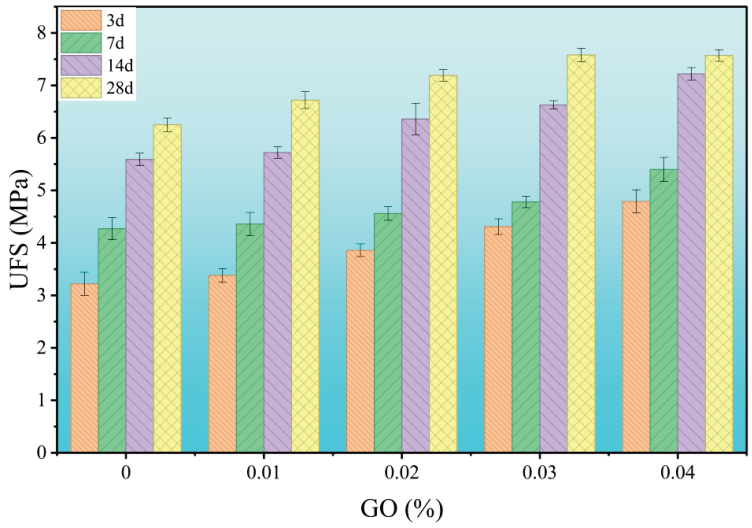

Figure 8. Effect of graphene oxide (GO) dosage on the flexural strength of hardened cement paste.

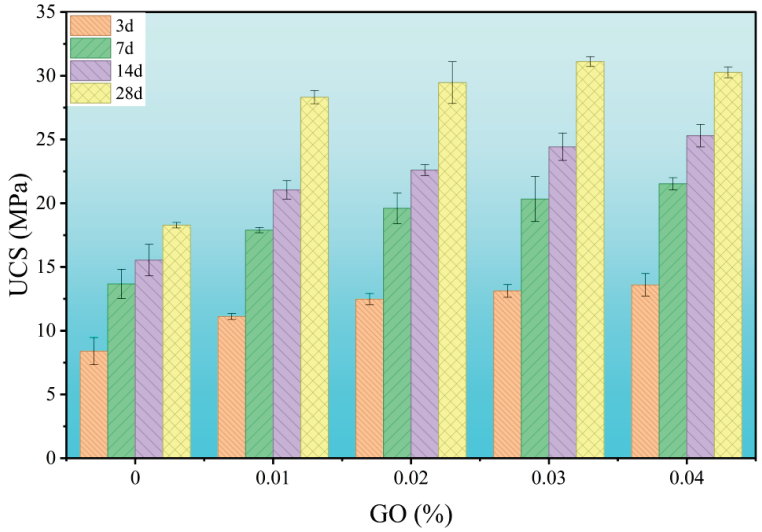

Figure 9. Effect of graphene oxide (GO) dosage on the compressive strength of hardened cement paste.

3.2.2. Effect of NS/GO Hybrids

Figures 10 and 11 illustrate the effect of hybrid NS/GO incorporation on the compressive and flexural strengths of hardened cement paste. At a low NS dosage (2 wt%), the addition of 0.01 wt% GO significantly enhanced early-age strength: the 3-d flexural strength increased from 3.46 MPa to 4.84 MPa, and the 7-d compressive strength increased from 17.37 MPa to 23.81 MPa. Furthermore, the 28-d compressive strength also rose from 25.37 MPa to 29.61 MPa, indicating a clear improvement in later-age strength. However, as the NS dosage increased to 3 wt% and 4 wt%, further GO addition resulted in an overall decline in strength, suggesting a negative interaction between excessive NS and GO. At a low GO dosage (e.g., 0.01 wt%), the incorporation of 2 wt% NS markedly enhanced early-age strength and improved later-age strength to some extent. Nevertheless, as the GO dosage increased, the beneficial effect of NS gradually diminished and even adversely influenced later-age strength development.

The results reveal a clear interactive effect between NS and GO in the hybrid system. An appropriate ratio (e.g., 2 wt% NS with 0.01 wt% GO) resulted in a synergistic enhancement. However, excessive dosage of either component led to composite strengths lower than those achieved with individual components, underscoring the critical importance of optimizing the component ratio. The strength data suggest an optimal dosage range for NS/GO hybrids, beyond which further addition may impair performance.

The evolution of mechanical properties observed in this study aligns with numerous existing research conclusions, revealing common mechanisms in nanomaterial-modified cement. The peak enhancement effect of NS at around 4 wt% is consistent with the findings of Supit and Sha et al. [37], who reported that NS enhances early and later-age strength through pozzolanic reaction and micro-filling effects, but its efficiency reaches a saturation point; excessive addition leads to particle agglomeration and increased water demand, resulting in diminished strength gain or even performance deterioration. The significant enhancement in compressive and flexural strength by GO at very low dosages can be attributed to its two-dimensional sheet structure, which guides the morphology of hydration products and enhances material toughness [38]. A key finding of this study is the synergistic effect observed at low NS/GO dosages and the antagonistic effect upon excessive dosage of either component. This aligns with the research conclusions of Du and Pang [39] on nanomaterial hybrid systems, indicating that the dispersion, interaction, and influence on the hydration process of different nanomaterials in the matrix vary significantly. Precise optimization of their hybrid ratio is essential for leveraging synergistic effects and avoiding performance offset. Therefore, the effectiveness of NS/GO hybrids is highly dependent on the dosage ratio, and further microstructural analysis is needed to elucidate the specific mechanisms underlying their synergistic or antagonistic interactions.

3.3. Analysis of Hydration Products and Solidification Mechanisms in Grouting Materials

3.3.1. SEM Analysis

Figure 12 presents representative scanning electron microscopy (SEM) images illustrating the microstructural morphology of 28-d cement pastes, highlighting the effects of different modification strategies. Figure 12 (A0), the unmodified cement, exhibits a typical loose and porous "coral-like" structure. Abundant hexagonal Portlandite ($Ca(OH)_2$) crystals (red arrows) are loosely stacked, with substantial micron-scale pores and cracks (red circles) forming an interconnected network. This microstructure explains the material's high permeability and relatively low mechanical strength.

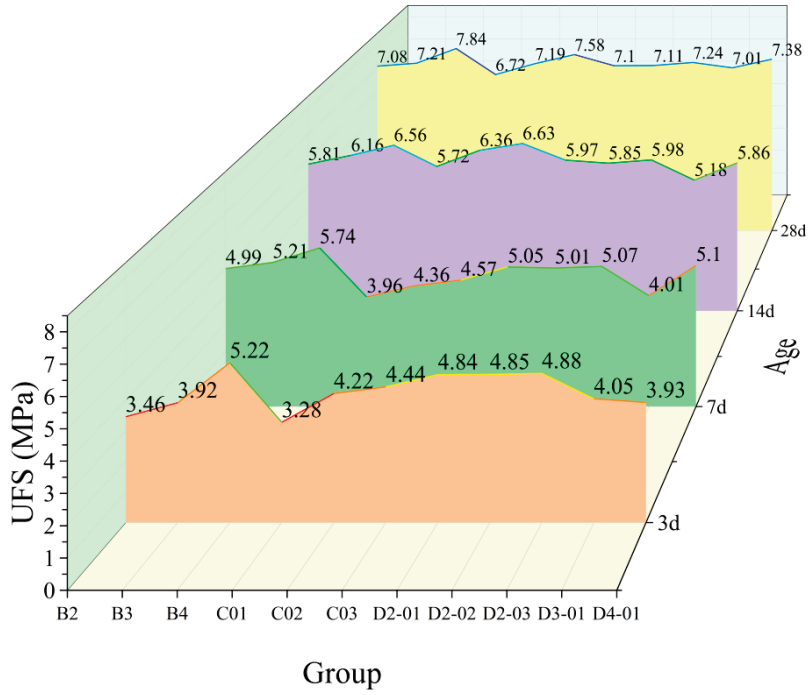

Figure 10. Effect of NS/GO hybrids on the flexural strength of hardened cement paste.

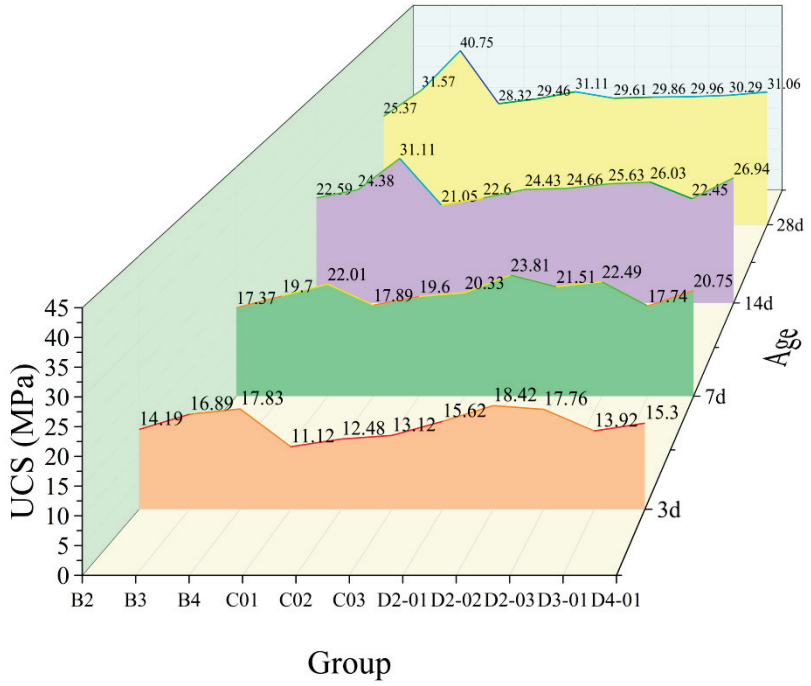

Figure 11. Effect of NS/GO hybrids on the compressive strength of hardened cement paste.

Figure 12 (B4) shows that the incorporation of NS fundamentally altered the precipitation, nucleation, and growth of hydration products, resulting in a distinctly different microstructure. The field of view is dominated by a dense, continuous "sponge-like" C–S–H gel matrix. Large $Ca(OH)_2$ crystals are substantially consumed and replaced by a tightly aggregated matrix comprising abundant nano-scale spherical/flocculent C–S–H gel particles (red arrows). These high-specific-surface-area nano-gel particles effectively fill primary pores and cracks and encapsulate unhydrated cement grains, thereby significantly refining the pore structure (note the markedly reduced pore size within the circles). This morphology underpins the superior performance of the B4 group and provides direct

visual evidence of NS's dual mechanisms: the "pozzolanic effect" consuming CH and the "micro-filler effect" optimizing porosity.

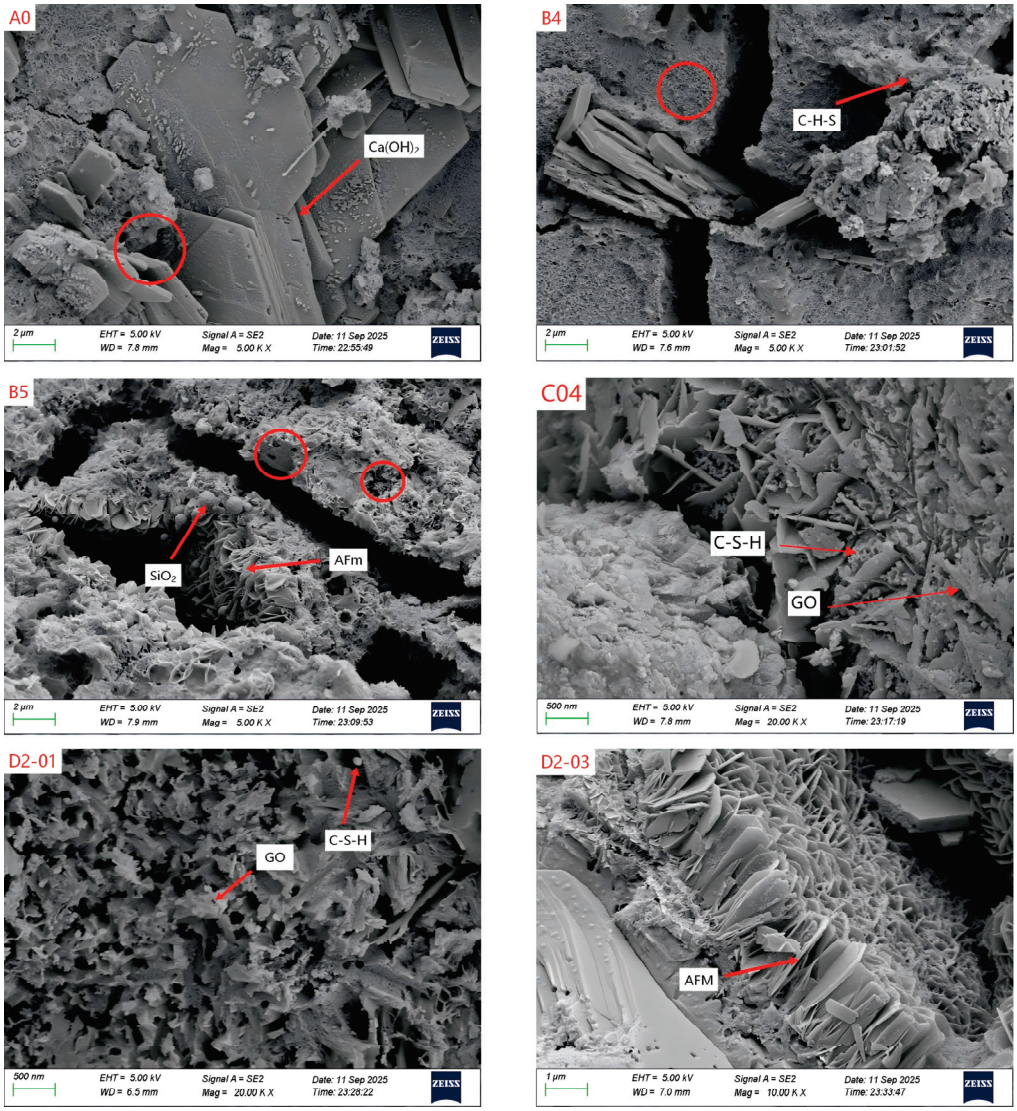

Figure 12. SEM images of different groups of samples.

Figure 12 (B5) indicates microstructural degradation at an NS dosage of 5 wt%. The sample displays a highly porous and loose morphology composed of irregular plate-like crystals stacked loosely, forming abundant sheltered pores and interconnected cracks (red circles). Some spherical particles (red arrows) failed to fill pores effectively or form a continuous matrix, suggesting that excessive NS led to agglomeration, hindering dense C–S–H gel formation and ultimately causing microstructural deterioration and performance regression.

Figure 12 (C04) shows that incorporating 0.04 wt% GO significantly optimized the microstructure. Hydration products transformed into a dense monolithic structure formed by intensive accumulation and interlocking of irregular plate-like crystals. Compared to group A0, pores were effectively filled with much finer material, greatly enhancing structural continuity. The rough surface of the filling material in the lower-left corner suggests stronger interfacial bonding. Abundant C–S–H gel particles are attached to GO sheets, indicating that GO nanosheets provide nucleation sites through their "templating effect," guide denser product arrangement, refine pores via the "micro-filler effect," and enhance

interfacial bond strength through "bridging" [40,41]. The synergy of these mechanisms underlies the excellent macroscopic performance of sample C04.

The comparison between Figure 12 (D2-01) and Figure 12 (D2-03) reveals a synergy-to-antagonism transition in the hybrid system. In D2-01, hydration products exhibit an interwoven, fluffy growth pattern. Plate-like and needle-like crystals cluster together, forming an open yet continuous structure with fine granular material, indicating favorable synergy: GO templates uniform growth, while NS optimizes pores through pozzolanic and micro-filling effects. In contrast, D2-03 is dominated by abundant regular, thin plate-like crystals stacked tightly in a "book-like" or fan-shaped arrangement, presenting a highly ordered but rigid laminated structure. This suggests excessive GO altered the hydration environment, dominated the process, inhibited C–S–H formation, and promoted lower-strength AFm phase formation. This structural change, combined with potential GO agglomeration, explains why D2-03's compressive strength, though slightly higher than D2-01, regressed compared to the C03 sample (0.03 wt% GO alone). This provides direct evidence of a synergy–antagonism transition, emphasizing the necessity of precise nanomaterial dosage control.

3.3.2. FTIR Analysis

Figure 13 presents the Fourier-transform infrared (FTIR) spectra of various samples at 28 days. The characteristic absorption band at ~1410 cm^{-1} is attributed to the asymmetric stretching vibration of the C–O bond in calcium carbonate ($CaCO_3$). Its presence, along with features at ~870 cm^{-1} (C–O out-of-plane bending) and ~710 cm^{-1} (C–O in-plane bending), indicates varying degrees of carbonation ($Ca(OH)_2 + CO_2 \rightarrow CaCO_3 + H_2O$) during preparation or testing. The band near ~960 cm^{-1} corresponds to Si–O stretching in calcium silicate hydrate (C–S–H) gel, whose intensity and profile indicate the amount and structure of C–S–H formed. The broad feature around ~450 cm^{-1} likely arises from bending vibrations of SiO_4^{4-} tetrahedra in unhydrated clinker (e.g., C_2S, C_3S) or quartz (SiO_2). Detailed vibrational assignments are summarized in Table 5.

Comparative analysis of the FTIR spectra provides insights into the influence of different admixtures.

First, comparing A0 and B4 reveals that B4 (4 wt% NS) shows a significantly enhanced absorption at 960 cm^{-1}, confirming that NS participated in the pozzolanic reaction ($Ca(OH)_2 + SiO_2 + H_2O \rightarrow$ C–S–H), promoting more C–S–H gel formation [42], consistent with improved mechanical performance. The weak feature around 440 cm^{-1} (Si–O bending) in A0 becomes a distinct peak in B4, due to Si–O bonds from incorporated NS nanoparticles and/or evolved clinker phases. The similar intensities of $CaCO_3$-related bands (1410 cm^{-1} and 870 cm^{-1}) indicate that NS did not significantly alter carbonation.

Comparing B4 and B5 shows that excessive NS (5 wt%) adversely affected hydration. B5 exhibits reduced intensity at 960 cm^{-1}, suggesting less C–S–H gel formation, likely due to particle agglomeration reducing reactive surface area, diminishing pozzolanic efficiency and interfering with normal hydration. This explains the macroscopic regression in B5.

Comparing A0 and C04, incorporating 0.04 wt% GO also markedly enhanced the C–S–H band intensity at 960 cm^{-1} (from 0.039 to 0.070), indicating promoted C–S–H formation due to GO's "templating effect" and "nucleation site effect." Its two-dimensional structure guides ordered growth and microstructural optimization. The $CaCO_3$-related bands remain consistent, showing no significant influence on carbonation.

Finally, D2-01 and D2-03 exhibit comparable intensities across all characteristic bands, indicating similarities in hydration product composition and structure, consistent with their similar macroscopic mechanical performance.

Note: The absence of OH or H_2O peaks in the FTIR spectra is attributed to the pre-drying treatment of the specimens prior to testing. The spectral range of 4000–2000 cm^{-1} was truncated as it showed no discernible peaks yet occupied significant space in the figure, thereby improving visual clarity while retaining all meaningful spectral features.

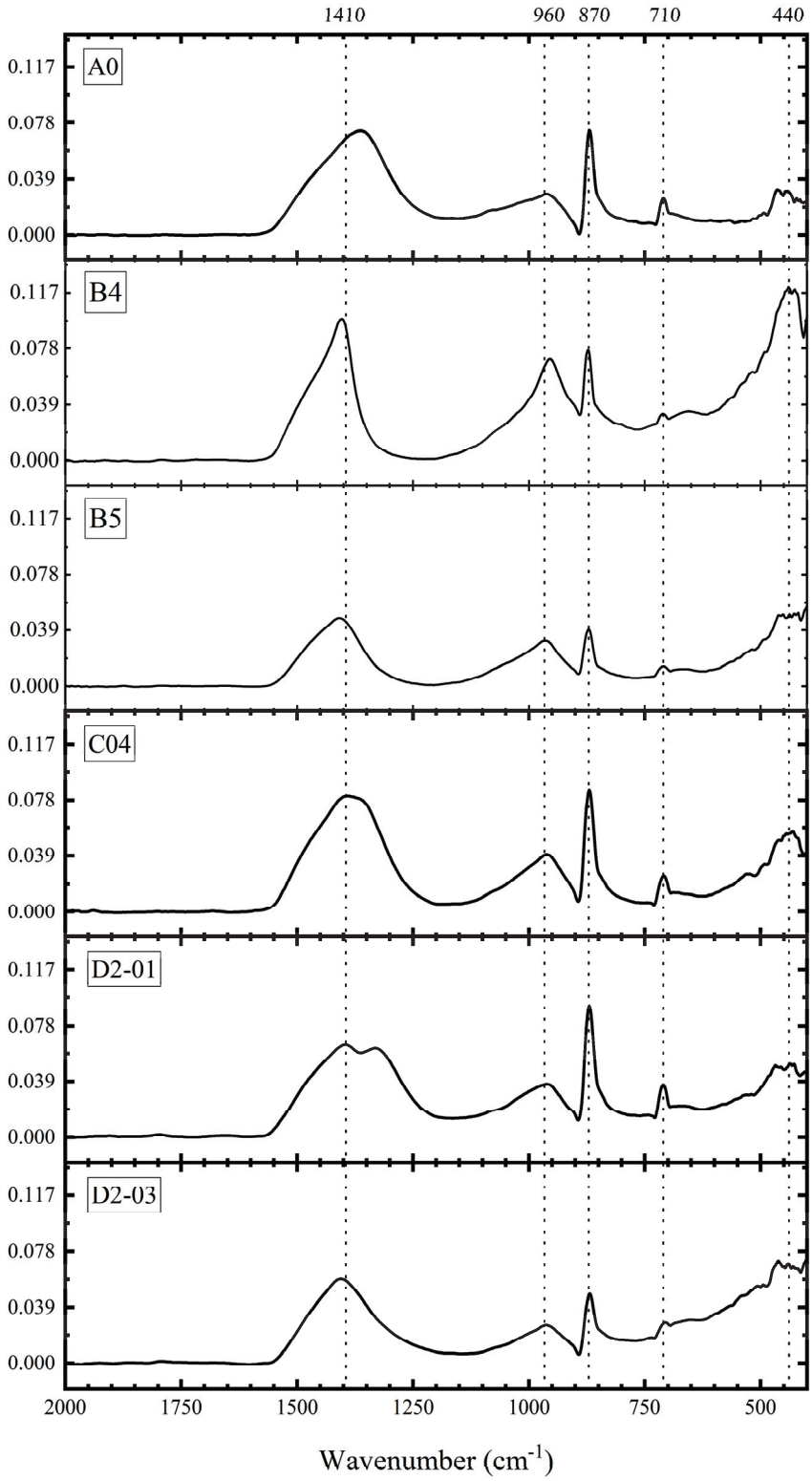

Figure 13. FTIR spectra of different groups of samples.

Table 5. Assignment of major FTIR absorption bands observed in the cement pastes.

Wavenumber (cm^{-1})	Vibration Assignment	Compound/Structure Indicated
~1410	C–O asymmetric stretching	Calcium carbonate ($CaCO_3$)
~960	Si–O stretching	Calcium silicate hydrate (C–S–H) gel
~870–880	C–O out-of-plane bending	Calcium carbonate ($CaCO_3$)
~710	C–O in-plane bending	Calcium carbonate ($CaCO_3$)
~430–450	Si–O bending	SiO_4^{4-} tetrahedron (in C_2S, C_3S, or quartz)

3.3.3. XRD Analysis

Figure 14 presents the X-ray diffraction (XRD) patterns of various samples at 28 days: (a) stacked patterns, (b) waterfall plot, and (c) comparative portlandite ($Ca(OH)_2$) characteristic peak intensity. Identified crystalline phases include quartz (SiO_2), ettringite ($Ca_6Al_2(SO_4)_3(OH)_{12}\cdot 26H_2O$/AFt), portlandite ($Ca(OH)_2$), dicalcium silicate ($Ca_2SiO_4/C_2S$), and tricalcium silicate (Ca_3SiO_5/C_3S), with C_2S and C_3S representing unhydrated clinker phases.

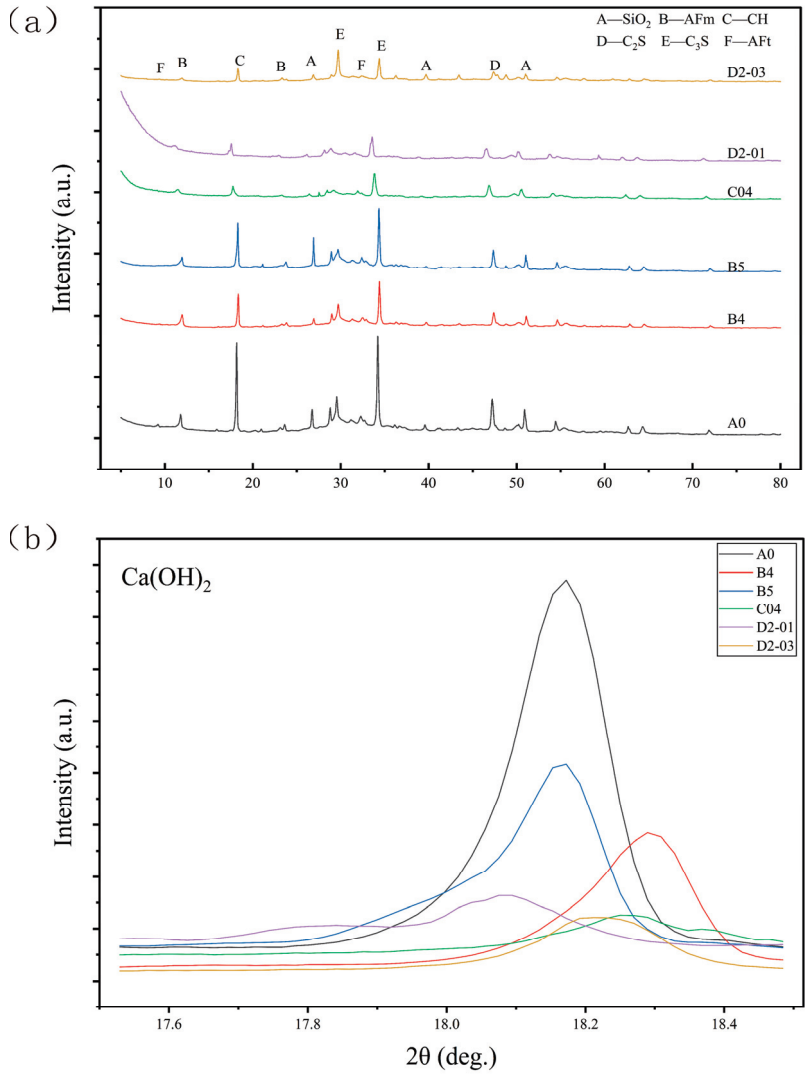

Figure 14. XRD patterns of different groups of samples: (**a**) stacked patterns (**b**) comparison of $Ca(OH)_2$ characteristic peak intensity.

The pozzolanic effect of NS is directly confirmed. Compared to A0, B4 (4 wt% NS) shows significantly reduced intensity of the $Ca(OH)_2$ peak at ~18° (2θ), indicating that reactive SiO_2 in NS consumed calcium hydroxide to form additional amorphous C–S–H gel. This microstructural modification underpins the enhanced mechanical properties of B4.

An optimal NS dosage is evident. At 5 wt% NS (B5), the $Ca(OH)_2$ peak reduction is less pronounced than in B4, suggesting agglomeration reduced specific surface area and reactivity, weakening the pozzolanic effect and causing performance regression.

The C04 sample (0.04 wt% GO) also shows a distinct decrease in $Ca(OH)_2$ peak intensity. This supports GO's physical toughening mechanisms (templating and bridging via its two-dimensional structure) and implies that its surface functional groups may catalyze hydration, promoting CH consumption and product formation, enhancing performance through a synergistic chemical pathway.

Furthermore, after the addition of NS/GO, the intensities of the crystalline diffraction peaks of both AFt and AFm were weakened. This might be because NS/GO altered the hydration path, causing the system to tend to form amorphous or gel-like calcium aluminate hydrates (such as the complex of $Al(OH)_3$ gel and C–S–H gel). This type of substance is difficult to be detected in the XRD pattern.

Critically, the GO/NS hybrid system exhibits a clear synergy–antagonism transition. The low-dosage hybrid (D2-01) shows $Ca(OH)_2$ peak intensity significantly lower than A0, indicating GO improved NS dispersion and reactivity, yielding synergistic enhancement. In contrast, the high-dosage hybrid (D2-03) shows less $Ca(OH)_2$ consumption than D2-01, revealing that excessive GO induced hetero-agglomeration, inhibiting NS activity and turning synergy into antagonism, leading to performance degradation. This provides a theoretical basis for rational design and dosage control of multi-nanomaterial systems in cementitious matrices.

3.3.4. MIP Analysis

Figures 15 and 16 present the pore size distribution and porosity characteristics at 28 days, measured by mercury intrusion porosimetry (MIP). Based on established criteria [43], pores were categorized into: micropores (MICP, <10 nm), medium capillary pores (MCP, 10–50 nm), large capillary pores (LCP, 50–1000 nm), and macropores (MACP, >1 μm).

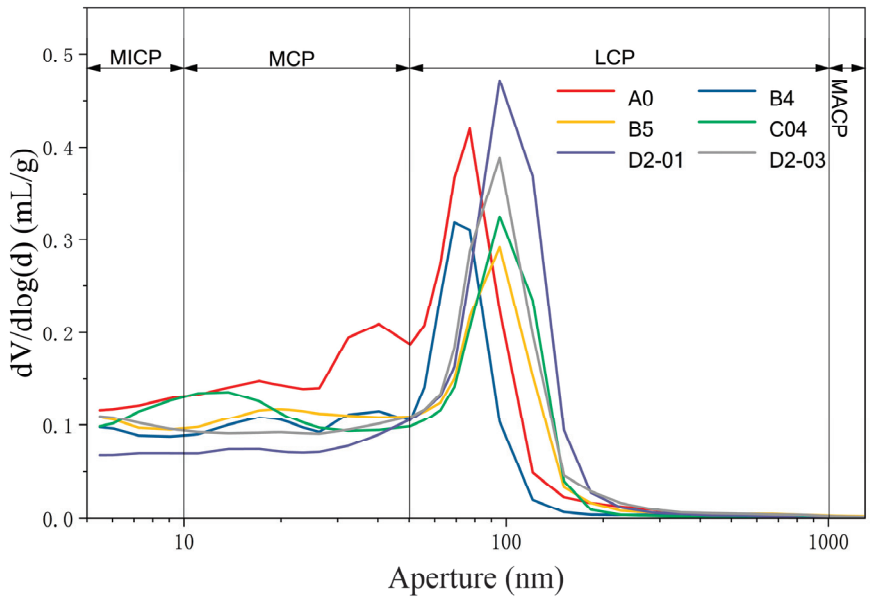

Figure 15. Pore size distribution of different sample groups.

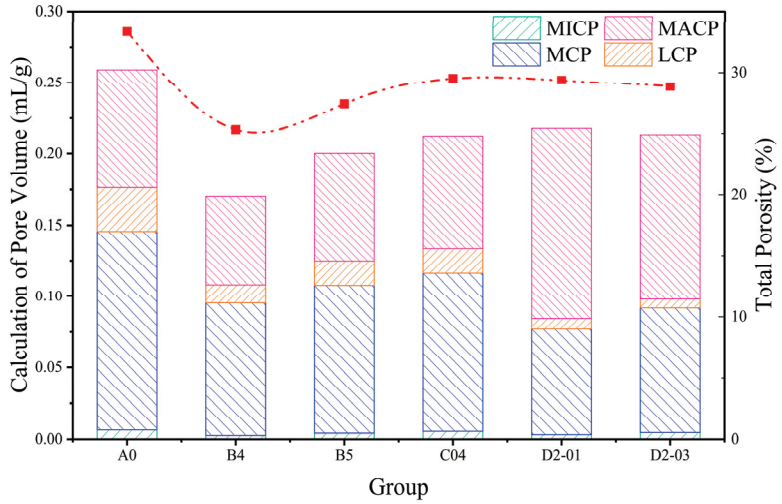

Figure 16. Porosity characteristics of different sample groups.

Analysis reveals that NS and GO composite modification exhibits complex behavior with synergistic and antagonistic effects. NS showed significant pozzolanic activity and micro-filling effect. B4 (4 wt% NS) had markedly reduced total pore volume versus A0. Macropore and medium capillary pore volumes decreased significantly, while micropore and medium capillary pore proportions increased, indicating NS consumes $Ca(OH)_2$ to form C–S–H gel clogging larger pores and acts as an ultra-fine filler, refining pores and reducing porosity. This dual mechanism explains the mechanical enhancement.

An optimal NS dosage limit was confirmed. At 5 wt% NS (B5), total pore volume rebounded, and the differential curve showed a higher macropore peak, suggesting agglomeration created defect centers introducing harmful large pores, deteriorating the pore structure.

GO exhibited a complementary mechanism. C04 (0.04 wt% GO) had slightly lower total pore volume than A0, with uniform reduction across all ranges and a flatter differential curve, indicating GO functions through templating and bridging, guiding a more uniform and dense microstructure, holistically optimizing pore distribution.

Notably, D2-03 had slightly lower total porosity than D2-01 and a relatively lower proportion of harmful macropores, explaining its marginally superior mechanical performance. Although both D2-01 and D2-03 had lower total porosity than A0, their macropore proportions were significantly higher, indicating GO/NS synergy might adversely affect pore size distribution. However, in D2-03, smaller pores were more refined, and GO's bridging effect strengthened the pore skeleton, compensating for increased macropores, yielding overall strength improvement.

4. Conclusions

This study systematically investigated the individual and synergistic effects of nanosilica (NS) and graphene oxide (GO) on the macroscopic properties and microstructure of cement-based grouting materials. The results provide both theoretical insights and experimental support for the precise design and application of nanomaterials in cementitious systems. The main conclusions are as follows:

1. Fresh State Properties: Both NS and GO significantly accelerated the setting time of cement paste and effectively reduced the bleeding rate. However, NS had a more detrimental impact on fluidity compared to GO. The hybrid system further shortened the setting process and improved stability, albeit at the cost of a more substantial reduction in fluidity.

2. Mechanical Properties: Both NS and GO significantly enhanced the compressive and flexural strength of cement paste at optimal dosages. The optimal dosage of NS was 4 wt%, while GO exhibited notable reinforcing effects within the range of 0.01–0.03 wt%. The hybrid system displayed a distinct transition from synergistic to antagonistic effects: a low-dosage combination (e.g., 2 wt% NS + 0.01 wt% GO) synergistically improved mechanical properties, increasing flexural and compressive strength by 13.5% and 45.5%, respectively, compared to the reference group. However, excessive dosage of either component (e.g., 5 wt% NS or 0.03 wt% GO in combination) resulted in reduced reinforcement efficiency, with performance even inferior to that of samples incorporating a single nanomaterial.
3. Microstructure:
    - NS enhances the matrix primarily through the pozzolanic reaction—consuming $Ca(OH)_2$ to form additional C–S–H gel—and a nano-filling effect that optimizes the pore structure. In contrast, GO improves performance via a templating effect and by providing nucleation sites that promote dense deposition of hydration products, along with a bridging effect that enhances overall integrity.
    - Excessive NS led to agglomeration, increasing the volume of harmful pores. Excessive GO resulted in abnormal morphology of hydration products (e.g., stacked plate-like AFm phases), inhibiting the formation of C–S–H gel.
    - In the hybrid system, GO improved the dispersion of NS and enhanced its pozzolanic effect. However, excessive GO induced hetero-agglomeration, which weakened the activity of NS and caused a transition from synergy to antagonism.
4. Pore Structure: NS mainly reduced medium and large capillary pores (>50 nm) and increased the proportion of fine pores (<50 nm), significantly decreasing total porosity. GO uniformly reduced pores across all size ranges, resulting in a more homogeneous pore size distribution. Although the hybrid system reduced total porosity, it also increased the proportion of large pores, the long-term durability implications of which require further investigation.
5. This study demonstrates that both NS and GO offer significant potential for modifying cement-based grouting materials, but their dosages must be strictly optimized. It is recommended that the NS dosage should not exceed 4 wt%, and the GO dosage should remain below 0.03 wt%. For hybrid systems, a low-to-medium dosage combination (e.g., 2 wt% NS + 0.01 wt% GO) is recommended to avoid agglomeration and antagonistic effects, thereby achieving synergistic performance enhancement.

Author Contributions: Conceptualization, G.Y. and Y.A.; methodology, L.L.; software, L.L.; validation, L.L., K.Y. and W.S.; formal analysis, J.Q.; investigation, L.L.; resources, J.D.; data curation, J.Q. and J.D.; writing—original draft preparation, L.L.; writing—review and editing, G.Y.; visualization, L.L.; supervision, Y.A. and J.D.; project administration, J.Q.; funding acquisition, L.L. All authors have read and agreed to the published version of the manuscript.

Funding: The research in this paper is supported by the Science and Technology Innovation Special Project of the Xiong'an New Area (2023XAGG0067), the National Natural Science Foundation of China (42293351, U2468221 and 42307228), and the National Key Research and Development Program of China (2023YFC3007100).

Data Availability Statement: The original contributions presented in this study are included in this article. Further inquiries can be directed to the corresponding author.

Acknowledgments: During the preparation of this manuscript/study, the authors used DeepSeek (V3.2) for the purposes of language polishing and translation assistance. The authors have reviewed and edited the output and take full responsibility for the content of this publication.

Conflicts of Interest: The authors declare no conflicts of interest.

Abbreviations

The following abbreviations are used in this manuscript:

NS	Nano-silica
GO	Graphene Oxide
PCE	Polycarboxylate Ether
FTIR	Fourier-Transform Infrared Spectroscopy
XRD	X-ray Diffraction
SEM	Scanning Electron Microscopy
MIP	Mercury Intrusion Porosimetry
UFS	Ultimate Flexural Strength
UCS	Ultimate Compressive Strength

References

1. Mehta, P.K.; Monteiro, P.J. *Concrete Microstructure, Properties, and Materials*; McGraw-hill: New York, NY, USA, 2006.
2. Scrivener, K.L.; Juilland, P.; Monteiro, P.J. Advances in understanding hydration of portland cement. *Cem. Concr. Res.* **2015**, *78*, 38–56. [CrossRef]
3. Sanchez, F.; Sobolev, K. Nanotechnology in concrete–a review. *Constr. Build. Mater.* **2010**, *24*, 2060–2071. [CrossRef]
4. Raki, L.; Beaudoin, J.; Alizadeh, R.; Makar, J.; Sato, T. Cement and concrete nanoscience and nanotechnology. *Materials* **2010**, *3*, 918–942. [CrossRef]
5. Du, H.; Dai Pang, S. Enhancement of barrier properties of cement mortar with graphene nanoplatelet. *Cem. Concr. Res.* **2015**, *76*, 10–19. [CrossRef]
6. Sanchez, F.; Zhang, L. Molecular dynamics modeling of the interface between surface functionalized graphitic structures and calcium–silicate–hydrate: Interaction energies, structure, and dynamics. *J. Colloid Interface Sci.* **2008**, *323*, 349–358. [CrossRef]
7. Shah, S.P.; Hou, P.; Cheng, X. Durability of cement-based materials and nano-particles: A review. In *Nanotechnology in Construction: Proceedings of NICOM5 2015*; Springer: Cham, Switzerland, 2015; pp. 15–24.
8. Du, M.; Yang, Y.; Miao, J.; Hou, R.; Zhai, K.; Yao, X. A deep learning-based study of the role of graphene oxide nanosheets on the microstructure of cement paste. *ACS Appl. Nano Mater.* **2025**, *8*, 14297–14306. [CrossRef]
9. Hu, J.; Lu, S.; Mao, X.; Luo, J.; Wang, S.; Gao, Y. Influence of nanosheet size and oxygen-containing functional group content on the reinforcing efficiency of graphene oxide on cementitious composites. *J. Mater. Sci.* **2025**, *60*, 7289–7306. [CrossRef]
10. Fan, L.; Zheng, J.; Wu, C.; Wang, H.; Li, F.; Song, F. Graphene oxide at carbon nanotubes/cement matrix abnormally enhance its hydration products and interlayer stress transfer at an important hydration accelerated period: Experimental study and molecular dynamics simulation. *Colloids Surf. A Physicochem. Eng. Asp.* **2025**, *717*, 136830. [CrossRef]
11. Zhang, H.; Gan, X.; Lu, Z.; Li, L.; Lu, L. Polycarboxylate superplasticizer-modified graphene oxide: Dispersion and performance enhancement in cement paste. *Nanomaterials* **2025**, *15*, 419. [CrossRef]
12. Hu, Z.; Wan, Y.; Duan, Y.; Shi, Y.; Gu, C.; Ma, R.; Dong, J.; Cui, D. A review of the impact of graphene oxide on cement composites. *Nanomaterials* **2025**, *15*, 216. [CrossRef]
13. Pan, Z.; He, L.; Qiu, L.; Korayem, A.H.; Li, G.; Zhu, J.W.; Collins, F.; Li, D.; Duan, W.H.; Wang, M.C. Mechanical properties and microstructure of a graphene oxide–cement composite. *Cem. Concr. Compos.* **2015**, *58*, 140–147. [CrossRef]
14. Lv, S.; Ma, Y.; Qiu, C.; Sun, T.; Liu, J.; Zhou, Q. Effect of graphene oxide nanosheets of microstructure and mechanical properties of cement composites. *Constr. Build. Mater.* **2013**, *49*, 121–127. [CrossRef]
15. Zhang, P.; Sun, Y.; Wei, J.; Zhang, T. Research progress on properties of cement-based composites incorporating graphene oxide. *Rev. Adv. Mater. Sci.* **2023**, *62*, 20220329. [CrossRef]
16. Li, X.; Liu, Y.M.; Li, W.G.; Li, C.Y.; Sanjayan, J.G.; Duan, W.H.; Li, Z. Effects of graphene oxide agglomerates on workability, hydration, microstructure and compressive strength of cement paste. *Constr. Build. Mater.* **2017**, *145*, 402–410. [CrossRef]
17. Vijayan, D.S.; Devarajan, P.; Sivasuriyan, A. A review on eminent application and performance of nano based silica and silica fume in the cement concrete. *Sustain. Energy Technol. Assess.* **2023**, *56*, 103105. [CrossRef]
18. Qing, Y.; Zenan, Z.; Deyu, K.; Rongshen, C. Influence of nano-sio2 addition on properties of hardened cement paste as compared with silica fume. *Constr. Build. Mater.* **2007**, *21*, 539–545. [CrossRef]
19. Ji, T. Preliminary study on the water permeability and microstructure of concrete incorporating nano-SiO_2. *Cem. Concr. Res.* **2005**, *35*, 1943–1947. [CrossRef]

20. Kim, G.; Suh, H.; Cho, S.; Im, S.; Nezhad, E.Z.; Seok, S.; Choi, C.; Bae, S. Synergistic strengthening mechanism of portland cement paste reinforced by a triple hybrid of graphene oxide, functionalized carbon nanotube, and nano-silica. *Constr. Build. Mater.* **2022**, *352*, 129017. [CrossRef]
21. Nguyen, H.D.; Zhang, Q.; Sagoe-Crentsil, K.; Duan, W. Graphene oxide-coated sand for improving performance of cement composites. *Cem. Concr. Compos.* **2021**, *124*, 104279. [CrossRef]
22. Bouibed, A.; Doufnoune, R. Synthesis and characterization of hybrid materials based on graphene oxide and silica nanoparticles and their effect on the corrosion protection properties of epoxy resin coatings. *J. Adhes. Sci. Technol.* **2019**, *33*, 834–860. [CrossRef]
23. Liu, C.; Chen, F.; Wu, Y.; Zheng, Z.; Yang, J.; Yang, B.; Yang, J.; Hui, D.; Luo, Y. Research progress on individual effect of graphene oxide in cement-based materials and its synergistic effect with other nanomaterials. *Nanotechnol. Rev.* **2021**, *10*, 1208–1235. [CrossRef]
24. Bai, S.; Jiang, L.; Xu, N.; Jin, M.; Jiang, S. Enhancement of mechanical and electrical properties of graphene/cement composite due to improved dispersion of graphene by addition of silica fume. *Constr. Build. Mater.* **2018**, *164*, 433–441. [CrossRef]
25. Mowlaei, R.; Lin, J.; de Souza, F.B.; Fouladi, A.; Korayem, A.H.; Shamsaei, E.; Duan, W. The effects of graphene oxide-silica nanohybrids on the workability, hydration, and mechanical properties of portland cement paste. *Constr. Build. Mater.* **2021**, *266*, 121016. [CrossRef]
26. Mohammed, A.; Sanjayan, J.G.; Duan, W.H.; Nazari, A. Incorporating graphene oxide in cement composites: A study of transport properties. *Constr. Build. Mater.* **2015**, *84*, 341–347. [CrossRef]
27. Li, H.; Zhang, Q.; Feng, G.; Mei, L.; Wang, Y.; Long, W. Multi-scale improved damping of high-volume fly ash cementitious composite: Combined effects of polyvinyl alcohol fiber and graphene oxide. *Constr. Build. Mater.* **2020**, *260*, 119901. [CrossRef]
28. Wang, D.; Fang, J.; Wang, Q.; Liu, Y. Utilizing desulphurized electrolytic-manganese residue as a mineral admixture: A feasibility study. *Cem. Concr. Compos.* **2022**, *134*, 104822. [CrossRef]
29. Kavussi, A.; Qazizadeh, M.J. Fatigue characterization of asphalt mixes containing electric arc furnace (EAF) steel slag subjected to long term aging. *Constr. Build. Mater.* **2014**, *72*, 158–166. [CrossRef]
30. *GB/T 17671-2021*; Methods of Testing Cements—Determination of Strength. Standards Press of China: Beijing, China, 2021.
31. Senff, L.; Labrincha, J.A.; Ferreira, V.M.; Hotza, D.; Repette, W.L. Effect of nano-silica on rheology and fresh properties of cement pastes and mortars. *Constr. Build. Mater.* **2009**, *23*, 2487–2491. [CrossRef]
32. Kong, D.; Su, Y.; Du, X.; Yang, Y.; Wei, S.; Shah, S.P. Influence of nano-silica agglomeration on fresh properties of cement pastes. *Constr. Build. Mater.* **2013**, *43*, 557–562. [CrossRef]
33. Jo, B.; Kim, C.; Tae, G.; Park, J. Characteristics of cement mortar with nano-SiO_2 particles. *Constr. Build. Mater.* **2007**, *21*, 1351–1355. [CrossRef]
34. Land, G.; Stephan, D. The influence of nano-silica on the hydration of ordinary portland cement. *J. Mater. Sci.* **2012**, *47*, 1011–1017. [CrossRef]
35. Wang, Q.; Li, S.; Pan, S.; Cui, X.; Corr, D.J.; Shah, S.P. Effect of graphene oxide on the hydration and microstructure of fly ash-cement system. *Constr. Build. Mater.* **2019**, *198*, 106–119. [CrossRef]
36. Liu, C.; Huang, X.; Wu, Y.; Deng, X.; Zheng, Z. The effect of graphene oxide on the mechanical properties, impermeability and corrosion resistance of cement mortar containing mineral admixtures. *Constr. Build. Mater.* **2021**, *288*, 123059. [CrossRef]
37. Suhendro, B. Toward green concrete for better sustainable environment. *Procedia Eng.* **2014**, *95*, 305–320. [CrossRef]
38. Cho, Y.; Yoo, S.; Jung, S.; Lee, K.; Kwon, S. Effect of Na_2O content, SiO_2/Na_2O molar ratio, and curing conditions on the compressive strength of fa-based geopolymer. *Constr. Build. Mater.* **2017**, *145*, 253–260. [CrossRef]
39. Wyrzykowski, M.; Terrasi, G.; Lura, P. Expansive high-performance concrete for chemical-prestress applications. *Cem. Concr. Res.* **2018**, *107*, 275–283. [CrossRef]
40. Kedir, A.; Gamachu, M.; Alex, A.G. Cement-based graphene oxide composites: A review on their mechanical and microstructure properties. *J. Nanomater.* **2023**, *2023*, 6741000. [CrossRef]
41. Alex, A.G.; Kedir, A.; Tewele, T.G. Review on effects of graphene oxide on mechanical and microstructure of cement-based materials. *Constr. Build. Mater.* **2022**, *360*, 129609. [CrossRef]
42. Murmu, P.P.; Kennedy, J.; Ruck, B.J.; Williams, G.V.M.; Markwitz, A.; Rubanov, S.; Suvorova, A.A. Effect of annealing on the structural, electrical and magnetic properties of Gd-implanted ZnO thin films. *J. Mater. Sci.* **2012**, *47*, 1119–1126. [CrossRef]
43. Rouquerol, J.; Avnir, D.; Fairbridge, C.W.; Everett, D.H.; Haynes, J.M.; Pernicone, N.; Ramsay, J.D.; Sing, K.S.W.; Unger, K.K. Recommendations for the characterization of porous solids (technical report). *Pure Appl. Chem.* **1994**, *66*, 1739–1758. [CrossRef]

Disclaimer/Publisher's Note: The statements, opinions and data contained in all publications are solely those of the individual author(s) and contributor(s) and not of MDPI and/or the editor(s). MDPI and/or the editor(s) disclaim responsibility for any injury to people or property resulting from any ideas, methods, instructions or products referred to in the content.

materials

MDPI

Article

Mechanisms for Migration of Alkali in Dolomitic Limestones

Xinyu Zhang, Wei Li *, Xiaojun Huang, Zhixin Wang and Min Deng *

College of Materials Science and Engineering, Nanjing Tech University, Nanjing 211816, China
* Correspondence: stevenlee187@outlook.com (W.L.); dengmin@njtech.edu.cn (M.D.)

Abstract: The alkali–dolomite reaction (ADR) describes the interaction between alkalis in concrete and dolomite which results in dedolomitization, leading to cracking and deterioration of the concrete. A large number of research has explored the chemical products associated with the ADR, mechanisms of expansion, and methods of identification, but our understanding of the occurrence and progression of the ADR chemical reaction is substantially limited. Key factors controlling the ADR chemical reaction are generally not understood. This paper investigates the migration process of alkali ions in dolomitic limestone and reaction process with dolomite crystals and alkali. Dolomitic limestone samples were selected for experimentation. The amount of Sodium (Na^+) was measured as a means of assessing alkali ion migration. We measured the degree of dedolomitization using X-ray diffraction (XRD). Microstructure was evaluated using field emission scanning electron microscopy (FESEM). This research provides new insights into dedolomitization. The pore network provides the physical pathway for alkali ion migration. Concentration gradients drive the migration of alkali ions, and their interactions control the efficiency of alkali ion migration.

Keywords: alkali–dolomite reaction (ADR); alkali ion migration; microstructure; dedolomitization

1. Introduction

Alkali–dolomite reaction (ADR, frequently referred to as alkali–carbonate reaction (ACR)) is a chemical reaction that can lead to the expansion and cracking of concrete that involves alkalis and dolomitic rocks [1–3]. ADR was first documented by Swenson in the 1950s when he was observing severely cracked concrete made with a carbonate rock in Kingston, Canada [4]. The cracks were different from those in the concrete due to alkali–silica reaction (ASR). He stated that aggregates with carbonate-bearing components contribute significantly to the expansion and cracking of concrete. After this, the same type of damage was found in Indiana, South Dakota, and Illinois in the United States [5,6]. Based on an organized study of the rock samples from various regions of China by Deng Min et al., findings to date suggest that there are active mineral constituents which may lead to alkali–carbonate reaction (ACR), found in different rock types which are widely spread throughout China [7–9].

Since then, there has been an interest in ADR and the research community has taken an interest in other countries as well [6,10–12].

The alkali–dolomite reaction is shown in Equation (1):

$$CaMg(CO_3)_2 + 2MOH \rightarrow Mg(OH)_2 + CaCO_3 + M_2CO_3 \quad (1)$$

where M represents the monovalent alkali cation (Na^+, K^+).

The mechanism of expansion of ADR has always been a considerable focus and a challenge in research. A number of mechanisms of expansion have been proposed but some mechanisms have been gradually refuted over time. Two most cited theories documented in the literature include the theories of Tang et al. [13–15] and the theory of Katayama et al. [16–19]. The theory, originally proposed by Tang and Deng [13–15] is outlined as follows: (1) the reagents migrate inward through the argillaceous network and are driven by the Gibbs free energy of the reaction; and (2) brucite and calcite grow in the limited space of the dolomite crystals creating crystallization pressure and resulting in expansion of rock. Tang et al.'s mechanism of expansion has flaws. The role of ion migration in ADR is unclear. The changes in Gibbs free energy are key to dedolomitization. However, Gibbs free energy does not drive alkalizing ion migration within rocks. Katayama and Grattan-Bellew [16–19] argued that simple dedolomitization is not sufficient for causing concrete expansion and cracking. They posited that the primary cause is alkali–silica reaction (ASR) caused by microcrystalline quartz. The mechanism of expansion proposed by Katayama et al. has its limitations. It is possible to decrease ASR by including 20% fly ash and 35% slag cement as bulk replacement materials; however, these scenarios did not decrease ADR. Chen et al. proposed a new alkaline medium, tetramethylammonium hydroxide (TMAH), that would react only with dolomite and not quartz. In their studies, dolomitic rock still had continual expansion with TMAH solution immersion, which terminates the argument meditating that ADR would not have expansion [20]. Mao has also confirmed compacted dolomite has significant expansive stresses in an alkaline solution. The osmosis theory, initially proposed by Hadley, was later questioned and recently interpreted by Milanesi et al. [21]. They consider that carbonate ions (CO_3^{2-}) from reactions play a crucial role in ADR expansion caused by dedolomitization. Even though there is a body of international research on the chemical reaction products, expansion mechanisms, and identification methods of ADR [22–28], its occurrence and development process remain unclear.

Currently, only a few studies were focused on the ion migration in alkali reactive aggregate. In ASR, researchers have proposed that the formation of an ASR gel can only be present at reactive silica sites with alkali and hydroxy ions migrating to these sites. Additionally, the rate of migration mainly depends on the concentration gradient of each reaction site [7]. However, none of these speculations are based on the results of experimental research, and researchers have paid little attention to ion migration in alkali reactive aggregate. Li et al. [29] have made some progress in the migration process of OH^- ions in dolostone. In his study, OH^- ions react with dolomite grains and form a nanofiltration-like structure that may block the migration of alkali ions and inhibit the dedolomitization process. Duke [30] proposed that dedolomitization only occurs at the aggregate edges. Calcium and magnesium ions will not diffuse, but carbonate ions can move freely. However, the key controlling factors remain unclear, and the key parameters driving ADR activity in dolomitic limestone are not clearly identified.

Moreover, systematic petrological approaches have been widely used to evaluate the alkali–aggregate reaction (AAR) process [29,31,32]. The polarizing microscopy has been employed to identify reaction characteristics for active silica phases and dolomite. With development of advanced imaging capabilities such as field emission scanning electron microscopy (FESEM) and backscattered electron imaging (BSE), these studies have determined the microstructure of reaction boundaries and elemental distributions using energy dispersive spectroscopy. These methods have created a relevance among mineral composition, microstructure, and reactive activity. Attending to the common approaches detailed above, the present study uses polarized light microscopy and FESEM/BSE as the principle analytical tools to evaluate the migration behavior of alkali ions within dolomitic limestone and examine reactions of alkali solutions with dolomite crystals.

2. Materials and Methods

2.1. Materials

This paper engaged dolomitic limestone BFL-1, ZC, YM, and SJW. BFL-1 was obtained from Shandong Province, China, ZC was obtained from Hebei Province, China and YM and SJW were obtained from Guizhou Province, China. Dolomitic limestones BFL-1 and ZC are classified as marine carbonate rocks and belong to the Cambrian system. After the end of the sedimentary period, an irregular dolomitization gave rise to a leopard-like structure. Dolomitic limestones YM and SJW belong to the Ordovician carbonate rocks, which are composed of light gray and gray microcrystalline fine-grained dolomites and limestones, and limestones and argillaceous dolomites build a layered structure with each other. Table 1 provides the chemical composition of dolomitic limestone. The results of MgO in dolomitic limestone BCL-1, ZC, YM, and SJW are 1.19%, 6.65%, 2.48%, and 2.55%, respectively. Figure 1 is the X-ray diffraction pattern of dolomitic limestone, determined in accordance with JY/T 0587-2020 [33]. The results indicate that dolomitic limestones BFL-1, ZC, YM, and SJW are principally composed of calcite, dolomite, and quartz crystals. YM also contains a small portion of illite crystals. The content of dolomite in dolomitic limestone was assessed using the XRD–Rietveld method. The amount of dolomite in dolomitic limestone BFL-1, ZC, YM, and SJW was 8.6%, 26.8%, 6.9%, and 16%, respectively.

Table 1. Chemical composition of rocks.

Rock	Chemical Composition/wt%							Loss	Total
	SiO_2	CaO	MgO	Al_2O_3	Fe_2O_3	K_2O	Na_2O		
BFL-1	3.93	52.34	1.19	0.70	0.25	0.16	0.15	40.57	99.35
ZC	2.01	47.07	6.65	0.85	0.25	0.13	0.12	41.43	98.66
YM	11.18	42.26	2.48	2.80	1.03	0.82	0.55	37.19	96.94
SJW	5.99	45.68	2.55	1.49	0.26	0.63	0.20	40.58	96.55

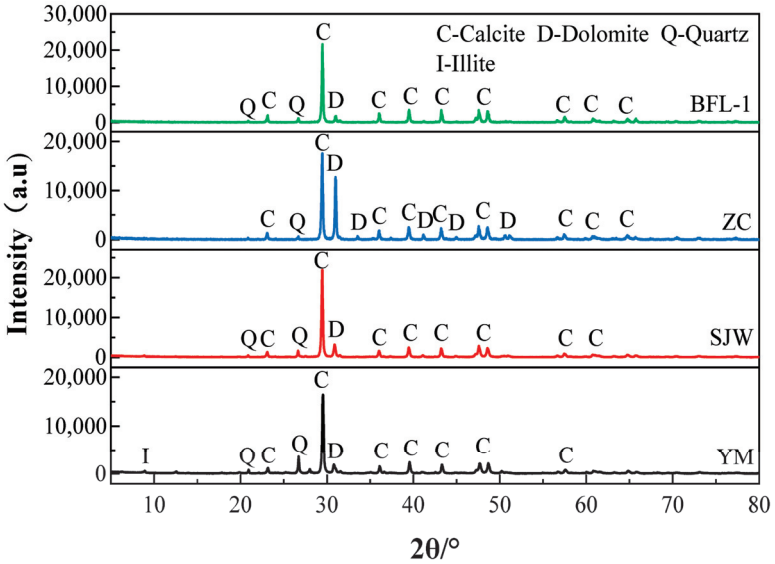

Figure 1. XRD patterns of rocks BFL-1, ZC, YM, and SJW.

Dolomitic limestone samples were selected and ground to pass a sieve size of 0.08 mm. A 30 g sample of the ground powder was weighed. The powder was added to a glass beaker and submerged in a constant temperature water bath of 60 °C. 3 hydrochloric acid was slowly added, drop by drop, while keeping stirring until evidence of bubbling dissipated, indicating that dissolution was complete (The hydrochloric acid reagent used in this paper

was sourced from Xilong Science Co., Ltd., located in Shantou, Guangdong Province, China). The solution was then filtered and the residue removed from the filter and dried in an oven at 60 °C for 24 h. The acid-insoluble substances in dolomitic limestone BFL-1, ZC, YM, and SJW were 4.22%, 3.50%, 21.75%, and 9.56%, respectively. Figure 2 shows the X-ray diffraction pattern of acid-insoluble substances in the rocks. From interpreting the XRD results we can see the acid-insoluble substances of dolomitic limestone YM and SJW were primarily quartz and illite. The dolomitic limestone YM also contained a small amount of microcline and albite. The acid-insoluble substances of dolomitic limestone BFL-1 and ZC were primarily quartz, with only a small amount of illite present. The results of quantitative analysis of each of the minerals of the acid-insoluble substances of rocks using the XRD–Rietveld method is shown in Table 2. The quartz minerals of dolomitic limestone BFL-1, ZC, YM, and SJW are 2.84%, 2.04%, 7.24%, and 3.50%, respectively. The clay minerals (illite) contents were 0.96%, 0.46%, 9.71%, and 5.38%, respectively.

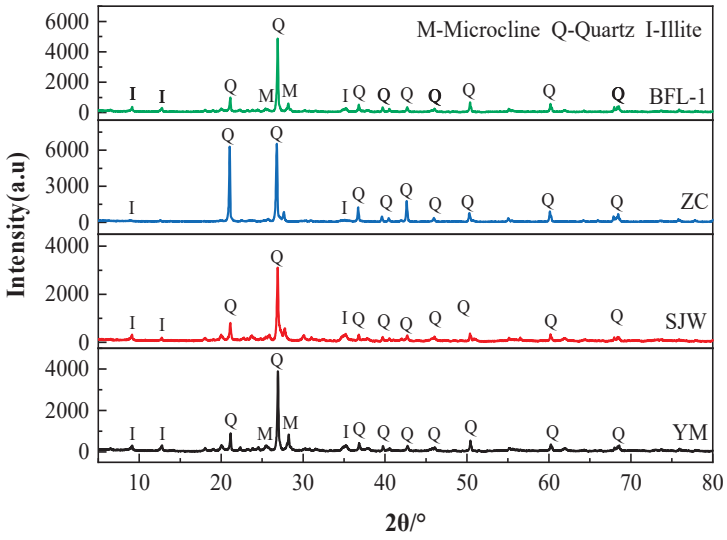

Figure 2. XRD patterns of acid-insoluble residues of dolomitic limestone.

Table 2. The content of minerals in acid-insoluble residues of dolomitic limestones.

Rocks	Mineral Content/wt%								AIR/%
	The Mineral Content in the Acid Insoluble				The Mineral Content in Raw Materials				
	Albite	Illite	Quartz	Microcline	Albite	Illite	Quartz	Microcline	
BFL-1	0.00	22.75	67.30	7.35	0.00	0.96	2.84	0.31	4.22
ZC	0.00	13.14	58.29	0.00	0.00	0.46	2.04	0.00	3.50
YM	13.81	44.64	33.29	8.16	3.00	9.71	7.24	1.77	21.75
SJW	0.00	56.28	36.61	0.00	0.00	5.38	3.50	0.00	9.56

The microstructure of the rock was observed by a Leica DM750P polarizing microscope (Leica Microsystems, Shanghai, China), and the results were shown in Figures 3–6. Figures 3–6 show microphotographs obtained from different areas using the same polarizer. The dolomitic limestone BFL-1 was mainly composed of micritic calcite and dolomite with a particle size from 10 to 60 μm. The dolomitic limestone ZC was mainly composed of calcite with a particle size of less than 20 μm and dolomite from 20 to 90 μm. A portion of the dolomite was in a mosaic structure, and the other dolomite was in a dispersed distributed structure. It also had a small amount of microcrystalline quartz. The dolomitic limestone YM was mainly composed of calcite from less than 20 μm and dolomite with a particle size from 10 to 40 μm. The dolomite was mainly presented with a mosaic structure,

and the other dolomite was in a dispersed distributed structure. It also contained a small amount of dispersed microcrystalline quartz. The dolomitic limestone SJW was mainly composed of calcite of different particle sizes, and dolomite with a particle size from 10 to 40 μm. The dolomite was mainly presented with a mosaic structure and a small amount distributed in a dispersed distributed structure, containing a small amount of dispersed microcrystalline quartz.

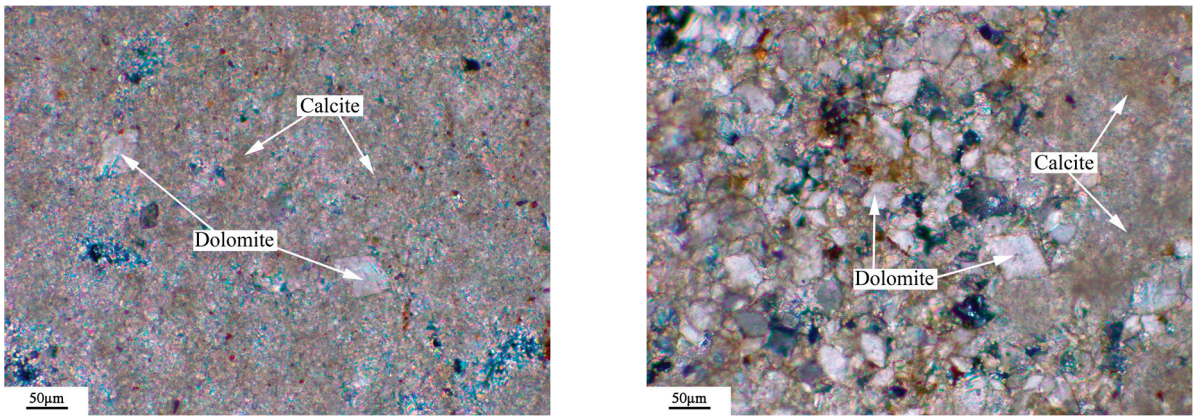

Figure 3. Polarizing microscope images: orthogonal polarizing microscope of BFL-1.

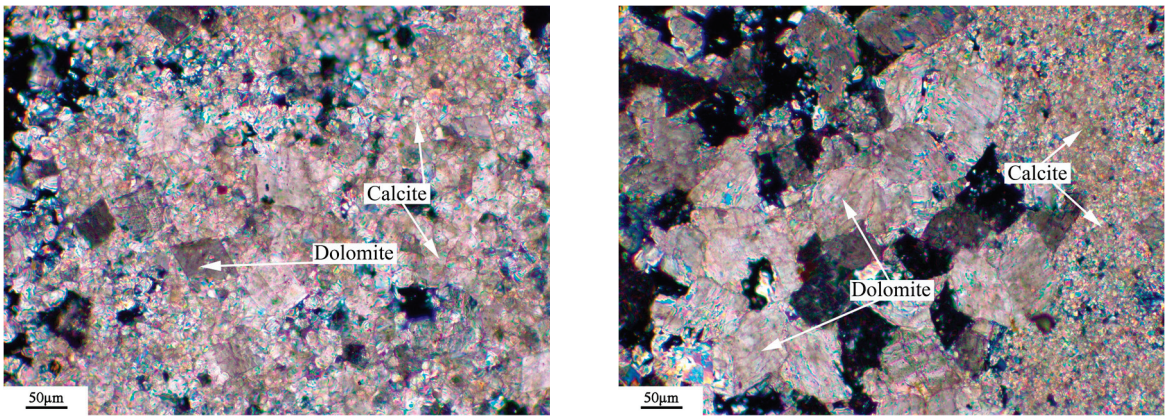

Figure 4. Polarizing microscope images: orthogonal polarizing microscope of ZC.

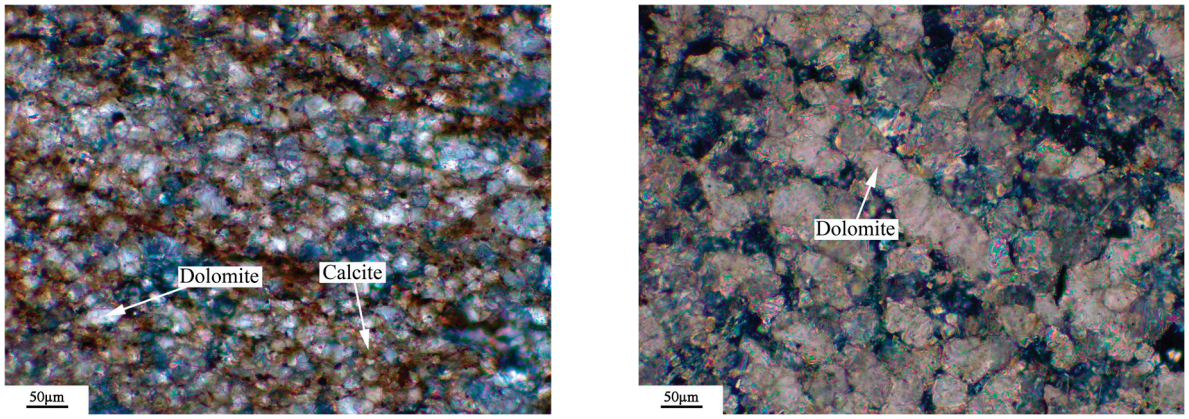

Figure 5. Polarizing microscope images: orthogonal polarizing microscope of YM.

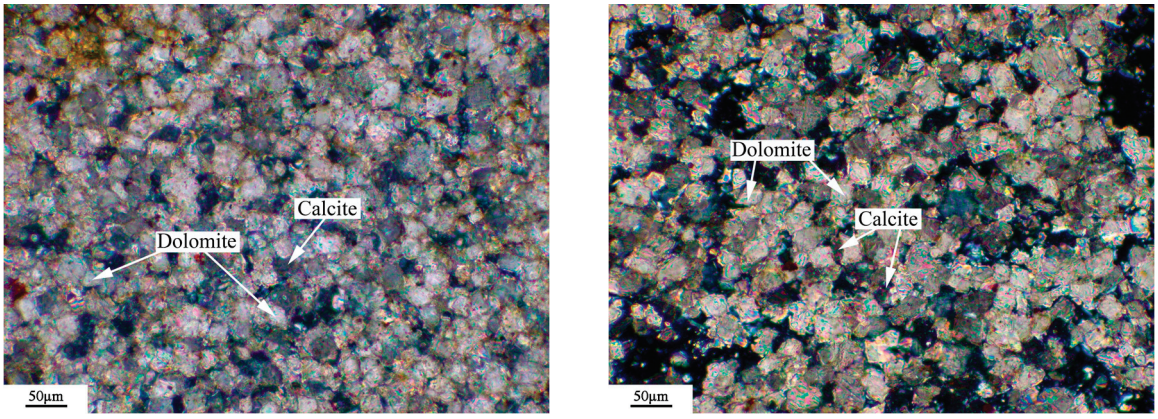

Figure 6. Polarizing microscope images: orthogonal polarizing microscope of SJW.

2.2. Analytical Methods

2.2.1. Migration Characterization of Na^+ Ions in Rocks

This paper aims to examine the migration of ions in rocks. Two approaches were adopted to achieve this goal: a column experiment to investigate ion migration in rock and an experiment to investigate ion migration in rocks of different particle sizes. The paper also characterizes Na^+ ion migration in rock columns. A core drilling device was used to procure cylindrical rock samples measuring Φ30 × 50 mm. Epoxy resin was uniformly applied onto the perimeter of the rock samples to prevent alkali ion migration into the sample matrix from the sides such that alkali ion could only migrate from the top and bottom surfaces of the sample (see Figure 7). The treated rock samples were immersed in 1 mol/L NaOH at 80 °C with a solid to liquid ratio of 1:5. Following curing for 14, 21, and 35 days the rock samples were removed and, using a slicing machine (Buehler Ltd., Shanghai, China), cut parallel to the top or bottom surface of the rock samples to produce rock slices. The rock slices were produced at 3 mm increments. After accounting for blade thickness of the cut (1.0 mm) the resultant rock slice was 2 mm thick. After each curing period, slices at the 0–2 mm, 3–5 mm, 6–8 mm, 9–11 mm, 12–14 mm, and 15–17 mm positions were cut. All rock slices were ground until they were below 0.080 mm. An amount of 1 g of the powder samples was added to 75 mL of deionized water and soaked for 24 h, then filtered to solid samples. The resultant filtrate was made up to 100 mL in a volumetric flask. The quantity of sodium ions (Na^+) in the various samples was examined based on the method according to ASTM D1976-20 [34] with a Thermo Fisher ICAP PRO ICP-MS (Thermo Fisher Scientific Inc. Shanghai, China).

Figure 7. Rock columns used for migration of Na^+ ions.

Characterization of Na^+ ion migration in rock particles of different particle sizes was explored. The dolomitic limestone was subjected to crushing using a jaw crusher (Wuxi Jianyi Instrument & Machinery Co., Ltd., Wuxi, China) followed by screening into rock

particles of 0.3–0.6 mm, 5–10 mm, and 10–16 mm through a vibrating screen. The rock particles were dried at 105 °C.

The prepared rock particles were immersed in 1 mol/L NaOH solution at 80 °C with a solid–liquid ratio of 1:5. After curing periods of 21, 35, 49, 72, 105, 135, 170, 210, 240, and 300 days, 15 g samples were taken from the rock particles for each particle size. The rock particles were washed with deionized water and dried in an oven at 105 °C for 10 h. The dry rock particles were ground to less than 0.080 mm using a vibration mill (RETSCH GmbH, Shanghai, China). An amount of 1 g of the powder samples was added to 75 mL of deionized water and soaked for 24 h, then filtered to solid samples. The resultant filtrate was made up to 100 mL in a volumetric flask. The quantity of Na^+ ions in the various samples was also examined using the Thermo Fisher ICAP PRO ICP-MS (Thermo Fisher Scientific Inc. Shanghai, China).

2.2.2. Determination of Degree of Dedolomitization

Quantitative determinations of dolomite in each sample were made using the XRD–Rietveld method [33]. The X-ray powder diffraction data were collected at room temperature, using a Rigaku Smart Lab 3 kW diffractometer (Rigaku Corporation, Beijing, China) with a scanning diffraction angle in the range of 17° to 70° at 1°/min. High Score Plus 3.0 software was used to determine the content of minerals in different reacted rock samples, and the degree of dedolomitization was calculated according to the decrease of the content of dolomite. Refinement quality was evaluated visually and through the (Rwp < 10% and GoF < 2). Figure 8 shows the XRD–Rietveld fitting results for rock sample ZC.

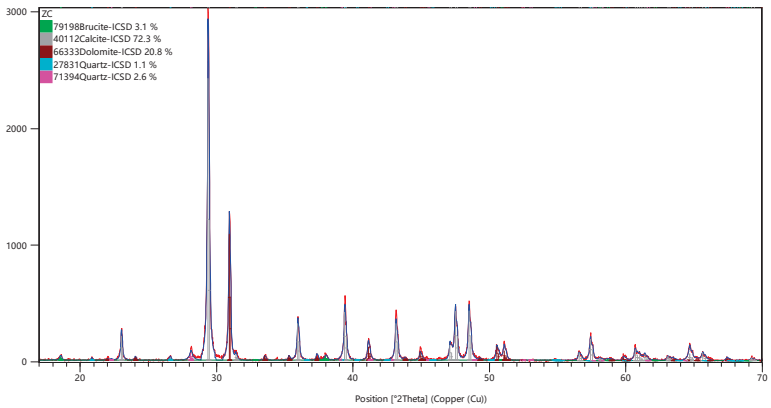

Figure 8. The XRD–Rietveld fitting results for rock sample ZC.

2.2.3. Determination of the Pore Structure of Rocks

The investigation of the porosity and pore size distribution of the rock samples was conducted via nitrogen adsorption method (N_2GA). The samples were analyzed with Gold APP V-Sorb 1800 Surface Area and Pore Size Analyzer (Gold APP Instruments Corporation Ltd., Beijing, China). A total of 5 g of samples with 0.16 mm to 0.32 mm particle size were weighed and applied to the specific surface area and pore size analyzer for determining the pore size distribution and the total pore volume of the rock particles.

2.2.4. Microstructural Analysis

After being immersed in a 1 mol/L NaOH solution at 80 °C for varying lengths of time, dolomitic limestone particles were rinsed with distilled water and dried in an oven at 105 °C for 10 h. Rock particles were stabilized in epoxy then polished using a Buehler Auto Met 250 grinding and polishing system (Buehler Ltd., Shanghai, China). The dolomite components of the rock samples were then analyzed in Zeiss Ultra55 FESEM and BSE (Carl Zeiss AG, Shanghai, China) to provide details of its morphology. The FESEM and

BSE imaging was performed at the most optimal imaging conditions of an acceleration voltage of 15 kV, a beam current of 5 nA, and a working distance of 8.5 mm. The depth of dedolomitization of dolomite was determined using the measurement tool function of Photoshop software (Version 21.0.1).

3. Results

3.1. The Amount of Na^+ Ion Migration in Rock Columns

Na^+ ion migration tests were utilized to quantitatively characterize ionic transport behavior of alkali ions in rocks. The amount of Na^+ ion migration in dolomitic limestone samples immersed in a 1 mol/L NaOH solution at 80 °C for different ages is illustrated in Figure 9. The amount of Na^+ ion migration discussed here represents the relative changes in Na^+ ions compared to the reference samples immersed in deionized water, which came from subtracting the initial Na^+ ion migration values from the reference samples. Due to the non-uniform distribution of mineral composition in the rock, this property will cause the measured Na^+ ion migration to vary to some extent.

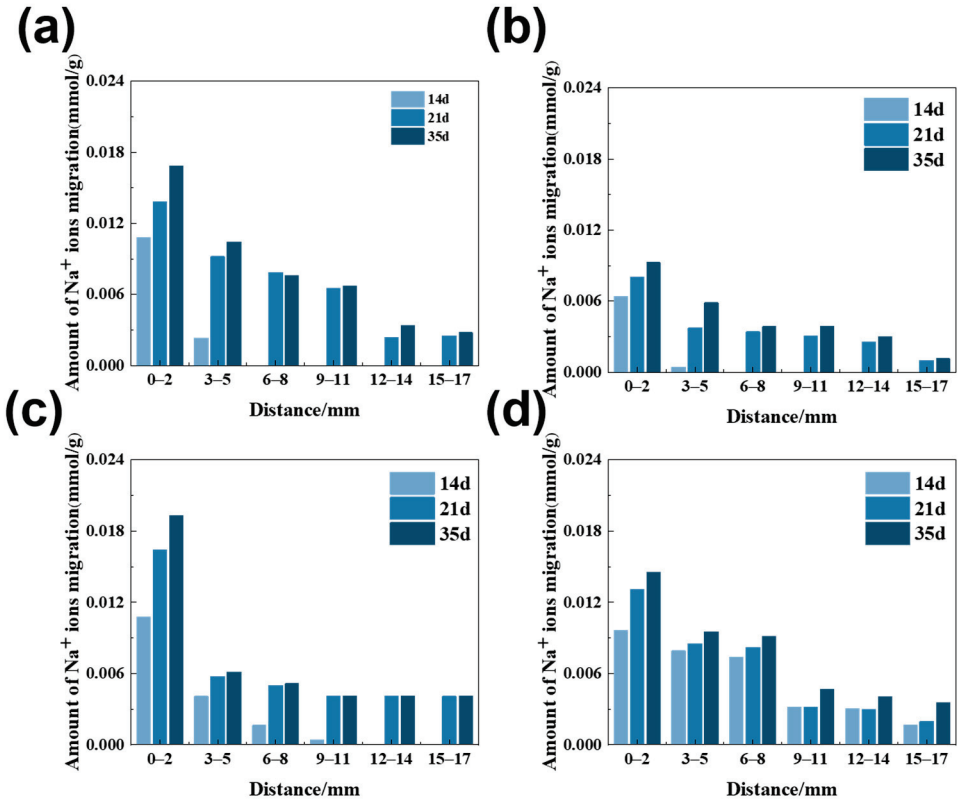

Figure 9. The amount of Na^+ ion migration in the rock columns of dolomitic limestones in a 1 mol/L NaOH solution at 80 °C ((**a**) BFL-1, (**b**) ZC, (**c**) YM, (**d**) SJW).

As shown in Figure 9, after the curing age of 14 days, the amount of Na^+ ion migration in dolomitic limestone BFL-1, ZC, YM, and SJW shows a predominant location from 0 to 5 mm in depth. The amount of migration decreases with depth and tends to stabilize. The amount of Na^+ ion migration in the middle of the column was relatively small. Over long curing age, Na^+ ions continued to migrate into the interior of the rock. After curing for 21 days, the amount of Na^+ ion migration stabilized; within the next observing 14 days of curing, increase in Na^+ ions migration was not significantly observed.

3.2. The Amount of Na^+ Ion Migration in Rocks of Different Sizes

The amount of Na^+ ion migration in dolomitic limestone with particle sizes of 0.3–0.6 mm, 5–10 mm, and 10–16 mm that were immersed in 1 mol/L NaOH solution at 80 °C is shown in Figure 10, in which the amount of Na^+ ion was calculated by subtracting the initial content of the reference samples immersed in deionized water from the Na^+ ion content in the cured specimens. There was some fluctuation in the data because of the non-uniform mineral distribution throughout the rock.

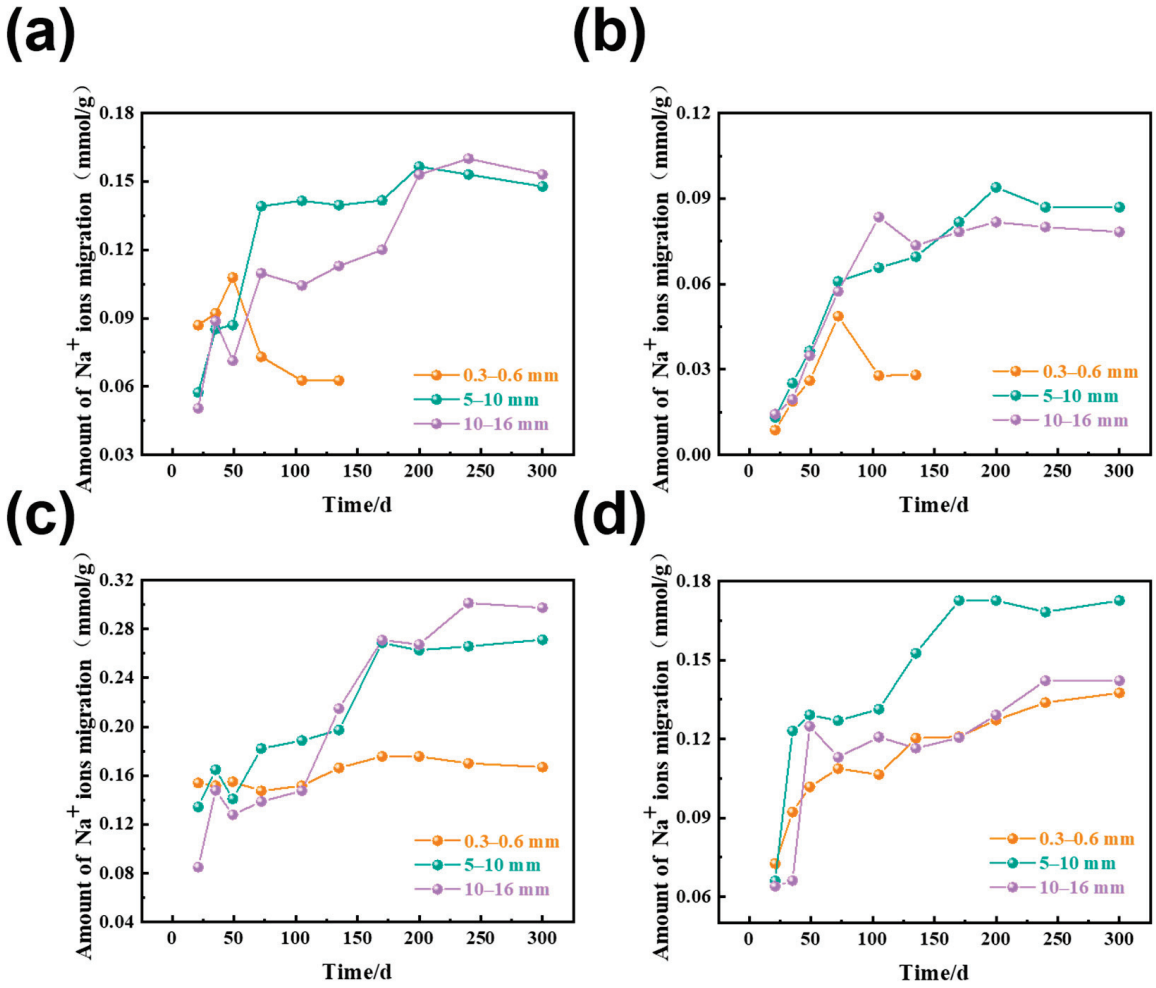

Figure 10. The amount of Na^+ ion migration in rocks of different sizes of dolomitic limestones in a 1 mol/L NaOH solution at 80 °C ((**a**) BFL-1, (**b**) ZC, (**c**) YM, (**d**) SJW).

As illustrated in Figure 10, during the 72 days of curing, the amount of Na^+ ion migrated in dolomitic limestone with varying particle sizes increased, although the total amounts of migration were small. The particle size of 5–10 mm had a significantly higher rate of migration than the other sizes. In dolomitic limestone with 0.3–0.6 mm particle sizes of BCL-1 and ZC, the dedolomitization was essentially complete and the rate of ion migration had stabilized after 135 days of curing. Subsequently, there were no additional measurements taken at the further ages of curing. The amount of Na^+ ion migrated in the larger particle sizes of dolomitic limestone had stabilized in the longer curing ages. At 170 days of curing, the amount of Na^+ migrated in dolomitic limestone ZC at particle sizes of 5–10 mm and 10–16 mm was 0.082 and 0.078 mmol/g, respectively. At 300 days of curing, the amount of Na^+ ion migrated in dolomitic limestone ZC at particle sizes of 5–10 mm and 10–16 mm was 0.086 and 0.079 mmol/g, respectively.

Comparing the Na^+ ion migration of dolomitic limestone with various particle sizes, the amount of Na^+ ion migration was relatively higher in dolomitic limestone with a particle size of 5–10 mm and lower in dolomitic limestone with a particle size of 0.3–0.6 mm. Na^+ ion migration in the dolomitic limestone that had a particle size of 10–16 mm was in between these two ranges of dolomitic limestone.

3.3. The Amount of Ca^{2+} and Mg^{2+} Ions Dissolution in Rocks of Different Sizes

To assess the potential effects of calcium and magnesium ions generated by the dissolution of the rocks on sodium ion migration behavior, rock samples were analyzed using ICP-MS to simultaneously measure the concentrations of calcium and magnesium ions. Figure 11 shows the dissolution of Ca^{2+} and Mg^{2+} in dolomitic limestone with particle sizes of 0.3–0.6 mm, 5–10 mm, and 10–16 mm that were immersed in 1 mol/L NaOH solution at 80 °C.

As illustrated in Figure 11, the solubility of calcium ions in NaOH solution is consistently increasing with additional reaction time; however, the overall dissolution remains marginal, with all dissolution values remaining below 0.016 mmol/g. Meanwhile, the solubility of magnesium ions did not vary significantly over time, and magnesium solubility remained low overall, with all dissolution values remaining below 0.0024 mmol/g.

3.4. Degree of Dedolomitization

The degree of dedolomitization was evaluated, and it was correlated with the amount of migration of alkali ions in the solution. The degree of dedolomitization in the dolomitic limestone for particle sizes of 0.3–0.6 mm, 5–10 mm, and 10–16 mm that were immersed in a 1 mol/L NaOH solution at 80 °C, as shown in Figure 12. There were some fluctuations in dedolomitization in the testing, which may be a result of the uneven distribution of dolomite in dolomitic limestone.

As illustrated in Figure 12, the degree of dedolomitization in dolomitic limestones of various particle sizes increases with an increase in curing time. The smaller sized dolomitic limestones observed a faster dedolomitization process and greater degree of dedolomitization than the larger particle sizes. Dolomitic limestone BFL-1 (0.3–0.6 mm particle size) showed 100% dedolomitization within 105 days, while the larger particle sizes (5–10 mm and 10–16 mm) showed less than 60% dedolomitization. It can be seen that only dolomitic limestones BFL-1 and ZC (0.3–0.6 mm particle size) reached complete dedolomitization of 100% dedolomitization after 105 days of curing time. However, for the dolomitic limestones SJW and YM with high clay content, some dolomites still did not react even after 300 days of curing for rocks with particle size of 0.3–0.6 mm. With increased curing age, dedolomitization of larger particle sizes tends to become slow. For dolomitic limestone ZC (particle size 5–10 mm), dedolomitization happens to 65% after 105 days of curing and 78% after 300 days of curing. For dolomitic limestone SJW (particle size 5–10 mm), 34% of dedolomitization occurs after 105 days of curing and the degree of dedolomitization reaction could only reach 44% after 300 days of curing. Within the samples, both the total reaction amount of dolomite and the degree of dedolomitization exhibited relatively high levels in dolomitic limestone ZC and relatively low values in dolomitic limestone BFL-1, YM, and SJW. Initial dedolomitization of dolomitic limestone YM and SJW primarily occurred in the first 170 days and then proceeded at a slower rate, which was similarly observed with Na^+ ion migration. Within 170 days, Na^+ ions moved into the rock interior, and showed little change after that point in time. Dedolomitization increased with Na^+ ion migration as there was an increased amount of Na^+ ions migrating into the rock interior. Hence, the dedolomitization process is also in part affected by the

alkali ion migration rate. When alkali ions rapidly migrate into rocks, dedolomitization occurs rapidly.

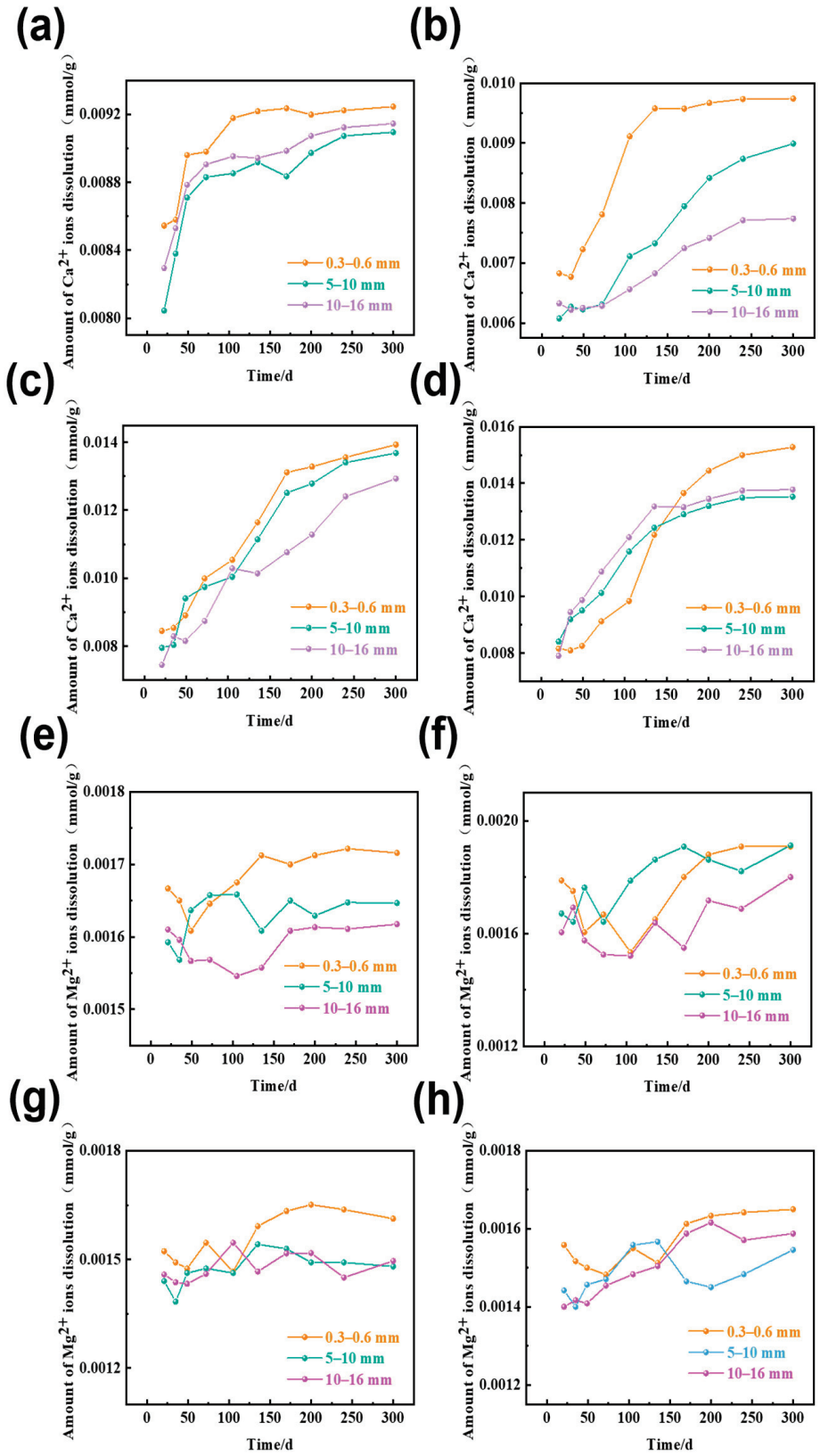

Figure 11. The amount of Ca^{2+} and Mg^{2+} ions dissolution in rocks of different sizes of dolomitic limestones in a 1 mol/L NaOH solution at 80 °C ((**a**) BFL-1- Ca^{2+}, (**b**) ZC- Ca^{2+}, (**c**) YM- Ca^{2+}, (**d**) SJW-Ca^{2+}, (**e**) BFL-1- Mg^{2+}, (**f**) ZC-Mg^{2+}, (**g**) YM-Mg^{2+}, (**h**) SJW-Mg^{2+}).

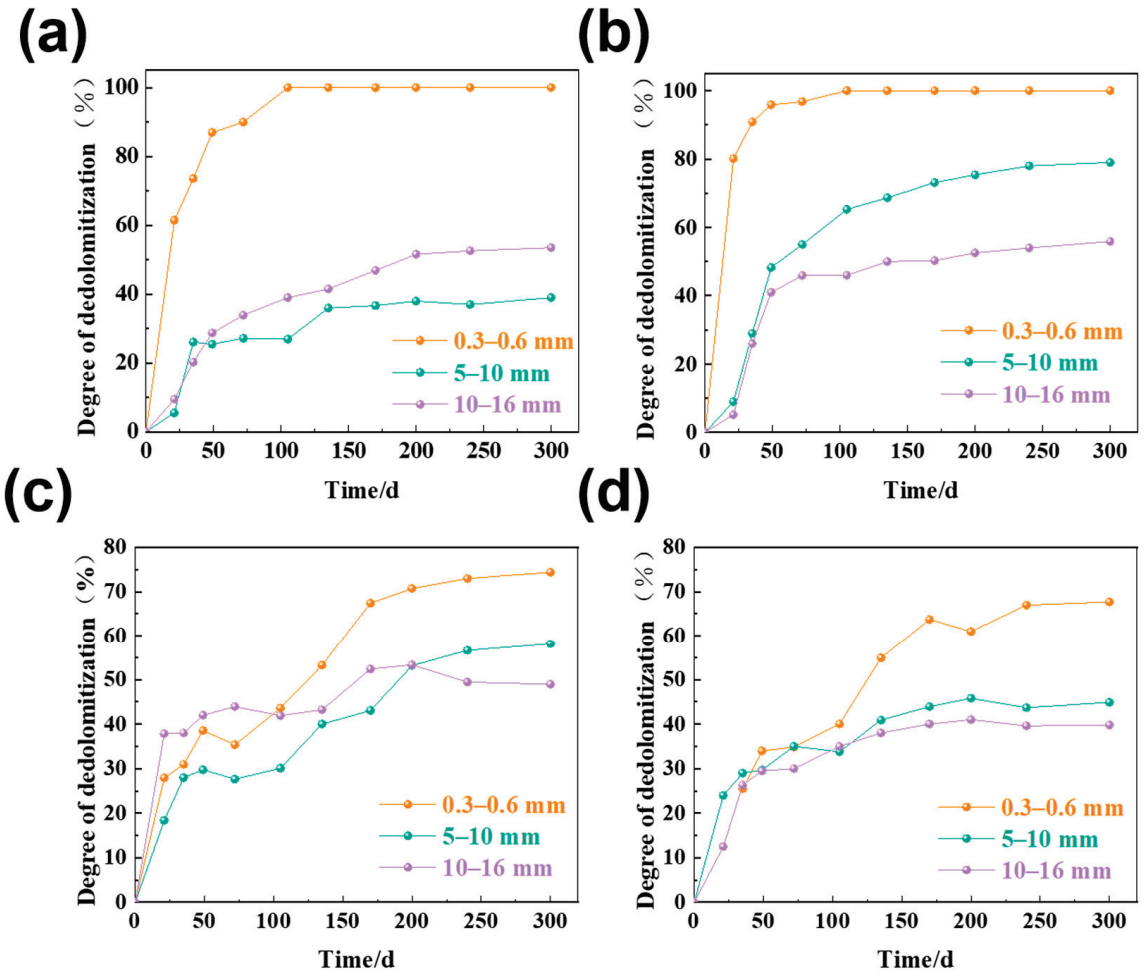

Figure 12. The degree of dedolomitization of different sizes of dolomitic limestones in a 1 mol/L NaOH solution at 80 °C ((**a**) BFL-1, (**b**) ZC, (**c**) YM, (**d**) SJW).

3.5. Pore Structure

The pore structure properties of rocks affect their transport mechanisms directly and are an important parameter for estimating the migration efficiency of alkali ions in rocks. Figure 13 shows the pore size distribution of rocks BFL-1, ZC, YM, and SJW, which was determined using the BET nitrogen adsorption method. The resultant total pore volume and pore volume for micropores (1–10 nm), mesopores (10–100 nm), and macropores (100–250 nm) is shown in Table 3. Figure 13 indicates that the rocks have a most probable pore diameter of approximately 100 nm. The rocks contain predominantly mesopores and macropores. The total pore volumes of dolomitic limestone BFL-1, ZC, YM, and SJW are 6.4, 3.2, 7.1, and 6.9 mm^3/g, respectively.

Table 3. The total pore volume of the rock and its pore volume by pore size.

No	Sample	Clay Minerals Contents/%	Total Pore Volume/(mm^3/g)	Micropore (1–10 nm) Volume/(mm^3/g)	Mesopore (10–100 nm) Volume/(mm^3/g)	Macropore (100–250 nm) Volume/(mm^3/g)
1	BFL-1	0.96	6.4	0.4	4.9	1.1
2	ZC	0.46	3.2	0.3	1.8	1.1
3	YM	10.04	7.1	0.7	5.3	1.1
4	SJW	5.42	6.9	0.7	5.0	1.2

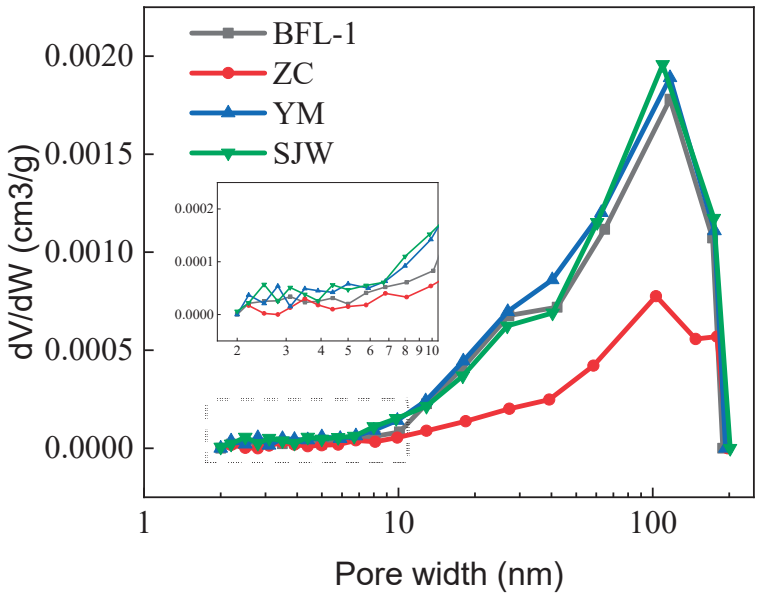

Figure 13. Pore size distribution of rocks BFL-1, ZC, YM, and SJW.

3.6. Microstructures of Dedolomitization

The use of FESEM and BSE to observe the sample surface in detail is a critical step in revealing its microstructure. The images taken using FESEM of 5–10 mm dolomitic limestone ZC as shown in Figures 14 and 15 show results after curing in a 1 mol/L NaOH solution at 80 °C for 72 days. Figure 14a shows a dolomite area displaying a mosaic structure in dolomitic limestone ZC. The dolomite area of approximately 400 μm around the particles shows that some dedolomitization occurs to produce fine products (see Figure 14b), while the internal area of approximately 400 μm distance from the edge of the particle does not exhibit a reaction. The contrast of the reaction zone and unreacted zone area (visible by the white dotted line) has a clear boundary where the two areas meet. Figure 15a shows a matrix that includes calcite and the dolomite area that has a localized mosaic structure within dolomitic limestone ZC. The left area shown on the image is the grayish-white matrix that includes calcite, etc., while the dark gray particle shown on the right is a dolomite crystal. The dolomite crystals located on the left and approximately 800 μm from the edge of the particle show some evidence of dedolomitization producing fine products, while the dolomite area on its right side does not have any visual evidence of the reaction (see Figure 15b). The dedolomitization area is approximately 100 μm wide.

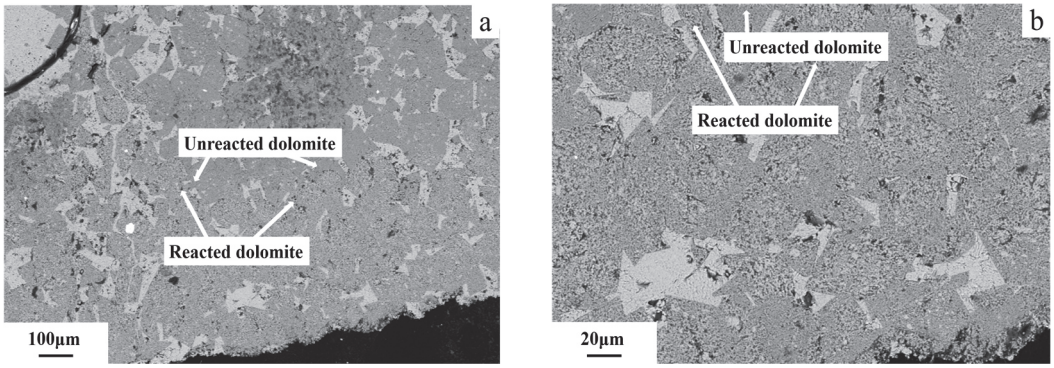

Figure 14. The FESEM images of dolomitic limestone ZC in 1 mol/L NaOH solution at 80 °C for 72 days: (**a**) reacted dolomite at the boundary (bottom zone) and unreacted dolomite in the inner zone (upper zone) and (**b**) magnified reacted dolomite at the boundary.

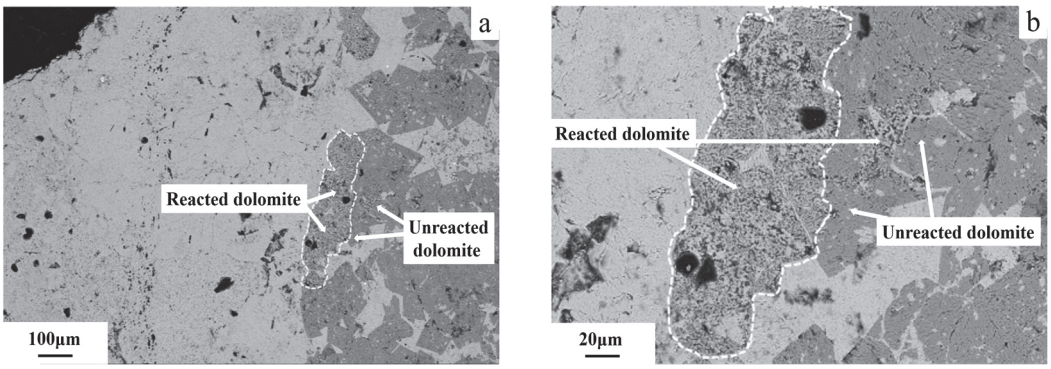

Figure 15. The FESEM images of dolomitic limestone ZC cured in 1 mol/L NaOH solution at 80 °C for 72 days: (**a**) reacted dolomite at the boundary (left zone) and unreacted dolomite in the inner zone (right zone) and (**b**) magnified reacted dolomite at the boundary and unreacted dolomite in the inner zone.

The FESEM image of the 5–10 mm dolomitic limestone BFL-1, after curing 1 mol/L NaOH solution at 80 °C for 72 days is shown in Figure 16. The dolomite in the dolomitic limestone BFL-1 is distributed in a dispersed manner. The dolomite within a distance of approximately 110 μm from the particle edge of the dolomitic limestone BFL-1 has been observed to dedolomitization, while the dolomite within the interior region of the dolomitic limestone has basically not reacted. The two dolomite crystals observed at the edge of the dolomitic limestone BFL-1 reveal that one of the dolomite crystals is undergoing dedolomitization, whereas the other side of the crystal remains unreacted (Figure 16a shows these dolomite crystals). In the dolomitic limestone BFL-1, Figure 16b shows the dolomite area that has a localized mosaic structure. Similar to the dolomite crystals noted previously in the dolomitic limestone BFL-1, the dolomite crystals within 80 μm from the edge of the dolomitic limestone BFL-1 have undergone dedolomitization, while the dolomite internal to the particle has remained non-reactive.

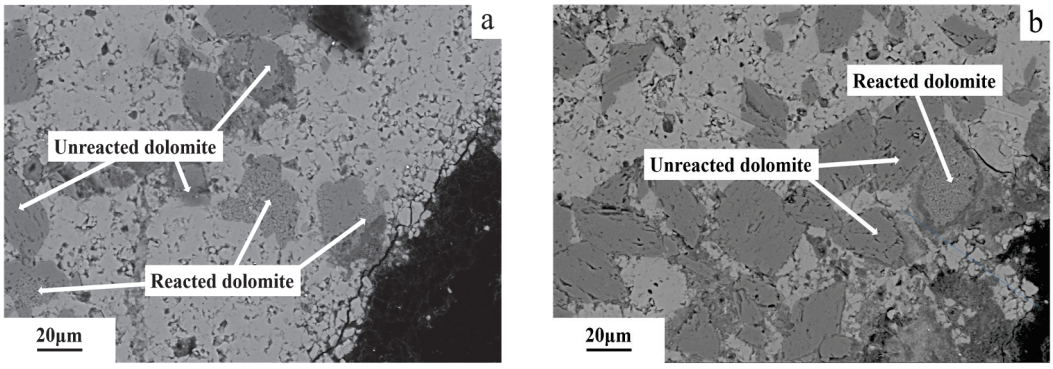

Figure 16. The FESEM images of dolomitic limestone BFL-1 in 5–10 mm cured in 1 mol/L NaOH solution at 80 °C for 72 days: (**a**) dolomite which distributed in a dispersed manner, (**b**) dolomite which had a localized mosaic structure.

The FESEM image of the dolomitic limestone YM with diameters of 5–10 mm after being cured in an 80 °C and 1 mol/L NaOH solution for 72 days is shown in Figure 17. Figure 17b presents a magnified view of the region outlined by the yellow rectangle in Figure 17a.The dolomite within the dolomitic limestone YM is distributed in a dispersed manner. The dolomite encircled by clay minerals within 50 μm from the edge of the particle has not undergone a visible dedolomitization.

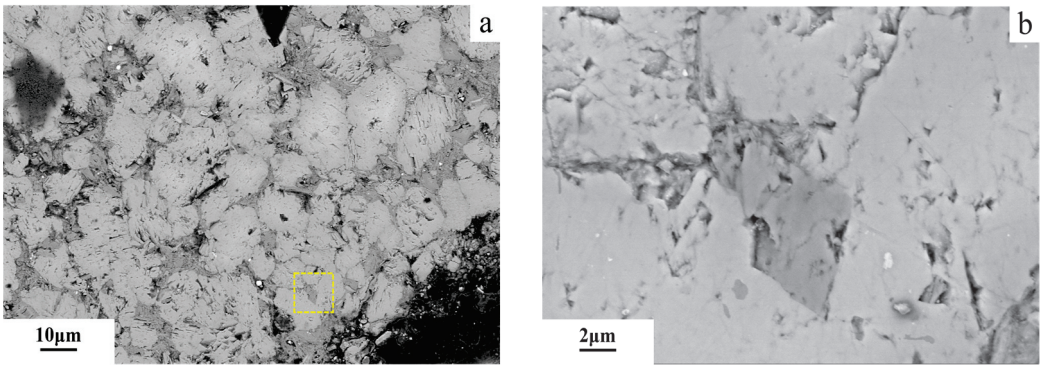

Figure 17. The FESEM images of dolomitic limestone YM in 5–10 mm cured in 1 mol/L NaOH solution at 80 °C for 72 days: (**a**) dolomite at the boundary, (**b**) magnified dolomite at the boundary.

The BSE images of 5–10 mm dolomitic limestone SJW with diameters of 5–10 mm after being cured in an 80 °C and 1 mol/L NaOH solution for 72 days is shown in Figure 18. The dolomite in this rock occurs as fine particles, and most of the dolomite has a mosaic structure. The dolomite particles within a distance of 80 μm from the edges of the particles have undergone dedolomitization.

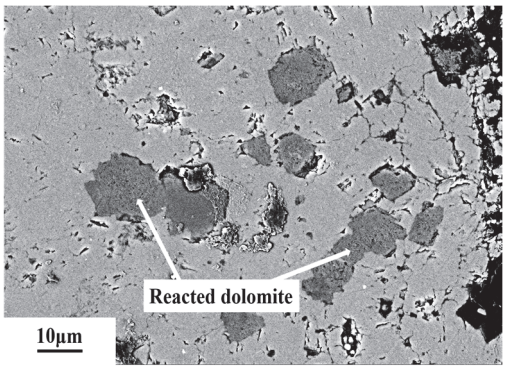

Figure 18. The BSE images of dolomitic limestone SJW in 5–10 mm cured in 1 mol/L NaOH solution at 80 °C for 72 days.

The BSE images of the edge regions of dolomitic limestone samples ZC and BCL-1, respectively, after curing in 1 mol/L NaOH solution at 80 °C for different times are shown in Figures 19 and 20. It is illustrated that after 49 days of curing, the dolomite at a proximity of 480 μm from the edge of the rock displayed dedolomitization, while the dolomite crystals appeared in fine-grain form (Figure 19a). At 72 days, the dedolomitization depth for dolomitic limestone ZC reached 550 μm (Figure 19b); at 105 days, the dedolomitization depth for dolomitic limestone ZC reached 630 μm (Figure 19c). The dolomite closest to the particle edge undergoes dedolomitization first. After the dolomite at the edge has entirely reacted, the dolomite within can begin to react. In this way, dedolomitization has gradually progressed into rock. As shown in Figure 20a, the dolomite at a distance of 50 microns from the edge of rock exhibited the start of dedolomitization after 49 days of curing. At 72 days, the depth of dedolomitization reached 84 μm (Figure 20b); at 105 days, the depth of dedolomitization reached 100 μm (Figure 20c). Similar to the previous result for dolomitic limestone ZC, dedolomitization progresses layer by layer into rock. After the dolomite at the edge has entirely reacted, the dolomite within can begin to react.

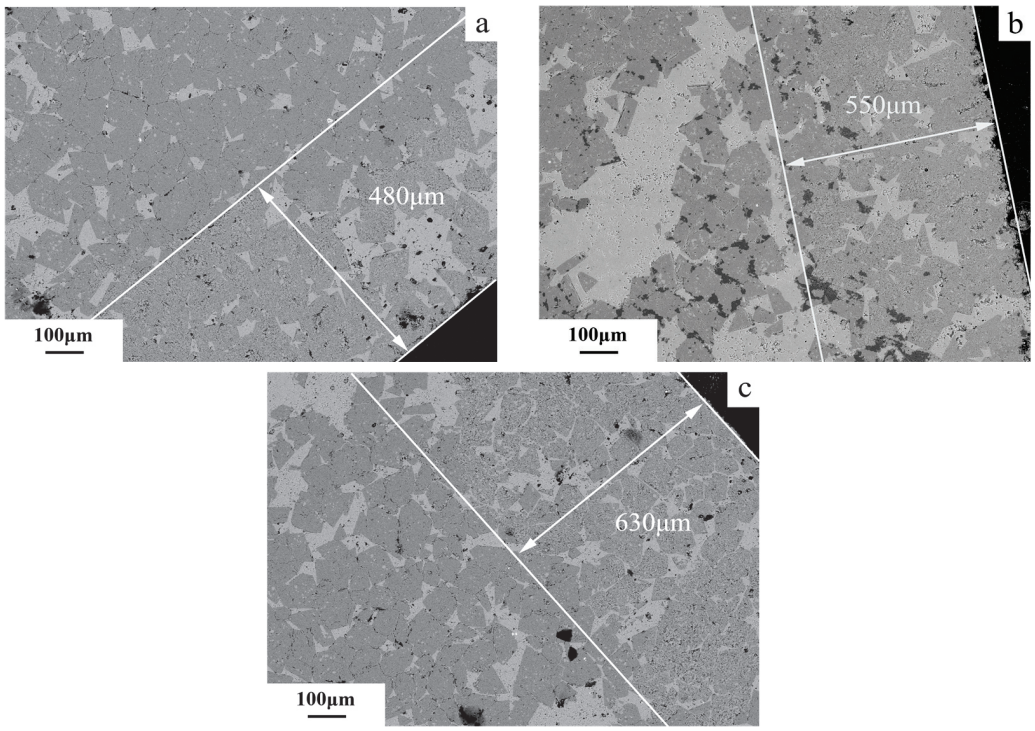

Figure 19. The BSE images of the boundary zone in rock ZC cured in 1 mol/L NaOH solution at 80 °C for different ages (**a**) 49 d, (**b**) 72 d, (**c**) 105 d.

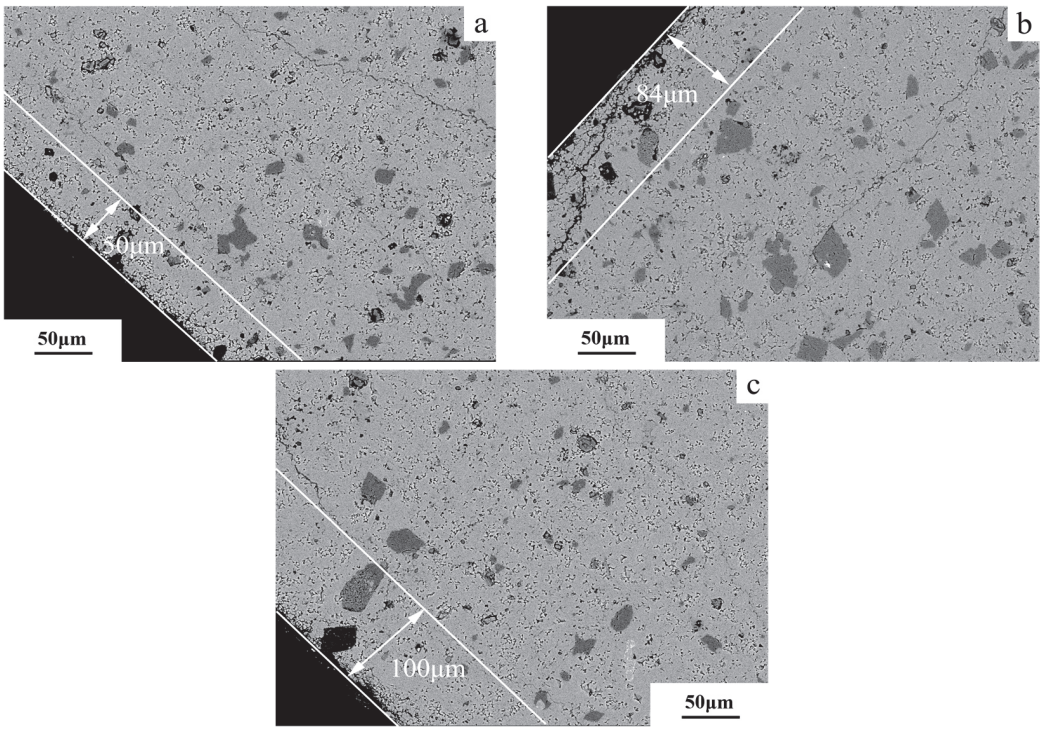

Figure 20. The BSE images of the boundary zone in rock BFL-1 cured in 1 mol/L NaOH solution at 80 °C for different ages (**a**) 49 d, (**b**) 72 d, (**c**) 105 d.

4. Discussion

This paper aims to examine the alkali ion migration mechanism in dolomitic limestone, thereby impacting dedolomitization. Accordingly, the purpose of the alkali discussion in this paper is to account for the findings based on these factors.

4.1. The Influence of Ca^{2+} and Mg^{2+} Ions Dissolution on Na^+ Ion Migration

When concentrations of solutions are less than 1 mol/L, the solubility of calcite is observed to increase with increasing concentrations of NaOH solution [35,36]. With time, NaOH gradually migrates into the interior of the rock matrix, increasing the concentration of alkaline species, promoting dissolution of calcite. As a result, Ca^{2+} ion leaching rates show an increasing trend with time. On the contrary, brucite solubility in alkaline solutions is considered very low, and dissolution is insensitive to alkaline concentrations [37]. Therefore, dissolution amount of Mg^{2+} ion remains low throughout the reaction time. As shown in Figures 10 and 11, while Ca^{2+} ion can be dissolved to a certain extent, the dissolution amount for Ca^{2+} ion is lower than Na^+ ion by one order of magnitude to more than ten times and for Mg^{2+} ion it will be two orders of magnitude or tens of times lower than Na^+ ions. Therefore, it is unlikely that Ca^{2+} and Mg^{2+} ions will significantly affect the diffusion behavior of Na^+ ions.

4.2. The Influence of Particle Size

The dolomitic limestone was cured in a 1 mol/L NaOH solution at 80 °C. Driven by the concentration gradient, Na^+ ions migrated through the calcite and clay mineral matrix in the rock. There was an upper limit to the migration process. As indicated in Figure 10a,b, after 105 days of curing, the migration of Na^+ ions reached equilibrium in BFL-1 and ZC where dolomite was completely reacted and the Na^+ migration was limited. When dolomite crystals were not present, the gaps between calcite crystals provided physical migration paths. The concentration difference of the alkali ions between the curing solution and the pore solution in calcite drove the migration of Na^+ and OH^- into the rock. However, the concentration of alkali ions in the pore solution of calcite was always lower than that of the curing solution.

For samples with dolomite crystals, when Na^+ ions migrate to the dolomite interface, dedolomitization occurs. This dedolomitization leads to the production of water-soluble Na_2CO_3 and consequently consumes OH^- ions and pulls additional OH^- ions into the reaction area. Meanwhile, Na^+ ions also enter the reaction zone accordingly. Figure 21 illustrates the dedolomitization mechanism occurring in dolomitic limestones with different particle sizes. In the examples from 0.3 to 0.6 mm sized dolomitic limestones, high dedolomitization occurred with low dolomite content, and therefore the amount of dolomite consumed per particle was low. However, in larger particle sizes the amount of dolomite consumed is greater, leading to a higher Na^+ ion migration associated with dedolomitization. This explains the lower Na^+ ion migration in 0.3–0.6 mm sized dolomitic limestones.

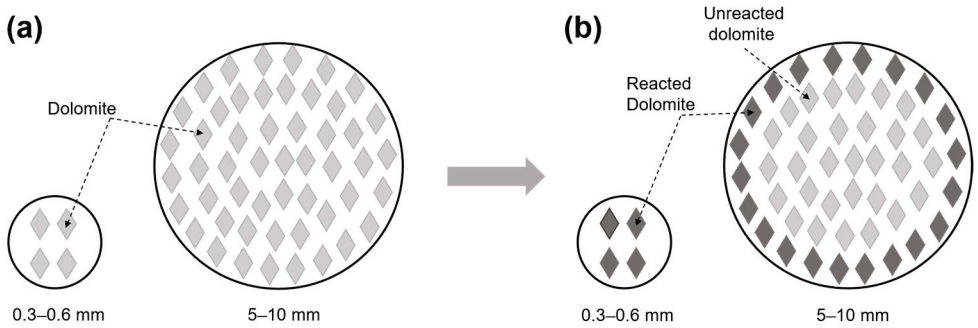

Figure 21. Schematic representation of the dedolomitization of dolomitic limestone with different grain sizes (**a**) before the dedolomitization, (**b**) after the dedolomitization.

Moreover, if the particle size is too large, the matrix impedes ion migration more readily. As shown in Figure 9, during migration experiment with Φ30 × 50 mm rock column, it could be seen that even the 0–3 mm thin slice had a lower Na^+ ion migration

amount that was dozens to hundreds of times lower than Na^+ ion migration amount in 10–16 mm dolomitic limestone. The size of rocks has a significant influence on alkali ion migration. This could explain the observation that 10–16 mm dolomitic limestone had a lower migration amount than 5–10 mm dolomitic limestone.

4.3. The Influence of Rock Pore Structure on Ion Migration

The formation process of small pores is primarily affected by clay minerals. For different rocks, micropore volumes tend to be larger in rocks with more clay minerals. When clay content surpasses 5%, micropore volume exceeds 0.7 mm^3/g and when clay content is less than 1%, micropore volume is less than 0.4 mm^3/g. Illite occurs with carbonate minerals (such as calcite and dolomite) in rocks. The dissolution of carbonate minerals can generate secondary pores, and the presence of illite can provide support for these micropores, preventing them from being compressed or plugged. Additionally, illite has a unique layered structure, with a certain amount of space between its layers [38].

Prior to the initiation of dedolomitization, alkali ion migration is primarily dependent on the porosity of the rock [39]. Porosity provides important pathways for alkali ion migration into the sample. Comparative study of different rock types indicates that the higher the clay content of a rock type, the greater the amount of Na^+ migrating into the rock. For example, dolomitic limestones containing less clay (ZC and BFL-1) only had Na^+ ions migrate into a depth of 3–5 mm after curing for 14 days, as shown in Figure 10. Meanwhile, dolomitic limestones containing more clay (YM and SJW) allowed Na^+ ions to migrate into a depth of 9–11 mm. In this early stage of ion migration, the migration of alkali ions is predominantly controlled by the pores between the crystals; therefore, the greater the porosity of the rock, the faster the alkali ion migration rate. Conversely, in rocks with lower clay content, due to their relatively low porosity, the amount of ion migration is also correspondingly lower.

4.4. Alkali Ion Migration After Dedolomitization

In the case of the alkali–aggregate reaction (ASR), alkali ions will migrate away from regions of high cement paste concentrations, into the interior of aggregates where there are lower cement paste concentrations. The migration of alkali ions to the interior of the aggregate is a diffusion process driven by the concentration gradient of alkali ions in solution [7,39]. Likewise, for the reaction removing dolomite to occur, the dolomite must be in contact with alkali ions. The same principle applies, whereby alkali ions will migrate toward the surface of the dolomite crystals, again driven by the concentration gradient. In ADR, OH^- ion chemically interact with dolomite and are consumed in the process. This consumption process leads to the further development of a concentration gradient in the reaction system. This concentration gradient promotes migration of OH^- ions to the reaction zone, thereby fast tracking dedolomitization. As shown in Figures 14 and 15, after curing in a 1 mol/L NaOH solution at 80 °C for 72 days, dolomite crystals that are 800 μm distant from the edge of dolomitic limestone ZC can react when there are no dolomite crystals at the boundary. This indicates that alkali ions can migrate through the pores into the deeper parts of the rock. When dolomite crystals exist at the boundary, the dolomite that is within about 400 μm of the edge of dolomitic limestone ZC particles shows dedolomitization while the internal dolomite has not undergone the reaction yet. Thus, this shows that dedolomitization limits ion migration into the interior of the rock.

As shown in Figure 19, after curing in a 1 mol/L NaOH solution at 80 °C for 105 days, alkali ions migrated into the rock particle, but the reaction depth was limited to 630 μm from the surface. This suggests that alkali ions chiefly react at the surface or near-surface where dolomite exists, rather deep in the rock. As shown in Figure 9, after curing in

a 1 mol/L NaOH solution at 80 °C for 35 days, the amounts of Na^+ ion migration of dolomitic limestone ZC and YM at depths of 0–2 mm reached 0.012 and 0.021 mmol/g, respectively. In contrast, the amounts of Na^+ ion migration in either sample at depths greater than 6 mm were only able to reach 0.004 and 0.005 mmol/g. The amounts of Na^+ ion migration are mainly concentrated within 0–2 mm, and the migration amount at a deeper position of 2 mm is relatively small. This is likely related to the fact that OH^- ions were preferentially reacting with the dolomite as they migrated, forming a concentration gradient that drew more OH^- ions to the reaction zone. This makes it difficult for OH^- ions to further penetrate into the interior of the rock. Once the dolomite is completely reacted, the alkali ions are free to migrate into the interior of the rock. Until that time, the reactions occurring within the reaction zone may have inhibited the migration of alkali ions so that the migration of ions was mainly concentrated in the surface layer of rock and the depth of dedolomitization was relatively shallow.

4.5. The Migration Mechanism of Alkali Ions

In Figure 22, the process of the migration of alkali ions in dolomitic limestone is illustrated. The dolomitic limestone sample was immersed in a 1 mol/L NaOH solution, and the alkali ions migrated through pores between the crystals, as shown in Figure 22a. During the alkali ions' migration process through the pores, OH^- ions interacted with the dolomite crystals, producing dedolomitization of the dolomite, which consumed a significant amount of OH^- ions and therefore reduce the concentration of OH^- ions in the reaction area. A concentration gradient is generated between the reaction area and the surrounding environment, which promotes the migration of alkali ions as shown in Figure 22b. Once dedolomitization was complete, alkali ions were no longer confined to the prior state and took the opportunity to migrate further away to deeper areas inside the rock, as shown in Figure 22c.

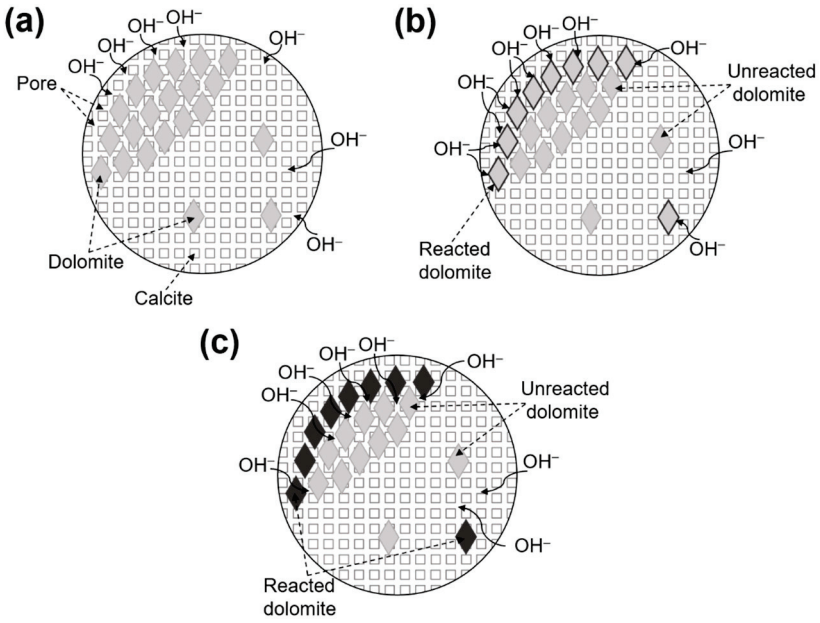

Figure 22. Migration processes of alkali ions (**a**) before the dedolomitization, (**b**) during the dedolomitization, (**c**) after the dedolomitization.

5. Conclusions

This paper evaluated the degree of dedolomitization with respect to the dolomitic limestone samples, BFL, ZC, YM, and SJW, by means of the XRD–Rietveld method. The amount of alkali ion migration was ascertained through ICP-MS. The microstructure

and dedolomitization process of dolomitic limestone were examined using FESEM, BSE, and polarizing microscopy. It should be noted that due to the inherent heterogeneity of dolomitic limestone samples studied, the quantitative results presented herein are primarily illustrative. The key value of this work lies in the elucidation of the mechanistic pathways rather than in providing universal quantitative parameters. This paper investigates the migration mechanism of alkali ions in dolomitic limestone. From our experiment work, the following conclusions can be drawn:

1. The pores between crystals are the physical pathways for the migration of alkali cations, whereas the concentration gradient established upon dedolomitization is a driving force for alkali ions migration. The interactions between pores and concentration gradient dictate the migration efficacy of alkali ions.
2. Clay minerals such as illite often have small crystal sizes and between these there is a large number of micropores (1–10 nm). These micropores provide efficient pathways for the migration of alkali ions.
3. The particle size has two effects on alkali ion migration: (a) Dedolomitization facilitates alkali ion migration. The smaller the size, the higher the degree of dedolomitization, but less dolomite content means less alkali ion will migrate after dedolomitization; and (b) The matrix has impediment effect on ion migration. The larger the size of the particle, the stronger the impediment effect.
4. The process of the migration of alkali ions in dolomitic limestone can be represented as: (a) alkali ions migrate in the pores between crystals and contact with dolomite crystals; (b) OH^- ions react with dolomite crystals and dedolomitization consumes OH^- ions and creates a concentration gradient; (c) alkali ions migrate to the dolomite reaction zone due to the concentration gradient; and (d) after dolomite crystals have reacted completely, alkali ions continue to migrate deeper into the rock.

Author Contributions: Conceptualization, X.Z.; Methodology, X.Z. and W.L.; Software, X.Z. and Z.W.; Validation, X.Z., W.L., X.H. and M.D.; Formal analysis, X.Z., X.H. and M.D.; Investigation, X.Z., X.H. and Z.W.; Resources, Z.W. and M.D.; Data curation, X.Z. and W.L.; Writing—original draft, X.Z.; Writing—review & editing, X.Z., W.L. and M.D.; Supervision, M.D. All authors have read and agreed to the published version of the manuscript.

Funding: The authors thank the Natural Science Foundation of Jiangsu Province (Grant No. BK20240563).

Data Availability Statement: The original contributions presented in this study are included in the article. Further inquiries can be directed to the corresponding authors.

Conflicts of Interest: The authors declare no conflict of interest.

References

1. Song, X.; Deng, M.; Li, W.; Lan, X.; Tang, M. Whether so-called Mg-Si gels are produced under dolomite-quartz system under alkaline conditions. *Cem. Concr. Res.* **2024**, *186*, 107701. [CrossRef]
2. Leemann, A.; Münch, B.; Lothenbach, B.; Bernard, E.; Trottier, C.; Winnefeld, F.; Sanchez, L. Alkali-carbonate reaction in concrete—Microstructural consequences and mechanism of expansion. *Cem. Concr. Res.* **2025**, *195*, 107903. [CrossRef]
3. Salim, M.U.; Mosaberpanah, M.A. The mechanism of alkali-aggregate reaction in concrete/mortar and its mitigation by using geopolymer materials and mineral admixtures: A comprehensive review. *Eur. J. Environ. Civ. Eng.* **2022**, *26*, 6766–6806. [CrossRef]
4. Swenson, E.G. A Reactive aggregate undetected by ASTM tests. *ASTM Bull.* **1957**, *226*, 48–51.
5. Yang, H.; Li, P.; Rao, M. Long term investigation and inhibition on alkali-aggregates reaction of three gorges dam concrete. *Constr. Build. Mater.* **2017**, *151*, 673–681. [CrossRef]
6. Hadley, D.W. Alkali reactivity of dolomitic carbonate rocks. *Highw. Res. Rec.* **1945**, *25*, 147–168.
7. Sims, I.; Poole, A.B. *Alkali-Aggregate Reaction in Concrete: A World Review*; CRC Press: Boca Raton, FL, USA, 2017.

8. Deng, M.; Xu, L.; Lan, X.; Tang, M. Microstructures and Alkali-Reactivity of Permian Emeishan Group Basaltic Rocks. In Proceedings of the 13th International Conference on Alkali Aggregate Reaction in Concrete, Trondheim, Norway, 16–20 June 2008.
9. Deng, M.; Han, S.; Lu, Y.; Lan, X.; Hu, Y.; Tang, M. Deterioration of concrete structures due to alkali-dolomite reaction in China. *Cem. Concr. Res.* **1993**, *23*, 1040–1046. [CrossRef]
10. Stukovnik, P.; Bosiljkov, V.B.; Marinsek, M. Acr progress in concretes with dolomite aggregate and blast furnace slag cem iii binder. *Ceram. Silik.* **2024**, *68*, 67–79. [CrossRef]
11. Zahedi, A.; Akpinar, P. A Case Study for exploring the alkali-aggregate reactivity of Cyprus aggregates. *Case Stud. Constr. Mater.* **2022**, *16*, e01000. [CrossRef]
12. Tong, L.; Tang, M. Expansion mechanism of alkali-dolomite and alkali-magnesite reaction. *Cem. Concr. Compos.* **1999**, *21*, 361–373. [CrossRef]
13. Tang, M.S.; Deng, M.; Lan, X.H.; Han, S. Studies on alkali-carbonate reaction. *Aci Mater. J.* **1994**, *91*, 26–29.
14. Deng, M.; Tang, M.S. Measures to inhibit alkali-dolomite reaction. *Cem. Concr. Res.* **1993**, *23*, 1115–1120. [CrossRef]
15. Tang, M. Classification of alkali aggregate reaction. In Proceedings of the 9th International Conference on Alkali Aggregate Reaction in Concrete, London, UK, 27–31 July 1992; pp. 6348–6353.
16. Katayama, T. The so-called alkali-carbonate reaction (ACR)—Its mineralogical and geochemical details, with special reference to ASR. *Cem. Concr. Res.* **2010**, *40*, 643–675. [CrossRef]
17. Katayama, T.; Jensen, V.; Rogers, C.A. The enigma of the 'so-called'alkali–carbonate reaction. *Proc. Inst. Civ. Eng. Constr. Mater.* **2016**, *169*, 223–232. [CrossRef]
18. Grattan-Bellew, P.E. Alkali-silica reaction—Canadian experience. In *The Alkali-Silica Reaction in Concrete*; CRC Press: Boca Raton, FL, USA, 1991; pp. 223–248.
19. Grattan-Bellew, P.E.; Mitchell, L.D.; Margeson, J.; Min, D. Is alkali–carbonate reaction just a variant of alkali–silica reaction ACR = ASR? *Cem. Concr. Res.* **2010**, *40*, 556–562. [CrossRef]
20. Chen, B.; Deng, M.; Huang, X.; Mo, L.; Huang, B.; Lan, X. Siliceous and dolomitic-bearing aggregates reaction in Tetramethylammonium hydroxide. *Constr. Build. Mater.* **2021**, *299*, 123948. [CrossRef]
21. Milanesi, C.A.; Marfil, S.A.; Locati, F. Expansive behavior of an alkali-carbonate reactive dolostone from Argentina: Proposal of an osmotic theory-based model to explain the expansion caused by the alkali attack. *Cem. Concr. Res.* **2020**, *138*, 106239. [CrossRef]
22. Ren, X.; Li, W.; Mao, Z.Y.; Deng, M. Inhibition of the alkali-carbonate reaction using fly ash and the underlying mechanism. *Crystals* **2020**, *10*, 484. [CrossRef]
23. Garcia, E.; Alfonso, P.; Tauler, E. Mineralogical Characterization of Dolomitic Aggregate Concrete: The Camarasa Dam (Catalonia, Spain). *Minerals* **2020**, *10*, 117. [CrossRef]
24. Garcıa, E.; Alfonso, P.; Tauler, E.; Galı, S. Surface alteration of dolomite in dedolomitization reaction in alkaline media. *Cem. Concr. Res.* **2003**, *33*, 1449–1456. [CrossRef]
25. Stukovnik, P.; Bosiljkov, V.B.; Marinsek, M. ACR in dolomitic aggregate concrete for an autogenous self-healing process. *Mater. Tehnol.* **2020**, *54*, 379–384. [CrossRef]
26. Milla, J.; Rupnow, T.; Saunders, W. *Effect of Clay Content on Alkali-Carbonate Reactive (ACR) Dolomitic Limestone*; Louisiana Transportation Research Center: Baton Rouge, LA, USA, 2021.
27. Dantas, S.R.A.; Bergmann, A.C.; Sanchez, L.F.M. Exploring the Effectiveness of TiO_2 Treatments to Mitigate Alkali-Aggregate Reaction (AAR). In Proceedings of the International Conference on Alkali-Aggregate Reaction in Concrete, Ottawa, ON, Canada, 18–24 May 2024; Springer Nature: Cham, Switzerland, 2024; pp. 515–522.
28. Leemann, A.; Münch, B.; Trottier, C.; Sanchez, L. Microstructural Consequences of Alkali-Carbonate Reaction. In Proceedings of the International Conference on Alkali-Aggregate Reaction in Concrete, Ottawa, ON, Canada, 18–24 May 2024; Springer Nature: Cham, Switzerland, 2024; pp. 87–94.
29. Li, W.; Deng, M.; Mo, L.; Panesar, D.K.; Mao, Z. Alkali carbonate reaction (ACR): Investigations on mechanism of dedolomitization of dolomite in dolostones. *Constr. Build. Mater.* **2022**, *351*, 128942. [CrossRef]
30. Duke, E.F. Reactions between dolomite and cement paste in deteriorated concrete. In Proceedings of the USA-Australia Workshop on High Performance Concrete, Sydney, Australia, 20–23 August 1997; pp. 20–23.
31. Pękala, A.; Vilcekova, S. Secondary mineralization processes in the assessment of alkaline reactivity of aggregates and durability of concrete. *Case Stud. Constr. Mater.* **2024**, *21*, e04113. [CrossRef]
32. Liu, X.; Mao, Z.; Yi, L.; Fan, Z.; Zhang, T.; Huang, X.; Deng, M.; Tang, M. Experimental Method for Evaluating the Reactivity of Alkali-Carbonate Reaction Activity. *Materials* **2022**, *15*, 2853. [CrossRef]
33. *JY/T 0587-2020*; General Rules for X-Ray Polycrystalline Diffractometry. Ministry of Education of PRC: Beijing, China, 2020.
34. *ASTM D1976-20*; Standard Test Method for Elements in Water by Inductively-Coupled Plasma Atomic Emission Spectroscopy. ASTM International: West Conshohocken, PA, USA, 2020.
35. Konno, H.; Nanri, Y.; Kitamura, M. Crystallization of aragonite in the causticizing reaction. *Powder Technol.* **2002**, *123*, 33–39. [CrossRef]

36. Simoni, M.; Hanein, T.; Woo, C.L.; Tyrer, M.; Nyberg, M.; Martinez, J.-C.; Quintero-Mora, N.I.; Provis, J.L.; Kinoshita, H. Decarbonisation of calcium carbonate in sodium hydroxide solutions under ambient conditions: Effect of residence time and mixing rates. *Phys. Chem. Chem. Phys.* **2022**, *24*, 16125–16138. [CrossRef]
37. Weiss, B.D.; Harasek, M. Solubility Data of Potential Salts in the MgO-CaO-SO_2-H_2O-O_2 System for Process Modeling. *Processes* **2021**, *9*, 50. [CrossRef]
38. Zheng, Y.H.; Baudet, B.A. Evolution of nano-pores in illite-dominant clay during consolidation. *Acta Geotech.* **2024**, *19*, 71–83. [CrossRef]
39. Gomez, L.; Perales, F.; Multon, S.; Socié, A.; Fournier, B.; Argouges, M. Numerical investigation of mechanisms affecting alkali-silica reaction advancement by reactive transport simulations. *Cem. Concr. Res.* **2025**, *190*, 107791. [CrossRef]

Disclaimer/Publisher's Note: The statements, opinions and data contained in all publications are solely those of the individual author(s) and contributor(s) and not of MDPI and/or the editor(s). MDPI and/or the editor(s) disclaim responsibility for any injury to people or property resulting from any ideas, methods, instructions or products referred to in the content.

materials

MDPI

Article

Influence of Clinker and Cinder Particle Gradation on the Properties of Blended Cement and Associated Mortars

Runze Shang [1], Dexiang Huang [2,3,4], Wenju Cai [2,3,4], Longlong Niu [1], Bi Chen [5], Xinyu Zhang [1], Wei Li [1,*] and Min Deng [1,*]

[1] College of Materials Science and Engineering, Nanjing Tech University, Nanjing 211816, China; runze12318@163.com (R.S.)
[2] Hefei Cement Research & Design Institute Corp., Ltd., Hefei 230051, China
[3] Anhui Provincial Key Laboratory of Green and Low-Carbon Technology in Cement Manufacturing, Hefei 230051, China
[4] CNBM (Hefei) Powder Technology Equipment Corp., Ltd., Hefei 230051, China
[5] College of Engineering Management, Nanjing Tech University, Nanjing 211816, China
* Correspondence: stevenlee187@outlook.com (W.L.); dengmin@njtech.edu.cn (M.D.)

Abstract: The high-hydrolysis reactivity cement clinker powder in cement plays a major role in cement's cementation, while low-hydrolysis reactivity mineral admixture powders, such as slag, m mainly serve as a filler. Through optimizing the particle matching of cement clinker powder and slag powder, the mechanical properties of cement can be enhanced. In this study, clinker and slag with differing levels of fineness were obtained by separate grinding, and the particle gradation of clinker powder and slag powder in the cement was optimized. Fine clinker particles were mixed with coarse slag particles to systematically explore their effects on the rheology of cement paste, the formation of hydration products, the evolution of the pore structure, and the material's mechanical properties. Through experimental tests and microscopic analysis, the mechanism whereby particle gradation is regulated by separate grinding was revealed. The findings of the study are as follows: with the same amount of cinder, finer clinker requires a higher water content of standard consistency. The addition of coarse cinder effectively reduces the standard-consistency water requirement of the blended cement. Fine grinding of coal cinder fails to enhance cement strength effectively but markedly raises the standard-consistency water demand. Thus, the specific surface area of coal cinder should be maintained at approximately 210 m^2/kg.

Keywords: grinding method; cement clinker; cinder; compressive strength; water requirement of standard consistency

1. Introduction

In 2024, China's total coal consumption was 5.96 billion tons, accounting for 53.2% of the country's total energy consumption [1]. Chinese coal-fired power plants generate approximately 600–700 million tons of solid industrial residues annually, primarily comprising fly ash (about 80–90%) and coal-fired slag (about 10–20%). Fly ash comprises fine particulate matter collected from flue gases, whereas coal-fired slag refers to the coarser residues accumulated at the bottom of the furnace (also referred to as bottom ash or cinder) [2].

Fly ash has been widely adopted in industrial applications, particularly as a cementitious additive in concrete and construction materials, owing to its favorable pozzolanic properties and consistent particle morphology [3,4]. However, the potential application

of cinder is fundamentally limited by its unstable structure and poor compaction characteristics, which seriously affect its functionality [5,6]. Therefore, only a limited fraction of cinder is utilized in subbase fill and brick manufacturing [7–9]. Over 85% of the cinder generated by coal-fired power plants is either stockpiled in open-air storage or disposed of in landfills, which has a significant impact on the surrounding air and soil [4,10,11]. Recent studies have confirmed the potential of cinder for use in construction applications. However, in China, its value-added utilization remains limited and is primarily restricted to brick production and road construction. Zhang et al. [12] prepared three different types of sintered bricks using lakebed mud, cinder, and sludge as the primary raw materials. Moreno Nabarro et al. [13], Fedorova and Shaforost [14], and other researchers have found that using cinder as a substitute for traditional road construction materials in road construction and maintenance applications can yield some economic benefits. In addition, cinder can be used to produce concrete [5,15]. Coarse aggregates can partially replace the stone, while fine aggregates can replace some of the sand and cement [16–19]. In recent years, much research has focused on using cinder to prepare concrete mixtures. However, bricks containing cinder are prone to cracking, and using cinder as a road base or fine aggregate fails to utilize its chemical properties, leading to resource waste. It is urgent to reasonably and fully develop and utilize cinder.

Cinder contains significant amounts of reactive components such as SiO_2 and Al_2O_3, which enable its use as a supplementary cementitious material. This application can help reduce cement consumption and enhance its added value in construction materials. However, its low early-age reactivity limits the incorporation ratio, hindering large-scale application. Existing technologies improve its reactivity through superfine grinding, but this results in high energy consumption and costs. Therefore, finding ways to increase the cinder content while reducing costs and improving cement strength has become a key challenge.

Cement-based materials are among the most widely used structural materials in modern construction projects, and their mechanical properties have a significant impact on both the engineering quality and durability. As core components, cement clinker and cinder not only influence the process of the hydration reaction but also directly determine the microstructure of the paste and its mechanical properties.

Composite cement is typically produced by blending Portland cement with supplementary cementitious materials (SCMs), including ground granulated blast-furnace slag, fly ash, or steel slag. Currently, the content of high-activity waste residues (such as slag and fly ash) in composite cement can reach 20–30%, while the content of low-activity waste residues (such as cinder and steel slag) is usually below 10% [20–23]. This preparation method is relatively simple, but the utilization of SCMs is low. When the content of these materials is higher, the early strength and other properties of the blended cement are poor, which limits the amount of SCMs that can be incorporated into the blended cement.

In addition, analyzing the particle size distribution of cement using the Rosin–Rammler–Bennet (RRB) distribution and the Fuller ideal packing curve [24,25] reveals that an insufficient amount of fine cement particles makes it difficult for the grinding system to achieve the ideal packing curve in a single process. Even when energy consumption is not considered, achieving the Fuller ideal packing curve through particle selection and blending would still lead to increased water demand, reduced early strength, poorer workability, and shrinkage cracking issues. This is evidently impractical and unsuitable for guiding production. Therefore, researchers recommend using a graded grinding process, where SCMs replace some of the fine cement particles. This approach not only optimizes the particle packing density but also mitigates the adverse effects of excessively fine cement particles [26,27].

In recent years, a large number of scholars have focused on the ultrafine grinding of low-grade SCMs, solid waste, or industrial by-products, and their subsequent blending with cement clinker. Kupwade-Patil et al. replaced Portland cement with finer volcanic ash components obtained through grinding and found that the finer volcanic ash components produced a more compact pore structure in the paste, thereby achieving higher compressive strength [28]. Carvalho et al. conducted experiments and found that replacing 25% of Portland cement with fine recycled powder in cement mortar resulted in almost the same compressive strength as the control group mortar [29]. Other researchers have found that, when the replacement rate of fine steel slag does not exceed 20%, its effect on the strength and drying shrinkage of ordinary concrete can be considered negligible [30]. Bui et al. found that, compared to the combination with fine cement, the composite of rice husk ash with coarse cement resulted in a higher increase in the relative strength of the paste [31]. Pormmoon et al. [32] found that micronized high-calcium and low-calcium coal bottom ash (D50 $\approx$ 4 μm) significantly improved the 28-day compressive strength of high-performance concrete while reducing chloride permeability and water adsorption. This was attributed to the filler effect of fine particles and pore refinement via pozzolanic reactions. Liew et al. [33] systematically studied the synergistic gradation effects of low-calcium coal bottom ash (LCBA) and ground granulated blast-furnace slag (GGBS). When 15% cement was replaced by LCBA combined with GGBS, the ternary blend achieved 58.1 MPa compressive strength (52.5 N grade) with 45% lower CO_2 emissions. These studies confirm that particle gradation optimization is critical for enhancing cement's mechanical properties and durability. They also propose a sustainable strategy: balancing performance and environmental benefits by tailoring fineness and calcium content [32,33]. Thus, integrating coal-based waste with clinker and slag, guided by particle design, could optimize cement performance while reducing environmental impact.

Despite extensive research on the use of cinder in cementitious materials, several critical gaps remain. First, most studies focus on ultrafine grinding of cinder to enhance reactivity, which incurs high energy costs without proportional strength gains. Second, the synergistic effects of particle gradation between clinker and cinder on hydration kinetics and pore structure evolution are poorly understood. Third, existing work rarely addresses the trade-off between water demand and mechanical properties when optimizing particle size distributions. This study fills these gaps by (1) proposing a cost-effective strategy combining fine clinker with coarse cinder to balance reactivity and water requirements, (2) systematically linking particle gradation to microstructure development through hydration heat and pore analysis, and (3) establishing an optimal fineness ratio (clinker: 498 m^2/kg; cinder: 210 m^2/kg) that outperforms conventional blends in terms of both strength and workability. These contributions advance the sustainable utilization of cinder while reducing grinding energy consumption.

2. Materials and Methods

2.1. Raw Materials

All raw materials, including cement clinker, cinder, and gypsum, were sourced from Hefei Southern Cement Co., Ltd., (Hefei, China). The mineral compositions of cement clinker and cinder were characterized by X-ray diffraction (XRD) following Chinese standard JY/T 0587-2020 [34]. The X-ray powder diffraction data were collected at room temperature using a Rigaku Smart Lab 3 kW diffractometer, Rigaku, Tokyo, Japan, and the scanning speed was 5°/min. Figure 1 shows the results. The mineral composition of cement clinker primarily consists of C_2S, C_3S, C_3A and C_4AF, while the cinder is mainly composed of vitreous material, containing small amounts of quartz and mullite.

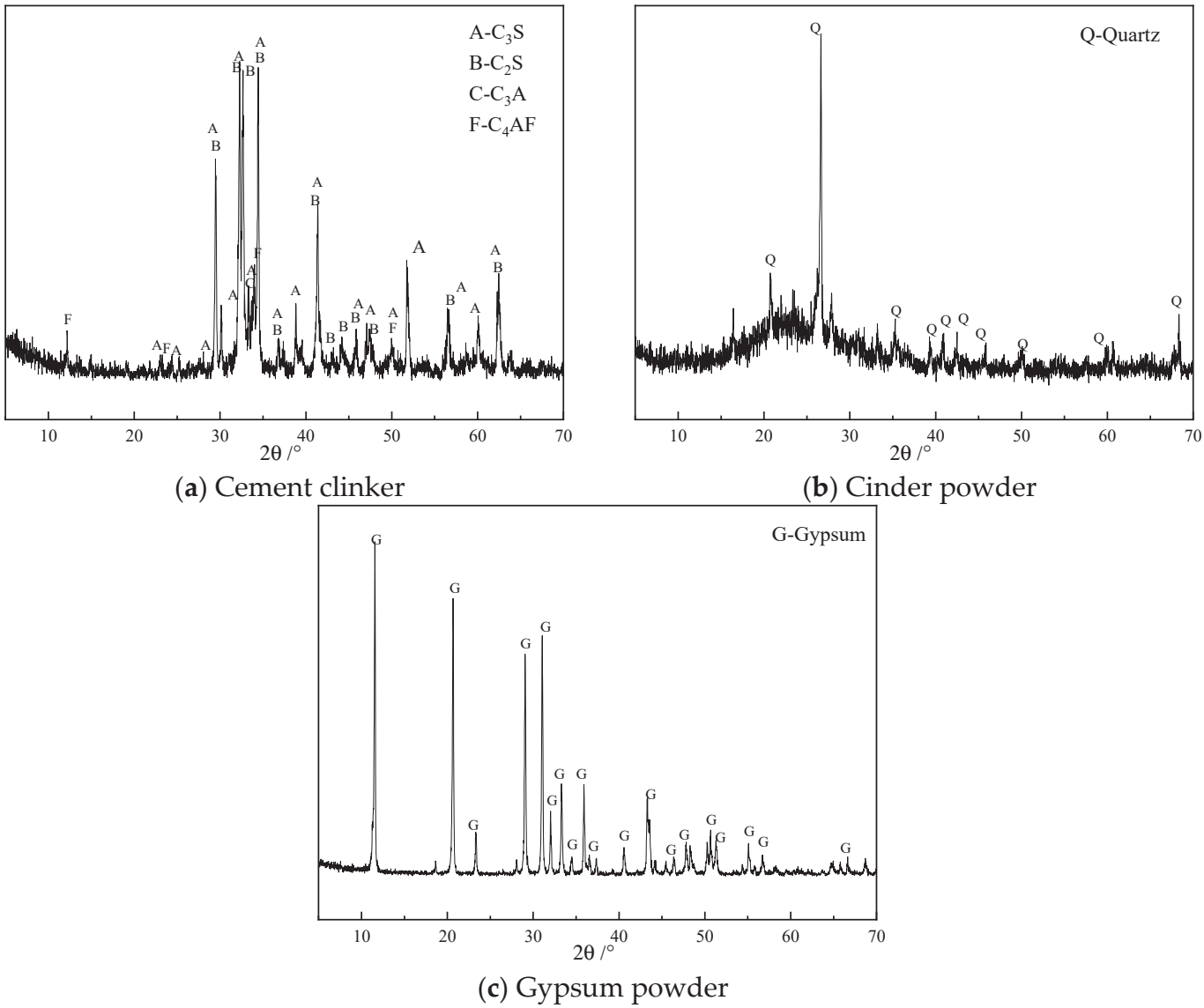

Figure 1. X-ray diffraction (XRD) pattern of cement clinker, cinder powder, and gypsum powder.

Cement clinker C was produced by Hefei South Cement Co., Ltd., (Hefei, China). The cinder and gypsum used were also from Hefei South Cement Co., Ltd. The chemical composition was determined following Chinese National Standard GB/T 176-2017 [35] for cement analysis. Table 1 shows the results. The main chemical components of the cinder are SiO_2, Al_2O_3, and Fe_2O_3. The primary chemical components of the gypsum are SO_3 and CaO.

Table 1. Chemical composition of cement clinker and cinder.

Sample	CaO	SiO_2	Fe_2O_3	Al_2O_3	MgO	K_2O	Na_2O	SO_3	Loss	Total
Clinker C	64.97	21.18	3.75	6.23	1.51	0.28	0.48	0.71	0.56	99.67
Cinder S	6.34	58.85	6.16	23.02	0.76	1.29	0.91	0.30	0.70	98.33
Gypsum G	32.52	1.48	0.13	0.50	0.32	0.12	0.15	43.46	21.10	99.78

2.2. Methods

2.2.1. Specific Surface of Cement—Blaine Method

The specific surface area was measured using an SBT-127 digital Blaine permeability (Wuxi, China) apparatus in accordance with GB/T 8074-2008 [36]: "Testing method for specific surface of cement—Blaine method".

2.2.2. Water Requirement of Standard Consistency

The test determines the water quantity needed for cement paste to reach 6 ± 1 mm plunger penetration in a Vicat apparatus, following GB/T 1346-2024 [37]. It mixes cement with varying water percentages until the standard penetration depth is achieved.

2.2.3. Mechanical Strength

The cement strength was determined according to GB/T 17671-2021 [38]. The experiment utilized standard sand with a water-to-cement ratio of 0.50. The specimens were cured under standardized conditions (20 °C, 95% relative humidity), and the compressive strength of the specimens was measured at curing ages of 3 days and 28 days.

2.2.4. Preparation of Cement Paste Samples

In the microstructure testing of cement paste, a cement paste with a water-to-binder ratio of 0.3 is prepared. The paste is sealed and cured in an environment at 20 °C. After curing for the specified age, the paste is removed and placed in alcohol to terminate the hydration before testing.

2.2.5. Heat of Hydration

The cement powder and water were first placed in a 20 °C environment to ensure that the material temperature matched the measurement ambient temperature. The heat of hydration was analyzed using the TAM AIR Thermstate90 calorimeter, manufactured by TA Instruments (New Castle, DW, USA), with a water-to-cement ratio of W/C = 0.5. The sample mass was approximately 5.00 g, and the temperature was maintained at a constant 20 °C.

2.2.6. Cement Paste Pore Structure

Mercury intrusion porosimetry was performed using the Micromeritics AutoPore IV 9610 (Norcross, GA, USA) instrument from the United States, which is one of the primary tools for testing the pore structure of cement paste. Prior to the pore structure analysis, the specimen was dehydrated in a vacuum oven at 105 °C for 4–5 h to eliminate capillary water and residual alcohol. Mercury intrusion porosimetry was then employed, where pressurized mercury was progressively forced into the accessible pores of the cement matrix while simultaneously recording both the intrusion pressure and cumulative mercury volume. This method has a test range of 7 nm to 200 μm.

3. Results and Discussion

3.1. Processing of Raw Materials

When grinding cement clinker with roller-ball mill, the granular clinker is crushed to a particle size less than 8 mm, and then it is ground and prepared by the laboratory roller press–mill–ball mill–powder concentrator system. Table 2 shows the specific surface area, sieve residue, and particle size of clinker and gypsum powder produced. The sample numbers in the table are represented by the raw material number followed by the D_{90} value (in μm).

Table 2. Specific surface area, sieve residue, and particle size of clinker and gypsum powder ground.

Numbering		C30	C27	C23	G
Specific Surface Area (m^2/kg)		368	422	498	174
Negative pressure sieve residue (%)	80 μm	0.0	0.0	0.0	4.1
	45 μm	0.0	0.0	0.0	43.4
Particle size (μm)	D_{10}	1.66	1.46	1.3	3.76
	D_{50}	10.96	9.15	7.13	31.06
	D_{90}	29.49	27.02	23.21	61.53

Figure 2 shows the particle size distribution of cement clinker. The frequency distribution of clinker particles ground in a roller press shows only one peak particle size and follows a skewed normal distribution.

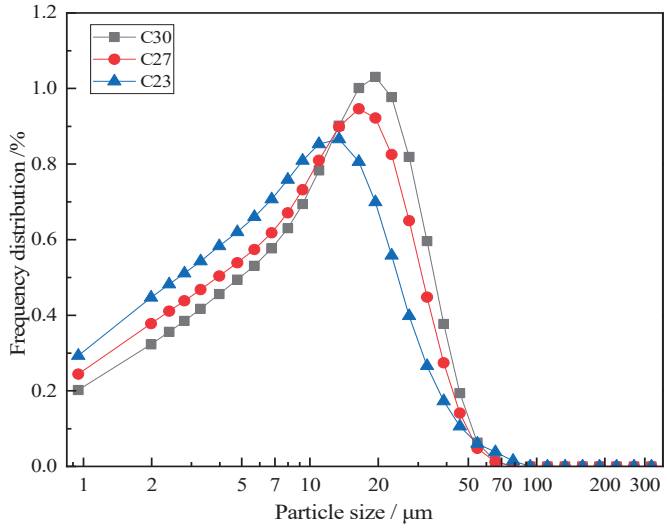

Figure 2. Frequency distribution of cement clinker powder.

By altering the powdering time and the rotational speed of the powder concentrator, five kinds of cinder powders with specific surface areas of approximately 106 m^2/kg, 210 m^2/kg, 260 m^2/kg, 300 m^2/kg, and 445 m^2/kg were obtained. Table 3 shows the specific surface area, sieve residue, and particle size distribution of the cinder. Figure 3 shows the laser particle size distribution of the cinder powder. The results indicate that the particle size distribution of the cinder powder exhibits only one peak particle size and follows a skewed normal distribution. The maximum observed particle diameter was below 200 μm, with the >45 μm fraction from negative pressure sieving showing an excellent correlation with laser diffraction measurements.

Table 3. Specific surface area, sieve residue, and particle size of the cinder.

Numbering		S91	S82	S69	S57	S33
Specific Surface Area (m^2/kg)		106	213	252	289	445
Negative pressure sieve residue (%)	80 μm	7.6	10.0	3.5	1.6	0.0
	45 μm	62.3	42.0	31.1	17.8	0.0
Particle size (μm)	D_{10}	23.86	4.36	4.07	3.52	2.39
	D_{50}	52.76	31.59	27.47	23.15	12.81
	D_{90}	90.96	81.73	68.92	57.44	33.13

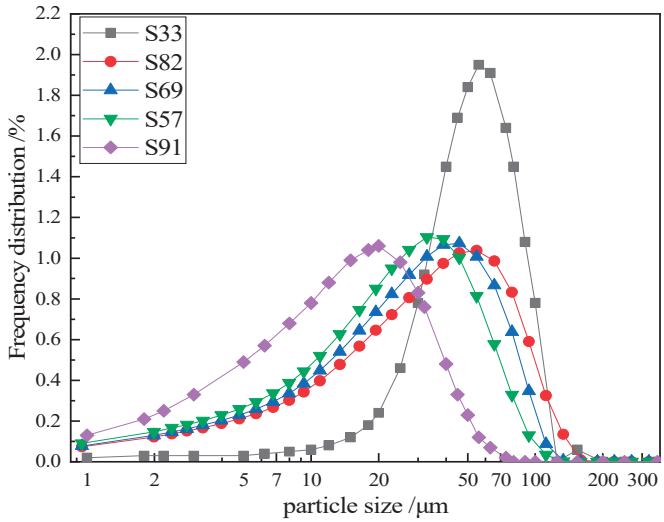

Figure 3. Frequency distribution of cinder powder particles.

The experiment used finer clinker powder, coarser cinder, and gypsum powder to create cement. The cinder powder was mixed at ratios of 15%, 20%, and 25%. The gypsum content in all cements was 5% across a total of 11 kinds of samples. The cement samples were labeled with the first letter of the clinker (C) + the D_{90} of the clinker powder + the first letter of the cinder (S) + the D_{90} of the cinder + the cinder content (in %). For example, C30S82-15 represents a mixture of clinker powder with a D_{90} of 30 μm and cinder powder with a D_{90} of 82 μm, with the cinder content being 15%.

3.2. Specific Surface Area and Fineness of Cement

Table 4 shows the specific surface area of cement prepared with clinker and cinder powders. When the cinder powder content was 15%, 20%, and 25%, the specific surface areas of the cements were 342–460, 337–448, and 332–438 m^2/kg, respectively. The content of particles larger than 45 μm was 6.01–8.47%, 7.27–10.19%, and 8.04–12.21%, respectively.

Table 4. Specific surface area of cement prepared with clinker and cinder powders.

No	The D_{90} (μm) of Clinker (C) Powder	The D_{90}/(μm) of Cinder (S) Powder	Cement Preparation Number	The Specific Surface Area of the Prepared Cement (m^2/kg)		
				15%S	20%S	25%S
1	30	82	C30S82	342	337	332
2		69	C30S69	348	343	342
3		57	C30S57	360	351	351
4		33	C30S33	379	387	391
5	27	82	C27S82	385	373	367
6		69	C27S69	387	384	371
7		57	C27S57	402	393	386
8	23	91	C23S91	433	414	386
9		82	C23S82	441	434	420
10		69	C23S69	447	445	424
11		57	C23S57	460	448	438

3.3. Uniformity Coefficient of Cement

Cementitious materials exhibit complex particle size distributions. Experimental data indicate that most cement systems conform to the Rosin–Rammler–Bennet (RRB)

distribution. The RRB equation's uniformity coefficient (n) effectively characterizes particle size distribution across varying fineness levels. The RRB equation is expressed as:

$$R(D_P) = 100\exp\left[-\left(\frac{D_P}{D_e}\right)^n\right] \quad (1)$$

where $R(D_p)$ represents the cumulative oversize percentage (%), D_p denotes the particle diameter (μm), and D_e is the characteristic particle size constant. The exponent n describes the distribution breadth, with smaller n values indicating broader distributions

Table 5 shows the uniformity coefficient (n) values for the blended cements. The results show that the n values for cinder-blended cements range from 0.932 to 1.132. The uniformity coefficient is smaller for blends of fine clinker (C23) and coarse cinder (S82), indicating a wider particle size distribution.

Table 5. The uniformity coefficient (n) values for blended cements.

No	The D_{90} (μm) of Clinker (C) Powder	The D_{90} (μm) of Cinder (S) Powder	Cement Preparation Number	The Uniformity Coefficient (n) of the Prepared Cement		
				15%S	20%S	25%S
1	30	82	C30S82	1.0417	1.0433	1.0358
2		69	C30S69	1.0685	1.0579	1.0489
3		57	C30S57	1.1078	1.1073	1.1202
4		33	C30S33	0.9978	0.9965	0.9962
5	27	82	C27S82	0.9858	0.9907	0.9866
6		69	C27S69	1.0203	1.0069	0.9989
7		57	C27S57	1.0519	1.0503	1.0472
8	23	91	C23S91	0.9881	0.9832	0.9812
9		82	C23S82	0.9340	0.9197	0.9191
10		69	C23S69	0.9398	0.9347	0.9526
11		57	C23S57	0.9851	0.9834	0.9823

3.4. Water Requirement of Standard Consistency for Cement

Figure 4 shows the water requirement of standard consistency for clinker-based blended cement pastes. Figure 5 shows the standard-consistency water requirement of cement pastes with added cinder. As the fineness of the cinder increases, the water requirement of the cement pastes increases. At the same cinder content, different blending methods result in significant differences in water requirements. The water requirement is relatively small for the blend of coarse cinder and clinker. The inverse correlation between cinder fineness and water demand matches findings from Pornmoon et al. [32], who noted a 15% increase in water demand for micronized cinder ($D_{50} \approx 4$ μm). However, our results demonstrate that coarser cinder ($D_{50} \approx 31$ μm) reduces the water requirement by 12–18%, surpassing the 8–10% improvement reported by Liew et al. [33] for GGBS blends. For the same cinder content, the cement with a C30S82 ratio generally has a smaller water requirement, while the cement with a C23S57 ratio has a larger water requirement.

Table 6. The minimum standard consistency water requirements of cinder-blended cement.

Cinder Dosage	Minimum Water Requirement of Standard Consistency (%)	Sample	Specific Surface Area (m^2/kg)	Uniformity Coefficient
15%	26.2	C23S91	433	0.988
20%	26.0	C23S91	414	0.983
25%	25.2	C23S91	386	0.981

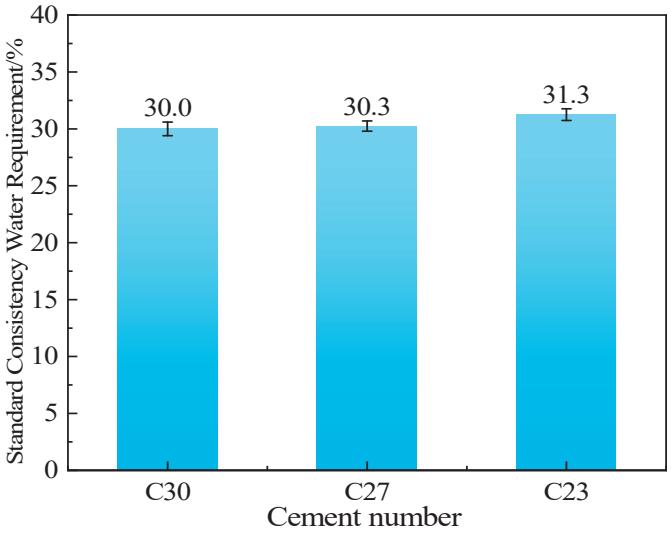

Figure 4. Water requirement of standard consistency for clinker-blended cement pastes.

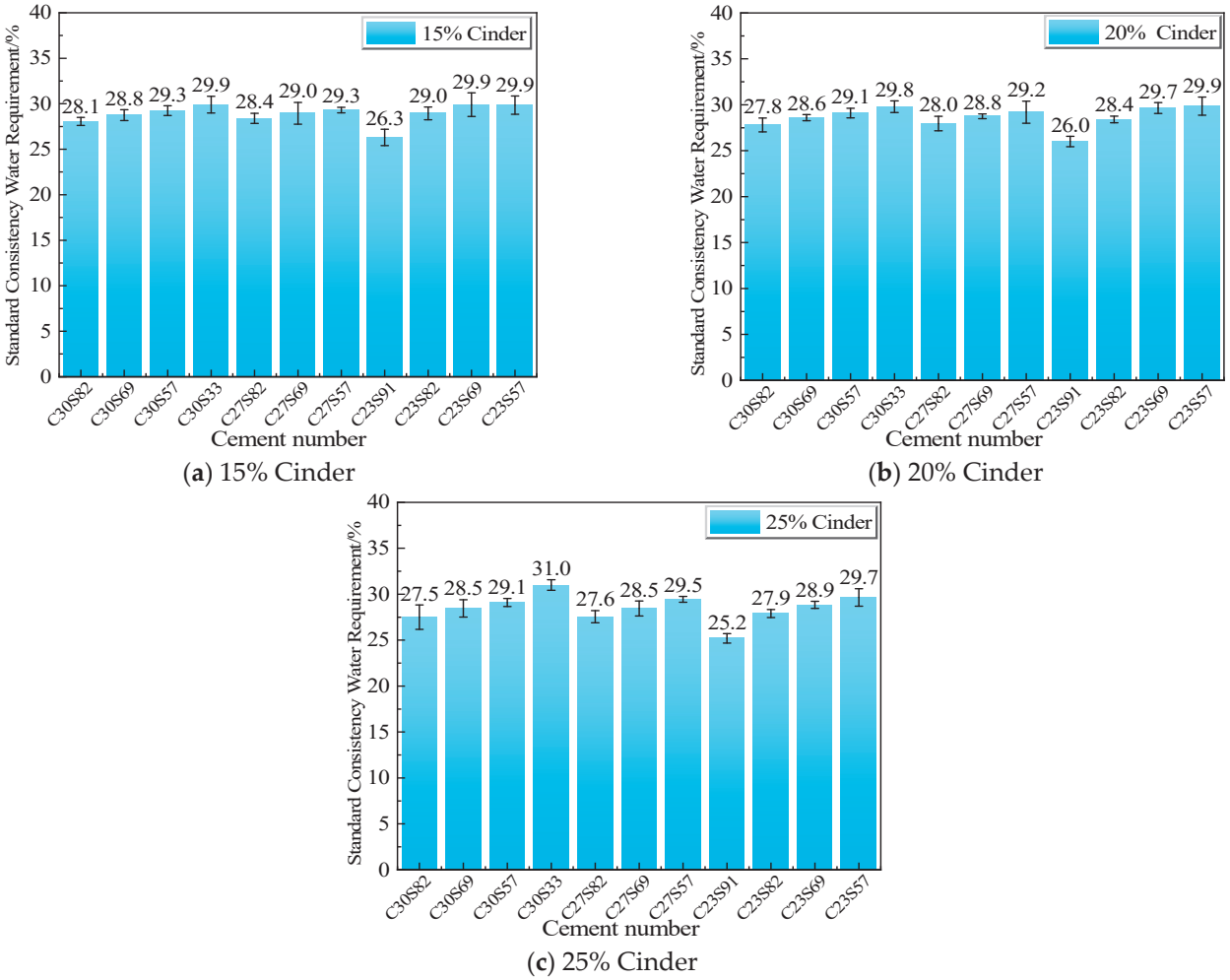

Figure 5. Water requirement of standard consistency for cement pastes blended with 15–25% cinder content.

Table 6 shows the minimum standard consistency water requirements for cement pastes blended with 15–25% cinder, along with their corresponding specific surface area and uniformity coefficient (n) values. The results indicate that, for the same amount of cinder, the blending of coarse cinder with coarse clinker results in a smaller water requirement.

When the amount of cinder is the same, the finer the clinker is, the greater the standard consistency water requirement is. Adding coarse cinder can effectively reduce the standard consistency water requirement of the mixed cement. Moreover, as the amount of cinder increases, the fineness decreases, and the effect of reducing the standard consistency water requirement of the mixed cement becomes more significant.

The fineness of the cement clinker has a significant influence on the standard water requirement of cement. After cement and water are mixed, the water must first fill the gaps between the particles and wet the surfaces of the particles to form a water film on the surface, enabling relative sliding between particles and thus achieving better fluidity. The finer the cement clinker particles are, the larger the specific surface area is, and the contact area with water increases significantly. This leads to an increase in the amount of water required to cover the particle surfaces and fill the gaps, resulting in an increase in the standard water requirement. Generally, the larger the particles are, the thicker the water film must be to achieve better fluidity. The powder particles with a larger n value require a thicker water film [25]. As shown in Table 5 and Figure 5, for samples with similar specific surface areas, as the n-value increases, the packing void ratio increases, requiring more free water to fill these voids, thus increasing the standard consistency water requirement. Therefore, when the amount of cinder added is the same, the higher the uniformity coefficient is, and the greater the standard consistency water requirement will be.

3.5. Strength of Compound Cement Mortar

The strength results of clinker with a D_{90} of 30, 27, and 23 μm (with 5% desulfurized gypsum) are shown in Table 7. The 28-day flexural strengths are 8.6, 8.5, and 8.2 MPa, and the 28-day compressive strengths are 59.0, 60.3, and 59.2 MPa, respectively. The cement fineness has little effect on the 28-day compressive strength.

Table 7. Flexural and compressive strength of clinker.

No	Clinker Number	Compressive Strength (MPa)		Flexural Strength (MPa)	
		3d	28d	3d	28d
1	C30	6.3	8.6	36.3	59.0
2	C27	6.7	8.5	37.9	60.3
3	C23	6.6	8.2	40.5	59.2

Figure 6 shows the strength of cement with 15–25% cinder. The differences in the 28-day compressive strengths of cement mixed with 15%, 20%, and 25% cinder are 4.5, 5.8, and 4.7 MPa, respectively. In the cement mixtures with different fineness levels in their clinker and slag, the strength of C23S91 always remains relatively low under different production volumes. This indicates that the slag particles should not be too coarse. However, in the C23 specimens, the influence of different slag fineness levels on the 28-day compressive strength is relatively small. The limited strength gain from fine cinder corroborates the findings of Carvalho et al. [25], who found that recycled powder fineness beyond 300 m^2/kg had diminishing returns. This suggests that grinding coal slag finely cannot effectively enhance the strength of cement but instead will significantly increase the water requirement of the standard consistency. Therefore, considering both strength and water requirements, the specific surface area of coal slag should be controlled at around 210 m^2/kg.

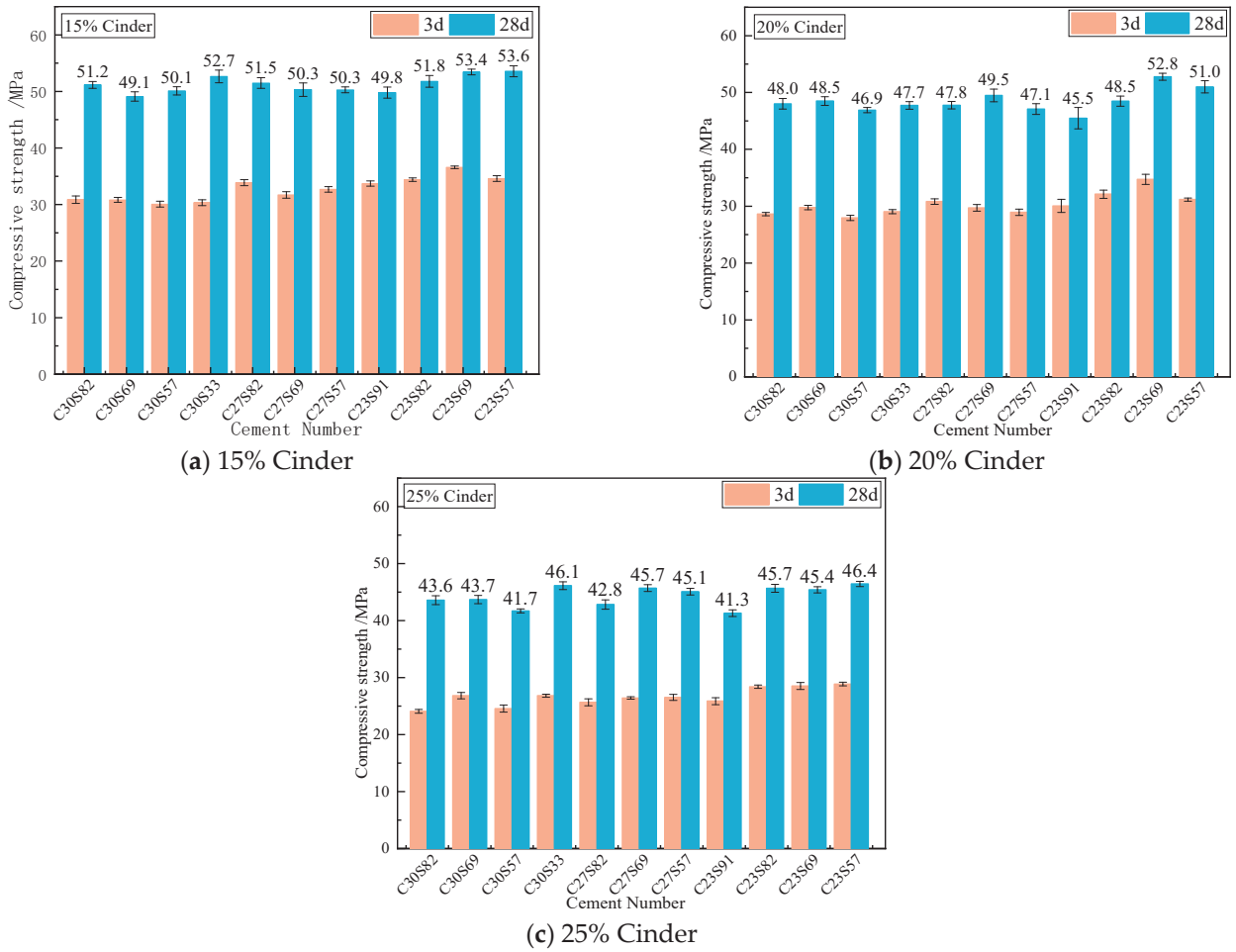

(**a**) 15% Cinder (**b**) 20% Cinder

(**c**) 25% Cinder

Figure 6. Compressive strength of cement mortar with 15–25% cinder.

Table 8 shows the cement samples with the best comprehensive performance. By comparing the fluidity and mechanical properties of cement, the optimal mixture ratio of cement with the best comprehensive performance is selected. The selection criterion for the best comprehensive performance is mainly based on the 28-day compressive strength, with the water content of standard consistency as a secondary indicator. Specifically, the 28-day compressive strength of each group of specimens is ranked from high to low. If the compressive strengths are similar, the standard consistency water content is further compared to select the one with lower water content to optimize workability and economy. Finally, the material with the best comprehensive performance should have both high mechanical properties and low water consumption. The combination of cement with 15–25% cinder content that achieves the best overall performance is all C23S82.

Table 8. Cement sample with the best comprehensive performance.

Cinder Dosage	The Sample with the Best Comprehensive Performance	28-Day Compressive Strength (MPa)	Water Requirement of Standard Consistency (%)
15%	C23S82	51.8	29.0
20%	C23S82	48.5	28.4
25%	C23S82	45.7	27.9

3.6. Hydration and Microstructure of Cement Paste

3.6.1. Hydration Products of Cement

Figure 7 shows the XRD spectra of cement pastes with 20% cinder after curing for 28 days. After 28 days of hydration, the cement paste primarily contains C2S, C3S, and calcium hydroxide. The diffraction peaks of C_2S and C_3S in the cement paste are relatively strong, indicating that some unhydrated clinker still remains after 28 days of hydration.

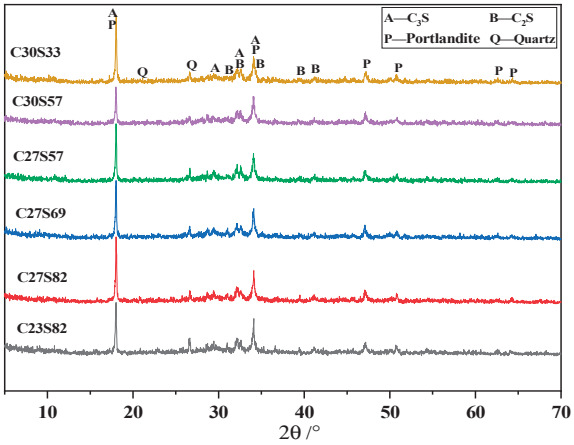

Figure 7. XRD pattern of the 28-day curing of cement pastes with cinder compound.

3.6.2. Compound Cement Hydration Heat

Figure 8 shows the hydration heat of pure cement. The finer the cement clinker, the earlier the second exothermic peak appears and the higher the heat release rate. The cement samples C23, C27, and C30 achieved maximum heat release rates of 4.7 mW/g, 4.0 mW/g, and 2.8 mW/g, respectively. The cumulative heat release after 72 h reached 312 J/g, 302 J/g, and 257 J/g, respectively. The earlier second exothermic peak in C23 blends reflects the accelerated nucleation of C-S-H due to higher clinker surface area. However, coarse cinder (S82) mitigates excessive heat release by diluting reactive sites, reducing cracking risk. This synergy—fine clinker providing nucleation centers and coarse cinder acting as a thermal buffer—explains the optimal performance of C23S82.

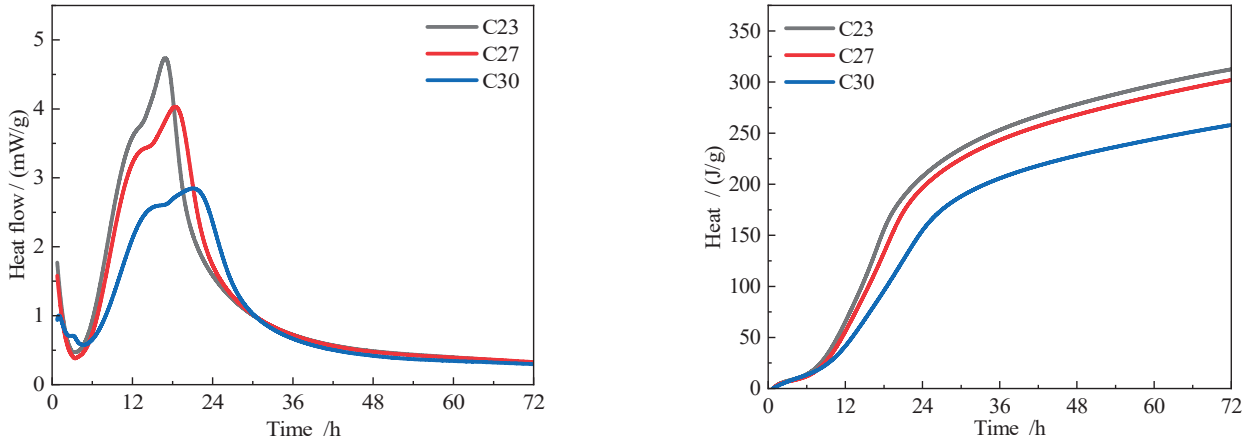

Figure 8. Hydration exothermic curves of cement.

Figure 9 shows the hydration heat of cement with 20% cinder. The experimental results show that the second exothermic peak of the cement primarily occurs around 24 h, and the incorporation of slag significantly reduces the heat release rate of this peak. Comparing samples with different slag contents, the second exothermic peak of C30S33

appears slightly earlier than that of C30S57, though the cumulative heat release at 72 h for both samples shows no significant difference. This suggests that fine slag promotes the hydration reaction of blended cement in the early stages (within 24 h) but has a minimal impact on the hydration process in the later stages (after 72 h). This phenomenon may be related to the micro-filler effect of the slag and the time-dependent activation of its latent reactivity. The pore refinement in C23S82 (Table 9) arises from two mechanisms: (1) fine clinker fills inter-cinder voids (physical effect), and (2) its rapid hydration generates secondary C-S-H that seals capillary pores (chemical effect). Coarse cinder's lower surface area limits water adsorption, preserving workability without compromising densification, as observed in similar studies [32,33].

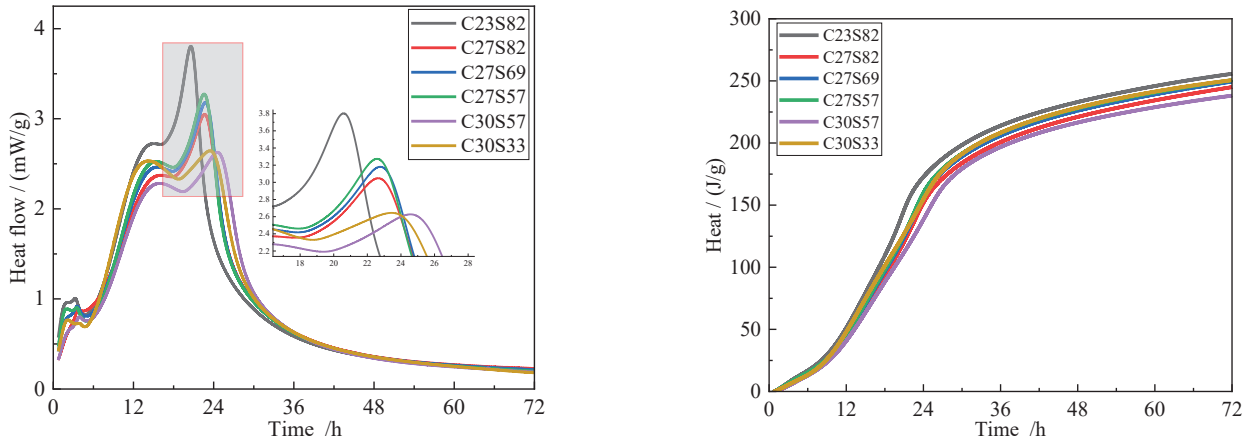

Figure 9. Hydration exothermic curves of cement blended with 20% cinder.

Table 9. Porosity and pore size distribution of cinder cement pastes.

Sample	Age (d)	Porosity (%)	Pore Size Distribution (%)				
			<10 nm	10–20 nm	20–50 nm	50–200 nm	>200 nm
C23S69	1	27.41	13.42	9.20	28.61	28.52	20.26
	3	25.90	15.48	8.30	25.78	26.30	24.14
	28	21.96	10.00	5.01	26.11	34.60	24.27
C30S69	1	30.80	11.22	9.98	33.40	24.53	20.88
	3	26.72	14.96	10.46	39.45	12.08	23.06
	28	22.82	14.00	4.99	34.14	22.07	24.81
C30S57	1	29.96	9.29	9.27	24.20	32.43	24.81
	3	25.82	14.71	9.54	27.99	23.83	23.93
	28	22.66	13.27	4.09	26.69	27.84	28.11
C30S33	1	29.15	14.62	10.37	34.99	24.12	15.91
	3	26.47	16.78	9.56	34.86	15.03	23.76
	28	21.83	14.27	5.73	34.68	20.41	24.91

3.6.3. Compound Cement Hole Structure

The mechanical strength, shrinkage behavior, and pore structure of cement pastes are closely related. Previous research classifies the pore size (d) of cement paste into four distinct categories based on their detrimental effects: pores below 20 nm, which are deemed harmless; pores ranging from 20 to 50 nm, classified as minimally harmful; pores between 50 and 200 nm, considered harmful; and pores exceeding 200 nm, which are highly harmful. Table 9 shows the porosity of hardened cement paste mixed with 20% cinder. As cement fineness and cinder fineness increase, the porosity at 28 days continuously decreases. The pores of 0 to 50 nm gradually increase, while the pores of >50 nm gradually decrease.

Specifically, the paste of C30S33 exhibits the lowest total porosity. Compared to C30S69, its porosity decreases from 22.82% to 21.83%, with a reduction of only 1%. This result indicates that, although fine slag can optimize the pore structure, its effect on reducing total porosity is limited, likely only contributing a mild physical filling effect. Figure 10 shows the pore size distribution of the cement paste with different clinker fineness and 20% cinder incorporation. The results show that the peak of the pore distribution in the cement paste appears in the 10–200 nm range. The most significant pore size in the cement paste is between 40–50 μm, exhibiting a distinct unimodal distribution characteristic.

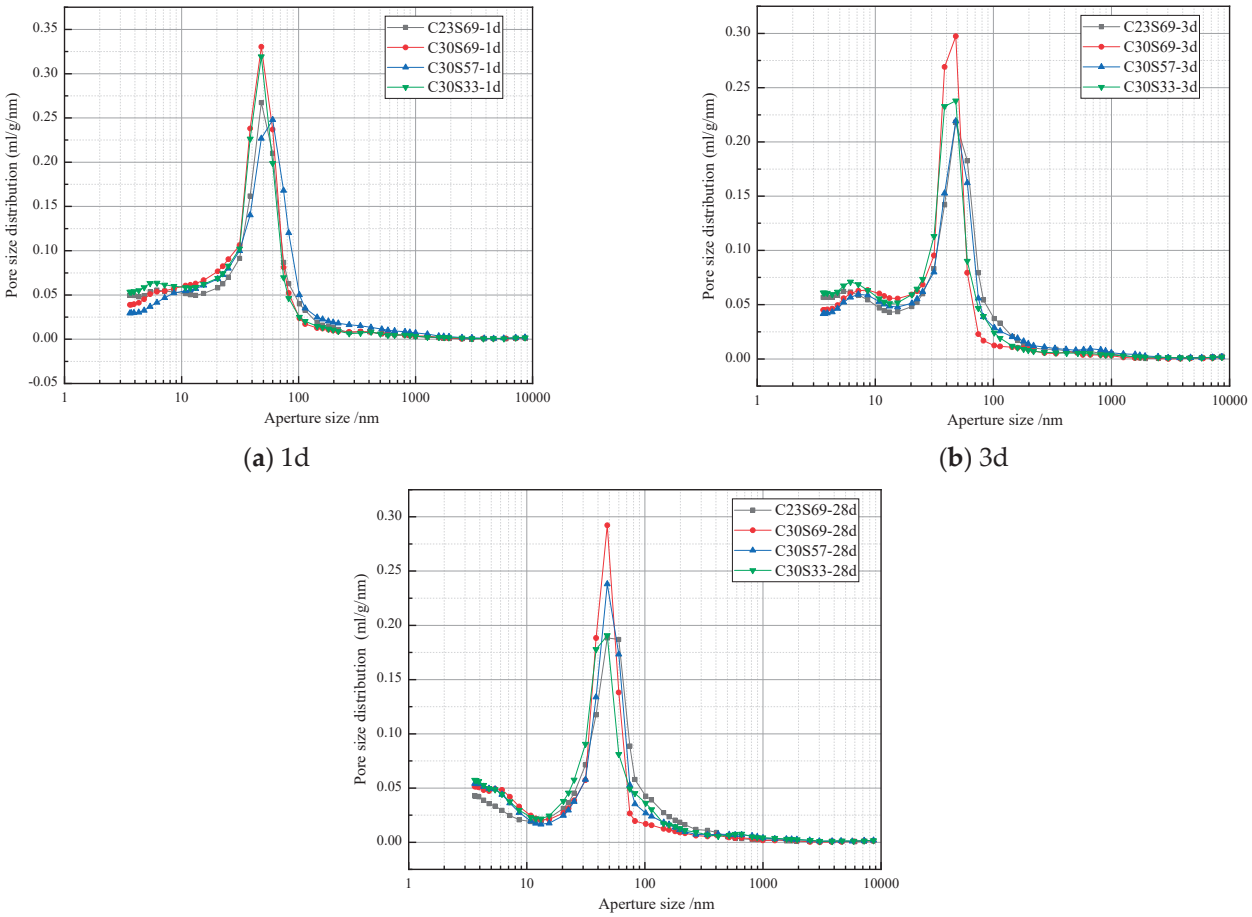

(**a**) 1d

(**b**) 3d

(**c**) 28d

Figure 10. Pore size distribution of cinder cement pastes (1d, 3d, 28d).

3.6.4. The Specific Microscopic Structure of Cement

Figure 11 shows BSEM images of C27S69 cement pastes at 1, 28, and 120 days of hydration. At 1 day, the hydration products around cinder particles appear loose and porous, indicating limited early reactivity. By 28 days, the microstructure becomes denser, with reduced porosity due to C-S-H gel formation. At 120 days, further densification occurs, and unhydrated clinker particles diminish significantly, confirming the long-term role of coarse cinder as a stable microaggregate. These observations align with the measured reduction in harmful pores (>50 nm) from 30.8% (1d) to 22.8% (28d) in Table 9.

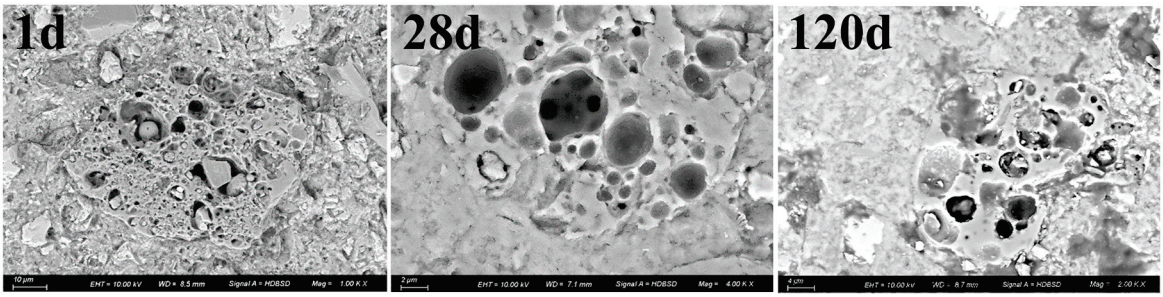

Figure 11. BSEM image of C27S69 cement pastes after being hydrated for 1d, 28d and 120d.

Figure 12 (C30S57 paste) reveals a compact ITZ between cinder particles and the cement matrix, with no visible cracks or voids. This contrasts with typical ITZs in fine-cinder blends (e.g., C30S33), where high water demand often leads to microcracking. The dense ITZ explains the superior mechanical performance of C30S57 (48.5 MPa at 20% cinder) compared to finer-cinder mixes, as it ensures effective stress transfer.

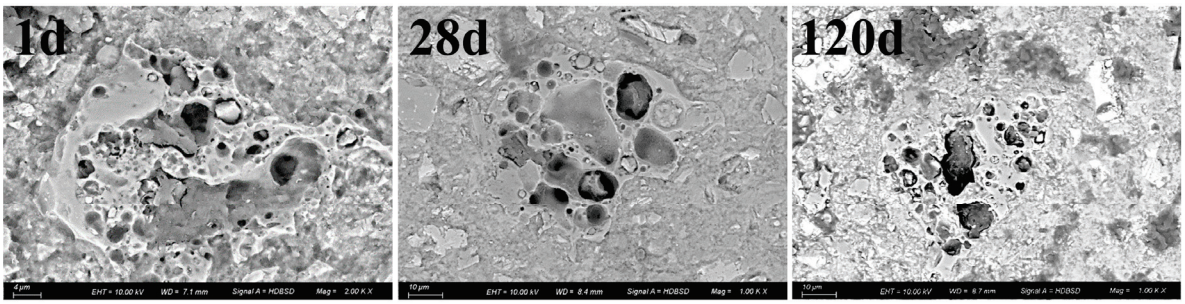

Figure 12. BSEM image of C30S57 cement pastes.

The EDS line scanning in Figure 13 (C27S69 at 120 days) shows uniform Ca and Si distribution around cinder particles, confirming their integration into the hydration products. Notably, Al and Fe signals from cinder remain localized, indicating minimal chemical dissolution. This supports the conclusion that coarse cinder primarily acts as a physical filler, while fine clinker drives hydration.

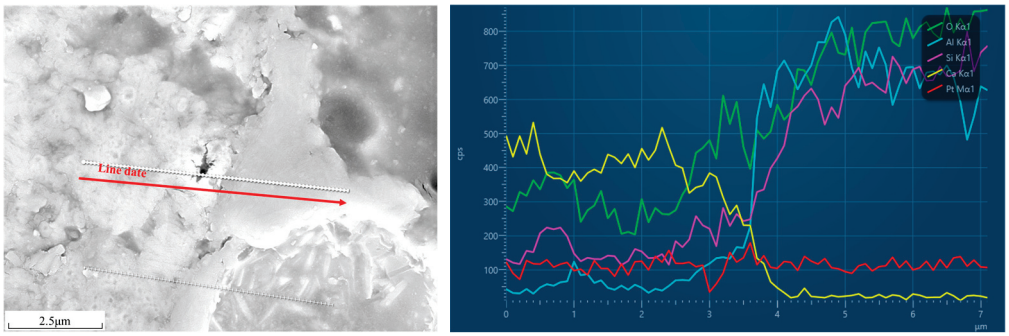

Figure 13. BSEM/EDS line scanning of C27S69 cement pastes after being hydrated for 120d.

4. Conclusions

This study systematically investigated the influence of clinker–cinder particle gradation on the properties of blended cement through controlled grinding and mixing strategies. The key findings and their implications are summarized as follows:

1. Blending fine clinker (specific surface area: 498 m^2/kg) with coarse cinder (210 m^2/kg) achieved the best balance between mechanical strength and workability. While finer

cinder increased water demand by 15–20%, it provided negligible strength improvements (<5%). This highlights the importance of prioritizing coarser cinder to reduce water requirements without sacrificing performance.

2. Coarse cinder ($D_{90} \approx 91$ μm) reduced the standard consistency water requirement by 12–18% compared to fine cinder ($D_{90} \approx 33$ μm), owing to its lower surface area and improved particle packing efficiency. This effect was amplified at higher cinder contents (25%), suggesting its suitability for high-volume SCM applications.
3. Cement blended with fine clinker and coarse cinder hydrates faster within the first day and reaches a higher degree of hydration, which is more beneficial for pore filling. Due to the initial packing voids of the particles, the porosity of the C30S33 blended cement paste after 28 days of curing was relatively low. Although the hydration heat results show that fine cinder benefits the hydration of cement, the effect is limited, and the contribution to strength is not significant.

This research provides an actionable framework for optimizing blended cements: (1) maximize clinker fineness to drive hydration, (2) limit cinder fineness to ~210 m^2/kg to control water demand, and (3) target a uniformity coefficient (n) of 0.93–0.98 for optimal packing.

Author Contributions: Methodology, R.S., L.N., B.C., X.Z., W.L. and M.D.; Software, R.S., L.N., B.C. and X.Z.; Validation, R.S., D.H., W.C., L.N. and W.L.; Formal analysis, R.S., L.N. and B.C.; Investigation, R.S., W.C., L.N. and X.Z.; Resources, D.H.; Data curation, D.H. and W.C.; Writing—original draft, R.S., X.Z. and M.D.; Writing—review & editing, R.S., W.L. and M.D.; Supervision, M.D. All authors have read and agreed to the published version of the manuscript.

Funding: This research was funded by Hefei Cement Research & Design Institute Co., Ltd. and to the Natural Science Foundation of Jiangsu Province (Grant No. BK20240563).

Institutional Review Board Statement: Not applicable.

Informed Consent Statement: Not applicable.

Data Availability Statement: The data presented in this study are available on request from the corresponding author. The data are not publicly available due to privacy.

Conflicts of Interest: Authors Dexiang Huang and Wenju Cai were employed by the company Hefei Cement Research & Design Institute Corp., Ltd., and CNBM (Hefei) Powder Technology Equipment Corp., Ltd. The remaining authors declare that the research was conducted in the absence of any commercial or financial relationships that could be construed as a potential conflict of interest.

References

1. Zhang, M.; Lv, T.; Deng, X.; Dai, Y.; Sajid, M. Diffusion of China's coal-fired power generation technologies: Historical evolution and development trends. *Nat. Hazards* **2019**, *95*, 7–23. [CrossRef]
2. Jayaranjan, M.L.D.; van Hullebusch, E.D.; Annachhatre, A.P. Reuse options for coal fired power plant bottom ash and fly ash. *Rev. Environ. Sci. Bio/Technol.* **2014**, *13*, 467–486. [CrossRef]
3. Orozco, C.; Babel, S.; Tangtermsirikul, S.; Sugiyama, T. Comparison of environmental impacts of fly ash and cinder as cement replacement materials for mass concrete and the impact of transportation. *Sustain. Mater. Technol.* **2024**, *39*, e00796.
4. Li, Y.; Liu, Y.; Gong, X.; Nie, Z.; Cui, S.; Wang, Z.; Chen, W. Environmental impact analysis of blast furnace cinder applied to ordinary Portland cement production. *J. Clean. Prod.* **2016**, *120*, 221–230. [CrossRef]
5. Carmona, M.O.; Paules, J.G.; Catalán, J.S.; Pousa, L.F.; Beltrán, R.A.; Sanz, F.Q. Recycling power plant cinder for use as aggregate in precast concrete components. *Mater. Constr.* **2010**, *60*, 99–113. [CrossRef]
6. Mohammed, S.A.; Koting, S.; Katman, H.Y.B.; Babalghaith, A.M.; Abdul Patah, M.F.; Ibrahim, M.R.; Karim, M.R. A Review of the Utilization of Coal Bottom Ash (CBA) in the Construction Industry. *Sustainability* **2021**, *13*, 8031. [CrossRef]
7. Ashish, D.K.; Verma, S.K.; Singh, J.; Sharma, N. Strength and durability characteristics of bricks made using coal bottom and coal fly ash. *Adv. Inconcrete Constr.* **2018**, *6*, 407–422.

8. Andreev, V.; Bryukhan, F. Some prospects for the use of ash and cinder wastes of coal power plants for production of building materials. *Resour. Conserv. Recycl.* **2010**, *54*, 1060–1066.
9. Siddique, R. Utilization of coal combustion by-products in sustainable construction materials. *Resour. Conserv. Ercycling* **2010**, *54*, 1060–1066. [CrossRef]
10. Argiz, C.; Menéndez, E.; Moragues, A.; Sanjuán, M.Á. Recent Advances in Coal Bottom Ash Use as a New Common Portland Cement Constituent. *Struct. Eng. Int.* **2014**, *24*, 503–508. [CrossRef]
11. Skoko, B.; Babić, D.; Marović, G.; Papić, S. Environmental radiological risk assessment of a coal ash and cinder disposal site with the use of the ERICA Tool. *J. Environ. Radioact.* **2019**, *208–209*, 106018. [CrossRef] [PubMed]
12. Zhang, Y.M.; Jia, L.T.; Mei, H.; Cui, Q.; Zhang, P.G.; Sun, Z.M. Fabrication, microstructure and properties of bricks fired from lake sediment, cinder and sewage sludge. *Constr. Build. Mater.* **2016**, *121*, 154–160. [CrossRef]
13. Moreno-Navarro, F.; Sol, M.; Rubio-Gámez, M.C.; Ramírez, A. Reuse of thermal power plant cinder in hot bituminous mixes. *Constr. Build. Mater.* **2013**, *49*, 144–150. [CrossRef]
14. Fedorova, N.V.S.D. The possibility of using of the thermal power plants ash and cinder wastes in the Rostov region road constructing. *Ekol. Promyshlennogo Proizbodstva* **2014**, *3*, 9–15.
15. Singh, M.; Siddique, R. Strength properties and micro-structural properties of concrete containing coal bottom ash as partial replacement of fine aggregate. *Constr. Build. Mater.* **2014**, *50*, 246–256. [CrossRef]
16. Singh, M.; Siddique, R. Effect of coal bottom ash as partial replacement of sand on workability and strength properties of concrete. *J. Clean. Prod.* **2016**, *112*, 620–630. [CrossRef]
17. Singh, M.; Siddique, R. Effect of coal bottom ash as partial replacement of sand on properties of concrete. *Resour. Conserv. Recycl.* **2013**, *72*, 20–32. [CrossRef]
18. Rafieizonooz, M.; Mirza, J.; Salim, M.R.; Hussin, M.W.; Khankhaje, E. Investigation of coal bottom ash and fly ash in concrete as replacement for sand and cement. *Constr. Build. Mater.* **2016**, *116*, 15–24. [CrossRef]
19. Kim, H.K.; Lee, H.K. Use of power plant bottom ash as fine and coarse aggregates in high-strength concrete. *Constr. Build. Mater.* **2011**, *25*, 1115–1122. [CrossRef]
20. Qian, J.; Shi, C.; Wang, Z. Activation of blended cements containing fly ash. *Cem. Concr. Res.* **2001**, *31*, 1121–1127. [CrossRef]
21. Li, D.; Shen, J.; Chen, Y.; Cheng, L.; Wu, X. Study of properties on fly ash-slag complex cement. *Cem. Concert. Res.* **2000**, *30*, 1381–1387. [CrossRef]
22. Aperador, W.; Duque, J.; Delgado, E. Comparison of electrochemical properties between portland cement, ground slag and fly ash. *Int. J. Electrochem. Sci.* **2016**, *11*, 3755–3766. [CrossRef]
23. Wang, Q.; Yan, P.Y.; Yang, J.W. Comparison of hydration properties between cement-GGBS-fly ash blended binder and cement-GGBS-steel cinder blended binder. *J. Wuhan Univ. Technol. Mater. Sci. Ed.* **2014**, *29*, 273–277. [CrossRef]
24. Liu, S.H.; Li, Q.L.; Song, J.W. Study on the grinding kinetics of copper tailing powder. *Powder Technol.* **2018**, *330*, 105–113. [CrossRef]
25. Qiao, L. Optimal particle size distribution of cement and its evaluation methods. *Cement* **2001**, *8*, 1–5.
26. Hu, R.; Lilin Wang, S. Optimization of cement particle gradation. *Cement* **2005**, *8*, 15.
27. Zhang, D. Discussion on the optimal particle size distribution of cement components. *Cement* **2008**, *6*, 24.
28. Kupwade-Patil, K.; Al-Aibani, A.F.; Abdulsalam, M.F.; Mao, C.; Bumajdad, A.; Palkovic, S.D.; Büyüköztürk, O. Microstructure of cement paste with natural pozzolanic volcanic ash and Portland cement at different stages of curing. *Constr. Build. Mater.* **2016**, *113*, 423–441. [CrossRef]
29. de Carvalho, J.M.F.; Schmidt, W.; Kuehne, H.C.; Peixoto, R.A.F. Influence of high-charge and low-charge PCE-based superplasticizers on Portland cement pastes containing particle-size designed recycled mineral admixtures. *J. Build. Eng.* **2020**, *32*, 101515. [CrossRef]
30. Wang, Q.; Shi, M.X.; Yang, J. Influence of classified steel cinder with particle sizes smaller than 20 μm on the properties of cement and concrete. *Constr. Build. Mater.* **2016**, *123*, 601–610.
31. Bui, D.D.; Hu, J.; Stroeven, P. Particle size effect on the strength of rice husk ash blended gap-graded Portland cement concrete. *Cem. Concr. Compos.* **2005**, *27*, 357–366. [CrossRef]
32. Pormmoon, P.; Sanit-in, P.K.; Jaturapitakkul, C.; Ban, C.C.; Tangchirapat, W. Strength, durability, and heat development characteristics of high-performance concrete containing ground coal bottom ash with low and high calcium. *Case Stud. Constr. Mater.* **2024**, *21*, e03845. [CrossRef]
33. Liew, J.J.; Cheah, C.B.; Khaw, K.L.P.; Siddique, R.; Tangchirapat, W. Blended cement and mortar with various low-calcium ground coal bottom ash content: Engineering characteristics, embodied carbon and cost analysis. *Constr. Build. Mater.* **2024**, *425*, 135987. [CrossRef]
34. *JY/T 0587-2020*; General Rules of Polycrystalline X-Ray Diffraction Method. Ministry of Education of PRC: Beijing, China, 2020.
35. *GB/T 176-2017*; Methods for Chemical Analysis of Cement. Ministry of Education of PRC: Beijing, China, 2017.

36. *GB/T 8074-2008*; Testing Method for Specific Surface of Cement—Blaine Method. Ministry of Education of PRC: Beijing, China, 2008.
37. *GB/T 1346-2024*; Test Methods for Water Requirement of Standard Consistency. Setting Time and Soundness of the Portland Cement, Ministry of Education of PRC: Beijing, China, 2024.
38. *GB/T 17671-2021*; Test Method of Cement Mortar Strength (ISO Method). Ministry of Education of PRC: Beijing, China, 2021.

Disclaimer/Publisher's Note: The statements, opinions and data contained in all publications are solely those of the individual author(s) and contributor(s) and not of MDPI and/or the editor(s). MDPI and/or the editor(s) disclaim responsibility for any injury to people or property resulting from any ideas, methods, instructions or products referred to in the content.

materials

MDPI

Article

Effect of Combined MgO Expansive Agent and Rice Husk Ash on Deformation and Strength of Post-Cast Concrete

Feifei Jiang [1], Yijiang Xing [2], Wencong Deng [2], Qi Wang [2], Jialei Wang [1,*] and Zhongyang Mao [3,*]

[1] School of Civil Engineering, Nantong Institute of Technology, Nantong 226000, China; 999620140019@just.edu.cn
[2] China State Construction Engineering (Macau) Co., Ltd., Macau 999078, China; xingyijiang@cohl.com (Y.X.); dengwencong@hotmail.com (W.D.); wangqi_2019@cohl.com (Q.W.)
[3] College of Materials Science and Engineering, Nanjing Tech University, Nanjing 211800, China
* Correspondence: wangjl@nit.zju.edu.cn (J.W.); mzy@njtech.edu.cn (Z.M.)

Abstract: This study investigates the effects of the combined addition of MgO expansive agent (MEA) and rice husk ash (RHA) on the performance of concrete. Results show that MEA absorbs water and competes with superplasticizers for adsorption, reducing early-age fluidity. In the later stages, its reaction with RHA generates M-S-H gel, accelerating slump loss. At early ages (up to 7 days), due to the slow hydration of MEA and partial replacement of cement, fewer hydration products are formed. Additionally, the pozzolanic reaction of RHA has not yet developed, resulting in the low early strength of concrete. In the later stages, $Mg(OH)_2$ fills pores and enhances compactness, while the pozzolanic reaction of RHA further optimizes the pore structure. The internal curing effect also provides the moisture needed for continued MEA hydration, significantly improving later-age strength. Moreover, in the post-cast strip of a tall building, the internal curing effect of RHA ensures the effective shrinkage compensation by MEA under low water-to-cement ratio conditions. The restraint provided by reinforcement enhances the pore-filling effect of $Mg(OH)_2$, improving concrete compactness and crack resistance, ultimately boosting long-term strength and durability.

Keywords: MgO expansion agent; post pouring strip; shrinkage cracks; tall buildings; rice husk ash

1. Introduction

With the increasing performance demands on concrete in modern construction, improving the durability, crack resistance, and strength of concrete has become a major focus of research. Cement concrete tends to shrink due to factors such as hydration heat [1] and drying shrinkage [2], leading to shrinkage cracks that compromise its long-term durability. This issue is particularly prominent in high-strength concrete with low water-to-binder ratios, where the risk of shrinkage cracking is significantly elevated [3–6].

In the foundation slab construction of tall buildings, post-cast strips serve as a critical structural measure to accommodate and release differential settlement. However, these strips are usually subjected to high-strength design requirements, low water-to-binder ratios, dense reinforcement, and severe external restraint. As a result, they experience significant autogenous and drying shrinkage, making them highly susceptible to early-age cracking [7]. Once cracks form, they not only reduce the structural integrity and water tightness, but also accelerate the ingress of harmful ions, leading to steel corrosion, durability degradation, and shortened service life [8–11].

Due to its advantages such as low water demand [12], stable hydration products [13,14], and controllable expansion behavior [15,16], MgO expansive agent (MEA) has been widely used for shrinkage compensation in concrete structures such as dams and airport pavements. However, some researchers have raised concerns regarding the potential reduction in compressive strength caused by the use of MEA. They argue that, while MEA hydration compensates for shrinkage through macroscopic expansion, it also increases the porosity of concrete, negatively impacting its strength. Wang [17] reported that replacing 8% of cement with MEA increased the porosity of concrete and reduced its compressive strength by 17.2%, 16.4%, and 14.6% at 3, 28, and 180 days, respectively. While such strength loss may be acceptable for structures with low strength requirements, such as dams, it is not tolerable in tall buildings, where concrete strength is a critical design parameter. Any reduction in strength could prevent the project from meeting acceptance standards, making this the first major limitation of MEA in high-rise construction.

Moreover, in large-volume high-strength concrete structures, moisture is rapidly consumed by cement hydration, and external curing water cannot effectively penetrate into the interior of the foundation slab. Under these conditions, whether MEA can continue to hydrate remains uncertain. Liu [18] found that curing humidity significantly affects MEA's hydration and expansion behavior. When the relative humidity falls below 80%, the MEA hydration becomes insufficient, reducing its shrinkage-compensating ability and resulting in net shrinkage of the concrete. Therefore, enhancing the degree of MEA hydration represents the second key challenge for its application in tall buildings.

To address the dual challenges of strength reduction and the insufficient hydration of MEA in mass concrete, our team innovatively proposed the combined use of MEA and rice husk ash (RHA). RHA has a highly porous internal structure and strong water-retention capability. It gradually releases stored water over time, thereby increasing the internal humidity [19] and promoting the sustained hydration of MEA under sealed or low-permeability conditions. A comprehensive study was conducted through laboratory tests on workability, shrinkage deformation, internal relative humidity, and compressive strength to investigate the synergistic effects of MEA and RHA on concrete performance. In addition, field applications were carried out to verify the effectiveness of this material system under real engineering conditions. The results demonstrated that the combined use of MEA and RHA effectively mitigates shrinkage cracking while maintaining high strength, offering a practical and durable solution for post-cast segments in the foundations of tall buildings.

2. Materials and Experimental Methods

2.1. Raw Materials and Mix Proportions

Cement: PO 42.5 grade Portland cement produced by Macau Cement Factory (Macao, China).

Coarse aggregate: Crushed granite with a continuous gradation of 5–20 mm, apparent density of 2575 kg/m^3.

Fine aggregate: River sand with a fineness modulus of 2.7.

MEA: High-activity MEA produced by Jiangsu Sobute New Materials Co., Ltd. (Nanjing, China), with an activity of 110 s measured by the citric acid method.

Water-reducing agent: Master Glenium SKY produced by Master Builders Solutions (Beachwood, OH, USA), a polycarboxylate-based high-performance water reducer.

RHA: Supplied by Shijiazhuang Xuhan New Materials Technology Co., Ltd. (Shijiazhuang, China), with a density of 2.21 g/cm^3 and a specific surface area of 23.9 m^2/g as measured by the BET method.

The main chemical components of RHA are listed in Table 1, expressed in wt.%. And the SiO_2 content in the rice husk ash is 78.25%. As shown in Figure 1, the XRD pattern of rice husk ash was obtained using a PANalytical X'Pert Pro MPD diffractometer produced by PANalytica (Eindhoven, Netherlands) with CuKα radiation, operating at 40 kV voltage and 40 mA current. The scan was conducted at a speed of 4°/min over a 2θ range of 5°–65°. The phase identification was performed using the PDF2-2004 ICDD database. SiO_2 is primarily present in the form of cristobalite, with characteristic crystalline peaks appearing at 2θ = 21.98°, 28.44°, 31.46°, and 36.08°, corresponding to crystal planes 101, 111, 102, and 200, respectively. The crystallinity of the rice husk ash, calculated using Jade software (MDI Jade 6.0), is 47.73%.

Table 1. Chemical composition of rice husk ash/%.

Chemicals	SiO_2	Al_2O_3	Fe_2O_3	CaO	MgO	SO_3	Na_2O	K_2O	Cl	LOI
RHA	78.25	0.33	0.28	0.933	0.395	0.143	0.053	0.052	0.016	19.548

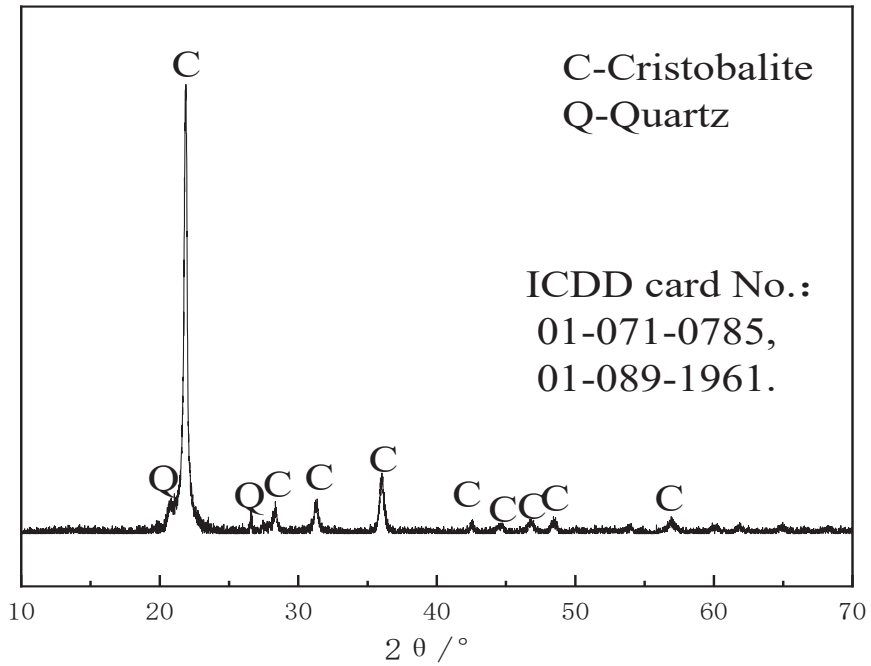

Figure 1. XRD pattern of rice husk ash.

The detailed concrete mix design is shown in Table 2. The initial concrete mix proportion was provided by the design institute and could not be modified at later stages. During the structural design phase, the required concrete strength was determined by the design institute, based on which the initial mix ratio was specified. This mix proportion was reviewed and confirmed by both the supervision unit and the material supplier, and therefore no changes were allowed. Consequently, the performance of the concrete was adjusted by incorporating MEA and RHA. To investigate the effects of different dosages of MEA and RHA on the performance of concrete, MEA and RHA were used as internal admixtures to replace cement by mass. The replacement ratios were 8% and 2%, corresponding to 36 kg and 9 kg, respectively [20]. The detailed concrete mix proportions are shown in Table 2, and four types of concrete were prepared: plain concrete (REF), concrete with 8% MEA (MC), concrete with 2% RHA (RC), and concrete with 8% MEA and 2% RHA (MR).

Table 2. Concrete mix design/kg·m^{-3}.

No.	Cement	Coarse Aggregate	Fine Aggregate	Water	Water Reducer	MEA	RHA
REF	450	980	740	172	5.7		
MC	414	980	740	172	5.7	36	
RC	441	980	740	172	5.7		9
MR	405	980	740	172	5.7	36	9

2.2. Experimental Methods

2.2.1. Laboratory Tests

(1) Autogenous Deformation Test

The autogenous deformation test was conducted under constant temperature and sealed conditions. A VWS-15 vibrating wire strain gauge produced by Nanjing Genan Industrial Co., Ltd. (Nanjing, China) was used. The gauge has a gauge length of 150 mm and a strain measurement range from −1500 με to 1500 με. The deformation was calculated using Equation (1):

$$\varepsilon = k\Delta F + (b - a)\Delta T \quad (1)$$

where ε is the autogenous deformation of concrete, 10^{-6}/F; k is sensitivity of the strain gauge, 10^{-6}/F; ΔF is the change in the measured value in real time relative to the base value of the vibrating modulus, F; b is temperature correction coefficient of the strain gauge, 10^{-6}/°C; a is linear thermal expansion coefficient of concrete, 10^{-6}/°C; ΔT is temperature change, °C.

PVC plastic buckets were used as casting molds, each with a diameter of 250 mm and a height of 300 mm. Freshly mixed concrete was poured into the buckets, compacted on a vibrating table until no air bubbles surfaced, then sealed with epoxy resin to prevent moisture exchange with the air. The sealed molds were then placed in a constant-temperature curing chamber at 20 °C. All casting and preparation were completed within 20 min. Finally, the strain of concrete with different mix proportions was recorded every 30 min to study its autogenous deformation. Detailed testing procedures are shown in Figure 2.

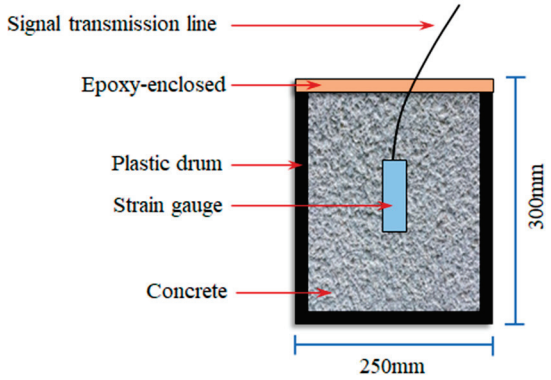

Figure 2. Autogenous deformation test of concrete.

(2) Compressive Strength Test

The compressive strength test was conducted in accordance with the method described in GB/T 50081-2002 [21]. Cubic specimens with a side length of 150 mm were used, with three specimens cast for each type of sample and their average taken as the test result. When the concrete cubes reached the specified curing age, they were removed from curing, and surface moisture was wiped off with a towel before performing the compressive strength

test. Three specimens were tested for each mix proportion, and the final result was taken as the average of the three specimens.

2.2.2. On-Site In Situ Tests

(1) Project Overview

The construction project is a tall building located in Macau. The development includes six towers, each 149.90 m tall with 50 floors and an additional basement level. The site area is approximately 20,000 m^2, with a total building area of about 330,000 m^2. The foundation consists of pile caps supported by bored piles and prestressed concrete piles, which are then connected via a bottom slab. Large-diameter bored piles are used for the tower foundations, while the podium foundations use high-strength prestressed pipe piles.

Due to the heavy self-weight of the main tower, the foundation experiences significantly more settlement than the podium, and the bearing capacity of the reclaimed land foundation is relatively low. If left unaddressed, differential settlement between the main tower and the podium may lead to additional internal stresses, which can cause cracks, tilting, and affect the building's safety and durability. Therefore, multiple post-cast settlement joints were installed between the main tower and the podium. The thickness of the post-cast joints is the same as that of the bottom slab, both being 1 m. Concrete is poured into the post-cast joint only after the differential settlement between the tower and podium has stabilized, thereby reducing the additional stress caused by settlement differences.

As shown in Figure 3, the post-cast joint serves as an important structural measure for releasing settlement deformation and is typically located at the junction between the main tower and the podium. The plan layout of the post-cast strip is shown in Figure 4. The top view of the high-rise building is shown in Figure 5. However, due to the heat of hydration and moisture evaporation, the concrete in the post-cast joints tends to shrink, leading to several potential problems. Firstly, shrinkage-induced cracks compromise structural integrity, reduce durability, and may even affect the mechanical performance of the joint. Secondly, shrinkage cracks can form water channels. In reclaimed land environments with high groundwater levels, this increases the risk of water ingress and threatens structural safety. Finally, cracks may lead to reinforcement corrosion. To compensate for the shrinkage of the post-cast joint concrete, a composite mixture of 8% MEA and 2% RHA was used in this project. The specific mix proportions are shown in Table 2.

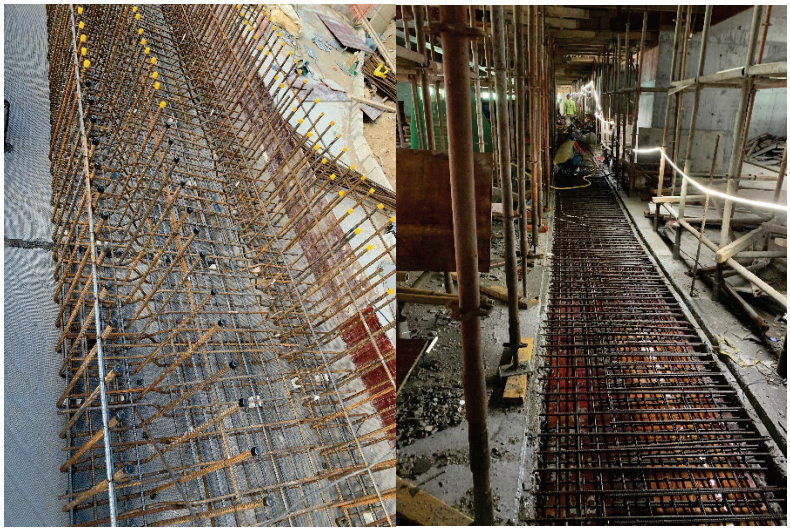

(**a**) (**b**)

Figure 3. Construction of the settlement post-cast joint: (**a**) Rebar binding; (**b**) Formwork and rebar installation.

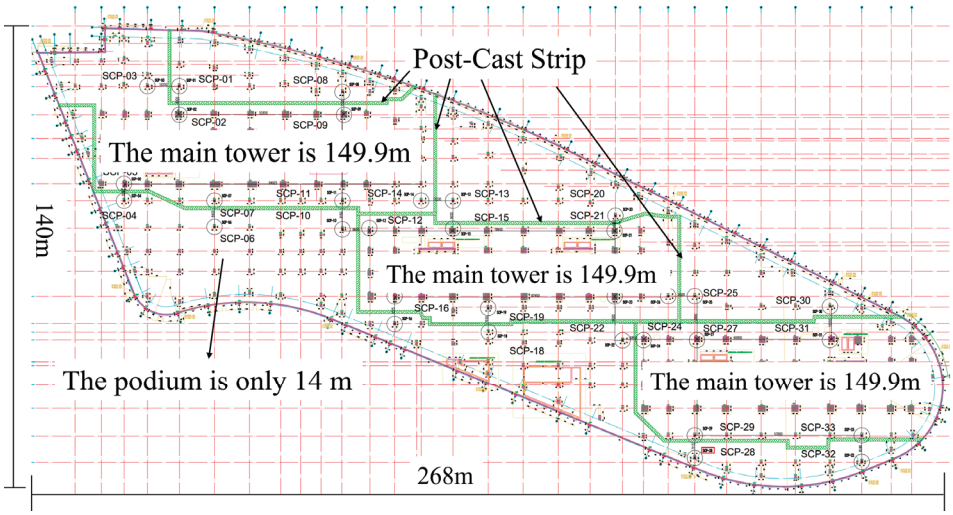

Figure 4. Schematic plan view of the post-cast strip layout.

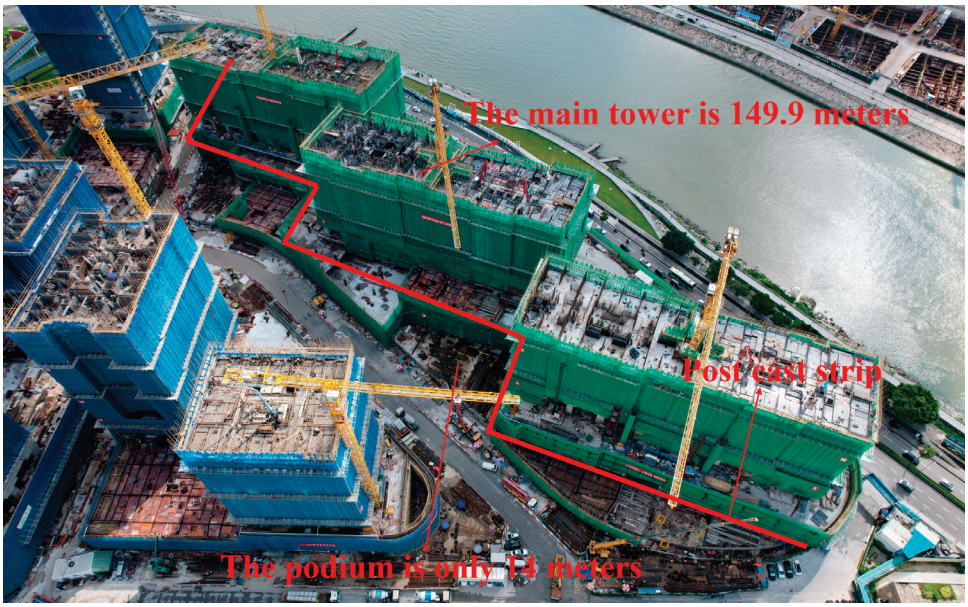

Figure 5. Top view of high-rise buildings.

(2) Concrete Pouring

As shown in Figure 6, in order to study the temperature, deformation, and humidity changes in the concrete, three strain gauges and hygrometers were embedded at different heights of the bottom slab. Strain Gauge No. 1 was placed near the surface (50 mm from the top surface) to measure the deformation of surface concrete. Strain Gauge No. 2 was embedded at the mid-depth (1/2 h = 650 mm) to measure the deformation in the center. Strain Gauge No. 3 was located near the bottom (50 mm from the bottom surface) to capture the deformation at the base.

As a comparison, a 150 cm concrete cube (without MEA and RHA) was cast and placed at ground level (to ensure it was in the same environmental conditions as the slab concrete with MEA). Strain Gauge No. 4 was used to measure its deformation. At the same positions, three hygrometers were also installed to monitor internal humidity changes in the concrete. The hygrometer was provided by Nanjing Genan Industrial Co., Ltd., with a measurement range of 10–100% RH and a sensitivity of 0.2% RH. The openings were sealed with rubber stoppers to prevent moisture exchange, ensuring accurate internal humidity measurements.

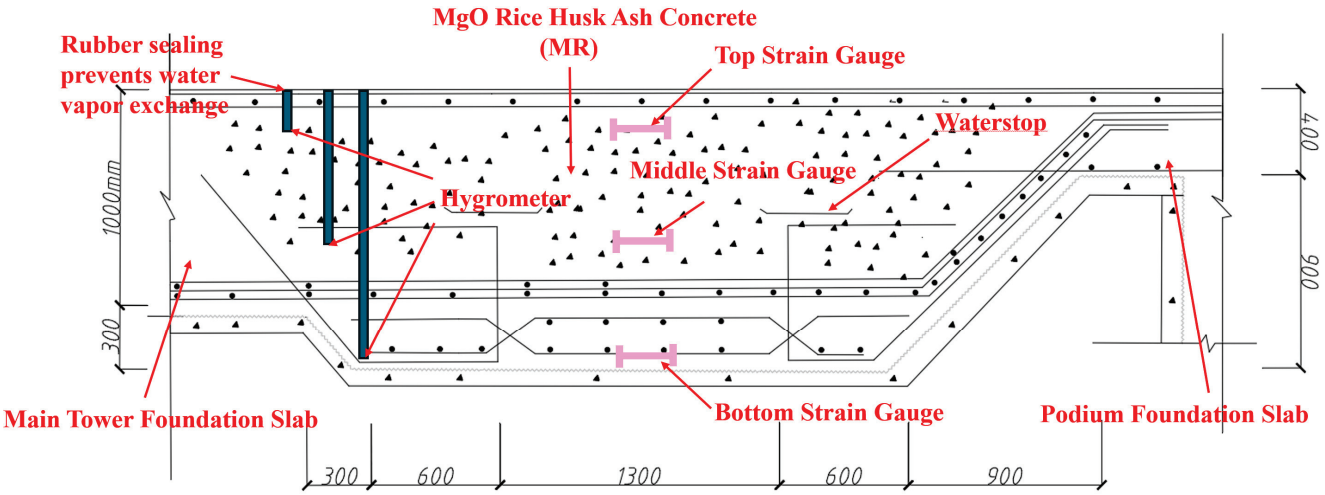

Figure 6. Post-cast concrete pouring and on-site testing.

To assess the degree of MEA hydration under real construction conditions, three reserved holes with a diameter of 80 mm and depths of 50 mm, 650 mm, and 1250 mm were made during the mass concrete casting. These holes were used to place neat paste specimens containing MEA and RHA, in order to study the effects of actual field conditions (temperature and humidity) on MEA hydration.

(3) Evaluation of the Hydration Degree of MEA

Neat paste specimens containing MEA and RHA were placed into the reserved holes in the concrete slab. After reaching the specified curing age, approximately 50 mg of each sample was taken. Hydration was stopped by soaking the samples in absolute ethanol for 3 days. The samples were then dried in a vacuum oven at 80 °C and ground into powder using an agate mortar.

The degree of hydration of MEA was determined using differential thermal analysis (DTA). The heating rate was 10 °C/min, with a temperature range from 30 °C to 1000 °C. Nitrogen gas was used as the protective atmosphere during heating. The hydration degree of MgO was calculated using Equation (2) [22]:

$$H_{\mathrm{MgO}} = \frac{40 \times Massloss_{\Delta T}}{D \times 18 \times (1 - Massloss_{950\ ^\circ\mathrm{C}})} \quad (2)$$

where H_{MgO} is the degree of MgO hydration, %; $Massloss_{\Delta T}$ is the mass loss percentage corresponding to the endothermic peak of $Mg(OH)_2$, %; $Massloss_{950\ ^\circ\mathrm{C}}$ is the mass loss percentage at 950 °C, %; and D is the dosage of MgO in the paste at the initial time, %.

(4) On-Site Strength Testing

During the post-casting concrete, standard concrete cube specimens (50 mm in side), without MEA and RHA, were cast simultaneously as control samples. To ensure the reliability of the data, three cubic specimens were cast, and their average value was taken as the compressive strength. At the specified curing ages, the compressive strength of the in-place concrete slab was tested using the rebound method, following the JGJ/T 23-2011 [23]. The compressive strength of the control cube specimens was tested according to the GBT 50107-2013 [24]. This approach was used to study the influence of MEA and RHA on concrete strength under actual construction conditions, in order to evaluate the feasibility of using MEA in mass concrete foundations.

(5) Pore Structure

Pore structure analysis was carried out using mercury intrusion porosimetry (MIP). For sample preparation, the neat paste specimens retrieved from the reserved holes in the slab were crushed in small fragments that were approximately 2 mm in size. These blocks were soaked in absolute ethanol for 24 h to terminate the hydration of cement and MEA. After ultrasonic cleaning, the samples were dried in a vacuum oven at 60 °C for 12 h and then sealed in airtight bags. For testing, two dried fragments were selected for MIP to analyze the pore structure, in order to assess the effects of MEA and RHA on the pore characteristics of the concrete.

3. Results and Discussion

3.1. Workability of Concrete

The workability of concrete incorporating both MEA and RHA is shown in Figure 7. The addition of MEA significantly reduced the fluidity of the concrete. There are three main reasons for this effect at the early stage. First, the water absorption of MEA affects the wetting and dispersion of cement particles. MEA has a large specific surface area and strong hydrophilic properties. When the mixing water enters the paste, MEA will preferentially absorb part of the free water, reducing the amount of free water around the cement particles, which prevents the cement particles from being fully wetted and dispersed evenly [25]. Second, MEA particles release Mg^{2+} ions during hydration. These cations interact with the negatively charged surfaces of cement particles, reducing the electrostatic repulsion between the particles and making it easier for them to cluster together. The flocculation effect is enhanced, and the flowability of the cement particles decreases, leading to the higher viscosity of the paste [26]. Third, MEA particles have a certain adsorptive capacity and will compete with cement particles for the adsorption of polycarboxylate superplasticizers, reducing the effective concentration of the superplasticizer on the cement surface and weakening the dispersion effect [27].

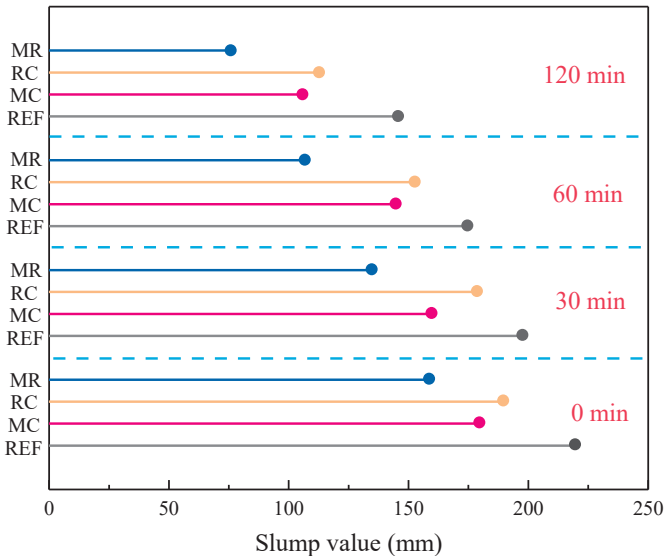

Figure 7. The effect of MEA and RHA on the workability of concrete.

In the later stages of hydration, MEA forms $Mg(OH)_2$, which interacts with other hydration products such as C-S-H gel to form a network structure. This increases the yield stress of the paste and further reduces fluidity [28]. Since the hydration rate of MEA is slower than that of cement, the viscosity effect of $Mg(OH)_2$ is not significant at early stages. However, as the hydration rate of MEA increases, its negative impact on

flowability becomes more pronounced, which is the main reason for the significant slump loss observed after 120 min in MEA-containing concrete.

When both MEA and RHA are used together, the SiO_2 in RHA can react with $Mg(OH)_2$ in the alkaline environment to form M-S-H gel through a pozzolanic reaction. The reaction equation is as follows:

$$SiO_2 + Mg(OH)_2 \rightarrow \text{M-S-H (hydrated magnesium silicate)} \quad (3)$$

The formation of M-S-H gel further reduces the free water, causing the paste to gradually thicken over time and accelerating the slump loss. This leads to a reduction in slump to 76 mm at 120 min, making pumping difficult. Therefore, from a construction perspective, the composite concrete should be completed within 120 min after mixing (including the total time for transportation and pouring).

3.2. Deformation Performance of Concrete

Figure 8 illustrates the deformation performance of concrete at different ages. It can be observed that ordinary concrete undergoes rapid shrinkage during the early stage (0–12 days). This shrinkage is primarily due to the reaction between cement and water, which produces hydration products with reduced volume. Since the hydration reaction occurs very quickly at early ages, the shrinkage increases rapidly, reaching −153 με at 12 days.

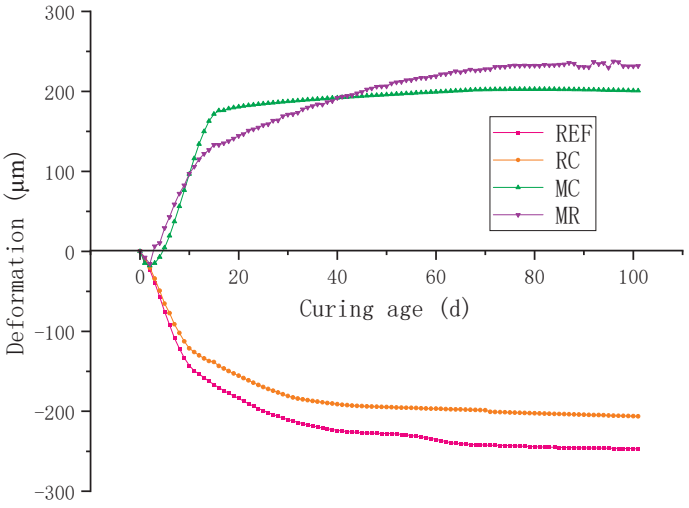

Figure 8. Deformation of concrete at different ages.

Subsequently, the cement hydration reaction slows down, and the shrinkage rate of the concrete decreases significantly. By 80 days, the shrinkage gradually increases to −244 με. After 80 days, the cement hydration is essentially complete, the shrinkage rate significantly decreases, and the shrinkage tends to stabilize, showing only slight fluctuations, eventually stabilizing at around −248 με. When such shrinkage is restrained, tensile stress develops inside the concrete, which is a major cause of early-age cracking in high-strength concrete [29].

With the addition of RHA alone, shrinkage is reduced, and the time for shrinkage to stabilize is shortened from 80 days to about 70 days. The first reason is that RHA is rich in SiO_2, which undergoes a secondary hydration reaction with $Ca(OH)_2$ to form the C-S-H gel, improving the compactness of the concrete and its resistance to shrinkage. The second reason is that the porous structure of RHA enables moisture redistribution. When free water is consumed, a relative humidity gradient forms inside the concrete, inducing

RHA to release moisture, which effectively reduces autogenous shrinkage. Additionally, due to the internal curing effect of RHA, the later hydration of cement is accelerated, thus shortening the overall shrinkage period [30].

When 8% MEA is added alone, the expansive behavior of MEA compensates for the shrinkage of the concrete. However, due to the intense early hydration of cement, significant early-age shrinkage still occurs, and since MEA hydrates more slowly than cement, a shrinkage of −15 με is observed at 0–2 days. As MEA gradually hydrates and expands, the overall deformation of the concrete shifts from shrinkage to expansion. At 15 days, the volume rapidly increases to 176 με. Thereafter, the expansion rate significantly decreases, and by 75 days, the concrete slowly expands to 201 με. After that, the expansion and shrinkage of the concrete essentially reach equilibrium, and the volume remains stable with no significant fluctuations [12,31].

When both 8% MEA and 2% RHA are added, the pozzolanic reaction of RHA consumes part of the calcium hydroxide, lowering the alkalinity of the pore solution and thus suppressing the hydration rate of MEA [12]. As a result, the early expansion is lower than that of the MEA-only mix. However, in the later stage, RHA's internal curing effect provides additional water for MEA hydration, leading to increased expansion. At 100 days, the expansion is 14.9% greater than that of the MEA-only mix, reaching 231 με.

3.3. Mechanical Properties of Concrete

The compressive strength of concrete at various curing ages is shown in Figure 9. In the early stages (3 and 7 days), the partial replacement of cement with MEA results in a reduction in the formation of cement hydration products (such as C-S-H gel), thereby decreasing the early strength. Moreover, the hydration rate of MEA is significantly slower than that of cement, and it does not sufficiently hydrate in the early stages to contribute to strength development, further limiting the early strength gain. As a result, the compressive strength of the MEA-containing concrete (MC) is 9.4% and 4.3% lower than that of the reference mix (REF) at 3 and 7 days, respectively. As the curing time increases, MEA gradually hydrates to form $Mg(OH)_2$, which precipitates and fills the pores within the concrete. This reduces porosity and enhances the compactness of the cement paste, thereby improving the later-age strength. By 28 days, the compressive strength of the MC mix exceeds that of REF by 2.7%.

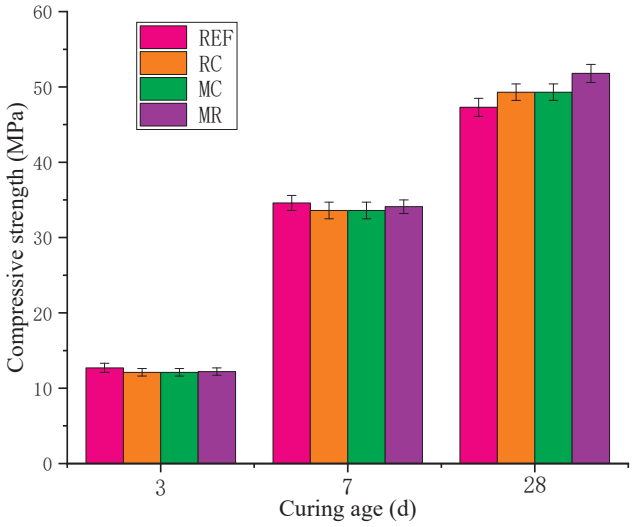

Figure 9. Compressive strength of concrete at different ages.

In ordinary cement systems, early strength primarily comes from hydration products such as C-S-H gel and $Ca(OH)_2$. However, RHA itself lacks early hydration activity

and does not directly produce strength-contributing substances, leading to reduced early strength [32]. Consequently, the 3-day and 7-day compressive strengths of the RHA-containing mix (RC) are 4.7% and 2.9% lower than those of the reference mix (REF), respectively. As the curing age increases, cement hydration gradually releases $Ca(OH)_2$, which accelerates the pozzolanic reaction of RHA. This reaction forms additional C-S-H gel, improving the density and strength of the cement paste. In addition, RHA particles can act as nucleation sites to promote a more uniform distribution of C-S-H gel, reduce large pore structures, and enhance later-age strength [33]. By 28 days, the strength of the RC mix exceeds that of REF by 4.2%.

When both MEA and RHA are used together, in the early stages (3 and 7 days), both the pozzolanic reaction of RHA and the hydration of MEA proceed relatively slowly, resulting in limited contributions to early strength. At 3 days, the compressive strength is 3.9% lower than REF. However, in the later stage (28 days), as the concrete continues to harden, cement hydration consumes water and causes internal drying. RHA, with its water storage capability, gradually releases moisture during this period [34], providing a favorable environment for continued MEA hydration, thus promoting the formation of $Mg(OH)_2$. Moreover, $Mg(OH)_2$ can react with SiO_2 in RHA to form magnesium silicate hydrate (M-S-H) [35]. The formation of M-S-H gel further optimizes the pore structure, enhances the compactness of the paste, reduces porosity, and significantly improves the long-term strength and durability of the concrete. As shown in Figure 10, it is precisely the synergistic effect of RHA and MEA that reduces the porosity and increases the density of the concrete, resulting in a 28-day compressive strength that is 9.5% higher than that of REF.

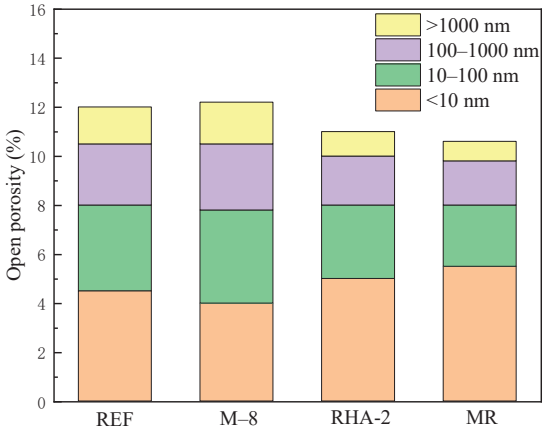

Figure 10. Pore structure of concrete at 28 days.

3.4. Field Test Results and Analysis

(1) Engineering Challenges of Post-Cast Concrete in Tall buildings

The post-cast concrete segments in tall buildings present several significant engineering challenges that necessitate advanced material solutions. First, these segments are massive in both area and thickness, leading to considerable temperature drop shrinkage and drying shrinkage after casting, which significantly increases the risk of shrinkage-induced cracking.

Second, the load conditions are highly complex. The post-cast segment must withstand a combination of static loads from the upper structure and dynamic loads such as vehicular traffic, thereby imposing stringent requirements on the compressive strength of the concrete.

Third, the project is located in a coastal reclamation area with a high groundwater level. As a critical part of the foundation system, the post-cast segment must provide

excellent waterproofing to prevent groundwater infiltration and ensure the long-term safety of the structure.

Fourth, the durability requirements are exceptionally high. Given the extended service life of tall buildings, the foundation concrete must possess excellent durability and crack resistance to withstand long-term mechanical and environmental stresses.

Fifth, the unique geological conditions pose additional structural demands. The project is situated in a reclaimed area with relatively soft foundation soil. Due to the significant difference in self-weight between the main tower and the podium, the post-cast segment experiences substantial bending moments after differential settlement. As a result, it is essential to address not only shrinkage issues but also the strength demands imposed by this complex stress state.

Lastly, high workability is required. As shown in Figure 3, dense reinforcement is arranged in the post-cast segment to resist the heavy load, resulting in very narrow rebar spacing. This hinders concrete flow and makes workability a critical property during construction.

In summary, the post-cast concrete in this project must simultaneously meet strict requirements for strength, workability, and shrinkage crack resistance under challenging engineering and environmental conditions. These factors underscore the necessity of employing an optimized material system—such as the combined use of MEA and RHA—to ensure both performance and durability.

(2) Measured Temperature of Concrete Slab

The temperature variation of the post-casting concrete after casting is shown in Figure 11. In the early stage, due to the rapid hydration and exothermic reaction of cement, the temperature rose sharply, reaching its peak at 2 days. Owing to the poor thermal conductivity of concrete and the large thickness of the slab, heat in the core was difficult to dissipate, with the maximum core temperature reaching 52.2 °C. In contrast, the surface layer could exchange heat with the atmosphere more efficiently, resulting in a faster heat dissipation and a peak temperature about 20% lower than the core, at 43.6 °C.

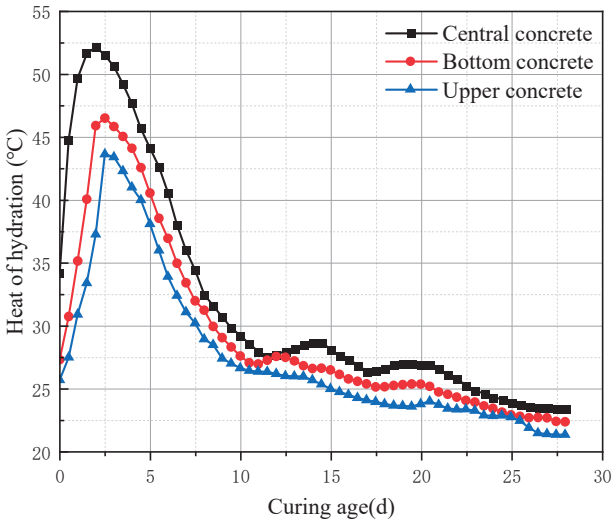

Figure 11. Measured temperatures of concrete at different locations.

In the middle stage, as cement continued to be consumed, the rate of heat release from hydration decreased, and the temperature dropped rapidly to 24 °C by day 15. At this point, thermal shrinkage led to significant volume contraction. Under the combined restraint of the foundation, formwork, and the early-cooled surface concrete, substantial

tensile stress developed inside the concrete, which is one of the main causes of cracking in mass concrete [36].

In the later stage, as the hydration reactions of the cementitious materials were essentially completed, no further heat was generated. The slab temperature gradually aligned with the ambient temperature, fluctuating slightly in response to environmental changes.

(3) Measured Deformation of the Concrete Slab

Figure 12 presents the measured deformation of concrete at different heights. In ordinary concrete, the volume continuously decreased after casting, with a shrinkage of 75 με observed by day 10. After adding the expansive agent, the MEA-induced expansion compensated for the shrinkage, and all three monitored positions exhibited varying degrees of expansion.

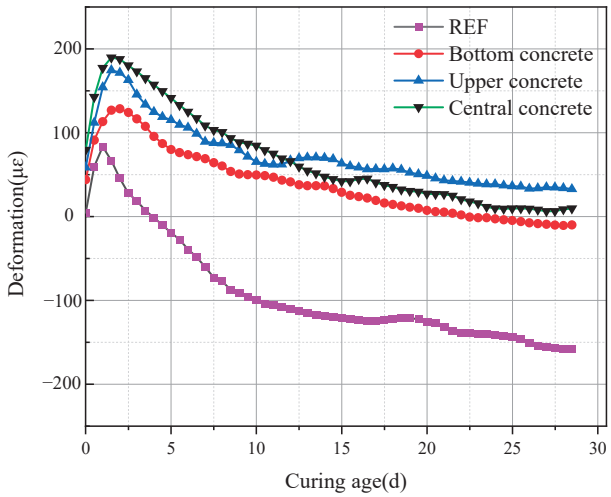

Figure 12. Measured deformation of concrete at different locations.

At the core, due to higher temperatures, the hydration rate of MEA was greater, resulting in significant early expansion. However, since the concrete had not yet fully hardened at this stage, part of the expansion was ineffective, leading to lower total long-term expansion at the core compared to the surface. At the surface, early temperature and hydration rate were lower; yet in the later stage, water supplementation through mist spraying promoted the sustained hydration of MEA, resulting in greater expansion than that observed at the core.

(4) Relative Humidity Inside Concrete at Different Positions

Figure 13 illustrates the internal relative humidity of concrete at different locations within the post-cast strip. After casting, hydration gradually consumed internal water, leading to a drop in internal humidity. The surface concrete, benefiting from external water curing, experienced a slower humidity decline, maintaining over 92% relative humidity even at day 15.

Due to the large thickness of the post-cast strip, external water has difficulty penetrating into the middle and lower sections. Moreover, the accumulation of hydration heat raises the temperature, causing intense cement hydration and rapid consumption of moisture, which results in a faster decline in humidity in the core and bottom areas [37]. RHA (rice husk ash), with its porous structure and internal curing effect, helped mitigate this moisture loss and promoted the continued hydration of both cement and MEA. As shown in Figure 13, the relative humidity in the core and bottom regions remained above 84% during the 15-day period, indicating that RHA effectively enhanced the moisture retention capability of the concrete.

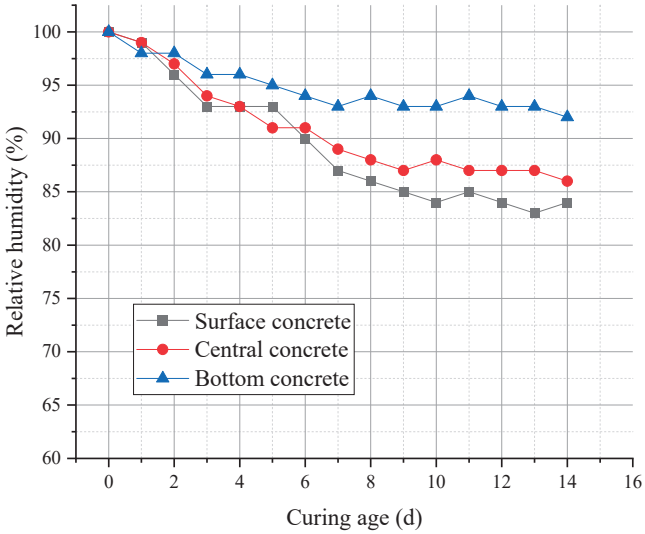

Figure 13. Relative humidity inside concrete at different locations.

The combination of RHA and MEA not only prevented shrinkage cracking in mass concrete but also supported the long-term hydration of MEA. The addition of RHA ensured that even under conditions of a low water-to-binder ratio and reduced humidity, MEA could still hydrate sufficiently and exhibit favorable expansion performance, thereby improving the long-term stability and strength of the concrete.

(5) Degree of MEA Hydration

The measured hydration degree of MEA at different locations of the concrete slab after on-site sampling is shown in Figure 14. After 3 d of casting, the hydration degree of MEA in the central region was 31.6%, which was 26.9% higher than that in the surface region (22.9%). This difference is primarily due to the higher temperature at the slab center, as MEA is highly sensitive to temperature and elevated temperatures can significantly accelerate its hydration [38].

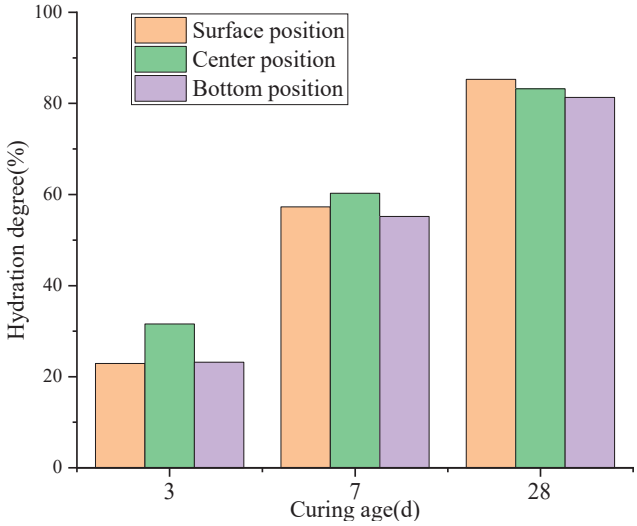

Figure 14. Hydration degree of MEA at different locations.

At 7 d, the degree of MEA hydration in the central region was 60.3%, which was 5.2% higher than that in the surface region (57.3%). The difference between the two was significantly reduced compared to that at 3 d, mainly because the temperature had decreased, leading to a reduced MEA hydration rate in the core region. Subsequently, as the

temperature further decreased and moisture was consumed, the MEA hydration rate in the central region slowed down markedly, further narrowing the gap with the surface region.

At 28 d, the MEA hydration degree in the surface region reached 85.3%, which was 2.5% higher than that in the central region. This was because, as the hydration of cement and MEA progressed, the free water in the core was gradually consumed, and external moisture could not penetrate into the central area. The resulting decline in humidity led to a lower MEA hydration rate. In contrast, the surface region received a continuous water supply due to curing, so its hydration rate during the later stage (7–28 days) was higher than that of the central region. The MEA at the bottom surface had a lower temperature than the core and lower humidity than the upper surface, so its hydration degree at 28 days was the lowest.

As shown in Figure 14, for the MEA hydration in the mass concrete floor slab, the early stage (0–3 d) was mainly controlled by temperature, while the middle and later stages (7–28 d) were mainly controlled by humidity. Due to the large dimensions of the floor slab in this high-rise building, with a maximum thickness of 1.3 m and a large amount of cement used, the heat of hydration was not easily dissipated, resulting in higher internal temperatures in the concrete. The higher the temperature, the greater the MEA hydration rate. At 3 days, the MEA hydration degree in different regions was all greater than 55%. In the later stages, due to the internal curing effect of rice husk ash, additional moisture was provided for MEA hydration, and the MEA hydration degree was greater than 80% in all regions.

(6) Measured Compressive Strength of Post-pour Concrete

Figure 15 shows the measured compressive strength of the post-pour concrete at different curing ages. The concrete strength increased with curing time. At early ages (3 days), the strength of MR concrete was similar to that of ordinary concrete. In the later stages, as MEA continued to hydrate and expand, the growth of magnesium hydroxide in the restricted pore size under the reinforcement restraint increased the density, and the strength gradually exceeded that of ordinary concrete. At 28 days, the strength was 10.5% higher than that of ordinary concrete. Based on the results of both deformation and strength tests, it can be concluded that the restrained expansion of MEA effectively mitigates shrinkage cracking and improves the concrete strength in high-strength-reinforced concrete for high-rise buildings.

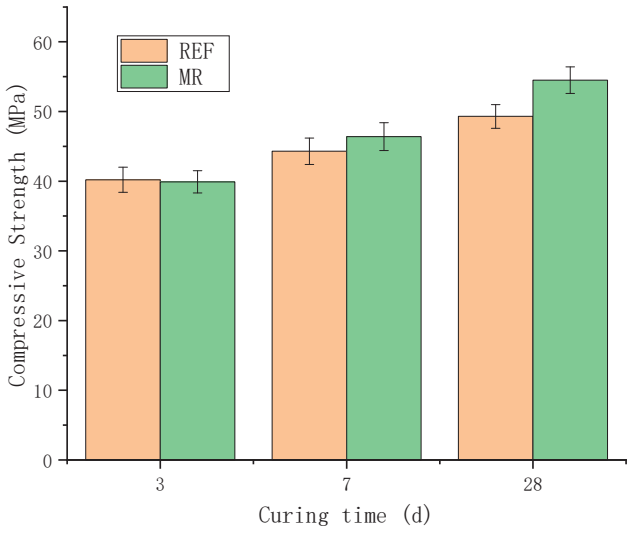

Figure 15. Compressive strength of concrete.

4. Conclusions

(1) The combined incorporation of MgO expansive agent (MEA) and rice husk ash (RHA) has demonstrated a synergistic effect on improving the crack resistance and durability of post-cast concrete used in tall building foundations. Their interaction effectively addresses both early-age shrinkage and long-term strength development.

(2) MEA provided expansion to counteract shrinkage; however, its hydration was limited in low-humidity, highly restrained environments. RHA, serving as an internal curing agent, improved internal moisture conditions, promoted the continuous hydration of MEA, and participated in pozzolanic reactions, forming additional C-S-H and M-S-H gels. This dual mechanism optimized the pore structure, enhanced matrix densification, and significantly reduced cracking risks.

(3) The composite mix showed reduced early-age workability due to the water absorption and ion exchange of MEA and the thickening effect of RHA. Slump loss was accelerated, and it is recommended that concrete be placed within 120 min of mixing to ensure good workability.

(4) Compared to conventional concrete, the composite concrete exhibited 10.5% higher 28 d compressive strength, while maintaining excellent shrinkage control. Field application demonstrated its suitability for high-strength, densely reinforced post-cast strips in tall buildings, offering a practical and effective approach to mitigating shrinkage-induced cracking in large-volume structural elements.

Author Contributions: Methodology, F.J., Q.W. and Z.M.; Software, Y.X.; Investigation, F.J. and Y.X.; Resources, F.J.; Data curation, J.W. and Z.M.; Writing—original draft, F.J. and Y.X.; Writing—review & editing, W.D., Q.W. and J.W.; Funding acquisition, W.D. All authors have read and agreed to the published version of the manuscript.

Funding: This research was funded by Jiangsu Marine Structure Service Performance Improvement Engineering Research Center; Nantong Building Structure Key Laboratory grant number CP12015005; Basic Science (Natural Science) Research Project of Higher Education Institutions in Jiangsu Province grant number 24KJD560004; Nantong Science and Technology Plan Project grant number JC2024040; Jiangsu University 'Blue Project'.

Institutional Review Board Statement: Not applicable.

Informed Consent Statement: Not applicable.

Data Availability Statement: The original contributions presented in this study are included in the article. Further inquiries can be directed to the corresponding authors.

Conflicts of Interest: Authors Yijiang Xing, Wencong Deng and Qi Wang were employed by the company China State Construction Engineering (Macau) Co., Ltd. The remaining authors declare that the research was conducted in the absence of any commercial or financial relationships that could be construed as a potential conflict of interest.

References

1. Kvocka, D.; Sustersic, J.; Pranjic, A.M.; Mladenovic, A. Mass Concrete with EAF Steel Slag Aggregate: Workability, Strength, Temperature Rise, and Environmental Performance. *Sustainability* **2022**, *14*, 15502. [CrossRef]
2. Mao, Y.G.; Liu, J.H.; Shi, C.J. Autogenous shrinkage and drying shrinkage of recycled aggregate concrete: A review. *J. Clean. Prod.* **2021**, *295*, 126435. [CrossRef]
3. Dhahir, M.K.; Marx, S. Shrinkage behaviour of high-strength concrete plates reinforced with carbon textile reinforcement. *Structures* **2024**, *69*, 107504. [CrossRef]
4. Stindt, J.; Forman, P.; Mark, P. Influence of Rapid Heat Treatment on the Shrinkage and Strength of High-Performance Concrete. *Materials* **2021**, *14*, 4102. [CrossRef] [PubMed]
5. Won, J.P.; Kim, S.H.; Lee, S.J.; Choi, S.J. Shrinkage and durability characteristics of eco-friendly fireproof high-strength concrete. *Constr. Build. Mater.* **2013**, *40*, 753–762. [CrossRef]

6. Pan, Z.F.; Meng, S.P. Three-level experimental approach for creep and shrinkage of high-strength high-performance concrete. *Eng. Struct.* **2016**, *120*, 23–36. [CrossRef]
7. Li, P.J.; Chen, M.J.; Sun, W.H. Numerical Simulation Analysis of the Full-Section Immersed Tube with the Post-Pouring Belt under Hydration Reaction. *Buildings* **2023**, *13*, 2377. [CrossRef]
8. Xu, F.; Yang, Z.; Liu, W.; Wang, S.; Zhang, H. Experimental investigation on the effect of sulfate attack on chloride diffusivity of cracked concrete subjected to composite solution. *Constr. Build. Mater.* **2020**, *237*, 117643. [CrossRef]
9. Ying, J.; Yan, H.; Huang, J.; Li, Z.A.; Chen, B. Simulation of concrete cracking and chloride diffusion under uniaxial compression. *J. Build. Eng.* **2024**, *96*, 110329. [CrossRef]
10. Neves, R.; Vicente, C.; Castela, A.; Montemor, M.F. Durability performance of concrete incorporating spent fluid cracking catalyst. *Cem. Concr. Compos.* **2015**, *55*, 308–314. [CrossRef]
11. Li, K.F.; Li, L. Crack-altered durability properties and performance of structural concretes. *Cem. Concr. Res.* **2019**, *124*, 105811. [CrossRef]
12. Mo, L.W.; Deng, M.; Tang, M.S.; Al-Tabbaa, A. MgO expansive cement and concrete in China: Past, present and future. *Cem. Concr. Res.* **2014**, *57*, 1–12. [CrossRef]
13. Kabir, H.; Hooton, R.D. Evaluating soundness of concrete containing shrinkage-compensating MgO admixtures. *Constr. Build. Mater.* **2020**, *253*, 119141. [CrossRef]
14. Tian, C.J.; Wang, Y.Z.; Qiu, K.; Yang, Q.L. Effects of submicron-MgO and nano-MgO on the expansion and microscopic properties of high-performance concrete. *J. Cent. South Univ.* **2022**, *29*, 3186–3200. [CrossRef]
15. Guo, J.J.; Zhang, S.W.; Guo, T.; Zhang, P. Effects of UEA and MgO expansive agents on fracture properties of concrete. *Constr. Build. Mater.* **2020**, *263*, 120245. [CrossRef]
16. Wang, A.G.; Sun, D.S.; Deng, M.; Chen, X.M.; Zhang, F.J. Influence of Restraint on Pore Structures and Air Permeability of Concrete Containing MgO-Type Expansive Agent. *Asian J. Chem.* **2013**, *25*, 5532–5534. [CrossRef]
17. Wang, L.; Song, X.; Yang, H.; Wang, L.; Tang, S.; Wu, B.; Mao, W. Pore Structural and Fractal Analysis of the Effects of MgO Reactivity and Dosage on Permeability and F–T Resistance of Concrete. *Fractal Fract.* **2022**, *6*, 113. [CrossRef]
18. Liu, K.; Cui, Y.; Yu, X. Analysis of the influence of MgO expansion agent on the expansion performance of cement mortar under constant humidity and variable humidity curing conditions. *Mater. Introd.* **2025**, *39*, 80–86. (In Chinese)
19. Wang, J.L.; Jiang, F.F.; Wang, R. Study on the interaction between limestone filler and rice husk ash on the rheological properties of cement composite pastes. *Constr. Build. Mater.* **2024**, *456*, 139247. [CrossRef]
20. Jiang, F.; Liu, R.; Mao, Z.; Deng, M. The combined effect of steel fiber and MgO on the deformation and mechanical properties of high-strength concrete. *J. Mater. Res. Technol.-JMRT* **2023**, *26*, 4296–4309. [CrossRef]
21. *GB/T 50081-2002*; Standard for Test Method of Mechanical Properties on Ordinary Concrete. China Architecture & Building Press: Beijing, China, 2002.
22. Mo, L.; Fang, J.; Huang, B.; Wang, A.; Deng, M. Combined effects of biochar and MgO expansive additive on the autogenous shrinkage, internal relative humidity and compressive strength of cement pastes. *Constr. Build. Mater.* **2019**, *229*, 116877. [CrossRef]
23. *JGJ/T23-2011*; Technical Specification for Inspection of Concrete Compressive Strength by Rebound Method. China Architecture & Building Press: Beijing, China, 2011.
24. *GBT50107-2013*; Standard for Test Methods of Concrete Strength. Standards Press of China: Beijing, China, 2013.
25. Li, S.K.; Mo, L.W.; Deng, M.; Cheng, S.K. Mitigation on the autogenous shrinkage of ultra-high performance concrete via using MgO expansive agent. *Constr. Build. Mater.* **2021**, *312*, 125422. [CrossRef]
26. Zhang, R.X.; Panesar, D.K. New approach to calculate water film thickness and the correlation to the rheology of mortar and concrete containing reactive MgO. *Constr. Build. Mater.* **2017**, *150*, 892–902. [CrossRef]
27. Wang, K.; Moon, J.; Du, H.J.; Xia, X.; Zhu, D.; Zhang, P.; Guo, J.J. Early-age shrinkage and hydration of concrete incorporating a mutually reinforcing systems of super absorbent polymers and MgO expansive agent under low humidity conditions. *Constr. Build. Mater.* **2024**, *417*, 135350. [CrossRef]
28. Jeon, I.K.; Woo, B.H.; Yoo, D.H.; Ryou, J.S.; Kim, H.G. Evaluation of the Hydration Characteristics and Anti-Washout Resistance of Non-Dispersible Underwater Concrete with Nano-SiO_2 and MgO. *Materials* **2021**, *14*, 1328. [CrossRef]
29. Liu, J.P.; Tian, Q.; Wang, Y.J.; Li, H.; Xu, W. Evaluation Method and Mitigation Strategies for Shrinkage Cracking of Modern Concrete. *Engineering* **2021**, *7*, 348–357. [CrossRef]
30. Endale, S.A.; Taffese, W.Z.; Vo, D.H.; Yehualaw, M.D. Rice Husk Ash in Concrete. *Sustainability* **2023**, *15*, 137. [CrossRef]
31. Mo, L.W.; Deng, M.; Tang, M.S. Effects of calcination condition on expansion property of MgO-type expansive agent used in cement-based materials. *Cem. Concr. Res.* **2010**, *40*, 437–446. [CrossRef]
32. Bandara, D.H.M.S. Development of blended cement utilizing the pozzolanic amorphous silica component of rice husk ash. *J. Natl. Sci. Counc. Sri Lanka* **1994**, *22*, 189–199. [CrossRef]

33. Rattanachu, P.; Toolkasikorn, P.; Tangchirapat, W.; Chindaprasirt, P.; Jaturapitakkul, C. Performance of recycled aggregate concrete with rice husk ash as cement binder. *Cem. Concr. Compos.* **2020**, *108*, 103533. [CrossRef]
34. Abellán-García, J. Effect of rice husk ash as partial replacement of ordinary Portland cement in ultra-high-performance glass concrete. *Eur. J. Environ. Civ. Eng.* **2024**, *28*, 661–683. [CrossRef]
35. He, P.P.; Poon, C.S.; Tsang, D. Comparison of glass powder and pulverized fuel ash for improving the water resistance of magnesium oxychloride cement. *Cem. Concr. Compos.* **2018**, *86*, 98–109. [CrossRef]
36. Yang, Y.; Yao, J.; Liu, J.; Kong, D.; Gu, C.; Wang, L. Evaluation of the thermal and shrinkage stresses in restrained concrete: New method of investigation. *Constr. Build. Mater.* **2024**, *411*, 134493. [CrossRef]
37. Chen, S.; Zhao, H.; Chen, Y.; Huang, D.; Chen, Y.; Chen, X. Experimental study on interior relative humidity development in early-age concrete mixed with shrinkage-reducing and expansive admixtures. *Constr. Build. Mater.* **2020**, *232*, 117204. [CrossRef]
38. Li, H.; Tian, Q.; Zhao, H.T.; Lu, A.Q.; Liu, J. Temperature sensitivity of MgO expansive agent and its application in temperature crack mitigation in shiplock mass concrete. *Constr. Build. Mater.* **2018**, *170*, 613–618. [CrossRef]

Disclaimer/Publisher's Note: The statements, opinions and data contained in all publications are solely those of the individual author(s) and contributor(s) and not of MDPI and/or the editor(s). MDPI and/or the editor(s) disclaim responsibility for any injury to people or property resulting from any ideas, methods, instructions or products referred to in the content.

materials

MDPI

Article

Application of Flotation Tailings as a Substitute for Cement in Concrete Structures for Environmental Protection and Sustainable Development—Part I: Sulfide Neutralization

Vanja Đurđevac [1,*], Novica Staletović [2], Lidija Đurđevac Ignjatović [1], Violeta Jovanović [3], Nikola Vuković [4] and Vesna Krstić [1,5,*]

[1] Mining and Metallurgy Institute Bor, Alberta Ajnštajna 1, 19210 Bor, Serbia; lidija.ignjatovic@irmbor.co.rs
[2] Faculty of Ecology and Environmental Protection, University "Union-Nikola Tesla", Cara Dušana 62-64, 11000 Belgrade, Serbia; nomstale@mts.rs
[3] Faculty of Management, Metropolitan University Belgrade, 11158 Belgrade, Serbia; violeta.jovanovic@metropolitan.ac.rs
[4] Institute for Technology of Nuclear and Other Mineral Raw Materials, Franchet d'Esperey 86, 11000 Belgrade, Serbia; n.vukovic@itnms.ac.rs
[5] Technical Faculty Bor, University of Belgrade, 19210 Bor, Serbia
* Correspondence: vanja.djurdjevac@irmbor.co.rs (V.Đ.); vesna.krstic@irmbor.co.rs (V.K.); Tel.: +381-605459270 (V.Đ.); +381-668088615 (V.K.)

Abstract: Flotation tailings (FT), as a product of the exploitation and processing of copper ore, represent a significant environmental and health risk due to the high content of heavy metals and sulfide compounds. Contemporary concepts of sustainable development and circular economy increasingly emphasize the need for rational use of resources and minimization of all types of waste, including mining waste. In this context, the reuse of flotation tailings in the construction industry represents a significant step towards closing the material flow in the mining and construction sectors. In order to reduce the negative impact of FT on the environment, the possibility of its application as a substitute for a portion of cement in the production of concrete was investigated. The main challenge is to reduce the negative impact of sulfides, originating from sulfide compounds, in order to achieve the desired concrete quality. Limestone aggregates of different size fractions (0/4, 4/8, 8/16 mm) were used for sulfide neutralization. Pyrite concentrate was used as a sulfide source, which together with FT provides the mixtures FT-7, FT-14, FT-25, and FT-40, with sulfur contents of 7.56, 13.84, 25.02, and 39.82%, respectively. FT mixtures were used as a substitute for Portland cement (PC) in the preparation of concrete. Test methods included XRD (X-ray diffraction), XRF (X-ray fluorescence), SEM (scanning electron microscopy), LP (leaching procedure), TCLP (toxicity characterization leaching procedure), assessment of acid eluate generation potential (AP—acid potential, NP—neutralization potential, and NNP—net neutralization potential), NEN (determination of heavy metals in cured concrete eluate), and UCS (uniaxial compressive strength of cured concrete). The results showed that the chemical characteristics of FT, as well as the chemical and mechanical properties of hardened concrete, allow the efficient use of these tailings in concrete mixes, which significantly utilizes FT, reduces the generation of mining waste, and contributes to the reduction of the negative impact on the environment and achieving sustainable development in mining.

Keywords: flotation tailings; sulfides; neutralization; hardened concrete; environmental protection; sustainable development

1. Introduction

The increase in production in the mining industry contributes to the growth of gross national income, the creation of new jobs, and the improvement of the living standard of the population [1]. However, given the scale and nature of the industry, negative environmental impacts are significant, including land degradation and air and water pollution [2]. The exploitation of ores, both by surface and underground methods, requires the occupation of a large area of land for the storage of waste rock and flotation tailings (FT). FT, which is a by-product of the processing of metallic ores (such as iron, copper, and zinc ores), contains a high percentage of pyrite and toxic heavy metals, including lead, zinc, arsenic, and mercury, which can cause serious environmental pollution [3,4].

Exposure of FT to the atmosphere and surface waters leads to its leaching, resulting in the leaching of heavy metals and the formation of acidic drainage waters due to the oxidation of pyrite in the presence of water and oxygen. Thus, as Saedi et al. [5] emphasized, there is pollution of surface and underground water, as well as soil pollution. In addition, the flotation dam used for FT storage is a potential source of pollution if it is damaged or demolished [6]. For the production of one kilogram of copper from ore, usually 987 kg of FT is allocated, which represents a major risk to the environment and human health [7]. According to estimates published by Cacciuttolo and Cano [8], in 2022, the total amount of FT at the global level reached 14 billion metric tons.

Given these challenges, the question is whether it is possible to reuse FT for product development, providing economic benefits and reducing environmental risks.

Unfortunately, the extraction of metals and other valuable components from tailings does not solve the problem of waste disposal. In recent years, research has focused on the use of flotation tailings (FT) in cement paste backfill (CPB) for the purpose of filling abandoned underground mines [9,10]. Research on the application of tailings rich in the sulfide mineral pyrite in cement pastes was conducted by Martins and colleagues [11]. The studies were carried out using different cement matrices (Portland cement (PC), calcium aluminate cement (CAC), and calcium sulfoaluminate cement (CSA)). Cement was replaced with 30% tailings, and the testing period lasted 200 days. The results showed that tailings act as a stable mixture in PC, while in CSA, they form additional hydration products containing sulfates. Despite the high pyrite content in the hydrated pastes, no formation of expansive phases due to pyrite oxidation—which would affect paste durability—was observed. CSA cement demonstrated ecological compatibility, as it proved most suitable for immobilizing arsenic, zinc, cadmium, chromium, and copper.

Portland cement (PC), as the most commonly used ingredient of concrete, accounts for about 75% of the total price of concrete, but at the same time it has a significant negative impact on the environment due to CO_2 emissions during its production, which accounts for approximately 5–7% of global CO_2 emissions [12]. Therefore, replacing a part of the cement with FT could bring multiple benefits in terms of emissions reduction and environmental pollution. By using mining waste as a secondary resource in construction, value is created from waste, which is in accordance with the principles of circular economy and sustainable development [13,14]. This approach directly contributes to the principles of sustainable development by reducing the impact of the mining industry's ecological footprint on the environment and promoting a circular economy, in accordance with the Sustainable Development Goals of the United Nations—especially goals 9 (Industry, innovation, and infrastructure), 11 (Sustainable cities and communities), 12 (Responsible consumption and production), and 13 (Climate action) [15].

Proper management and reuse of flotation tailings (FT), which contain heavy metals and sulfide minerals, would help ensure environmental protection. Using FT as a cement substitute in concrete production could address the release of heavy metals, the issue of

tailings disposal, and the prevention of pollutant leaching into the environment [16]. Saedi and colleagues [5] used tailings with different sulfur contents—0.4% and 19%—as a partial cement replacement in proportions ranging from 20% to 80%. The results of the TCLP test showed that with increasing curing time, the leaching rate of toxic metals (cadmium, chromium, cobalt, lead, zinc, copper) decreased. The compressive strength of samples containing 20% tailings with 0.4% and 19% sulfur content increased over time, indicating that up to 20% of the cement can be replaced with tailings. However, the high sulfide content in tailings poses a problem, as it affects the formation of hydration products and leads to the creation of sulfide salts, which in turn weaken concrete quality.

Grinding FT results in finely ground materials that can be used as supplementary cementitious materials (SCMs). This fine material can act as an inert filler in concrete, providing more nucleation sites for hydration products [17]. Gutteridge and colleagues [18] found that inert fine materials exhibit a filler effect when replacing cement up to 20%. In the case of using fine sulfide tailings in mortar, low replacement ratios can improve mortar properties, even if the tailings have low pozzolanic properties or hydraulic reactivity [19]. These properties still require further investigation.

FT, as a by-product of the exploitation and processing of copper ores, represents a significant ecological challenge due to the presence of heavy metals and sulfide compounds. In order to reduce its negative impact on the environment, the possibility of using FT in combination with pyrite concentrate, as a substitute for part of the cement in the production of concrete, was investigated. Although the presence of sulfur from sulfide compounds can cause problems in the quality of concrete, the use of limestone aggregates allows the neutralization of these negative effects, thereby contributing to sustainable development through the use of mining waste in the construction industry.

2. Theory

Pyrite oxidation, as a key process in the creation of acid mine drainage (AMD), is a complex biogeochemical phenomenon that includes numerous reactions, both abiotic and biotic, with the role of various factors such as pH, temperature, presence of microbial catalysts, and oxygen concentration. The process mainly takes place in three phases: initial oxidation of pyrite by oxygen; oxidation of ferrous ions (Fe^{2+}) to ferric ions (Fe^{3+}); and in the final phase, when Fe^{3+} becomes the dominant oxidizing agent for pyrite.

2.1. Theoretical Basis of Pyrite Oxidation

Oxidation of pyrite in tailings, due to exposure to atmospheric influences, is a process through which pyrite oxidizes in the presence of oxygen and water. This biogeochemical process generates acidic solutions that affect the formation of AMD, the precipitation of soluble iron minerals, and the formation of acidic sulfate soils in the environment. Pyrite oxidation has a negative impact on the environment because it contributes to the mobilization of heavy metals and sulfates in natural watercourses, which has long-term effects on environmental pollution. This process is described in detail by Nordstrom [20].

I reaction: In the initial phase of oxidation, in a neutral and slightly basic environment, the oxidizing agent is oxygen. The oxidation of sulfur to sulfate leads to a decrease in pH, which can drop to as low as 4.5, shown by Reaction (1) [21]:

$$2FeS_{2(S)} + 7O_{2(g)} + 2H_2O \rightarrow 2Fe^{2+}_{(aq)} + 4SO^{2-}_{4(aq)} + 4H^{+}_{(aq)} \quad (1)$$

II reaction: The oxidation reaction of Fe^{2+} to Fe^{3+} is slow and determines the rate of the pyrite oxidation process, Reaction (2). The concentration of dissolved Fe^{3+} ions decreases

due to the precipitation of $Fe(OH)_3$. Bacteria such as *Thiobacillus ferrooxidans* can accelerate this reaction by increasing the rate of oxidation up to 6 times [22]:

$$4Fe^{2+}_{(aq)} + O_{2(g)} + 4H^{+}_{(aq)} \rightarrow 4Fe^{3+}_{(aq)} + 2H_2O_{(aq)} \quad (2)$$

III reaction: In highly acidic conditions (pH < 3), Fe^{3+} ions become the main oxidizing agent for pyrite [22,23]. Reaction (3) [24] shows how Fe^{3+} rapidly oxidizes pyrite in the presence of water and at low pH, which is crucial for the generation of acid mine drainage.

$$FeS_{2(S)} + 14Fe^{3+}_{(aq)} + 8H_2O_{(aq)} \rightarrow 15Fe^{2+}_{(aq)} + 2SO^{2-}_{4(aq)} + 16H^{+}_{(aq)} \quad (3)$$

If the pH is >4.5, hydrolysis and precipitation of Fe^{3+} as $Fe(OH)_3$ occurs, reducing the amount of oxidizing agent in the solution decreases, Reaction (4):

$$Fe^{3+}_{(aq)} + 3H_2O_{(aq)} \rightarrow Fe(OH)_{3(s)} + 3H^{+}_{(aq)} \quad (4)$$

If a neutralizing mineral, such as calcite ($CaCO_3$), is present in the system where the pyrite oxidation process takes place, the pH increases, and the rate of oxidation decreases. Reaction (5) shows the dissolution of calcite, which neutralizes the acidity:

$$CaCO_{3(s)} + 2H^{+}_{(aq)} \rightarrow Ca^{2+}_{(aq)} + H_2O_{(aq)} + CO_{2(g)} \quad (5)$$

Figure 1 shows the scheme of pyrite oxidation and acid neutralization, resulting from the reaction between pyrite and calcite. In the form of the algorithm in Figure 1, the reactions from (1) to (5) are presented.

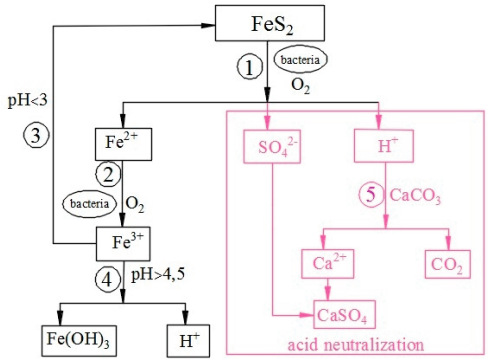

Figure 1. Schematic representation of pyrite oxidation and acid neutralization by calcite. The numbers from (1) to (5) represent the corresponding reactions (1) through (5).

Figure 2 shows the Eh-pH diagrams of the systems C-Ca-Fe-S-H_2O (blue color) and Fe-O_2-H_2O (red color) at standard conditions, calculated with HSC Chemistry software [25]. The vertical blue band indicates the measured stable pH range of the seepage water, which is key to understanding the chemical reactions and stability of sulfide compounds in the system. These diagrams are important for the analysis of sulfide neutralization in flotation tailings, which are used as a substitute for cement in concrete structures. The presented data, shown in Figure 2, contribute to a better understanding of the process of neutralization and stabilization of sulfides, which enables a more efficient application of FT in concrete structures while reducing the negative impact on the environment and promoting sustainable development.

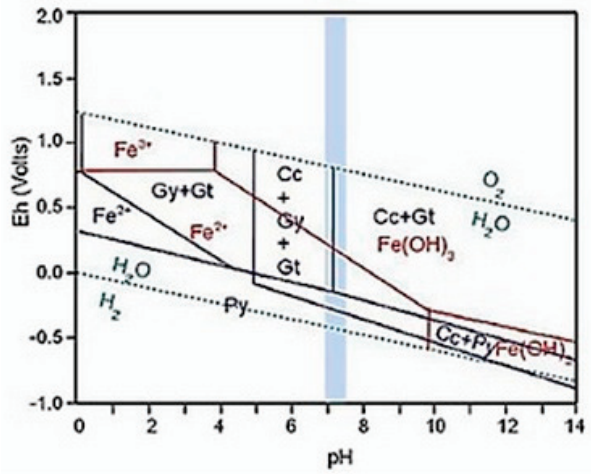

Figure 2. Eh—pH diagrams of C—Ca—Fe—S—-H_2O (blue) and Fe—-O_2—-H_2O (red) systems at standard conditions (calculated using HSC Chemistry). Vertical blue bar: measured stable pH range of the seepage water [25].

The key reaction, which defines the rate of pyrite oxidation and the formation of AMD, is the oxidation of Fe^{2+} in the presence of oxygen, as shown by Reaction (2). This reaction belongs to a group of very slow reactions under abiotic conditions. However, when occurring under biotic conditions in the presence of bacteria, it proceeds much faster. Because of this phenomenon, it was concluded that certain bacteria can act as catalysts for the Fe^{2+} ion oxidation reaction. There is a wide range of bacteria that can contribute to the biogeochemical oxidation of Fe^{2+} ions in the natural environment. This group of bacteria includes *Thiobacillus*, which are acidophilic and require pH < 3 for optimal growth and have been found in sulfide mine tailings [26,27]. Three species of *Thiobacillus* have been isolated from acidic mine waters [24]: *Thiobacillus ferrooxidans*, *Thiobacillus thiooxidans*, and *Thiobacillus acidophilus*.

2.2. Mechanism of Oxidation of Fe^{2+} Ions by Bacteria

Thiobacillus bacteria obtain energy by oxidizing reduced sulfur compounds. *Thiobacillus ferrooxidans* bacteria use iron (Fe^{2+}) as an electron donor for their metabolic activity. The process of oxidizing Fe^{2+} to Fe^{3+} allows bacteria to obtain the energy needed for growth and the production of biologically important molecules, such as ATP and NADPH [28]. The efficiency of this process in bacteria is limited, as it has been found that only 3.2 to 30% of the energy produced by the oxidation of Fe^{2+} can be used for bacterial growth [29,30]. These bacteria are not only important for the oxidation of pyrite but also for sulfides and elemental sulfur.

Chemiosmosis, a process in which the energy from the oxidation of Fe^{2+} is used to transport protons (H^+) across the cell membrane, explains the link between ATP production and Fe^{2+} oxidation [31–33].

2.3. Prevention and Remediation of Acidic Mine Drainage Waters

Acid mine drainage (AMD) is created in the vicinity of abandoned mines and tailings by the oxidation of mine waste, which is rich in sulfide minerals. Oxidation of pyrite, a sulfide mineral, in the presence of oxygen, bacteria, and water produces sulfuric acid and metal. The resulting oxidation products are responsible for the formation of low pH, high concentrations of sulfide ions, and heavy metals in AMD. AMD has a negative impact on the environment, as it can cause pollution of river watercourses and soil.

In active mines, the prevention of AMD is carried out by filling tailings, diverting water and making limestone trenches around the mine [34]. To solve the AMD problem, it

is necessary to control the oxidation of Fe^{2+} ions, Reaction (2), which determines the rate of pyrite oxidation. Two ways of controlling the reaction have been proposed: thermodynamic control and kinetic control [35]. Two remedial systems can be used in vulnerable places where AMD has formed: active or passive AMD treatments [36].

3. Methods and Materials

3.1. Methods

XRF analysis was performed on a Rigaku Supermini 200 device and is a semi-quantitative analysis. The elemental analyzer Leco CS844 Carbon/Sulfur Determinator (St. Joseph, MI, USA) was used to determine the total sulfur in the FT. To determine the mineralogical composition of the FT and the concrete composite, an XRD analysis was used, performed with a RigakuMiniFlex 600 instrument with a D/teXUltra 250 high-speed detector and an X-ray tube with a copper anode (Tokyo, Japan). Recording conditions were angle range 3–90°, step 0.02°, recording speed 10°/min. The X-ray tube voltage was 40 kV, and the current was 15 mA. Mineral identification was performed in PDXL 2 Version 2.4.2.0 software, and the obtained diffractograms were compared with data from the ICDD PDF-2 2015 database. The detection limit of XRD analysis was about 1%.

The morphology of the concrete was analyzed with a JEOL JSM-IT300LV scanning electron microscope (SEM), operated at 20 kV (Tokyo, Japan). EDS spectra were recorded using an Oxford Instruments (Abingdon, UK) Xmax 50 mm^2 energy dispersive X-ray spectrometer (EDS). SEM analysis was performed on sample C2/25 after 120 days of stabilization. The analysis was performed on the pre-fracture surface of concrete. The sample was subjected to XRD analysis, after which it was coated with gold (thickness 15 nm) using a JEOL JFC-1300 Auto Fine Coater for SEM-EDS analysis (Tokyo, Japan).

According to the standard SRPS EN 12457-2:2008 [37], a leaching procedure (LP) was carried out, based on which FT was characterized by compliance testing, which provides data on the leaching of granular waste materials and sludges with a liquid–solid ratio of 10 L/kg and a particle size of <4 mm. The aim of these tests is to identify heavy metals in the eluate after leaching the waste material. The tested samples were brought into contact with distilled water during continuous mixing at 10 revolutions per minute at room temperature (20 ± 2) °C, with a contact time of 24 h, without pH control. After filtration, the concentrations of the metals present (Ag, As, Ba, Be, Cd, Co, Cr, Cu, Mo, Ni, Pb, Sb, Se, Sn, V, and Zn) were determined by optical emission spectrometry of inductively coupled plasma on an ICP-OES SPECTRO CIROS Λ-125-770 nm, SPECTRO ARCOS ICP-OES analyzer, according to the standard SRPS EN ISO 11885:2007 [38]. Tests were performed in duplicate, and the results were evaluated in accordance with the relevant rulebook on categories, testing, and classification of waste, Annex 10 [39]. The TCLP test was performed to determine the toxic characteristics of tailings samples FT-7, FT-14, FT-25, and FT-40 and concrete C1/40 and C3/40 after 28 and 90 days according to US EPA standard 1311 [40]. The test material was extracted for 18 h with a slightly acidic liquid at 20 times its weight and stirred at 30 rpm at room temperature (20 ± 2) °C. After stirring, the solution was filtered, and a few drops of 1 N HNO_3 were added. The content of heavy metals was determined using ICP-OES, according to the standard SRPS EN ISO 11885:2007 [38].

3.2. Preparation of Concrete Samples and Their Mix Designs

Concrete samples were made by mixing PC, aggregate, FT, and water. Portland cement brand PC 42.5N was used as a binder in the concrete. In the experiment, crushed separated natural limestone aggregate of fractions 0/4 mm, 4/8 mm and 8/16 mm was used as aggregate. Flotation tailings and pyrite concentrate, both by-products of copper ore processing at the Veliki Krivelj mine (Bor, Serbia), were used in this study. Adding pyrite

concentrate to FT resulted in FT with a certain sulfur content. By replacing cement with FT, in different ratios (Table 1), and mixing with water (water/cement ratio of 0.5) according to the SRPS EN 206-1 standard [41], a concrete composite was obtained that was cast in molds of dimensions 15 × 15 × 15 cm and 10 × 10 × 10 cm. After 24 h, the hardened concrete was removed from the mold and treated under controlled conditions (temperature (20 ± 2)°C and humidity of 95%) for further testing of the concrete characteristics.

Table 1. Marking of concrete samples with different proportions of PC, FT, and sulfur in FT.

Sample Abbreviation			Sample Composition
C100			**100%PC**
PC80-FT20 (C1)	PC80-FT20/7	C1/7	80%PC, 20%FT and 7.56% S in FT
	PC80-FT20/14	C1/14	80%PC, 20%FT and 13.84% S in FT
	PC80-FT20/25	C1/25	80%PC, 20%FT and 25.02% S in FT
	PC80-FT20/40	C1/40	80%PC, 20%FT and 39.82% S in FT
PC40-FT60 (C2)	PC40-FT60/7	C2/7	40% PC, 60% FT and 7.56% S in FT
	PC40-FT60/14	C2/14	40% PC, 60% FT and 13.84% S in FT
	PC40-FT60/25	C2/25	40% PC, 60% FT and 25.02% S in FT
	PC40-FT60/40	C2/40	40% PC, 60% FT and 39.82% S in FT
PC20-FT80 (C3)	PC20-FT80/7	C3/7	20% PC, 80% FT and 7.56% S in FT
	PC20-FT80/14	C3/14	20% PC, 80% FT and 13.84% S in FT
	PC20-FT80/25	C3/25	20% PC, 80% FT and 25.02% S in FT
	PC20-FT80/40	C3/40	20% PC, 80% FT and 39.82% S in FT

PC—Portland cement, FT—flotation tailings, S—sulfur.

3.3. Flotation Tailings and Aggregate

Mixtures of FT and pyrite concentrate were prepared to achieve theoretical sulfur contents of 7%, 14%, 25%, and 40% and were denoted as FT-7, FT-14, FT-25, and FT-40, while the real concentrations of sulfur in the mixtures were 7.56, 13.84, 25.02, and 39.82%, respectively. Table 2 shows the content of oxides and total sulfur, loss on ignition in samples FT-7, FT-14, FT-25 and FT-40.

Table 2. Chemical composition of PC, FT-7, FT-14, FT-25, and FT-40.

Component (wt.%)	PC	FT-7	FT-14	FT-25	FT-40
SiO_2	24.56	60.21	56.31	52.14	40.21
Al_2O_3	4.85	17.68	14.61	8.99	4.66
Fe_2O_3	3.87	9.21	16.76	29.44	45.45
CaO	62.59	4.49	4.56	2.83	0.67
K_2O	0.83	1.64	1.2	0.9	0.58
Na_2O	0.45	1.2	1.07	0.95	0.85
MgO	2.01	1.66	0.78	0.96	0.22
P_2O_5	0.027	0.12	0.078	0.089	0.05
SO_3	0.80	0.19	0.43	1.47	3.46
Cl^-	n.d. *	n.d. *	n.d. *	n.d. *	n.d. *
Total S	0.32	7.56	13.84	25.02	39.82
Loss on ignition	-	7.99	12.75	17.29	25.71

* n.d.—not detected.

The mineralogical composition of FT was determined by XRD analysis, as shown in Figure 3. Pyrite is the most abundant sulfide phase identified in all samples. Also, quartz and clinochlore are represented in all samples, while FT-7 and FT-25 additionally contain illite and albite, and FT-14 contains illite.

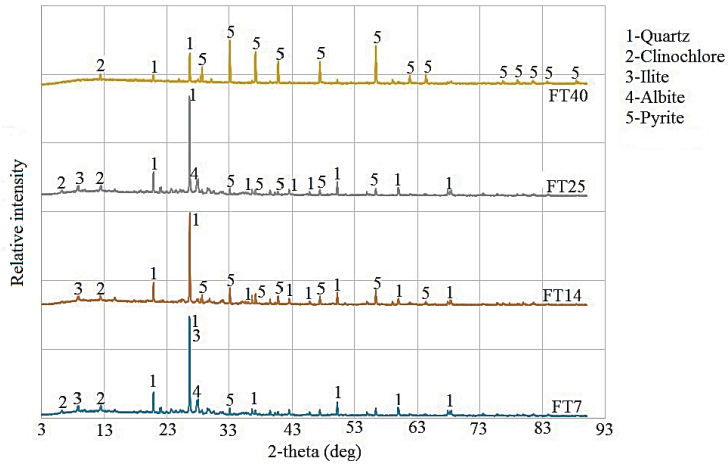

Figure 3. XRD analysis of flotation tailings mixtures FT-7, FT-14, FT-25, and FT-40.

The particle size distributions (PSDs) of flotation tailings FT-7, FT-14, FT-25, and FT-40 were determined in accordance with the SRPS EN 17892-4 standard [42]. The PSD curves are presented using a semi-logarithmic graph showing the relationship between particle size and cumulative fraction content (Figure 4). Table 3 shows the values for d_{10}, d_{50}, and d_{90}, as well as the specific gravity (SG) of the PC, FT-7, FT-14, FT-25, and FT-40.

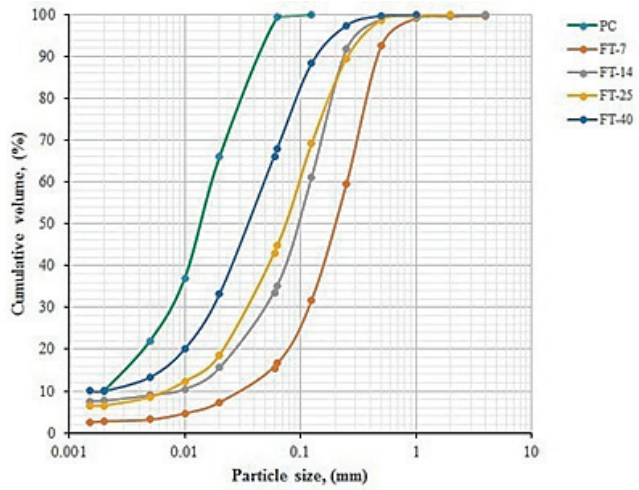

Figure 4. PSD of PC, FT-7, FT-14, FT-25, and FT-40.

Table 3. Physical properties of PC, FT-7, FT-14, FT-25, and FT-40.

Sample Label	d_{10} (μm)	d_{50} (μm)	d_{90} (μm)	SG (g/cm^3)
PC	2.01	14.1	44.3	3.050
FT-7	30.1	205.2	470.2	2.826
FT-14	9.1	98.2	240.3	2.962
FT-25	7.2	75.3	260.2	3.463
FT-40	2.2	36.3	140.3	4.342

d—diameter (the equivalent particle diameter).

By comparing the d_{90} results for the samples FT-7, FT-14, FT-25, and FT-40, with values of 470.2, 240.3, 260.2, and 140.3 μm, respectively, to that of PC (d_{90} = 44.3 μm), it is evident that the FT samples contained coarser fractions than PC. Based on the PSD analysis, FT-7 had the coarsest fraction (d_{90} = 470.2 μm), which will delay the onset of the pozzolanic reaction and cause the material to behave as an inert filler during the early stages of hardening [17]. In later stages of hardening, FT-7 will exhibit chemical reactivity and initiate a pozzolanic reaction, due to its high SiO_2 content (60.21%), as shown in Table 2 [17].

The FT-14, FT-25, and FT-40 samples will provide a physical contribution in concrete, meaning they will behave as inert fillers whose fine particles create additional nucleation sites for the hydration products—a phenomenon known as the heterogeneous nucleation effect [17].

An analysis of the d_{10}, d_{50}, and d_{90} values for FT-7, FT-14, FT-25, and FT-40 shows that samples with higher sulfur content (FT-25 and FT-40) exhibited a finer particle structure compared to those with lower sulfur content (FT-7 and FT-14). The fine fractions in the samples originated from sulfide minerals present in the tailings [19].

Specific gravity (SG) values range from 2.826 g/cm^3 for low-sulfur samples (FT-7) to 4.342 g/cm^3 in high-sulfur tailings (FT-40). This significant variation in SG is related to the variable chemical and mineralogical composition of the FT samples. Nevertheless, the measured SG values fell within the range defined by the specific gravity of quartz (SG_quartz = 2.65 g/cm^3) and pyrite (SG_pyrite = 5.00 g/cm^3) [19].

In the experiment, crushed separated natural aggregate of limestone with the fraction sizes of 0/4, 4/8, and 8/16 mm was used as an aggregate. The minerals present in the aggregate were also determined by XRD analysis (Figure 5).

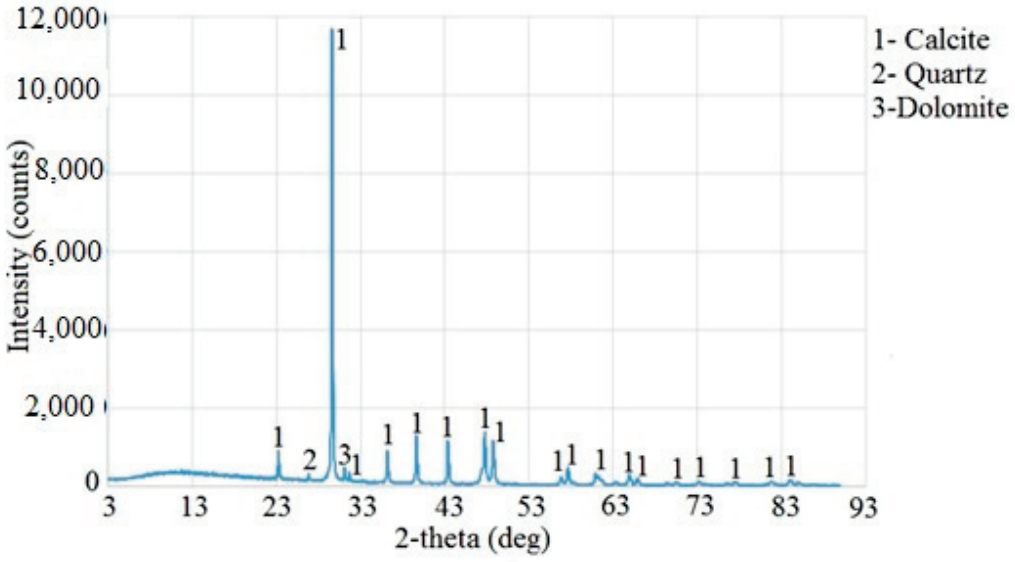

Figure 5. XRD analysis of limestone aggregates.

3.4. Examination Methodology

3.4.1. Assessment of the Potential of Creating Acidic Eluates

According to the standard SRPS EN 15875:2013 [43], a static test was performed to determine the acid and neutralization potential of waste containing sulfides. This standard determines the potential of sulfide-containing waste to form acidic leachate in landfills. The standard determines the method of determining the acid potential (AP) and neutralization potential (NP) of the material. From the obtained results, the net neutralization potential (NNP) was determined. AP is the maximum potential of acid formation from the sample under the assumption that all sulfur originates from pyrite and that acidity will result from

its complete oxidation [43], as shown in Equation (6), where S% is the percentage of total sulfur in the sample and is expressed in kilograms of carbonate per one ton of sample, [kg $CaCO_3$/t]:

$$AP = S\% \times 31.25 \quad (6)$$

The percentages of total sulfur in the examined tailings samples FT-7, FT-14, FT-25, and FT-40 were 7.56, 13.84, 25.02, and 39.82%, respectively. The measuring unit for AP represents the required amount of $CaCO_3$ to neutralize the acidity of one ton of waste.

The neutralization potential (NP) represents the ability of the sample to neutralize the resulting acidity [43]. It is determined by adding hydrochloric acid (HCl) to the sample, then titrating it with sodium hydroxide (NaOH) to determine the amount of acid consumed by the sample. The unit of measurement for NP is expressed in kilograms of carbonate per one ton of sample, [kg $CaCO_3$/t]. NP is calculated according to Equation (7), where N is the normality [mol/L], V is the volume [ml], and W is the mass of the sample [g]:

$$NP = [(N \times V)HCl - (N \times V)\ NaOH] \times 50/W, \quad (7)$$

The net neutralization potential (NNP) is calculated as the difference between NP and AP, according to Equation (8):

$$NNP = NP - AP \quad (8)$$

If the value of NNP <-20 and NP/AP is less than 1, it indicates that the sample has the potential to generate acidic leachate because the acid potential of AP (sulfides = pyrite) is greater than the neutralization potential of NP. If the value of NNP > 20 and NP/AP is greater than 3, it means that the sample does not have the potential to generate acidic drainage water because the neutralization potential of NP (carbonates = calcite) is sufficient to neutralize the sample. If $-20 <$ NNP < 20 and NP/AP is between 1 and 3, the acid potential is uncertain; therefore, it is necessary to perform a kinetic test [44].

3.4.2. Assessment of Leaching of Heavy Metals from Monolithic Waste

In laboratory conditions, the leaching of hardened concrete was simulated to determine the amount of heavy metals in the eluate. The test was performed according to the EA NEN 7375:2004 standard [45]. After 28 days of pouring the concrete composite into $15 \times 15 \times 15$cm molds and curing in controlled conditions (temperature (20 ± 2) °C and air humidity 95%), the concrete cubes were immersed in a container with distilled water—"tank test". After the 0.25th, 1st, 2.25th, 4th, 9th, 16th, 36th, and 64th days after immersing the cubes, the eluate was separated, filtered, acidified, and saved for further analysis. The separated eluates, after the specified periods, were analyzed by ICP-OES SPECTRO CIROS to quantify the heavy metals prescribed by the Regulations on Categories, Testing and Classification of Waste, Annex 8, Article 2 [40]. The obtained results of the analysis were compared with the same rulebook [40].

3.4.3. Compressive Strength

The compressive strength test of hardened concrete was performed according to the SRPS EN 12390-3:2019 standard [46]. With this method, the change in compressive strength during the curing period was monitored. The test was performed on the samples from Table 1 for a period of 28, 90, 120, 180, and 360 days from the day of pouring the concrete composite into molds $10 \times 10 \times 10$ cm. The testing was done on three test bodies on the 3000 kN MATEST compression machine. After the finished care of the concrete blocks, a test must be carried out within 10 h to ensure that the sample does not lose moisture. The concrete cube is placed in the compression machine so that the force acts normal to the direction of pouring. The calculation of the compressive strength is determined according

to Equation (9) [46], where fc represents the compressive strength [MPa], F is the maximum breaking load [N], and A_c represents the cross-sectional area of the sample affected by the compressive force [mm^2]:

$$f_c = F/A_c \quad (9)$$

3.4.4. Concrete Porosity

The apparent porosity of permeable concrete is calculated according to Equation (10) [47]:

$$p = \left[1 - \frac{m_2 - m_1}{\rho \times V}\right] \times 100\% \quad (10)$$

where p represents the apparent porosity expressed in [%], V is the volume of the dry sample [cm^3], m_1 is the mass of the sample measured by immersing the sample in water [g], m_2 is the mass of the sample after 48 h immersion in water [g], and ρ is the density of water [g/cm^3].

4. Results and Discussion

4.1. XRD Analysis

Semi-quantitative XRD analysis detected the minerals that make up the structure of concrete, based on which the quality and strength of concrete can be predicted. The analysis did not determine the formation of sulfate compounds gypsum, and ettringite. Figure 6 shows the comparative diffractograms of the samples from Table 1 after 28 and 120 days after casting the concrete composite into plastic molds.

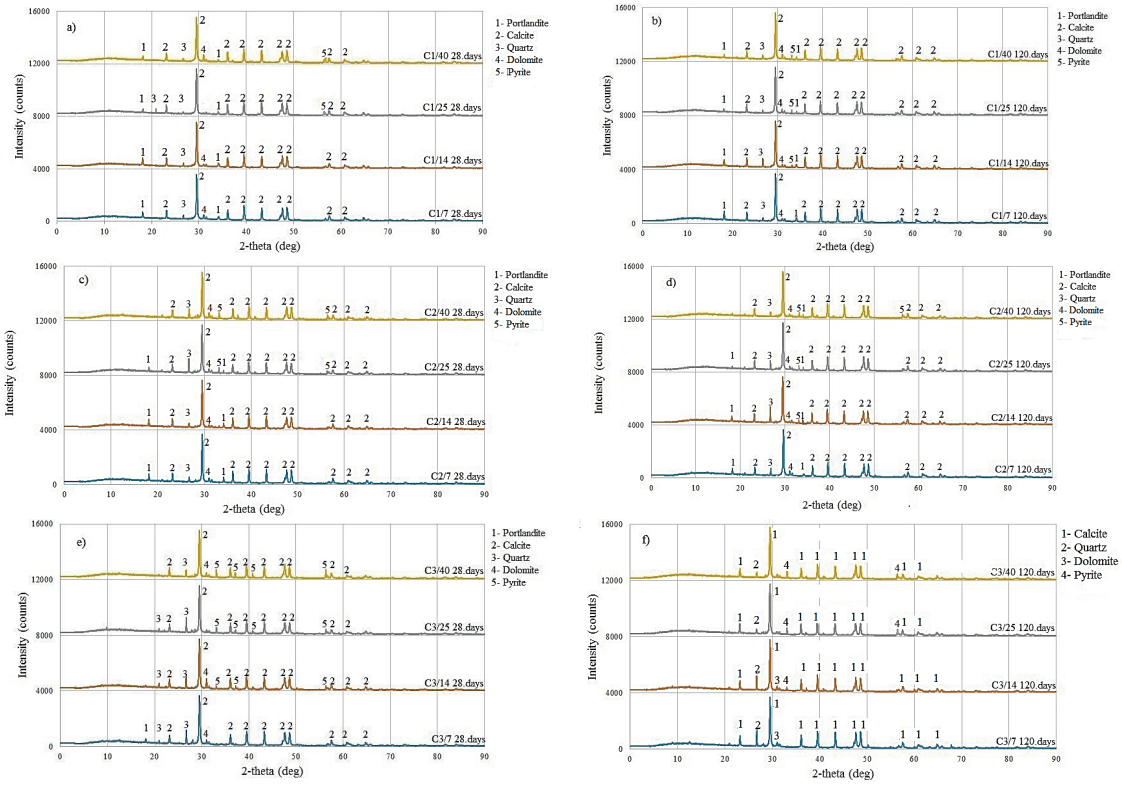

Figure 6. XRD analysis of samples: C1/7, C1/14, C1/25, and C1/40 after (**a**) 28 days and (**b**) 120 days; C2/7, C2/14, C2/25, and C2/40 after (**c**) 28 days and (**d**) 120 days; and C3/7, C3/14, C3/25, and C3/40 after (**e**) 28 days and (**f**) 120 days.

In sample C1 (PC80-FT20), shown in Figure 6a,b, 20% of PC was replaced with FT. The analysis showed that portlandite and calcite, quartz, and dolomite minerals were present in

all samples. Portlandite is a cement hydration product that affects the strength of concrete. According to Šestoperov (Grdić) [48], at most 10% of portlandite is formed during the hydration of cement in concrete. Calcite is the structural mineral of limestone aggregate, while quartz is present in FT. For C1/25 and C1/40, after 28 days, and C1/14, C1/25, and C1/40, after 120 days, the presence of pyrite was observed, which was expected due to the high concentration of sulfur in the concrete.

In sample C2 (PC60-FT40), shown in Figure 6c,d, 60% of PC was replaced with FT. Portlandite was detected in all samples, except for sample C2/40, which is attributed to a lower amount of cement and a higher amount of sulfide. No cement hydration products were formed in such hardened concrete [49–51]. A reduced cement content results in fewer hydration products, thereby decreasing compressive strength. In samples with higher concentrations of sulfur after 28 days (C2/25 and C2/40) and after 120 days (C2/14, C2/25, and C2/40), sulfide mineral pyrite was observed.

In sample C3 (PC20-FT80), shown in Figure 6e,f, 80% of PC was replaced with FT. No cement hydration products were detected in these samples, except for sample C3/7 after 28 days. This absence is attributed to the significantly reduced cement content and increased sulfide concentration, as was also observed in sample C2. The presence of the sulfide mineral pyrite was evident in all samples except C3/7 after 28 and 120 days. These samples are expected to exhibit the lowest compressive strength.

4.2. Scanning Electron Microscopy (SEM)

Using SEM-EDS, the morphology and chemical composition of the control concrete sample C100 (100% cement) and the representative sample C2/25 (40% PC and 60% FT containing 25% sulfur) were analyzed after 120 days of curing. The cement hydration products tobermorite (C-S-H gel), portlandite ($Ca(OH)_2$), and ettringite ($3CaO{\cdot}Al_2O_3{\cdot}3CaSO_4{\cdot}32H_2O$) were detected in the sample C100 (Figure 7). Hydration products formed in the voids and pores of the concrete matrix, thereby reducing porosity and contributing to the development of a compact microstructure [5].

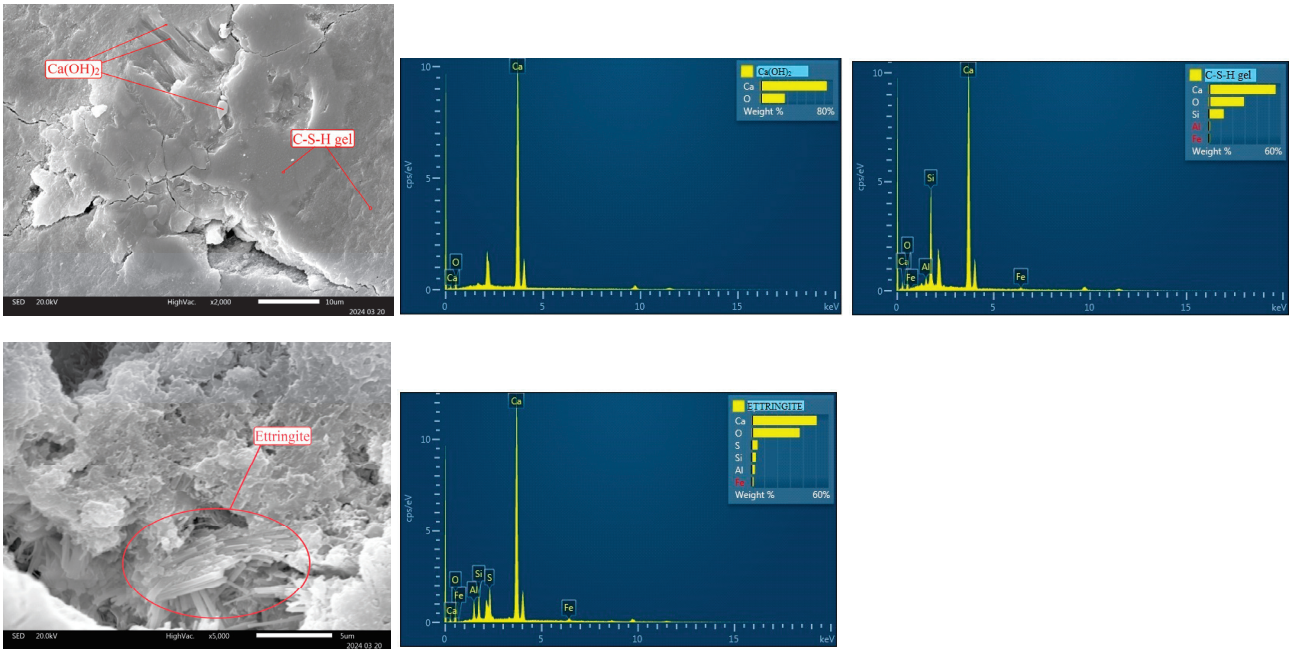

Figure 7. SEM images and EDS analyses of the control sample C-100.

The C2/25 sample was taken as a representative sample for the analysis because the analysis of the compressive strength results showed the regularity of the reduction of the

compressive strength in proportion to the percentage of cement in the concrete, which is clearly expressed in the C2/14, C2/25, and C2/40 samples. Therefore, C2/25 was selected to present the morphology of the concrete and to show that the sulfur present in the concrete had no significant influence on the hydration of the cement or on the formation of new compounds (Figure 8). The obtained structure of C2/25 was homogeneous, without cracks and voids, and with the following cement hydration products: tobermorite, portlandite, ettringite, and tetracalcium aluminate hydrate ($4CaO \cdot Al_2O_3 \cdot 13H_2O$).

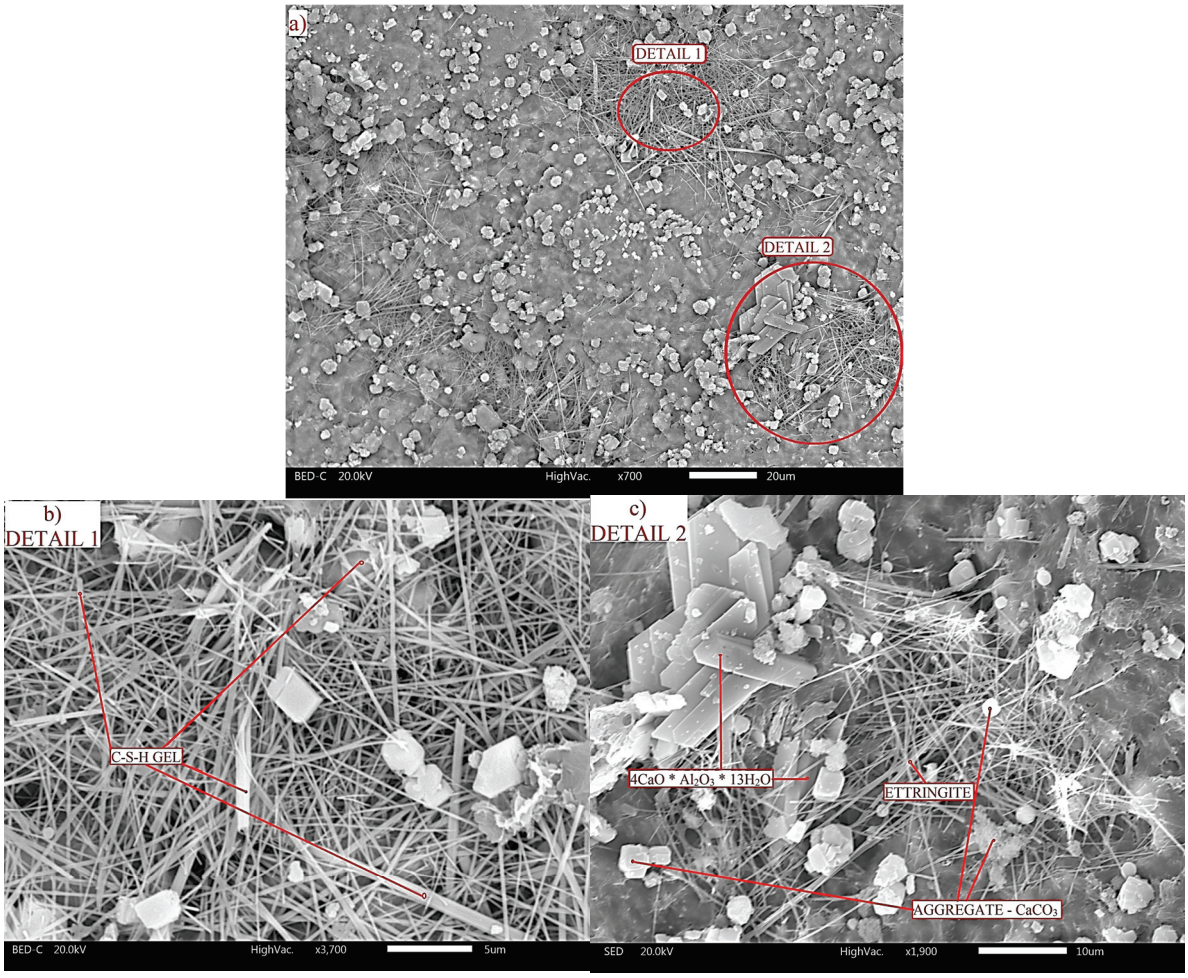

Figure 8. SEM image of representative sample C2/25 (**a**), with details 1 (**b**) and 2 (**c**).

Needle-like C-S-H gel [52] and plate crystals of portlandite are formed during the hydration of alite (C_3S) and belite (C_2S). C-S-H gel and portlandite, according to Bušatlić et al. [53], occupy about 50–60% and 20–25% of the volume of hardened hydrated cement paste, respectively. C-S-H gel is an amorphous phase [54] that plays a key role in determining the durability and mechanical properties of cementitious materials [55]. During cement hydration, C-S-H gel and portlandite fill the voids that were previously filled with water, which is why they are considered the binding phase of the cement paste. Mohamed et al. [56] explained that the fine fractions of limestone aggregate, which consists of calcite, represent nucleation points for the formation of C-S-H gel and portlandite ($Ca(OH)_2$). The fine particles originating from the flotation tailings (FT) incorporated in the concrete also serve as nucleation sites for the formation of cement hydration products [17].

Ettringite is formed by hydration of tricalcium-aluminate (C_3A) in the presence of gypsum ($CaSO_4 \cdot 2H_2O$), and it consists of long needle crystals that form a network that fills the pores and cavities (Figure 8c).

Another product of hydration of tricalcium aluminate in the presence of portlandite and at a low concentration of sulfate ions (0.296 g SO_3/1 g C_3A) [53] is tetracalcium-aluminate hydrate ($4CaO{\cdot}Al_2O_3{\cdot}13H_2O$ or C_4AH_{13}; Figure 8c).This hydration reaction is the main cause of flash setting, which leads to irreversible hardening of the cement paste. The structure of the hydrate C_4AH_{13}, according to Grdić [48], consists of hexagonal plate crystals that gradually transform into the higher stable cubic form C_3AH_6.

The presented morphology of C2/25 indicates that the structure of the sample is homogeneous, which makes the sample slightly porous, which reduces the diffusion of oxygen and water through the concrete and prevents the oxidation of pyrite from the tailings. SEM and XRD analysis showed that no new compounds were formed during the hardening of the concrete, which indicates that there was no oxidation of pyrite in the concrete.

One of the catalysts of pyrite oxidation is the bacterium *Thiobacillus ferrooxidans*. Sampson et al. [57] explained that the presence of this bacterium on the pyrite surface causes mineral erosion. Figure 9 shows a pyrite grain in sample C2/25, indicating that the grain surface is undamaged, i.e., there was no mineral erosion, confirming the absence of *Thiobacillus ferrooxidans* in the concrete.

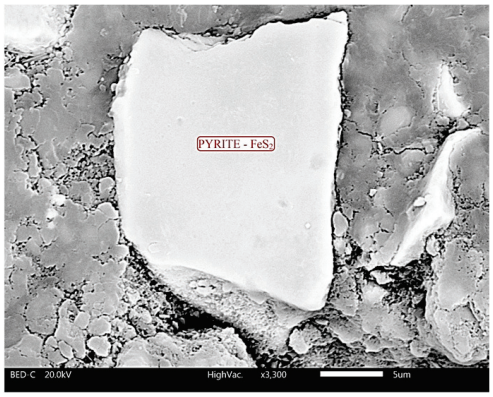

Figure 9. Pyrite grain in sample C2/25.

4.3. Uniaxial Compressive Strength

Uniaxial compressive strength tests were performed on the control sample C-100 and the samples from Table 1, C1 (PC80-FT20), C2 (PC40-FT60), and C3 (PC20-FT80), depending on the sulfur content in the flotation tailings (FT), after 28, 90, 120, 180, and 360 days of curing. The comparison of results was performed on samples with the same content of PC and FT, but with different concentrations of sulfur in the FT and curing time. This analysis aimed to determine whether the sulfur present in FT causes concrete degradation during the curing time.

Table 4 shows the measured and mean values of the uniaxial compressive strength of samples C-100, C1, C2, and C3 during the hardening period, for better visibility and easier interpretation of the obtained results. The standard deviation was determined based on the data presented in the tables, using a 95% confidence level. For statistical data analysis, Student's t-distribution (*t*-test) was applied with degrees of freedom equal to $n - 1$. In our case, for five measurements, this corresponds to 4 degrees of freedom, and the corresponding t-value at the 95% confidence level was 2.7764, with the results shown in Table 3.

Table 4. Measured and mean values of uniaxial compressive strength of control sample C-100 and samples C1, C2, and C3 during the period of curing.

FT with Different Sulfur Content	C1 (PC80-FT20)						
	Uniaxial Compressive Strength, [MPa]					Mean Value of Uniaxial Compressive Strength, [MPa]	StDEV
	28 Day	90 Day	120 Day	180 Day	360 Day		
C-100	38.97	40.68	41.88	42.87	43.21	41.52	2.151
C1/7	42.33	42.44	43.08	43.57	43.91	43.07	0.855
C1/14	42.15	42.36	43.68	43.91	44.01	43.22	1.109
C1/25	29.88	30.61	30.85	31.02	31.35	30.74	0.685
C1/40	28.38	28.74	29.95	31.39	31.97	30.09	1.961
FT with Different Sulfur Content	**C2 (PC40-FT60)**						
	Uniaxial Compressive Strength, [MPa]					Mean Value of Uniaxial Compressive Strength, [MPa]	StDEV
	28 Day	90 Day	120 Day	180 Day	360 Day		
C-100	38.97	40.68	41.88	42.87	43.21	41.52	2.151
C2/7	23.02	24.45	27.04	27.83	27.98	26.06	2.748
C2/14	12.49	14.32	14.9	16.66	16.97	15.07	2.270
C2/25	12.58	14.52	15.98	15.98	16.02	15.02	1.866
C2/40	14.09	15.54	16.42	16.55	16.91	15.90	1.404
FT with Different Sulfur Content	**C3 (PC20-FT80)**						
	Uniaxial Compressive Strength, [MPa]					Mean Value of Uniaxial Compressive Strength, [MPa]	StDEV
	28 Day	90 Day	120 Day	180 Day	360 Day		
C-100	38.97	40.68	41.88	42.87	43.21	41.52	2.151
C3/7	3.30	4.40	6.46	7.48	7.89	5.91	2.465
C3/14	3.45	5.11	6.74	7.22	7.92	6.09	2.235
C3/25	3.15	4.91	6.61	7.16	7.93	5.95	2.382
C3/40	4.01	6.03	6.23	6.60	7.77	6.13	1.691

Yellow: Control sample; Green: samples where 20% of PC is replaced by FT (FT with pozzolanic properties); Pink: samples where the compressive strength is proportional to the learning PC (FT with filler properties).

Table 4 presents the uniaxial compressive strength results of samples C-100, C1/7, and C1/14 after 360 days of curing, namely, 43.21, 43.91, and 44.01 [MPa], respectively. For samples C1/7 and C1/14, the compressive strength was expected to be 20% lower than that of sample C-100 (≈34.57 MPa), due to the 20% reduction in PC in samples C1/7 and C1/14. The results showed that there was no decrease in the compressive strength of the C1/7 and C1/14 samples, which means that 20% of FT-7 and FT-14 effectively replaced 20% of the PC.

The compressive strength results of samples C-100 and C2/7 after 360 days of curing were 43.21 and 27.98 [MPa], respectively. According to the proportion of PC in the sample, C2/7 had 40% PC, so the compressive strength of the C2/7 sample was expected to be 60% lower than the compressive strength of C-100. The test results showed that the compressive strength of sample C2/7 corresponded to that of a sample containing 60% PC, which means that there was a replacement of about 20% of the cement with FT-7.

As can be seen in Table 4, the compressive strengths of samples C1/25, C1/40, C2/14, C2/25, C2/40, C3/7, C3/14, C3/25, and C3/40 were lower in proportion to the reduction in the PC content in the samples. For example, C1/25 (80% PC) had a mean value of compressive strength of 30.74 MPa, and the control sample C-100 had 41.52 MPa; thus,

it follows that the mean value of compressive strength of C1/25 was 25.96% lower than control sample C-100, which corresponded to a reduction of PC participation of 20% in the sample. Sample C2/25 (40% PC) had a mean compressive strength of 15.02 MPa, and control sample C-100 was 41.52 MPa, with the mean compressive strength of C2/25 being 62.83% lower than control sample C-100, which corresponded to a 60% decrease in PC participation in the sample. Sample C3/25 (20% PC) had a mean value of compressive strength of 5.92 MPa, and the control sample C-100 was 41.52 MPa, with the mean value of compressive strength of C2/25 being 85.74% less than the control sample C-100, which corresponded to an 80% decrease in PC participation in the sample.

According to the regularities shown, it can be concluded that FT-7 in samples C1 and C2, as well as FT-14 in sample C1, can replace 20% of PC. The results of previous research, ratio of mechanical results, and the number of tailings showed that FT can replace fine aggregate from 10 to 40%, and PC from 5 to 20% [58]. In order for FT to replace PC, it must have pozzolanic properties, which are proven according to the SRPS EN 450-1:2014 standard [59]. By summarizing the results of the chemical properties shown in Table 2, a comparison of the results with the requirements of the relevant standard was carried out, according to which FT-7 is classified as pozzolan of class C.

Due to the coarse particle content in FT-7, as shown in Table 3, in the early stages of curing, pozzolanic reactions will be delayed, and the sample will behave as an inert filler. As the curing time increases, the pozzolanic activity of FT-7 will gradually increase [17]. FT-14 does not meet the criteria of the standard, due to the high value of the loss on ignition of 12.75%, according to the standard it is max 9%, which is why it is not classified as a pozzolanic material. Deniz Adigüzel et al. [58] formed a diagram of the dependence of the relative change in compressive strength on the number of oxides in the tailings SiO_2, Al_2O_3, and Fe_2O_3 (Figure 10), which showed that tailings with $SiO_2 + Al_2O_3 + Fe_2O_3 > 75\%$ can have compressive strengths from 10% lower to 5% higher than the reference value.

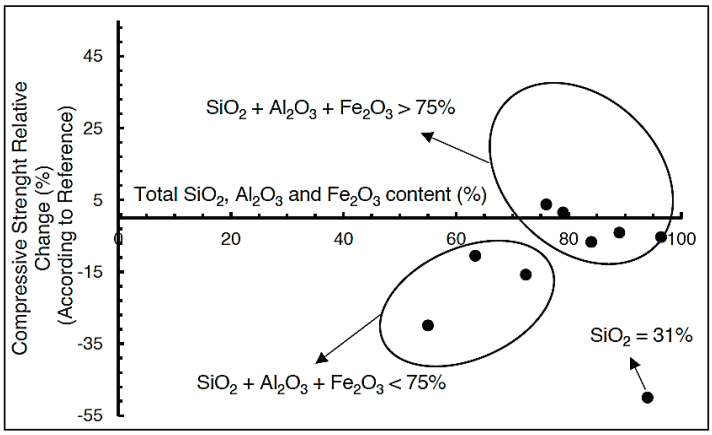

Figure 10. Influence of the sum of oxides SiO_2, Al_2O_3, and Fe_2O_3 on compressive strength [59].

In FT-14, the sum of SiO_2, Al_2O_3, and Fe_2O_3 oxides was 87.68% (see Table 2), which according to the diagram means that it can be expected that the compressive strength will range from 10% lower to 5% higher than the reference sample. FT-14 had a high percentage of SiO_2, 56.31% (Table 2), which reacts with portlandite to form calcium-silicate hydrate (C-S-H gel) responsible for the mechanical properties of concrete [58]. Sulfur, found in FT, reacts with tricalcium aluminate hydration products to form ettringite and gypsum, which lead to expansion of concrete and increase in volume, which negatively affect the mechanical properties of concrete [58]. In samples C1/7, C1/14, and C2/7, no formation of ettringite occurred, which was proven by XRD analysis (Figure 6a,b).

In samples C1, C2, and C3, the flotation tailings showed the characteristics of an inert filler in concrete. The term filler refers to particles with a maximum size of 250 μm and that they are inert, but not without influence [60,61]. Fillers can fill the intergranular space between the cement grains in concrete, thereby reducing porosity and increasing the compressive strength of concrete [62]. This is known as the fill effect. Fillers can also serve as nucleation sites for cement hydrates. This property depends on the particle size and develops in the early stage of solidification [60,61,63–66].

In samples FT-7, FT-14, FT-25, and FT-40, the contents of particles smaller than 250 μm were 59.50%, 91.70%, 89.50%, and 97.40%, respectively (see Figure 4). Samples FT-14, FT-25, and FT-40 met the conditions of the filler, due to the high content of particles smaller than 250 μm. The fine particles in FT-14, FT-25, and FT-40 samples will create spaces within the concrete where the nucleation of hydration products can occur [17].

Sulfur present in samples FT-7, FT-14, FT-25, and FT-40 in concentrations of 7.56%, 13.84%, 25.02%, and 39.82%, respectively, formed ettringite during cement hydration, which has a negative effect on the mechanical properties of concrete and leads to its degradation. In concrete samples where tailings, which contain sulfur, are used as a substitute for cement, the aggregate is natural sand, a significant decrease in compressive strength was observed with a greater participation of tailings in the sample without any clear regularity [5]. The solution to this problem is the neutralization of sulfur, which, in this paper, was achieved by using limestone as an aggregate in concrete, as will be described in detail later in the paper. By neutralizing the sulfur in the FT samples, it was found that the FT acted as a partially inert filler.

Concrete porosity is shown in Table 5 and was calculated according to Formula (10) [47] on samples C1, C2, and C3, with FT having the lowest and highest sulfur concentration.

Table 5. Comparative table of porosity and uniaxial compressive strength of samples C1, C2, and C3.

Sample Code		Porosity [%]	Porosity StDEV	Mean Value of Uniaxial Compressive Strength [MPa]	StDEV
C1 (PC80-FT20)	T-7	3.24	1.331	43.07	2.151
	T-40	6.61	1.530	30.09	1.961
C2 (PC40-FT60)	T-7	6.82	1.594	26.06	2.748
	T-40	8.76	1.004	15.90	1.404
C3 (PC20-FT80)	T-7	9.08	1.783	5.91	2.151
	T-40	9.56	1.706	6.13	1.691

Table 5 presents the porosity results of samples C1, C2, and C3 and the dependence of compressive strength on porosity. By comparing the porosity results of the mentioned samples with the porosity values of porous concrete, where the porosity is 15–30% [67], we can conclude that samples C1, C2, and C3 were not porous concrete. The effect of porosity on compressive strength is that with increasing porosity, compressive strength decreases, due to a decrease in the homogeneity of the sample.

The small porosity of the concrete indicates the homogeneity of the samples. Sample homogeneity is one of the basic characteristics that determine a sample's mechanical properties, specifically compressive strength. The homogeneity of the sample was achieved by forming a sufficient amount of hydration product (C-S-H gel and portlandite), proportional participation of cement in the sample, neutralization of sulfur, use of limestone as an aggregate in the sample, and the property of FT to act as a filler in the sample due to the high percentage of fractions smaller than 250 μm.

4.4. Assessment of Acid Formation Potential—Static Test

In this work, a static test was performed according to SRPS EN 15875:2013 [43] on samples FT-7, FT-14, FT-25, and FT-40 in order to characterize the FT samples based on their potential for acid formation. Based on the test results (Table 6), it can be concluded that all FT samples have a potential for acid formation. The main cause for the creation of acidic drainage is the presence of pyrite in the tailings, which during oxidation, in the presence of water and oxygen, produces acid and metal ions [68]. The low neutralization potential of the samples, due to the low content of alkaline oxides K_2O+CaO+MgO, <8 wt% [68], is also one of the reasons for the potential for acid formation.

Table 6. Results of the static test and characterization of the FT samples.

Static Test	FT-7	FT-14	FT-25	FT-40
S, [%]	7.56	13.84	25.02	39.82
AP, [$CaCO_3$ kg/t]	236.25	432.50	781.88	1244.38
NP, [$CaCO_3$ kg/t]	13.13	5.25	4.25	11.75
NNP, [$CaCO_3$ kg/t]	−223.13	−427.25	−777.63	−1256.13
NP/AP	0.06	0.01	0.01	−0.01
K_2O+CaO+MgO, [%]	7.79	6.54	4.69	1.47
Sample characterization	PAF *	PAF *	PAF *	PAF *

AP—acidity potential, NP—neutralization potential, NNP—net neutralization potential. * PAF—potentially acid-forming.

At flotation tailings disposal sites, the potential of the tailings to form acids has a negative impact on the environment, due to the creation of acidic drainage waters. Tailings, with acid-forming potential, when used in concrete, can lead to the degradation of the concrete structure. This problem can be solved by neutralizing the sulfide in FT.

In this work, the neutralization of FT acidity was achieved by using limestone as an aggregate in concrete. The basic mineral of limestone is calcite ($CaCO_3$), which is also the most commonly used mineral for neutralization [69]. A static test was performed on a representative sample C3/40 (Table 7), where the share of PC (20%), FT (80%), and sulfur concentration in FT was 39.82%, and limestone was used as aggregate. In order for the sample to meet the requirements of NAF characterization (no potential for acid formation), it is necessary that NNP > 20 and NP/AP be greater than 3 [44]. Sample C3/40 met the stated conditions, NNP = 559.23 [$CaCO_3$ kg/t] and NP/AP = 4.18, which means that the neutralization of sulfur in the sample using limestone aggregate was achieved.

Table 7. Results of static test C3/40.

Sample	S, [%]	AP, [$CaCO_3$ kg/t]	NP, [$CaCO_3$ kg/t]	NNP, [$CaCO_3$ kg/t]	NP/AP	Sample Characterization
C3/40	5.62	175.63	734.85	559.23	4.18	NAF *

* NAF—not acid-forming.

4.5. The Process of Leaching Toxic Elements

The TCLP method [17] was performed on samples of flotation tailings FT-7, FT-14, FT-25, and FT-40 and concrete C1/40 and C3/40 after 28 and 90 days in order to determine the toxic characteristics of the samples.

Table 8 presents the results of FT testing, where the concentrations of toxic elements in FT samples were lower than the threshold concentrations for non-hazardous waste

according to the rulebook on categories, testing, and classification of waste [39]. Based on these results, FT is classified as non-hazardous waste.

Table 8. Chemical analysis of the eluate obtained by the TCLP method on samples FT-7, FT-14, FT-25, and FT-40.

Parameter	Unit	FT-7	FT-14	FT-25	FT-40	Reference Value for Non-Hazardous Waste *
Sb	mg/L	<0.006	<0.006	<0.006	<0.006	15
As	mg/L	<0.020	<0.020	<0.020	<0.020	5
Cu	mg/L	4.9	16.9	2.9	1.2	25
Ba	mg/L	0.080	0.063	0.061	0.036	100
Cd	mg/L	0.004	0.041	<0.004	0.007	1
Mo	mg/L	<0.007	<0.007	<0.007	<0.007	350
Ni	mg/L	0.024	0.030	0.008	<0.007	20
Pb	mg/L	0.27	0.15	0.080	1.0	5
Se	mg/L	<0.004	<0.004	<0.004	<0.004	1
Cr	mg/L	0.045	0.034	0.010	0.015	5
Zn	mg/L	2.3	2.0	0.73	0.51	250
Hg	mg/L	<0.0005	<0.0005	<0.0005	<0.0005	0.2
V	mg/L	<0.007	<0.007	<0.007	<0.007	24
Ag	mg/L	<0.005	<0.005	<0.005	<0.005	5

* Annex 10 of the rulebook on categories, testing, and classification of waste (Sl gl RS 56/2010, 93/2019, 39/2021, 65/2024), Article 1, Parameters for testing the toxic characteristics of waste intended for disposal [39].

The test results of FT-40, C1/40, and C3/40 after 28 and 90 days are shown in Table 9. C1/40 and C3/40 were taken as concrete test samples due to the higher content of sulfur in FT, which is included in the composition of concrete, in order to see the influence of sulfur and the amount of cement on the leaching of toxic elements. The amounts of tested toxic elements were lower than the permitted limits given by the rulebook [39], which classifies samples C1/40 and C3/40 as non-hazardous waste, i.e., materials that do not pose a harmful impact. It can be seen that the leaching of toxic elements was less in samples with a lower participation of FT. For example, copper leaching in concrete C1/40 after 28 days was 0.55 mg/L, and in sample C3/40, after 28 days, it was 1.11 mg/L. The reason for this is the lower participation of cement in concrete, which led to the formation of less hydration products (C-S-H gel), which resulted in greater leaching of toxic elements. The product of cement hydration, C-S-H gel, plays an important role in the stabilization of heavy metals in concrete [69]. In general, the use of flotation tailings, as a replacement for cement in concrete, contributes to the stabilization/solidification of heavy metals within the concrete matrix, thereby reducing the leaching of toxic elements into the environment. The results show that the amount of leaching of toxic elements decreased with the curing time.

Table 9. Chemical analysis of the eluate obtained by the TCLP method on samples FT-40, C1/40, and C3/40 after 28 and 90 days.

Parameter	Unit	FT-40	C1/40 after 28 Days	C3/40 after 28 Days	C1/40 after 90 Days	C3/40 after 90 Days	Reference Value for Non-Hazardous Waste *
Sb	mg/L	<0.006	0.003	0.005	0.001	0.004	15
As	mg/L	<0.020	0.0092	0.013	0.0088	0.010	5
Cu	mg/L	1.2	0.55	1.11	0.45	0.96	25
Ba	mg/L	0.036	0.021	0.033	0.018	0.03	100
Cd	mg/L	0.007	0.003	0.006	0.002	0.005	1
Mo	mg/L	<0.007	0.003	0.005	0.001	0.005	350
Ni	mg/L	<0.007	0.004	0.006	0.002	0.004	20
Pb	mg/L	1.0	0.23	0.88	0.12	0.64	5
Se	mg/L	<0.004	0.002	0.003	0.001	0.002	1
Cr	mg/L	0.015	0.0082	0.011	0.0061	0.0098	5
Zn	mg/L	0.51	0.25	0.43	0.11	0.31	250
Hg	mg/L	<0.0005	0.0002	0.0004	0.0001	0.0003	0.2
V	mg/L	<0.007	0.002	0.006	0.001	0.004	24
Ag	mg/L	<0.005	0.002	0.004	0.001	0.003	5

* Annex 10 of the rulebook on categories, testing, and classification of waste (Sl gl RS 56/2010, 93/2019, 39/2021, 65/2024), Article 1, Parameters for testing the toxic characteristics of waste intended for disposal [39].

4.6. Assessment of Leaching of Heavy Metals from Monolithic Waste

The heavy metal leaching method was performed on samples C1/6, C3/6, C1/14, C3/14, C1/25, C3/25, C1/40, and C3/40 in order to determine the amount of leached heavy metals under the influence of atmospheric conditions. In this paper, detailed test results are not presented, but only summary findings relevant to the classification of samples are given. In the second part of this paper (Part II), a complete analysis of the assessment of leaching of heavy metals from monolithic waste will be presented.

The classification and evaluation of FT pollution was conducted based on the results of leaching of heavy metals, according to the SRPS EN 12457-2 standard [37], on samples FT-6, FT-14, FT-25, and FT-40. By comparing the values, it can be seen that all the parameters met the conditions of non-hazardous waste. Samples FT-6, FT-14, FT-25, and FT-40 were classified as non-hazardous waste.

Cumulative leaching of heavy metals per unit area of the sample, as well as the rate and nature of leaching, was determined using the leaching test for monolithic waste, in accordance with the EA NEN 7375:2004 standard [45]. Based on the obtained results, the impact of samples FT-6, FT-14, FT-25, and FT-40 on the environment was determined.

The values of the measured cumulative leaching of heavy metals (ε_n^*) for samples C1/7, C3/7, C1/14, C3/14, C1/25, C3/25, C1/40, and C3/40 after 64 days of testing met the criteria for non-hazardous waste, which can be disposed of in landfills designated for such waste, in accordance with the rulebook [39], These findings will be discussed in greater detail in the second part of this paper (Part II).

5. Conclusions and Future Perspectives

Research on the application of FT as a substitute for cement in concrete structures provides a significant contribution to environmental protection, resource conservation, and

the sustainable development of the construction industry. FT, which until now has been an environmental problem due to the high content of heavy metals and sulfide compounds, can be effectively converted into a valuable construction material, which achieves multiple benefits: reduction of mining waste, saving of natural raw materials/resources, and reduction of CO_2 emissions through reduced consumption of Portland cement. This approach represents a concrete example of the implementation of the circular economy in mining and construction and can contribute to the development of sustainable cities, which is in line with the global Sustainable Development Goals (SDGs).

The results of this study indicate that the use of limestone, as a crushed separated natural aggregate, incorporated as a structural component in concrete, enabled the neutralization of sulfides originating from pyrite, which is a component of flotation tailings (FT). This conclusion is supported by the following findings:

- Acid generation potential analysis (static test) showed that the representative sample C3/40 (comprising 20% Portland cement (PC) and 80% FT, with a sulfur concentration in FT of 39.82%) has no acid generation potential (NAF). This confirms the effective neutralization of sulfides in the sample.
- Uniaxial compressive strength tests of samples C1, C2, and C3 after 360 days revealed values comparable to those recorded at 28 days. This indicates the absence of concrete degradation due to sulfide presence, further supporting the successful sulfide neutralization process.
- Microstructural and chemical analysis of sample C2/25, conducted using SEM-EDS, revealed a homogeneous structure without cracks or voids. The presence of hydration products—C-S-H gel, portlandite, ettringite, and tetracalcium aluminate hydrate—confirms that sulfides present in the concrete do not interfere with cement hydration or the formation of new compounds.
- Environmental impact assessments showed that all tested samples are environmentally benign. This was demonstrated using both the TCLP (Toxicity Characteristic Leaching Procedure) and heavy metal leaching tests on monolithic waste. TCLP analysis confirmed no leaching of toxic elements (Sb, As, Cu, Ba, Cd, Mo, Ni, Pb, Hg) from the samples. Furthermore, the leaching test for monolithic waste demonstrated that after 64 days, the eluates met the criteria for non-hazardous waste suitable for disposal at designated non-hazardous waste landfills.

However, further research is needed to optimize the relationships between flotation tailings, cement, and other components of concrete mixtures. Special emphasis should be placed on the long-term stability of concrete under conditions of different temperature and humidity regimes, as well as on extended testing of the toxicity and ecological impact of concrete with flotation tailings in real-world applications Additionally, it is recommended to explore the potential for applying this technology at a larger industrial scale, in order to reduce the environmental impact of the construction industry, while also enabling the maximum utilization of mining waste.

Future perspectives in this research area include the development of new technologies for more efficient sulfide neutralization, as well as the integration of environmental criteria in concrete production. Also, the application of flotation tailings in other industries, such as the production of cement and construction materials, could further contribute to sustainability and reduction of mining waste.

Author Contributions: Conceptualization, V.Đ. and V.K.; Methodology, V.Đ. and L.Đ.I.; Validation, N.S., N.V. and V.K.; Formal analysis, N.S., L.Đ.I., V.J. and N.V.; Investigation, V.Đ. and L.Đ.I.; Resources, L.Đ.I.; Writing—original draft, V.Đ. and V.K.; Writing—review & editing, V.J., N.V. and

V.K.; Visualization, V.J.; Supervision, N.S., N.V. and V.K.; Funding acquisition, V.Đ. All authors have read and agreed to the published version of the manuscript.

Funding: The research presented in this paper was done with the financial support of the Ministry of Science and Technological Development and Innovation of the Republic of Serbia, with the Contract No. 451-03-136/2025-03/200052.

Institutional Review Board Statement: Not applicable.

Informed Consent Statement: Not applicable.

Data Availability Statement: The data presented in this study are available on request from the corresponding author due to all data will be available in the future doctoral thesis defended by Vanja Đurđevac.

Conflicts of Interest: The authors declare no conflicts of interest.

References

1. Nuorivaara, T.; Björkqvist, A.; Bacher, J.; Serna-Guerrero, R. Environmental remediation of sulfidic tailings with froth flotation: Reducing the consumption of additional resources by optimization of conditioning parameters and water recycling. *J. Environ. Manag.* **2019**, *236*, 125–133. [CrossRef] [PubMed]
2. Castillo Araiza, R.; Rodrigues, A.; Fournier, B.; Duchesne, J. A new accelerated testing scheme to evaluate the potential oxidation reaction of sulfide-bearing aggregates in concrete specimens. *Cement Concr. Res.* **2024**, *180*, 107507. [CrossRef]
3. Mafra, C.; Bouzahzah, H.; Stamenov, L.; Gaydardzhiev, S. Insights on the effect of pyrite liberation degree upon the acid mine drainage potential of sulfide flotation tailings. *Appl. Geochem.* **2020**, *123*, 104774. [CrossRef]
4. De Carvalho, A.L.C.B.; de Albuquerque, V.A.; Blannin, R.; Escobar, A.G.; Frenzel, M.; Rudolph, M.; Silva, A.C.; Goldmann, D. A study on the desulfurization of sulfidic mine tailings for the production of a sulfur-poor residue. *Miner. Eng.* **2023**, *202*, 108285. [CrossRef]
5. Saedi, A.; Jamshidi-Zanjani, A.; Khodadadi Darban, A.; Mohseni, M.; Nejati, H. Utilization of lead–zinc mine tailings as cement substitutes in concrete construction: Effect of sulfide content. *J. Build. Eng.* **2022**, *57*, 104865. [CrossRef]
6. Saedi, A.; Jamshidi-Zanjani, A.; Mohseni, M.; Khodadadi Darban, A. Effect of mechanochemical activation on hydration properties of lead-zinc sulfide tailings for concrete construction. *Case Stud. Constr. Mater.* **2023**, *18*, e01996. [CrossRef]
7. Mends, E.A.; Tita, A.M.; Hussaini, S.; Thella, J.S.; Pan, L.; Chu, P. Investigation of leaching of nickel sulfide flotation tailings to recover valuable metals. *Miner. Eng.* **2024**, *212*, 108716. [CrossRef]
8. Cacciuttolo, C.; Cano, D. Environmental impact assessment of mine tailings spill considering metallurgical processes of gold and copper mining: Case studies in the Andean countries of Chile and Peru. *Water* **2022**, *14*, 3057. [CrossRef]
9. Đurđevac Ignjatović, L.; Krstić, V.; Radonjanin, V.; Jovanović, V.; Malešev, M.; Ignjatović, D.; Đurđevac, V. Application of cement paste in mining works, environmental protection and sustainable development goals in the mining industry. *Sustainability* **2022**, *14*, 7902. [CrossRef]
10. Lu, H.J.; Qi, C.C.; Chen, Q.S.; Gan, D.Q.; Xue, Z.L.; Hu, Y.J. A new procedure for recycling waste tailings as cemented paste backfill to underground stopes and open pits. *J. Clean. Prod.* **2018**, *188*, 601–612. [CrossRef]
11. Martins, N.P.; Helser, J.; Plötze, M.; Snellings, R.; Habert, G. Effect of sulfidic mine tailings used as mineral admixtures on the hydration of common and alternative cement. *Mater. Struct.* **2024**, *57*, 19. [CrossRef]
12. Na, H.; Eom, Y.; Yoo, K.; Diaz Alorro, R. A review on the reprocessing of sulfide tailings for resource recovery and AMD prevention using mineral processing methods. *Miner. Eng.* **2024**, *218*, 109025. [CrossRef]
13. Pomponi, F.; Moncaster, A. Circular economy for the built environment: A research framework. *J. Clean. Prod.* **2017**, *143*, 710–718. [CrossRef]
14. Barbosa Júnior, I.D.O.; Macêdo, A.N.; Martins, V.W.B. Construction industry and its contributions to achieving the SDGs proposed by the UN: An analysis of sustainable practices. *Buildings* **2023**, *13*, 1168. [CrossRef]
15. United Nations. *Transforming Our World: The 2030 Agenda for Sustainable Development*; United Nations: New York, NY, USA, 2015.
16. Dandautiya, R.; Singh, A.P. Utilization potential of fly ash and copper tailings in concrete as partial replacement of cement along with life cycle assessment. *Waste Manag.* **2019**, *99*, 90–101. [CrossRef] [PubMed]
17. Zunino, F.; Lopez, M. Decoupling the physical and chemical effects of supplementary cementitious materials on strength and permeability: A multi-level approach. *Cem. Concr. Compos.* **2016**, *65*, 19–28. [CrossRef]
18. Gutteridge, W.A.; Dalziel, J.A. Filler cement: The effect of the secondary component on the hydration of Portland cement: Part, I. A fine non-hydraulic filler. *Cem. Concr. Res.* **1990**, *20*, 778–782. [CrossRef]

19. Martins, N.P.; Srivastava, S.; Simão, F.V.; Niu, H.; Perumal, P.; Snellings, R.; Ilikainen, M.; Chambart, H.; Habert, G. Exploring the Potential for Utilization of Medium and Highly Sulfidic Mine Tailings in Construction Materials: A Review. *Sustainability* **2021**, *13*, 12150. [CrossRef]
20. Nordstrom, D.K. Aqueous pyrite oxidation and the consequent formation of secondary iron minerals. In *Acid Sulfate Weathering*; Kittrick, J.A., Fanning, D.S., Hossner, L.R., Eds.; Soil Science Society of America: Madison, WI, USA, 1982; pp. 37–56.
21. Singer, P.C.; Stumm, W. Kinetics of the oxidation of ferrous iron. In Proceedings of the Second Symposium on Coal Mine Drainage Research, Pittsburgh, PA, USA, 14–15 May 1968; pp. 12–34.
22. Smith, E.E.; Svanks, K.; Shumate, K.S. Sulfide to sulfate reaction studies. In Proceedings of the Second Symposium on Coal Mine Drainage Research, Pittsburgh, PA, USA, 14–15 May 1968; pp. 1–11.
23. Garrels, R.M.; Thompson, M.E. Oxidation of pyrite in ferric sulfate solution. *Am. J. Sci.* **1960**, *258*, 57–67.
24. Singer, P.C.; Stumm, W. *Oxygenation of Ferrous Iron*; Rep. 14010-06/69; FWQA: Lakeland, FL, USA, 1969.
25. Moricz, F.; Madai, F.; Walder, I.F. Pyrite oxidation under circumneutral pH conditions. In Proceedings of the 23rd Conference on Earth Science and Environmental Protection, Miskolc, Hungary, 27–29 September 2012; Available online: https://www.researchgate.net/publication/328530759 (accessed on 4 March 2025).
26. Trafford, B.D.; Bloomfield, C.; Kelso, W.I.; Pruden, G. Ochre formation in field drains in pyritic soils. *J. Soil Sci.* **1973**, *24*, 453–460. [CrossRef]
27. Amaro, A.M.; Chamorro, D.; Seeger, M.; Arrendondo, R.; Perrano, I.; Jerez, C.A. Effect of external pH perturbations on in vivo protein synthesis by the acidophilic bacterium Thiobacillus ferrooxidans. *J. Bacteriol.* **1991**, *173*, 910–915. [CrossRef] [PubMed]
28. Suzuki, I. Mechanisms of inorganic oxidation and energy coupling. *Annu. Rev. Microbiol.* **1974**, *28*, 85–101. [CrossRef] [PubMed]
29. Temple, K.L.; Colmer, A.R. The autotrophic oxidation of iron by a new bacterium: *Thiobacillus ferrooxidans*. *J. Bacteriol.* **1951**, *62*, 605–611. [CrossRef]
30. Lyalikova, N.N. A study of chemosynthesis in *Thiobacillus ferrooxidans*. *Microbiologiya* **1958**, *27*, 556–559.
31. Hooper, A.B.; DiSpirito, A.A. In bacteria which grow in simple reductants, generation of proton gradient involves extra cytoplasmic oxidation of substrate. *Microbial. Rev.* **1985**, *49*, 140–157. [CrossRef]
32. Ingledew, W.J.; Cobley, J.G. A potentiometric and kinetic study on the respiratory chain of ferrous iron-grown *Thiobacillus ferrooxidans*. *Biochim. Biophys. Acta* **1980**, *590*, 141–158. [CrossRef] [PubMed]
33. Ingledew, W.J. Thiobacillus ferrooxidans—The bioenergetics of an acidophilic chemolithotroph. Biochim. *Biophys. Acta* **1982**, *683*, 89–117.
34. Skousen, J.; Foreman, J. Water management techniques for acid mine drainage control. *Green Lands* **2000**, *30*, 44–53.
35. Singer, P.C.; Stumm, W. Acid mine drainage: The rate determining step. *Science* **1970**, *167*, 1121–1123. [CrossRef]
36. Kirby, D. Effective Treatment Options for Acid Mine Drainage in the Coal Region of West Virginia. Master's Thesis, Marshall University, Huntington, WV, USA, 2014.
37. *SRPS EN 12457-2:2008*; Characterization of Waste—Leaching—Compliance Test for Leaching of Granular Waste Materials and Sludges—Part 2: One Stage Batch Test at a Liquid-Solid Ratio of 10 l/kg for Materials with a High Content Solids and Particle Size of Less than 4 mm (with Decreasing Particle Size, or Without Decreasing). Institute for Standardization of Serbia: Belgrade, Serbia, 2008.
38. *SRPS EN ISO 11885:2007*; Water Quality—Determination of Selected Elements by Inductively Coupled Plasma Optical Emission Spectrometry (ICP-OES). Institute for Standardization of Serbia: Belgrade, Serbia, 2007.
39. Regulation on Categories, Testing, and Classification of Waste. Official Gazette of the RS, No. 56/2010, 93/2019, 39/2021, 65/2024. (In Serbian). Available online: https://www.paragraf.rs/propisi/pravilnik-kategorijama-ispitivanju-klasifikaciji-otpada.html (accessed on 13 March 2025).
40. U.S. EPA. *Method 1311, Toxicity Characteristic Leaching Procedure*; U.S. Environmental Protection Agency: Washington, DC, USA, 1992. Available online: https://www.epa.gov/sites/default/files/2015-12/documents/1311.pdf (accessed on 13 March 2025).
41. *SRPS EN 206-1:2011*; Concrete—Part 1: Specification Performance, Production and Conformity. Institute for Standardization of Serbia: Belgrade, Serbia, 2011.
42. *SRPS EN ISO 17892-4*; Geotechnical Investigation and Testing—Laboratory Testing of Soil—Part 4: Determination of Particle Size Distribution. Institute for Standardization of Sebia: Belgrade, Serbia, 2016.
43. *SRPS EN 15875:2013*; Characterization of Waste—Static Test for Determination of Acid Potential and Neutralization Potential of Sulfidic Waste. Institute for Standardization of Serbia: Belgrade, Serbia, 2013.
44. Karlsson, T.; Räisänen, M.L.; Lehtonen, M.; Alakangas, L. Comparison of static and mineralogical ARD prediction methods in the Nordic environment. *Environ. Monit. Assess.* **2018**, *190*, 719. [CrossRef]
45. *NEN 7375*; Leaching Characteristics of Moulded or Monolithic Building and Waste Materials—Determination of Leaching of Inorganic Components with the Diffusion Test—"The Tank Test". Netherlands Normalisation Institute Standard: Amsterdam, The Netherlands, 2004.

46. *SRPS EN 12390-3:2019*; Testing Hardened Concrete—Part 3: Compressive Strength of Test Specimens. Institute for Standardization of Serbia: Belgrade, Serbia, 2019.
47. Xiong, B.; Wu, X.; Liu, W.; Lu, X.; Gao, H.; Lv, W. Influence of different aggregate characteristics on pervious concrete. *Constr. Build. Mater.* **2025**, *460*, 139789. [CrossRef]
48. Grdić, Z. *Concrete Technology*; Printing House "SVEN": Niš, Serbia, 2011; ISBN 978-86-80295-94-7.
49. Koohestani, B.; Belem, T.; Koubaa, A.; Bussiere, B. Experimental investigation into the compressive strength development of cemented paste backfill containing Nano-silica. *Cem. Concr. Compos.* **2016**, *72*, 180–189. [CrossRef]
50. Koohestani, B. Effect of saline admixtures on mechanical and microstructural properties of cementitious matrices containing tailings. *Constr. Build. Mater.* **2017**, *156*, 1019–1027. [CrossRef]
51. Dong, Q.; Liang, B.; Jia, L.; Jiang, L. Effect of sulfide on the long-term strength of lead-zinc tailings cemented paste backfill. *Constr. Build. Mater.* **2019**, *200*, 436–446. [CrossRef]
52. Wang, L.; Guo, F.; Lin, Y.; Yang, H.; Tang, S.W. Comparison between the effects of phosphorous slag and fly ash on the C-S-H structure, long-term hydration heat and volume deformation of cement-based materials. *Constr. Build. Mater.* **2020**, *250*, 118807. [CrossRef]
53. Bušatlić, I.; Bušatlić, N.; Merdić, N.; Haračić, N. *Basics of Portland Cement Chemistry and Technology*; Printing House Fojnica d.d.: Fojnica, Bosnia and Herzegovina, 2020; pp. 171–176. Available online: https://www.researchgate.net/publication/343994073 (accessed on 20 April 2025). ISBN 978-9958-17-168-0.
54. Geng, Z.; Tang, S.; Wang, Y.; A, H.; He, Z.; Wu, K.; Wang, L. Stress relaxation properties of calcium silicate hydrate: A molecular dynamics study. *J. Zhejiang Univ.-Sci. A Appl. Phys. Eng.* **2024**, *25*, 97–115. [CrossRef]
55. Wang, L.; Jin, M.; Zhou, S.; Tang, S.; Lu, X. Investigation of microstructure of C-S-H and micro-mechanics of cement pastes under NH4NO3 dissolution by 29Si MAS NMR and microhardness. *Measurement* **2021**, *185*, 110019. [CrossRef]
56. Mohamed, A.R.; Elsalamawy, M.; Ragab, M. Modeling the influence of limestone addition on cement hydration. *Alex. Eng. J.* **2015**, *54*, 1–5. [CrossRef]
57. Sampson, M.I.; Phillips, C.V.; Ball, A.S. Investigation of the attachment of Thiobacillus ferrooxidans to mineral sulfides using scanning electron microscopy analysis. *Miner. Eng.* **2000**, *13*, 643–656. [CrossRef]
58. Adiguzel, D.; Tuylu, S.; Eker, H. Utilization of tailings in concrete products: A review. *Constr. Build. Mater.* **2022**, *360*, 129574. [CrossRef]
59. *SRPS EN 450-1:2014*; Fly Ash for Concrete—Part 1: Definition, Specifications and Conformity Criteria. Institute for Standardization of Serbia: Belgrade, Serbia, 2014.
60. Sigvardsen, N.M.; Nielsen, M.R.; Potier, C.; Ottosen, L.M.; Jensen, P.E. Utilization of Mine Tailings As Partial Cement Replacement. *Mod. Environ. Sci. Eng.* **2018**, *4*, 365–374.
61. Moosberg-Bustnes, H.; Lagerblad, B.; Forssberg, E. The function of fillers in concrete. *Mater. Struct.* **2004**, *37*, 74–81. [CrossRef]
62. Wang, C.; Wang, C.; Xiong, Z.; Wang, Y.; Han, Y. Experimental study of high-flow and low-expansion backfill material. *PLoS ONE* **2020**, *15*, e0236718. [CrossRef]
63. Ye, G.; Liu, X.; De Schutter, G.; Poppe, A.-M.; Taerwe, L. Influence of limestone powder used as filler in SCC on hydration and microstructure of cement pastes. *Cem. Concr. Compos.* **2007**, *29*, 94–102. [CrossRef]
64. Deschner, F.; Winnefeld, F.; Lothenbach, B.; Seufert, S.; Schwesig, P.; Dittrich, S.; Goetz-Neunhoeffer, F.; Neubauer, J. Hydration of Portland cement with high replacement by siliceous fly ash. *Cem. Concr. Res.* **2012**, *42*, 1389–1400. [CrossRef]
65. Nonat, A. Interactions between chemical evolution (hydration) and physical evolution (setting) in the case of tricalcium silicate. *Mater. Struct.* **1994**, *27*, 187–195. [CrossRef]
66. Lawrence, P.; Cyr, M.; Ringot, E. Mineral admixtures in mortars effect of type, amount and fineness of fine constituents on compressive strength. *Cem. Concr. Res.* **2005**, *35*, 1092–1105. [CrossRef]
67. Pervious Concrete: Guideline to Mixture Proportioning, NRMCA Engineering Division, NRMCA Publication Number: 2PE001, Version 1, February 2009. Available online: https://www.nrmca.org/wp-content/uploads/Pervious_Concrete_Guideline_Mixture_Proportioning.pdf (accessed on 13 March 2025).
68. da Silva, R.G.; Couto, D.; Tavares, A.; Ribeiro, M.M.; Chaves, L.; Guimarães, L.; Fonseca, K.; Silva, A.C. Static tests to assess acid mine drainage potential of copper sulfide flotation tailings. *Tecnol. Metal Mater. Min.* **2023**, *20*, e2792. [CrossRef]
69. Saedi, A.; Jamshidi-Zanjani, A.; Mohseni, M.; Darban, A.K. Mechanical activation for sulfidic tailings treatment by tailings: Environmental aspects and cement consumption reduction. *Case Stud. Constr. Mater.* **2023**, *19*, e02632. [CrossRef]

Disclaimer/Publisher's Note: The statements, opinions and data contained in all publications are solely those of the individual author(s) and contributor(s) and not of MDPI and/or the editor(s). MDPI and/or the editor(s) disclaim responsibility for any injury to people or property resulting from any ideas, methods, instructions or products referred to in the content.

materials

MDPI

Article

Methods for Quantitative Determination of Iron Sulfides in Rocks

Zhixin Wang [1], Shaoping Wang [2], Wei Li [1,*], Bing Cao [2], Xiaojun Huang [1], Xin Chuai [2], Xinyu Zhang [1] and Min Deng [1,*]

[1] College of Materials Science and Engineering, Nanjing Tech University, Nanjing 211816, China; 202261203229@njtech.edu.cn (Z.W.)
[2] Nanshan Mining Company Ltd., Anhui Maanshan Iron and Steel Mining Resources Group, Maanshan 243000, China
* Correspondence: stevenlee187@outlook.com (W.L.); dengmin@njtech.edu.cn (M.D.)

Abstract: When iron sulfides are used as aggregate in concrete production, it easily oxidizes to form harmful substances such as sulfates. This results in acid corrosion and internal sulfate attack (ISA), significantly reducing concrete durability. To date, the quantification methods for iron sulfides in aggregates remain inaccurate, often neglecting pyrrhotite (a type of iron sulfide). No standardized methods or threshold values for the sulfide content in aggregates have been established, nor have technical guidelines for the application of sulfide-containing aggregates, limiting their use. This study proposes an on-site quantification procedure for determining the pyrite and pyrrhotite content in tailings using a selective chemical dissolution process. An orthogonal experiment was designed to determine the optimal dissolution conditions by considering four factors: particle size, reaction temperature, acid concentration, and reaction time. The pyrrhotite quantification method showed a relative standard deviation (RSD) of 3.60% (<5%) and a mean relative error of 3.19% (<5%), while the pyrite quantification method showed an RSD of 3.11% (<5%) with a mean relative error of 4.70% (<5%). The results were further optimized under engineering conditions to reduce costs and enable on-site quantification without relying on complex precision instruments. The quantitative results of pyrite in mineral samples were verified by the XRD internal standard method, and the error was less than 0.6%. This approach ensures the effective monitoring and management of sulfide content in concrete aggregates, promoting the practical application of sulfur-bearing aggregates.

Keywords: pyrite; selective dissolution; quantitative analysis; aggregate

1. Introduction

In the 20th century, sulfide-containing aggregates (mostly from tailings) were widely used in concrete in Europe and America to reduce the construction costs [1–4]. These rocks contained sulfides like pyrite, which later oxidized, causing expansion and cracking, and progressively deteriorated the concrete [5–8]. In Massachusetts, eastern U.S., extensive cracking damage has occurred in numerous residential concrete foundations due to the oxidation of iron sulfide minerals in coarse aggregate stone, affecting over 45,000 households [9]. In Spain, the use of pyrite-containing aggregates in construction has led to numerous cases of oxidation-induced structural damage [10]. In 1992, iron-sulfide-bearing aggregates are used in the Grosse and Taiscon dams, which subsequently led to severe concrete cracking problems. Since 2004, concrete expansion and rapid deterioration have been observed within 2 to 5 years after construction in Trois-Rivières,

Quebec, Canada [11,12]. In eastern Connecticut, USA, numerous homes incorporating pyrrhotite-bearing aggregates have exhibited cracking and structural damage after 25 years of service [13].

Metal sulfide tailings exposed to air undergo oxidation over time, generating multiple hazardous substances that cause severe environmental damage [6,14–17]. Metal sulfides in mine tailings are highly reactive. Pyrite (FeS_2), in particular, easily reacts with oxygen when exposed to air or oxygen-containing water [18,19]. In wet conditions, pyrite slowly dissolves, releasing large amounts of H^+. At the same time, heavy metals like Zn^{2+}, Cu^{2+}, Cd^{2+}, and Pb^{2+} inside the mineral also dissolve out [20]. It is most accepted that the process mainly includes the following steps [21–23]:

When exposed to the environment, pyrite reacts with water and oxygen, producing Fe^{2+} and $SO_4{}^{2-}$, and releasing large amounts of H^+, as shown in Equation (1).

$$2FeS_2 + 7O_2 + 2H_2O \rightarrow 2Fe^{2+} + 4H^+ + 4SO_4{}^{2-} \quad (1)$$

The generated Fe^{2+} is unstable in the environment and is rapidly oxidized by oxygen to Fe^{3+}, as shown in Equation (2).

$$4Fe^{2+} + O_2 + 4H^+ \rightarrow 4Fe^{3+} + 2H_2O \quad (2)$$

Due to the substantial H^+ production from Equation (1), the environmental acidity progressively increases. When the pH falls below 3.5, Fe^{3+} acts as a potent oxidant to further oxidize pyrite, as shown in Equation (3).

$$FeS_2 + 14Fe^{3+} + 8H_2O \rightarrow 15Fe^{2+} + 16H^+ + 2SO_4{}^{2-} \quad (3)$$

The Fe^{2+} produced in Equation (3) reacts with environmental oxygen via Equation (2), forming the highly oxidative Fe^{3+}. This cyclic process leads to the continuous accumulation of Fe^{3+} and $SO_4{}^{2-}$, accompanied by the progressive acidification (pH decrease) of the environment [24].

The use of iron sulfides as an aggregate in concrete poses risks due to oxidation and sulfate formation. The accurate quantification of iron sulfides content is essential in order to ensure concrete durability.

Luo conducted a qualitative and quantitative analysis of pyrite materials using analytical transmission electron microscopy (AEM/EDS), which enables the precise quantitative analysis of micron- and nano-scale regions in pyrite materials [25]. McDougall, H. conducted a quantitative phase analysis of pyrite concentrate powder using X-ray diffraction [26]. Del Real I proposed a method for the accurate quantification of pyrite using synchrotron-based X-ray fluorescence [27]. The study by Bolin, TB quantified the pyrite content by combining the sulfur K-edge X-ray absorption near-edge structure (S-XANES) third-derivative analysis with wet chemical methods [28].

These methods all require expensive and sophisticated instrumentation, making them unsuitable for a reproducible on-site quantitative analysis. Alternatively, some standard methods employ acid dissolution techniques, where the soluble sulfur content is assumed to represent the pyrite content. The national standard GB/T 31288 [29] establishes the technical requirements for iron tailings sand used in concrete, concrete products and mortar. It specifies that the sulfide and sulfate content (calculated as SO_3) in iron tailings sand should not exceed 0.50%. This method specifies dissolving the sample in HCl, followed by the determination of the dissolved $SO_4{}^{2-}$ content using the barium chloride titration method. The obtained $SO_4{}^{2-}$ concentration is then converted to SO_3 content, representing the total sulfides and sulfates in the sand. However, since pyrite is insoluble in HCl, this method cannot evaluate the potential hazards from sulfur present in pyrite form, representing a significant limitation in assessing the complete sulfur-related risks of iron tailings sand.

The European standard EN 12620:2008 [30] specifies that the pyrrhotite content in aggregates, calculated as sulfur, must not exceed 0.1%. Currently, no other countries or regions have established limit standards for the iron sulfide mineral content in aggregates. Similarly, ACI 201.2R [31] does not provide specific regulations on this matter.

Jana [13] found that Canadian aggregates containing 0.3% pyrrhotite caused severe concrete cracking. To mitigate this, they recommend either avoiding pyrrhotite-containing aggregates, using aggregates with a sulfur content below 0.1%, or establishing sulfur threshold limits specific to different iron sulfide mineral types.

The oxidation of pyrrhotite is more significant than that of pyrite due to its higher reactivity. Existing methods primarily focus on the quantification of pyrite, lacking the ability to distinguish and identify pyrite and pyrrhotite. Furthermore, some standards fail to effectively quantify pyrite, highlighting the need for improved analytical approaches.

This study aims to determine the content of sulfide minerals (including pyrite and pyrrhotite) in tailings using a stepwise chemical dissolution method. An HCl solution was used to selectively dissolve pyrrhotite first, followed by an HNO_3 solution to dissolve pyrite due to its higher oxidizing power. The results were validated by a quantitative analysis using XRD. The effects of the sample particle size, solution concentration, reaction temperature, and reaction time on the analysis of the sulfide mineral content will be examined to establish suitable sample sizes and experimental conditions.

2. Materials and Methods

2.1. Materials

2.1.1. Pyrrhotite

The pyrrhotite samples used in this experiment are collected from the Huangganglang iron mine in Chifeng, Inner Mongolia, China. After crushing and sieving, the samples were classified into three particle size fractions: 0.015–0.030 mm, 0.030–0.045 mm, and 0.045–0.075 mm. Table 1 shows the elemental compositions of different size of pyrrhotite with Thermo ARL 9900 X-ray fluorescence (XRF), from Thermo, Waltham, MA, USA. The pyrrhotite with three different particle sizes are mainly composed of Fe and S, with trace amounts of impurity elements like Pb, Zn, and Si. Figure 1 shows distinct characteristic diffraction peaks of pyrrhotite (Fe_7S_8), galena (PbS), and sphalerite (ZnS). The X-ray powder diffraction data were collected at room temperature using a Rigaku SmartLab 3 kW diffractometer, from Rigaku, Tokyo, Japan.

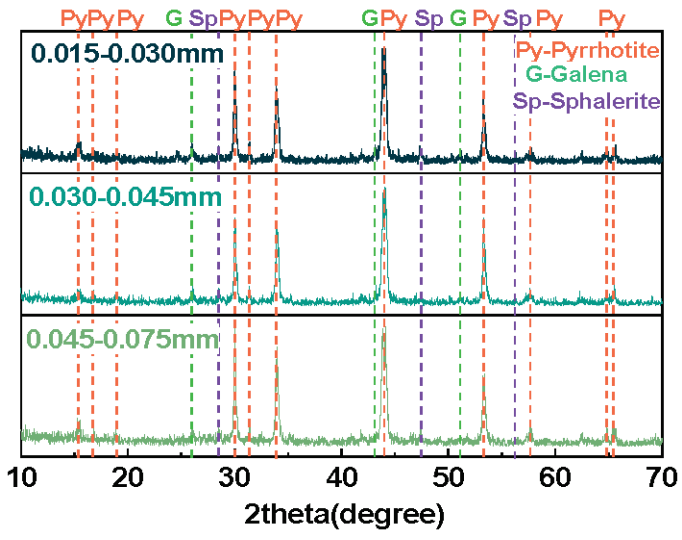

Figure 1. XRD patterns of pyrrhotite in 0.015–0.030 mm, 0.030–0.045 mm, and 0.045–0.075 mm.

Table 1. Elemental compositions of pyrrhotite in 0.015–0.030 mm, 0.030–0.045 mm, and 0.045–0.075 mm.

Particle Size/mm	Elemental Composition/wt%							
	Fe	S	Pb	Zn	Si	Cu	Sb	Al
0.015–0.030	58.42	33.84	2.23	0.95	0.49	0.20	0.19	0.11
0.030–0.045	60.33	34.18	0.95	0.47	0.39	0.09	0.07	0.05
0.045–0.075	59.19	35.15	1.36	0.72	0.37	0.15	0.12	0.07

2.1.2. Pyrite

The pyrite samples used in this experiment are collected from the Shangbao mining area in Hunan, China. After crushing and sieving, the samples were classified into three particle size fractions: 0.015–0.030 mm, 0.030–0.045 mm, and 0.045–0.075 mm. Table 2 shows the elemental compositions of different sizes of pyrite. The pyrite with three different particle sizes is mainly composed of Fe and S. Figure 2 shows distinct characteristic diffraction peaks of pyrite.

Table 2. Elemental compositions of pyrite in 0.015–0.030 mm, 0.030–0.045 mm, and 0.045–0.075 mm.

Particle Size/mm	Elemental Composition/wt%							
	S	Fe	Si	Ca	W	Mg	Al	Cl
0.015–0.030	48.79	47.05	0.57	0.30	0.18	0.10	0.04	0.03
0.030–0.045	46.62	49.62	0.48	0.23	0.11	0.06	0.03	0.03
0.045–0.075	47.95	49.06	0.44	0.19	0.10	0.05	0.03	0.03

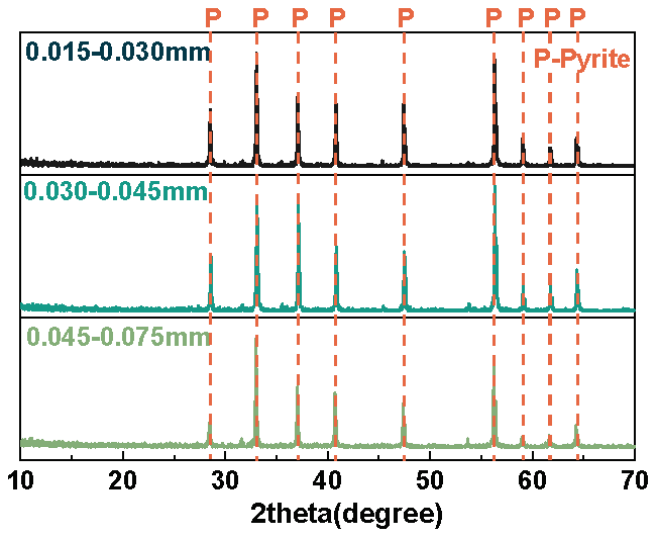

Figure 2. XRD patterns of pyrite in 0.015–0.030 mm, 0.030–0.045 mm, and 0.045–0.075 mm.

2.1.3. Iron Ore Tailings

Samples numbered 1–3 are the crushed stone, while samples numbered 4–6 are the manufactured sand. There samples are collected from the maanshan iron and steel mining resources group in Anhui, China. The blended samples are ground using a vibratory mill to ensure they passed through a 0.075 mm standard sieve. Figure 3 shows that Samples 1–6 are primarily composed of feldspar, with minor amounts of amphibole, chlorite, mica, calcite, quartz, magnetite, and pyrite. Figure 4 shows the micrograph obtained by optical microscope. Pyrite is dispersed throughout the sample, locally exhibiting a mosaic texture, with minor amounts of pyrite coexisting with magnetite.

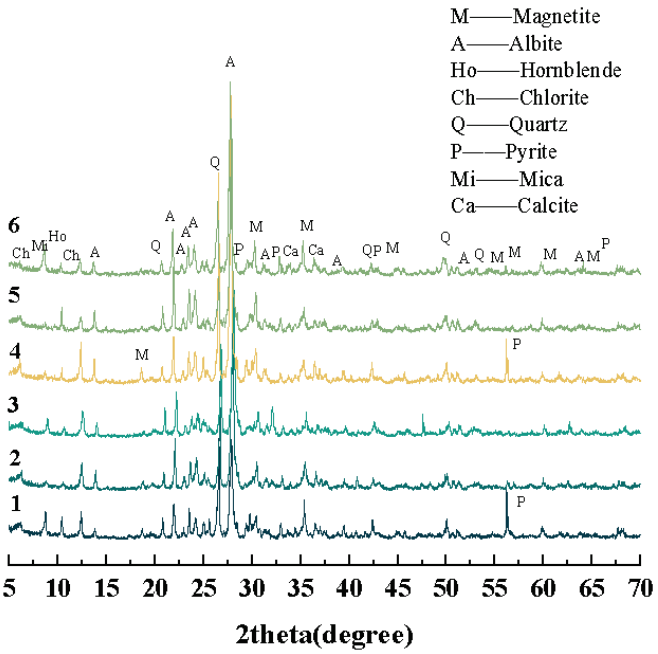

Figure 3. XRD patterns of sample 1–6.

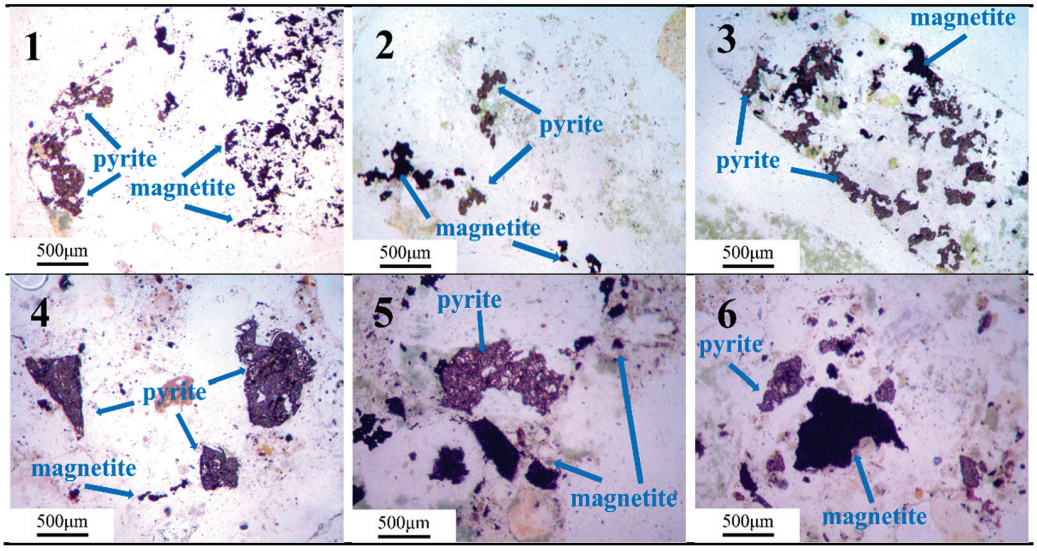

Figure 4. Micrographs of samples 1–6.

2.2. Methods and Device

2.2.1. Chemical Dissolution Method

In the presence of HCl solutions, pyrrhotite can undergo complete dissolution, resulting in the production of H_2S and elemental sulfur. H_2S-containing gas is absorbed by $CuSO_4$ solution, forming CuS precipitate. The amount of H_2S is quantified by measuring the precipitate. Elemental sulfur, which is highly soluble in carbon disulfide, can be quantified by evaporating carbon disulfide. By measuring these two sulfur-containing products, the sulfur content in the pyrrhotite sample can be accurately quantified. The value of x in pyrrhotite was determined by X-ray diffraction analysis to calculate the pyrrhotite content in the sample. At the same time, the filtrate after the reaction can be analyzed for soluble sulfate content (as SO_3 mass fraction). (As shown in Figure 5).

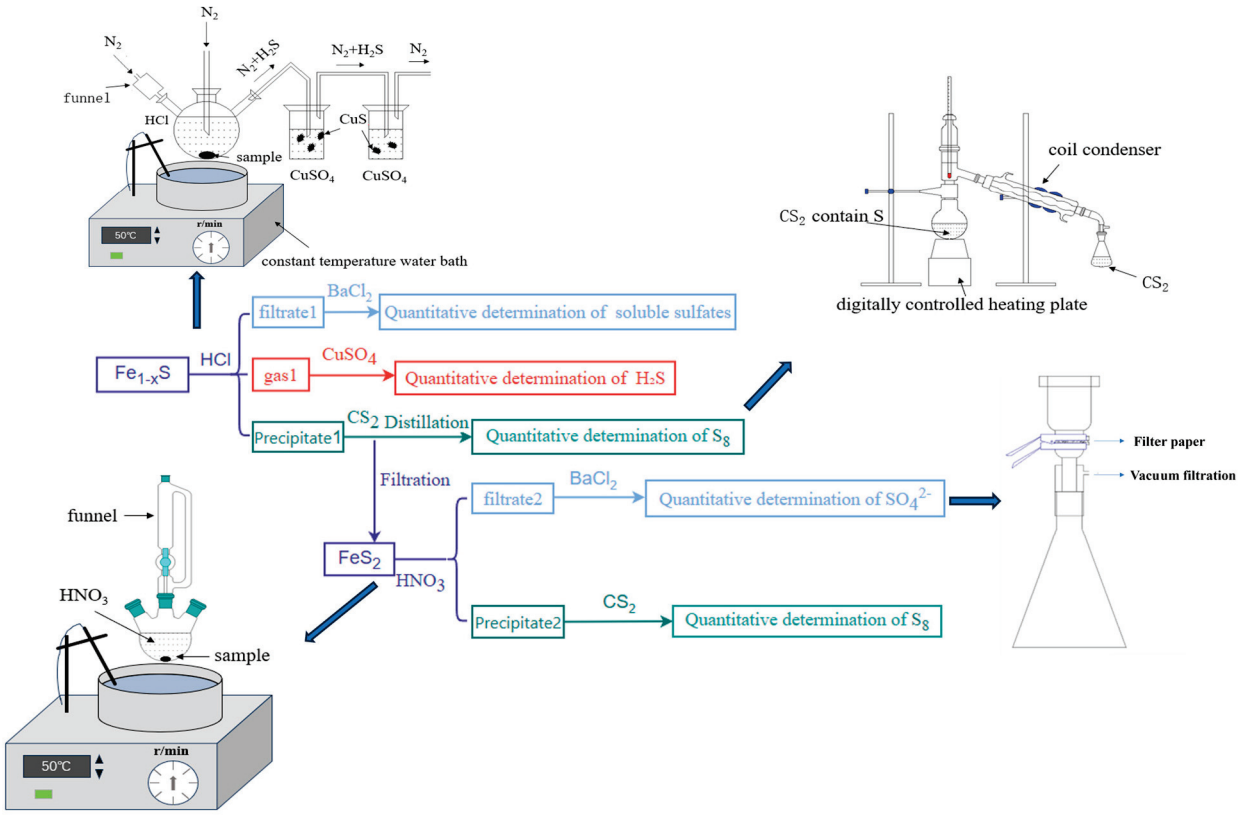

Figure 5. Experimental procedure and equipment diagram.

The experimental procedures are as follows:

1. The pyrrhotite was added to HCl, and the evolved gas was purified using two gas-washing bottles containing $CuSO_4$ solution.
2. After the reaction is complete, the reaction mixture is filtered. The filtrate (Filtrate 1) is added with $BaCl_2$ to form precipitate $BaSO_4$, which allows for the quantitative determination of soluble sulfate content.
3. While the filter precipitate (precipitate 1) was dried, the dried precipitate 1 was then washed with CS_2, followed by filtration. The solution was evaporated to recover elemental sulfur.
4. The precipitate in the two gas-washing bottles is filtered, dried, and weighed to obtain the mass of CuS.
5. The presence of sphalerite and galena as impurities in the pyrrhotite ore introduces analytical interference, as these minerals are also soluble in HCl. This may affect the accuracy of sulfur quantification. To quantitatively analyze the Pb^{2+} and Zn^{2+} ion concentrations in the sample, H_2SO_4 is added to the filtrate to precipitate Pb^{2+} ions as $PbSO_4$. The resulting $PbSO_4$ precipitate is dissolved in a pH 5.7 buffer solution (acetic acid/sodium acetate), and the lead content is determined via EDTA complexometric titration. In an ammoniacal medium with the presence of an oxidizing agent, Fe^{2+} interference is precipitated and separated. $Na_2S_2O_3$ and NH_4F are used as masking agents to eliminate the interference from Cu^{2+} and Al^{3+}. Zn^{2+} content is determined by EDTA standard solution titration at pH 5.5–6.0, using xylenol orange as the indicator.

Unlike pyrrhotite, pyrite has a more stable crystal structure and does not dissolve in HCl solution. Figure 6 shows the X-ray diffraction pattern of the reaction product from pyrite and HCl. However, it can dissolve completely in strongly oxidizing HNO_3 solution. During the dissolution of pyrite, sulfur in pyrite is oxidized to SO_4^{2-} ions and partially to elemental sulfur. The SO_4^{2-} ions in the solution can be quantified by

adding saturated $BaCl_2$ solution to form $BaSO_4$ precipitate. Elemental sulfur is dissolved in CS_2 and recovered through distillation for quantitative analysis. By combining the measured masses of SO_4^{2-} ions and elemental sulfur, the sulfur content in the pyrite can be quantified. The pyrite content in the sample was quantified based on its stoichiometric chemical composition. (As shown in Figure 5).

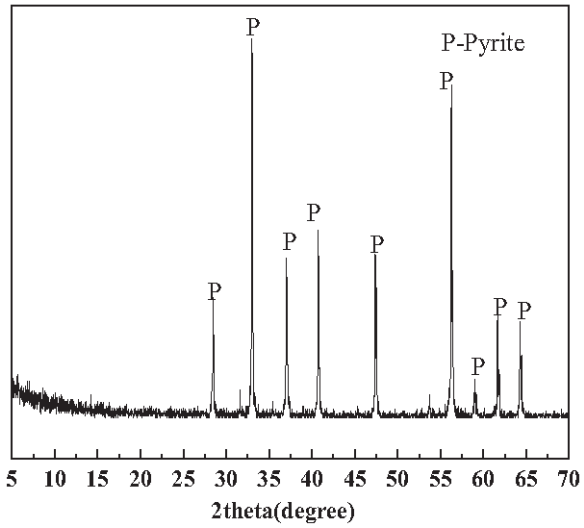

Figure 6. XRD pattern of the reaction product from pyrite treated with 1:1 HCl solution at 80 °C for 1 h.

The experimental procedures are as follows:

1. The pyrite was added to HNO_3 solution.
2. After the reaction was completed, the mixture was filtered through filter paper to obtain precipitate 2, while filtrate 2 was diluted to 100 mL. $BaCl_2$ solution was added to filtrate 2 to quantitatively precipitate SO_4^{2-} ions.
3. The remaining precipitate was dried, washed with carbon disulfide, and filtered. The resulting solution was then distilled to recover elemental sulfur.

2.2.2. The Internal Standard Method of XRD

The samples were completely crushed and processed into crushed stone with particle sizes of 5–25 mm and sand with a fineness modulus of approximately 2.80. All samples were thoroughly mixed and approximately 30–50 g of the samples taken and pulverized using a vibrating mill for later use. Quantitative analysis of pyrite in crushed stone and sand samples was conducted using the XRD internal standard method, with analytical-grade ZnO as the internal standard. A 2.0 g mixed sample was prepared by mixing according to the proportions presented in Table 3 and ground in an agate mortar for 20 min. The samples were tested in the 31~35° range with a scanning speed of 0.02°/s. Figure 7 shows the X-ray diffraction pattern of pyrite and ZnO. Figure 8 shows the areas of pyrite and ZnO were calculated using the MDI Jade 6 software for fitting, and the resulting calibration curve.

Table 3. Determination of pyrite content in samples by XRD internal standard method.

Sample	**Percentage/%**				
Albite	94	93	91	89	87
Pyrite	1	2	4	6	8
ZnO	5	5	5	5	5

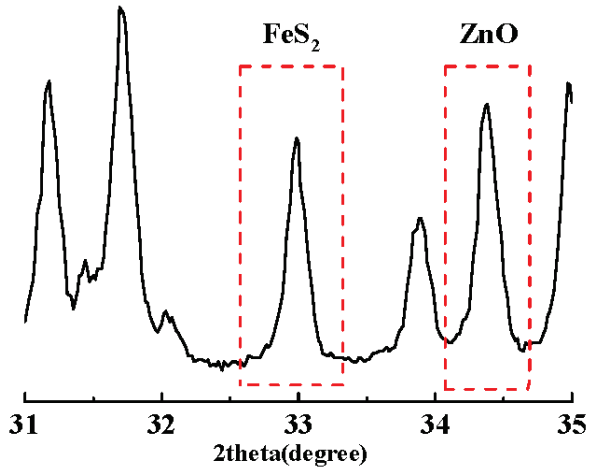

Figure 7. Diffraction peaks of pyrite and ZnO.

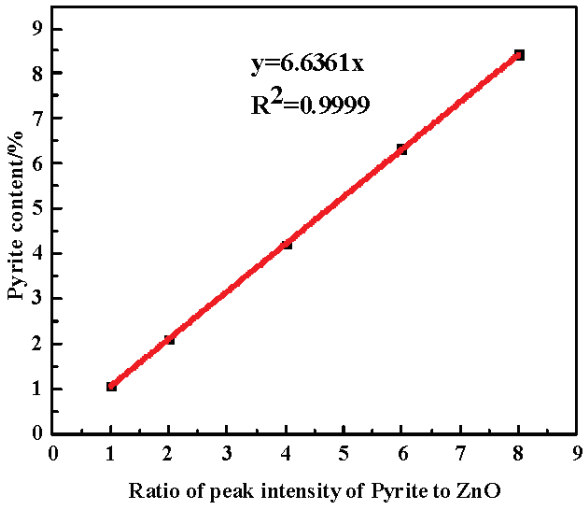

Figure 8. The standard working curve of the internal standard method.

2.3. Orthogonal Design of Experiments

Four main factors (particle size, reaction temperature, reaction concentration, and reaction time) are each set at three levels. Each combination was tested in triplicate. Two L9(3^4) orthogonal tables which are presented in Tables 4 and 5 were employed to conduct experiments for optimizing quantitative conditions, ultimately determining the best process conditions for quantifying iron sulfide in the samples.

Table 4. Orthogonal experimental design table for reaction between pyrrhotite and HCl.

Level	A Particle Size/mm	B Temperature/°C	C HCl Concentration	D Time/h
1	0.015–0.030	20	1:1	1.5
2	0.030–0.045	50	1:3	2.0
3	0.045–0.075	80	1:5	2.5

Table 5. Orthogonal experimental design table for reaction between pyrite and HNO3.

Level	A Particle Size/mm	B Temperature/°C	C HNO_3 Concentration	D Time/h
1	0.045–0.075	20	1:1	0.5
2	0.030–0.045	50	2:1	1.0
3	0.015–0.030	80	3:1	1.5

3. Results and Discussion

3.1. Quantification of Pyrrhotite

Under the nine experimental conditions of the orthogonal design table, approximately 0.5 g of the sample was weighed (accuracy: ±0.0001 g) and reacted with 50 mL of acids (HCl) at varying concentrations. The evolved gases were purified by passing through two gas-washing bottles, each containing 500 mL of 1 mol/L $CuSO_4$ solution.

The Pb^{2+} and Zn^{2+} in the filtrate are quantitatively analyzed. Subsequently, corrections are made for their contributions based on the chemical formulae of PbS and ZnS.

The pyrrhotite content was quantified based on the calculated mass of sulfur in individual components, as shown in Equations (4) and (5).

$$m_{\text{total S}} = m_{\text{elemental S}} + m_{\text{Sin } H_2S} - m_{\text{Sin PbS}} - m_{\text{Sin ZnS}} \quad (4)$$

$$w_{Fe_7S_8} = \frac{m_{\text{total S}} \times 2.61}{m_{\text{sample}}} \quad (5)$$

where $M_{Fe_7S_8} = 669.23$ g/mol and $M_S = 32.06$g /mol. This yields a conversion factor of 2.61 for transforming the sulfur mass to a pyrrhotite mass.

Table 6 shows the quantitative analysis results of sulfur-containing products. The analysis of pyrrhotite in the sample was performed based on its chemical formula Fe_7S_8, with the sulfur content calculated accordingly.

Table 6. Experimental results of pyrrhotite.

Experiment	A	B	C	D	Sample/g	Elemental Sulfur/g	CuS/g	Fe_7S_8/%
1	A1 *	B1	C1	D1	0.4997	0.0120	0.1653	33.15
2	A1	B2	C2	D2	0.5007	0.0189	0.1067	26.41
3	A1	B3	C3	D3	0.4873	0.0250	0.3520	72.91
4	A2	B1	C2	D3	0.5051	0.0000	0.0000	0.00
5	A2	B2	C3	D1	0.5340	0.0239	0.4276	81.85
6	A2	B3	C1	D2	0.4974	0.0184	0.4867	83.32
7	A3	B1	C3	D2	0.4995	0.0000	0.0000	0.00
8	A3	B2	C1	D3	0.5041	0.0261	0.4611	88.70
9	A3	B3	C2	D1	0.5000	0.0295	0.4026	83.17

* A1 represents factor A at level 1.

Figure 9 shows the presence of unreacted pyrrhotite in the X-ray diffraction pattern. In experiments 4 and 7, no precipitate was observed in the gas-washing bottle, showing no H_2S gas was generated. Adding a $BaCl_2$ solution to the filtrate produced no white precipitate, indicating no SO_4^{2-} ions were formed. The CS_2 dissolved and no elemental sulfur was detected after distillation. Therefore, pyrrhotite in experiments 4 and 7 did not react with HCl. The reaction rates of pyrrhotite in experiments 1, 2, and 3 were 33.15%, 26.41%, and 72.91%, respectively. The residue contained unreacted pyrrhotite and sphalerite, indicating that the reaction between pyrrhotite and hydrochloric acid was incomplete under the particle size range of 0.015–0.030 mm.

The concentration of the reference value in Table 7 was determined by an XRF analysis and calculated after excluding the interference of sulfur from the associated galena and sphalerite phases.

Table 7 shows the following significance ranking of four influencing factors: R2 > R3 > R4 > R1. This indicates that the reaction temperature exerts the most substantial effect on the pyrrhotite quantification, followed by the solution concentration, reaction time, and particle size. The optimal conditions are determined to be A3B3C1D1, corresponding to a particle size of 0.045–0.075 mm, reaction temperature of 80 °C, HCl concentration of 1:1, and reaction time of 1.5h.

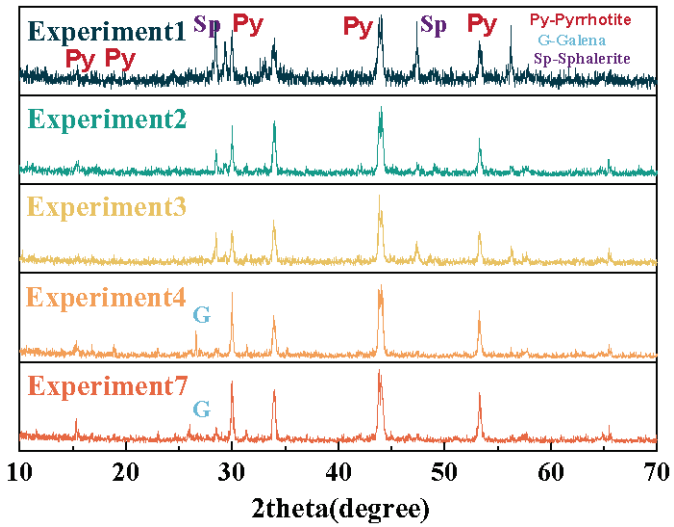

Figure 9. Mineral composition of HCl acid insoluble residues of pyrrhotite.

Table 7. Orthogonal experimental intuitive analysis of pyrrhotite.

Experiment	A	B	C	D	The Reacted Fe_7S_8/%	Reference Value/%	Ratio/%
1	1	1	1	1	33.15	83.32	60.21
2	1	2	2	2	26.41	83.32	68.30
3	1	3	3	3	72.91	83.32	12.50
4	2	1	2	3	0.00	85.32	100.00
5	2	2	3	1	81.85	85.32	4.07
6	2	3	1	2	83.32	85.32	2.34
7	3	1	3	2	0.00	87.30	100.00
8	3	2	1	3	88.70	87.30	1.60
9	3	3	2	1	83.17	87.30	4.73
k1	47.00	86.74	21.38	23.00			
k2	35.47	24.66	57.68	56.88			
k3	35.44	6.52	38.86	38.03			
Range	11.56	80.21	36.29	33.88			
Optimization Plan	A3	B3	C1	D1			

Besides the optimization plan, the results also indicate that, at a temperature range of 50–80 °C, particle sizes of 0.030–0.075 mm, a reaction time of over 1.5 h, and an HCl concentration exceeding 25%, the quantitative analysis of pyrrhotite becomes more accurate. However, when measuring tailings samples, the particle size distribution may not be as distinct. Therefore, it is necessary to test whether the optimal experimental conditions remain reasonable under a particle size range of below 0.075 mm and make further optimizations accordingly. The ratio in the quantitative results under the 1:1 HCl solution condition in Table 7 is significantly smaller, so the adjustment of the reaction temperature is preferred when optimizing the conditions.

The pyrrhotite sample is dissolved in the 1:1 HCl solution at 80 °C for 1.5 h. Figure 10 shows no detectable pyrrhotite diffraction peaks, confirming complete dissolution under these conditions.

Pyrrhotite is dissolved in a 1:1 HCl solution at 50 °C for 1.5 h. Figure 11 shows no detectable pyrrhotite diffraction peaks, also confirming complete dissolution under these conditions.

When the temperature was reduced to 20 °C, Figure 12 shows that pyrrhotite did not fully react.

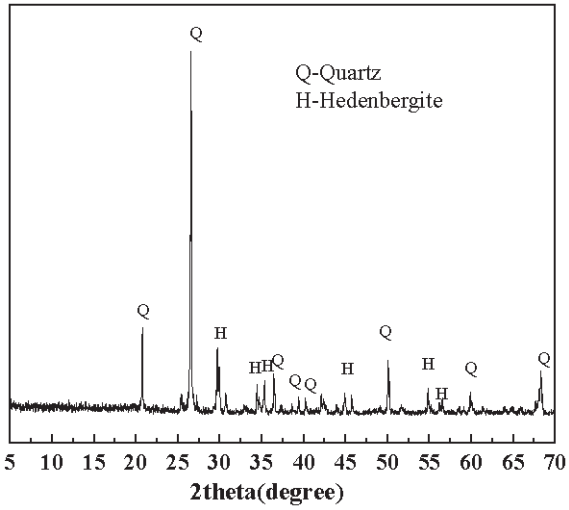

Figure 10. XRD pattern of pyrrhotite reacted with 1:1 HCl solution at 80 °C for 1.5 h.

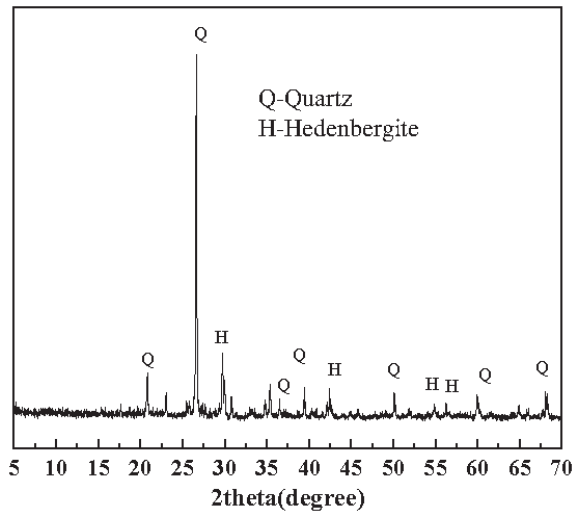

Figure 11. XRD pattern of pyrrhotite reacting with 1:1 HCl solution at 50 °C for 1.5 h.

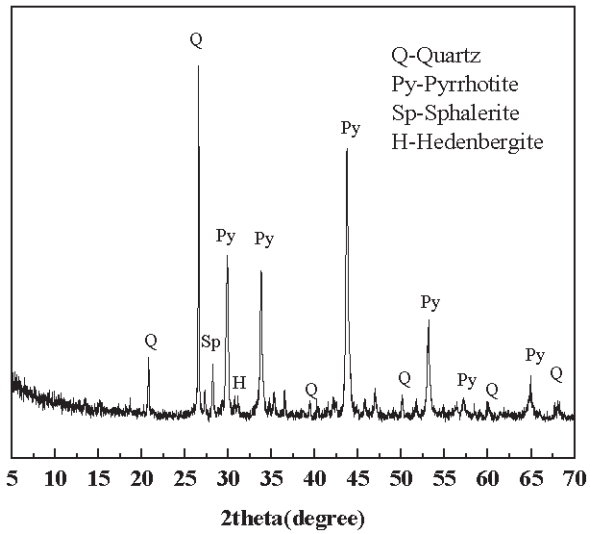

Figure 12. XRD pattern of pyrrhotite reacting with 1:1 HCl solution at 20 °C for 1.5 h.

For an accurate quantitative analysis of pyrrhotite in practical samples, complete dissolution can be achieved by grinding the sample to all pass a 0.075 mm sieve, followed by a reaction with a 1:1 HCl solution at 50 °C for 1.5 h.

3.2. Quantification of Pyrite

Under the nine experimental conditions of the orthogonal design table, approximately 0.5 g of the sample was weighed (accuracy: ±0.0001 g) and reacted with 50 mL of acids (HNO_3) at varying concentrations. Dilute the filtrate to 100 mL, take 5 mL of the filtrate, and add the $BaCl_2$ solution to test for SO_4^{2-}. Table 8 shows the experimental results are presented. During the quantification of SO_4^{2-} ions, the $BaCl_2$ solution is added to the boiling solution, resulting in the formation of $Ba(NO_3)_2$ precipitate after standing. Originally, boiling was intended to promote the crystallization of barium sulfate precipitate, but it resulted in the formation of barium nitrate precipitate. Figure 13 shows boiling can lead to the formation of $Ba(NO_3)_2$ precipitate. $Ba(NO_3)_2$ has a stable crystalline form and is very difficult to dissolve in water and acid, with the result being on the high side. At room temperature, adding a $BaCl_2$ solution, letting it stand for 4 h, and washing the precipitate with warm water can avoid the effect of $Ba(NO_3)_2$ on the results.

Table 8. The content of pyrite measured by barium sulfate gravimetric method.

Experiment	A	B	C	D	Sample/g	Elemental Sulfur/g	$BaSO_4$/(g/5 mL)	FeS_2/%
1	A1	B1	C1	D1	0.5120	0.0032	0.0721	73.57
2	A1	B2	C2	D2	0.5084	0.0000	0.0933	94.35
3	A1	B3	C3	D3	0.5067	0.0000	0.0949	96.29
4	A2	B1	C2	D3	0.4966	0.0025	0.0906	94.74
5	A2	B2	C3	D1	0.4982	0.0000	0.0939	96.90
6	A2	B3	C1	D2	0.5020	0.0000	0.0857	87.77
7	A3	B1	C3	D2	0.5082	0.0000	0.0906	91.66
8	A3	B2	C1	D3	0.5064	0.0000	0.0911	92.49
9	A3	B3	C2	D1	0.5008	0.0000	0.0916	94.04

Figure 13. The boiling step caused the formation of $Ba(NO_3)_2$ precipitate.

The pyrite content was quantified based on the calculated mass of sulfur in individual components, as shown in Equations (6) and (7).

$$m_{\text{total S}} = m_{\text{elemental S}} + m_{\text{Sin } SO_4^{2-}} \tag{6}$$

$$w_{FeS_2} = \frac{m_{\text{total S}} \times 1.87}{m_{\text{sample}}} \tag{7}$$

where $M_{FeS_2} = 119.97$ g/mol and $M_S = 32.06$ g/mol. This yields a conversion factor of 1.87 for transforming the sulfur mass to a pyrrhotite mass.

The results in Table 8 indicate that, at 20 °C, with HNO_3 concentrations of 1:1 and 2:1, the reaction between pyrite and HNO_3 primarily produces SO_4^{2-} ions, while a small amount of elemental sulfur is also formed. The elemental sulfur formed is mainly retained in the precipitate. When the HNO_3 concentration is 3:1, pyrite (0.015–0.030 mm) reacts completely to form SO_4^{2-} ions, with no elemental sulfur generated. As the reaction temperature increases to 50 °C and 80 °C, the elemental sulfur is further oxidized, resulting in no elemental sulfur, and all sulfur in the pyrite is converted to SO_4^{2-} ions in the liquid phase. In the seventh experiment, the complete conversion of sulfur to SO_4^{2-} ions was achieved even at 20 °C, primarily due to the high HNO_3 concentration (3:1) and the small particle size (0.015–0.030 mm) of pyrite, which, together, facilitated the oxidation of elemental sulfur at relatively low temperatures. Therefore, increasing the HNO_3 concentration and reducing the particle size of pyrite effectively promote the conversion of elemental sulfur at low temperatures, ensuring that sulfur exists entirely as SO_4^{2-} ions in the liquid phase and reducing the need for additional quantitative steps.

Pyrite undergoes a complete reaction under standard conditions (particle size of 0.015–0.075 mm, temperature of 20–80 °C, HNO_3 concentration exceeding 50%, and reaction time over 0.5 h). Significantly lower results are observed only under extreme conditions (particle size of 0.045–0.075 mm, 20 °C, dilute HNO_3 1:1, and a reaction time of 0.5 h, as demonstrated in Experiment 1). To ensure a complete reaction, avoid combinations of extreme parameters (e.g., coarse particles, low temperature, dilute acid, and a short reaction time). Adjusting any single parameter (e.g., reducing the particle size, increasing the temperature, using more concentrated HNO_3, or extending the reaction time) is sufficient to achieve full reaction.

Figure 14 shows that the precipitate is $BaSO_4$, with no impurities such as $Ba(NO_3)_2$ detected.

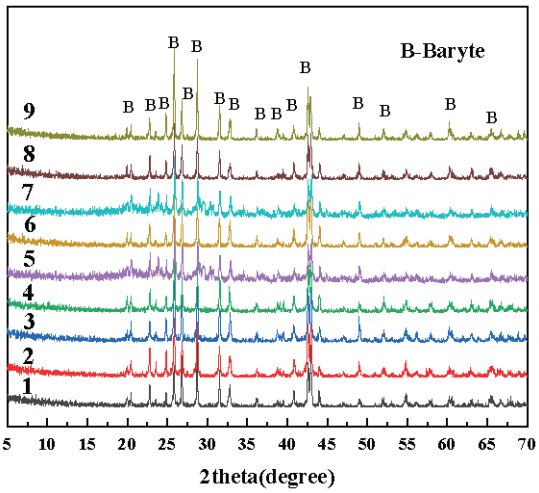

Figure 14. $BaSO_4$ precipitate after incinerating at 950 °C.

Within the defined parameter range in Table 9, R4 > R1 > R2 > R3. The significance of the four factors is ranked as follows: the reaction time, sample particle size, reaction temperature, and HNO_3 concentration. The reaction time and sample particle size have the greatest impact on the quantitative results of pyrite, followed by the reaction temperature, while the effect of the HNO_3 concentration is minimal. The optimal conditions are A3B3C2D2, corresponding to a particle size of 0.015–0.030 mm, reaction temperature of 80 °C, HNO_3 concentration of 2:1, and reaction time of 1 h.

The results indicate that, at a temperature range of 20–80 °C, particle sizes of 0.015–0.075 mm, a reaction time of over 0.5 h, and an HNO_3 concentration exceeding 50%, the quantitative analysis of pyrite is accurate. However, when measuring tailings samples,

the particle size distribution may not be as distinct. Therefore, it is necessary to test whether the optimal experimental conditions remain reasonable under a particle size range of below 0.075 mm and make further optimizations accordingly.

Table 9. Orthogonal experimental results and analysis of pyrite.

Experiment	A	B	C	D	The Reacted FeS_2/%	Reference Value/%	Ratio/%
1	1	1	1	1	73.57	89.71	17.99
2	1	2	2	2	94.35	89.71	5.18
3	1	3	3	3	96.29	89.71	7.34
4	2	1	2	3	94.74	87.22	8.62
5	2	2	3	1	96.90	87.22	11.10
6	2	3	1	2	87.77	87.22	0.63
7	3	1	3	2	91.66	91.28	0.41
8	3	2	1	3	92.49	91.28	1.33
9	3	3	2	1	94.04	91.28	3.02
k1	10.17	9.01	6.65	10.70			
k2	6.78	5.87	5.61	2.07			
k3	1.59	3.66	6.28	5.76			
Range	8.58	5.34	1.04	8.63			
Optimization Plan	A3	B3	C2	D2			

The pyrite completely dissolves after reacting with the 2:1 HNO_3 solution at 80 °C for 1 h. Further optimization of the reaction conditions is recommended, under the two tested conditions: (1) a reaction temperature of 50 °C, a 2:1 HNO_3 solution, and a reaction time of 1 h, and (2) a reaction temperature of 80 °C, a 1:1 HNO_3 solution, and a reaction time of 1 h. Due to the small amount of filter residue, the X-ray diffraction analysis pattern is not feasible. The filter residue was ground and redissolved in a concentrated 2:1 HNO_3 solution at 80 °C to verify the complete pyrite dissolution by quantifying SO_4^{2-} ions in the resulting filtrate. Figure 15 shows it is $Ba(NO_3)_2$. No characteristic peaks of barium sulfate are detected, confirming that the pyrite in the sample is completely decomposed under the tested conditions.

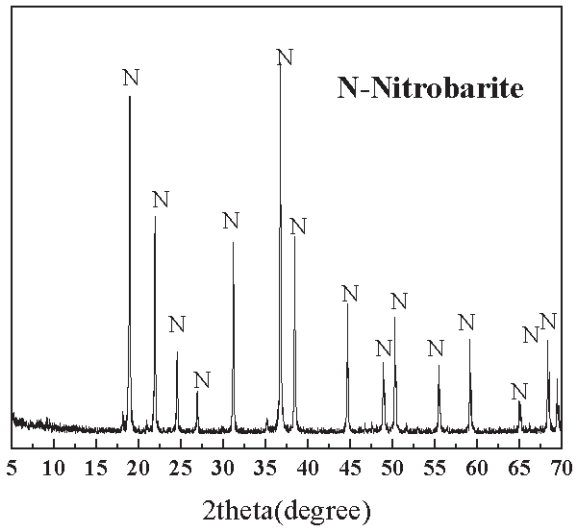

Figure 15. XRD pattern of the white precipitate after redissolution.

Further optimization of the reaction conditions: Pyrite is reacted with a 1:1 HNO_3 solution at 50 °C for 1 h. Figure 16 shows significant pyrite characteristic diffraction peaks in the residue, indicating that the pyrite did not fully react.

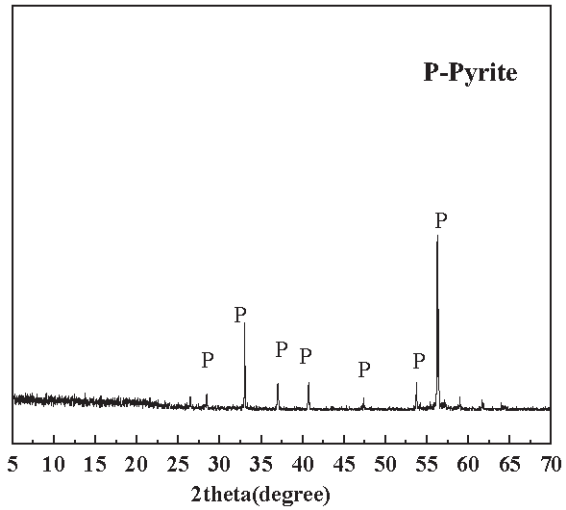

Figure 16. XRD pattern of pyrite reacting with 1:1 HNO_3 solution at 50 °C for 1 h.

For an accurate quantitative analysis of pyrite in practical samples, complete dissolution can be achieved by grinding the sample to below 0.075 mm, followed by a reaction with a 1:1 HNO_3 solution at 80 °C for 1 h.

3.3. Quantification of Iron Sulfide in Iron Ore Tailings

3.3.1. Quantification with Chemical Dissolution Methods

Iron ore tailings samples were first dissolved in HCl. Quantitative pyrrhotite was reacted with 1:1 HCl at 50 °C for 1.5 h. The residue was then dissolved in carbon disulfide, and the filtrate was used to distill elemental sulfur. After drying the residue, HNO_3 was added, and the mixture was reacted with a 1:1 HNO_3 solution at 80 °C for 1 h. The resulting filtrate was diluted to 100 mL. From this, 5 mL was taken and mixed with the excess $BaCl_2$ solution, left to stand for at least 4 h, washed with hot water 8 to 10 times, and then ashed at 350 °C, followed by calcination at 950 °C. Table 10 shows the quantitative results of sulfide iron and soluble sulfate in the samples.

Table 10. Quantitative results of soluble sulfate and iron sulfide.

Sample	Soluble Sulfates (in Terms of SO_3/%)	$Fe_{1-x}S$ (in Terms of $Fe_{1-x}S$ Mass/%)	FeS_2 (in Terms of FeS_2 Mass/%)
1	0.09	0.00	3.20
2	0.10	0.00	0.80
3	0.09	0.00	5.62
4	0.10	0.00	6.47
5	0.12	0.00	1.71
6	0.10	0.00	2.87

3.3.2. Quantification with the Internal Standard Method of XRD

The quantitative analysis using the internal standard method determined the pyrite content as follows: 2.77% in crushed stone sample 1, 1.10% in crushed stone sample 2, 6.13% in crushed stone sample 3, 5.95% in manufactured sand sample 4, 1.87% in manufactured sand sample 5, and 2.63% in manufactured sand sample 6.

Figure 17 shows that chemical dissolution approach achieves comparable pyrite content measurement (deviation <0.6%) to the internal standard method of XRD. The selected samples are representative. The deviation in results for Sample 1 is +0.43%, Sample 2 is −0.3%, Sample 3 is −0.51%, Sample 4 is +0.52%, Sample 5 is −0.16%, and Sample 6 is +0.24%.

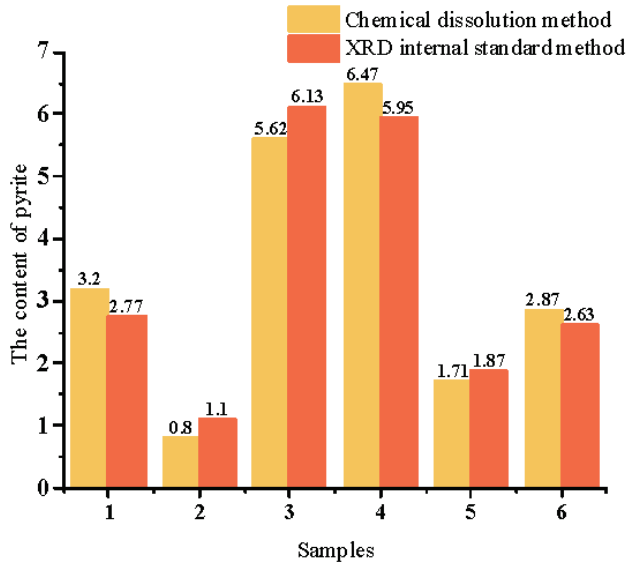

Figure 17. Quantitative results of pyrite.

4. Discussion

4.1. Optimization of Experimental Conditions

The initial experimental design using three particle size ranges (0.015–0.030 mm, 0.030–0.045 mm, and 0.045–0.075 mm) provided a detailed characterization of individual minerals. Industrial applications require more cost-effective and practical conditions. To address this, we optimized the protocol by (1) setting the particle size to <0.075 mm, and (2) reducing the reaction temperature for pyrrhotite from 80 °C to 50 °C and decreasing the HNO_3 concentration for pyrite from 2:1 to 1:1, significantly lowering the energy and reagent consumption. The test results confirmed complete reactions under the optimized conditions, enabling a wider field application of this technique.

4.2. Accuracy and Precision of Chemical Dissolution Methods

For pyrrhotite quantification, orthogonal tests 1, 2, 3, 4, and 7 showed that the quantitative analysis could not be effectively completed under the current experimental conditions. Under suitable conditions (tests 5, 6, 8, and 9), the average quantitative result was 84.26% with a standard deviation of 3.03 and a relative standard deviation (RSD) of 3.60% (<5%), showing a good repeatability and high precision. The absolute errors were 3.47, 2.00, 1.40, and 4.13, with relative errors of 4.07%, 2.34%, 1.60%, and 4.73%, respectively. The mean absolute error (MAE) was 2.75 and mean relative error (MRE) was 3.19% (<5%), showing a good accuracy and agreement with reference values.

For pyrite quantification under proper conditions (excluding test 1), the average measured value was 93.53%, with a standard deviation of 2.91 and a relative standard deviation of 3.11% (<5%), showing good repeatability and high precision. The mean absolute error was 4.17 and mean relative error was 4.70% (<5%), showing a high accuracy and good agreement with reference values.

For mineral samples, the pyrite content determined by chemical methods ranged from 0.8% to 6.47%, while XRD with the internal standard method yielded 1.1% to 6.13%. The error between these methods varied between −0.51% and +0.52%.

The method demonstrates high precision, repeatability, and accuracy in the quantitative analysis of both iron sulfide minerals (pyrrhotite and pyrite) under suitable conditions, showing a good agreement with the XRD internal standard method, making it a reliable analytical technique.

4.3. Method Comparisons

The chemical dissolution method proposed in this study complements various analytical techniques reported in the literature (e.g., EDS, XRD, synchrotron XRF, and S-XANES) in terms of objectives, applicability, and limitations. Luo et al. [25] achieved a quantitative analysis of pyrite thin specimens using EDS, but this method requires stringent sample preparation (thin specimens) and struggles to distinguish the dissolution selectivity between pyrrhotite and pyrite. Mcdougall et al. [26] employed XRD for the quantitative phase analysis, which can differentiate between mineral phases but relies on standard samples and lacks sensitivity for low-content phases. Del Real et al. [27] combined multiple microanalytical techniques (e.g., synchrotron XRF) for elemental mapping, providing a high spatial resolution, but the equipment is costly and unsuitable for batch sample processing. Bolin [28] used S-XANES to directly determine the pyrite content, which is sensitive to sulfur speciation but requires synchrotron radiation, limiting its application in conventional laboratories.

In contrast, the chemical dissolution method in this study enables the differentiation and quantification of multi-phase sulfides by optimizing the acid system, allowing the simultaneous quantitative analysis of soluble sulfates, pyrrhotite, and pyrite. However, a limitation of the chemical method is its susceptibility to interference from associated minerals (e.g., other sulfides or oxides).

5. Conclusions

In this study, an on-site quantification procedure was proposed for determining the pyrite and pyrrhotite content in tailings using a selective chemical dissolution process. Sulfur-containing products were quantitatively analyzed, and the iron sulfide content was calculated based on chemical formulae, excluding the interference of galena and lead sulfide in the quantification process.

(1) The optimal quantitative conditions were determined as grinding pyrrhotite to 0.045–0.075 mm, followed by digestion in 1:1 HCl at 80 °C for 1.5 h, while pyrite required finer grinding to 0.015–0.030 mm with a subsequent treatment in 2:1 HNO_3 at 80 °C for 1 h to achieve complete dissolution.
(2) The pyrrhotite quantification method exhibited a relative standard deviation (RSD) of 3.60% (<5%) and a mean relative error of 3.19% (<5%), while the pyrite quantification method showed an RSD of 3.11% (<5%) with a mean relative error of 4.70% (<5%).
(3) The dissolution process was improved, the cost was reduced, and on-site well completion was achieved. The quantitative results of pyrite in mineral samples were verified by the XRD internal standard method, and the error was less than 0.6%.

Author Contributions: Methodology, Z.W., S.W., W.L., X.H. and M.D.; Software, Z.W., S.W. and M.D.; Validation, Z.W., S.W., W.L., X.H. and X.C.; Formal analysis, Z.W., W.L., B.C., X.H. and X.C.; Investigation, Z.W., X.H., X.C. and X.Z.; Resources, B.C. and X.Z.; Data curation, Z.W., B.C. and M.D.; Writing—original draft, Z.W. and X.Z.; Writing—review & editing, Z.W., W.L., X.Z. and M.D. All authors have read and agreed to the published version of the manuscript.

Funding: This research was funded by Natural Science Foundation of Jiangsu Province (Grant No. BK20240563).

Institutional Review Board Statement: Not applicable.

Informed Consent Statement: Not applicable.

Data Availability Statement: The original contributions presented in this study are included in the article. Further inquiries can be directed to the corresponding authors.

Acknowledgments: We would like to thank the Natural Science Foundation of Jiangsu Province.

Conflicts of Interest: Authors Shaoping Wang, Bing Cao and Xin Chuai were employed by the company Nanshan Mining Company Ltd., Anhui Maanshan Iron and Steel Mining Resources Group. The remaining authors declare that the research was conducted in the absence of any commercial or financial relationships that could be construed as a potential conflict of interest.

References

1. Saedi, A.; Jamshidi-Zanjani, A. Addition of silane nanoparticles combined with mechanical activation for efficient reuse of sulfidic tailings for concrete construction. *Dev. Built Environ.* **2025**, *21*, 100606. [CrossRef]
2. Li, L.J.; Mao, X.C.; Liu, Z.K.; Wang, Y.C.; Li, D.X.; Ai, Q.X.; Wang, Y.Q. Variation of chalcophile elements in base metal sulfide minerals from the Jinchuan magmatic Ni—Cu sulfide deposit, NW China: Implications for mineral exploration. *J. Geochem. Explor.* **2024**, *259*, 107440. [CrossRef]
3. Li, S.; Xiao, W.; Chen, C.; Sang, M.; Mao, Q.; Gao, L.; Xia, F.; Li, X.; Du, X. Two-episode mineralization in the Haerdaban Pb—Zn deposit, NW China: Insights from sulfide trace elements, in situ S—Pb isotopes, and Rb-Sr geochronology. *Precambrian Res.* **2024**, *412*, 107550. [CrossRef]
4. Wang, Y.; Lai, J.; Cao, Y.; Brzozowski, M.; Mao, X.; Peng, H.; Ai, Q. Controls on the metal tenors of sulfide ores in the Jinchuan Ni-Cu-PGE sulfide deposit, NW China: Implications for the formation of distinct textural types of sulfide ores in magma conduits. *Ore Geol. Rev.* **2023**, *163*, 105810. [CrossRef]
5. Zhong, R.; Wille, K. Deterioration of residential concrete foundations: The role of pyrrhotite-bearing aggregate. *Cem. Concr. Compos.* **2018**, *94*, 53–61. [CrossRef]
6. Glasser, F.P.; Marchand, J.; Samson, E. Durability of concrete—Degradation phenomena involving detrimental chemical reactions. *Cem. Concr. Res.* **2008**, *38*, 226–246. [CrossRef]
7. Rodrigues, A.; Duchesne, J.; Fournier, B.; Durand, B.; Rivard, P.; Shehata, M. Mineralogical and chemical assessment of concrete damaged by the oxidation of sulfide—Bearing aggregates: Importance of thaumasite formation on reaction mechanisms. *Cem. Concr. Res.* **2012**, *42*, 1336–1347. [CrossRef]
8. Schmidt, T.; Leemann, A.; Gallucci, E.; Scrivener, K. Physical and microstructural aspects of iron sulfide degradation in concrete. *Cem. Concr. Res.* **2011**, *41*, 263–269. [CrossRef]
9. Jana, D. Cracking of residential concrete foundations in eastern Connecticut, USA from oxidation of pyrrhotite. *Case Stud. Constr. Mater.* **2022**, *16*, e00909. [CrossRef]
10. Marcelino, A.P.; Calixto, J.M.; Gumieri, A.G.; Caldeira, C.L.; Delbem, I.D.; Ferreira, M.C. A feasible evaluation protocol to determine the most reactive sulfide-bearing aggregate for use in concrete. *Constr. Build. Mater.* **2020**, *242*, 118031. [CrossRef]
11. Strongman, K.R.; Gibson, H.L.; Howard, A.E.; Lafrance, B.; Hamilton, M.A. Relative timing and controls on advanced argillic and conventional alteration of the Neoarchean Onaman volcanogenic massive sulfide deposit, Ontario, Canada. *Can. J. Earth Sci.* **2025**, *62*, 41–65. [CrossRef]
12. Titon, B.; Duchesne, J.; Fournier, B.; Rodrigues, A. Concrete deterioration due to sulfide-bearing aggregates: Mineralogical and chemical characteristics of pyrrhotite in concrete aggregates from Trois-Rivières, Canada. *Constr. Build. Mater.* **2025**, *458*, 139670. [CrossRef]
13. Jana, D. Pyrrhotite Epidemic in Eastern Connecticut: Diagnosis and Prevention. *Aci Mater. J.* **2020**, *117*, 61–70. [CrossRef]
14. Fan, Z.; Zou, D.; Zhang, M.; Qin, S.; Liu, T. Numerical modeling of unidirectional sulfate attack on tunnel lining concrete considering water evaporation at free face. *Cem. Concr. Res.* **2025**, *190*, 107813. [CrossRef]
15. Nehdi, M.L.; Suleiman, A.R.; Soliman, A.M. Investigation of concrete exposed to dual sulfate attack. *Cem. Concr. Res.* **2014**, *64*, 42–53. [CrossRef]
16. Ragoug, R.; Metalssi, O.O.; Barberon, F.; Torrenti, J.M.; Roussel, N.; Divet, L.; de Lacaillerie, J.B.D.E. Durability of cement pastes exposed to external sulfate attack and leaching: Physical and chemical aspects. *Cem. Concr. Res.* **2019**, *116*, 134–145. [CrossRef]
17. Andrews, A.; Nyarko, E.F.; Adjaottor, A.A.; Nsiah-Baafi, E.; Adom-Asamoah, M. Reuse and stabilization of sulphide mine tailings as fine aggregate for construction mortar. *J. Clean. Prod.* **2022**, *357*, 131971. [CrossRef]
18. Rimstidt, J.; Vaughan, D.J. Pyrite oxidation: A state-of-the-art assessment of the reaction mechanism. *Geochim. Cosmochim. Acta* **2003**, *67*, 873–880. [CrossRef]
19. Janzen, M.P.; Nicholson, R.V.; Scharer, J.M. Pyrrhotite reaction kinetics: Reaction rates for oxidation by oxygen, ferric iron, and for nonoxidative dissolution. *Geochim. Cosmochim. Acta* **2000**, *64*, 1511–1522. [CrossRef]
20. Hamilton, I.C.; Woods, R. An investigation of surface oxidation of pyrite and pyrrhotite by linear potential sweep voltammetry. *J. Electroanal. Chem.* **1981**, *118*, 327–343. [CrossRef]
21. Oliveira, I.; Cavalaro, S.H.; Aguado, A. New kinetic model to quantify the internal sulfate attack in concrete. *Cem. Concr. Res.* **2013**, *43*, 95–104. [CrossRef]

22. Wang, H.; Dowd, P.A.; Xu, C. A reaction rate model for pyrite oxidation considering the influence of water content and temperature. *Miner. Eng.* **2019**, *134*, 345–355. [CrossRef]
23. Chirita, P.; Schlegel, M.L. Pyrite oxidation in air-equilibrated solutions: An electrochemical study. *Chem. Geol.* **2017**, *470*, 67–74. [CrossRef]
24. Belzile, N.; Chen, Y.W.; Cai, M.F.; Li, Y. A review on pyrrhotite oxidation. *J. Geochem. Explor.* **2004**, *84*, 65–76. [CrossRef]
25. Luo, T.; Guo, Y.; Deng, Z.; Liu, X.; Sun, Z.; Qi, Y.; Yang, M. Energy-dispersive X-ray spectroscopy for the quantitative analysis of pyrite thin specimens. *J. Wuhan Univ. Technol.-Mater. Sci. Ed.* **2023**, *38*, 1304–1310. [CrossRef]
26. Mcdougall, H.; Hibberd, M.; Tong, A.; Neville, S.; Peterson, V.; Didier, C. Preparation of pyrite concentrate powder from the Thackaringa mine for quantitative phase analysis using X-ray diffraction. *J. Appl. Crystallogr.* **2022**, *55*, 1572–1582. [CrossRef]
27. Del Real, I.; Smieska, L.; Thompson, J.F.H.; Martinez, C.; Thomas, J.; Layton-Matthews, D. Using multiple micro-analytical techniques for evaluating quantitative synchrotron-XRF elemental mapping of hydrothermal pyrite. *J. Anal. At. Spectrom.* **2019**, *34*, 1724–1738. [CrossRef]
28. Bolin, T.B. Direct Determination of Pyrite Content in Argonne Premium Coals by the Use of Sulfur X-ray Near Edge Absorption Spectroscopy (S-XANES). *Energy Fuels* **2010**, *24*, 5479–5482. [CrossRef]
29. *GB/T 31288*; Iron Tailings Sand. Standardization Administration of China: Beijing, China, 2014. (In Chinese)
30. *EN 12620:2008*; Aggregates for Concrete. European Committee for Standardization: Brussels, Belgium, 2008.
31. *ACI 201.2R*; Guide to Durable Concrete. Asian Culinary Institute (ACI): Singapore, 2016.

Disclaimer/Publisher's Note: The statements, opinions and data contained in all publications are solely those of the individual author(s) and contributor(s) and not of MDPI and/or the editor(s). MDPI and/or the editor(s) disclaim responsibility for any injury to people or property resulting from any ideas, methods, instructions or products referred to in the content.

materials

MDPI

Article

Utilization of Low-Grade Limestone and Solid Waste for the Preparation of High-Belite Portland Cement

Jiapeng Duan, Yu Zhang *, Suwei Xia, Zian Geng and Wenbo Xin *

State Key Laboratory of Materials-Oriented Chemical Engineering, College of Materials Science and Engineering, Nanjing Tech University, Nanjing 211816, China

* Correspondence: zhangyuzeus@njtech.edu.cn (Y.Z.); xinwenbo@njtech.edu.cn (W.X.)

Abstract: In this study, high-belite Portland cement clinker was successfully prepared by using low-grade limestone and solid-waste calcium carbide slag and steel slag, achieving resource utilization while reducing CO_2 emissions caused by raw materials decomposition in the cement industry. Using X-ray diffraction, microscopic images, thermogravimetric analysis, and differential scanning calorimetry, the physicochemical reaction process, phase composition, and microscopy of clinker were studied. The results indicated that the high-belite Portland cement clinker can be successfully produced at 1340 °C for 1 h with a belite content of 58.6% and an alite content of 24.2% when the composition of raw material was suitable. Meanwhile, the content of high-reactive-phase α-C_2S can reach 1.4%. Via microscopic viewing, C_2S and C_3S were interphase distributed and well developed. In this study, the CO_2 emission of the prepared high-belite Portland cement clinker was 54.67% lower than that of ordinary Portland cement clinker. All the above results confirm that high-belite Portland cement clinker can be produced using low-grade limestone and solid wastes, which can significantly reduce CO_2 emission during Portland clinker production and promote an innovative approach to the cement industry.

Keywords: low-grade limestone; high belite; Portland cement; lower CO_2 emission

1. Introduction

Based on global cement production in 2023, China remains the world's largest cement producer, accounting for about 52% of the global total. According to the national statistics, the total cement production in China reached 2.02 billion tons in 2023 [1], ranking the first in the world for almost 40 years. Normally, there are 0.6 tons of CO_2 emission for each ton of Portland cement clinker production, resulting a total of 1.21 billion tons of CO_2 emission in the cement industry in China in 2023. In 2023, China's total carbon emission amounted to 12.6 billion tons [2], of which cement clinker production contributed 9.6% to the overall emission. The low-carbon development of the cement industry is crucial for China to achieve carbon neutrality. Reducing CO_2 emission during the calcination process of Portland cement is considered one of the best pathways to decrease overall CO_2 emission in cement production. High-belite cement (HBC) is a type of Portland cement characterized by belite (C_2S) as its primary mineral phase, with the C_2S content exceeding 40%. As belite Portland cement, it is a Portland clinker mainly composed of belite mineral phases. In cement clinker, compared with alite, belite has a lower early hydration activity and mainly contributes to the later-phase strength, while alite mainly determines the early strength of cement. In the cement industry, HBC typically contains 40–50% C_2S and 25–30% alite (C_3S) [3].

The substitution of HBC for ordinary Portland cement (PC) can significantly lower the quality requirements for raw materials, enabling the use of low-grade limestone (LGL)

in place of high-grade limestone. Additionally, CO_2 emission is significantly reduced. In the aspects of phase mineralization of Portland cement clinker, the formation enthalpy of C_3S is 1810 kJ/kg, while the enthalpy of C_2S is 1350 kJ/kg [4]. Moreover, the calcination temperature for HBC is lower than that of PC [5]. Consequently, this reduced calcination temperature leads to decreased heat consumption during clinker production, thereby mitigating the environmental impact associated with cement manufacture. Moreover, HBC exhibits low heat of hydration, superior high-temperature stability, exceptional resistance to chemical attack, and a gradual early strength development, followed by a significant long-term strength gain.

HBC can utilize low-grade raw materials or solid waste as substitutes for high-grade limestone owing to its lower requirements for raw materials quality. This provides a new solution for the utilization of LGL and solid wastes. Jihane Moudar et al. [6] successfully prepared belite using waste glass and shells instead of traditional raw materials. Their study demonstrated that the 90-day hydration strength of cement mortar reached 30.05 MPa after blending the synthesized C_2S with shellac and gypsum. M.K. Enríquez et al. [7] further investigated the use of paper sludge, cement kiln dust, and rice husk ash as complete substitutes for natural raw materials in belite cement clinker production. Their research revealed that HBC clinker could be manufactured using 20–25% paper sludge, 60–69% cement kiln dust, and 9–11% rice husk ash. These studies collectively demonstrate the feasibility and environmental benefits of incorporating low-quality raw materials and waste streams into HBC production, aligning with global sustainability goals while maintaining or enhancing cement properties. In addition, the water–cement ratio of cement paste has a significant impact on rheological and time-varying properties, which, in turn, has a huge influence on its mechanical properties [8–12].

Calcium carbide slag, a by-product generated from the hydrolysis of calcium carbide to produce acetylene gas, poses significant environmental hazard when accumulated in large quantities. It has been extensively utilized in various sectors, including building materials, chemical engineering, and pollution abatement [13]. The primary constituent of calcium carbide slag is $Ca(OH)_2$, which can be thermally decomposed into CaO at elevated temperatures and subsequently utilized as a raw material in cement production. Relative to limestone, calcium carbide slag exhibits lower decomposition heat and does not release CO_2 during the process, thereby offering significant advantages in terms of energy conservation and emission reduction [14]. Moreover, 1 ton of calcium carbide slag can substitute for 1.28 tons of limestone, thereby reducing CO_2 emission by 0.56 tons. This approach effectively achieves the objective of "treating waste with waste" [15]. Yifan Gao et al. [16] prepared belite cement using solid waste materials, including calcium carbide slag, silica fume, and laterite. The Ca^{2+} ions in the calcium carbide slag can be substituted by other ions present in these waste materials. The resulting belite cement exhibits superior long-term strength compared to ordinary Portland cement. Low-grade limestone, a by-product of limestone mining operations, has gained increasing attention for resource utilization as high-grade limestone resources gradually deplete. The resource utilization of LGL has become one of the important directions in the development of the cement industry. Tamma VR et al. [17] prepared limestone-based cement by partially substituting LGL for cement clinker. Research findings indicate that when the substitution ratio is 15%, the performance of the resulting limestone-based cement is equivalent to that of 43-grade ordinary Portland cement. Liu Zhenhe et al. [18] successfully developed cement clinker utilizing low-grade limestone, achieving a 28-day compressive strength exceeding 55 MPa.

The aforementioned research demonstrates that belite cement clinker can be successfully synthesized from low-grade raw materials and solid waste. In this study, high-belite Portland cement clinker was produced using calcium carbide slag, steel slag, LGL, and

clay. The reactivity of low-grade limestone was enhanced via mechanical activation. This approach not only facilitates the resource utilization of LGL and solid wastes but also significantly reduces CO_2 emission during the cement production. Furthermore, high-belite Portland cement exhibits superior chemical properties and a broader range of applications compared to conventional Portland cement. The technical roadmap of this article is shown in Figure 1 as follows:

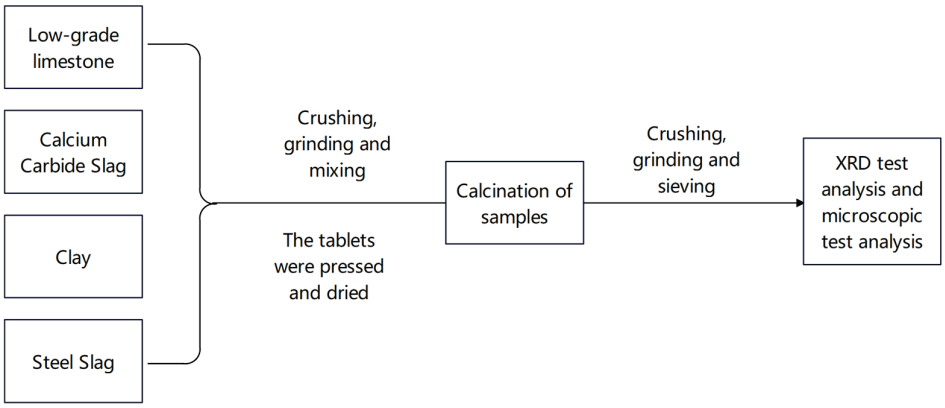

Figure 1. Technical roadmap.

2. Experimental Section

2.1. Raw Materials

The raw materials utilized in this study include LGL (Conch Cement, Huainan, China), calcium carbide slag (Conch Cement, Huainan, China), clay (Shijiazhuang, China), and steel slag (Maanshan, China). Table 1 provides the chemical compositions of the raw materials. Figure 2 illustrates the X-ray diffraction (XRD) patterns of the raw materials, where the main substances in calcium carbide slag are $Ca(OH)_2$ and $CaCO_3$. For low-grade limestone, the main substances are $CaCO_3$ and SiO_2. In clay, the main components are SiO_2 and silicate minerals. The composition of steel slag is relatively complex. Besides $CaCO_3$ and Fe_2O_3, there are also mineral phases from clinker, such as C_2S, etc. The particle size distributions of the raw materials are shown in Figure 3a, and the median particle sizes of the LGL, calcium carbide slag, clay, and steel slag are 6.113 μm, 8.278 μm, 11.986 μm, and 14.785 μm, respectively. Additionally, the LGL underwent graded grinding to pass through 200-mesh (74 μm) and 400-mesh (34 μm) square hole sieves, designated as LS-200 and LS-400, and their particle size distributions are shown in Figure 3b. The median particle sizes of LS-200 and LS-400 are 6.133 μm and 4.907 μm, respectively.

Table 1. Chemical compositions of raw materials (wt.%).

Materials	LOSS	SiO_2	Al_2O_3	Fe_2O_3	CaO	MgO	K_2O	Na_2O	SO_3
Low-grade limestone	31.01	19.90	6.49	2.13	36.14	1.88	1.29	0.40	0.17
Calcium carbide slag	25.95	2.90	1.42	0.46	68.50	0.12	0.03	0	0.44
Clay	12.38	63.59	11.45	1.03	6.10	2.24	2.48	0.45	0
Steel slag	−0.70	14.02	4.14	24.35	43.28	5.36	0.02	0.08	0.16

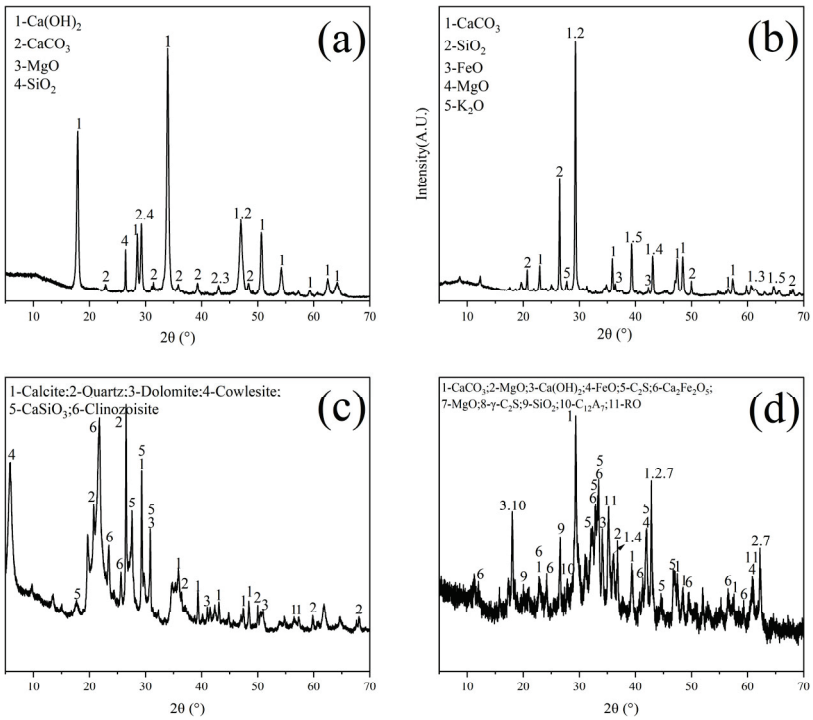

Figure 2. XRD diagram of raw materials. (**a**) Calcium carbide slag, (**b**) low-grade limestone, (**c**) clay, and (**d**) steel slag.

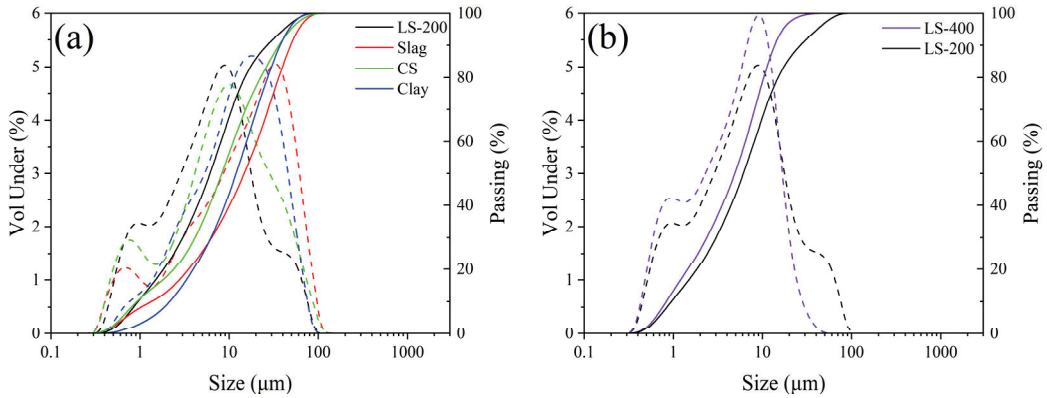

Figure 3. Particle size distribution of raw materials. Solid line: passage rate; dashed line: volume ratio. (**a**) Particle size distribution of raw materials, (**b**) Particle size distribution of different limestone.

LGL contains a higher proportion of SiO_2 than common limestone and exhibits differences in reactivity during calcination with $CaCO_3$. Thermogravimetric (TG) and differential scanning calorimetry (DSC) analyses of low-grade limestone and common limestone are shown in Figure 4, where it was observed that low-grade limestone releases less CO_2 during thermal decomposition. The DSC curve of common limestone shows more pronounced peaks and valleys, indicating a higher energy barrier for calcite decomposition [19]. The impurities present in LGL are beneficial to reduce the decomposition temperature, which starts at 645.3 °C, while the decomposition temperature of common limestone is 684.5 °C.

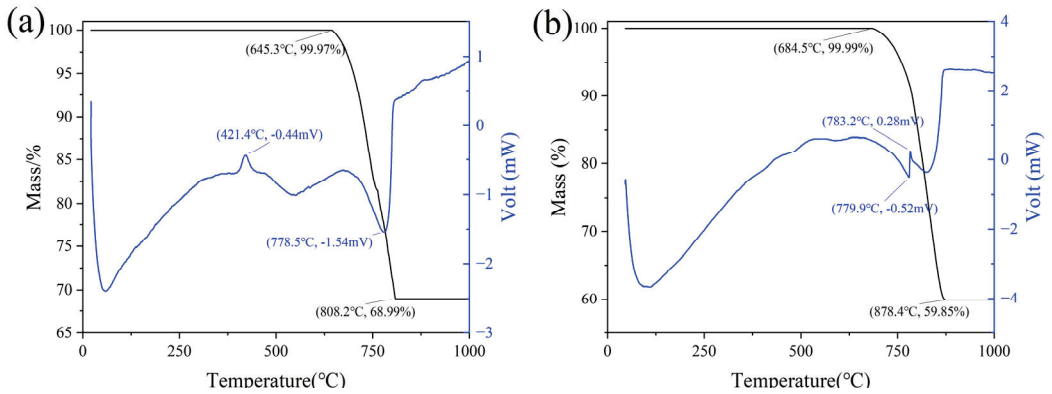

Figure 4. Comparison of TG−DSC between low−grade limestone and common limestone. (**a**) low−grade limestone, (**b**) common limestone.

The mineral-phase composition in cement clinker can be controlled by adjusting three critical parameters: the limestone saturation factor (KH), the silica modulus (SM), and the alumina modulus (IM). By optimizing the values of these parameters, the initial mineral composition of the cement clinker can be initially set. The calculation formulas are as follows [20]:

$$KH = \frac{CaO - 1.65Al_2O_3 - 0.35Fe_2O_3}{2.8SiO_2} \quad (1)$$

$$SM = \frac{SiO_2}{Al_2O_3 + Fe_2O_3} \quad (2)$$

$$IM = \frac{Al_2O_3}{Fe_2O_3} \quad (3)$$

The chemical composition of the raw materials and the three parameters are illustrated in Table 2. This study aims to incorporate LGL and calcium carbide slag, among other solid wastes, into cement clinker production. By precisely adjusting the proportions of each raw material, a set of parameters are prepared (KH = 0.70–0.90, SM = 2.5 ± 0.1, and IM = 1.2 ± 0.1). Specifically, high-belite Portland cement clinker is produced by systematically varying the KH value, while the values of SM and IM are constant.

Table 2. Composition of clinker ratios.

	Low-Grade Limestone	Calcium Carbide Slag	Clay	Steel Slag	KH	SM	IM
A	16.5	52.5	20	11	0.72	2.4	1.3
B	15	54	20	11	0.74	2.4	1.3
C	13.5	55.5	20	11	0.76	2.4	1.3
D	13	56.75	20	10.25	0.78	2.5	1.3
E	11	58	20	11	0.80	2.4	1.3
F	12.5	58	19	10.5	0.82	2.4	1.3
G	11.5	59	19	10.5	0.84	2.4	1.3
H	10	60	19	11	0.86	2.4	1.2
I	9	61.5	19	10.5	0.88	2.4	1.3
J	7.5	62.5	19	11	0.90	2.4	1.2

Samples are prepared with the specified ratio according to Table 2. For each specimen, 50 g of the mixture was combined with 8% deionized water and thoroughly blended for 12 h. Subsequently, a tablet press was utilized to form a square piece with a thickness of

about 4 cm. The prepared sample was then placed in an oven at 105 °C for 24 h to dry. The dried square pieces were then transferred to a box-type resistance furnace for sintering. The temperature was increased at a rate of 10 °C per minute, held at 900 °C for 30 min, and further heated to the target temperature with subsequent insulation. The detailed sintering procedure is illustrated in Figure 5.

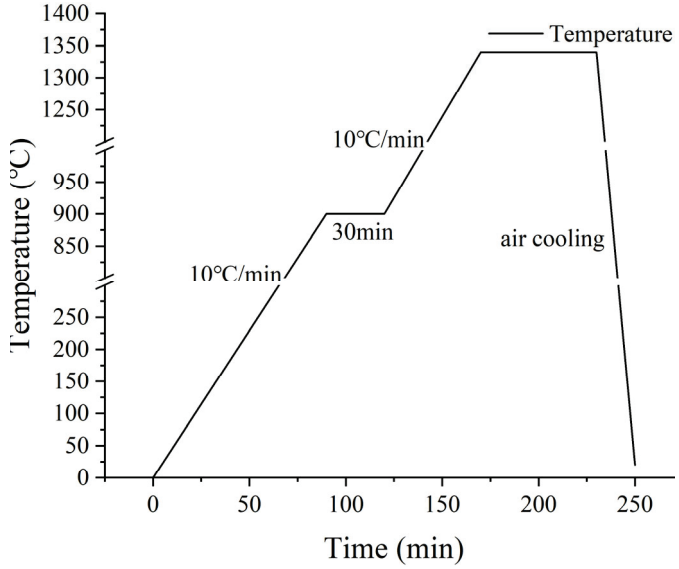

Figure 5. Calcination process.

2.2. Measurement Methods

The XRD measurements were conducted using a SmartLabTM diffractometer from Rigaku, Tokyo, Japan. The instrument was equipped with a copper target (CuKα, λ = 0.154 nm), and the data were collected from 5° to 70° with a step size of 0.01° at 5°/min. The X-ray tube operated at 40 kV and 40 mA. Prior to the XRD tests, the samples were milled to a particle size of ≤45 μm to minimize preferred orientations.

Mineral-phase identification was performed using Search Match software (Version 4.0), which allows for rapid and accurate determination of the corresponding mineral PDF cards. Table 3 presents the CIF files corresponding to the clinker mineral phases used in this experiment. Quantitative analysis of the cement clinker was performed using the Rietveld method with High Score Plus. During the calculation process, the weighted profile residual (Rwp) was minimized to ≤10.0%, and the Goodness of Fit (G) was maintained at ≤2.0 [21].

Table 3. ICSD numbers of mineral phase.

Phase	ICSD Number
M1-C_3S	81100 [22]
M3-C_3S	94742 [23]
α-C_2S	81099 [24]
β-C_2S	81096 [25]
γ-C_2S	81095 [26]
C_3A	1841 [27]
C_4AF	9197 [28]
CaO	75785 [29]

TG-DSC curves were conducted using a STA 449F5 instrument (NETZSCH, Selb, Germany). The heating rate was 10 °C/min, with a temperature range of 20–1500 °C under an air atmosphere for the initial tests. For hydrated samples, the same heating rate was applied within a temperature range of 20–1000 °C under a nitrogen (N_2) atmosphere.

Microscopic images were captured on internal cross-sections of the samples with a Gemini 300 scanning electron microscope (ZEISS, Oberkochen, Germany) at an accelerating voltage of 3.0 kV. And the samples were sprayed with gold before the experiment

3. Results and Discussion

Low-KH (0.72–0.80) clinker was calcined at temperatures of 1260 °C, 1300 °C, 1340 °C, and 1380 °C, each with a sintering time for 1 h. It was observed that a melting phenomenon occurred during calcination at 1380 °C (Figure 6). Quantitative XRD analysis (Rwp $\leq$ 10%, G $\leq$ 2.0) of samples calcined below 1340 °C revealed that the primary mineral phase was C_2S, comprising 70–80%, with C_3S present in trace amounts (0–10%), as shown in Figures 7 and 8. Given the predominance of C_2S and the relatively low content of C_3S, the resulting clinker exhibits insufficient strength for practical applications and is, therefore, unsuitable for manufacturing purposes.

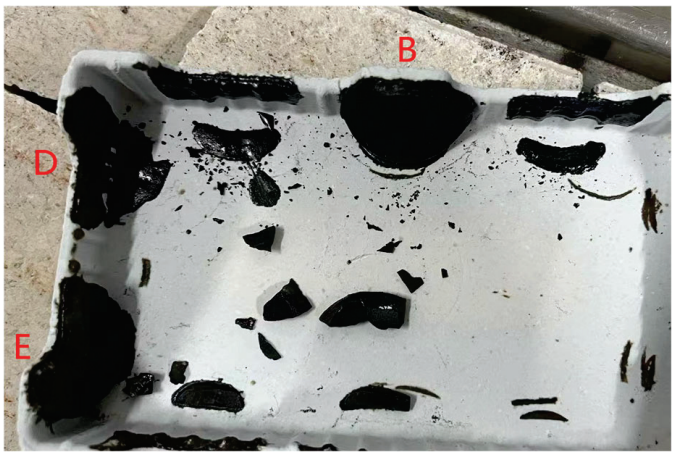

Figure 6. Low-KH clinker sample photo (B, D, E represent clinker with a low KH ratio).

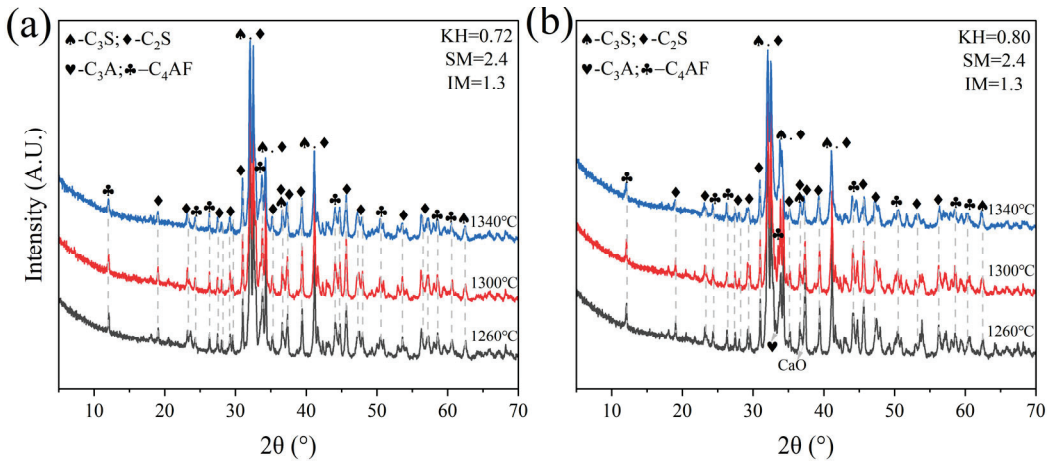

Figure 7. XRD analysis patterns of samples A and E. (**a**) sample A, (**b**) sample E.

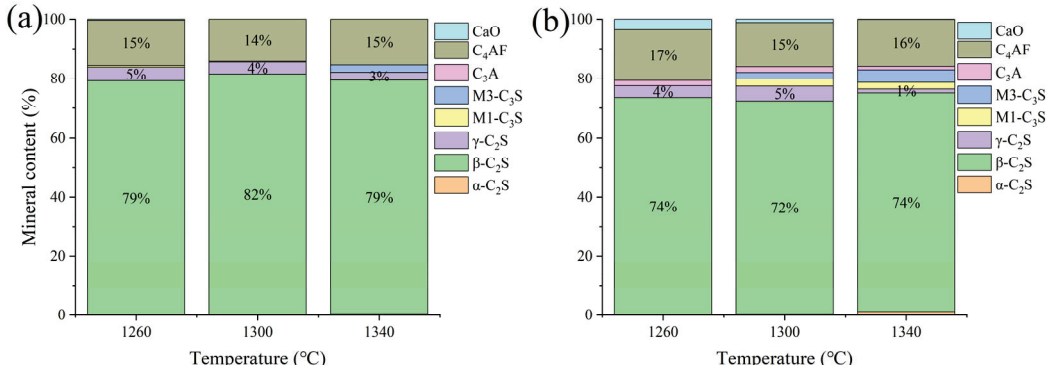

Figure 8. The proportion of major mineral components in samples A and E. (**a**) sample A, (**b**) sample E.

Sample F was subjected to calcination at temperatures of 1300 °C, 1340 °C, and 1380 °C with a sintering time of 1 h. It was observed that calcination at 1380 °C resulted in significant melting and obvious adherence to the crucible. Calcination at 1300 °C and 1340 °C proceeded normally. XRD analysis (Figure 9) revealed that at 1300 °C, a substantial amount of f-CaO remained unreacted, with C_2S comprising 77% of the main mineral phase and C_3S only 2.7%. At 1340 °C, the main mineral phase was also predominantly C_2S (77%), with a C_3S content of 2.7%.

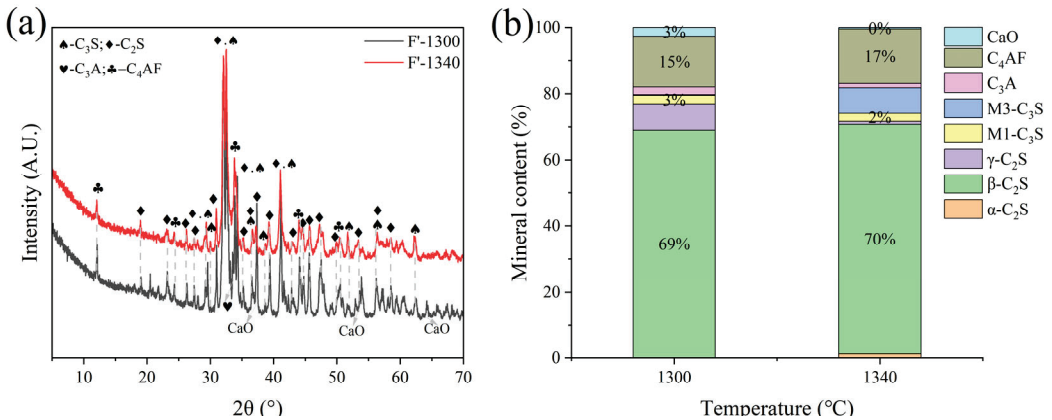

Figure 9. XRD analysis and mineral composition ratios of sample F. (**a**) XRD of sample F, (**b**) mineral content of sample F.

G and H were calcined at temperatures of 1300 °C, 1340 °C, 1380 °C, and 1400 °C for 1 h. The XRD and mineral composition of samples H and G are shown in Figures 10 and 11. Calcination at 1300 °C resulted in a significant amount of f-CaO and pulverization, while the diffraction peaks corresponding to f-CaO disappeared at 1340 °C. The quantitative analysis shows that the C_2S in the clinker was 68.5%, and the C_3S was only 13.3% when the sample G was calcined at 1340 °C. C_2S and C_3S were 51.9% and 28.5%, respectively at 1380 °C, but the C_3A content was slightly higher at 1.7%. The clinker at 1400 °C was 54.7% C_2S and 24.5% C_3S, but the content of γ-C_2S was too high. The H sample exhibited 58.6% C_2S and 24.2 % C_3S at 1340 °C, 50.4% C_2S and 30.1% C_3S at 1380 °C, and 43.4% C_2S and 35.8% C_3S at 1400 °C. TG-DSC analysis of the H sample (Figure 12) showed two significant mass losses of 9.00% and 9.12% at temperatures of 368–513 °C and 606–833 °C, respectively, corresponding to the decomposition of $Ca(OH)_2$ and $CaCO_3$. The DSC curves revealed an endothermic peak at 108.07 °C due to the evaporation of free water in the raw material, as well as peaks at 480.9 °C and 782.9 °C, which corresponded to the decomposition of $Ca(OH)_2$ and $CaCO_3$, consistent with the TG data. Additionally, an exothermic peak at 1269.0 °C was observed, likely resulting from the thermal effect of

C_2S formation during solid-phase precipitation, while a peak at 1342.6 °C was attributed to the sintering of the molten phase, representing the thermal effect of C_3S formation [30]. XRD and mineral-phase composition analysis concluded that more C_3S would be produced in sample H at the same calcination temperature, which is favorable for clinker strength. In addition, more calcium carbide slag could be used in sample H mixing to reduce CO_2 emission more effectively.

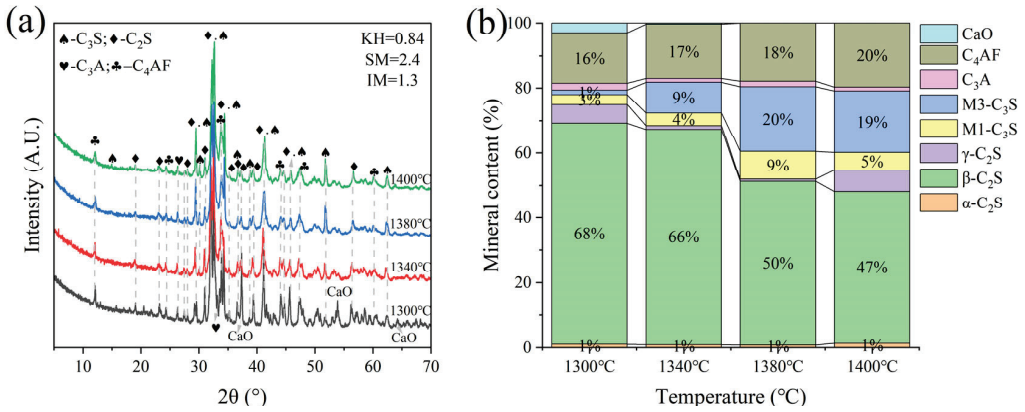

Figure 10. XRD analysis and mineral composition ratios of sample G. (**a**) XRD of sample G, (**b**) mineral content of sample G.

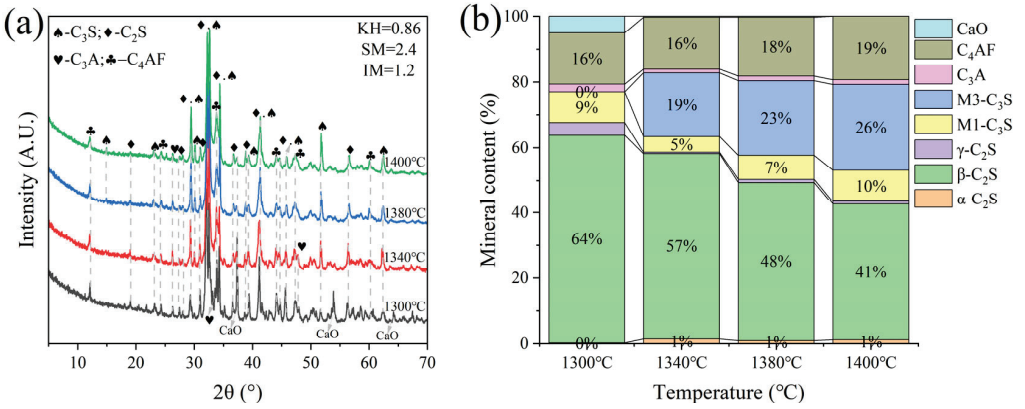

Figure 11. XRD analysis and mineral composition ratios of sample H. (**a**) XRD of sample H, (**b**) mineral content of sample H.

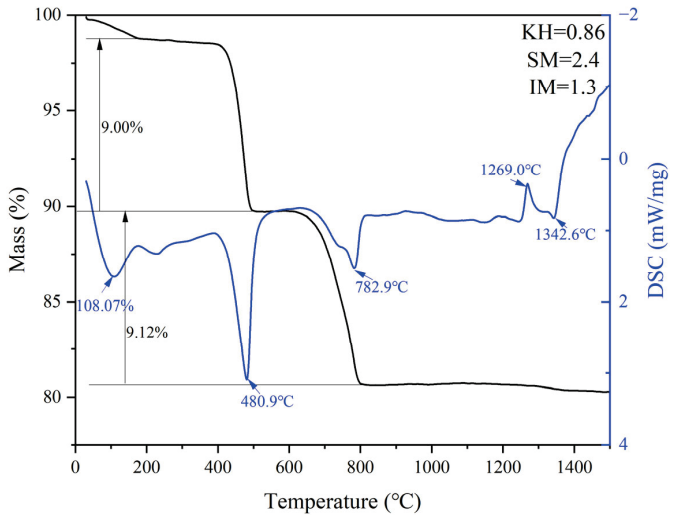

Figure 12. TG-DSC curves of sample H.

As shown in Figure 13, there is unreacted CaO in the clinker at a low calcining temperature. At this time, the content of β-C_2S in the clinker accounts for more than 60%, and a large amount of β-C_2S makes it easy to produce more γ-C_2S during cooling. Meanwhile, the C3S in the clinker calcined at 1300 °C is of the M1 type, which is related to the presence of trace mineralization ions in the raw material, which can promote the transformation of the M3 type to the M1 type. With the increase in calcination temperature, CaO in clinker reacts with C_2S to form C_3S, M3-C_3S begins to appear, and the content gradually increases, but the change in M1-C_3S content floats less, which is limited by the content of mineralization ions. When the calcination temperature was increased to 1380 °C, the content of C_3S in clinker was 30%. Trace mineralization ions in the raw material have a positive effect on the calcination of clinker, which can promote the generation of highly active minerals, such as M1-C_3S and α-C_2S. In addition, the increase in calcination temperature promotes the conversion of C_2S to C_3S, and the CaO content in clinker is also reduced. However, the clinker intermediate phases, constituting C_4AF and C_3A generation, were basically unchanged.

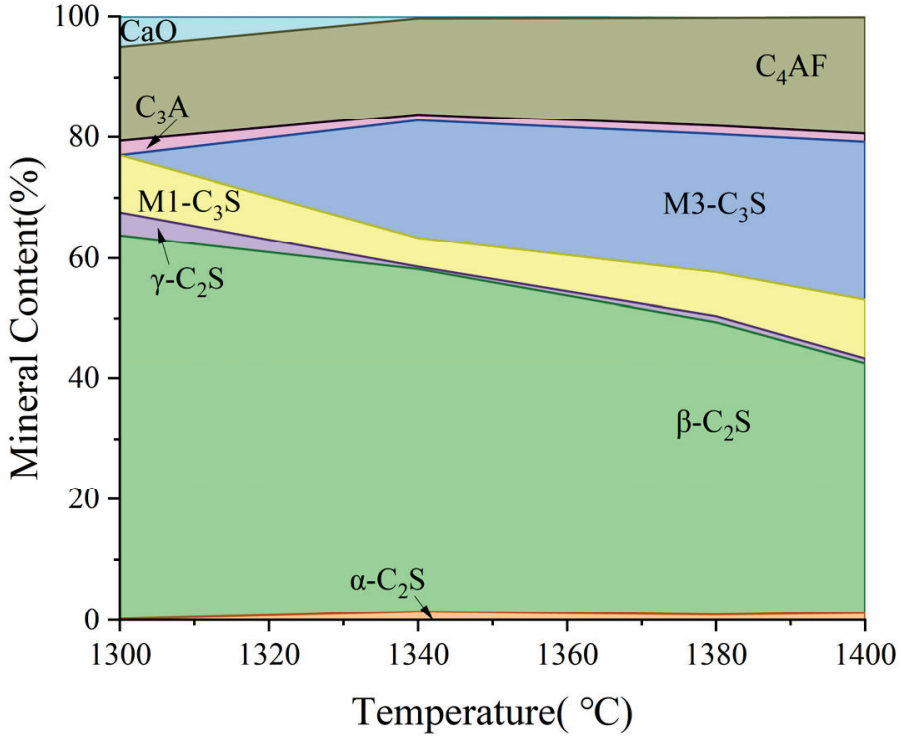

Figure 13. Effect of calcination temperature on mineral-phase formation.

For samples I and J, calcination experiments were performed at temperatures of 1340 °C, 1380 °C, and 1400 °C, each with a one-hour sintering period. XRD qualitative and quantitative analyses indicated that the C_3S content in cement clinker calcined at 1340 °C exceeded 30% (Figures 14 and 15). However, due to an imbalanced mineral-phase composition, characterized by a lower KH value and an excessively high IM value, the formation of C_3S from C_2S and CaO was hindered. The high IM values resulted in increased liquid-phase viscosity, complicating mass diffusion and thereby reducing the contribution of C_3S to the clinker's mineral-phase composition [31]. It was determined that the clinker prepared with the KH = 0.86 ratio is more suitable for use in production. Additionally, insulation time experiments were conducted on sample H to determine the optimal sintering duration.

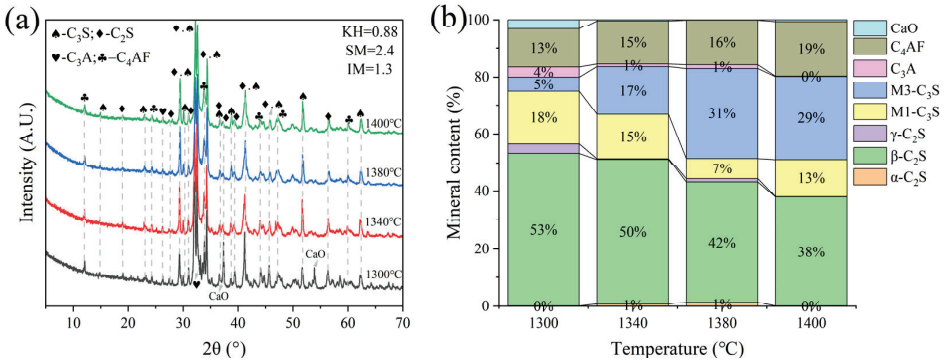

Figure 14. XRD analysis and mineral composition ratios of sample I. (**a**) XRD of sample I, (**b**) mineral content of sample I.

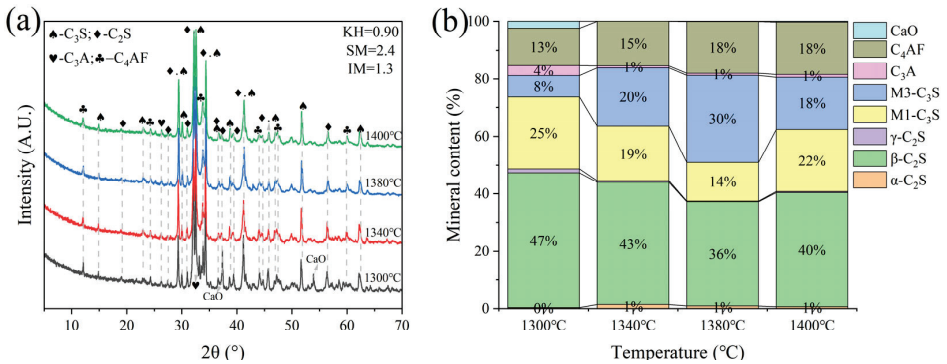

Figure 15. XRD analysis and mineral composition ratios of sample J. (**a**) XRD of sample J, (**b**) mineral content of sample J.

Due to the minimal difference in mineral-phase composition between calcination temperatures of 1340 °C and 1380 °C, microscopic image analysis was conducted at both temperatures to further determine the optimal calcination temperature. The figure below shows the microscopic image analysis of cement clinker prepared at 1340 °C and 1380 °C with KH = 0.86 (Figure 16). For the sample calcined at 1340 °C with a one-hour sintering period, the main mineral phases were C_2S and C_3S, with C_2S particles surrounded by the liquid phase [32]. The C_2S mineral phase had an average particle size of approximately 30 μm, while the C_3S mineral phase had an average particle size of about 20 μm and a length-to-width ratio of 2.5. In contrast, the C_3S mineral phase significantly increased in samples calcined at 1380 °C. Quantitative analysis indicated that calcination at 1340 °C was more appropriate.

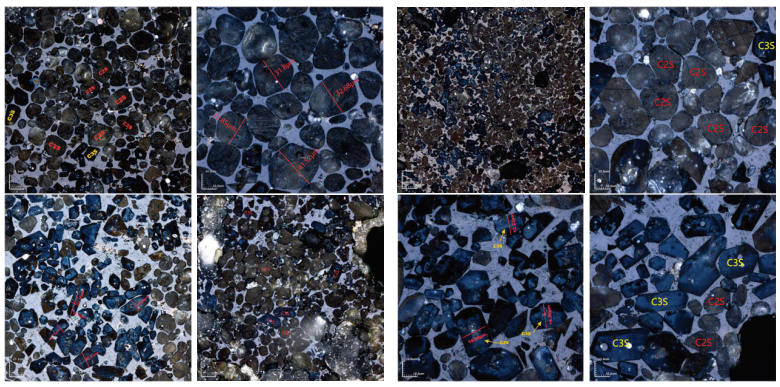

Figure 16. Microscopic images of sample H sintered at 1340 °C and 1380 °C for 1 h. (**Left**): 1340 °C, (**Right**): 1380 °C.

Different sintering time experiments were conducted for sample H under the desired ratio, with sintering times of 0 min, 30 min, 60 min, and 90 min. XRD and microscopic analyses revealed distinct f-CaO diffraction peaks, with quantitative analysis indicating a higher f-CaO content at a calcination temperature of 1340 °C when the sintering time was reduced to 0 min in Figure 17. Additionally, the C_3S content significantly increased at a sintering time of 90 min. The mineral-phase composition at 30 min closely matched that observed at 60 min, meeting the requirements of the mineral-phase ratio of high-belite Portland cement clinker. Microscopic image analysis (Figure 18) further identified numerous voids and the incomplete development of small crystal particles at a sintering time of 30 min. This observation highlights that 60 min is the optimal sintering time, as it provides the most balanced mineral-phase composition while minimizing issues related to incomplete crystal formation.

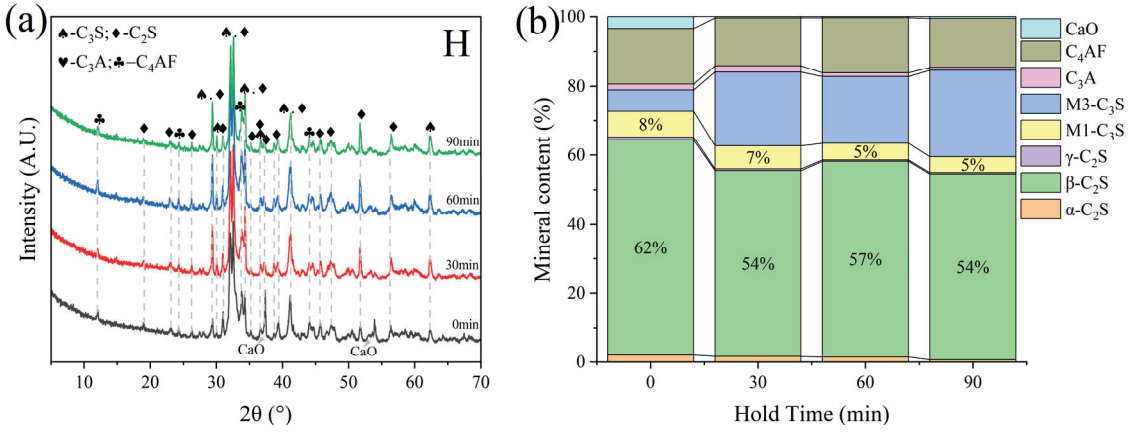

Figure 17. XRD and mineral content of sample H under varying sintering time conditions. (**a**) XRD of sample H, (**b**) mineral content of sample H.

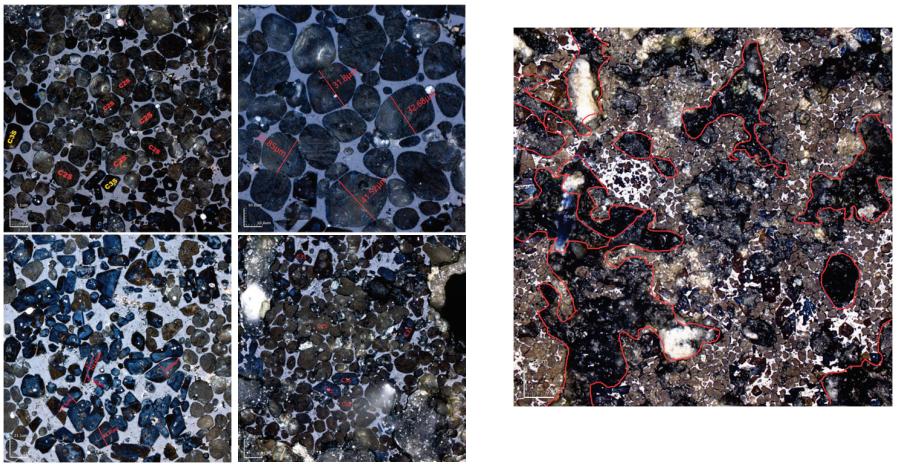

Figure 18. Microscopic images of sample H sintered at 1340 °C for 30 min and 1 h. (**Left**): 1 h; (**Right**): 30 min.

Due to the significant SiO_2 content in LGL, its crystallinity can adversely affect clinker properties. To address this issue, the limestone was classified and ground into various particle sizes, followed by sieving through 200-mesh and 400-mesh square-hole sieves to ensure uniform fineness before batching for clinker preparation under identical calcination conditions. XRD analysis indicated that varying limestone grain sizes do not significantly influence the C_4AF and C_3A mineral-phase contents in Figures 19 and 20. For sample H, the mineral composition remains consistent when using 400-mesh sieved limestone,

whereas for sample G, the effect of limestone fineness is more pronounced due to a higher proportion of limestone in raw meal preparation (11.5% in sample G compared to 10% in sample H). This underscores the importance of controlling the limestone fineness according to specific requirements.

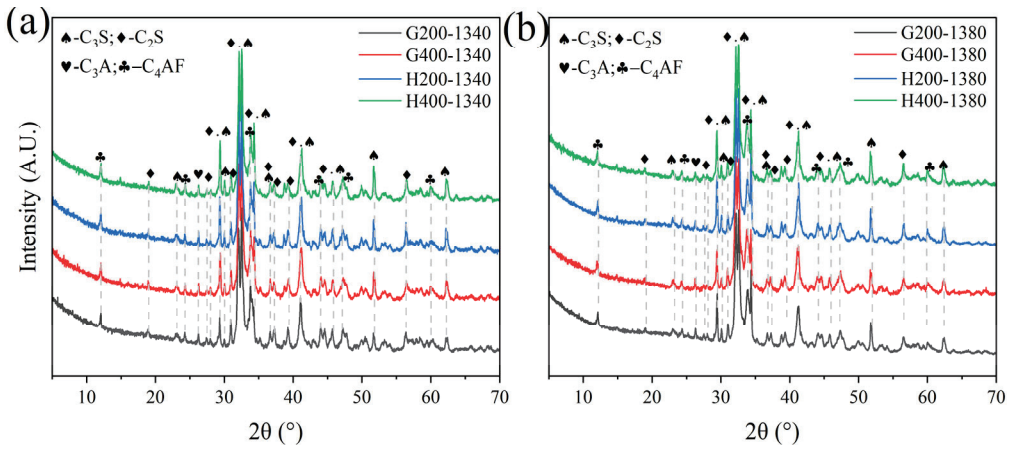

Figure 19. XRD of samples G and H calcined with limestone feedstocks of varying fineness.

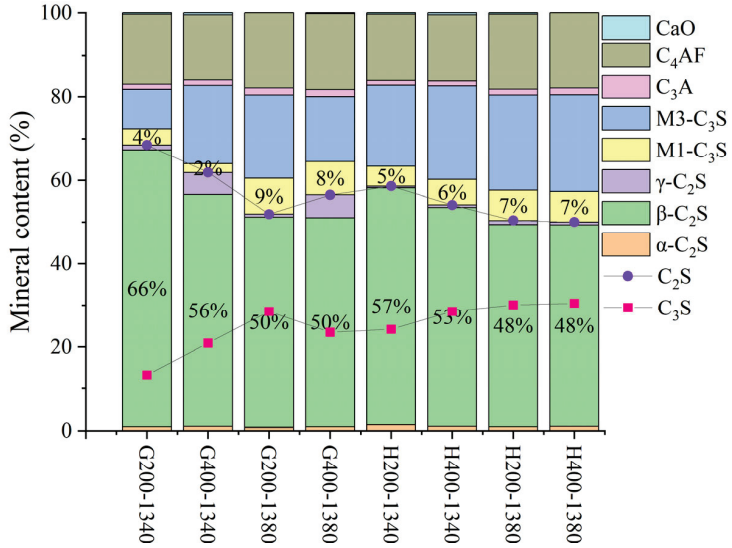

Figure 20. The mineralogical composition of samples H and G following calcination with limestone feedstocks of varying fineness.

In this experiment, utilizing low-grade limestone and calcium carbide slag to replace high-quality limestone for clinker calcination can significantly reduce the CO_2 emission due to the decomposition of raw materials in the production of cement process. Because the main component of calcium carbide slag is $Ca(OH)_2$, CaO and H_2O are produced during decomposition, and there is no CO_2 emission; for this reason, according to the TG-DSC curve of sample H, the H_2O produced during calcination is analyzed to calculate the required CaO, as shown in Equations (4)–(7). And the percentage of CO_2 reduction is calculated by replacing $CaCO_3$, as shown in Figure 21.

$$Ca(OH)_2 \rightarrow CaO + 2H_2O \quad (4)$$

$$CaCO_3 \rightarrow CaO + CO_2 \quad (5)$$

$$m_{2CO_2} = \frac{11}{9} m_{H_2O} \quad (6)$$

$$R_{CO_2} = \left(1 - \frac{m_2CO_2}{m_{1CO_2} + m_{2CO_2}}\right) \times 100\% \quad (7)$$

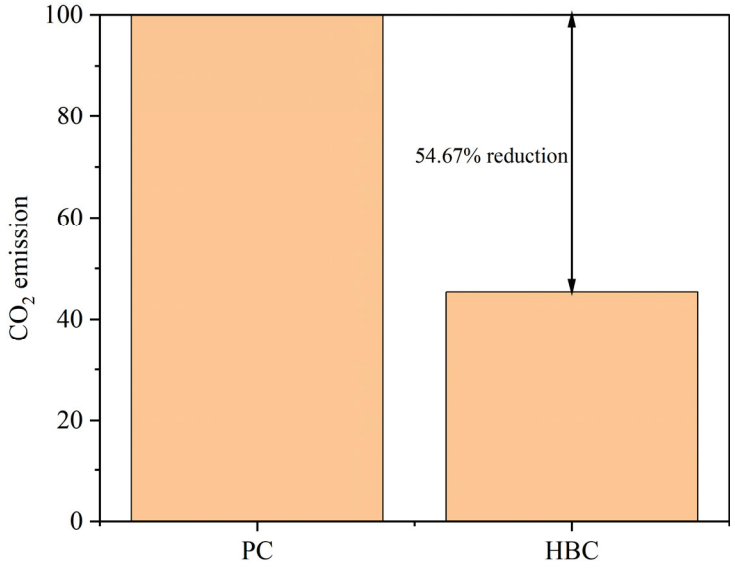

Figure 21. Comparison of CO_2 emissions between HBC and PC.

Here, R_{CO_2} is the proportion of CO_2 emission reduction, m_{1CO_2} is the reduced CO_2 emissions during calcination, and m_{2CO_2} is the CO_2 emissions from calcination.

4. Conclusions

In this study, high-belite Portland cement clinker was prepared using LGL and solid waste materials (calcium carbide slag and steel slag). The effects of varying KH values, calcination temperatures, and sintering times on clinker formation were systematically investigated. Additionally, a preliminary exploration of the influence of fineness of limestone on clinker calcination was conducted. The conclusions drawn from this study are summarized as follows:

High-belite Portland cement was successfully prepared by changing the KH value and calcining system. A too-low or too-high KH will cause the content of C_2S and C_3S in the clinker mineral phase to be either too high or too low. High-belite Portland cement clinker with KH = 0.86 was successfully prepared at 1340 °C in 1 h, where the mineral phase of β-C_2S can reach 56.8%, and the α-C_2S can be up to 1.4%. The early hydration activity of α-C_2S is higher than that of β and γ, which can make up for the defect of low early hydration strength of high-belite Portland cement clinker.

In this research, the difference in fineness (6.133 μm and 4.907 μm) of LGL may not affect the mineral composition of the high-belite Portland cement clinker. This may be due to LGL occupying a relatively small proportion of raw material combinations. Further investigations need to be performed.

Overall, the high-belite Portland cement clinker prepared from low-grade limestone and solid wastes can effectively reduce CO_2 emission. In this study, the CO_2 emission of the prepared high-belite Portland cement clinker was 54.67% lower than that of ordinary Portland cement clinker.

Author Contributions: Conceptualization, Y.Z. and W.X.; Methodology, J.D., Y.Z. and W.X.; Validation, Y.Z. and W.X.; Formal analysis, J.D.; Investigation, J.D., S.X. and Z.G.; Data curation, J.D., S.X. and Z.G.; Writing—original draft, J.D.; Writing—review & editing, Y.Z. and W.X. All authors have read and agreed to the published version of the manuscript.

Funding: This research was funded by National Natural Science Foundation of China grant number 52302024 and National Key R & D Program of China grant number 2021YFB3802002.

Institutional Review Board Statement: Not applicable.

Informed Consent Statement: Not applicable.

Data Availability Statement: The original contributions presented in this study are included in the article. Further inquiries can be directed to the corresponding authors.

Conflicts of Interest: The authors declare that they have no conflicts of interest related to this work. We declare that we do not have any commercial or associative interests that represents a conflict of interest in connection with the work submitted.

References

1. National Bureau of Statistics. *Statistical Communique of the People's Republic of China on the 2023 National Economic and Social Development*; National Bureau of Statistics: Beijing, China, 2024; pp. 4–21.
2. IEA. *CO2 Emissions in 2023*; IEA: Paris, France, 2024.
3. Cuesta, A.; Ayuela, A.; Aranda, M.A.G. Belite cements and their activation. *Cem. Concr. Res.* **2021**, *140*, 106319. [CrossRef]
4. Kurdowski, W.; Duszak, S.; Trybalska, B. Belite produced by means of low-temperature synthesis. *Cem. Concr. Res.* **1997**, *27*, 51–62. [CrossRef]
5. Hanein, T.; Galvez-Martos, J.-L.; Bannerman, M.N. Carbon footprint of calcium sulfoaluminate clinker production. *J. Clean. Prod.* **2018**, *172*, 2278–2287. [CrossRef]
6. Moudar, J.; El Fami, N.; Diouri, A.; Taibi, M.H. Characterization of belitic cement mortars elaborated from shell and glass powders, microstructure and mechanical properties. *Constr. Build. Mater.* **2023**, *379*, 131189. [CrossRef]
7. Enriquez, M.K.; Tobon, J.I.; Ramirez, J.H. Use of industrial wastes for the synthesis of belite clinker. *Mater. Constr.* **2020**, *70*, e226. [CrossRef]
8. Yang, Z.; Liu, Y.; Chen, M.; Wang, X.; Ye, C.; Li, X.; Chen, W.; Yang, Y.; Wang, B.; Li, C.; et al. Influence of Coupling Effects between Gravel Soil Porosity and Cement Grout Weight on Diffusion Laws and Morphologies of Penetration Grouting. *Appl. Sci.* **2022**, *12*, 7601. [CrossRef]
9. Zhiquan, Y.; Xiangdong, N.; Kepeng, H.; Wei, L.; Yanhui, G. Relationships between water-cement ratio and rheological characteristics of Power-law cement grouts. *Electron. J. Geotech. Eng.* **2015**, *20*, 5825–5831.
10. Yang, Z.; Qian, S.; Hou, K. Time-dependent behavior characteristics of Power-law cement grouts applied in geotechnical engineering. *Electron. J. Geotech. Eng.* **2015**, *20*, 1017–1024.
11. Yang, Z.Q.; Hou, K.P.; Guo, T.T. Research on Time-Varying Behavior of Cement Grouts of Different Water-Cement Ratios. *Appl. Mech. Mater.* **2011**, *71–78*, 4398–4401. [CrossRef]
12. Yang, Z.Q.; Hou, K.P.; Guo, T.T. Study on the Effects of Different Water-Cement Ratios on the Flow Pattern Properties of Cement Grouts. *Appl. Mech. Mater.* **2011**, *71–78*, 1264–1267. [CrossRef]
13. Zhao, X.J.; Yang, Z.J.; Lin, X.W.; Ma, H.; Shen, W.H. Development status of comprehensive utilization of carbide slag. *China Chlor Alkali* **2016**, *7*, 43–47.
14. Ding, Q.S.; Tang, G.H.; Lu, S.B. Development of New Technology for Production of Cement Clinker with Carbide Slag in Replacement of Limestone. In Proceedings of the International Symposium on Cement and Concrete and Canmet/ACI International Symposium on Concrete Technology for Sustainable Development, Xi'an, China, 19–22 September 2006; pp. 274–282.
15. Zeng, X.J.; Chen, P.; Wang, Y.P. Production technology progress of cement made of acetylene slag home and abroad. *China Cem.* **2018**, *9*, 79–85.
16. Gao, Y.; Li, Z.; Zhang, J.; Zhang, C.; Chen, J. Synthesis, Characterization and Properties of Solid Waste Based High Belite Cement. *Chem. Lett.* **2021**, *50*, 128–130. [CrossRef]
17. Tamma, V.R.; Pancharathi, R.K.; Bibekananda, M.; Pallapothu, S.N.R.G. Strength and microstructure characteristics of low-grade (LG) limestone-based cements for a sustainable concrete. *Environ. Dev. Sustain.* **2024**, *26*, 22907–22927. [CrossRef]
18. Liu, Z.H.; Guo, Y.H.; Liu, S.F. Application of low grade limestone in cement clinker production. *Cement* **2024**, *4*, 49–51. [CrossRef]
19. Zhao, P. Performance of Belite-Barium Calcium Sulphoaluminate Cement Preparaed by Low Grade Raw Materials and Industrial Wastes. Master's Thesis, University of Jinan, Jinan, China, 2011.
20. Wu, H.M. Cement clinker rate value and its application in batching. *China Cem.* **2013**, *7*, 70–74.
21. Hu, Y.; Li, W.; Ma, S.; Wang, Q.; Zou, H.; Shen, X. The composition and performance of alite-ye'elimite clinker produced at 1300 °C. *Cem. Concr. Res.* **2018**, *107*, 41–48. [CrossRef]
22. Mumme, W.G. Crystal structure of tricalcium silicate from a Portland cement clinker and its application to quantitative XRD analysis. *Neues Jahrb. Für Mineral. Monatshefte.* **1995**, *4*, 146–160.

23. De La Torre, A.G.; Bruque, S.; Campo, J.; Aranda, M.A.G. The superstructure of C_3S from synchrotron and neutron powder diffraction and its role in quantitative phase analyses. *Cem. Concr. Res.* **2002**, *32*, 1347–1356. [CrossRef]
24. Mumme, W.G.; Hill, R.J.; Bushnell-wye, G.; Segnit, E.R. Rietveld crystal structure refinements, crystal chemistry and calculated powder diffraction data for the polymorphs of dicalcium silicate and related phases. *Neues Jb Miner Abh.* **1995**, *169*, 35–68.
25. Yamnova, N.A.; Zubkova, N.V.; Eremin, N.N.; Zadov, A.E.; Gazeev, V.M. Crystal structure of larnite β-Ca_2SiO_4 and specific features of polymorphic transitions in dicalcium orthosilicate. *Crystallogr. Rep.* **2011**, *56*, 210–220. [CrossRef]
26. Gobechiya, E.R.; Yamnova, N.A.; Zadov, A.E.; Gazeev, V.M. Calcio-olivine γ-Ca_2SiO_4: I.: Rietveld refinement of the crystal structure. *Crystallogr. Rep.* **2008**, *53*, 404–408. [CrossRef]
27. McMurdie, H.F. The Structure of Tricalcium Aluminate. *J. Res. Natl. Bur. Stand.* **1941**, *27*, 499–505. [CrossRef]
28. Jupe, A.C.; Cockcroft, J.K.; Barnes, P.; Colston, S.L.; Sankar, G.; Hall, C. The site occupancy of Mg in the brownmillerite structure and its effect on hydration properties: An X-ray/neutron diffraction and EXAFS study. *J. Appl. Crystallogr.* **2001**, *34*, 55–61. [CrossRef]
29. Chmaissem, O.; Huang, Q.; Putilin, S.N.; Marezio, M.; Santoro, A. Neutron powder diffraction study of the crystal structures of $HgBa_2CuO_4$+δ and $HgBaO_2$. *Phys. C Supercond* **1993**, *212*, 259–265. [CrossRef]
30. Blancovarela, M.T.; Palomo, A.; Vazquez, T. Effect of fluorspar on the formation of clinker phases. *Cem. Concr. Res.* **1984**, *14*, 397–406. [CrossRef]
31. Huang, L.; Song, W.; Li, H.; Zhang, H.; Yang, Z. Effects of aphthitalite on the formation of clinker minerals and hydration properties. *Constr. Build. Mater.* **2018**, *183*, 275–282. [CrossRef]
32. Londono-Zuluaga, D.; Tobón, J.I.; Aranda, M.A.G.; Santacruz, I.; De la Torre, A.G. Clinkering and hydration of belite-alite-ye'elimite cement. *Cem. Concr. Compos.* **2017**, *80*, 333–341. [CrossRef]

Disclaimer/Publisher's Note: The statements, opinions and data contained in all publications are solely those of the individual author(s) and contributor(s) and not of MDPI and/or the editor(s). MDPI and/or the editor(s) disclaim responsibility for any injury to people or property resulting from any ideas, methods, instructions or products referred to in the content.

materials

MDPI

Article

Influence of Raw Material Fineness on Clinker Burnability and Cement Performance

Shanshi Chen, Xinjian Yue and Yongmin Zhou *

College of Materials Science and Engineering, Nanjing Tech University, South Puzhu Road No. 30, Nanjing 211816, China; 202261203311@njtech.edu.cn (S.C.); 202261203299@njtech.edu.cn (X.Y.)
* Correspondence: yongminzhou@njtech.edu.cn; Tel.: +86-139-5183-2092

Abstract: The particle size of raw materials is crucial for clinker formation, ultimately affecting cement performance. However, the specific effects of the fineness of individual raw materials on clinker burnability remain insufficiently understood. In this study, the fineness of limestone, shale, and iron-bearing materials was systematically varied to explore its influence on raw meal burnability and the resulting cement properties. Raw materials were prepared with controlled residue levels (5–20%) retained on an 80 μm sieve. Their impact was evaluated based on free lime content (f-CaO), clinker phase composition, cement strength development, and hydration behavior. Among the variables studied, limestone fineness was found to be the predominant factor affecting f-CaO levels, confirming its dominant role in governing clinker burnability. In contrast, fineness adjustments of aluminosilicate and iron-bearing components produced comparatively minor effects. Despite variations in raw meal fineness, clinkers produced with sieve residues between 10% and 15% exhibited consistent phase compositions, primarily comprising tricalcium silicate (C_3S), dicalcium silicate (C_2S), tricalcium aluminate (C_3A), and tetracalcium aluminoferrite (C_4AF). Furthermore, cement pastes derived from these clinkers demonstrated similar setting times, mechanical strengths, and hydration product assemblages. These results highlight the robustness of cement performance with respect to moderate variations in raw material fineness, particularly when limestone fineness is adequately controlled.

Keywords: cement raw materials; particle size distribution; clinker sintering; cement performance

1. Introduction

Clinker formation is governed by a combination of raw meal chemistry [1,2], calcination temperature [3,4], and particle size distribution (PSD) [5], with the latter exerting a pronounced influence on solid-state reaction interfaces, diffusion pathways, and reaction kinetics [6]. Among these factors, PSD plays a critical role in determining the thermal behavior during sintering and the evolution of clinker phase assemblages.

Previous studies have identified an optimal specific surface area range of 250–320 m^2/kg as favorable for the formation of major silicate phases, particularly C_3S and C_2S [7]. In contrast, excessively broad or ultra-fine PSDs can hinder the formation of a homogeneous liquid phase, reduce thermal efficiency during calcination, promote ring formation, and ultimately compromise both clinker quality and kiln operational stability [8–10]. Al-Salmany and Al-Hazaa [11] emphasized that particle size uniformity is vital for achieving stable sintering. When raw meal particles are refined below 80 μm, the resulting increase in surface area and reduction in diffusion distances enhance the

reactivity between CaO and SiO_2, promoting C_3S formation and minimizing residual free lime (f-CaO) [12]. However, overly fine raw meals with specific surface areas exceeding 400 m^2/kg may induce localized high-viscosity liquid phases, which obstruct effective heat transfer and impede reaction kinetics [13,14]. These effects destabilize the thermal regime and impair clinker formation. Consequently, optimization of raw meal PSD should prioritize both balance and uniformity, rather than indiscriminate fineness.

In addition to PSD, the alkali content of raw materials—though typically present in minor quantities—can influence the clinkerization process. Alkali oxides such as Na_2O and K_2O contribute to early liquid phase formation, affecting sintering temperature and phase evolution, particularly the development of C_3A and C_4AF [15]. Moreover, alkalis can lower the eutectic point of the melt, potentially interacting with PSD effects on reaction kinetics. While this study focuses primarily on PSD, alkali contents were controlled during raw meal preparation to isolate the influence of particle fineness from compositional variability [16].

Grinding and blending strategies also significantly affect clinker reactivity and cement performance. Garces-Vargas et al. [17] reported that non-optimized blending and grinding techniques may disrupt synergistic reactions among raw meal components, thereby limiting hydration activity and early strength development. Therefore, understanding the contribution of individual constituent fineness to overall reactivity is essential for improving clinker formation, enhancing energy efficiency, and reducing CO_2 emissions [18,19].

Beyond clinker formation, raw material PSD directly influences the rheological properties and hydration kinetics of cementitious systems, which are critical in engineering applications such as grouting and soil stabilization. Prior research has shown that variations in cement fineness and composition significantly affect the time-dependent viscosity and flow characteristics of cement-based suspensions [20–22]. These findings underscore the broader relevance of raw material PSD control across the entire cement production and application spectrum.

In this study, the influence of raw material fineness on clinker burnability, mineral phase development, and cement performance is systematically investigated. Using controlled proportions of limestone, shale, and industrial by-products—namely iron tailings or copper slag—the effect of fineness variation was evaluated based on sieve residue values ranging from 5% to 20% at 80 μm. The assessment focused on f-CaO content, clinker mineralogy, and the compressive strength development of the produced cement, providing insight into the mechanistic role of individual raw material fineness in determining raw meal reactivity.

Unlike conventional approaches that regulate the overall fineness of the raw mix, this study independently adjusts the fineness of limestone, shale, and iron-bearing components. This approach aims to identify the dominant constituent influencing clinker burnability and cement strength, offering both empirical evidence and theoretical guidance for targeted PSD optimization. The findings hold significant implications for enhancing process efficiency, clinker quality, and sustainability in cement manufacturing.

Furthermore, the incorporation of industrial solid wastes such as copper slag and iron tailings into cement raw mixes has attracted increasing interest due to its potential to reduce natural resource consumption and environmental impacts. Rich in Fe_2O_3 and SiO_2, these materials function as effective corrective components in clinker production while contributing to waste valorization and carbon footprint reduction. Their use aligns with global efforts toward sustainable construction and circular economy practices. Recent studies have further validated their viability—for example, copper slag as a supplementary raw material in clinker formulation [23], and iron tailings enhancing the performance and reducing the environmental load of blended cement systems [24].

2. Materials and Methods

2.1. Materials

As depicted in Figure 1, the raw materials for this study were sourced as follows: limestone (X), shale (X), and iron tailings from Zhejiang Xindu Cement Co. (Jiaxing, China), and limestone (H), shale (H), and copper slag from Hejiashan Cement Co. (Jiangshan, China). Gypsum, in the form of analytical reagent (AR)-grade calcium sulfate dihydrate, was provided by Xilong Chemical Co. (Shantou, China) In this study, iron tailings and copper slag were utilized as ferriferous corrective materials to effectively adjust the Fe_2O_3 content of the raw mix, ensuring it meets the requirements for clinker mineral formation. Their use also promotes the resource utilization of industrial solid wastes, contributing to reductions in both production costs and carbon emissions [25,26].

Figure 1. Raw materials used in this study.

The chemical compositions of the milled raw materials were analyzed by X-ray fluorescence (XRF; Spectro, Bruker, Billerica, MA, USA), with the results summarized in Table 1. Mineralogical phases were identified through X-ray diffraction (XRD) using Cu Kα radiation, and the corresponding diffractograms are shown in Figure 2. Material densities were determined using a pycnometer and are reported in Table 2.

Table 1. Chemical composition of cement raw materials measured by XRF (wt.%).

Raw Material Name	CaO	SiO_2	Al_2O_3	Fe_2O_3	LOI [1]	MgO	SO_3	K_2O	Na_2O
Limestone (X)	48.22	7.18	2.65	0.54	40.34	0.77	0.12	0.2	0.09
Shale (X)	0.83	67.54	14.47	6.43	4.9	1.2	0.05	2.99	0.44
Iron Tailings	14.38	45.12	4.06	22.64	9.84	3.27	0.22	0.47	0.16
Gypsum	48.51	---	---	---	20.12	---	31.21	---	---
Limestone (H)	51.19	5.58	0.66	0.26	40.15	0.78	0.06	0.06	0.06
Shale (H)	0.73	62.74	14.83	8.35	6.16	2.77	0.32	2.06	0.31
Copper Slag	2.96	30.97	3.23	58.49	0	1.85	0.12	0.54	0.33

[1] LOI refers to the percentage of mass loss upon heating to 950 °C.

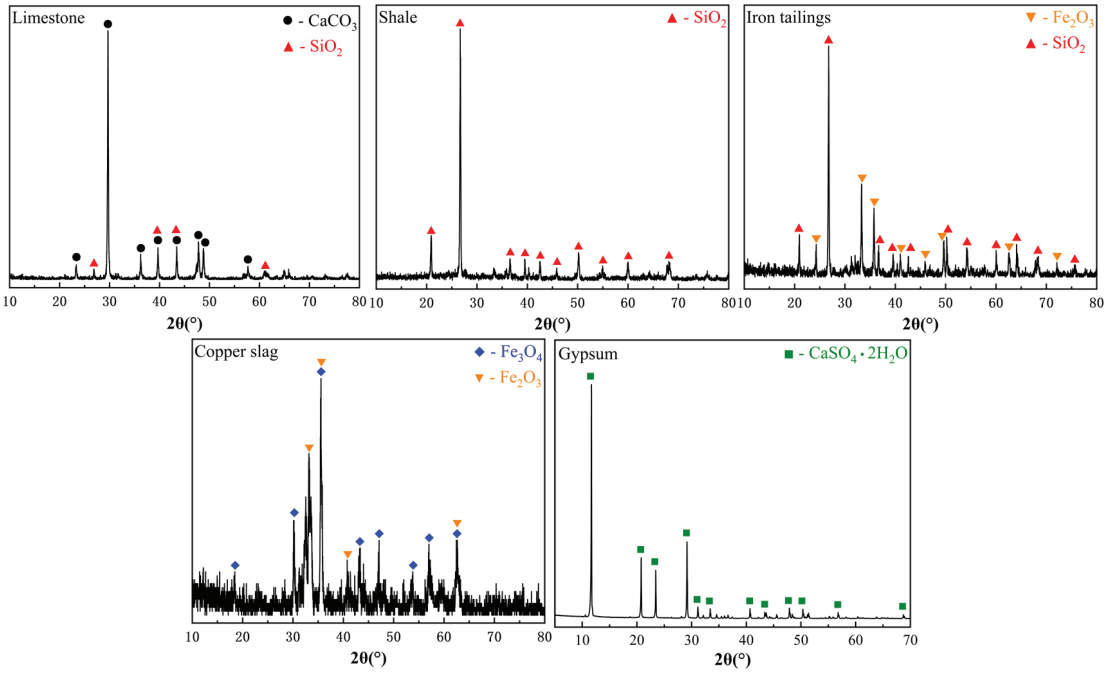

Figure 2. XRD patterns of various cement raw materials.

Table 2. Hardness and density of cement raw materials.

Raw Material	Limestone (X)	Shale (X)	Iron Tailings	Limestone (H)	Shale (H)	Copper Slag
Density (g/cm^3)	2.59	2.51	2.85	2.61	2.54	3.66

2.2. Methods

2.2.1. Raw Meal Proportioning for Cement Production

Drawing on the chemical compositions presented in Table 1, two distinct raw meal formulations were developed through an optimization strategy to produce two types of Portland cement. The lime saturation factor (KH) was controlled at 0.9 ± 0.1, the silica modulus (SM) at 2.6 ± 0.1, and the alumina modulus (IM) at 1.6 ± 0.1 [27]. During the proportioning process, two of the three targeted modulus values were strictly maintained, while the third was adjusted as closely as possible to ensure a well-balanced raw mix with favorable burnability. The final raw meal compositions and corresponding modulus values of the resulting clinkers are presented in Table 3.

Table 3. Raw meal proportioning schemes for cement production.

	Raw Material Proportion (wt%)			KH [1]	SM [2]	IM [3]
X	Limestone (X)	Shale (X)	Iron Tailings	0.9	2.39	1.65
	86.4	8.09	5.5			
H	Limestone (H)	Shale (H)	Copper Slag	0.9	2.5	1.39
	84.84	13.37	1.79			

[1] KH = $\frac{\omega(CaO)-1.65\cdot\omega(Al_2O_3)-0.35\cdot\omega(Fe_2O_3)}{2.8\cdot\omega(SiO_2)}$. [2] SM = $\frac{\omega(SiO_2)}{\omega(Al_2O_3)+\omega(Fe_2O_3)}$. [3] IM = $\frac{\omega(Al_2O_3)}{\omega(Fe_2O_3)}$.

2.2.2. Preparation of Raw Material Powder Samples with Varying Fineness

Raw materials were ground using appropriate techniques to achieve the target fineness levels, as specified in Table 4. Each material was milled separately to attain 80 μm sieve residues of 5%, 10%, 15%, and 20% (hereafter, all residue values refer to the 80 μm sieve).

This fineness range was selected based on typical fineness control practices in cement plants and preliminary trials. This range effectively captures the influence of particle size on burnability without introducing excessive grinding effort or compromising material stability. While broader or finer ranges could be explored in future studies, the chosen interval was sufficient to observe meaningful differences among raw materials under practical conditions.

Table 4. Fineness of different raw materials.

Limestone (X)		Limestone (H)		Shale (X)		Shale (H)		Copper Slag		Iron Tailings	
Sample ID	Sieve Residue (%)	Sample ID	Sieve Residue (%)	Sample ID	Sieve Residue (%)	Sample ID	Sieve Residue (%)	Sample ID	Sieve Residue (%)	Sample ID	Sieve Residue (%)
XS-1	5	HS-1	5	XY-1	5	HY-1	5	XT-1	5	HT-1	5
XS-2	10	HS-2	10	XY-2	10	HY-2	10	XT-2	10	HT-2	10
XS-3	15	HS-3	15	XY-3	15	HY-3	15	XT-3	15	HT-3	15
XS-4	20	HS-4	20	XY-4	20	HY-4	20	XT-4	20	HT-4	20

Ground samples were sealed in plastic bags and stored prior to use. Particle size distributions (PSD) at each fineness level were measured using a laser diffraction analyzer (90PlusPALS, Brookhaven, Nashua, NH, USA), while specific surface areas were determined via nitrogen adsorption. All samples were oven-dried for 10 h before analysis. The PSD profiles of the ground H-type raw materials are shown in Figure 3. The corresponding D10, D50, D90 values and average particle sizes for each fineness level are summarized in Table 5.

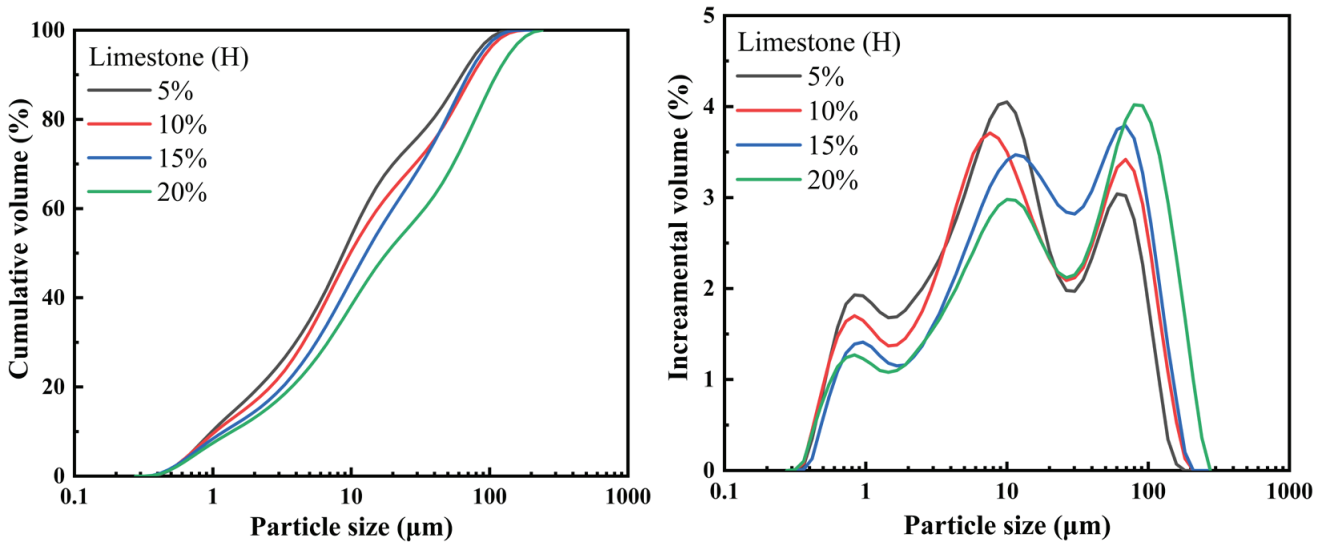

Figure 3. *Cont.*

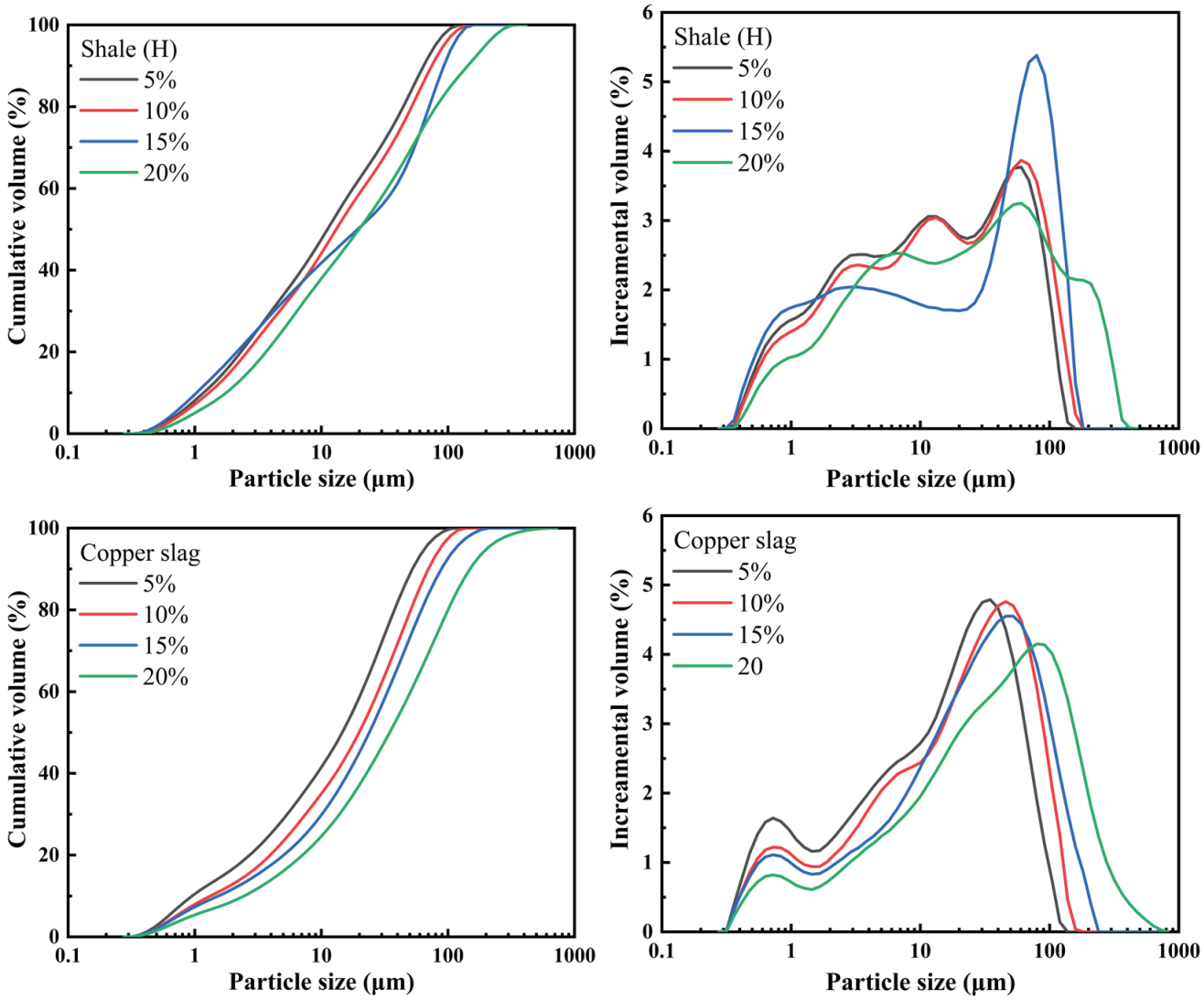

Figure 3. PSD of ground raw materials.

Table 5. PSD of raw materials.

	D10% (μm)	D50% (μm)	D90% (μm)
HS-5%	0.983	8.772	63.179
HS-10%	1.043	9.844	75.232
HS-15%	1.198	12.77	84.154
HS-20%	1.373	18.069	112.184
HY-5%	1.174	11.183	64.241
HY-10%	1.296	13.097	74.438
HY-15%	1.032	19.363	92.726
HY-20%	1.767	19.863	143.182
HT-5%	0.95	14.644	52.428
HT-10%	1.327	19.877	70.038
HT-15%	1.535	23.907	88.528
HT-20%	2.455	34.687	149.078

2.2.3. Preparation of Cement Clinker

Based on the proportioning schemes outlined in Table 3, the raw materials were blended in a V-type mixer for 10 min, then compacted into cylindrical pellets (Φ17 × 13 mm^3) using a steel mold. The pellets were placed in crucibles and subjected to thermal processing in

a high-temperature electric furnace, with the heating rate controlled at 10 °C/min. The samples were first preheated at 950 °C for 30 min to ensure complete decomposition of calcium carbonate, then sintered at 1450 °C for another 30 min to facilitate clinker formation. After firing, the clinkers were rapidly cooled to approximately 25 °C using forced air.

2.2.4. Preparation of Cement Paste and Mortar

Following Chinese National Standard GB 175-2023, Portland cement was produced by blending 95 wt.% ground clinker with 5 wt.% calcium sulfate dihydrate (gypsum) in a V-type mixer for 10 min. The standard consistency water demand and setting times of the cement paste were determined following GB/T 1346-2011. Cement mortar was prepared as per the guidelines in GB/T 17671-2021.

Compressive and flexural strength tests were separately performed using an electronic universal testing machine (CDT1305-2, Mesiste Industrial Co., Ltd., China). Each strength value represents the average of three mortar specimens. For hydration analysis, cement paste samples cured for 28 days were crushed, immersed in absolute ethanol for 72 h to halt hydration, and then dried in a vacuum oven at 50 °C.

3. Structure and Discussion

3.1. Influence of Raw Material Particle Size Distribution on the Burnability of Raw Meal

3.1.1. Burnability Test of Raw Meal

Burnability tests of cement raw meal were carried out following the Chinese National Standard GB/T 26566-2011. Limestone, shale, and iron-bearing corrective materials were individually ground to obtain a 10% residue on an 80 μm sieve, resulting in a raw meal with a similar 10% residue at the same sieve size. Following pre-calcination at 950 °C for 30 min, the raw meal samples were calcined for 30 min at three different temperatures: 1350 °C, 1400 °C, and 1450 °C. After calcination, the clinkers were air-cooled to room temperature.

The f-CaO content in the clinkers was determined using the glycerol–ethanol method outlined in GB/T 176-2017. The results are presented in Table 6.

Table 6. f-CaO content in cement clinker.

	1350 °C	**1400 °C**	**1450 °C**
X	3.12 wt.%	1.84 wt.%	0.98 wt.%
H	2.38 wt.%	1.16 wt.%	0.62 wt.%

As illustrated in Table 6, the f-CaO content in the clinker gradually declines as the calcination temperature rises. At 1450 °C, the f-CaO content in both X and H clinkers falls below 1.5 wt.%, indicating complete calcination under these conditions. These values meet the requirements specified in the Chinese National Standard GB/T 21372-2024.

3.1.2. Influence of Fineness of Silica-Alumina Raw Materials on the Burnability of Raw Meal

The fineness of limestone and iron-bearing corrective materials was maintained with a residue of 10% on the 80 μm sieve. The effect of the fineness of silica-alumina raw materials on the burnability of the raw meal was investigated by varying their particle size. The calcination temperature was set at 1450 °C. The specific proportioning scheme is provided in Table 7, and the experimental results are presented in Figure 4.

Table 7. Burnability proportioning scheme with varying fineness of silica-alumina raw materials.

Sample ID	Limestone			Shale			Iron Tailings or Copper Slag			Raw Meal Fineness (%)
	Raw Material ID	Sieve Residue (%)	Blend Ratio (%)	Raw Material ID	Sieve Residue (%)	Blend Ratio (%)	Raw Material ID	Sieve Residue (%)	Blend Ratio (%)	
X-01	XS-2	10	86.4	XY-1	5	8.09	XT-2	10	5.51	9.60
X-02	XS-2	10	86.4	XY-2	10	8.09	XT-2	10	5.51	10.00
X-03	XS-2	10	86.4	XY-3	15	8.09	XT-2	10	5.51	10.40
X-04	XS-2	10	86.4	XY-4	20	8.09	XT-2	10	5.51	10.81
H-01	HS-2	10	84.84	HY-1	5	13.37	HT-2	10	1.79	9.33
H-02	HS-2	10	84.84	HY-2	10	13.37	HT-2	10	1.79	10.00
H-03	HS-2	10	84.84	HY-3	15	13.37	HT-2	10	1.79	10.67
H-04	HS-2	10	84.84	HY-4	20	13.37	HT-2	10	1.79	11.34

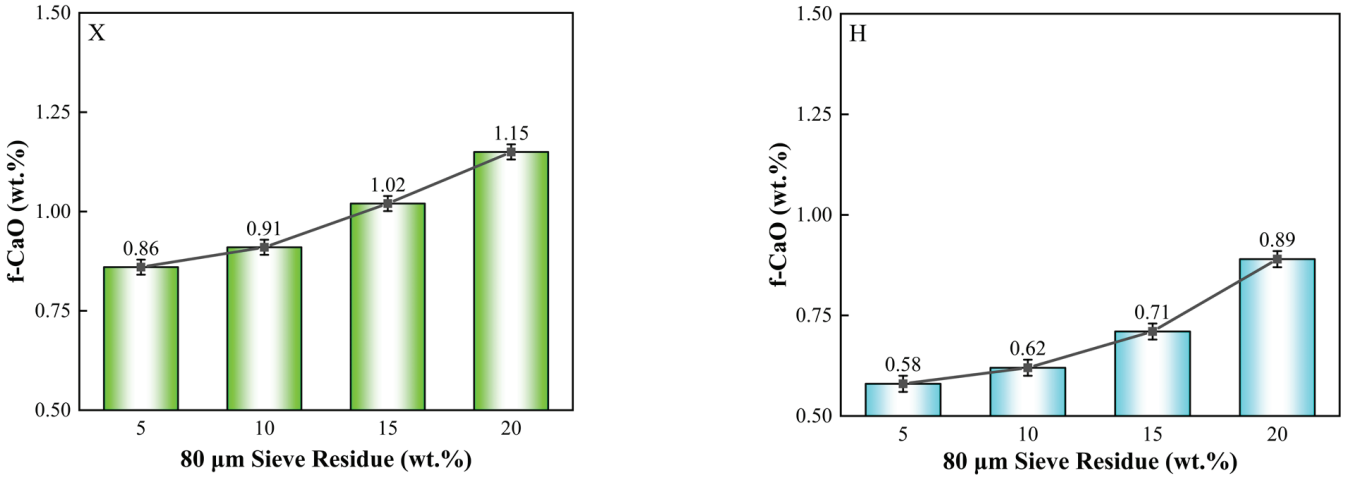

Figure 4. Comparison of burnability of raw meal with varying fineness of silica-alumina raw materials.

As shown in Figure 4, within the residue range of 5% to 20%, the impact of shale fineness on the burnability of the raw meal is limited. As the shale residue increases, the burnability of the raw meal slightly decreases. At a residue of 5%, the f-CaO content is 0.86% for X and 0.58% for H. When the residue increases to 20%, the f-CaO content rises to 1.15% for X and 0.89% for H.

Further comparison reveals that, as the shale residue increases from 5% to 20%, the f-CaO content increases by 0.29% in the X group (with a shale mass fraction of 8.09%) and by 0.31% in the H group (with a shale mass fraction of 13.37%). The increase in both cases is small, indicating that, within this range of fineness, the effect of shale fineness on the burnability of the raw meal is minor and can be considered a secondary factor.

3.1.3. Influence of Fineness of Iron-Bearing Corrective Materials on the Burnability of Raw Meal

Based on the conclusions from Section 3.1.2, it was observed that when the shale residue increased from 10% to 15%, the f-CaO content in the clinker changed by less than 0.2%. Therefore, shale with a residue of 15% was selected for subsequent experiments. The fineness of limestone and shale was kept constant, while the fineness of iron tailings and copper slag was varied to examine the effect of the particle size of iron-bearing corrective materials on the burnability of the raw meal. The experimental proportioning scheme is outlined in Table 8, and the results are presented in Figure 5.

Table 8. Burnability proportioning scheme with varying fineness of iron-bearing corrective materials.

Sample ID	Limestone			Shale			Iron Tailings or Copper Slag			Raw Meal Fineness (%)
	Raw Material ID	Sieve Residue (%)	Blend Ratio (%)	Raw Material ID	Sieve Residue (%)	Blend Ratio (%)	Raw Material ID	Sieve Residue (%)	Blend Ratio (%)	
X-05	XS-2	10	86.4	XY-3	15	8.09	XT-1	5	5.51	10.13
X-06	XS-2	10	86.4	XY-3	15	8.09	XT-2	10	5.51	10.40
X-07	XS-2	10	86.4	XY-3	15	8.09	XT-3	15	5.51	10.68
X-08	XS-2	10	86.4	XY-3	15	8.09	XT-4	20	5.51	10.96
H-05	HS-2	10	84.84	HY-3	15	13.37	HT-1	5	1.79	10.58
H-06	HS-2	10	84.84	HY-3	15	13.37	HT-2	10	1.79	10.67
H-07	HS-2	10	84.84	HY-3	15	13.37	HT-3	15	1.79	10.76
H-08	HS-2	10	84.84	HY-3	15	13.37	HT-4	20	1.79	10.85

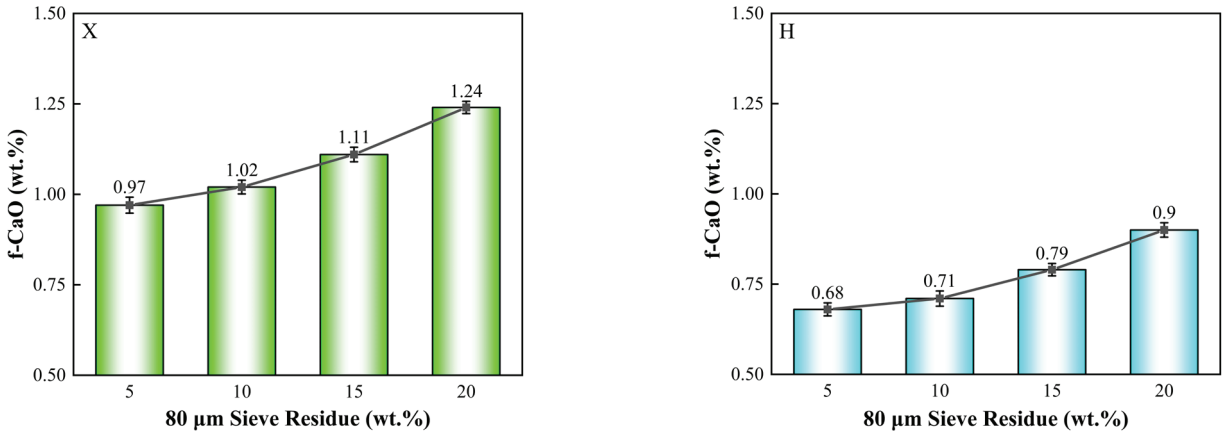

Figure 5. Comparison of burnability of raw meal with varying fineness of iron-bearing corrective materials.

As shown in Figure 5, within the residue range of 5% to 20%, the effect of the fineness of iron-bearing corrective materials on the burnability of the raw meal is limited. The experimental data indicate that, as the residue increases from 5% to 20%, the f-CaO content in X clinker rises from 0.97% to 1.24%, an increase of 0.27%. In H clinker, f-CaO increases from 0.68% to 0.90%, an increase of 0.22%. Thus, within this fineness range, the particle size of iron-bearing corrective materials has a minor effect on the burnability of the raw meal and can be considered a secondary factor in the context of this study.

3.1.4. Influence of Fineness of Calcareous Raw Materials on the Burnability of Raw Meal

Based on the findings from Section 3.1.3, when the residue of iron tailings in X increased from 10% to 15%, and the residue of copper slag in H increased from 10% to 20%, the change in f-CaO content was less than 0.2%. Therefore, iron tailings with a residue of 15% and copper slag with a residue of 20% were selected for subsequent experiments. The fineness of shale and iron-bearing corrective materials was kept constant, while the fineness of limestone was varied to study its impact on the burnability of the raw meal. The experimental proportioning scheme is outlined in Table 9, and the results are presented in Figure 6.

Table 9. Burnability proportioning scheme with varying fineness of calcareous raw materials.

Sample ID	Limestone			Shale			Iron Tailings or Copper Slag			Raw Meal Fineness (%)
	Raw Material ID	Sieve Residue (%)	Blend Ratio (%)	Raw Material ID	Sieve Residue (%)	Blend Ratio (%)	Raw Material ID	Sieve Residue (%)	Blend Ratio (%)	
X-09	XS-1	5	86.4	XY-3	15	8.09	XT-4	15	5.51	6.36
X-10	XS-2	10	86.4	XY-3	15	8.09	XT-4	15	5.51	10.68
X-11	XS-3	15	86.4	XY-3	15	8.09	XT-4	15	5.51	15.00
X-12	XS-4	20	86.4	XY-3	15	8.09	XT-4	15	5.51	19.32
H-09	HS-1	5	84.84	HY-3	15	13.37	HT-4	20	1.79	6.61
H-10	HS-2	10	84.84	HY-3	15	13.37	HT-4	20	1.79	10.85
H-11	HS-3	15	84.84	HY-3	15	13.37	HT-4	20	1.79	15.09
H-12	HS-4	20	84.84	HY-3	15	13.37	HT-4	20	1.79	19.33

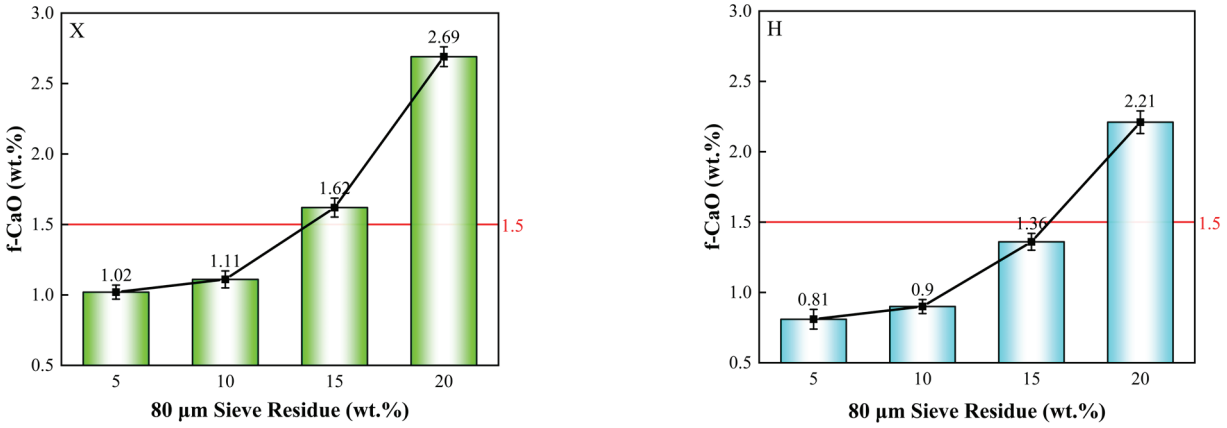

Figure 6. Comparison of burnability of raw meal with varying fineness of calcareous raw materials.

As shown in Figure 6, the fineness of limestone significantly affects the burnability of the raw meal. As the primary source of CaO, limestone constitutes more than 80% of the raw meal. The experimental results show that, as the residue of limestone increases from 5% to 20%, the f-CaO content in X clinker rises from 1.02% to 2.69%, and in H clinker, from 0.81% to 2.21%. This suggests that a higher limestone residue leads to an increase in f-CaO content in the clinker, indicating incomplete reaction of CaO. Therefore, optimizing the fineness of limestone is a crucial method for improving the burnability of the raw meal.

Since the f-CaO content in X clinker with a limestone residue of 15% is 1.62%, which exceeds the 1.5% upper limit set by the Chinese National Standard GB/T 21372-2024, additional experiments were conducted with limestone residues of 13% and 14%. The results are presented in Table 10.

Table 10. f-CaO content of X group with limestone residues of 13% and 14%.

sieve residue (%)	13	14
f-CaO (wt.%)	1.39	1.51

The experimental results demonstrate that when the limestone residue in the X group is 13%, the f-CaO content of the clinker meets the national standard.

The raw meal burnability tests indicate that finer control over PSD facilitates clinker phase formation. This may allow for a reduction in sintering temperature, thereby lowering fuel consumption and CO_2 emissions during clinker production. However, achieving such

benefits requires avoiding overly coarse raw meal preparation. While direct quantification of energy savings was beyond the scope of this study, the results suggest that PSD optimization could serve as a viable strategy to improve thermal efficiency and environmental performance in cement manufacturing.

3.2. Comparison of Chemical and Mineralogical Characteristics of Clinker Before and After Formula Optimization

Based on the findings from Section 3.1, when the residue of limestone, shale, and iron tailings in X raw meal is 13%, 15%, and 15%, respectively, and in H raw meal, the residue of limestone, shale, and iron tailings is 15%, 15%, and 20%, the f-CaO content in the clinker remains below 1.5%. Therefore, following this fineness optimization scheme, two sets of comparative experiments were designed: one with coarse and fine raw meal and the other with a finer raw meal. These experiments aim to explore the impact of comprehensive raw material particle size control on clinker firing characteristics. The specific raw meal proportioning scheme is outlined in Table 11, and the XRD results are presented in Figure 7.

Table 11. Comparison analysis scheme of coarse and fine raw meal.

Sample ID	Limestone		Shale		Iron Tailings or Copper Slag		Raw Meal Fineness (%)
	Sieve Residue (%)	Blend Ratio (%)	Sieve Residue (%)	Blend Ratio (%)	Sieve Residue (%)	Blend Ratio (%)	
X1	10	86.4	10	8.09	10	5.51	10
X2	13	86.4	15	8.09	15	5.51	13.27
H1	10	84.84	10	13.37	10	1.79	10
H2	15	84.84	15	13.37	20	1.79	15.09

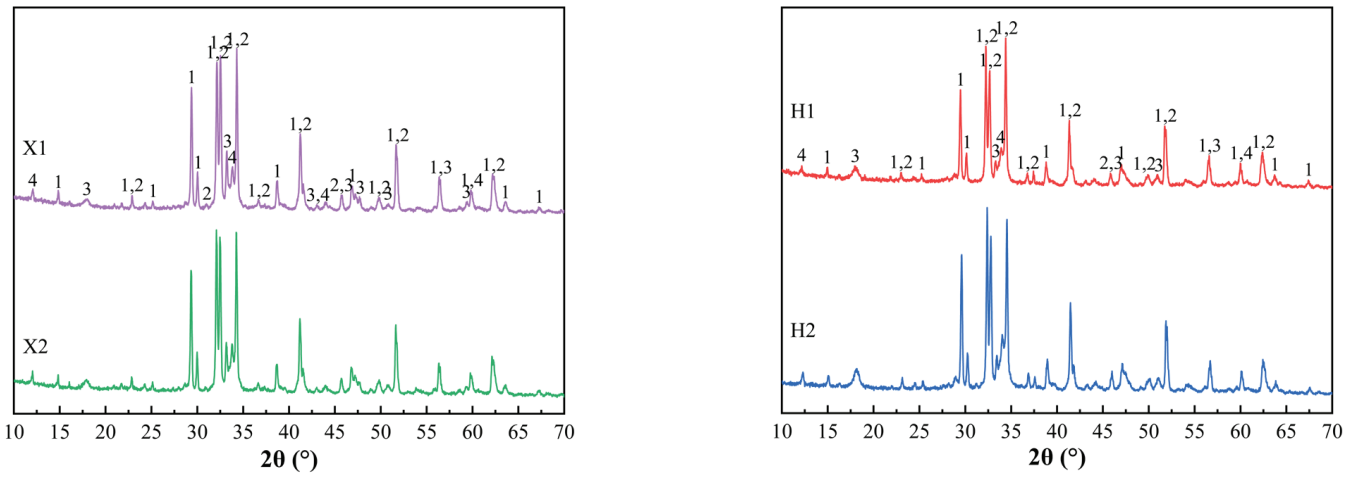

Figure 7. XRD analysis of X1, X2, and H1, H2 clinkers.

From the XRD analysis results of X1, X2, H1, and H2 clinkers shown in Figure 7, it is evident that the diffraction peaks of the mineral phases C_3S, C_2S, C_3A, and C_4AF are consistent in both peak position and intensity, indicating no significant change in the major mineral composition. Although X1 and X2, as well as H1 and H2, correspond to raw materials with different particle sizes, the diffraction peak positions and relative intensities of mineral phases in each sample group are largely consistent. This suggests that,

under identical firing conditions, the mineral composition of the clinker remains stable, predominantly consisting of C_3S, C_2S, C_3A, and C_4AF.

Further comparison of the XRD patterns of X1 vs. X2 and H1 vs. H2 reveals that the characteristic diffraction peaks of C_3S and C_2S consistently appear at their typical 2θ positions, with minimal differences in peak shape and intensity. Similarly, the characteristic peaks of C_3A and C_4AF maintain high consistency, indicating that the mineral phases of raw meals with different particle sizes are essentially the same under the same firing conditions [28].

In conclusion, within the residue range of 10–15%, variations in raw meal fineness have a minimal effect on the major mineral composition of the clinker. The differences in raw meal particle size within this range have a limited impact on the formation of key mineral phases, thereby maintaining the consistency of clinker composition.

3.3. Comparison of Cement Performance and Hydration Products Before and After Formulation Optimization

Changes in raw material fineness not only affect the burnability of clinker but may also influence cement performance. To comprehensively assess the impact of the proposed fineness optimization on cement quality, it is essential to further investigate its effects on the properties of cement mortar and paste, ensuring the stability of the final product's performance.

Therefore, in this section, cement is prepared using both the pre-optimization raw material fineness scheme (X1, H1) and the post-optimization scheme (X2, H2). The mechanical properties and hydration products are tested to evaluate the effect of raw material fineness optimization on cement performance.

3.3.1. Comparison of Cement Performance

The setting time, standard consistency, and stability of the four cement samples were tested, with the results summarized in Table 12.

Table 12. Setting time and standard consistency of cement.

Sample ID	Solidification Time (min)		Standard Consistency (%)	Stability (mm)	Specific Surface Area (m^2/kg)
	Initial Condensation	Complete Condensation			
X0	158	249	25.6	1.5	337
X1	164	263	26.9	1.9	331
H0	122	225	24.1	0.8	343
H1	127	232	24.9	1.5	336
Standard	≥45	≤390	---	≤5	300–400

As shown in Table 12, the setting time, standard consistency, soundness, and specific surface area of all six cement samples meet the requirements specified in the Chinese National Standard for Portland cement (GB 175-2023). Furthermore, the difference in standard consistency between X2 and X1, as well as between H2 and H1, is less than 1.5%, and the changes in initial and final setting times remain within 10 min. This indicates that the adjustments in fineness did not cause any significant performance fluctuations [29].

The compressive and flexural strengths of the cement mortar after 28 days of curing were measured, and the results are presented in Figure 8.

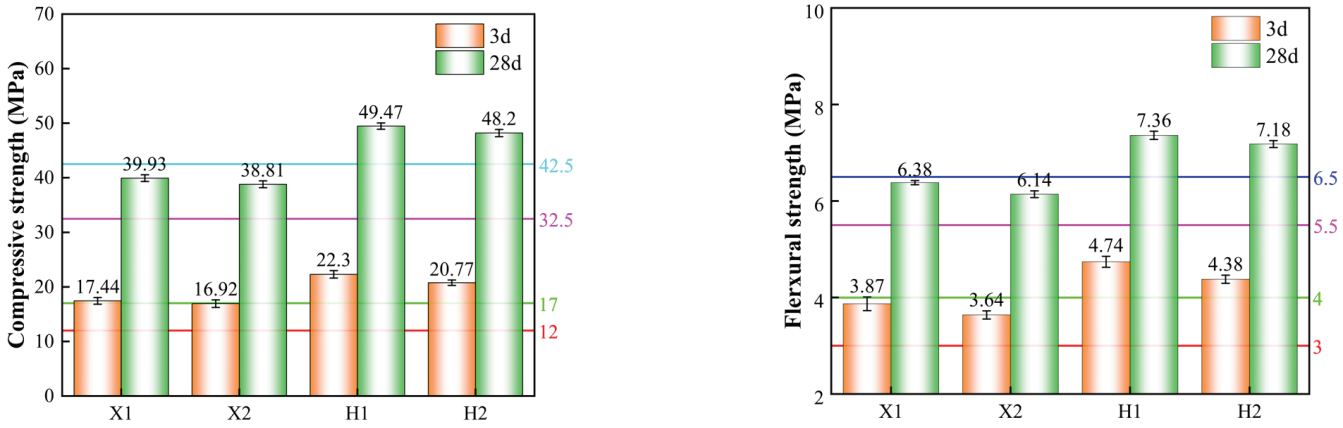

Figure 8. Compressive and flexural strengths of cement mortar.

As shown in Figure 8, the 3-day flexural and compressive strengths of the H1 and H2 cement samples were 4.74 MPa and 4.38 MPa, and 22.3 MPa and 20.77 MPa, respectively. The 28-day flexural and compressive strengths were 7.36 MPa and 7.18 MPa, and 49.47 MPa and 48.2 MPa, respectively, meeting the requirements for a 42.5 grade cement. The 3-day flexural and compressive strengths of the X1 and X2 cement samples were 3.87 MPa and 3.64 MPa, and 17.44 MPa and 16.92 MPa, respectively, while the 28-day flexural and compressive strengths were 6.38 MPa and 6.14 MPa, and 39.93 MPa and 38.81 MPa, respectively, meeting the requirements for a 32.5 grade cement.

These results suggest that the raw material fineness optimization scheme maintains stable mechanical properties without significantly altering the cement's setting time or standard consistency, indicating that the optimization does not adversely affect cement performance.

3.3.2. XRD Comparison of Cement Paste

Cement paste was prepared, and XRD analysis was conducted on the hydration products after 28 days of curing, as shown in Figure 9.

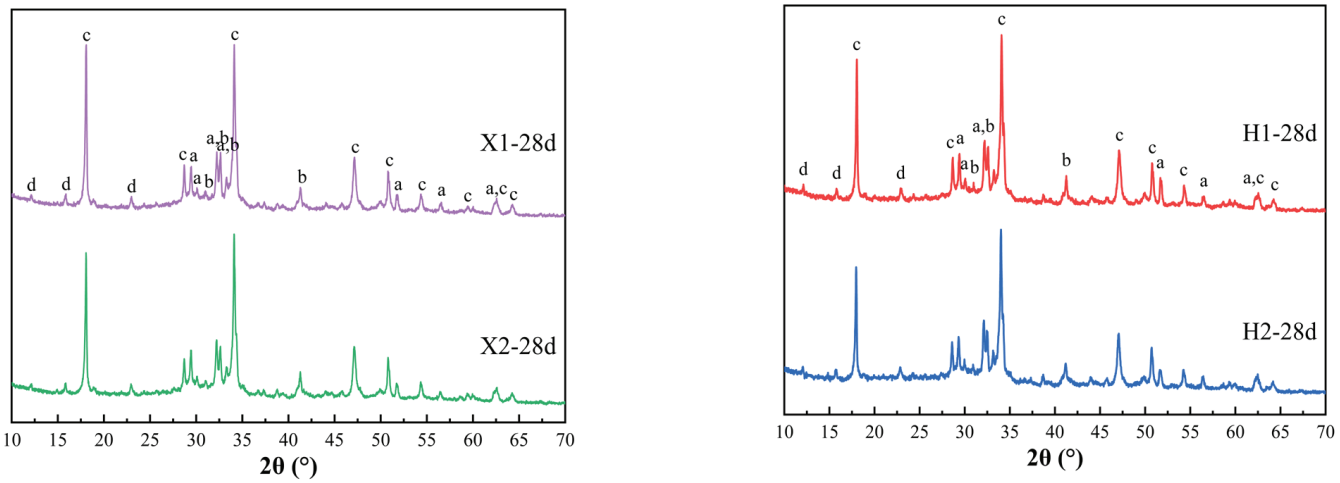

Figure 9. XRD of the 28-day hydration products of X1, X2, H1, and H2.

Analysis of the XRD patterns of the X1, X2, H1, and H2 samples at 28 days of curing reveals the presence of calcium hydroxide ($Ca(OH)_2$) and ettringite (AFt) in all samples, while certain amounts of unhydrated tricalcium silicate (C_3S) and dicalcium silicate (C_2S)

remained. This indicates that the hydration product composition is consistent across all samples, with similar levels of unreacted materials.

Comparison of the intensity of the C_3S and C_2S diffraction peaks among the four groups of samples shows minimal variation in peak intensity, suggesting that the hydration degree of the cement prepared under different raw material fineness conditions is essentially the same at this age. The variation in raw material fineness within the 10–15% sieve residue range does not significantly affect the residual unhydrated minerals. $Ca(OH)_2$, the primary alkaline product of C_3S and C_2S hydration, exhibits clear diffraction peaks in all samples with consistent peak intensities, indicating similar levels of hydration reaction [30]. AFt is also present in all samples, with comparable peak intensities, suggesting that its formation is similar across the samples [31].

In conclusion, the differences in the types and relative contents of hydration products at 28 days are minimal among the four cement samples, indicating that variations in raw material fineness within the 10–15% sieve residue range do not significantly influence the cement's hydration behavior.

3.3.3. TG-DTG Comparison of Cement Paste

Figure 10 presents the TG-DTG curves of the hydration products of cement paste cured for 28 days. As shown in Figure 10(1,2), the DTG curves of H1, H2, X1, and X2 display two major peaks and one minor peak. The weight loss observed between approximately 50 °C and 200 °C corresponds to AFt and C-S-H gel. The peak between 450 °C and 550 °C is associated with the decomposition of calcium hydroxide ($Ca(OH)_2$) [32], leading to the release of water and the formation of CaO. The minor peak between 680 °C and 750 °C is attributed to the decomposition of carbonate phases [33], primarily resulting from the reaction of hydration products with atmospheric CO_2.

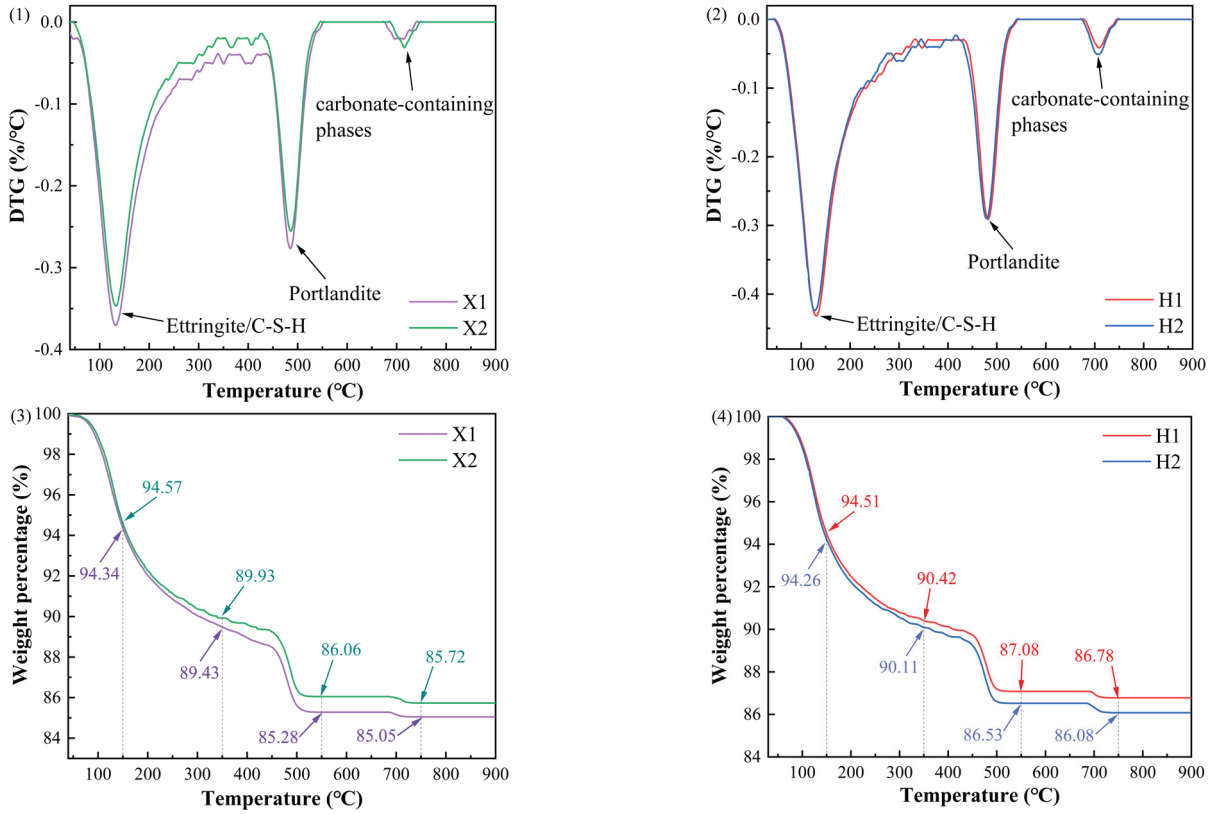

Figure 10. TG-DTG curves of the hydration products of cement paste cured for 28 days.

Decomposition peaks of ettringite, C-S-H gel, and calcium hydroxide, along with the presence of carbonate phases, are observed in all samples. According to studies by Fang and Chang [34], and Šavija and Luković [35], the carbonation of ettringite, C-S-H gel, and calcium hydroxide accounts for 70–80% of the total carbonation, while the remaining carbonation could be attributed to partial carbonation of the hydrated clinker or other byproducts.

As shown in Figure 10(3,4), the TG curves indicate that at 900 °C, the mass loss of X1 and X2 is 13.94% and 14.72%, respectively, while for H1 and H2, it is 13.22% and 13.92%. The difference does not exceed 0.8%, suggesting that the hydration degree and thermal stability of the samples are consistent.

Therefore, the types and decomposition behavior of the hydration products of X2 and X1, as well as H2 and H1, are essentially identical, indicating that variations in raw material fineness within the 10–15% sieve residue range do not significantly affect the cement's hydration reaction. The decomposition peak of Portlandite between 400–500 °C is nearly identical for all samples, supporting the conclusion that the cement samples exhibit similar hydration degrees at 28 days, with no significant differences caused by changes in raw material fineness. The mass loss data suggest that the quantity of hydration products for the slightly coarser cement is comparable to that of the finer cement, indicating that the basic performance of the cement is unaffected.

These findings suggest that a differentiated grinding strategy could be implemented in cement plants—specifically, applying finer grinding to limestone while allowing coarser grinding of shale and iron-bearing materials. Such an approach could optimize energy consumption during raw material preparation without compromising clinker quality or cement performance.

4. Conclusions

An analysis was conducted on the burnability of clinker prepared from raw materials with varying fineness, including limestone, shale, and iron corrective materials. Additionally, a comparison and performance testing of cement prepared from coarser and finer raw materials were carried out. The following conclusions were drawn:

Effect of Raw Material Fineness on Clinker Burnability: The influence of different raw materials on the burnability of the clinker varies. Within the range of 5–20% sieve residue at 80 μm, variations in the fineness of silicate-aluminate and iron corrective materials have a minimal impact on burnability, indicating that these are not the primary factors. In contrast, the fineness of calcareous raw materials significantly affects the f-CaO content, making it a key factor controlling the burnability of clinker.

Impact of Fineness on Mineral Composition: Changes in raw material fineness have a limited impact on the major mineral composition of the clinker. A comparison of XRD patterns for clinker produced from raw materials with different fineness shows that, within the sieve residue range of 10–15%, the content of major minerals in the clinker remains largely unchanged. This suggests that fluctuations in fineness within this range do not significantly influence mineral formation.

Adaptability of Cement Performance to Raw Material Fineness: Cement performance demonstrates strong adaptability to variations in raw material fineness. Cement prepared from clinker produced at different fineness levels was subjected to mechanical property testing and hydration product analysis. The results indicate that, within the aforementioned range of fineness variation, no significant differences were observed in terms of strength, hydration product types, or relative content. This suggests that a moderate increase in sieve residue of raw materials does not significantly impact the final performance of the

cement. The results support the feasibility of a selective grinding strategy to improve energy efficiency while maintaining overall cement quality.

Author Contributions: Conceptualization, S.C., X.Y. and Y.Z.; Methodology, S.C., X.Y. and Y.Z.; Validation, S.C. and Y.Z.; Formal analysis, S.C.; Investigation, S.C.; Data curation, S.C.; Writing—original draft, S.C.; Writing—review & editing, Y.Z. All authors have read and agreed to the published version of the manuscript.

Funding: This research received no external funding.

Institutional Review Board Statement: Not applicable.

Informed Consent Statement: Not applicable.

Data Availability Statement: The original contributions presented in this study are included in the article. Further inquiries can be directed to the corresponding author.

Conflicts of Interest: The authors declare no conflict of interest.

References

1. Isteri, V.; Ohenoja, K.; Hanein, T.; Kinoshita, H.; Kletti, H.; Rössler, C.; Tanskanen, P.; Illikainen, M.; Fabritius, T. Ferritic calcium sulfoaluminate belite cement from metallurgical industry residues and phosphogypsum: Clinker production, scale-up, and microstructural characterisation. *Cem. Concr. Res.* **2022**, *154*, 106715. [CrossRef]
2. Tepeli, D. Development of Chemometrics Method Based on Infrared Spectroscopy for the Determination of Cement Composition and Process Optimization. Master's Thesis, Izmir Institute of Technology, Urla, Türkiye, 2021.
3. Huang, L.; Cheng, G.L.; Huang, S.W. Effects of Calcination Conditions on the Formation and Hydration Performance of High-Alite White Portland Cement Clinker. *Materials* **2020**, *13*, 494. [CrossRef] [PubMed]
4. Huang, X.; Zhang, J.F.; Zhang, K.C. Effect of boron oxide on stability of high-ferrite Portland cement clinker in low-temperature calcination. *Sci. Rep.* **2024**, *14*, 31825. [CrossRef]
5. Castillo, J.A.; Wilhelmsson, B.; Broström, M.; Eriksson, M. Phase evolution of cement raw meal in a high-CO_2 atmosphere. *Cem. Concr. Res.* **2025**, *193*, 107874. [CrossRef]
6. Ervik, T.K.; Hammer, S.E.; Noto, H.; Ellingsen, D.G.; Thomassen, Y.; Weinbruch, S.; Benker, N.; Berlinger, B. Physicochemical characterization of particulate matter in a cement production plant. *Environ. Sci.-Process. Impacts* **2022**, *24*, 1243–1256. [CrossRef]
7. Aguirre Castillo, J.; Broström, M.; Eriksson, M. Phase evolution and burnability of cement raw meal. *Adv. Cem. Res.* **2023**, *35*, 577–587. [CrossRef]
8. Radu, D.; Ghizdavet, Z. Raw materials' clinker burnability vs. Oxides acidity/basicity. *Rev. Romana De Mater./Rom. J. Mater.* **2017**, *47*, 282–287.
9. Mohamed, Y.; Kasif, A.; Alla, E.A.A.; Elmahadi, M. Calculation of the formation process of clinker inside the rotary cement kiln. *Proc. Voronezh State Univ. Eng. Technol.* **2018**, *80*, 233–239. [CrossRef]
10. Nuhu, S.; Ladan, S.; Umar Muhammad, A. Effects and Control of Chemical Composition of Clinker for Cement Production. *Int. J. Control Sci. Eng.* **2020**, *10*, 16–21. [CrossRef]
11. Ali, A.; Al-Salmany, S.H.A.-H. Redesigning Raw Materials Mixture Burning Behavior and Effect on Portland Cement Productivity. *Iraqi Geol. J.* **2025**, *58*, 207–218. [CrossRef]
12. Elmrabet, R.; Hmidani, Y.; Mariouch, R.; Elharfi, A.; Elyoubi, M.S. Influence of raw meal composition on clinker reactivity and cement proprieties. *Mater. Today Proc.* **2021**, *45*, 7680–7684. [CrossRef]
13. Costa, A.R.D.; Coppe, M.V.; Bielefeldt, W.V.; Bernal, S.A.; Black, L.; Kirchheim, A.P.; Gonçalves, J.P. Thermodynamic modelling of cements clinkering process as a tool for optimising the proportioning of raw meals containing alternative materials. *Sci. Rep.* **2023**, *13*, 17589. [CrossRef]
14. Siame, M.C.; Zvarivadza, T.; Onifade, M.; Simate, I.N.; Lusambo, E. Dynamic Simulation of Heat Distribution and Losses in Cement Kilns for Sustainable Energy Consumption in Cement Production. *Sustainability* **2025**, *17*, 553. [CrossRef]
15. Herfort, D.; Macphee, D. Components in Portland Cement Clinker and Their Phase Relationships. In *Lea's Chemistry of Cement and Concrete*; Butterworth-Heinemann: Oxford, UK, 2019; pp. 57–86.
16. Ceplak, B. Influence of Alkalis on the Phase Development of Belite-Sulfoaluminate Clinkers. *J. Ceram.-Silik.* **2022**, *66*, 527–539. [CrossRef]
17. Garces-Vargas, J.F.; Díaz-Cardenas, Y.; Zunino, F.; Ribalta-Quesada, J.; Scrivener, K.; Martirena, F. The Challenge of Grinding Ternary Blends Containing Calcined Clays and Limestone. *Minerals* **2022**, *12*, 1170. [CrossRef]

18. Antunes, M.; Santos, R.L.; Pereira, J.; Rocha, P.; Horta, R.B.; Colaço, R. Alternative Clinker Technologies for Reducing Carbon Emissions in Cement Industry: A Critical Review. *Materials* **2022**, *15*, 209. [CrossRef]
19. Sousa, V.; Bogas, J.A. Comparison of energy consumption and carbon emissions from clinker and recycled cement production. *J. Clean. Prod.* **2021**, *306*, 127277. [CrossRef]
20. Ding, Y.; Yang, Y.; Zhu, Y.; Zhang, J.; Guo, Y.; Chen, X. Hydration-time-dependent rheological behaviors of Newtonian cement grouts with different water cement ratios. *Nongye Gongcheng Xuebao/Trans. Chin. Soc. Agric. Eng.* **2020**, *36*, 161–167. [CrossRef]
21. Yang, Z.; Liu, Y.; Chen, M.; Wang, X.; Ye, C.; Li, X.; Chen, W.; Yang, Y.; Wang, B.; Li, C.; et al. Influence of Coupling Effects between Gravel Soil Porosity and Cement Grout Weight on Diffusion Laws and Morphologies of Penetration Grouting. *Appl. Sci.* **2022**, *12*, 7601. [CrossRef]
22. Yang, Z.; Qian, S.; Hou, K. Time-dependent behavior characteristics of Power-law cement grouts applied in geotechnical engineering. *Electron. J. Geotech. Eng.* **2015**, *20*, 1017–1024.
23. Silva, Y.F.; Burbano-Garcia, C.; Araya-Letelier, G.; González, M. Short- and long-term experimental performance of concrete with copper slag: Mechanical and physical properties assessment. *Case Stud. Constr. Mater.* **2024**, *20*, e03302. [CrossRef]
24. Zhang, B.; Muhammad, F.; Yu, T.; Fahimizadeh, M.; Hassan, M.A.S.; Liang, J.; Ning, X.A.; Yuan, P. Harnessing iron tailings as supplementary cementitious materials in Limestone Calcined Clay Cement (LC3): An innovative approach towards sustainable construction. *Constr. Build. Mater.* **2024**, *453*, 139111. [CrossRef]
25. Luo, L.; Zhang, Y.M.; Bao, S.X.; Chen, T.J. Utilization of Iron Ore Tailings as Raw Material for Portland Cement Clinker Production. *Adv. Mater. Sci. Eng.* **2016**, *2016*, 1596047. [CrossRef]
26. Wang, J.P.; Erdenebold, U. A Study on Reduction of Copper Smelting Slag by Carbon for Recycling into Metal Values and Cement Raw Material. *Sustainability* **2020**, *12*, 1421. [CrossRef]
27. Darmanto, P.S.; Amalia, A. Analysis of high clinker ratio of Portland Composite Cement (PCC). *S. Afr. J. Chem. Eng.* **2020**, *34*, 116–126. [CrossRef]
28. Sazonova, N.; Skripnikova, N.; Lucenko, A.; Novikova, L. Cement clinker structure during plasma-chemical synthesis and its influence on cement properties. *IOP Conf. Ser. Mater. Sci. Eng.* **2015**, *71*, 012018. [CrossRef]
29. Hansen, B.S.; Howard, I.L.; Shannon, J.; Cost, T.; Wilson, W.M. Portland-Limestone Cement Fineness Effects on Concrete Properties. *Aci Mater. J.* **2020**, *117*, 157–168. [CrossRef]
30. Wang, J.; Guo, R.; Wu, A.; Xiao, B.; Ruan, Z. Strength and Microstructural Characteristics of Activated Fly Ash–Cement Paste. *Processes* **2024**, *12*, 2356. [CrossRef]
31. de Matos, P.R.; Andrade Neto, J.S.; Jansen, D.; De la Torre, A.G.; Kirchheim, A.P.; Campos, C.E.M. In-situ laboratory X-ray diffraction applied to assess cement hydration. *Cem. Concr. Res.* **2022**, *162*, 106988. [CrossRef]
32. Wang, Q.; Yao, G.; Zhu, X.N.; Wang, J.X.; Wu, P.; Lyu, X.J. Preparation of Portland Cement with Gold Ore Tailings. *Adv. Mater. Sci. Eng.* **2019**, *2019*, 1324065. [CrossRef]
33. Abdalqader, A.F.; Jin, F.; Al-Tabbaa, A. Development of greener alkali-activated cement: Utilisation of sodium carbonate for activating slag and fly ash mixtures. *J. Clean. Prod.* **2016**, *113*, 66–75. [CrossRef]
34. Fang, Y.; Chang, J. Microstructure changes of waste hydrated cement paste induced by accelerated carbonation. *Constr. Build. Mater.* **2015**, *76*, 360–365. [CrossRef]
35. Šavija, B.; Luković, M. Carbonation of cement paste: Understanding, challenges, and opportunities. *Constr. Build. Mater.* **2016**, *117*, 285–301. [CrossRef]

Disclaimer/Publisher's Note: The statements, opinions and data contained in all publications are solely those of the individual author(s) and contributor(s) and not of MDPI and/or the editor(s). MDPI and/or the editor(s) disclaim responsibility for any injury to people or property resulting from any ideas, methods, instructions or products referred to in the content.

materials

MDPI

Article

Insights into Hydration Kinetics of Cement Pastes Evaluated by Low-Field Nuclear Magnetic Resonance: Effects of Super-Absorbent Polymer as Internal Curing Agent and Calcium Oxide as Expansive Agent

Meixin Liu [1], Yuan Hu [1], Jing Li [2], Xiaolin Liu [1], Huiwen Sun [1], Yunfei Di [1], Xia Wu [1] and Junyi Zhang [1,*]

[1] College of Civil and Transportation Engineering, Hohai University, Nanjing 210098, China; liumeix1999@163.com (M.L.); 18705609882@163.com (X.L.)
[2] The Huaihe River Commission of the Ministry of Water Resources, Bengbu 233001, China
* Correspondence: jyzh@hhu.edu.cn

Abstract: Understanding the hydration kinetics of cement paste is essential for adjusting the early-age performance of concrete. Low-field nuclear magnetic resonance (LF-NMR) has emerged as an innovative technique to evaluate cement hydration progress by analyzing the evolution of transverse relaxation time (T_2) signals. This study provides insights into the influence of a super-absorbent polymer (SAP) as an internal curing agent and calcium oxide (CaO) as an expansive agent (EA) on LF-NMR spectroscopy of cement paste for the first time. The chemical compositions of the cement and CaO-based EA were determined by X-ray fluorescence, while the morphological characterizations of the cement, SAP and CaO-based EA materials were characterized by scanning electron microscopy. Based on the extreme points in the first-order derivatives of the T_2 signal maximum amplitude curve, the hydration progress was analyzed and identified with four stages in detail. The results showed that the use of the SAP with a higher content retarded the hydration kinetics more evidently at a very early age, thus prolonging the duration of the induction and acceleration stages. The use of the CaO-based EA shortened the induction, acceleration and deceleration stages, which verified its promotion of hydration kinetics in the presence of the SAP. The combination of 3 wt% SAP and 2 wt% CaO consumed more water content synergistically in the first 100 h by hydration reactions. These findings revealed the roles of SAP and CaO-based EA (commonly adopted for low-shrinkage concrete) in adjusting hydration parameters and the microstructure evolution of cement-based materials, which would further offer fundamental knowledge for the early-age cracking control of concrete structures.

Keywords: cement paste; hydration kinetics; super-absorbent polymer (SAP); CaO-based expansive admixture; low-field nuclear magnetic resonance (LF-NMR)

1. Introduction

The generation of cracks in concrete can provide permeable invasion pathways for corrosive media and then induce subsequent propagation and further expansion of the cracks, which will aggravate the performance deterioration of a concrete structure [1,2]. The cracking of concrete at an early age could be one of the most common problems in practical concrete engineering, and volume deformation is one of the key factors that lead to early-age cracks [3,4]. Incorporating an expansive admixture can compensate for the shrinkage volumetric deformation of concrete, which is regarded as an effective approach

to mitigating shrinkage-induced cracking [5,6]. Meanwhile, an internal curing admixture is favorable for reserving the internal humidity of concrete and helps to prevent cracks caused by autogenous shrinkage [7–9]. Specifically, calcium oxide (CaO) has been proven to possess a fast expansion function and extensive adaptability in different environmental conditions [10]. In addition, the use of a super-absorbent polymer (SAP) can alleviate the autogenous shrinkage effectively and enhance the long-term hydration degree of concrete, which has little effect on the mechanical strength of concrete compared with other internal curing materials [11,12]. Hence, these two chemical admixtures are often incorporated simultaneously for the shrinkage and cracking control of concrete [13–15].

Understanding the hydration kinetics of concretes with CaO or SAP can be crucial for tailoring their fresh and hardened properties. Wczelik et al. [16] investigated the hydration kinetics of cement-based materials by isothermal calorimetry and reported that the first exothermic peak was heightened and broadened with the addition of an expansive additive, while the second exothermic peak was lowered. Zhao et al. [17] found that the expansion additive could shorten the setting and hardening of fresh cement-based materials. Wang et al. [18] used quantitative X-ray diffraction (QXRD) to investigate the influence of SAP incorporation on cement hydration and assess the hydration degree and found that an SAP as an internal curing admixture slightly decreased the hydration degree at an early age. An environmental advanced scanning electron microscope (ESEM) was also utilized to observe the absorption behavior of SAP particles in a cement pore solution and their shape variations, which could facilitate understanding the mechanism for SAPs restraining concrete autogenous shrinkage during the specific hydration progress of cement [19].

On the other hand, the hydration kinetics of cementitious binders have a direct effect on the physical and mechanical properties of early-age concrete. Some conventional techniques have been adopted to characterize hydration, such as isothermal calorimetry, electrical resistivity measurement, scanning electron microscopy (SEM) and transmission electron microscopy (TEM) [16,20–22]. To be specific, isothermal calorimetry has been commonly employed for the evaluation of hydration kinetics, but at the later stage, its signal usually becomes too weak after hydration for several days. Electrical impedance spectroscopy was also developed as a non-contact measurement technique for hydration characterization. Nevertheless, analyzing the alternating electric current would be complicated, and the frequency variation also affects resistivity. Furthermore, it is difficult to realize the continuous monitoring of hydration via SEM and TEM observation approaches, and the pre-drying treatment will also change the microstructure of cement samples.

Therefore, low-field nuclear magnetic resonance (LF-NMR), as a novel approach, was proposed to investigate hydration kinetics and the microstructure evolution of a cement paste by assessing the relaxation time of hydrogen protons in pores [23,24]. Considering that LF-NMR is a type of non-destructive, non-invasive and in situ continuous characterization, it shows significant advantages compared with other conventional measurement approaches. Wang et al. [25] used an LF-NMR spectrometer to characterize the hydration kinetics of cement paste and pointed out that the hydration periods could be clearly described by the evolution of the longitudinal relaxation time (T_1) signal. Similarly, monitoring the intensity of the transverse relaxation time (T_2) signal of LF-NMR of the cement paste could also characterize the hydration kinetics, which presented a good agreement with other evaluation approaches [26]. In addition, the measurement of the T_2 signal required much shorter time and possessed higher robustness than that of the T_1 signal, by which the hydration mechanism could be revealed according to the time-dependent curve of the T_2 signal [27].

According to the cement chemistry theory, the multi-stage hydration progress could be analyzed and identified by establishing a hydration model, which can be adopted to

quantify the hydration kinetics as well as divide several specific hydration periods for cement-based materials [28,29]. The determination of the dynamic hydration model can unravel the relation between hydration kinetics and various influential factors. However, little research has focused on the coupled effects of an SAP and CaO on cement hydration for shrinkage control, particularly using an advanced characterization technique like LF-NMR. This research gap shed light on the urgent need and significance for a comprehensive understanding of how these chemical admixtures interact to change the hydration kinetics and microstructure evolution of cement-based materials.

Since there is still little research focusing on the hydration characteristics of cement-based materials with CaO as the expansive admixture (EA) and an SAP as the internal curing admixture concurrently, the influences of the water-to-cement ratio (w/c), SAP and CaO-based EA on essential parameters of hydration models were analyzed for the first time in this research. Specifically, the effects of the SAP and/or CaO-based EA incorporation on durations of hydration stages (including the induction, acceleration, deceleration and stable stages) were investigated based on the second-order differential functions of T_2 signal curves. The findings are expected to provide fundamental knowledge for optimizing the design of low-shrinkage concrete.

2. Materials and Methods

2.1. Materials

Portland cement with a strength grade of 52.5 (P·I 52.5) in compliance with Chinese Standard GB 175-2023 [30] was chosen in this study, which possessed a specific surface area of 373.2 m^2/kg. A commercially available concrete expansive admixture (EA) with CaO as the active component was used, which had a restrained expansion ratio of 0.18% after water curing for 7 days (according to Chinese Standard GB/T 23439-2017) [31]. A super-absorbent polymer (SAP) with a particle size of 75–95 μm was also employed as the internal curing admixture, which presented a spherical shape and possessed a water absorption capacity of 19.7 g per gram according to the tea bag method. The tea bag method was adopted to measure the absorption capacity of the SAP as $(m3 - m2 - m0)/(m2 - m1)$, where m1 is the mass of an empty tea bag, m2 is the mass after loading with the SAP, m3 is the swollen mass after immersion in the test solution and m0 is the average liquid absorption mass of ten tea bags.

2.2. Methods

2.2.1. Sample Preparation

The water-to-cement ratio (w/c) was designed at 0.30, 0.35 or 0.40 for the cement paste mixture. For keeping consistent with practical cases, the dosage of the SAP was 0.15 wt% or 0.30 wt% (by mass of cement), while the dosage of the CaO-based EA was 2.0 wt% or 3.0 wt% (by mass for the replacement of cement). The mixing proportions of all samples are provided in Table 1, in which the "CP" series represents blank samples, while the "CP_S" series denotes samples containing the SAP.

The stirring and homogenization processes are as follows. First, the cement, EA and SAP solids were dry-mixed using a mechanical mixer for 2 min to ensure a uniform distribution of the dry materials. Then, mixing water was added to the container and further mixed with the low speed of 140 rev/min for 60 s. Afterwards, the mixing speed was increased to 285 rev/min for another 150 s, which led to the adequate dispersion state of the fresh cement paste.

Table 1. Mix proportions of cement paste samples.

Sample	*w/c*	SAP (%)	EA (%)	Extra Water for SAP Absorption (%)
0.30CP	0.30	0	0	0
0.40CP	0.40	0	0	0
0.35CP	0.35	0	0	0
0.35CP_S015	0.35	0.15	0	2.96
0.35CP_S03	0.35	0.30	0	5.91
0.35CP_S03C2	0.35	0.30	2.0	5.91
0.35CP_S03C3	0.35	0.30	3.0	5.91

2.2.2. Morphology Analysis

The microscopic morphologies of the cement, the SAP and the CaO-based EA were examined using scanning electron microscopy (SEM) (Sigma300, ZEISS, Oberkochen, Germany). Nonconductive samples were coated with a 30 s gold film to improve conductivity.

2.2.3. Chemical Composition Analysis

The chemical composition of the cement and CaO-based EA was determined using an X-ray fluorescence spectrum analyzer (ZSX primus II, Rigaku, Tokyo, Japan). Powder samples of about 3 g were dried and passed through a 200-mesh sieve and then exposed to X-rays to emit fluorescence for data collection.

2.2.4. Hydration Characteristics Analysis

The experiment utilized an LF-NMR instrument (PQ-001, Niumag, Suzhou, China), as shown in Figure 1. This device is equipped with a low magnetic field with a field strength of only 0.42 T. The frequency was set at 18 MHz. The temperature of the magnet was controlled at 32 ± 0.02 °C, and the laboratory temperature was maintained at 20 ± 2 °C. The measurement of the transverse relaxation time T_2 was carried out using the Carr–Purcell–Meiboom–Gill (CPMG) method.

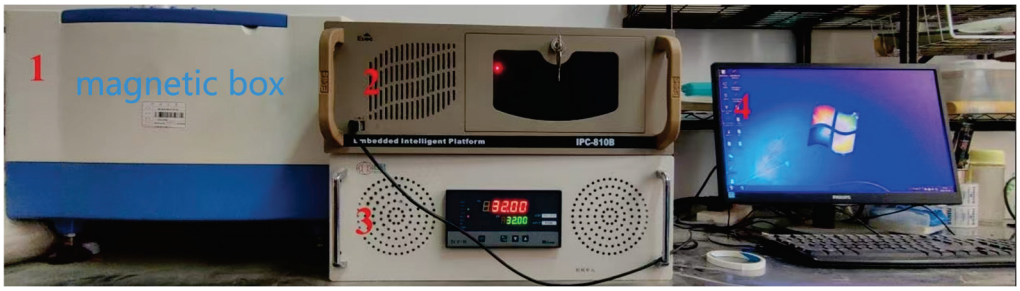

Figure 1. LF-NMR instrument: (1) magnetic box; (2) spectrum system and controlling machine; (3) console unit; (4) displayer.

2.3. Hydration Kinetic Characterizations

Fresh mixture was filled into the glass tube to evaluate the hydration kinetics immediately based on the LF-NMR spectroscopy, with a magnetic field intensity of 0.42 T and a proton resonance frequency of 18 MHz. Then, the sample together with the tube was stored in an incubator with a constant temperature of 20 °C during the testing intervals. The detailed calibration process and parameter information for the LF-NMR measurement were consistent with the previous studies [23,24], and the transverse relaxation (T_2) signal of the cement paste sample was calculated by the Carr–Purcell–Meiboom–Gill (CPMG) sequence analysis.

For example, the amplitude of the T_2 signal by a single transient measurement is shown in Figure 2a, in which the maximum value could indicate the free water amount in the sample. The signal intensity of the physically bound water is expressed by absorbance units (a.u.s). Then, the time-dependent evolution curve of the maximum T_2 amplitude could be plotted according to the long-term continuous measurements, as shown in Figure 2b. Based on the first-order (and further second-order) derivatives of this curve, the extreme points in Figure 3a (corresponding to the zero points in Figure 3b) were calculated to separate the hydration process as different stages. Specifically, the initial pre-induction period was not analyzed here owing to the time consumption from adding water to the first measurement, and thus the subsequent four stages were identified including the induction (dormant) stage, acceleration stage, deceleration stage and steady stage.

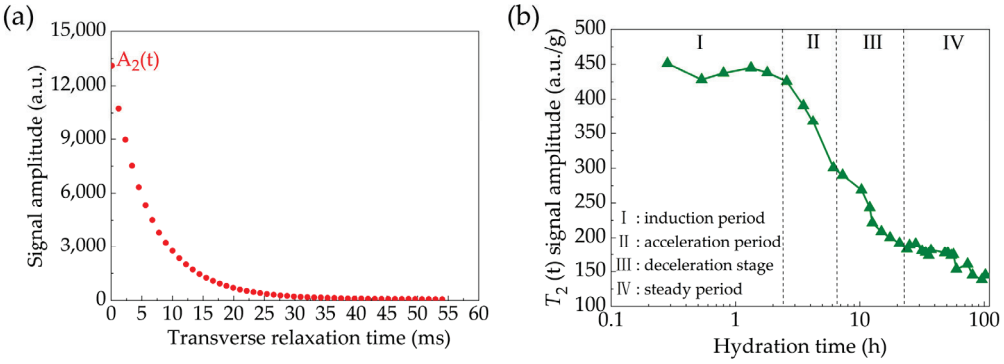

Figure 2. (**a**) First wave of T_2 signal; (**b**) time-dependent evolution of T_2 signal maximum amplitude by unit mass of sample.

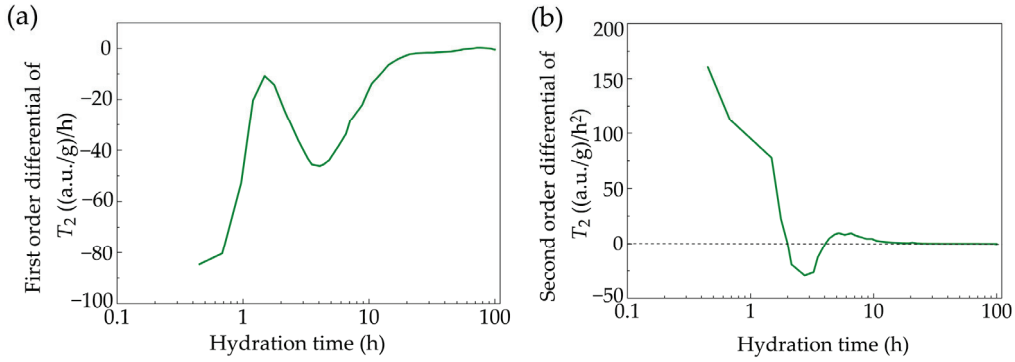

Figure 3. (**a**) First-order and (**b**) second-order differential of T_2 signal maximum amplitude.

Moreover, TAM Air isothermal calorimetry (TA Instruments, New Castle, DE, USA) was used to characterize the hydration kinetics of the cement paste samples by monitoring the heat release under a 20 °C constant temperature condition for parallel comparison.

3. Results and Discussion

3.1. Morphology and Compositions

The microstructure morphologies of the raw materials observed by the scanning electron microscope (SEM) are presented in Figure 4. The SEM micrographs revealed the mineralogical phases in Figure 4a, including angular C_3S (tricalcium silicate, 10–50 μm, distinct cleavage planes), sub-rounded C_2S (dicalcium silicate, 5–20 μm, surface etching), porous C_3A aggregates (tricalcium aluminate, 2–10 μm), and equant C_4AF crystals (tetracalcium ferroaluminate, 3–15 μm). The chemical compositions of the cement and CaO-based EA are shown in Table 2, which were analyzed by X-ray fluorescence (XRF) spectroscopy.

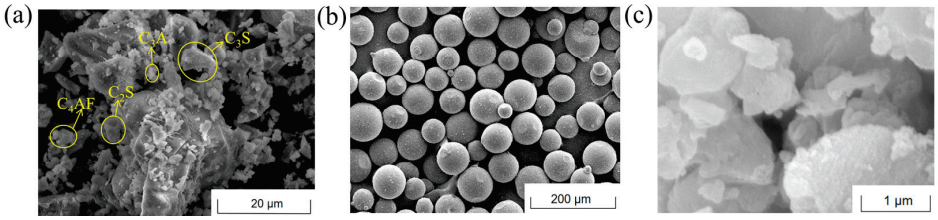

Figure 4. SEM observation images of raw materials: (**a**) cement; (**b**) SAP; (**c**) CaO-based EA.

Table 2. Chemical compositions of cement and CaO-based EA (wt%).

Material	CaO	SiO_2	Al_2O_3	Fe_2O_3	MgO	K_2O	Na_2O	TiO_2	SO_3	LOI
Cement	64.77	19.62	4.53	3.15	0.89	0.64	0.07	0.26	2.40	1.67
EA	84.32	3.38	4.93	1.20	1.26	—	—	—	2.57	2.34

3.2. Comparison of LF-NMR and IC Results

The heat flow of the plain cement paste sample with a w/c of 0.35 being obtained by isothermal calorimetry and the first-order differential curve of the T_2 signal maximum amplitude from LF-NMR characterization were collected and are compared in Figure 5. At a very early age of the hydration process, the reaction of C_3A minerals first occurred once the solids contacted with water, after the dissolution of clinker minerals. The ettringite (AFt) hydrates formed rapidly to entry the pre-induction period, which was the main factor that resulted in the generation of the first exothermic peak. Afterward, the speed of the hydration reactions tended to slow down and enter into a short induction period, with the gradual accumulation of hydration products. In the later stage during the hydration for a further several hours, the second exothermic peak appeared with the intense formation of $Ca(OH)_2$ and C-S-H gel products, indicating that a large amount of heat was released and thus the overall hydration kinetics were accelerated again. Finally, abundant hydration products filled the space that was occupied by water previously and then formed a network structure interlinked with hydration products, which decreased the contact area of the un-hydrated cement particles with water and thus led to the deceleration stage. A shoulder occurred in the NMR result curve at approximately 17 h, which could also be found in the heat flow curve at around 17 h, representing the transformation of AFt to calcium aluminate mono-sulfate (AFm). Ultimately, the hydration rate and exothermic rate tend to be stable. Thereby, the time-dependent hydration kinetics of the cement paste being indicated by LF-NMR showed a strong relation with the results obtained from traditional IC technique, which provide a convincing technique for monitoring the hydration process and investigating the role of CaO-based EA and SAP.

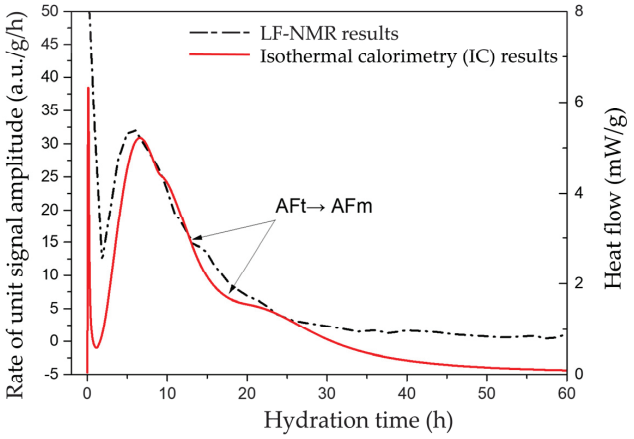

Figure 5. Comparative analysis of LF-NMR and isothermal calorimetry measurements for cement paste with w/c = 0.35.

3.3. Influence of w/c on Hydration Stages

The time-dependent evolution of the T_2 signal maximum amplitude collected from the LF-NMR characterization is exhibited in Figure 6, which involves samples with three different w/c values (0.30, 0.35 or 0.40). Generally, it can be clearly observed that the intensity of the signal indicating the physically bound water showed similar decreasing tendencies with prolonged hydration time for all the samples. On the other hand, the T_2 signal intensity became stronger with a higher w/c value, as expected, as the higher water content in the mixture means more physically bound water was contained by unit mass of cement paste. The influence of the mixture w/c value on each hydration stage was further analyzed, which was divided by the zero points in the second-order differential curve. The detailed parameters of every typical hydration period, including the initial stage, the acceleration stage, the deceleration stage and the steady stage for all samples, are provided in Table 3 and Figure 7.

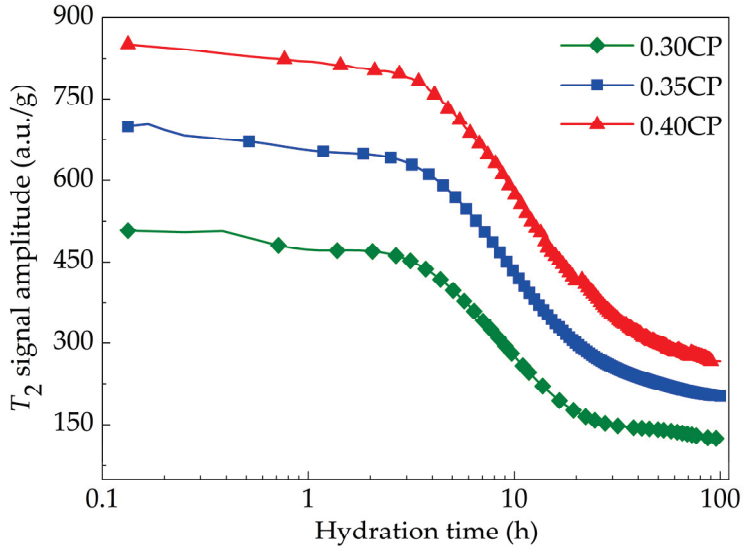

Figure 6. Time-dependent evolution of T_2 signal amplitude for cement paste samples with variable w/c values.

Table 3. The starting and terminal time points of each hydration stage for cement paste samples with variable w/c values.

Sample	Hydration Time (Hours:Minutes)			
	Induction Stage	Acceleration Stage	Deceleration Stage	Steady Stage
0.30CP	[0*,1:31]	[1:31,4:55]	[4:55,34:08]	[34:08,100*]
0.35CP	[0*,1:43]	[1:43,5:22]	[5:22,36:15]	[36:15,100*]
0.40CP	[0*,1:58]	[1:58,5:40]	[5:40,38:05]	[38:05,100*]

Note: The 0* indicates the time point at which the first measurement was taken but not the cement coming into contact with water. The 100* indicates the end of the measurement.

During the induction stage, the T_2 signal amplitude initially showed a rapid decreasing tendency. In the later portion of induction stage, a slower decreasing rate could be found for the T_2 signal amplitude, owing to the formation of a protective membrane [32]. The early-age hydrates contributed to the generation of membranes being composed of C-S-H gel, covering the surface of the un-hydrated cement grains and impeding the successional permeation of cationic/anionic ions in the solution, which hindered the hydration during the later induction stage. In the acceleration stage, the decreasing rate of T_2 signal amplitude became higher again with the supersaturation of calcium ions, and the promoted precipitation of $Ca(OH)_2$ crystals consumed water rapidly in fresh cement paste mixture. These hydration reactions led to the fast-decreasing curve of T_2 signal amplitude during

this stage. At the terminal of the acceleration stage, the T_2 signal intensities decreased to 402.3, 563.9 and 700.3 a.u./g for the 0.30CP, 0.35CP and 0.40CP samples, respectively. Taking a closer looking at the data, the average decline rates during the total acceleration stage were 20.3, 23.6 and 28.4 a.u./g/h for the 0.30CP, 0.35CP and 0.40CP samples, respectively. The results implied that water consumption by hydration reactions would be significantly more severe with a higher w/c of cement paste during the acceleration stage.

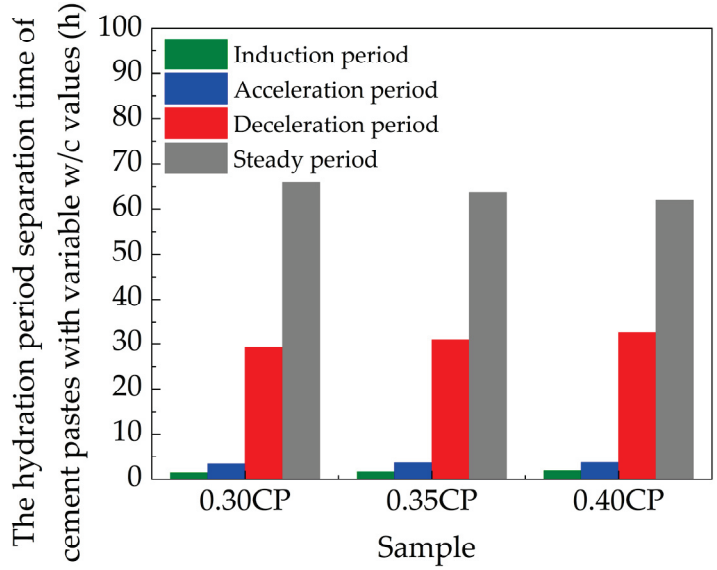

Figure 7. The duration of hydration stages for cement paste samples with variable w/c values.

After the acceleration stage, the hydration of the cement paste entered in the deceleration stage as the generation of a large quantity of hydration products. At the end of deceleration stage, the T_2 signal intensities further decreased to 146.2, 243.3 and 320.6 a.u./g for the 0.30CP, 0.35CP and 0.40CP samples, respectively. At the end of the deceleration stage, the reaction rate of hydration became quite slow, which manifested as the relative steady signal intensity, implying less variation in the physically bound water amount. The hydration time points for reaching the last steady hydration stage were about 34.1, 36.3 and 38.1 h for the 0.30CP, 0.35CP and 0.40CP samples, respectively. Hence, it took a longer time for the cement paste with a higher w/c ratio to achieve a stable hydration state. Additionally, it is worth noting that although the curves in Figure 6 exhibited slightly falling tendencies in the steady stage, the decreasing rates were substantially lower than before and could even actually be neglectable with the time prolonging because the horizontal axis for the time mark was on a logarithmic scale. Overall, a higher water content in the mixture resulted in the longer duration of every hydration stage, which may be explained by the higher dilution degree of the cementitious mixture causing a delayed hydration progress.

Zhao investigated the hydration process of Portland cement with w/c values of 0.3, 0.35 and 0.4. According to their results, with the increase in w/c from 0.3 to 0.35 or 0.4, the induction stage was prolonged by 6.2% or 9.7%, the acceleration time was prolonged by 2.9% or 6.4%, and the deceleration time was prolonged by 14.5% or 64.5%. The T_2 signal amplitude per unit mass increased with a higher w/c. In the steady stage, the hydration reaction rate was extremely small, the content of physically bound water in cement paste was very little and hydration tended to become steady [33].

3.4. Influence of SAP on Hydration Stages

The influence of the SAP content on the time-dependent evolution of the T_2 signal maximum amplitude is presented in Figure 8. It can be clearly seen that the T_2 signal intensity (denoting the amount of physically bound water) became stronger with the higher

SAP dosage, which meant that the addition of the SAP could help to reserve the water content in the fresh cementitious mixture and reduce the water consumption amount during hydration reactions. However, the use of the SAP did not affect the overall trend of the T_2 signal amplitude curve. The detailed parameters of the typical hydration periods involving cement paste samples with variable SAP dosages are provided in Table 4 and Figure 9. Then, the effect of the SAP on every specific hydration stage was further discussed accordingly.

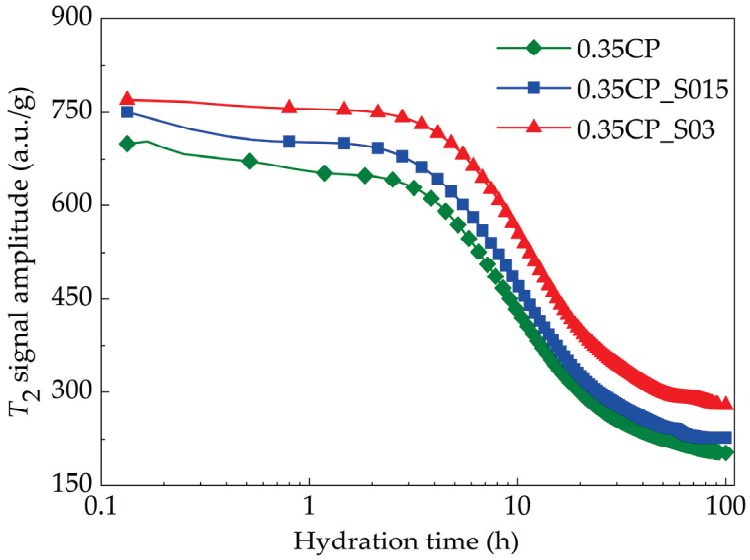

Figure 8. Time-dependent evolution of T_2 signal amplitude for cement paste samples with variable SAP dosages (w/c = 0.35).

Table 4. The starting and terminal time points of each hydration stage for cement paste samples with variable SAP dosages (w/c = 0.35).

Sample	Hydration Time (Hours:Minutes)			
	Induction Stage	Acceleration Stage	Deceleration Stage	Steady Stage
0.35CP	[0*,1:43]	[1:43,5:22]	[5:22,36:15]	[36:15,100*]
0.35CP_S015	[0*,1:53]	[1:53,5:45]	[5:45,36:32]	[36:32,100*]
0.35CP_S03	[0*,2:06]	[2:06,6:55]	[6:55,37:28]	[37:28,100*]

Note: The 0* indicates the time point at which the first measurement was taken but not the cement coming into contact with water. The 100* indicates the end of the measurement.

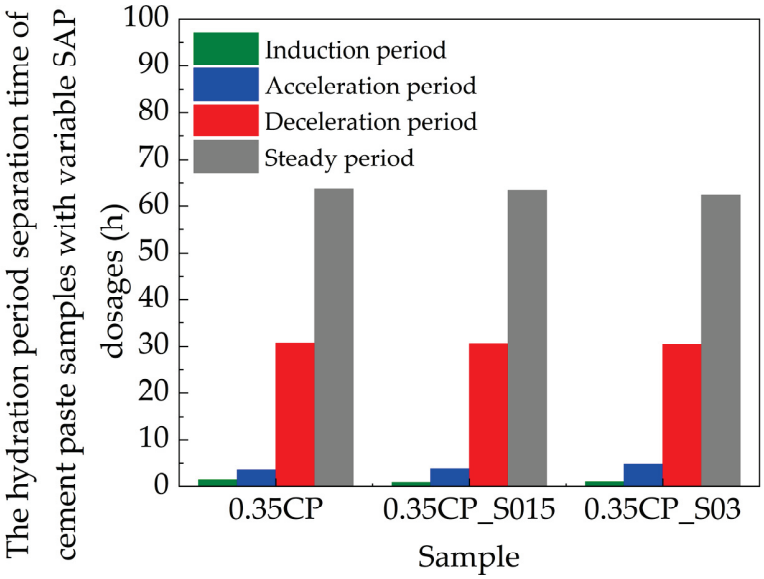

Figure 9. The duration of hydration stages for the cement paste samples with variable SAP dosages (w/c = 0.35).

Firstly, the duration of the induction stage continued for 1.72, 1.88 and 2.10 h for the 0.35CP, 0.35CP_S015 and 0.35CP_S03 samples, respectively. Hence, the incorporation of the SAP with a higher content prolonged the induction stage of cement hydration more evidently, owing to the increased total water amount in mixtures at the beginning. Meanwhile, after incorporating 0.15% or 0.30% SAP, the T_2 signal intensity increased from 649.2 to 695.0 or 749.7 a.u./g at the end of induction period and subsequently delayed the onset of later exothermic peaks. Then, the acceleration stage of the 0.35CP, 0.35CP_S015 and 0.35CP_S03 samples continued for 3.64, 3.87 and 4.82 h, respectively. During this stage, the cement pastes gradually hardened and formed a dense skeleton, which could wrap the hydration products together with the un-hydrated cement grains. It is obvious that the higher SAP content prolonged the duration of the acceleration stage significantly, since the SAP particles started to continuously release water during this stage, which could be driven by the concentration gradient difference of ions in the liquid phase. In other words, the addition of the SAP was equivalent to the entrainment of extra water being effective for hydration reactions. This function of SAP particles would decrease the concentration of calcium ions in a pore solution, which may explain the extended duration of the acceleration stage. Such a retardation effect of the SAP on hydration was also in accordance with other previous results by isothermal calorimetry [18,19].

As for the subsequent deceleration stage, the differential calculation results showed that it terminated at 36.25, 36.53 and 37.47 h for the 0.35CP, 0.35CP_S015 and 0.35CP_S03 samples, respectively. So, the addition of a higher SAP content could slightly extend the ending time point of the deceleration stage, at which the T_2 signal intensities were decreased from 243.3 to 265.7 and 323.1 a.u./g for the 0.35CP_S015 and 0.35CP_S03 samples, respectively. During this period, the SAP particles could release water gradually with the descending internal humidity in the cement paste and thus were able to endow the hardened materials with a sufficient and uniform distribution of interior moisture, which contributed to the promotion of the holistic hydration degree for the cement-based materials. Finally, the samples entered into the steady stage, and their curves presented horizontal extending trends, which suggested that the hydration reactions became much slower or even nearly static. The long-term signals also revealed that the quantity of physically free water in the hardened cement paste was enhanced by the incorporation of the SAP, which indicated that it can release water continuously for realizing a long-term internal curing effect, which would mitigate the self-desiccation of concrete and thus reduce the shrinkage and cracking risks [14]. After hydration for 100 h, the T_2 signal amplitude values of the 0.35CP, 0.35CP_S015 and 0.35CP_S03 samples were 203.2, 227.4 and 279.3 a.u./g, respectively, at the ending time point of measurement.

Similarly, Zhang et al. employed isothermal calorimetry to investigate the influence of an SAP at dosages of 0.2%, 0.4%, 0.6% and 1.0% (by cement mass) on the early hydration kinetics of Portland cement (w/c = 0.5). The results demonstrated that the SAP modified the hydration process without altering the duration of the induction stage nor the timing of the acceleration stage onset. However, the SAP significantly increased the heat evolution rate during the acceleration period and elevated the main exothermic peak value compared to the control group without SAP addition [34].

3.5. Influence of CaO on Hydration Stages

The use of the CaO-based EA may also exert significant influences on the hydration kinetics of the cement paste. This section focuses on the effect of the CaO-based EA with the dosages of 0, 2% and 3% and with the presence of the SAP as an internal curing admixture simultaneously. The time-dependent evolution of the T_2 signal amplitude for these shrinkage-compensating cement pastes with different contents of the CaO-based

EA are exhibited in Figure 10. Considering the fact that the hydration of cement usually requires a higher amount of water than that of a CaO-based EA with equivalent mass [35], the replacement of cement by more EA resulted in less water being consumed by hydration. Hence, when the w/c ratio was constant, using the CaO-based EA as a binder component to partially replace the cement may have facilitated the generation of more free water in early-age mixture. Correspondingly, the time portions for each hydration stage were further determined as listed in Table 5, and the division results are depicted in Figure 11.

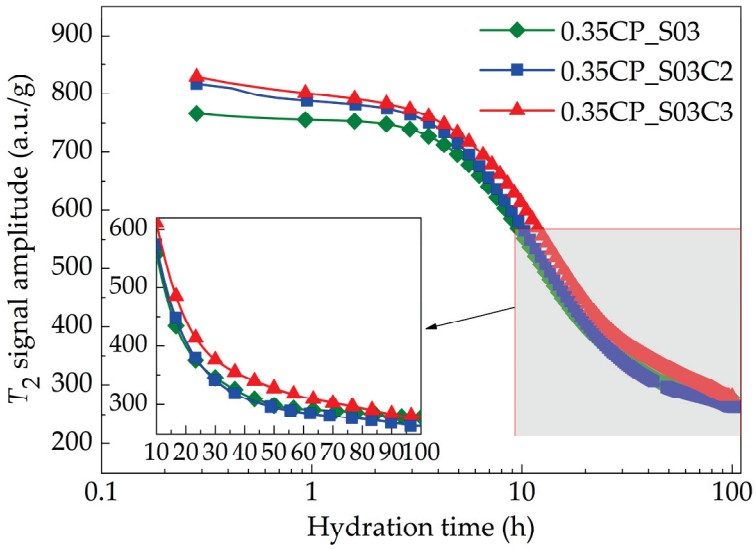

Figure 10. Time-dependent evolution of T_2 signal amplitude for cement paste samples with constant SAP and variable CaO dosages (w/c = 0.35).

Table 5. The starting and terminal time points of each hydration stage for cement paste samples with constant SAP and variable CaO dosages (h).

Sample	Hydration Time (Hours:Minutes)			
	Induction Stage	Acceleration Stage	Deceleration Stage	Steady Stage
0.35CP_S03	[0*,2:06]	[2.:06,6:55]	[6:55,37:28]	[37:28,100*]
0.35CP_S03C2	[0*,2:04]	[2:04,6:29]	[6:29,36:17]	[36:17,100*]
0.35CP_S03C3	[0*,1:56]	[1:56,6:11]	[6:11,35:32]	[35:32,100*]

Note: The 0* indicates the time point at which the first measurement was taken but not the cement coming into contact with water. The 100* indicates the end of the measurement.

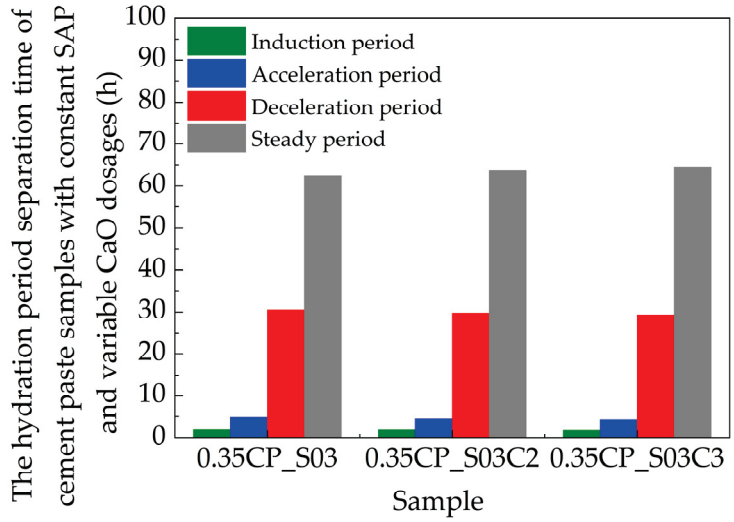

Figure 11. The duration of hydration stages for cement paste samples with constant SAP and variable CaO dosages (w/c = 0.35).

For the induction stage, the incorporation of the CaO-based EA led to stronger T_2 signal intensities, which was possibly because the addition of the CaO-based EA modified the particle-packing states of solids and thus released more free water from deflocculation for the fresh mixture initially [36]. At the end of the induction stage, the T_2 signal maximum amplitudes of the 0.35CP_S03, 0.35CP_S03C2 and 0.35CP_S03C3 cement paste samples were 749.7, 777.3 and 787.5 a.u./g, respectively. On the other hand, plenty of calcium ions could be released by the dissolution of the CaO-based EA admixture, which may shorten the elapsed time being required for approaching its over-saturation concentration point [37]. So, the duration of the induction stage could be shortened with a higher content of the CaO-based EA. Then, when reaching the terminal time point of the acceleration hydration stage, the T_2 signal amplitude intensities of the 0.35CP_S03, 0.35CP_S03C2 and 0.35CP_S03C3 samples were 641.4, 669.7 and 702.9 a.u./g, respectively. During this period, the corresponding average descending rates of the 0.35CP_S03 and 0.35CP_S03C2 samples were as high as 22.47 and 24.29 a.u./g/h, which indicated the promoted hydration reactions of cement clinker minerals to consume free or physically bound water and motivate the generation of hydration products more rapidly. In other words, it is interesting to note that the time-dependent signal curves exhibited a faster descending tendency when adding the CaO-based EA, probably because the dissolution of CaO can enhance the concentration of calcium ions in a solution [38]. Furthermore, it can be obviously found that the T_2 signal amplitude curves of the 0.35CP_S03C2 and 0.35CP_S03C3 samples were rather close, with not very obvious variation between them if the dosage of the CaO-based EA increased from 2% to 3%.

Afterward, for the subsequent deceleration stage, the overall consumption rate of free water or physically bound water became obviously slower for all these mixtures. Specifically, the T_2 signal amplitude values of the 0.35CP_S03 and 0.35CP_S03C2 samples decreased to 323.1 and 319.5 a.u./g at the end of deceleration stage, when the terminal time points were about 37.5 and 36.3 h from adding water. Thereby, the incorporation of the CaO-based EA shortened both the acceleration and deceleration stages, which verified the promotion effect of the CaO-based EA on the hydration kinetics of the cement paste with the presence of the SAP for internal curing. After about 20 h, the hardened cement pastes gradually entered into the steady stage. The amplitude values of the T_2 signal fluctuated just around 278.3, 263.1 and 283.4 a.u./g for the 0.35CP_S03, 0.35CP_S03C2 and 0.35CP_S03C3 samples, respectively, after hydration for 100 h. In addition, regarding the 0.35CP_S03C2 sample, it consumed more water in the hydration reactions during the whole measurement period compared with the other two samples, as verified by the largest variation in T_2 signal amplitude values at the beginning and ultimate moments. This indicated that 2 wt% could be a suitable dosage of CaO-based EA for reaching a more effective promotion effect on the hydration kinetics of cement paste.

Similarly, Zhao et al. used the LF-NMR technique to study the effect of a CaO-MgO blended EA on the early-age hydration of a cement paste with a w/c of 0.35. The results showed that with the increase in the CaO-MgO blended EA, the amount of transverse relaxation T_2 signal in the induction period increased, and the induction stage was shortened by 16.0% and 20.3%, respectively, when the dosage of the CaO-MgO blended EA was increased from 0 to 2% and 4%. The use of the CaO-MgO blended EA was able to increase the concentration of Ca^{2+} in the pore solution of the cement slurry to shorten the duration of the induction period. However, with the increase in the CaO-MgO blended EA, the T_2 signal intensity in the stable period decreased [39].

4. Research Significance

The experimental results provide valuable insights into advancing cement-based material technology. The identified hydration stages and their dependence on the w/c ratio offer a scientific basis for optimizing concrete mix designs, particularly in controlling setting times and strength development. The SAP addition strategy demonstrates potential for developing internal curing concrete systems, which could significantly improve durability in dry climates or water-scarce regions. Furthermore, the synergistic effects of the SAP and CaO-based EA open new possibilities for designing shrinkage-compensated concrete, addressing a critical challenge in modern construction. These findings lay a solid foundation for developing high-performance concrete with enhanced performance and sustainability. In the future, more in-depth investigations will be carried out to further explore the coupled effects of SAPs and CaO on the volume deformation and cracking tendency of early-age cement-based materials, based on the hydration analysis results in this study.

5. Conclusions

According to the experimental investigations, some major conclusions can be obtained as follows:

(1) For fresh cement paste samples, the time-dependent evolution of transverse relaxation time (T_2) signal maximum amplitude presented a descending tendency with prolonged hydration time. Based on the extreme points in the first-order derivatives of the T_2 signal maximum amplitude curve, the hydration progress could be further identified with four different stages.

(2) With the increase in the water-to-cement ratio (w/c) in the cementitious mixture, all the stages in hydration progress (including induction, acceleration, deceleration and steady stages) became longer, which could be explained by more physically bound or free water in the mixture that led to a higher dilution degree.

(3) The incorporation of the super-absorbent polymer (SAP) with a higher content could retard the hydration kinetics more evidently at a very early age and thus prolong the duration of the induction and acceleration stages. Afterwards, the SAP also exhibited an effective promotion on the overall hydration degree of the cement-based materials at later stages.

(4) Adding the CaO-based expansive admixture (EA) shortened the induction, acceleration and deceleration stages of the cement paste, which confirmed its promotion effect on hydration kinetics with the presence of the SAP. The combination of 3 wt% SAP and 2 wt% CaO could consume more water synergistically by hydration reactions in the first 100 h.

Author Contributions: Conceptualization, M.L.; Validation, H.S., Y.D. and J.Z.; Formal analysis, M.L. and X.W.; Investigation, M.L. and X.L.; Resources, X.L.; Writing—original draft, M.L.; Writing—review & editing, J.L. and J.Z.; Visualization, Y.H.; Supervision, J.Z.; Project administration, M.L.; Funding acquisition, J.L. All authors have read and agreed to the published version of the manuscript.

Funding: This research was funded by the Guangxi Science and Technology Program under Grant (Guike AA23062034), the Research on Key Technologies for Improving the Quality and Safety Assurance of the Huai River to Sea Waterway Phase II Project (RHSD2/FW-2024-03), and the Technology Project of State Grid Jiangsu Electric Power Co., Ltd. (J2023094).

Data Availability Statement: The original contributions presented in the study are included in the article, further inquiries can be directed to the corresponding author.

Conflicts of Interest: The authors declare no conflict of interest.

References

1. Zhang, Y.; Liu, X.; Xu, Z.; Yuan, W.; Xu, Y.; Yao, Z.; Liu, Z.; Si, R. Early-Age Cracking of Fly Ash and GGBFS Concrete Due to Shrinkage, Creep, and Thermal Effects: A Review. *Materials* **2024**, *17*, 2288. [CrossRef] [PubMed]
2. Gamage, N.; Patrisia, Y.; Gunasekara, C.; Law, D.W.; Houshyar, S.; Setunge, S. Shrinkage Induced Crack Control of Concrete Integrating Synthetic Textile and Natural Cellulosic Fibres: Comparative Review Analysis. *Constr. Build. Mater.* **2024**, *427*, 136275. [CrossRef]
3. Ning, Z.; Liu, Y.; Wang, W.; Dong, J.; Meng, X.; Wang, Q. Crack propagation and non-uniform deformation analysis in hydraulic asphalt concrete: Insights from X-ray CT scanning and digital volume correlation. *Constr. Build. Mater.* **2024**, *411*, 134704. [CrossRef]
4. Yang, Y.; Ma, L.; Huang, J.; Gu, C.; Xu, Z.; Liu, J.; Ni, T. Evaluation of the Thermal and Shrinkage Stresses in Restrained High-Performance Concrete. *Materials* **2019**, *12*, 3680. [CrossRef] [PubMed]
5. Shrestha, A.; Ahmad, N.; Zhang, Z.; Rawat, S.; Li, L. Effect of United Expanding Admixture on Autogenous Shrinkage and Early Age Mechanical Properties of High-Strength Engineered Cementitious Composites. *Buildings* **2024**, *14*, 2868. [CrossRef]
6. Liu, L.; Chen, H.; He, Z.; Wang, P.; Cui, J.; Cai, X.; Sun, Y. Effect and Mechanism of Compound Expansive Agent on Rheological, Mechanical, and Shrinkage Properties of UHPC. *Constr. Build. Mater.* **2024**, *444*, 137730. [CrossRef]
7. Wang, Y.; Xue, S.; Li, X.; Geng, Y.; Rong, H. Autogenous Shrinkage of High-Performance Concrete Subjected to Different Curing Temperatures. *Constr. Build. Mater.* **2024**, *447*, 138069. [CrossRef]
8. Li, S.; Liu, S.; Jiang, C. Analysis of the Influence and Mechanism of Diatomaceous Earth Internal Curing on the Autogenous Shrinkage and Early Crack Resistance of Cement-Based Materials with Low Water-Binder Ratio. *Appl. Sci.* **2024**, *14*, 5397. [CrossRef]
9. Ghanem, H.; Ramadan, R.; Khatib, J.; Elkordi, A. A Review on Chemical and Autogenous Shrinkage of Cementitious Systems. *Materials* **2024**, *17*, 283. [CrossRef] [PubMed]
10. Zhang, Y.; Pan, Y.; Ren, T.; Liang, H.; Zhang, J.; Zhang, D. The Application of Calcium-Based Expansive Agents in High-Strength Concrete: A Review. *Buildings* **2024**, *14*, 2369. [CrossRef]
11. Shen, Y.; Wang, Z.; Zhou, Y.; Du, J.; Lai, J.; Qian, K.; Ruan, S.; Bi, Y.; Qian, X. The Influence of Nano-Silica Composite Superabsorbent Polymer on the Autogenous Shrinkage of Mortar. *Constr. Build. Mater.* **2024**, *442*, 137683. [CrossRef]
12. Han, Y.; Xie, Y.; Li, W.; Yue, Q.; Liu, Y.; Peng, B. Using SAP to Control the Deformation of Shrinkage-Compensating Concretes at Early Age. *Constr. Build. Mater.* **2024**, *416*, 135139. [CrossRef]
13. Yang, G.; Wang, H.; Wan-Wendner, R.; Hu, Z.; Liu, J. Cracking Behavior of Ultra-High Strength Mortar with CaO-Based Expansive Agent and Superabsorbent Polymer. *Constr. Build. Mater.* **2022**, *357*, 129281. [CrossRef]
14. Wang, K.; Moon, J.; Du, H.; Xia, X.; Zhu, D.; Zhang, P.; Guo, J. Early-Age Shrinkage and Hydration of Concrete Incorporating a Mutually Reinforcing Systems of Super Absorbent Polymers and MgO Expansive Agent Under Low Humidity Conditions. *Constr. Build. Mater.* **2024**, *417*, 135350. [CrossRef]
15. Liu, L.; Fang, Z.; Huang, Z.; Wu, Y. Solving Shrinkage Problem of Ultra-High-Performance Concrete by a Combined Use of Expansive Agent, Super Absorbent Polymer, and Shrinkage-Reducing Agent. *Compos. Part B Eng.* **2022**, *230*, 109503. [CrossRef]
16. Nocuń-Wczelik, W.; Bochenek, A.; Migdał, M. Calorimetry and Other Methods in the Studies of Expansive Cement Hydrating Mixtures. *J. Therm. Anal. Calorim.* **2012**, *109*, 529–535. [CrossRef]
17. Zhao, H.; Xiang, Y.; Liu, J.; Zhang, Z.; Jia, R.; Yao, T.; Li, H.; Xu, W.; Tian, Q. Effects of Reinforcement on Autogenous Deformation of Early-Age Concrete Containing CaO-Based Expansion Agent. *Constr. Build. Mater.* **2022**, *320*, 126197. [CrossRef]
18. Wang, H.; Liu, Z.; Wang, F.; Zhang, J.; Guo, L.; Zhang, Y.; Li, Y.; Lin, J.; Lu, Z.; Jiang, J. Deciphering the Influence of Superabsorbent Polymers on Cement Hydration and Portlandite Formation. *Constr. Build. Mater.* **2024**, *418*, 135455. [CrossRef]
19. Schroefl, C.; Snoeck, D.; Mechtcherine, V. A Review of Characterisation Methods for Superabsorbent Polymer (SAP) Samples to Be Used in Cement-Based Construction Materials: Report of the RILEM TC 260-RSC. *Mater. Struct.* **2017**, *50*, 197. [CrossRef]
20. Bortoletto, M.; Sanches, A.O.; Santos, J.A.; da Silva, R.G.; Tashima, M.M.; Paya, J.; Soriano, L.; Borrachero, M.V.; Malmonge, J.A.; Akasaki, J.L. New Insights on Understanding the Portland Cement Hydration Using Electrical Impedance Spectroscopy. *Constr. Build. Mater.* **2023**, *407*, 133566. [CrossRef]
21. Dong, P.; Allahverdi, A.; Andrei, C.M.; Bassim, N.D. The Effects of Nano-Silica on Early-Age Hydration Reactions of Nano Portland Cement. *Cem. Concr. Compos.* **2022**, *133*, 104698. [CrossRef]
22. de Matos, P.R.; Neto, J.S.A.; Jansen, D.; De la Torre, A.G.; Kirchheim, A.P.; Campos, C.E. In-Situ Laboratory X-Ray Diffraction Applied to Assess Cement Hydration. *Cem. Concr. Res.* **2022**, *162*, 106988. [CrossRef]
23. Xiang, Y.; Zhao, H.; Hu, D.; Yun, W.; Wang, Y.; Xu, W. Hydration Characteristics of Cementitious Materials with Manufactured Sand from Various Lithologies and Differential Effect of CaO-MgO Blend Expansion Agent. *Constr. Build. Mater.* **2024**, *433*, 136773. [CrossRef]

24. Zhao, H.; Li, X.; Chen, X.; Qiao, C.; Xu, W.; Wang, P.; Song, H. Microstructure Evolution of Cement Mortar Containing MgO-CaO Blended Expansive Agent and Temperature Rising Inhibitor Under Multiple Curing Temperatures. *Constr. Build. Mater.* **2021**, *278*, 122376. [CrossRef]
25. Wang, B.; Faure, P.; Thiery, M.; Baroghel-Bouny, V. ^{1}H NMR Relaxometry as an Indicator of Setting and Water Depletion During Cement Hydration. *Cem. Concr. Res.* **2013**, *45*, 1–14. [CrossRef]
26. Bortolotti, V.; Fantazzini, P.; Mongiorgi, R.; Sauro, S.; Zanna, S. Hydration Kinetics of Cements by Time-Domain Nuclear Magnetic Resonance: Application to Portland-Cement-Derived Endodontic Pastes. *Cem. Concr. Res.* **2012**, *42*, 577–582. [CrossRef]
27. Ji, Y.; Pel, L.; Sun, Z. NMR Study on the Early-Age Hydration and Ion Binding of the Cement Paste Prepared with NaCl Solutions. *Cem. Concr. Compos.* **2022**, *129*, 104489. [CrossRef]
28. Rusu, M.M.; Faux, D.; Ardelean, I. Monitoring the Effect of Calcium Nitrate on the Induction Period of Cement Hydration via Low-Field NMR Relaxometry. *Molecules* **2023**, *28*, 476. [CrossRef] [PubMed]
29. She, A.; Yao, W.; Wei, Y. In-Situ Monitoring of Hydration Kinetics of Cement Pastes by Low-Field NMR. *J. Wuhan Univ. Technol. Mater. Sci. Ed.* **2010**, *25*, 692–695. [CrossRef]
30. *GB 175-2023*; Common Portland Cement. China Standards Press: Beijing, China, 2023.
31. *GB/T 23439-2017*; Expansive Agents for Concrete. China Standards Press: Beijing, China, 2017.
32. Scrivener, K.; Ouzia, A.; Juilland, P.; Mohamed, A.K. Advances in Understanding Cement Hydration Mechanisms. *Cem. Concr. Res.* **2019**, *124*, 105823. [CrossRef]
33. Zhao, H.; Xiang, Y.; Xu, W.; Chen, X.; Zhu, Y.; Wu, H.; Liu, S. Effects of Water-cement Ratio and Hydration Heat Regulating Materials on Hydration Process of Early-age Cementitious Materials. *J. Wuhan Univ. Technol. Mater. Sci. Edit.* **2023**, *38*, 88–96. [CrossRef]
34. Zhang, G.; Wang, Y.; He, R.; Wang, P. Effects of super absorbent polymer on the early hydration of Portland cement highlighted by thermal analysis. *J. Therm. Anal. Calorim.* **2017**, *129*, 45–52. [CrossRef]
35. Qi, T.; Zhou, W.; Liu, X.; Wang, Q.; Zhang, S. Predictive Hydration Model of Portland Cement and Its Main Minerals Based on Dissolution Theory and Water Diffusion Theory. *Materials* **2021**, *14*, 595. [CrossRef] [PubMed]
36. Londero, C.; Klein, N.S.; Mazer, W. Study of Low-Cement Concrete Mix-Design Through Particle Packing Techniques. *J. Build. Eng.* **2021**, *42*, 103071. [CrossRef]
37. Zhao, H.; Jiang, K.; Di, Y.; Xu, W.; Li, W.; Tian, Q.; Liu, J. Effects of Curing Temperature and Superabsorbent Polymers on Hydration of Early-Age Cement Paste Containing a CaO-Based Expansive Additive. *Mater. Struct.* **2019**, *52*, 108. [CrossRef]
38. Zhang, J.; Chen, T.; Gao, X.; Tian, W.; Jiao, D.; Zhu, X. Rheological concerns arising from the use of anti-freezing additives in cement mortar with/without SP and AEA for low-temperature construction. *Cem. Concr. Compos.* **2023**, *142*, 105220. [CrossRef]
39. Zhao, H.; Xiang, Y.; Liu, J.; Chen, X.; Xu, W.; Li, H. Influences of Calcium Oxide-Magnesium Oxide Blended Expansive Agent and Temperature Rising Inhibitor on Hydration Characteristic of Early-Age Cement Paste. *J. Chin. Ceram. Soc.* **2021**, *49*, 2509–2517.

Disclaimer/Publisher's Note: The statements, opinions and data contained in all publications are solely those of the individual author(s) and contributor(s) and not of MDPI and/or the editor(s). MDPI and/or the editor(s) disclaim responsibility for any injury to people or property resulting from any ideas, methods, instructions or products referred to in the content.

materials

MDPI

Article

Redispersible Acrylic Ester Polymers: Effect of Polymer Property Changes Due to Polymerization Method Modification and Functional Additives on the Performance of Polymer Cement Mortar

Jeong-Bae Lee

Department of Smart Construction and Environmental Engineering, Daejin University, Pochon 11159, Republic of Korea; jblee@daejin.ac.kr

Abstract: This paper presents an experimental study aimed at improving the performance of polymer cement mortar by evaluating the properties of acrylic ester redispersible polymers, synthesized using a change in polymerization method from emulsion monomer to monomer dropwise addition methods, along with the use of a functional additive in the form of a foaming agent. To achieve the research objectives, a polymer with a glass transition temperature of −11 °C was synthesized by fixing the monomer ratio, particle-size distribution, and glass transition temperature, and the physical properties of the polymer cement mortar were assessed. The results showed that polymers synthesized using the modified polymerization method increased elongation at break and possessed a 35% smaller average particle size. The use of the foaming agent also resulted in enhanced tensile strength. The polymer cement mortars made with these respective polymers demonstrated improvements in compressive strength 11~25%, flexural strength 53~77%, bond strength 78~113%, volumetric changes 65~88%, and water absorption 30~70%. These findings suggest that changes in the polymerization method and the incorporation of functional additives influence the average particle size and air entrainment control properties of the polymers, thereby positively impacting the performance of the cement hydrates.

Keywords: emulsion monomer dropping; monomer dropping; average particle size; cement mortar

1. Introduction and Motivation

Cement mortar and concrete, widely used as repair materials for concrete structures, are convenient to use and inexpensive but have disadvantages such as low tensile and flexural strength, high drying shrinkage, low bond strength, and poor chemical and freeze–thaw resistance. To overcome these weaknesses, polymers are incorporated into cement mortar and concrete.

The use of polymers in cement mortar and concrete was first introduced by Cresson in 1923, and the research on the polymer forms currently in use was published by Lefebure in 1924. Since then, significant research and development has been conducted to utilize polymers in mortar and concrete, leading to the production of polymer-modified materials in several countries for the last 70 years [1]. During the 1920s and 1930s, polymer-modified cement mortar and concrete were developed using natural rubber latex, and in the 1940s, research on synthetic latex, chloroprene rubber latex, and polyacrylic ester latex for polymer-modified cement mortars began. By the late 1940s, these materials had seen diverse applications. In the 1960s, the use of styrene-butadiene rubber, polyacrylic ester, and polyvinylidene chloride-vinyl chloride in mortar and concrete became more widespread. This led to the advancement of polymer-modified cement mortar and concrete in several countries. Additionally, methylcellulose, a water-soluble polymer, was applied to polymer-modified cement mortar for ceramic tile adhesives [2].

Shibazaki introduced research on polymer-modified cement mortars using hydrophilic polymers such as hydroxyethyl cellulose and polyvinyl alcohol [3]. Shiyun and Zhiyuan studied polymer-modified cement mortar using composite polymer latexes which showed that mixing two different polymer latexes can complement the disadvantages of each polymer [4].

In 1933, Sugita et al. researched the microstructure and the complex mechanism of latex paste and mortar, discovering that a large amount of polymer particles and hydrated cement form layers through interfacial action within the aggregate and cement particles [5]. Geist, who developed PVAC mortar, found that particle sizes between 1 and 5 μm or 2 and 5 μm produce maximum strength [6]. In 1964, Ohama et al. studied the monomer ratios of EVA, SBR, and poly styrene-butyl acryl ester, concluding that the monomer ratio affects the strength of latex mortars within the same range as the polymer–cement ratio [7]. In 1987, they introduced a mechanism involving interactions between the polymer and carboxyl groups [8].

Today, the construction industry demands high-performance materials for improving the durability of structures and applying advanced construction methods. Polymer-modified cement mortar and concrete are receiving attention in this context. In general, polymer-modified cement mortar is a composite material consisting of cement and polymers mixed for cement modifications. Compared to standard cement mortar, it demonstrates superior workability, repairability, flexural and tensile strength, flexural toughness, adhesion, waterproofing, resistance to chloride ion penetration, resistance to carbonation, freeze–thaw resistance, abrasion resistance, and impact resistance [9,10]. Due to these advantages, polymer-modified cement mortars are widely used around the world in high-performance building exterior materials, flooring, coatings, waterproofing materials, decorative coatings, and for repairing and reinforcing reinforced concrete structures [11].

The characteristics of polymer-modified cement mortar and concrete are affected by the properties of the polymer film formed inside the mortar. Thus, the polymer film formation process is closely related to the properties of polymer-modified cement mortar and concrete. Understanding the inherent properties of polymers, such as the strength and elongation of the polymer film, the minimum film formation temperature (MFT), the glass transition temperature (Tg), the melting point (Tm), and the lower temperature limits, is crucial before applying them to cement mortar and concrete. Among these, Tg is a key factor in determining the degree and form of film formation within cement mortar and concrete [12].

Since the 2010s, research utilizing natural polymers such as starch, cactus extract, casein, rice, and eggs has reported that polymer incorporation affects the durability and waterproofing of mortar [13,14]. Research on the fire resistance of polymer-modified mortars has also been conducted, evaluating characteristics such as heat resistance, residual bond strength, and tensile strength [15–17]. Although various studies on polymer-modified mortars have been carried out, there is still a lack of research focused on improving the performance of polymer-modified cement mortar by modifying polymer properties through synthesis processes.

This paper evaluates the improvement in the performance of polymer-modified cement mortars using polymers with a glass transition temperature of −11 °C, which were identified as suitable for cement modifications in previous studies. These polymers were modified through changes in synthesis methods and the use of additives, and their effects on the performance of cement pastes were studied.

2. Research Objectives and Scope

In this paper, the glass transition temperature used was −11 °C (AC3), which demonstrated the best overall performance in previous research [18] evaluating the physical properties of acrylic-based redispersible powder polymers synthesized with varying monomer ratios. Based on the selected monomer ratio, the characteristics of polymer-modified

cement mortars were evaluated using polymers whose performance was modified through two methods.

There are several methods to improve the performance of polymers used in cement mixtures. Common approaches include adjusting the hardness through molecular weight control, adding functionality through functional monomers, and using additives such as dispersants and thickeners. These methods allow for the modification of polymer properties to achieve the most suitable characteristics for specific applications.

This research employed two methods: using a defoamer as a functional additive to control the entrained air within the polymer and modifying the polymerization method; specifically, the polymerization method from emulsion monomer to monomer dropping systems to reduce the polymer particle size and achieve stable synthesis. Additionally, modified polyvinyl alcohol was replaced with polyvinyl alcohol, which is used as protective colloid, to further enhance the performance of the polymer.

The research content and methods of this paper are as follows:

(1) Polymers were synthesized based on a glass transition temperature of −11 °C (AC3) according to the monomer ratio. Two types of polymers were synthesized: a polymer modified with a defoamer as a functional additive (defoamer-modified acrylic latex; DMAC) and a polymer synthesized by changing the emulsion polymerization method and protective colloid (polymerization-modified acrylic latex; PMAC). The basic properties of these redispersible powder polymers were evaluated.

(2) The glass transition temperature was measured using a differential scanning calorimeter, and the tensile strength was measured according to KS M 3381 (testing method for tensile properties of glass-fiber-reinforced plastics) [19]. Additionally, the average particle size was analyzed using a particle-size analyzer.

(3) Polymer-modified cement mortar was prepared using the synthesized redispersible powder polymers. The polymer-modified cement mortar was made by incorporating 5% of the total binder with redispersible powder polymer, while maintaining an air content of 4.5 ± 1.5% and a flow value of 155 ± 10 mm to ensure consistent workability. The setting time, compressive strength, flexural strength, bond strength, length change, and water absorption of the polymer-modified cement mortars were measured at various curing ages and compared with standard cement mortar and a polymer-modified cement mortar before performance modification.

3. Overview of Experiments

3.1. Materials Used

The cement used in this study was Type 1 Ordinary Portland Cement, as specified in KS L 5201 [20]; its chemical composition and physical properties are shown in Table 1. The physical properties of the standard sand are also shown in Tables 1 and 2.

Table 1. Chemical composition and physical properties of Ordinary Portland Cement.

Chemical Composition		**Physical Properties**		
SiO_2	21.7	Density (g/cm^2)		3.15
Al_2O_3	5.7	Specific surface area (m^2/kg)		328
Fe_2O_3	3.2	Setting Time (min)	Initial Set	221
CaO	63.1		Final Set	361
MgO	2.8	Compressive Strength (MPa)	3 days	22.6
SO_3	2.2		7 days	31.6
Ig. loss	1.3		28 days	38.7

Table 2. Physical properties of silica sand.

Number	Size (mm)	Density (g/cm^3)	Absorption Rate (%)	Organic Impurities
6	≤0.67	2.61	0.91	None

Additionally, the physical properties of the silica fume (hereafter referred to as SF) used in this study are shown in Table 3. A melamine-based powdered superplasticizer was used in the preparation of both cement mortar and polymer-modified cement mortar.

Table 3. Physical properties of silica fume.

Category	Classification	Characteristic Value
Chemical Properties (%)	SiO_2	91.2
	Al_2O_3	1.3
	Fe_2O_3	0.8
	CaO	0.7
	MgO	0.3
	Na_2O	0.5
	K_2O	0.8
Physical Properties	Density (g/cm^2)	2.2
	Specific Surface Area (m^2/kg)	20,470

3.2. Experimental Mix Proportion

3.2.1. Polymer Synthesis

The acrylic ester copolymer emulsion composition used in this study consisted of a hydrophilic ethylene-unsaturated monomer and a hydrophobic ethylene-unsaturated monomer. Methyl (meth)acrylate (MMA) was used as the hydrophilic ethylene-unsaturated monomer, while butyl (meth)acrylate (BA), ethyl acrylate (EA), and 2-ethylhexyl acrylate (2-EHA) were used as the hydrophobic ethylene-unsaturated monomers, with the monomer ratios adjusted accordingly. The glass transition temperature (Tg) of the synthesized emulsion was fixed at −11 °C. The compositions of the reference polymer AC3 and the performance-modified polymers DMAC and PMAC are shown in Table 4.

Table 4. Monomer composition ratio.

Category	AC3	DMAC	PMAC
Tg (°C)	−11	−11	−11
MMA (%)	45	45	45
BA (%)	30	30	30
EA (%)	5	5	5
2-EHA (%)	20	20	20

3.2.2. Polymer Cement Mortar

The mix proportions of the polymer cement mortar used in this study are shown in Table 5.

Table 5. Mix proportions of polymer cement mortar.

Type	Binder (Weight Ratio)			S (Weight Ratio)	SP** (B×%)	W/B* (%)	Defoamer/Polymer (%)
	C	SF	P***				
Control	1.0	-	-	2.45	0.5	54.0	-
AC3	0.9	0.5	0.5	2.45	0.5	50.0	2.0
DMAC	0.9	0.5	0.5	2.45	0.5	50.0	2.0
PMAC	0.9	0.5	0.5	2.45	0.5	50.0	2.0

B*: C + SF + P; SP**: Super Plasticizers; P***: Polymer.

3.3. Experimental Method

3.3.1. Performance of Redispersible Powder Polymer

(1) Glass transition temperature

The thermal properties, specifically the glass transition temperature (Tg), of the polymers synthesized with the monomer ratios shown in Table 4 were measured. To measure Tg, a portion of the polymer film, which was dried in an oven, was sampled and scanned using differential scanning calorimetry (DSC) at a rate of 10 °C/min over a range of −50 °C to 50 °C. The theoretical calculation of Tg without experimental testing is shown in Equations (1)–(4):

$$T_{wt} = (T_{wt}1 + T_{wt}2 + T_{wt}3 + \ldots + T_{wt}n) \quad (1)$$

$$T_{gt} = (T_g1 + T_g2 + T_g3 + \ldots + T_gn) \quad (2)$$

$$T_g1, T_g2, T_g3, \ldots, T_gn = (K + T_{gm}) \quad (3)$$

$$T_{wt}/T_g = \{(T_{wt}1/T_g1) + (T_{wt}2/T_g2) + (T_{wt}3/T_g3) + \ldots + (T_{wt}n/T_gn)\} \quad (4)$$

where:

T_{wt}: Total weight of the monomer
T_{gt}: Total glass transition temperature (sum of the glass transition temperature of individual monomers and absolute temperature)
T_{gm}: Glass transition temperature of the monomers used as raw materials
K: Absolute temperature

(2) Tensile Strength

To evaluate the properties of the synthesized polymer, specimens were prepared by drying in an oven at 40 °C for 48 h. The tensile strength and elongation were measured according to KS M 3381, "Test Method for Strength of Glass Fiber Reinforced Plastics" [19]. Each powdered polymer was redispersed by diluting 20% in water, then molded on a glass plate and dried to form films. These films were cut into specimens of 10 mm × 30 mm and tested using a tensile-strength-measuring device.

(3) Average Particle Size

To analyze the particle size of the synthesized redispersible polymer, the average particle size of the powder polymer was measured using a particle-size analyzer.

(4) Microstructure Analysis

To observe the morphology of polymer films formed inside the cement paste, analyses were conducted using scanning electron microscopy (SEM) and energy dispersive X-ray spectroscopy (EDS).

3.3.2. Performance of Polymer Cement Mortar

(1) Setting Time

To determine the setting characteristics of the polymer cement mortar, the setting time of the mortar was measured according to KS F2436, "Test Method for Setting Time of Concrete by Penetration Resistance" [21].

(2) Flow and Air Content

To measure the flow and air content of the polymer cement mortar, the flow and air content of the mortar were kept constant. The flow of the mortar was measured using a flow table according to KS F 2476, "Test Method for Polymer Cement Mortar", [22] after preparing the mortar. The air content was measured according to KS L 3136, "Test Method for Measuring the Air Content of Hydraulic Cement Mortar" [23].

(3) Compressive Strength

To measure the compressive strength of the polymer cement mortar, 50 × 50 × 50 mm cube molds were used to prepare the specimens. After curing for 48 hours at a temperature of 20 ± 2 °C and relative humidity above 90%, the specimens were demolded and water-cured for 5 days at 20 ± 2 °C. Then, they were cured at 20 ± 2 °C and 60 ± 10% relative humidity for 21 days. The compressive strength was measured on days 3, 7, 28, and 56 according to the test method specified in KS L 5105 [24].

$$f_m = P/A \quad (5)$$

where:

f_m: Compressive Strength (Mpa)
P: Total maximum load (N)
A: Area of loaded surface (mm^2)

(4) Flexural Strength

To measure the flexural strength of the polymer cement mortar, 40 × 40 × 160 mm prismatic molds were used to prepare the specimens. After molding, the specimens were cured in the same manner as the compressive strength specimens. The flexural strength was measured on day 28 according to the test method specified in KS F 2476 [22].

$$S_f = 0.0028P \quad (6)$$

where:

S_f: Flexural Strength (Mpa)
P: Total maximum load (N)

(5) Bond Strength

To measure the bond strength of the polymer cement mortar, a base concrete specimen (600 × 600 × 100 mm) with a compressive strength of approximately 50 MPa was prepared. Mortar was applied to the specimen at a thickness of 5 mm. Bond strength was measured on days 7, 14, and 28 by attaching a 40 × 40 mm top tensile jig, following the bond strength test methods specified in KS F 4715 [25], JIS A 6909 [26], and JIS A 6910 [27] (thin coating materials).

$$S_t = P/A \quad (7)$$

where:

f_m: Bond Strength (Mpa)
P: Total maximum load (N)
A: Area of loaded specimen (mm^2)

(6) Volume Change

To measure the volume change of the polymer cement mortar, the length change of each polymer cement mortar was compared to that of standard cement mortar. A 25 × 25 × 285 mm prismatic mortar specimen for length change was prepared and cured in the same way as the compressive strength specimens. The length change was measured over 56 days at 20 ± 2 °C and 60 ± 10% relative humidity using a dial gauge method

according to KS F 2424, "Test Method for Length Change of Mortar and Concrete" [28] and calculated as per Equation (5).

$$Lt = \{(L_0 - L_n)/L_0\} \times 100 \quad (8)$$

where:

L_t: Length change rate (%)
L_0: Length of the mortar before immersion
L_n: Length of the mortar at n days of immersion

(7) Water Absorption

To evaluate the resistance of the polymer cement mortar to water absorption, a water absorption test was conducted in accordance with KS F 2476, "Test Method for Polymer Cement Mortar" [22].

The polymer cement mortar specimens were prepared based on each mix proportion and cured for 28 days. After curing, the specimens were dried in an oven at 80 ± 2 °C for 24 h. The initial weight of the dried specimens was measured, and the specimens were immersed in water at 20 ± 2 °C. The weight of the specimens was measured at 1, 3, 5, 9, 24, and 48 h of immersion. The water absorption rate was calculated using Equation (6).

$$W_a = \frac{W_1 - W_0}{W0} \times 100 \quad (9)$$

W_a: Water absorption rate (%)
W_1: Weight of the specimen at each immersion time (g)
W_2: Weight of the specimen before immersion (g)

4. Results of Experiments

In this study, redispersible powder polymers were synthesized based on the monomer ratio of AC3, which has a glass transition temperature of −11 °C. Two types of polymers were produced: one combined with a functional additive and another with modified protective colloid and polymerization method. The functional additive used was a defoamer, which aimed to prevent performance degradation caused by excessive entrained air in the redispersible powder polymer. Additionally, modified polyvinyl alcohol (PVOH) was used as the protective colloid, and the polymerization method was changed from the emulsion monomer dropping system to the monomer dropping system.

4.1. Physical Properties of Polymers

The redispersible powder polymers were analyzed for melting point, glass transition temperature (Tg), tensile strength, and particle-size distribution. The glass transition temperature was measured using differential scanning calorimetry (DSC), and the tensile strength and elongation were measured using a tensile strength tester (AGS-500G, Shimadzu, Kyoto, Japan). To analyze the particle size of PMAC and AC3, a particle-size analyzer was used to determine the average particle size of the powder polymers.

The physical properties of the polymers are presented in Table 6 and Figures 1–6. As the analysis results show, the theoretical Tg remained the same since there was no change in the monomer ratio. Additionally, the modification of the polymerization method and the use of a defoamer did not affect the glass transition temperature. The Tg values measured using DSC were approximately 10 °C higher than the theoretical Tg. This discrepancy is due to the fact that the theoretical Tg is calculated based on the inherent glass transition temperature of each monomer, which matches the measured value when the polymer is in its emulsion state. However, the presence of this anti-caking agent, which is applied onto the surface of the powdered polymer particles to prevent them from clumping and to ensure long-term preservation, causes the Tg of the redispersible powder resin to be higher

than the theoretical Tg when analyzed using DSC. Once redispersed, the polymer behaves according to its original Tg characteristics (18).

Table 6. Characteristics of polymer powder.

Category	AC3	DMAC	PMAC
Theoretical Tg (°C)	−11	−11	−11
Measured Tg (°C)	5.64	5.64	5.64
Tensile Strength of 20% Dispersion Film (MPa)	10.5	11.0	10.5
Elongation of 20% Dispersion Film (%)	150	150	150
Average Particle Size (nm)	831	-	290

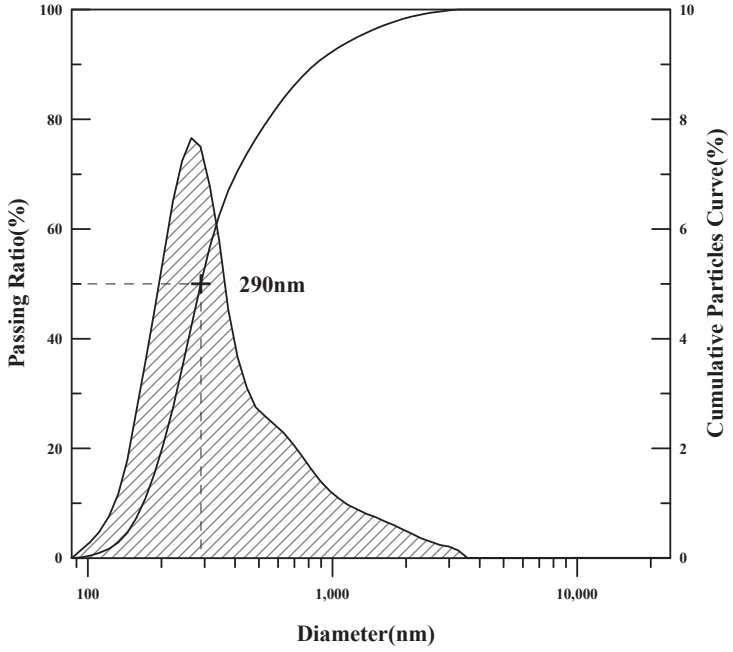

Figure 1. Particle-size analysis results (PMAC).

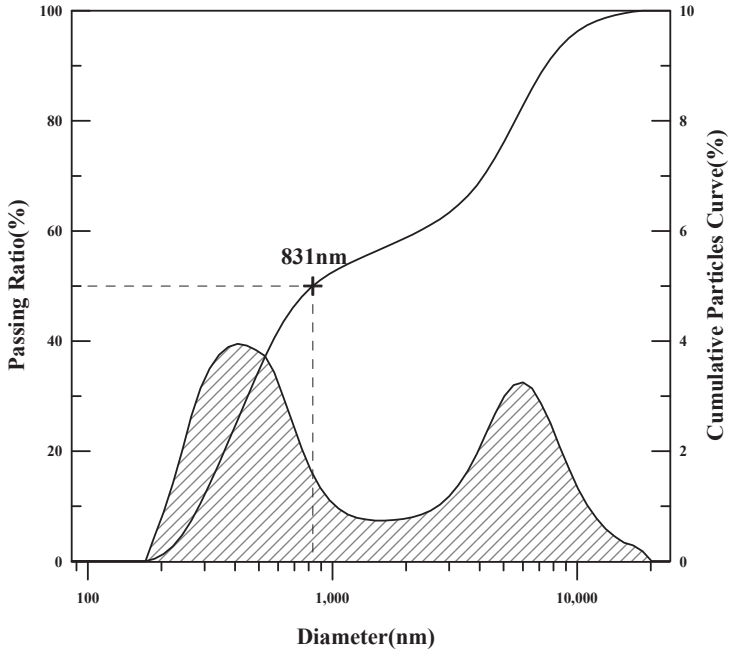

Figure 2. Particle-size analysis results (AC3).

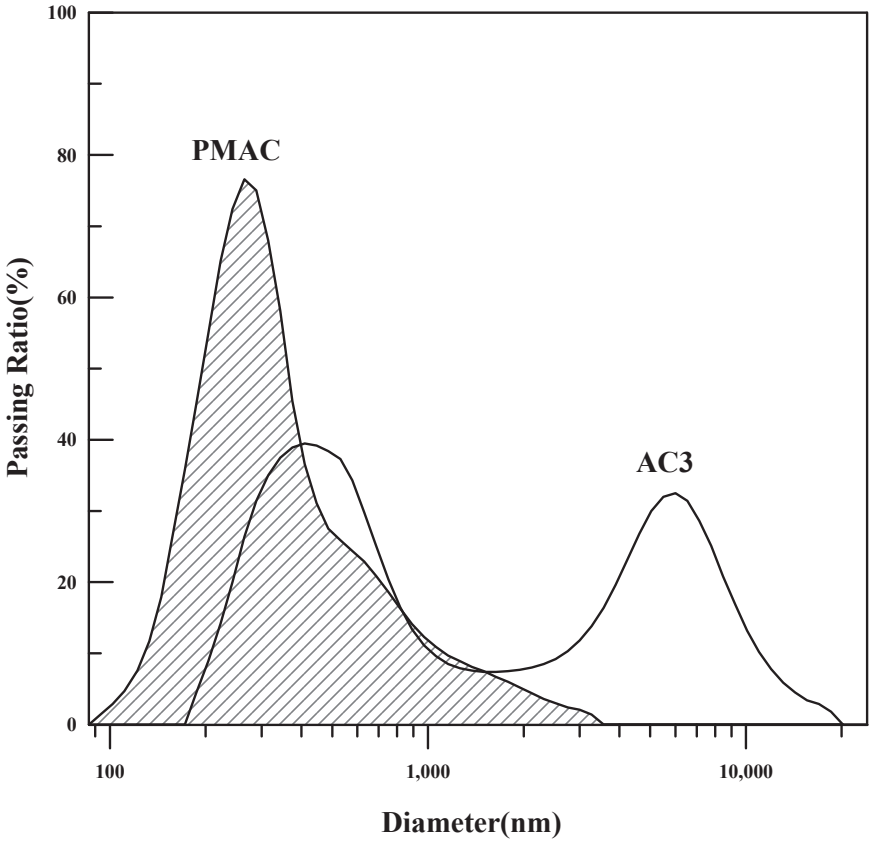

Figure 3. Changes in particle-size distribution due to polymerization method modification.

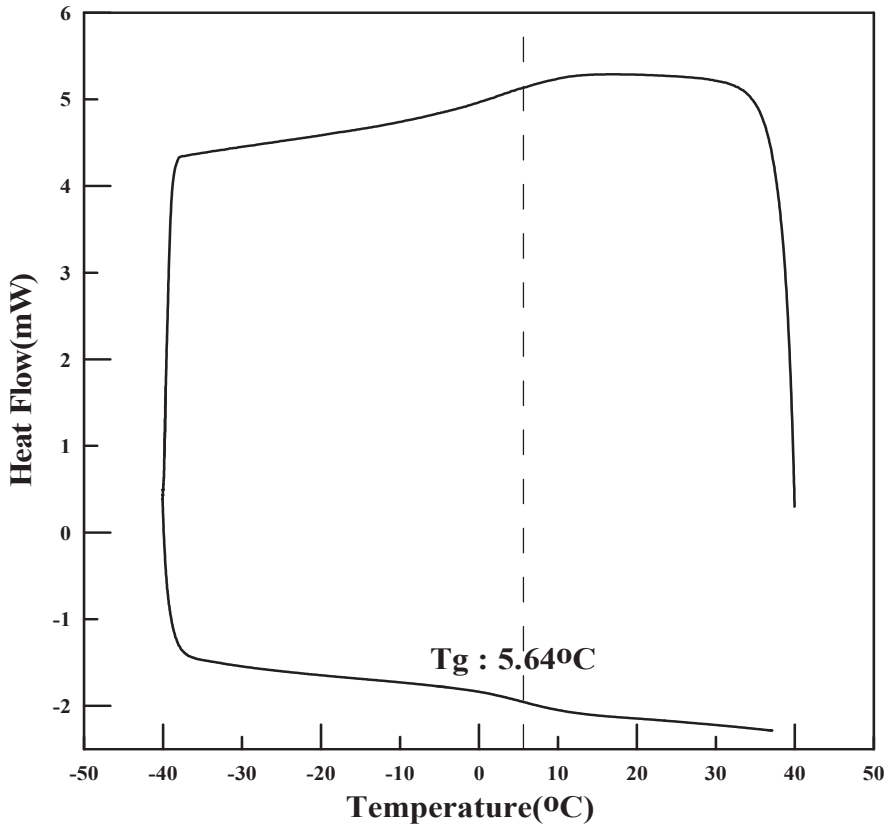

Figure 4. DSC measurement results (DMAC).

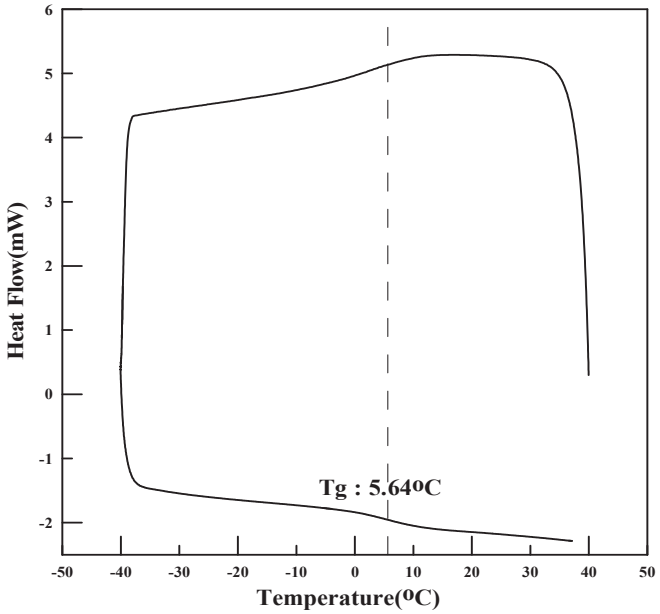

Figure 5. DSC measurement results (PMAC).

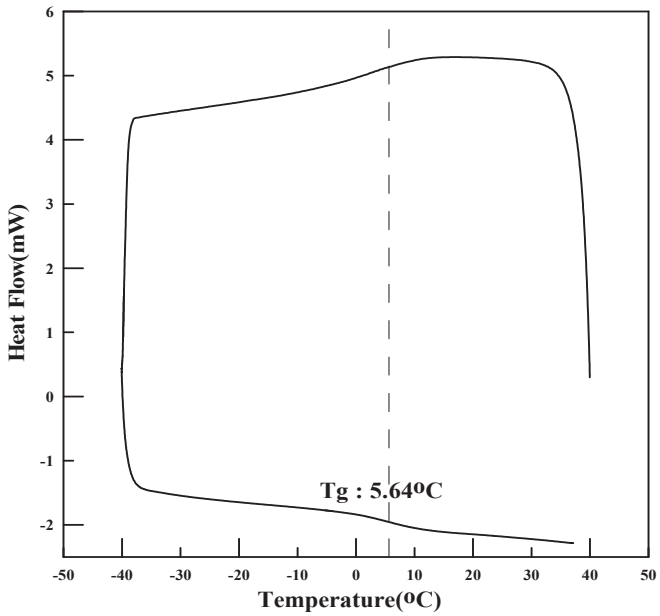

Figure 6. DSC measurement results (AC3).

In terms of tensile strength, DMAC indicated a slightly higher value. Furthermore, the film elongation of PMAC, which was synthesized using a modified polymerization method, was 46% higher.

The average particle-size analysis revealed that the particles of PMAC, synthesized with the modified polymerization method, were 35% smaller than those of AC3. Since DMAC was synthesized using the same polymerization method as AC3, the average particle size was the same. The increase in tensile strength and slight decrease in elongation for DMAC are likely due to the suppression of air bubbles within the polymer, which resulted in stronger films. In the case of PMAC, the significant reduction in average particle size is attributed to the characteristics of the monomer dropping system and the modified protective colloid.

These results suggest that the use of modified polymers could lead to improved performance in polymer cement mortars.

4.2. Physical Properties of Polymer Cement Mortar

4.2.1. Flowability and Setting Characteristics

(1) Flowability

Table 7 summarizes the air content and flow values for the polymer cement mortar and standard cement mortar, which were prepared using AC3, DMAC, and PMAC, organized by polymer type.

Table 7. Flow and air content of polymer cement mortar.

Category	Theoretical Tg (°C)	Defoamer/ Polymer (%)	W/B (%)	Flow (%)	Air Content (%)
Theoretical Tg (°C)	-	-	54.0	164	5.6
AC3	−11	2.0	50.0	160	5.2
DMAC	−11	2.0	50.0	154	4.6
PMA	−11	2.0	50.0	157	5.9

As shown in the results of the experiment, the air content of DMAC, which includes a defoamer, was reduced by approximately 10% compared to AC3 (before the addition of the defoamer). This indicates that the addition of a defoamer during the polymerization stage effectively controls entrained air. In this study, a defoamer was added after polymerization to maintain a consistent air content, but post-addition alone was not able to control the entrained air. Therefore, the addition of a defoamer during the polymerization stage is considered to be a more effective method. This is because controlling the entrained air reduces the pore volume inside the cement mortar and increases the number of fine pores, thereby improving compressive strength.

In the case of PMAC, compared to AC3, there was a slight decrease in flow and a small increase in air content. However, overall, PMAC had similar behavior to AC3.

Generally, an increase in air content tends to enhance flowability, but in polymer cement mortar using PMAC, the flowability did not increase despite the rise in air content. It is assumed that the particle size of PMAC, produced with a modified polymerization method, was smaller than that of AC3, leading to an increase in the specific surface area of the polymer in contact with water within the polymer cement mortar. In other words, the increase in fine particles resulted in higher viscosity of the polymer cement mortar, leading to reduced flowability.

(2) Setting Characteristics

To compare the setting characteristics of polymer cement mortar using DMAC, PMAC, and AC3 with ordinary cement mortar, the setting time of the mortar was measured according to KS F 2436, "Test Method for Setting Time of Concrete by Penetration Resistance" [21]. The results of the setting time test are summarized by polymer type in Figure 7.

As seen in Figure 7, polymer cement mortar tends to have a delayed setting time compared to ordinary cement mortar.

Additionally, there was no significant difference in the setting time between AC3, which used the original polymer, and PMAC, which used the modified polymer. This is likely because both polymers had the same glass transition temperature. However, DMAC showed a slightly faster initial setting compared to AC3 and PMAC. This trend is attributed to the defoamer added during the polymerization process, which controlled the entrained air in the polymer, leading to a reduction in air voids within the polymer cement mortar. The reduction in internal voids increased the penetration resistance, as the voids were reduced, hindering the penetration of the needle, thus resulting in higher penetration resistance values.

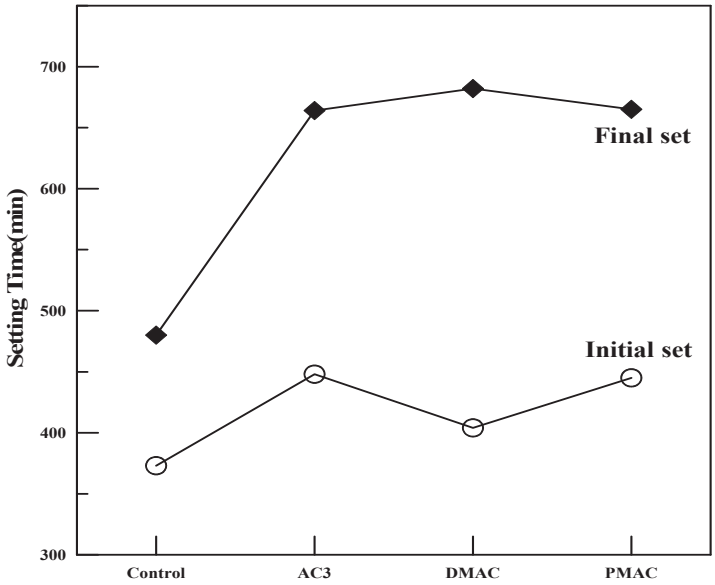

Figure 7. Changes in setting time of mortar due to polymer performance modifications.

In the case of PMAC, the initial setting time was delayed compared to AC3, but the final setting time occurred earlier, showing the same trend compared to DMAC. This can be explained by the smaller polymer particle size, which increases the number of polymer particles surrounding the cement particles, thereby hindering the hydration of water and cement, delaying the initial setting. Additionally, the faster redispersible rate of the finer polymer particles in water accelerated the formation of polymer films within the polymer cement mortar, increasing the penetration resistance and causing the final setting to occur earlier.

4.2.2. Strength Characteristics

(1) Compressive Strength

The compressive strength of polymer cement mortar and ordinary cement mortar prepared with the three types of powder polymers was measured at 3, 7, 28, and 56 days of curing. The results are summarized in Table 8.

Table 8. Compressive strength of polymer cement mortar.

Type	Compressive Strength (MPa)			
	3 Days	7 Days	28 Days	56 Days
Control	12.9 (100)	23.0 (100)	32.4 (100)	35.8 (100)
AC3	14.4 (112)	23.7 (103)	36.7 (113)	43.3 (121)
DMAC	20.2 (157)	33.2 (144)	44.1 (136)	47.6 (133)
PMAC	17.3 (134)	28.4 (123)	40.6 (125)	48.0 (134)

The compressive strength ratio of the polymer cement mortar relative to 100 for the control (ordinary cement mortar).

To evaluate the compressive strength development characteristics of polymer cement mortar using the three types of powder polymers, the compressive strength ratio of polymer cement mortar to cement mortar at each curing age is shown in Figure 8. As illustrated in Figure 8, both DMAC and PMAC had a 20–40% increase in compressive strength compared to AC3. Furthermore, compared to ordinary cement mortar, the compressive strength increased by approximately 30–50%, indicating that the use of modified polymers effectively enhances the strength of polymer cement mortar.

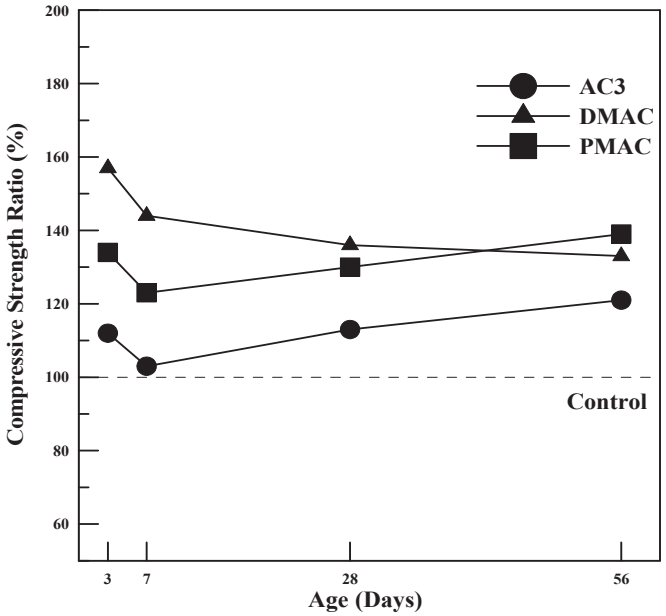

Figure 8. Compressive strength ratio of polymer cement mortar.

When comparing DMAC and PMAC, which utilize different methods for performance improvement, slightly different trends were observed. DMAC showed the best compressive strength results up to 28 days, while PMAC indicated the highest strength at 56 days. These results suggest that the method of controlling entrained air to improve performance is particularly effective in enhancing early strength. On the other hand, in the case of improving performance by modifying the emulsion polymerization method, the reduction in polymer particle size accelerated the formation of polymer films within the polymer cement mortar. This led to the creation of denser films, which suppressed moisture evaporation inside the mortar and allowed the hydration process to continue over an extended period. As a result, strength tends to increase over time with greater gains at longer curing ages compared to the early stages.

(2) Flexural Strength

Table 9 summarizes the flexural strength at 28 and 56 days for polymer cement mortars prepared using AC3, DMAC, and PMAC, along with the flexural strength ratio of polymer cement mortar compared to ordinary cement mortar at the same curing ages.

Table 9. Flexural strength of polymer cement mortar.

Type	Flexural Strength (MPa)		Flexural Strength Ratio (%)	
	28 Days	56 Days	28 Days	56 Days
Control	6.5	7.0	100	100
AC3	9.4	10.7	145	153
DMAC	11.3	11.9	174	170
PMAC	10.8	12.4	166	177

To examine the flexural strength development characteristics of polymer cement mortar before and after performance modification, the flexural strength ratio of the specimens at 28 and 56 days is summarized in Figure 9. As shown in Figure 9, DMAC and PMAC had a 15–20% increase in flexural strength at 28 days compared to AC3, and an 11–16% increase at 56 days. Notably, PMAC showed more than a 10% increase in flexural strength even after 28 days, indicating a continued improvement at longer curing ages.

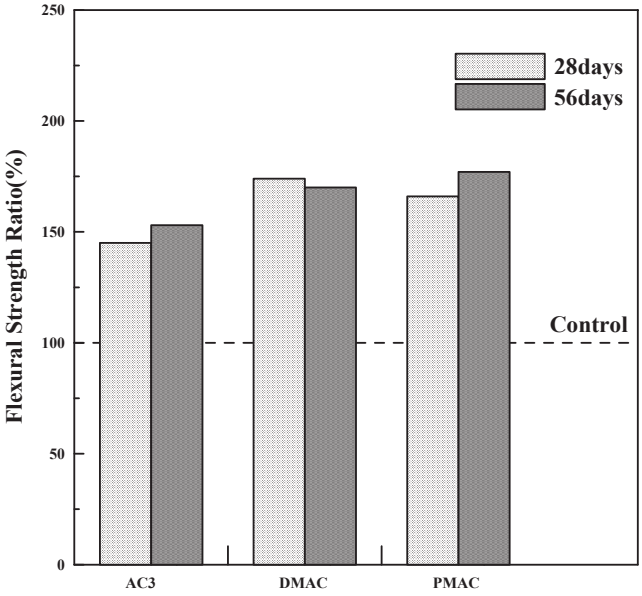

Figure 9. Flexural strength ratio of polymer cement mortar.

The reason for these results, similar to the compressive strength findings, is likely due to the control of entrained air, which reduces overall porosity while increasing fine pores. Additionally, the smaller polymer particle size likely enabled faster penetration between the aggregate and cement, enhancing the bond strength.

This is believed to be due to the infiltration of small polymer particles into the relatively large spaces within the cement matrix, resulting in a denser comatrix structure.

(3) Bond Strength

Figure 10 summarizes the bond strength measurements at 7, 14, and 28 days for polymer cement mortar prepared using AC3, DMAC, and PMAC, as well as ordinary cement mortar. As shown in Figure 10, the bond strength of all polymer cement mortars was 2 to 3 times higher than that of ordinary cement mortar, and bond strength increased with curing time. Additionally, DMAC and PMAC showed higher bond strength compared to AC3, with PMAC exhibiting a 20–50% increase in bond strength.

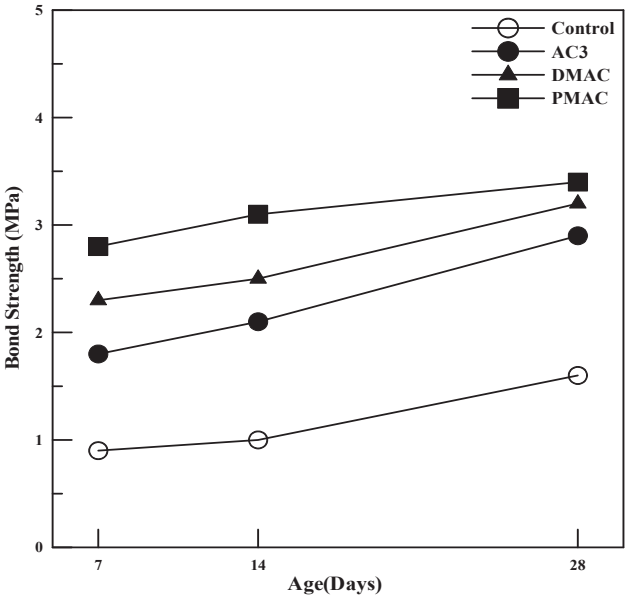

Figure 10. Bond strength of polymer cement mortar at different curing ages.

To evaluate the bond strength development characteristics of the improved polymer cement mortars, bond strength was measured up to 28 days, and the bond strength ratio of polymer cement mortar to ordinary cement mortar at each curing age is summarized in Figure 11. As seen in Figure 11, the bond strength ratio at 28 days tends to be lower compared to that at 14 days.

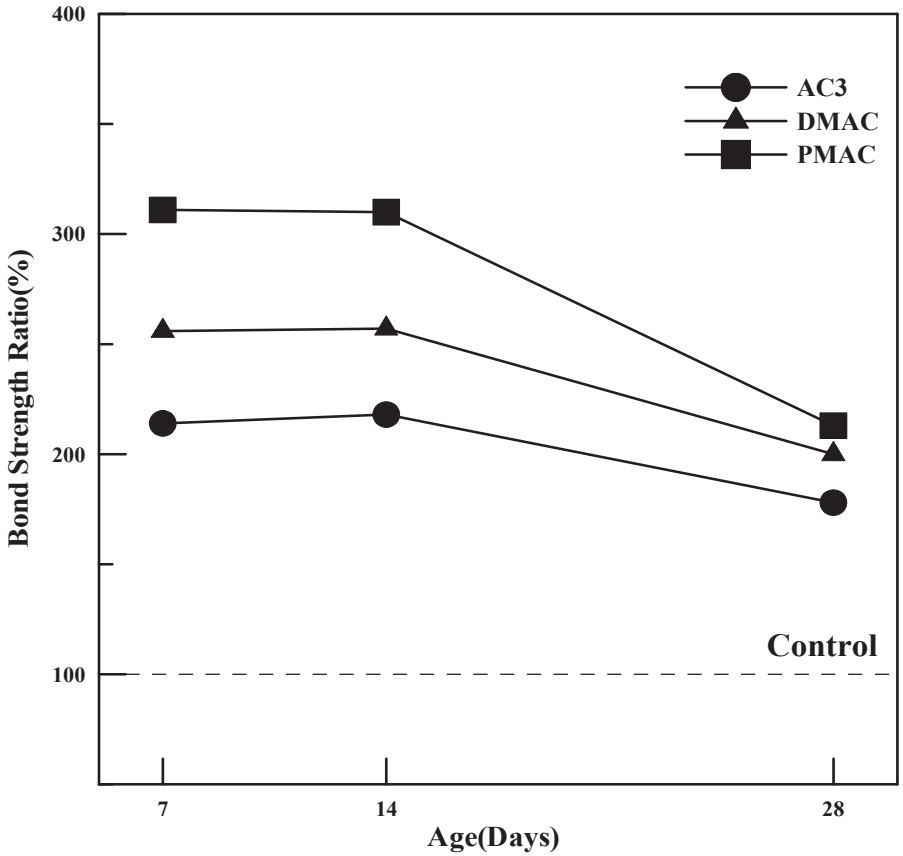

Figure 11. Bond strength ratio of polymer cement mortar.

The reason for this trend is that in ordinary cement mortar, the bond strength increases as the cement hydrates and bonds with the base concrete. Therefore, the bond strength is relatively low at early curing stages and tends to increase significantly at later stages as hydration progresses. In contrast, in polymer cement mortar, the bond is formed through the polymer film that connects the interface between the base concrete and the mortar in the early curing stages, resulting in a higher bond strength ratio at the early ages. In other words, the bond strength of cement mortar is enhanced by cement hydration, whereas, in polymer cement mortar, the polymer film serves as an adhesive.

In the case of DMAC, the reduction in internal voids due to the control of entrained air contributes to the improved bond strength. For PMAC, the smaller polymer particles quickly penetrate the interface between the base concrete and the polymer cement mortar, enhancing the bonding strength from the early curing stages.

4.2.3. Volume Change

To examine the volume change of polymer cement mortar with performance-improved polymers, polymer cement mortar was prepared using three types of redispersible powder polymers: AC3, DMAC, and PMAC. The length changes up to 56 days of curing were measured according to KS F 2424 [27], and the results are shown in Figure 12.

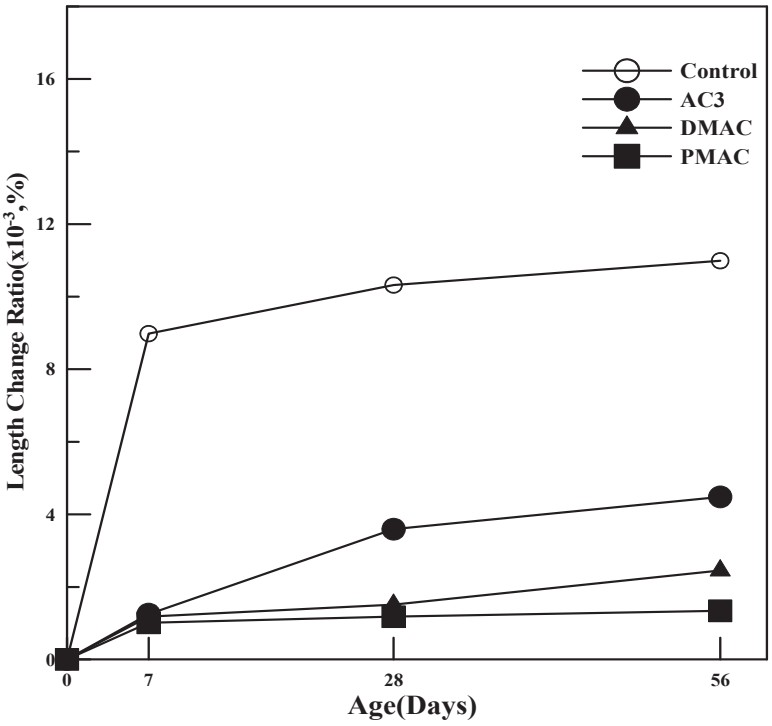

Figure 12. Length change rate of polymer cement mortar.

As shown in Figure 12, the mortars incorporating the three types of powder polymers demonstrated smaller length changes compared to ordinary cement mortar, indicating reduced volume change regardless of the polymer type used. Furthermore, DMAC and PMAC, which used performance-enhanced polymers, showed improved shrinkage compared to AC3, indicating the effectiveness of polymer performance improvement.

In particular, PMAC, which was improved through modification of the polymerization method, demonstrated the smallest length change rate, indicating stable shrinkage behavior. This is likely due to the smaller polymer particle size, which allows for the rapid and dense formation of an impermeable polymer film within the polymer cement mortar. This film effectively suppresses moisture evaporation, leading to reduced drying shrinkage compared to the pre-improved polymer.

4.3. Water Absorption

In general, the water absorption and permeability of polymer cement mortar and concrete tend to decrease as the polymer-to-cement ratio increases, rather than being impacted by the type of polymer used [29]. To achieve polymer cement mortar and concrete with good waterproofing performance, it is important to form a continuous polymer film to create a sealing effect or fill large voids with polymer particles.

In this study, to assess the impact of redispersible powder polymers on waterproofing performance, the water absorption rates of ordinary cement mortar and polymer cement mortars using AC3, DMAC, and PMAC were measured.

The results of the water absorption test for polymer cement mortars using AC3, DMAC, and PMAC, as well as ordinary cement mortar, are summarized in Figure 13. As shown in Figure 13, the 48 h water absorption rate of ordinary cement mortar was 8.4%, while AC3 showed a 72.6% improvement, DMAC a 30.9% improvement, and PMAC a 40.5% improvement, indicating enhanced waterproofing performance. These results are consistent with the findings of Song Hae-Ryong et al. [30], and the observed trend is likely due to the reduced water–binder ratio, which made the structure denser, and the formation of an impermeable polymer film that prevented water absorption.

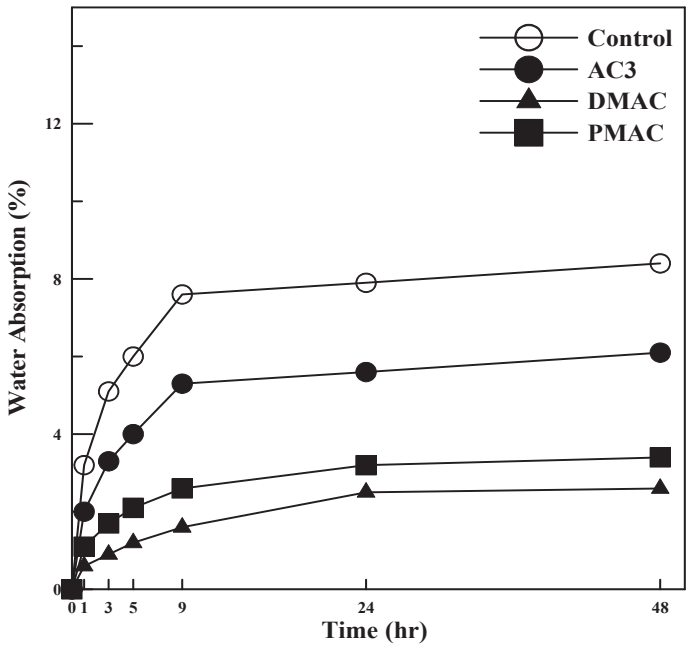

Figure 13. Water absorption test results.

In particular, DMAC and PMAC, which were modified for improved performance, demonstrated significantly enhanced waterproofing performance compared to the pre-improvement polymers, showing that the use of functional additives and changes to the emulsion polymerization method were effective in improving water absorption resistance.

4.4. Microstructure Analysis

A microstructure analysis was conducted using a scanning electron microscope (SEM) and energy dispersive X-ray spectroscopy (EDS) to observe the morphology of the polymer films formed inside the polymer cement paste by the performance-modified polymers.

Figures 14 and 15 show the SEM images and EDS analysis results for the DMAC polymer film, while Figures 16 and 17 show the SEM images and EDS analysis results for the PMAC polymer film. As seen in the figures, the performance-enhanced polymers penetrated the pores of the cement paste and formed films. The EDS analysis confirmed that the primary component of the formed polymer film is carbon (C).

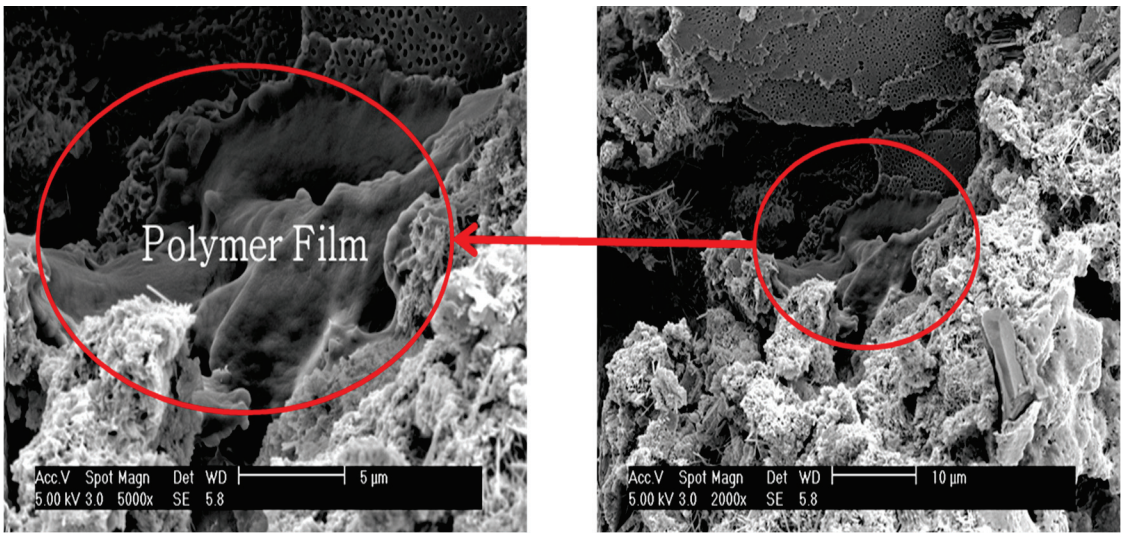

Figure 14. SEM image of polymer film (DMAC).

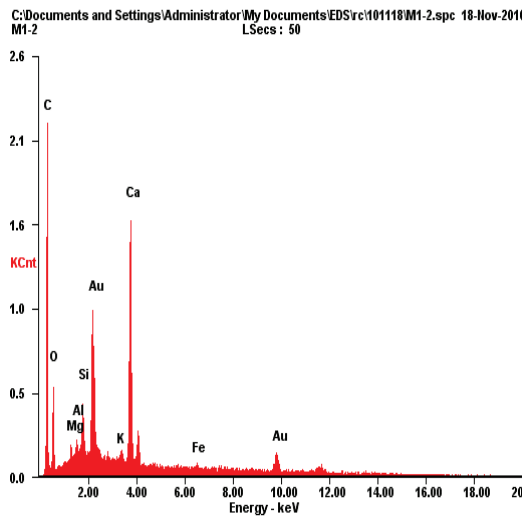

Element	Wt %	At %
C K	39.34	70.51
O K	11.66	15.68
MgK	0.53	0.47
AlK	0.41	0.32
SiK	1.59	1.22
K K	0.61	0.33
CaK	14.57	7.82
FeK	0.76	0.29
AuL	30.54	3.34

Figure 15. EDS analysis results of polymer film (DMAC).

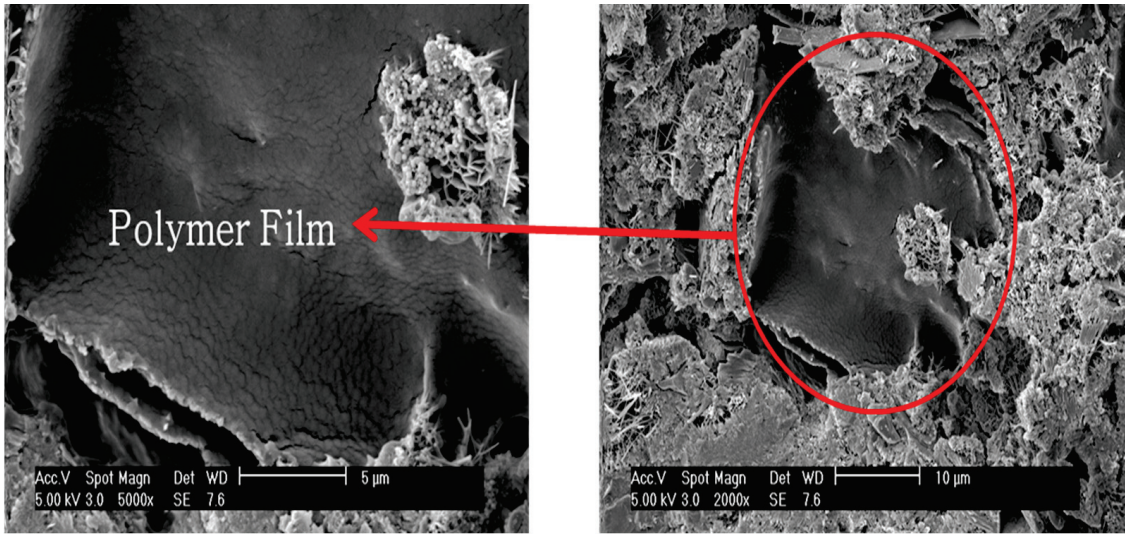

Figure 16. SEM image of polymer film (PMAC).

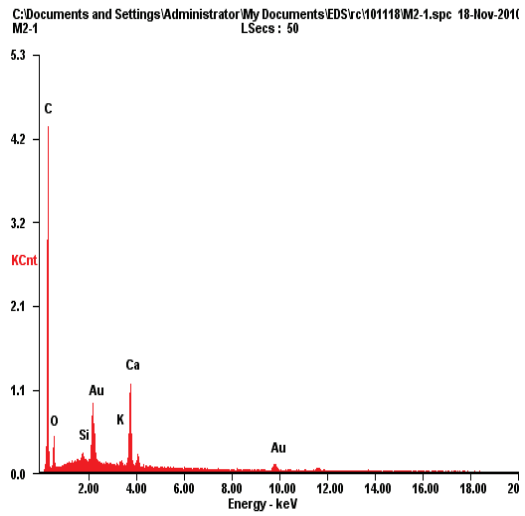

Element	Wt %	At %
C K	58.92	84.57
O K	8.30	8.94
SiK	0.43	0.26
K K	0.53	0.23
CaK	9.36	4.03
AuL	22.46	1.97

Figure 17. EDS analysis results of polymer film (PMAC).

The formed polymer film is considered to create a comatrix within the mortar, enhancing properties such as bond strength, flexural strength, and water absorption rate.

5. Conclusions

This study on cementitious materials using polymers modified through changes in the synthesis method and the addition of additives led to the following conclusions:

(1) In terms of tensile strength, DMAC showed higher values, while PMAC exhibited a 46% increase in elongation compared to AC3, and its average particle size decreased by approximately 35%.
(2) The compressive strength of the mortar increased by 20–40% for both DMAC and PMAC compared to AC3, and by 30–50% compared to ordinary cement mortar.
(3) The flexural strength of the mortar increased by 15–20% at 28 days for DMAC and PMAC compared to AC3, and by 11–16% at 56 days. In particular, PMAC showed more than a 10% improvement in flexural strength even after 28 days, indicating long-term strength improvement.
(4) The bond strength of all polymer cement mortars was 2–3 times higher than that of ordinary cement mortar, with bond strength increasing as the curing age progressed. DMAC and PMAC also showed improved bond strength compared to AC3, with PMAC exhibiting a 20–50% increase in strength.
(5) Compared to ordinary cement mortar, all mortars using the three types of powder polymers had smaller length change rates, indicating reduced volume change. Additionally, DMAC and PMAC, which used performance-modified polymers, showed improved shrinkage behavior compared to AC3, demonstrating the effectiveness of the polymer modifications.
(6) The water absorption test results showed that, compared to ordinary cement mortar, AC3 improved water absorption by 72.6%, DMAC by 30.9%, and PMAC by 40.5%, indicating enhanced waterproofing performance.

It was determined that the smaller the particle size of the polymer, the more effective its use, allowing for the production of a denser structure in polymer cement mortar by suppressing bubble formation. This is expected to enable effective use in repairing various types of concrete structures, such as buildings, wastewater treatment plants, bridges, dams, and roads.

Funding: This research was supported by a Korea Agency for Infrastructure Technology Advancement (KAIA) grant funded by the Korean government (MOLIT) (RS-2023-00250434).

Institution Review Board Statement: Not applicable.

Informed Consent Statement: Not applicable.

Data Availability Statement: The original contributions presented in the study are included in the article, further inquiries can be directed to the corresponding author.

Acknowledgments: The author would like to thank Youngjun Lee for their assistance in conducting the experimental research.

Conflicts of Interest: The author declares no conflict of interest.

References

1. Ohama, Y. Polymer-based Admixtures. *Cem. Concr. Compos.* **1998**, *20*, 189–212. [CrossRef]
2. Wagner, H.B. Methycellulose in Water Retentive Hydraulic Cements. *Ind. Eng. Chem.* **1960**, *52*, 233–234. [CrossRef]
3. Shibazaki, T. Properties of Masonry Cement Modified with Water Soluble Polymers. *Semento-Gijutsu-Nempo* **1964**, *17*, 94–199.
4. Shiyun, Z.; Zhiyuan, C. Properties of Latex Blends and Its Modified Cement Mortars. *Cem. Concr. Res.* **2002**, *32*, 1515–1524.
5. Sugita, J.; Takigi, S.; Mashino, M.; Sakai, E. Composite Mechanism of Polymer Modified Cement. Extended Abstracts. *Cem. Concr. Res.* **1933**, *25*, 127–135.
6. Geist, J.M.; Amagna, S.V.; Mellor, B.B. Improved Portland Cement Mortars with Polyvinyl Acetate Emulsions. *Ind. Eng. Chem.* **1953**, *45*, 759–769. [CrossRef]

7. Ohama, Y.; Ibe, H.; Mine, H.; Kato, K. Cement Mortars Modified by SBR Latexes with Variable Bound Styrene. *Rubber Chem. Technol.* **1964**, *37*, 558–569. [CrossRef]
8. Ohama, Y. Principle of Latex Modification and Some Typical Properties of Latex-Modified Mortars and Concretes. *ACI Mater. J.* **1987**, *84*, 511–518.
9. Schneider, S.I.; DeWacker, D.R.; Palmer, J.G. *Redispersible Polymer Powders for Tough, Flexible Cement Mortars, Polymer-Modified Hydraulic-Cement Mixtures, STP 1176*; American Society for Testing and Materials: Philadelphia, PA, USA, 1993; pp. 76–89.
10. Ohama, Y.; Shiroishida, K.; Miyake, T. *Thermal Resistance of Polymer Modified Mortars. Proceedings of the Twenty-Fifth Japan Congress on Materials Research*; The Society of Materials Science: Kyoto, Japan, 1982; pp. 234–238.
11. ACI Committee 548. *Guide for the Use of Polymers in Concrete*; American Concrete Institute: Detroit, MI, USA, 1992.
12. Zhao, S. Microstructure of Polymer Cement Concrete. Ph.D. Thesis, Delft University of Technology, Delft, The Netherlands, 1995.
13. Pintea, A.O.; Manea, D.L. New Types of Mortars Obtained by Admixing Traditional Mortars with Natural Polymers to Increase Physico-Mechanical Performances. *Procedia Manuf.* **2019**, *32*, 201–207. [CrossRef]
14. Pintea, A.O.; Nanea, D.L. Influence of Natural Organic Polymers upon the Mechanical Properties of Plaster Mortars. *Procedia Manuf.* **2020**, *46*, 165–172. [CrossRef]
15. Hwang, E.H.; Song, M.K.; Kim, Y.Y. Hot Water Resistance of Polymer Mortar Composites Depending on Unsaturated Polyester Resin Types. *Appl. Chem. Eng.* **2018**, *29*, 201–208.
16. Jang, K.Y.; Ryu, D.W. Residual Bond Strength of Polymer-modified Mortars Using Re-dispersible Polymer Powder at Elevated Temperature. *Concr. Inst.* **2019**, *31*, 339–346. [CrossRef]
17. You, K.; Hyung, W. Bond Strength and Tensile Strength of Polymer-Modified Mortar Using Styrene and Butyl Acrylate. *Polymer* **2014**, *38*, 820–826.
18. Kim, S.-S.; Lee, J.-B.; Cho, T.-J.; Hooton, R.D. Determination of Optimum Glass Transition Temperature of Acrylic Acid Ester Copolymer to Improve Performance of Cement Matrixes. *ACI Mater. J.* **2014**, *111*, 521–529.
19. *KS M 3381*; Testing Method for Tensile Properties of Glass Fiber Reinforced Plastics. Korean Standards Association: Seoul, Republic of Korea, 2009.
20. *KS L 5201*; Portland Cement. Korean Standards Association: Seoul, Republic of Korea, 2021.
21. *KS F 2436*; Standard Test Method for Setting Times of Concrete Mixture by Penetration Resistance. Korean Standards Association: Seoul, Republic of Korea, 2022.
22. *KS F 2476*; Standard Test Method for Polymer-Modified Cement Mortar. Korean Standards Association: Seoul, Republic of Korea, 2019.
23. *KS L 3136*; Standard Test Method for Air Content of Hydraulic Cement Mortar. Korean Standards Association: Seoul, Republic of Korea, 2021.
24. *KS L 5105*; Test Method for compressive Strength of Hydraulic Cement Mortar. Korean Standards Association: Seoul, Republic of Korea, 2022.
25. *KS F 4715*; Wall Coatings for Thin Textured Finishes. Korean Standards Association: Seoul, Republic of Korea, 2023.
26. *JIS A 6909*; Coating Materials for Textured Finishes of Buildings. Japanese Industrial Standards: Tokyo, Japan, 2014.
27. *JIS A 6910*; Test Certificate Impact Test of Multi-Layer Acrylic Paint. Japanese Industrial Standards: Tokyo, Japan, 1988.
28. *KS F 2424*; Standard Test Method for Length Change of Mortar and Concrete. Korean Standards Association: Seoul, Republic of Korea, 2020.
29. Ohama, Y. Study on Properties and Mix Proportioning of Polymer-Modified Mortars for Buildings. *Rep. Build. Res. Inst.* **1973**, *65*, 74. (In Japanese)
30. Song, H.-R.; Hyung, W.-G.; Kim, W.-K.; Soh, Y.-S. Effect of Glass Transition Temperature on Strength Properties of Polymer-Modified Mortar Using Polymer Dispersion. *Proc. Korea Concr. Inst. Annu. Conf.* **2001**, *13*, 1011–1016.

Disclaimer/Publisher's Note: The statements, opinions and data contained in all publications are solely those of the individual author(s) and contributor(s) and not of MDPI and/or the editor(s). MDPI and/or the editor(s) disclaim responsibility for any injury to people or property resulting from any ideas, methods, instructions or products referred to in the content.

materials

MDPI

Article

Performance Research and Engineering Application of Fiber-Reinforced Lightweight Aggregate Concrete

Feifei Jiang [1], Wencong Deng [2], Qi Wang [2], Jialei Wang [1,*] and Zhongyang Mao [3]

[1] School of Civil Engineering, Nantong Institute of Technology, Nantong 226000, China; 999620140019@just.edu.cn
[2] China State Construction Engineering (Macau) Co., Ltd., Macau 999078, China; deng_wencong@163.com (W.D.); wangq202312@163.com (Q.W.)
[3] College of Materials Science and Engineering, Nanjing Tech University, Nanjing 211800, China; mzy@njtech.edu.cn
* Correspondence: wangjl@nit.zju.edu.cn

Abstract: Low strength and low impact toughness are two of the main issues affecting the use of lightweight aggregate concrete in harsh cold environments. In this study, the strength of concrete was improved by adding high-strength fibers to bear tensile stress and organize crack propagation. Four sets of comparative experiments were designed with freeze–thaw cycles of 0, 50, 100, and 150 to study the mechanical properties of fiber-reinforced lightweight aggregate concrete under freeze–thaw conditions. A detailed study was conducted on the effects of freeze–thaw on the compressive strength, flexural strength, impact toughness, and microstructure of concrete with different fiber contents (3, 6, and 9 kg/m^3). The results show that for ordinary lightweight aggregate concrete, under the freeze–thaw cycle, the internal pore water of the concrete froze and generated expansion stress, resulting in tensile cracks inside the concrete. The cracks gradually accumulated and expanded, ultimately leading to cracking and damage of concrete structures. After 150 cycles, the strength loss rate exceeded 25%. When adding a reasonable amount of fiber (6 kg/m^3), the fiber took on the tensile stress and hindered the development of internal cracks, significantly enhancing the splitting tensile strength, flexural strength, and impact toughness of lightweight aggregate concrete. And the failure pattern of concrete was significantly improved. At the beginning of the freeze–thaw cycle, the internal tensile stress was less than the fiber tensile strength and the fiber–matrix bonding strength, and the strength reduction rate of the concrete was slow. Relying on the friction absorption capacity between the fiber and the matrix, the fiber used its own deformation to resist the tensile stress. In the late stage of the freeze–thaw cycle, due to the destruction of the fiber–matrix transition zone structure, the bond strength decreased, the crack resistance and toughening effect decreased, and the strength of the concrete decreased rapidly. Moreover, the reduction in impact toughness was greater than the compressive strength and flexural strength under static load.

Keywords: fiber; lightweight aggregate concrete; mechanical properties; microstructure; freeze–thaw

1. Introduction

In cold regions, building materials often face freeze–thaw cycles, leading to gradual deterioration of material properties and seriously affecting the service life and safety of structures [1,2]. As one of the most widely used building materials, concrete's frost resistance directly affects the durability of engineering structures [2–4]. However, traditional concrete has many internal pores and is prone to water absorption. After multiple freeze–thaw cycles, it is prone to cracking, which in turn affects its mechanical properties [5,6]. In recent years, lightweight aggregate concrete has been widely used in construction projects due to its light weight, good thermal insulation performance, and good frost resistance [7–10].

Lightweight aggregate concrete is a concrete material made by replacing ordinary aggregates with lightweight aggregates (such as ceramic particles, expanded shale, etc.), which

can effectively reduce the weight of structures and is widely used in construction projects, especially in super-high-rise buildings and cold regions [11–14]. Yoon has found that replacing natural stones with lightweight aggregates reduces the self-weight by 25–30%. This not only reduces the requirement for the bearing capacity of beams and columns, but also reduces the size of foundations and supporting components, reduces the use of steel and concrete, and ultimately achieves the goals of weight reduction and material conservation [15]. However, lightweight aggregate concrete also faces the challenge of freeze–thaw cycles, and its mechanical performance changes under multiple freeze–thaw cycles have not been fully studied. Moreover, Safwan has found that due to its porous nature, lightweight aggregate has a lower strength, and the aggregate is prone to cracking when subjected to tensile and shear forces. Once it cracks, the low strength of the aggregate makes it difficult to prevent crack propagation, resulting in a lower residual strength of the concrete after cracking [16]. Therefore, how to improve the strength of lightweight aggregate concrete is currently a research hotspot. Li [17] carried out rapid freeze–thaw tests on concrete specimens and analyzed the damage evolution law of concrete under uniaxial compression with different freeze–thaw damage degrees. It was found that the compression failure of specimens after freeze–thaw damage showed more obvious brittle characteristics. Therefore, how to improve the strength of lightweight aggregate concrete and improve the toughness after freeze–thaw damage is the current research hotspot.

Fiber-reinforcement technology is widely used in the research and engineering practice of concrete to improve its strength and toughness. Fibers can not only effectively improve the tensile strength and crack resistance of concrete, but also enhance its toughness and impact resistance. Guler's research found that adding 0.75% fibers increased the compressive strength, tensile strength, and flexural strength of concrete by 1.1%, 73.4%, and 47.9%, respectively [18]. However, freeze–thaw cycles can damage the bond strength between fibers and the matrix, reducing the performance of fiber-reinforced concrete [19–21]. Especially in cold regions, frequent freeze–thaw cycles can cause the expansion of microcracks inside concrete and the deterioration of the material structure, thereby reducing its bearing capacity and service life. Zeng found that after 150 freeze–thaw cycles, the strength of fiber-reinforced concrete decreased by 17–38% [22]. How to improve the frost resistance of fiber-reinforced concrete is currently a key issue restricting its promotion in cold regions of China. Dong [23] found that micropores in lightweight aggregate can provide "buffer space" during freeze–thaw cycles. These pores help to reduce the concentration of freeze–thaw stress and prevent cracks in concrete. In addition, lightweight aggregate concrete can absorb and store water, provide more uniform ice crystal distribution at low temperatures, reduce internal stress, and help to avoid water concentration in the same place. Therefore, lightweight aggregate can improve the frost resistance of concrete.

Through the above analysis, the replacement of natural aggregate with lightweight aggregate can reduce the self-weight of the structure and improve the frost resistance of concrete. Fiber can improve the toughness and strength of lightweight aggregate concrete. Considering the natural conditions of cold winter in cold regions of China, and the adverse factors of a lack of natural aggregate, this paper uses lightweight aggregate and plastic steel fiber to prepare fiber-reinforced lightweight aggregate concrete. Compared with steel fibers and basalt fibers commonly used in engineering, plastic steel fibers have the advantages of a large elastic modulus, high tensile strength, and non-rusting [24]. The effect of fiber on the mechanical properties and microstructure of lightweight aggregate concrete under freeze–thaw cycles was studied in detail. The research results are conducive to improving the durability of concrete structures in severe cold regions.

2. Materials and Methods

2.1. Materials

Cement: PO 42.5 ordinary Portland cement. The main chemical composition of the cement is shown in Table 1. Coarse aggregate: spherical fly ash ceramsite produced by Baotou Jingzheng Ceramsite Co., Ltd. (Baotou, China), with a particle size of 5–20 mm,

a bulk density of 0.97 g/cm^3, an apparent density of 1.76 g/cm^3, and a water absorption rate of 12.25%. Fine aggregate: river sand, bulk density was 1.58 g/cm^3, apparent density was 2.46 g/cm^3. Fiber: High-performance special-shaped plastic steel fiber produced by Zhejiang Ningbo Dacheng New Materials Co., Ltd. (Ningbo, China). The diameter was 1.2 mm, the length was 30 mm, the density was 0.97 g/cm^3, the elastic modulus was 9884 MPa, the tensile strength was 543 MPa, and the elongation was 14.1%. Water reducer: naphthalene-based B2 high-efficiency water reducer produced by Jiangsu Subote New Materials Co., Ltd. (Nanjing, China), with a water reduction rate of 20%.

Table 1. Chemical composition of cement (%).

CaO	SiO_2	Al_2O_3	Fe_2O_3	MgO	SO_3	K_2O	Loss	Total
61.12	22.24	6.40	3.08	2.20	1.88	0.47	1.53	98.92

2.2. Methods

(1) The mix proportion of fiber-reinforced lightweight aggregate concrete was designed with reference to the loose volume method in the Technical Specification for Lightweight Aggregate Concrete (JGJ51-2002) [25]. The specific mix proportions are shown in Table 2. Considering the strength and workability requirements of concrete, the fiber content was initially set to 0 kg/m^3, 3 kg/m^3, 6 kg/m^3, and 9 kg/m^3, respectively.

(2) Previous studies have shown that as the fiber content increases, the fibers tend to clump and become difficult to stir. The experiment used a small, forced concrete mixer for mixing, with mixing performed in stages. The lightweight aggregate was pre-wetted for 1 h before mixing. After the specimens were formed, they were cured in a standard curing room for 28 days before being taken out for freeze–thaw testing.

(3) In order to study the effect of freeze–thaw cycles on the mechanical properties of fiber-reinforced lightweight aggregate concrete, comparative tests were conducted with freeze–thaw cycles of 0, 50, 100, and 150 times, respectively, while keeping other test environments and material components unchanged. Compressive and flexural tests of fiber-reinforced lightweight aggregate concrete under different freeze–thaw cycles were carried out to study the influence of freeze–thaw cycles on the mechanical strength of fiber-reinforced lightweight aggregate concrete. The freeze–thaw test was conducted following the "Standard for Test Methods of Long-Term and Durability Performance of Ordinary Concrete" (GB/T50082-2009) [26]. After being cast, the concrete was cured for 24 days, then soaked in water at a temperature of (20 $\pm$ 2) °C for 4 days before the freeze–thaw testing began. Each freeze–thaw cycle was completed within 4 h, with the specimen's temperature controlled at a minimum of -17 ± 2 °C and a maximum of 5 ± 2 °C.

(4) Impact toughness can characterize the ability of concrete materials to absorb energy under dynamic loads. The higher the impact toughness of concrete, the stronger its ability to resist dynamic loads, and vice versa. The impact resistance test of fiber-reinforced lightweight aggregate concrete was carried out according to the concrete impact resistance test method, and the effects of the freeze–thaw cycles and fiber content on the impact toughness of lightweight aggregate concrete were analyzed. The test used a drop hammer impact tester, as shown in Figure 1, with a drop hammer mass of 3 kg and an impact height of 300 mm.

(5) A scanning electron microscope (SU3500, HITACHI, Tokyo, Japan) was used to scan the fiber–matrix interface transition zone. The effects of freeze–thaw cycles on the interface transition zone were compared to analyze the internal mechanism of changes in the macroscopic properties of concrete.

Table 2. Mix proportion of lightweight aggregate concrete (kg/m^3).

Cement	Sand	Lightweight Aggregate	Water Reducer	Water
440	764	598	6.6	140.8

Figure 1. Impact test equipment for fiber-reinforced lightweight aggregate concrete.

3. Results and Discussion

3.1. Effect of Fiber Content on Compressive Strength

The compression failure morphology of ordinary lightweight aggregate concrete is shown in Figure 2. There was a hoop effect between the test block and the pressure plate of the press, and the failure was manifested as two conical failures at the upper and lower apex angles. From the failure section, most of the cracks passed through the aggregate, the lightweight aggregate itself was damaged, and the stress on the aggregate reached its strength limit. It was very different from ordinary concrete under compression. When ordinary concrete was compressed and damaged, the aggregate was not damaged due to its high strength. The damage occurred in the weaker matrix and interface. This shows that the self-strength of the lightweight aggregate had a great influence on the compressive strength of the fiber-reinforced lightweight aggregate concrete. The strength was further reduced after freezing and thawing, and large pieces of concrete peeled off on the side.

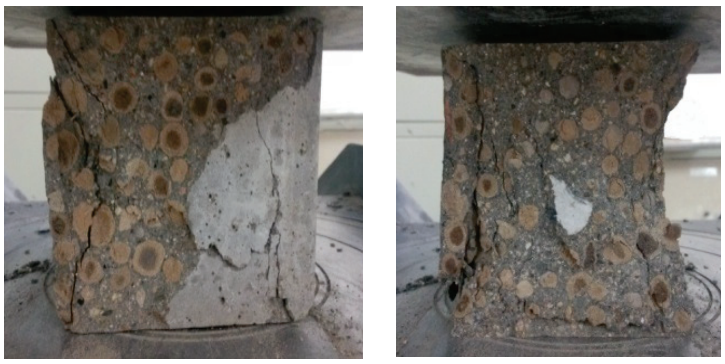

(**a**) No freeze–thaw (**b**) Freeze–thaw cycles 150 times

Figure 2. Compressive failure form of ordinary lightweight aggregate concrete.

It can be seen from Figure 3 that after adding fibers, the surface of the unfrozen–thawed test block was smooth, and there was no exposure of fibers and aggregates. There was a crack at the damaged area with a larger width, but no large-scale whole-piece falling off occurred. Due to the restraining effect of the fibers on the cracks, the fiber-reinforced lightweight aggregate concrete test block showed a certain ductility when it was destroyed, and the integrity was good after destruction. The surface of the test block after the freeze–thaw cycle

was rough and uneven, some fibers and aggregates were exposed, and there was a whole-piece falling off on the side. This is mainly due to the fact that after multiple freeze–thaw cycles, frost heave cracks were generated inside the test block, and there were large initial defects [27,28]. After being compressed, the internal cracks further expanded and gradually penetrated to the surface, causing overall peeling.

(**a**) No freeze–thaw (**b**) Freeze–thaw cycles 150 times

Figure 3. Failure form of fiber-reinforced lightweight aggregate concrete under compression.

Figure 4 shows the measured compressive strength of the concrete. The strength of the concrete showed a trend of first decreasing, then increasing, and then decreasing again with the increase in the fiber content. After freeze–thaw, the strength of each specimen decreased to varying degrees. The main reasons may be as follows: (1) Concrete with a content of 3 kg/m^3 has too few fibers, which cannot effectively bear the tensile stress caused by compression and have little effect on crack limitation. At the same time, the addition of fibers introduces a weak interface between the fibers and matrix, which is not as dense as ordinary concrete structures, resulting in lower strength compared to ordinary concrete [29]. (2) When the dosage is 9 kg/m^3, due to too many fibers, the weak surface of the fibers in contact with the cement matrix increases, and the fibers are not fully wrapped by the cement slurry, resulting in more defects and a decrease in the bond strength between the fibers and the cement slurry, leading to a decrease in the concrete strength [30]. (3) The concrete fiber content with a dosage of 6 kg/m^3 is moderate, and the strength is significantly improved. The fibers suppress the development of cracks without introducing too much of a weak interface with the mortar.

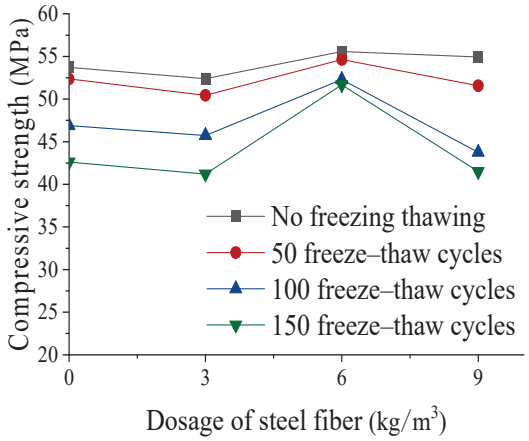

Figure 4. Effect of fiber content on compressive strength.

3.2. Effect of Freeze–Thaw Cycles on Compressive Strength

The effects of freeze–thaw cycles on the compressive strength and strength loss rate are shown in Figure 5. As the number of freeze–thaw cycles continued to increase, the

concrete strength loss rate continued to increase, and the compressive strength gradually decreased. In the early stage of the freeze–thaw cycle (0 to 50 times), the compressive strength decreased slowly, and the strength loss rate was controlled within 2–6%. In the late stage of the freeze–thaw cycles (100 to 150 times), the compressive strength decreased rapidly, and the strength loss rate could reach as high as 24.5%. This is because during the freeze–thaw cycle, the pore water inside the concrete freezes and produces expansion stress, resulting in tensile cracks inside the concrete. Under the action of repeated freeze–thaw cycles, the cracks gradually accumulate and expand, eventually leading to the destruction of the concrete structure and a reduction in the compressive strength.

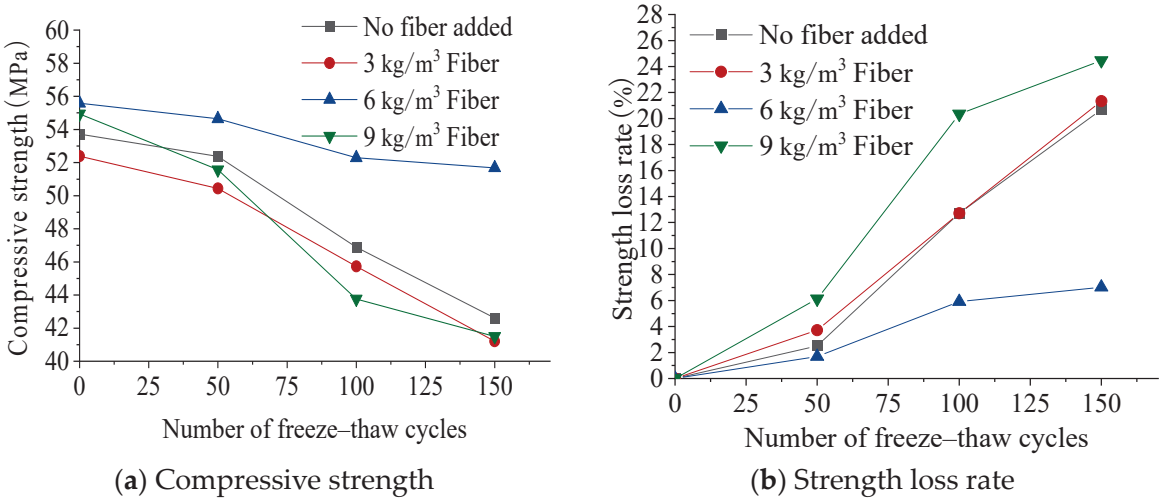

(**a**) Compressive strength (**b**) Strength loss rate

Figure 5. Effect of freeze–thaw cycles on concrete compressive strength and strength loss rate.

As can be seen from Figure 5b, the compressive strength loss rate of the lightweight aggregate concrete with a fiber content of 6 kg/m^3 was the smallest, which was 13.7% lower than that of ordinary concrete. The strength reduction rate was significantly lower than that of the other fiber-reinforced lightweight aggregate concretes. This was because the reasonable fiber content enabled the slurry to fully wrap the fibers, resulting in a high fiber–matrix interface bonding strength, a dense structure, and few defects.

3.3. Effect of Freeze–Thaw Cycles on Splitting Tensile Strength

Figure 6 shows the influence of freeze–thaw cycles on the splitting tensile strength. When the fiber content was low (0 kg/m^3, 3 kg/m^3, and 6 kg/m^3), the splitting tensile strength of the concrete decreased relatively slowly in the early stage of freeze–thaw, and gradually accelerated with the increase in freeze–thaw cycles in the later stage. When the fiber content increased to 9 kg/m^3, the loss rate of the splitting tensile strength was much higher than that of other concretes. This is because adding too much fiber increased the interface between the fiber and the cement matrix, and the damage to the interface area caused by freeze–thaw action also increased, resulting in a decrease in the bond strength between the fiber and the matrix. When the concrete was subjected to splitting load, the fiber with a low bond strength with the matrix would not be able to effectively disperse the stress concentration at the tip of the crack, and the fiber that can continue to bear tensile stress was greatly reduced, thereby reducing the splitting tensile strength of the concrete. The concrete with a fiber content of 6 kg/m^3 had the smallest strength loss rate due to its reasonable content.

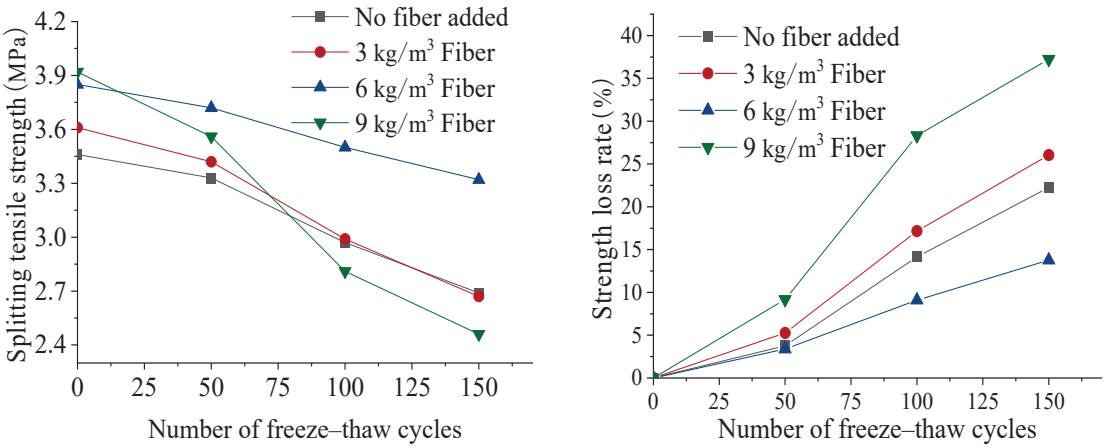

(**a**) Splitting tensile strength (**b**) Strength loss rate

Figure 6. Effect of freeze–thaw cycles on splitting tensile strength and strength loss rate.

3.4. Effect of Freeze–Thaw Cycles on Flexural Strength

Flexural strength is an important indicator of concrete's tensile properties. The fiber-reinforced lightweight aggregate concrete was subjected to flexural tests using the three-point loading method, and the failure morphology is shown in Figure 7. Comparison with Figure 7 shows that the lightweight aggregate concrete without fibers fractured brittlely under load. When the first main crack appeared on the lower surface of the specimen, the cracks rapidly expanded upward, causing the specimen to break suddenly. Lightweight aggregate concrete with 6 kg/m^3 fiber showed good ductility characteristics under load. When cracks appeared on the surface of the specimen, the cracks slowly extended with the increase in load. When the specimen was destroyed, the crack width was small due to the constraint of the fiber, and the cracking changed from a main crack to parallel fine cracks. Finally, the specimen remained as a whole when it was destroyed.

(**a**) Unmixed fiber (**b**) 6 kg/m^3 fiber

Figure 7. Flexural failure morphology of lightweight aggregate concrete.

Figure 8 shows the change in flexural strength. As can be seen from Figure 8a, the flexural strength of the concrete gradually decreased with the increase in the number of freeze–thaw cycles. The rate of decrease was slow in the early stage of the freeze–thaw cycle; the flexural strength decreased rapidly in the later stage. Because the elastic modulus of the fiber was much smaller than that of the concrete matrix, the fiber and the matrix could not deform synchronously. When the load exceeded the tensile strength of the matrix, the matrix cracked and partially stopped working. This part of the load was borne by the fiber. At this time, the concrete relied on the tensile strength of the fiber itself and the friction between the fiber and the matrix to consume energy at the same time. When the tensile stress was higher than the bonding strength between the fiber and matrix, the fiber would slip or even pull out. According to the above mechanism, the bonding strength

between the fiber and the matrix had a great influence on the overall flexural strength of the concrete, and repeated freeze–thaw cycles greatly weakened the bonding strength, resulting in a decrease in the flexural strength.

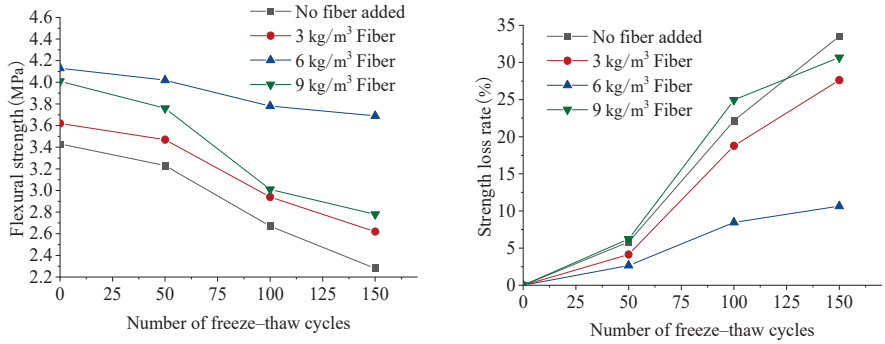

(**a**) Flexural strength (**b**) Strength loss rate

Figure 8. Effect of freeze–thaw cycles on flexural strength.

As can be seen from Figure 8b, with the increase in freeze–thaw cycles, the flexural strength loss rate of lightweight aggregate concrete with a fiber content of 6 kg/m^3 is 22.9% lower than that of ordinary concrete and was also much lower than that of concrete with a content of 3 kg/m^3 and 9 kg/m^3. This was because under repeated freeze–thaw cycles, a large fiber content would cause the interface defects to gradually increase with the accumulation of freeze–thaw damage, while fewer fibers could not effectively share the tensile stress. In addition, freeze–thaw cycles would greatly reduce the bonding strength between the fiber and the matrix, leading to accelerated damage to the flexural strength of fiber-reinforced lightweight aggregate concrete.

3.5. Effect of Freeze–Thaw Cycles on Impact Toughness

The effect of freeze–thaw cycles on the initial crack energy consumption is shown in Figure 9. The initial crack energy consumption of lightweight aggregate concrete without freeze–thaw cycles increased with the increase in the fiber content, mainly because the initial crack in the concrete was related to the number of fibers distributed horizontally in the bottom tensile zone, that is, the bottom fibers could effectively offset part of the impact energy consumption [31]. With the increase in freeze–thaw cycles, the impact toughness of the fiber-reinforced coarse aggregate concrete decreased rapidly, and the influence of freeze–thaw damage on the impact toughness was greater than the compressive strength and flexural strength under static load. Before freeze–thaw, the initial crack energy of the fiber concrete (6 kg/m^3) was 76% greater than that of ordinary concrete, but after the cycle, it was only 49% greater. This was mainly because the freeze–thaw cycle destroyed the bonding strength of the fiber–matrix interface and reduced the ability of the fiber to withstand impact loads.

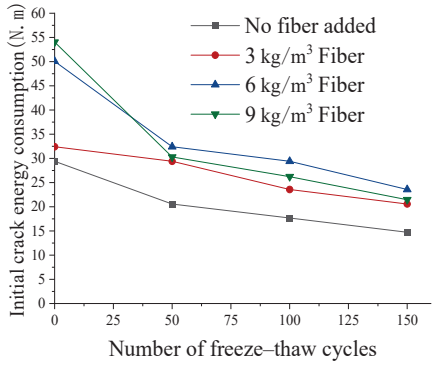

Figure 9. Effect of freeze–thaw cycle on initial crack energy consumption.

The destruction energy consumption of different specimens is shown in Figure 10. The damage energy consumption of lightweight aggregate concrete increased with the increase in fiber content. The addition of fiber significantly improved the energy consumption ability of concrete to resist damage. The damage energy consumption of lightweight aggregate concrete without fiber and with a fiber content of 3 kg/m^3 is much lower than that of lightweight aggregate concrete with a fiber content of 6 kg/m^3 and 9 kg/m^3. With the increase in freeze–thaw cycles, the destructive energy consumption gradually decreased. Freeze–thaw had a greater weakening effect on the destructive energy consumption of concrete with a higher fiber content. However, lightweight aggregate concrete with fiber added still had a stronger ability to offset the impact energy consumption after freeze–thaw cycles than that without fiber.

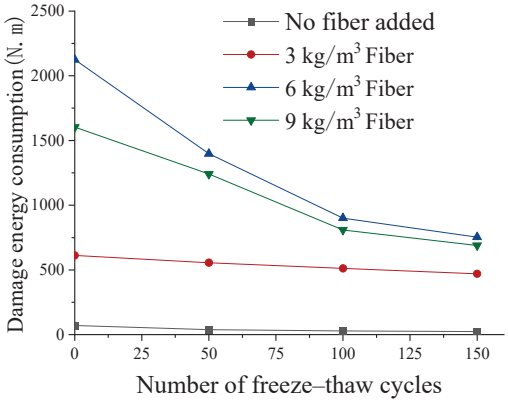

Figure 10. Effect of freeze–thaw cycles on damage energy consumption.

3.6. Microstructure of Fiber–Matrix Interface Transition Zone

The fiber–matrix interface of fiber-reinforced lightweight aggregate concrete before freeze–thaw is shown in Figure 11. There was a clear boundary between the fiber and the matrix, some pores existed in the interface transition zone, many coarse needle-like and columnar calcium aluminates spanned between the C-S-H gels, and a large number of gelled particles and some coarse crystals accumulated on the fiber surface. The fibers were different from lightweight aggregates, as the surface of the fibers was hydrophobic. Due to the micro-bleeding effect, water was concentrated on the fiber surface, which resulted in a thicker water film layer. This reduced the ion concentration and reduced the formation of hydration products on the fiber surface, affecting the bonding strength between the fiber and cement matrix. The fiber–matrix interface transition zone is mainly composed of three parts. The first part is a double-layer membrane, which mainly contains $Ca(OH)_2$ crystals and hydrated calcium silicate gel. The second part is the $Ca(OH)_2$-rich area. There are some pores inside this part, which make the structure not dense, resulting in a weak bond between the fiber and the matrix. The third part is the porous area, which has a large porosity and is another weak link in the interface layer. Therefore, when the fiber content is too large (9 kg/m^3), a large number of weak fiber–matrix interfaces were brought into the composite system, which reduced the strength.

The fiber–matrix interface of fiber-reinforced lightweight aggregate concrete after 150 freeze–thaw cycles is shown in Figure 12. Due to freeze–thaw, ettringite and CSH gel broke and separated in the fiber–matrix interface area, resulting in wider gaps, which reduced the integrity of the fiber–matrix interface and ultimately resulted in the fiber being unable to effectively exert its reinforcement, toughening, and crack resistance capabilities. Therefore, the tensile strength, flexural strength, and impact toughness were reduced due to the effects of freeze–thaw. According to osmotic pressure theory, the solution in the macropores in the transition zone froze first, and the ion concentration in the solution increased, forming a concentration difference with the nearby small pores of the cement matrix. Under the action of this concentration difference, the pore solution in the smaller pores in the matrix migrated to the macropores in the interface transition zone, thereby

generating osmotic pressure, which led to the partial rupture of the columnar calcium aluminate and CSH gel that acted as a bridge in the interface transition zone, resulting in a decrease in the bonding strength between the fiber and the matrix, and ultimately leading to the attenuation of the mechanical properties of the concrete. At the same time, due to the inherent microcracks in the concrete caused by freezing and thawing, the initial strength of the concrete was reduced. In the subsequent load test, the cracks would further expand under the load and cause structural damage. Therefore, the performance of concrete is influenced by both the fiber content and freeze–thaw cycles. The decline rate of the compressive strength, splitting compressive strength, and flexural strength of concrete with a different fiber content and different freeze–thaw time are shown in Table 3.

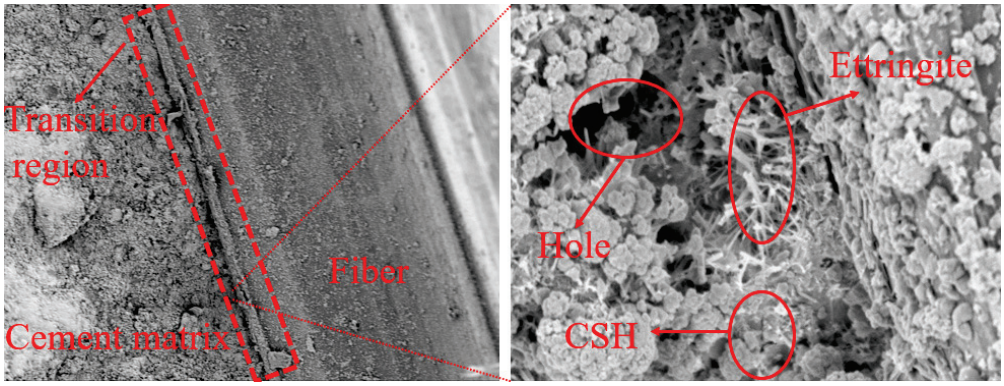

Figure 11. Microstructure of the transition zone between fibers and matrix interface before freeze–thaw cycles.

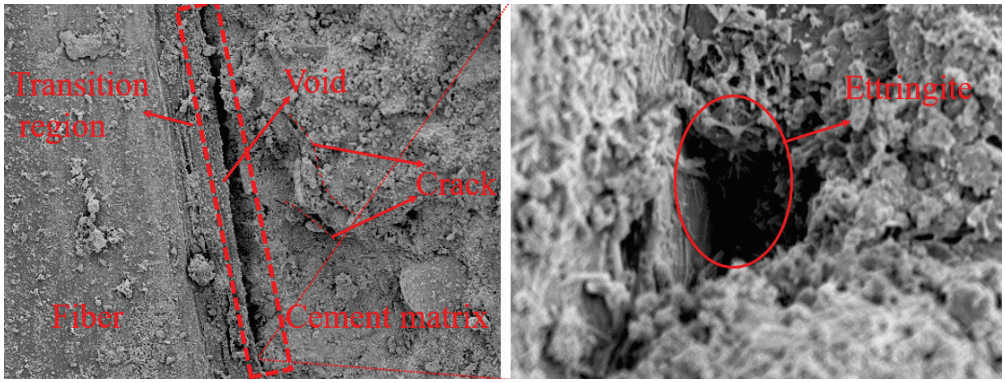

Figure 12. Microstructure of the transition zone between fibers and matrix interface after freeze–thaw cycles.

Table 3. Decline rate of mechanical properties after freeze–thaw cycle.

Mechanical Property	Freeze–Thaw	0 kg/m^3 Fiber	3 kg/m^3 Fiber	6 kg/m^3 Fiber	9 kg/m^3 Fiber
Compressive Strength	50	2.51%	3.72%	1.69%	6.13%
	100	12.71%	12.71%	5.92%	20.35%
	150	20.68%	21.34%	7.02%	24.46%
Tensile Strength	50	3.76%	5.26%	3.38%	9.18%
	100	14.16%	17.17%	9.09%	28.32%
	150	22.25%	26.04%	13.77%	37.24%
Flexural Strength	50	5.83%	4.14%	2.66%	6.23%
	100	22.16%	18.78%	8.47%	24.94%
	150	33.53%	27.62%	10.65%	30.67%

Through the above analysis and comparison with the literature [32], it can be found that the freeze–thaw damage of fiber-reinforced lightweight aggregate concrete is obviously different from that of ordinary concrete. During freezing and thawing, the water in the pores of ordinary concrete freezes and expands, forming an ice wedge effect, which leads to the continuous expansion of pores and cracks, reducing the strength of the matrix. For fiber-reinforced lightweight aggregate concrete, freeze–thaw not only affects the strength of the matrix, but also leads to the deterioration of the microstructure of the fiber–matrix transition zone, which directly leads to the reduction in the bond force between the fiber and the matrix. With the increase in freeze–thaw cycles, the "bridging" effect of the fiber continues to weaken, and the fiber is difficult to effectively prevent the expansion of cracks, resulting in a significant decline in the tensile strength and flexural strength of the concrete. The damage of these microstructures can well explain why the macro mechanical properties are reduced. These macroscopic performance deteriorations are directly related to the damage of the microstructure in the transition zone.

3.7. Engineering Application

The construction project was a super-high-rise building in China. Six 149.90 m residential buildings with 50 floors and a 1-floor basement were built in the project. The project covered an area of about 20,000 m^2 and a building area of about 330,000 $m^{2.}$ The project was located in the reclamation area, with loose soil and a low bearing capacity, so the project adopted a high-strength prestressed concrete pipe pile foundation, with a diameter of 600 mm and a depth of about 43 m. At the same time, in order to reduce the self-weight of the structure, fiber-reinforced lightweight aggregate concrete was used in the backfilling works such as sunken toilets.

The following advantages of fiber-reinforced lightweight aggregate concrete are mainly considered:

(1) Light weight

The project is located in the reclamation area. The soil in the reclamation area is relatively soft and the foundation condition is poor. The use of traditional heavy filling materials will increase the self-weight of buildings, thus increasing the risk of foundation settlement. Lightweight aggregate concrete has the characteristics of light weight, which can effectively reduce the structural load of the building, reduce the uneven settlement of the foundation, and improve the stability of the building.

(2) Good thermal insulation performance

The thermal conductivity of lightweight aggregate concrete is small, which can effectively reduce the heat loss, reduce building energy consumption, and improve the comfort of residents in winter. At the same time, it can also avoid the freeze–thaw damage of concrete in winter.

(3) Good crack resistance and impermeability

Fiber can effectively improve the crack resistance of lightweight aggregate concrete and avoid shrinkage cracking of concrete. The toilet is a high-humidity environment, and there is often water vapor and drops. Fiber-reinforced lightweight aggregate concrete can effectively prevent the penetration and absorption of water, keep the interior of the toilet dry, and prevent the breeding of mold.

In the backfilling construction of the sunken bathroom, preparatory work was first completed, including cleaning the base layer and preparing materials and equipment for the fiber-reinforced lightweight aggregate concrete. During base layer cleaning, it was ensured that there was no debris or standing water, and waterproofing treatment was conducted if necessary. Next, formwork and partitioning were carried out, with templates set in the construction area to ensure concrete molding quality, and pipeline positions were reserved where needed. The concrete was mixed according to the proportions in Table 2, with fibers added in two stages and mixed thoroughly to ensure an even distribution of

fibers. After pouring, it was compacted with a vibrator, with special attention paid to the compactness of corners. After leveling the surface, wet curing was performed, keeping the concrete surface moist for about seven days to ensure adequate strength development. The measured rebound strength of the concrete is shown in Table 4. At 28 days, the strength reached 52.3 MPa, exceeding the design strength. As shown in Figure 13, a high-pressure water test (water pressure greater than 3 bars) was conducted, with each 10 square meters tested for 5 min, and no leakage points were found. As shown in Figure 14, the concrete surface remained intact without cracks, and there was no seepage after the water immersion test.

Table 4. Measured rebound strength of concrete.

Curing Time	3 Day	7 Day	28 Day
Rebound strength	35.2	46.1	52.3

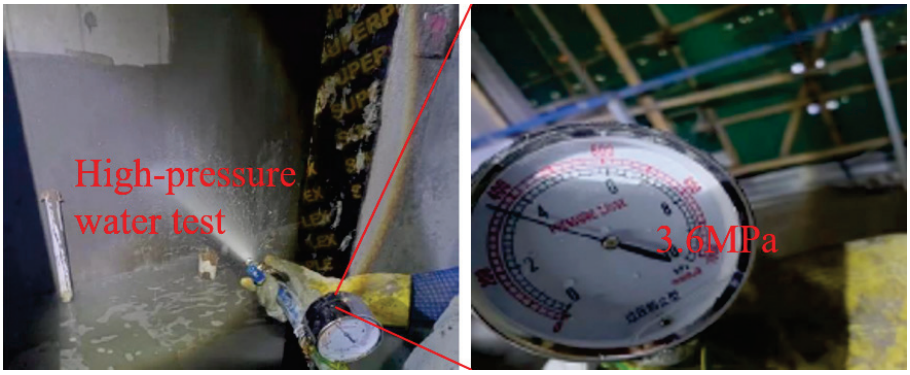

Figure 13. High-pressure water test.

(**a**) Before construction (**b**) After construction

Figure 14. Construction of toilet backfill concrete.

4. Conclusions

(1) A reasonable amount of fiber (6 kg/m^3) can significantly enhance the splitting tensile strength, flexural strength, and impact toughness of lightweight aggregate concrete, and can significantly improve the damage pattern of concrete. When the fiber content is too small (3 kg/m^3), it cannot effectively bear the tensile stress generated by compression and has limited restraint on cracks. At the same time, the addition of fibers introduces a weak fiber–matrix interface, resulting in lower strength than fiber-free concrete. When the dosage is too large (9 kg/m^3), because there are too many fibers, the weak surface of the interface between the fibers and the cement matrix increases, and the fibers are not fully wrapped by the cement slurry, resulting in more defects. This leads to a reduction in the bonding strength between the fibers and the cement paste, and ultimately a reduction in the strength of the concrete. Therefore, it is necessary to set the fiber content reasonably.

(2) During the freeze–thaw cycle, the pore water inside the concrete freezes and generates tensile stress, and tensile cracks are generated inside the concrete. Under the action of repeated freeze–thaw cycles, the cracks gradually accumulate and expand, eventually leading to the destruction of the concrete structure. Freeze–thaw cycles have a great impact on the strength of ordinary lightweight aggregate concrete. After 150 freeze–thaw cycles, the strength loss rate exceeds 25%.

(3) After adding fiber, the fiber bears the tensile stress and hinders the development of internal cracks. After 150 freeze–thaw cycles, the compressive and flexural strength losses of the concrete with 6 kg/m^3 fiber were reduced by 13.7% and 22.9%, respectively, compared with the concrete without fiber, and the initial cracking energy consumption and failure energy consumption under the impact load are also significantly increased. In the early stages of the freeze–thaw cycle, the strength decreases slowly and the matrix cracks. This part of the load is transferred to the fibers. At this time, the concrete relies on the tensile capacity of the fibers themselves and the friction generated by the fibers and the matrix to simultaneously dissipate energy. This increases the residual strength of the concrete after cracking. At this time, the tensile stress is lower than the tensile strength of the fiber and the fiber–matrix bonding strength, and the fiber absorbs external force through its own deformation ability. However, in the later stages of the freeze–thaw cycle, the tensile stress is greater than the bonding force between the fibers and the matrix, and the fibers will slip or even pull out, losing their gradual toughening effect, resulting in a rapid reduction in the concrete strength.

(4) The influence of freeze–thaw damage on the impact toughness is greater than the compressive strength and flexural strength under static load. Before freeze–thaw, the initial crack energy of the fiber concrete (6 kg/m^3) is 76% greater than that of ordinary concrete, but after the cycle, it is only 49% greater. This is mainly because the freeze–thaw cycle destroys the bonding strength of the fiber–matrix interface and reduces the ability of the fiber to withstand impact loads. The performance of concrete is influenced by both the fiber content and freeze–thaw cycles.

(5) In this research, the effect of the freeze–thaw cycle on the performance of fiber-reinforced lightweight aggregate concrete under laboratory conditions was studied in detail. Due to the limitations of the experimental conditions and time, the impact of real natural conditions (temperature, humidity, salt exposure) on concrete had not been studied at this stage. Considering that different temperatures, humidity, and other natural environments will have different effects on concrete, the future performance research of lightweight aggregate concrete in a natural environment will be very meaningful.

Author Contributions: Methodology, F.J.; Formal analysis, Q.W. and Z.M.; Investigation, F.J. and W.D.; Resources, F.J.; Data curation, W.D., Q.W., J.W. and Z.M.; Writing—original draft, F.J. and J.W.; Writing—review & editing, J.W. All authors have read and agreed to the published version of the manuscript.

Funding: The project was funded by Science and Technology Plan Project of Suzhou: 2023SS14; Basic Science (Natural Science) Research Project of Higher Education Institutions in Jiangsu Province: 24KJD560004; Jiangsu University 'Blue Project': 2024.

Institutional Review Board Statement: Not applicable.

Informed Consent Statement: Not applicable.

Data Availability Statement: The original contributions presented in the study are included in the article, further inquiries can be directed to the corresponding author.

Conflicts of Interest: Authors Wencong Deng and Qi Wang were employed by the company China State Construction Engineering (Macau) Co., Ltd. The remaining authors declare that the research was conducted in the absence of any commercial or financial relationships that could be construed as a potential conflict of interest.

References

1. Hasholt, M.T.; Jensen, O.M. Environmental Assessment of Frost-resistant Concrete with Superabsorbent Polymers. *Nord. Concr. Res.* **2020**, *63*, 43–62.
2. Dong, X.; Yu, T.; Zhang, Q.; Bui, T.Q. Multiscale freezing-thaw in concrete: A numerical study. *Compos. Struct.* **2023**, *309*, 116758. [CrossRef]
3. Liu, X.; Yan, Z.; Wang, D.; Zhao, R.; Niu, D.; Wang, Y. Corrosion cracking behavior of reinforced concrete under freeze-thaw cycles. *J. Build. Eng.* **2023**, *64*, 105610. [CrossRef]
4. Ma, Z.; Zhao, T.J.; Yang, J. Fracture Behavior of Concrete Exposed to the Freeze-Thaw Environment. *J. Mater. Civ. Eng.* **2017**, *29*, 04017071. [CrossRef]
5. Taheri, B.M.; Ramezanianpour, A.M.; Sabokpa, S.; Gapele, M. Experimental evaluation of freeze-thaw durability of pervious concrete. *J. Build. Eng.* **2021**, *33*, 101617. [CrossRef]
6. Zhao, R.; Shi, C.; Zhang, R.; Wang, W.; Zhu, H.; Luo, J. Study on the Freeze-Thaw Resistance of Concrete Pavements in Seasonally Frozen Regions. *Materials* **2024**, *17*, 1902. [CrossRef]
7. Wongkvanklom, A.; Posi, P.; Khotsopha, B.; Ketmala, C.; Pluemsud, N.; Lertnimoolchai, S.; Chindaprasirt, P. Structural Lightweight Concrete Containing Recycled Lightweight Concrete Aggregate. *KSCE J. Civ. Eng.* **2018**, *22*, 3077–3084. [CrossRef]
8. Alani, A.A. Lightweight concrete containing recycled aggregates. *Mag. Civ. Eng.* **2024**, *17*, 12804.
9. Muhtar. Performance-based experimental study into quality zones of lightweight concrete using pumice aggregates. *Case Stud. Constr. Mater.* **2023**, *18*, e01960.
10. González-Betancur, D.; Hoyos-Montilla, A.A.; Tobón, J.I. Sustainable Hybrid Lightweight Aggregate Concrete Using Recycled Expanded Polystyrene. *Materials* **2024**, *17*, 2368. [CrossRef]
11. Deng, P.; Wang, Y.; Sun, Y.; Liu, Y.; Guo, W. Bond durability of basalt-fiber-reinforced-polymer bars embedded in lightweight aggregate concrete subjected to freeze-thaw cycles. *Struct. Concr.* **2021**, *22*, 2829–2848. [CrossRef]
12. Zeng, Y.; Li, X.; Tang, A.; Zhao, N.; Li, L.; Jia, S. Axial compressive behavior of basalt and polyacrylonitrile fibers reinforced lightweight aggregate concrete with industrial waste ceramsite-lytag after freeze-thaw cycles. *J. Build. Eng.* **2023**, *76*, 107402. [CrossRef]
13. Cai, B.; Wang, S.; Fu, F.; Duan, W.; Wang, L. Experimental study on steel-fiber-reinforced scoria aggregate concrete subjected to freeze-thaw cycles and then exposure to elevated temperatures. *Fire* **2023**, *6*, 119. [CrossRef]
14. Gou, H.; Sofi, M.; Zhang, Z.; Zhu, H.; Zhu, M.; Mendis, P. Durability development of lightweight and high-strength engineered cementitious composites subject to combined sulfate-chloride attack under freeze-thaw cycles. *Constr. Build. Mater.* **2023**, *408*, 133659. [CrossRef]
15. Yoon, J.Y.; Kim, J.H. Mechanical properties of preplaced lightweight aggregates concrete. *Constr. Build. Mater.* **2019**, *216*, 440–449. [CrossRef]
16. Al-sayed; Wang, X.; Peng, Y.J. Simulation of Fracture Process of Lightweight Aggregate Concrete Based on Digital Image Processing Technology. *CMC-Comput. Mater. Contin.* **2024**, *79*, 4169–4195. [CrossRef]
17. Li, P.; Li, J.; Fan, L.; Mi, S.D.; Li, J.Y.; Liu, H.Q.; Peng, S.Q.; Huang, W.Q. Experimental Investigation into Lightweight High Strength Concrete with Shale and Clay Ceramsite for Offshore Structures. *Sustainability* **2024**, *16*, 1148. [CrossRef]
18. Guler, S.; Yavuz, D.; Korkut, F.; Ashour, A. Strength prediction models for steel, synthetic, and hybrid fiber reinforced concretes. *Struct. Concr.* **2019**, *20*, 428–445. [CrossRef]
19. Wang, Y.; Xie, M.; Zhang, J. Mechanical properties and damage model of modified recycled concrete under freeze-thaw cycles. *J. Build. Eng.* **2023**, *78*, 107680. [CrossRef]
20. Wu, Y.; Dai, J.; Shi, B.; Wu, B. The strength and elastic modulus of pervious concrete considering pore and fiber during freeze-thaw cycles. *Sustainability* **2022**, *14*, 16217. [CrossRef]
21. Zhao, Y.-R.; Wang, L.; Lei, Z.-K.; Han, X.-F.; Xing, Y.-M. Experimental study on dynamic mechanical properties of the basalt fiber reinforced concrete after the freeze-thaw based on the digital image correlation method. *Constr. Build. Mater.* **2017**, *147*, 194–202. [CrossRef]
22. Zeng, Y.; Meng, S.; Xu, H.; Yuan, S.; Lang, W.; Chen, W. Strength attributes of fiber-reinforced lightweight aggregate concrete incorporating Lytag ceramsite under freeze-thaw environment. *J. Build. Eng.* **2023**, *65*, 105804. [CrossRef]
23. Dong, W.; Shen, X.-D.; Xue, H.-J.; He, J.; Liu, Y. Research on the freeze-thaw cyclic test and damage model of Aeolian sand lightweight aggregate concrete. *Constr. Build. Mater.* **2016**, *123*, 792–799. [CrossRef]
24. Li, G.; Xu, Z.; Niu, J. Numerical Simulation of Microscopic Failure Process of Plastic Steel Fiber Lightweight Aggregate Concrete. *Mater. Rev.* **2018**, *32*, 2412–2417.
25. *JGJ51-2002*; Technical Specification for Lightweight Aggregate Concrete. China Construction Industry Press: Beijing, China, 27 September 2002.
26. *GB/T50082-2009*; Standard for Test Methods for Long Term Performance and Durability of Ordinary Concrete. China Construction Industry Press: Beijing, China, 30 November 2009.
27. Xu, F.; Li, T.; Li, C.; Li, Z.; Wang, S.; Zhao, N. Compressive behavior, microstructural properties, and freeze-thaw behavior of tailing recycled aggregate concrete with waste polypropylene fiber addition. *Materials* **2021**, *14*, 6712. [CrossRef]

28. Wu, X.; Tian, J.; Ma, H.; Zheng, Y.; Hu, S.; Wang, W.; Du, Y.; Huang, W.; Sun, C.; Zhu, Z. Investigation on interface fracture properties and nonlinear fracture model between ecc and concrete subjected to salt freeze-thaw cycles. *Constr. Build. Mater.* **2020**, *259*, 119785. [CrossRef]
29. Li, F.; Chen, D.; Lu, Y.; Zhang, H.; Li, S. Influence of mixed fibers on fly ash based geopolymer resistance against freeze-thaw cycles. *J. Non Cryst. Solids* **2022**, *584*, 121517. [CrossRef]
30. Lu, J.; Liu, J.; Yang, H.; Wan, X.; Gao, J.; Zhang, J.; Li, P. Experimental investigation on the mechanical properties and pore structure deterioration of fiber-reinforced concrete in different freeze-thaw media. *Constr. Build. Mater.* **2022**, *350*, 128887. [CrossRef]
31. Zhang, Z.W.; Zhang, Z.H.; Wang, X.; Zhou, C.H. Dynamic and static interfacial bonding properties of cfrp-concrete subjected to freeze-thaw cycles. *Structures* **2022**, *37*, 947–959. [CrossRef]
32. Lv, D.; Liu, H.; He, F.; Wang, W.; Miao, Q.; Li, H.; Wang, F.; Zhao, J.; Shi, C. Freeze-Thaw Damage Characteristics of Concrete Based on Compressive Mechanical Properties and Acoustic Parameters. *Materials* **2024**, *17*, 1010. [CrossRef]

Disclaimer/Publisher's Note: The statements, opinions and data contained in all publications are solely those of the individual author(s) and contributor(s) and not of MDPI and/or the editor(s). MDPI and/or the editor(s) disclaim responsibility for any injury to people or property resulting from any ideas, methods, instructions or products referred to in the content.

materials

MDPI

Article

Influence of Grinding Aids on the Grinding Performance and Rheological Properties of Cementitious Systems

Yahya Kaya [1], Hatice Gizem Şahin [1], Naz Mardani [2] and Ali Mardani [1,*]

[1] Department of Civil Engineering, Bursa Uludag University, Bursa 16059, Turkey; 512126007@ogr.uludag.edu.tr (Y.K.); 532026001@ogr.uludag.edu.tr (H.G.Ş.)
[2] Department of Mathematics Education, Bursa Uludag University, Bursa 16059, Turkey; nazmardani@uludag.edu.tr
* Correspondence: alimardani@uludag.edu.tr

Abstract: The cement industry is of great importance in terms of raw materials consumed, energy consumed, and greenhouse gases emitted. Grinding aids (GA) are used to reduce energy consumption and costs, as well as to reduce the amount of CO_2 released into the environment. In this study, the effect of GA-polycarboxylate ether-based water-reducing admixture (PCE) compatibility on some fresh, rheological and hardened state properties of cementitious systems was investigated. In order to investigate the rheological properties and thixotropic behavior of the mixtures, a total of 51 cement paste mixtures were prepared, containing 4 different types (molasses, MEG, DEA and ethanol) and ratios (0.025, 0.05, 0.75 and 0.1) of GAs and 2 different ratios (0.08% and 0.16%) of PCE in addition to the control mixture. In addition, the effect of the used GAs on the grinding efficiency and compressive strength value was investigated. Additionally, the predictability of the type of GA, dosage and cure time using the Taguchi method was investigated. It was determined that the highest grinding performance was obtained in mixtures containing MEG. It was determined that in cement paste mixtures containing GAs, the dynamic yield stress and viscosity values generally decrease with the increase in PCE usage rate up to a certain value, and these values may increase if the PCE usage increases further. It was determined that such behavior is not present in cement paste mixtures containing GAs and that the structural build-up value of the mixtures generally increases with the increase in the PCE admixture usage rate. It was determined that the use of GAs had a positive effect on 28-day compressive strength.

Keywords: grinding aids; polycarboxylate ether-based water-reducing admixture; grinding efficiency; rheological property; thixotropic behavior; GA–PCE compatibility

1. Introduction

Greenhouse gas emissions, air pollution and climate change are among the leading factors that cause global problems [1–5]. In the solution process of these problems, issues such as developing alternatives to products that cause CO_2 emissions during production, renewable energy sources and energy efficiency have gained importance [6,7]. The cement industry causes great harm to the environment in terms of energy, raw material consumption and CO_2 emissions. The amount of electricity spent in the cement industry constitutes 2% of the electricity used worldwide and 5% of the electricity used in the industry. However, it accounts for 5–7% of global CO_2 emissions [8]. Approximately 1.2 tons of raw materials and 130 kWh of energy are consumed to produce one ton of cement, resulting in approximately 1 ton of CO_2 [9,10]. In cement production, approximately 35% of the energy consumed is spent in the clinker grinding phase. In addition, a significant portion of the energy consumed in the grinding phase is wasted by converting into heat, sound and vibration. As a result of studies conducted to reduce both the energy consumption and cost and the amount of CO_2 released into the environment, the use of grinding aids (GA) has come to the fore [11–13].

GAs adsorb on the surfaces of the grains with the help of the highly polar functional groups they contain (-OH, -NH_2, -COOR, -SO_3, etc.) [14,15]. Adsorbed GAs neutralize the electrical charges on the surface, preventing the cracks formed in the clinker from closing, particles from coming together and sticking to the mill surface and/or balls [15,16]. Thus, grinding efficiency is ensured. It is known that cement grains produced using GAs contain finer cement particles despite having the same Blaine fineness value. In addition, cements produced using GAs and cements produced without GAs create differences in important properties such as surface energy [17]. This situation significantly affects the hydration reactions of cement, cement–admixture compatibility and rheological properties of cement pastes.

Plank et al. [18] emphasized that GAs have a similar mechanism to polycarboxylate ether-based water-reducing admixtures (PCE) in terms of adsorption onto the cement grain. Therefore, the adsorption of PCE onto the cement grain may be negatively affected in systems containing GAs. It was stated that in case of binder–admixture incompatibility, negative effects such as rapid or slow setting [10], segregation [19], loss of consistency and increased shrinkage [19–21] may occur in cementitious systems. Some of these negativities may be due to their binding properties, while others may be due to admixture properties. Since the used GAs affect the cement properties, the cement–PCE compatibility of the cements in which GAs are used during production should be examined comprehensively. The effects on both the cement surface properties and hydration reactions vary depending on the type, dosage and chemical content of the GAs used [22–25]. Some studies examining the compatibility of cements produced with GAs with PCE are summarized below.

In a study conducted by Sun et al. [26], the compatibility of cements produced using 0.01, 0.02, 0.03 and 0.04% glycerin-type GAs with PCE was examined. It was observed that the flow performance of PCE was higher when the Ga dosage was less than 0.02%. It was determined that PCE was adsorbed at a lower rate in cements containing more than 0.02% GA. In another study, the effect of the use of GAs on the surface energy of the cement grain was investigated by Prziwara and Kwade [27]. On the one hand, it was stated that GAs adsorbed on the cement grain and caused the surface energy to decrease. On the other hand, it was emphasized that the cements produced using GAs may have higher surface energy compared to the grains without GAs due to the fact that they consist of smaller grains. This situation revealed that there are different opinions about the adsorption of PCE to cements containing GAs. It was stated by Karakuzu et al. [28] that PCE adsorption is seriously affected by the high positive charge density of the cement surface. It was emphasized by Sun et al. [26] that the cement surface load density can vary depending on the type of GA and the usage rate. Accordingly, the degree of adsorption of PCE to cement varies in cements containing GAs. As understood from the literature, it is necessary to examine the PCE compatibility of cementitious systems in the presence of GAs. It was reported by Mardani-Aghabaglou et al. [10] that the determination of rheological parameters of cementitious systems is one of the most reliable methods in terms of examining cement–admixture compatibility. However, studies examining the effect of cements produced with GAs on the rheological properties of cementitious systems are very limited.

With the Taguchi method, variables caused by uncontrollable factors that are not taken into account by traditional experimental design can be controlled [29]. In this method, the objective function values are converted to the signal-to-noise (S/N) ratio to measure the performance characteristics of the levels of control factors against the factors in question [29]. The S/N ratio is defined as the desired signal ratio for the undesired random noise value and shows the quality characteristics of the experimental data [30]. In this direction, it is known that the Taguchi method is used in experiments that require excessive energy and time.

In this study, GA–PCE compatibility was investigated in terms of rheological properties and thixotropic behavior of cement pastes. While rheological properties of mixtures were investigated with dynamic yield stress and viscosity values, thixotropic behavior was interpreted with structural build-up (A_{thix}) behavior. The effect of used GAs on grinding

efficiency and compressive strength values of mixtures was also investigated. In addition, the predictability of GA type, dosage and curing time was investigated with the Taguchi method.

2. Materials and Methods

2.1. Materials

The cements produced within the scope of this study were obtained by grinding 96% clinker and 4% gypsum in a laboratory-type ball mill until the target Blaine fineness value (3900 ± 100 cm^2/g) was reached. The cements obtained are CEM I 42.5R-type cements in accordance with TS EN 197-1 Standard [31]. The chemical properties of clinker and gypsum given by the company are shown in Table 1.

Table 1. Some chemical properties of clinker and gypsum [29].

	SiO_2	Al_2O_3	Fe_2O_3	CaO	MgO	SO_3 *	Na_2O	K_2O	Cl *	C_3S	C_2S	C_3A	C_4AF	Loss of Ignition
Clinker	21.52	5.43	3.31	65.38	1.04	0.38	0.48	0.54	0.01	56.51	19.06	8.79	10.07	0.52
Gypsum	4.98	1.21	0.83	28.94	0.83	39.67	0.25	0.19						

* According to TS EN 197-1, $SO_3 \leq 3.5\%$ and $Cl^- \leq 0.01$.

Some properties of the GAs and PCE used in this study are shown in Tables 2 and 3, respectively.

Table 2. Some chemical properties of the used GAs and PCE.

Admixture Name	Molecular Weight (g/mol)	Alkaline Content (%) (Na_2O)	Density (g/cm^3)	Solid Content (%)	Chloride Content (%)	pH, 25 °C	Boiling Point	Number of OH Groups It Contains
Diethanol amine (DEA)	105.14	<10	1.097	50.0	<0.1	11.0	271	2
Monoethyleneglycol (MEG)	62.07	<10	1.112	50.0	<0.1	8.2	197	2
Ethanol	46.07	<10	0.789	50.0	<0.1	7.4	157	1
PCE	19,000	<10	1.06	32	<0.1	4.56	-	-

Table 3. Some chemical and physical properties of molasses used as GAs.

Name	Solid Content (%)	Sugar Content (%)	Raffinose (%)	pH 25 °C	Betaine (%)
Molasses	52.7	0.4	0.8	6.6	2.4

In the production of mortar mixtures, washed river sand aggregate with a grain diameter of 0–4 mm, in accordance with TS EN 196-1 Standard [32], was used. The saturated surface dry specific gravity of the aggregate according to TS EN 1097-6 Standard [33] was measured as 2.64 and its water absorption capacity as 1.2%.

2.2. Preparation of Mixtures and the Test Method

2.2.1. Preparation of Mixtures

In order to determine the rheological properties and thixotropic behavior, the w/c ratio was kept constant as 0.35 in the produced paste mixtures. For this purpose, in addition to the control mixture, a total of 51 cement paste mixtures containing 4 different types (molasses, MEG, DEA and ethanol) and ratios (0.025, 0.05, 0.75 and 0.1) of GAs and 2 different ratios (0.08% and 0.16%) of PCE were prepared. The mixtures were named according to the type of GA, GA usage rate and PCE usage rate. For example, the mixture

containing 0.050% ethanol and 0.08% PCE was named as 0.05 ethanol 0.08%. The rheological properties of the prepared mixtures were evaluated in terms of dynamic yield stress and viscosity parameters and thixotropic properties were evaluated in terms of structural build-up (A_{thix}) development.

Within the scope of this study, mortar mixtures were produced in accordance with ASTM C109 Standard [34]. In determining the PCE requirements for the target flow value of the mixtures, the water/binder ratio, sand/binder ratio and target flow value were kept constant as 0.485, 2.75 and 190 ± 20 mm, respectively. All mixtures were prepared in a Hobart mixer.

2.2.2. The Test Method

The Grinding Process

The clinker grinding process was carried out in a Bond-type laboratory-type mill with a 1.5 kW motor power and a capacity of 5 kg located in the Bursa Uludag University Construction Materials Laboratory. The Blaine fineness value of the obtained cements was determined by an automatic Blaine measuring device, and the particle size distributions were determined by a Malvern/Zetasizer Nano ZSP brand particle size determination device (Malvern, UK). In the grinding processes, the Blaine fineness value was measured after 30 min and 50 min of grinding. In addition, the number of revolutions applied until the target Blaine fineness value of 3900 ± 100 cm^2/g was reached was determined. The energy consumed was determined based on the number of revolutions applied. The energy consumed in the production of cements was calculated according to Equation (1).

$$Eg = (220 \times Tö \times A \times 1000)/(m \times Tg) \quad (1)$$

Here, Eg is the grinding energy (kWh/ton), Tö is the grinding time (hour), A is ampere, m is the mass of ground material (kg) and Tg is the mill factor (constantly taken as 4 from the grinding mill manufacturer). Optimum grinding conditions were determined based on the energy consumed.

The Rheology Test

The rheological properties and structural recovery development of the mixtures produced within the scope of this study were examined. In the scope of this study, an MCR52-Anton Paar rheometer (Istanbul, Turkey) with a ball diameter of 8 mm was used (Figure 1a). The ambient temperature was kept constant at 20 ± 2 °C during the measurement. The applied rheological measurement process is shown in Figure 1b.

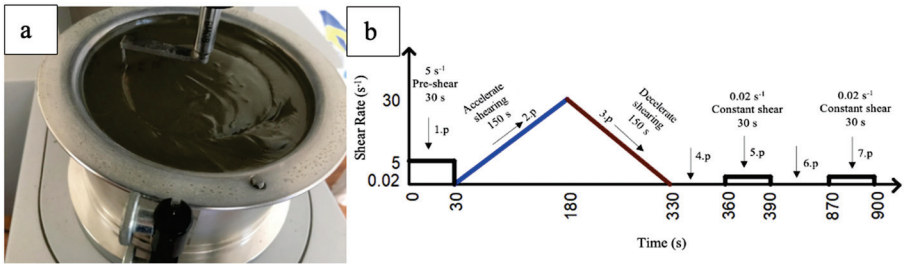

Figure 1. (**a**) Measuring device and (**b**) rheological measurement process.

The rheological properties of the mixtures (yield stress and final viscosity value) were obtained by drawing shear stress–shear rate and viscosity–shear rate graphs for each mixture, using the Herschel–Buckley model shown in Equation (2) on the raw data determined in the 3rd period. In Figure 2, as an example, the shear stress–shear rate and viscosity–deformation rate graphs of control mixture produced within the scope of this study are shown.

$$\tau = \tau_0 + b\dot{\gamma}^p \quad (2)$$

Here, τ is the shear stress (Pa), τ_0 is the yield stress (Pa), b is the Herschel–Bulkley consistency coefficient, $\dot{\gamma}$ is the shear rate (s^{-1}) and p is the Herschel–Bulkley index.

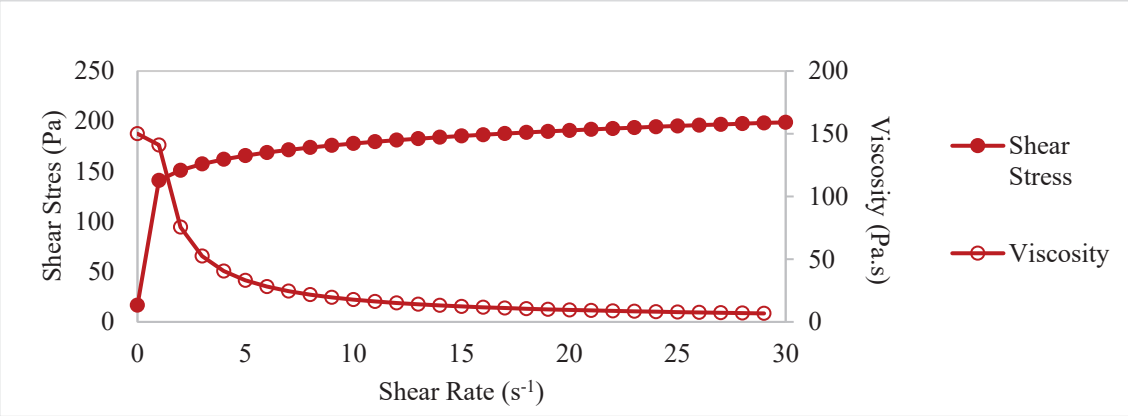

Figure 2. Shear stress–shear rate and viscosity–deformation rate graphs of control mixture.

The rheological measurement method consists of 7 periods. The shear rate and durations to which the mixtures are exposed in each period are shown in Figure 1b. The dynamic yield stress and viscosity values of the mixtures were determined using the 3rd period data. The maximum shear stress obtained from the 5th and 7th periods was selected as the static yield stress.

During the static shear test, the deformation rate to which the cementitious systems are exposed is very low and the mixture is not disturbed at all. In this case, only structural recovery is present in the mixtures. The structural recovery development (A_{thix}) was determined using the static yield stresses obtained as a result of this test. The value in question was calculated with the help of Equation (3).

$$A_{thix} = \frac{\tau_{s,f} - \tau_{s,i}}{t_d} \quad (3)$$

Here, A_{thix} represents the structural recovery development (Pa/s), $\tau_{s,f}$ represents the static yield stress value (Pa) obtained from the 7th period, $\tau_{s,i}$ represents the static yield stress value (Pa) obtained from the 5th period, and t_d represents the waiting time (s).

Flow and Compressive Strength

The flow value was determined in accordance with ASTM C1437 [35] and the compressive strength values in the prepared mixtures were determined according to ASTM C109 Standards.

Design of Experiments with the Taguchi Method

Within the scope of this study, ANOVA and the Taguchi method were applied to determine the optimum combination of grinding parameters. In the Taguchi method, nominal best, largest best, smallest best methods depending on the characteristic type are used to calculate signal-to-noise (S/N) ratios [29]. In this study, the "biggest is best" as shown in Equation (4) proposed by Mandal et al. [36] is used as the objective function.

$$S/N = -10 \times \log(\Sigma(1/Yi^2)/n) \quad (4)$$

where Yi is the data observed in the i-th experiment and n is the number of observations of the experiment.

In this study, the control factors were selected as GA type, GA dosage and curing time. The levels of the selected factors are shown in Table 4. In order to determine the optimum compressive strength value and analyze the effects of the factor parameters, the

most appropriate orthogonal array was selected as L16(4^2 2^1). The L16 mixed orthogonal array shown in Table 5 was used to analyze the experimental results.

Table 4. Factor parameters and their levels.

Parameters	Symbol	Levels 1	Levels 2	Levels 3	Levels 4
GA Type	A	Molasses	MEG	DEA	Et
GA Dosage	B	0.025	0.05	0.075	0.1
Cure Duration	C	7	28	-	-

Table 5. Taguchi L16(4^2 2^1) orthogonal layout.

Experiment No.	Factor A	Factor B	Factor C
1	Molasses	0.025	7
2	Molasses	0.05	7
3	Molasses	0.075	28
4	Molasses	0.1	28
5	MEG	0.025	7
6	MEG	0.05	7
7	MEG	0.075	28
8	MEG	0.1	28
9	DEA	0.025	28
10	DEA	0.05	28
11	DEA	0.075	7
12	DEA	0.1	7
13	Ethanol	0.025	28
14	Ethanol	0.05	28
15	Ethanol	0.075	7
16	Ethanol	0.1	7

3. Experimental Results and Discussion

3.1. Grinding Efficiency

The Blaine fineness values of the cements with and without GAs after 30 min and 50 min grinding and the amount of energy consumed for the target Blaine fineness value are given in Table 6. In order to better understand the grinding efficiency of the GA types, the average grinding efficiencies are given in Figure 3 and the particle size distributions of the cements produced are given in Figure 4.

Regardless of the use of GAs, the fineness value of the cements increased as expected with the increase in grinding time from 30 min to 50 min. When the cements subjected to the 30 min grinding process were analyzed, it was found that the lowest Blaine fineness value belonged to the control cement without GAs. Compared to the control cement, cements containing molasses, MEG, DEA and ethanol-type GAs were measured to have 6-15-10% and 9% higher Blaine fineness values after 25 min of grinding, respectively. Among the GA types, the most successful performance on the early grinding time was observed with the glycol-based admixture, while the lowest performance was obtained with molasses admixture. Similarly, it was reported by Assaad et al. [37] that the performance of glycol-based admixtures was high at early grinding time. It was found that there was no significant increase in grinding efficiency with the increase in the rate of GA utilization regardless of the type of GA. It was found that the highest performance was obtained in molasses, MEG and ethanol types at 0.075% and in DEA at 0.025% of GA.

When the cements subjected to the 50 min grinding process were analyzed, it was found that the control cement without GAs had the lowest Blaine fineness value. It was determined that the use of molasses, MEG, DEA and ethanol increased the Blaine fineness values of the cements by 7-15-11% and 10%, respectively. After 30 min grinding, it was seen that the admixture performances continue similarly at 50 min grinding. It was determined that no significant pattern was observed with the increase in the rate of GA use.

Table 6. Grinding efficiencies.

Cements	30 Min Specific Surface Area (cm^2/g)	30 Min Relative Fineness Increase (%)	50 Min Specific Surface Area (cm^2/g)	50 Min Relative Fineness Increase (%)	Blaine Fineness at the End of the Milling Process (cm^2/g)	Time to Reach Target Blaine Fineness Value (min)	Energy Consumption (kWh/tone)	Relative Energy Efficiency Increase (%)
C	2180	-	3130	-	4100	96.00	47.200	-
0.025 Molasses	2325	6.65	3325	6.23	4050	85.48	42.960	8.98
0.05 Molasses	2260	3.67	3290	5.11	4100	84.41	42.448	10.07
0.075 Molasses	2390	9.63	3400	8.63	4095	83.55	42.036	10.94
0.1 Molasses	2250	3.21	3410	8.95	4100	82.30	41.436	12.21
0.025 MEG	2440	11.93	3450	10.22	4140	81.31	40.963	13.22
0.05 MEG	2500	14.68	3625	15.81	4170	80.24	40.450	14.30
0.075 MEG	2595	19.04	3660	16.93	4180	79.48	40.082	15.08
0.1 MEG	2520	15.60	3665	17.09	4150	80.26	40.457	14.29
0.025 DEA	2550	16.97	3570	14.06	4200	81.48	41.042	13.05
0.05 DEA	2350	7.80	3415	9.11	4140	80.83	40.730	13.71
0.075 DEA	2350	7.80	3470	10.86	4210	80.18	40.418	14.37
0.1 DEA	2360	8.26	3470	10.86	4200	82.83	41.688	11.68
0.025 Ethanol	2270	4.13	3310	5.75	4165	85.88	43.150	8.58
0.05 Ethanol	2390	9.63	3550	13.42	4180	81.94	41.262	12.58
0.075 Ethanol	2450	12.39	3605	15.18	4220	79.69	40.184	14.86
0.1 Ethanol	2385	9.40	3390	8.31	4210	82.81	41.678	11.70

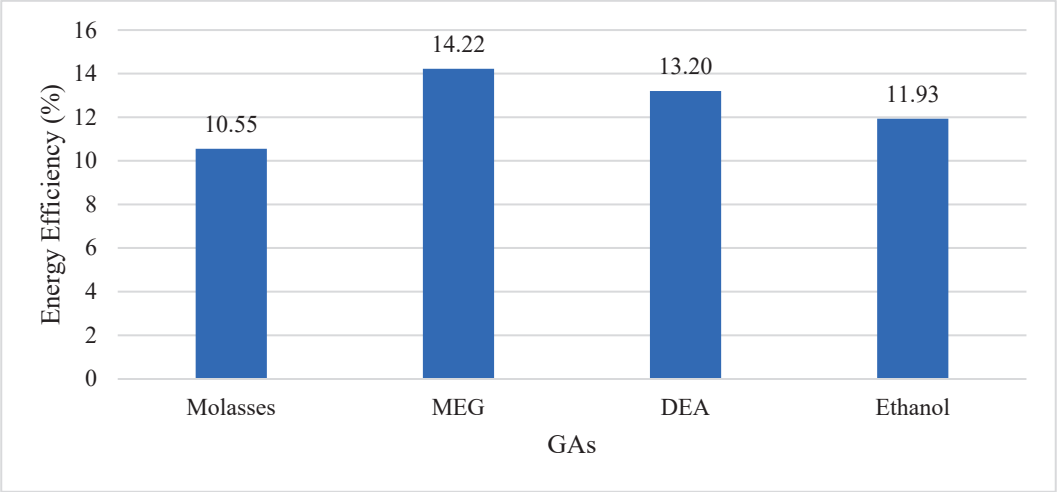

Figure 3. Average energy efficiency of Gas.

While 47.2 kWh/ton of energy was consumed to achieve the target Blaine fineness of 4100 ± 100 cm^2/g in control cement, the average energy consumed in cements containing molasses, MEG, DEA and ethanol was 42.22, 40.49, 40.97 and 41.57 kWh/ton, respectively (Figure 3). It was found that the highest grinding performance was achieved by using MEG with an energy efficiency of about 14.22% compared to the control cement. The lowest grinding performance was obtained when molasses admixture was used with 10.55% compared to the control cement (Figure 3).

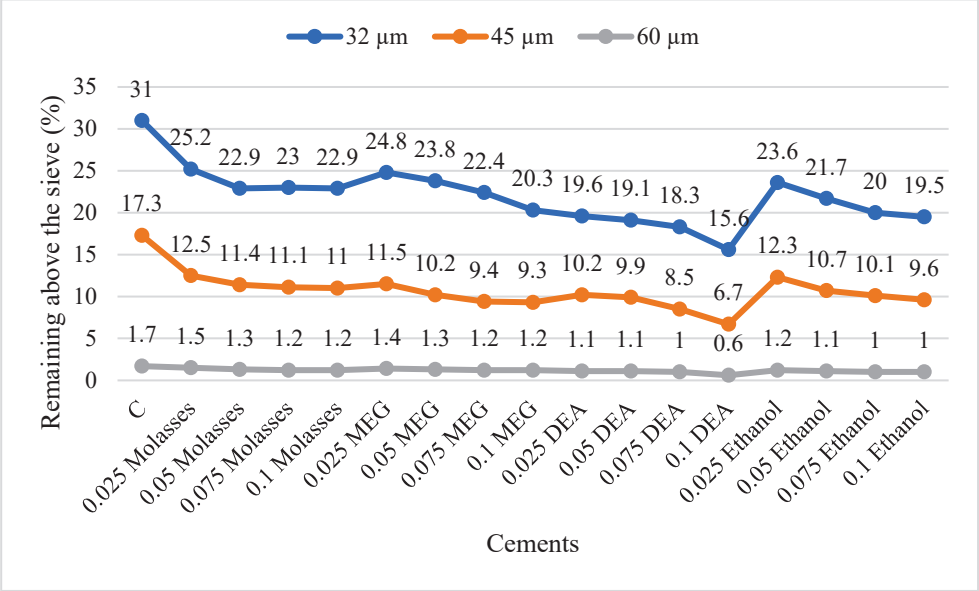

Figure 4. Particle size distributions of cements.

By adsorbing on the surface of the particles, GAs reduce the electrical charges generated by friction during grinding and the surface energies of the particles, which increase with the decrease in the size of the particles [38]. It has been emphasized by researchers that the dispersion effect of GAs adsorbed on the particle surface is related to the changing surface properties of the particles such as surface energy, zeta potential, and flocculation energy [39,40]. Since GAs adsorb on particles with the help of hydroxyl groups (-OH), the number of hydroxyl groups they have also affects their performance [14]. As can be seen from Table 2, the admixtures with the highest grinding performance have 2 hydroxyl groups in the molecular formula. In addition, Vieira and Peres [41] revealed in their study that the pH of the admixture used can have an effect on the grinding performance. In this study, it was observed that grinding efficiency increased with increasing pH. This indicates that the high grinding performance of DEA and MEG admixtures may also be related to the high pH value (Table 2).

It was found that the optimum grinding performance was observed for all GAs, regardless of the type of GA, when 0.075% SCT was used. In the literature, there are studies showing that the GA dosage reduces the efficiency after a certain point [42]. This is thought to be related to the powder fluidity of cement grains produced with GAs. When more than a certain amount of GA is used, cement grains may show sliding behavior at the collision point of the balls and cause a decrease in grinding performance [29].

Particle size distributions of cements with target Blaine fineness values are shown in Figure 4.

Since the particle size distribution of cements with the same Blaine fineness value may differ, it is known that Blaine fineness is not sufficient as a precise fineness criterion [42]. For this reason, the effect of the use of GAs on the particle size distribution was investigated. As can be seen from Figure 4, it was observed that the particle size distribution of the cements narrowed and a finer size range was obtained with the use of GAs and the increase in the utilization rate, regardless of the type of GA. In the studies conducted in the literature [15,42–45], it has been explained that cements obtained by using GAs result in narrower particle size distribution and smoother granular product formation compared to cements obtained without GAs. Accordingly, it was emphasized that the fine particle ratio increased. In grinding processes without GAs, the cement particles are agglomerated and coated on the balls, making the size reduction process difficult. Cements containing larger particles are obtained by grinding the grains agglomerated between the balls. For

this reason, admixtures that prevent agglomeration by adsorbing to the particles cause a narrower particle size distribution.

3.1.1. Flow Performance and Compressive Strength

The PCE requirements and 1-, 7- and 28-day compressive strength values of the mixtures for the target flow value are given in Table 7.

Table 7. PCE requirements and compressive strength values of the mixtures.

Mixtures	Fresh State Unit Volume Weight (kg/m^3)	PCE Requirement for Target Flow Value (%)	Compressive Strength (MPa)		
			1 Day	7 Day	28 Day
C	2.220	0.253	11.07	30.19	45.78
0.025 Molasses	2.318	0.250	11.81	28.37	47.86
0.05 Molasses	2.332	0.267	12.16	26.12	52.38
0.075 Molasses	2.281	0.241	10.80	25.64	50.80
0.1 Molasses	2.292	0.242	10.05	26.67	51.25
0.025 MEG	2.280	0.282	10.98	28.23	45.34
0.05 MEG	2.326	0.272	11.45	31.44	46.39
0.075 MEG	2.358	0.265	10.54	30.74	52.67
0.1 MEG	2.325	0.261	10.00	30.62	46.83
0.025 DEA	2.320	0.250	15.03	38.20	41.67
0.05 DEA	2.312	0.247	10.34	32.40	45.36
0.075 DEA	2.437	0.238	8.87	26.70	44.95
0.1 DEA	2.342	0.235	8.80	27.80	44.35
0.025 Ethanol	2.339	0.250	10.31	30.12	43.46
0.05 Ethanol	2.351	0.252	11.87	29.90	48.45
0.075 Ethanol	2.327	0.247	10.17	31.20	48.77
0.1 Ethanol	2.342	0.244	8.63	27.98	49.35

When Table 7 is analyzed, it is observed that the PCE requirement for the target flow value increases with the use of GAs. This is thought to be due to the presence of finer particles due to the GA content (Figure 4). It was found that the early age strengths of the cements containing GAs were generally lower than the control mix. Each mortar mixture was prepared according to PCE requirements for target flow value. The PCE requirement for target flow value is generally increased in mixes containing GAs. This is thought to slow down the setting of these mixes, resulting in poor performance compared to the control mix [16].

When the 28-day mixtures were analyzed, it was determined that the GA content positively affected the compressive strength except for the mixtures containing DEA. In this context, it was determined that mixtures containing molasses, MEG and ethanol increased the compressive strength by 5–15%. It was determined that the highest strength performance was found in the mixtures containing molasses. Another reason for the high strength of the mixtures containing GAs compared to the control mixture is PSD. PSD is known to be an important parameter in the strength of cement [7,13,46,47]. Increasing the amount of fines decreases the proportion of non-hydrated particles. This has a positive effect on the strength of cement [7]. It reveals that the presence of GAs is effective in the progressive processes in hydration reactions. Considering that hardened cement pastes are porous materials, their porosity and pore structure are important factors affecting mechanical strength. Another critical factor in determining strength is the bulk strength of hardened cement pastes, which is governed primarily by the degree of hydration and the microstructure of cement hydrates.

3.1.2. Dynamic Yield Stress, Viscosity Values and Structural Build-Up (A_{thix}) Development of Mixtures

Dynamic yield stress and viscosity values of the cement paste mixtures produced within the scope of this study are shown in Table 8.

In order to clearly determine the effect of PCE usage rate, GA type and GA usage rate on the rheological properties of cement pastes, the effect of each parameter was evaluated separately.

When the rheological properties of mixtures without PCE are examined, it was seen that the rheological properties are negatively affected regardless of the type and dosage of GA. Assaad and Issa [15] reported that GAs negatively affect the fresh state and rheological properties of cementitious systems. When the particle size distribution (PSD) of the mixtures with GAs is examined, it is observed that the fine grain ratio increases as the GA dosage increases in cements with the same Blaine fineness value. It is thought that this situation may increase the PCE requirement and negatively affect the rheological properties.

When the effect of PCE usage rate on the dynamic yield stress and viscosity values of the mixtures was examined, decreases were detected in the dynamic yield and viscosity values of the mixtures due to the increase in the PCE usage rate, as expected in the control mixture without GAs. It is known that this situation is due to the electrostatic repulsion and steric repulsion forces acting between cement grains according to the colloidal dispersion stability theory [10,48]. However, it was understood that such behavior was not present in cement paste mixtures containing GAs. In these mixtures, it was determined that the dynamic yield stress and viscosity values generally decrease with an increase in PCE usage rate up to 0.08%, and these values may increase when PCE usage increases. Similarly, in a study conducted by Maybury et al. [49], it was determined that the mixtures exhibited shear thickening behavior when different additives with electrostatic and steric repulsion were added to the systems. It was reported by the researchers that this situation occurred due to the clustering of free polymer chains.

When the mixtures with 0.025% GA were examined, it was determined that the mixtures with the highest dynamic yield stress and viscosity values were the DEA and control mixtures, respectively. As the amount of admixture increased, it was understood that the mixture containing molasses and DEA generally had the highest value. Similarly, when the mixtures with 0.050% and 0.075% GA amounts were examined, regardless of the PCE usage rate, it was determined that the mixtures with the highest dynamic yield stress and viscosity values were the mixtures containing molasses and DEA. When the mixtures with 0.1% GA amount were examined, it was determined that the mixture with the highest dynamic yield stress and viscosity value was the mixture containing DEA. In the mixtures where the PCE usage amount was 0.08%, it was determined that the mixture containing molasses and MEG had the highest dynamic yield stress and viscosity value. In the mixture containing 0.16% PCE, it was determined that the highest dynamic yield stress and viscosity values were in the mixture containing DEA and MEG, respectively. As a result, it was determined that the additive containing molasses was generally the most effective on rheological parameters. As a result, it was determined that the additive containing molasses was generally the most effective on rheological parameters. Similarly, in a study conducted by Gao et al. [50], it was determined that the water requirement of the mixtures increased with the addition of molasses up to a certain dosage. However, it has been reported that adding molasses after a certain dosage does not increase the water requirement of the mixtures and even causes it to decrease. Researchers have stated that this situation is due to the development of cement particle fineness and specific surface with molasses dosage. It has been reported that the effect of using high amounts of molasses in reducing the water requirement is since molasses has a slight water-reducing effect in concrete [51,52].

Table 8. Rheological properties of the mixtures.

Mixture	Rheological Parameters	PCE Dosage (%)		
		0	**0.08**	**0.16**
C	Dynamic yield stress (Pa)	16.70	10.57	6.12
	Apparent viscosity (Pa·s)	6.63	5.8	5.67
	A_{thix} (Pa/s)	0.56	0.63	0.5
0.025 Ethanol	Yield stress (Pa)	35	10.46	18.54
	Apparent viscosity (Pa·s)	5	5.33	5.09
	A_{thix} (Pa/s)	0.33	0.7	0.67
0.05 Ethanol	Yield stress (Pa)	37.31	23.11	29.25
	Apparent viscosity (Pa·s)	5.59	5.52	5.24
	A_{thix} (Pa/s)	0.48	0.57	0.79
0.075 Ethanol	Yield stress (Pa)	14.55	38.12	27.68
	Apparent viscosity (Pa·s)	7.22	6.25	4.82
	A_{thix} (Pa/s)	0.7	0.67	0.71
0.1 Ethanol	Yield stress (Pa)	42.89	29.38	31.95
	Apparent viscosity (Pa·s)	6.43	6.07	6.08
	A_{thix} (Pa/s)	0.72	0.66	0.92
0.025 MEG	Yield stress (Pa)	39.4	35.65	40.37
	Apparent viscosity (Pa·s)	6.3	6.2	6.55
	A_{thix} (Pa/s)	0.46	0.65	0.65
0.05 MEG	Yield stress (Pa)	47.95	38.48	40.35
	Apparent viscosity (Pa·s)	6.9	6.02	6.04
	A_{thix} (Pa/s)	0.54	0.65	0.76
0.075 MEG	Yield stress (Pa)	39.98	34.34	48.42
	Apparent viscosity (Pa·s)	6.17	8.27	7.07
	A_{thix} (Pa/s)	0.44	0.74	0.76
0.1 MEG	Yield stress (Pa)	37.39	16.24	47.59
	Apparent viscosity (Pa·s)	6.27	8.32	6.97
	A_{thix} (Pa/s)	0.56	1.2	1.59
0.025 DEA	Yield stress (Pa)	43.36	45.48	48.46
	Apparent viscosity (Pa·s)	5.9	5.8	6.74
	A_{thix} (Pa/s)	0.4	0.46	0.46
0.05 DEA	Yield stress (Pa)	40.36	43.69	51.68
	Apparent viscosity (Pa·s)	5.29	5.62	6.67
	A_{thix} (Pa/s)	0.35	0.39	0.55
0.075 DEA	Yield stress (Pa)	41.45	47.19	55.94
	Apparent viscosity (Pa·s)	5.54	6.38	7.23
	A_{thix} (Pa/s)	0.39	0.51	0.59
0.1 DEA	Yield stress (Pa)	57.39	50.94	58.38
	Apparent viscosity (Pa·s)	6.99	6.28	6.79
	A_{thix} (Pa/s)	0.31	0.42	0.35
0.025 Molasses	Yield stress (Pa)	43.1	46.26	61.78
	Apparent viscosity (Pa·s)	6.2	6.55	6.64
	A_{thix} (Pa/s)	0.48	0.61	0.75
0.05 Molasses	Yield stress (Pa)	50.58	50.89	63.51
	Apparent viscosity (Pa. s)	7.14	7.41	6.39
	A_{thix} (Pa/s)	0.51	0.68	0.72
0.075 Molasses	Yield stress (Pa)	57.7	53.51	49.39
	Apparent viscosity (Pa·s)	7.83	7.14	6.11
	A_{thix} (Pa/s)	0.56	0.72	1.2
0.1 Molasses	Yield stress (Pa)	48.12	57.85	38.14
	Apparent viscosity (Pa·s)	5.98	7.72	6.57
	A_{thix} (Pa/s)	0.42	0.74	0.73

A_{thix} values of the mixtures are shown in Table 3. When the effect of the PCE usage rate on the A_{thix} value of the mixtures was examined, as expected in the control mixture without GAs, decreases were detected in the A_{thix} values of the mixtures due to the increase in the PCE usage rate. This situation was similar to the trend measured in the rheological parameters of the mixtures. However, it was determined that such behavior was not present in the cement paste mixtures containing GAs and the structural recovery value of the mixtures generally increased with the increase in the PCE usage rate.

When the mixtures without PCE and with 0.025% and 0.050% GA amounts were examined, it was determined that the mixture with the highest A_{thix} value was the control mixture. It was determined that the structural build-up values of the mixtures changed depending on the type of GA with the increase in the PCE usage rate, and when the mixtures containing 0.08% PCE and 0.025% GA were examined, the mixture with the highest A_{thix} value was the mixture containing MEG. It was determined that the highest structural build-up rate belonged to the mixture using molasses when the GA usage rate was 0.050%. When the mixtures without PCE and with 0.075% GA were examined, it was determined that the mixture with the highest A_{thix} value was the mixture containing ethanol. In the mixture containing 0.08% and 0.16% PCE, the highest A_{thix} value was found to be in the mixture containing MEG. When the mixtures without PCE and with 0.1% GA were examined, it was determined that the mixture with the highest A_{thix} value was the mixture containing ethanol. In the mixture containing 0.08% PCE, it was determined that the highest A_{thix} value was in the mixture containing molasses. In the mixture containing 0.16% PCE, it was determined that the highest A_{thix} value was in the mixture containing MEG.

3.2. Evaluation of Analysis Results

3.2.1. Analysis of Signal-to-Noise (S/N) Ratios

Compressive strength values were measured experimentally for each combination of control factors with the experimental design. The data obtained were processed using Taguchi techniques and optimization of the measured grinding factors was achieved by signal-to-noise (S/N) ratios. The highest value of compressive strength is important to improving the quality of concrete. Therefore, the "higher is better" equation was used to calculate the S/N ratio. S/N ratios and mean values for the grinding parameters are shown in Table 9.

Table 9. Experimental results, S/N ratios and mean values.

Experiment No.	Control Factors			Compressive Strength (MPa)	S/N Ratio for Compressive Strength	Means for Compressive Strength
	GA Type	GA Dosage	Days			
1	Molasses	0.025	7	28.37	29.06	28.37
2	Molasses	0.05	7	26.12	28.34	26.12
3	Molasses	0.075	28	50.8	34.12	50.8
4	Molasses	0.1	28	51.25	34.19	51.25
5	MEG	0.025	7	28.23	29.01	28.23
6	MEG	0.05	7	31.44	29.95	31.44
7	MEG	0.075	28	51.67	34.26	51.67
8	MEG	0.1	28	46.83	33.41	46.83
9	DEA	0.025	28	41.67	32.40	41.67
10	DEA	0.05	28	45.36	33.13	45.36
11	DEA	0.075	7	26.7	28.53	26.7
12	DEA	0.1	7	27.8	28.88	27.8
13	Et	0.025	28	43.46	32.76	43.46
14	Et	0.05	28	48.45	33.71	48.45
15	Et	0.075	7	31.2	29.88	31.2
16	Et	0.1	7	27.98	28.94	27.98

The effect of each control factor on the compressive strength was analyzed using a "S/N response table" and a "means table". The results of the S/N and mean response of the compressive strength values are shown in Table 10.

Table 10. Response table for S/N and significance for compressive strength values.

Response Table for Signal-to-Noise Ratios				Response Table for Means			
Level	**GA Type**	**GA Dosage**	**Days**	**Level**	**GA Type**	**GA Dosage**	**Days**
1	31.43	30.81	29.07	1	39.13	35.43	28.48
2	31.66	31.28	33.5	2	39.54	37.84	47.44
3	30.74	31.7		3	35.38	40.09	
4	31.32	31.36		4	37.77	38.46	
Delta	0.92	0.89	4.42	Delta	4.16	4.66	18.96
Rank	2	3	1	Rank	3	2	1

This table, prepared using the Taguchi technique, shows the optimum levels of control factors for the highest compressive strength value. The level values of the control factors given in Table 10 are shown graphically in Figure 5. The optimum processing parameters of the control factors to achieve the highest compressive strength value can be easily determined from these graphs. The best level for each control factor was found according to the highest S/N ratio and the lowest mean value in the levels of that control factor. As a result, it was found that the highest compressive strength was obtained by curing MEG at 0.075 dosage for 28 days.

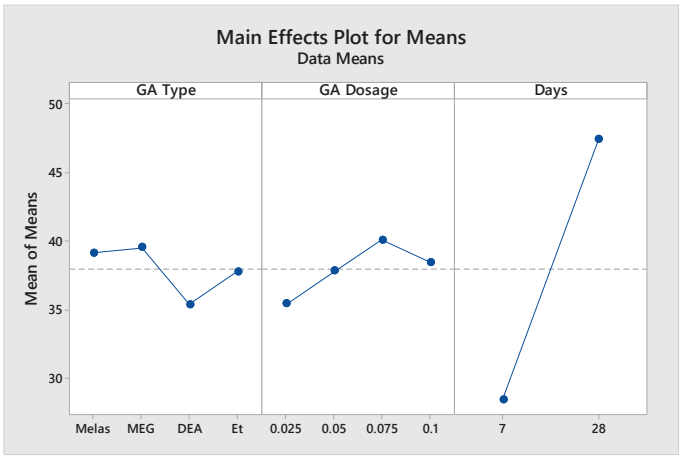

(**a**)

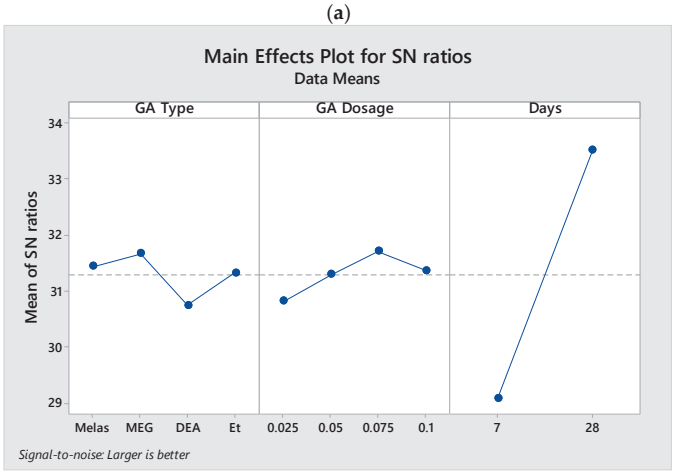

(**b**)

Figure 5. Influence degrees and significance graph of factor parameters for high compressive strength value (**a**) according to S/N ratio and (**b**) according to mean values.

3.2.2. The ANOVA Method

In this study, ANOVA was used to analyze the effects of GA type, dosage and curing time on compressive strength. The ANOVA results for the compressive strength value are shown in Table 11. This analysis was performed at 5% significance level and 95% confidence level. The significance of the control factors in ANOVA was determined by comparing the F values of each control factor. Moreover, if the P value of each control factor is less than 0.5, it means that the data are significant. The effect ratio in the last column of Table 11 shows the percentage value of each parameter contribution indicating the degree of impact on process performance. The percentage error of the ANOVA model was 2.38%.

Table 11. ANOVA results for the energy consumed.

Source	Degre of Freedom (DoF)	Sum of Squares (SS)	Mean Square (MS)	F-Value	*p*-Value	Impact Rates (%)
GA Type	3	42.25	14.08	3.03	0.093168	2.71%
GA Dosage	3	44.82	14.94	3.22	0.082825	2.87%
Days	1	1437.36	1437.36	309.42	0	92.04%
Error	8	37.16	4.65			2.38%
Total	15	1561.59				100.00%

3.2.3. Estimation of Optimum Grinding Conditions by the Taguchi Method and Comparison with Experimental Results

For the Taguchi method, verification tests were performed at optimum and random levels of control factors. The results obtained are shown in Table 12. It is understood from the results that the predicted values and experimental data are quite close. Kıvak [25] reported that error values should be less than 20% for reliable statistical analysis. In this direction, it was understood that the data obtained were at an acceptable level. Therefore, the results obtained from the validation tests reflect successful optimization.

Table 12. Comparison of experimental results and Taguchi predictions.

	Taguchi Method		
	Experimental Result	**Estimate**	**Error (%)**
0.05 Molasses 28 Day	52.38	50.49	3.74
0.25 Ethanol 7 Day	29.90	27.77	7.67

4. Conclusions

The results obtained from this study in which the effects of different types and dosages of GAs on grinding efficiency, rheological properties and compressive strength of cementitious systems were investigated are summarized below:

- It was determined that the highest and lowest grinding performance among the GAs was obtained when MEG and molasses admixtures were used, respectively.
- It was observed that the highest grinding performance, regardless of the type of GA, was obtained when 0.075% by mass of GA was used.
- It was found that the use of GAs increased the PCE requirement for the target spread value, had a negative effect on the early age strength but had a positive effect on the 28-day compressive strength.
- Decreases in the dynamic threshold shear stress, viscosity and A_{thix} values of the mixtures were measured due to the increase in the PCE utilization rate in the control mixture without GAs.
- The blends with the highest dynamic threshold shear stress and viscosity values were molasses 0.050–0.16% and MEG 0.1–0.08%, while the blends with the lowest values were control 0.16% and ethanol 0.075–0.16%, respectively.

- The mixture with the highest A_{thix} value was MEG 0.1–0.16%, while the mixture with the lowest value was Dea-0.1–0%.
- Optimum levels of control factors on compressive strength were determined using S/N ratios. It was found that the GA dosage was a more important parameter compared to the type of GA.
- The margin of error of the predictions compared to the experimental results was found to be acceptable.

Author Contributions: Conceptualization, Y.K., H.G.Ş., N.M. and A.M.; methodology, Y.K., H.G.Ş., N.M. and A.M.; software, Y.K., H.G.Ş., N.M. and A.M.; validation, Y.K., H.G.Ş., N.M. and A.M.; formal analysis, Y.K., H.G.Ş., N.M. and A.M.; investigation, Y.K., H.G.Ş., N.M. and A.M.; resources, Y.K., H.G.Ş., N.M. and A.M.; data curation, Y.K., H.G.Ş., N.M. and A.M.; writing—original draft preparation, Y.K., H.G.Ş., N.M. and A.M.; writing—review and editing, Y.K., H.G.Ş., N.M. and A.M.; visualization, Y.K., H.G.Ş., N.M. and A.M.; supervision, A.M.; project administration, A.M. All authors have read and agreed to the published version of the manuscript.

Funding: The authors express their appreciation for the assistance provided by the Scientific and Technological Research Council of Turkey (TUBITAK) under Grant No: 222M425. They also recognize the contributions of the Bursa Uludag University Science and Technology Centre (BAP) under grant numbers FGA-2024-1754. The primary and secondary authors extend their gratitude to TUBITAK for the 2211A scholarship received during their doctoral studies.

Institutional Review Board Statement: This study did not require ethical approval.

Informed Consent Statement: Not applicable.

Data Availability Statement: The original contributions presented in the study are included in the article, further inquiries can be directed to the corresponding author.

Conflicts of Interest: The authors declare no conflicts of interest.

References

1. Sezer, A.; Boz, A.; Tanrinian, N. An investigation into strength and permittivity of compacted sand-clay mixtures by partial replacement of water with lignosulfonate. *Acta Phys. Pol. A* **2016**, *130*, 23–27. [CrossRef]
2. Yüksel, C.; Mardani-Aghabaglou, A.; Beglarigale, A.; Yazıcı, H.; Ramyar, K.; Andiç-Çakır, Ö. Influence of water/powder ratio and powder type on alkali–silica reactivity and transport properties of self-consolidating concrete. *Mater. Struct.* **2016**, *49*, 289–299. [CrossRef]
3. Yiğit, B.; Salihoğlu, G.; Mardani-Aghabaglou, A.; Salihoğlu, N.K.; Özen, S. Recycling of sewage sludge incineration ashes as construction material. *J. Fac. Eng. Archit. Gazi Univ.* **2020**, *35*, 1647–1664.
4. Bayqra, S.H.; Mardani-Aghabaglou, A.; Ramyar, K. Physical and mechanical properties of high volume fly ash roller compacted concrete pavement (A laboratory and case study). *Constr. Build. Mater.* **2022**, *314*, 125664. [CrossRef]
5. Durgun, M.Y.; Özen, S.; Karakuzu, K.; Kobya, V.; Bayqra, S.H.; Mardani-Aghabaglou, A. Effect of high temperature on polypropylene fiber-reinforced mortars containing colemanite wastes. *Constr. Build. Mater.* **2022**, *316*, 125827. [CrossRef]
6. Boesch, M.E.; Hellweg, S. Identifying Improvement Potentials in Cement Production with Life Cycle Assessment. *Environ. Sci. Technol.* **2010**, *44*, 9143–9149. [CrossRef]
7. Zhang, Y.M.; Napier-Munn, T.J. Effects of particle size distribution, surface area and chemical composition on Portland cement strength. *Powder Technol.* **1995**, *83*, 245–252. [CrossRef]
8. Madlool, N.A.; Saidur, R.; Hossain, M.S.; Rahim, N.A. A critical review on energy use and savings in the cement industries. *Renew. Sustain. Energy Rev.* **2011**, *15*, 2042–2060. [CrossRef]
9. ICS. *Cement Technology Roadmap 2009 Carbon Emission Reduction Up to 2050*; World Business Council for Sustainable Development: Conches-Geneva, Switzerland, 2009.
10. Mardani-Aghabaglou, A. *Portland Çimentosu ve Süperakışkanlaştırıcı Katkı Uyumunun Incelenmesi, Doktora Tezi*; Ege Üniversitesi Fen Bilimleri Enstitüsü, İnşaat Mühendisliği Anabilim Dalı: İzmir, Turkey, 2016.
11. Deniz, V. A Study on the Specific Rate of Breakage of Cement Materials in a Laboratory Ball Mill. *Cem. Concr. Res.* **2003**, *33*, 439445. [CrossRef]
12. Jankovic, A.; Valery, W.; Davis, E. Cement grinding optimisation. *Miner. Eng.* **2004**, *17*, 1075–1081. [CrossRef]
13. Zhang, T.; Gao, J.; Hu, J. Preparation of polymer-based cement grinding aid and their performance on grindability. *Constr. Build. Mater.* **2015**, *75*, 163–168. [CrossRef]
14. Jeknavorian, A.A.; Barry, E.F.; Serafin, F. Determination of grinding aids in Portland cement by pyrolysis gas chromatography-mass spectrometry. *Cem. Concr. Res.* **1998**, *28*, 1335–1345. [CrossRef]

15. Assaad, J.J.; Issa, C.A. Effect of clinker grinding aids on flow of cement-based materials. *Cem. Concr. Res.* **2014**, *63*, 1–11. [CrossRef]
16. Kobya, V.; Kaya, Y.; Mardani-Aghabaglou, A. Effect of amine and glycol-based grinding aids utilization rate on grinding efficiency and rheological properties of cementitious systems. *J. Build. Eng.* **2022**, *47*, 103917. [CrossRef]
17. Katsioti, M.; Tsakiridis, P.E.; Giannatos, P.; Tsibouki, Z.; Marinos, J. Characterization of various cement grinding aids and their impact on grindability and cement performance. *Constr. Build. Mater.* **2009**, *23*, 1954–1959. [CrossRef]
18. Plank, J.; Sachsenhauser, B.; De Reese, J. Experimental determination of the thermodynamic parameters affecting the adsorption behaviour and dispersion effectiveness of PCE superplasticizers. *Cem. Concr. Res.* **2010**, *40*, 699–709. [CrossRef]
19. Mardani-Aghabaglou, A.; Boyacı, O.C.; Hosseinnezhad, H.; Felekoğlu, B.; Ramyar, K. Effect of gypsum type on properties of cementitious materials containing high range water reducing admixture. *Cem. Concr. Compos.* **2016**, *68*, 15–26. [CrossRef]
20. Şahin, H.G.; Mardani, A.; Özen, S.; Emin, A. Utilization of high-range water reducing admixture having air-entraining agents in cementitious systems. *J. Build. Eng.* **2023**, *64*, 105565. [CrossRef]
21. Özen, S.; Altun, M.G.; Mardani-Aghabaglou, A.; Ramyar, K. Effect of main and side chain length change of polycarboxylate-ether-based water-reducing admixtures on the fresh state and mechanical properties of cementitious systems. *Struct. Concr.* **2021**, *22*, E607–E618. [CrossRef]
22. Mardani-Aghabaglou, A.; Felekoğlu, B.; Ramyar, K. Effect of Cement C3A Content on Properties of Cementitious Systems Containing High-Range Water-Reducing Admixture. *J. Mater. Civ. Eng.* **2017**, *29*, 04017066. [CrossRef]
23. Aytekin, B.; Mardani-Aghabaglou, A. Sustainable materials: A review of recycled concrete aggregate utilization as pavement material. *Transp. Res. Rec.* **2022**, *2676*, 468–491. [CrossRef]
24. Assaad, J.J.; Asseily, S.E.; Harb, J. Use of cement grinding aids to optimise clinker factor. *Adv. Cem. Res.* **2010**, *22*, 29–36. [CrossRef]
25. Şahin, H.G.; Biricik, Ö.; Mardani-Aghabaglou, A. Polycarboxylate-based water reducing admixture–clay compatibility; literature review. *J. Polym. Res.* **2022**, *29*, 33. [CrossRef]
26. Sun, Z.; Liu, H.; Ji, Y.; Pang, M. Influence of glycerin grinding aid on the compatibility between cement and polycarboxylate superplasticizer and its mechanism. *Constr. Build. Mater.* **2020**, *233*, 117104. [CrossRef]
27. Prziwara, P.; Kwade, A. Grinding aids for dry fine grinding processes–Part I: Mechanism of action and lab-scale grinding. *Powder Technol.* **2020**, *375*, 146–160. [CrossRef]
28. Karakuzu, K.; Kobya, V.; Mardani-Aghabaglou, A.; Felekoğlu, B.; Ramyar, K. Adsorption properties of polycarboxylate ether-based high range water reducing admixture on cementitious systems: A review. *Constr. Build. Mater.* **2021**, *312*, 125366. [CrossRef]
29. Kaya, Y.; Kobya, V.; Mardani, A.; Mardani, N.; Beytekin, H.E. Effect of Grinding Conditions on Clinker Grinding Efficiency: Ball Size, Mill Rotation Speed, and Feed Rate. *Buildings* **2024**, *14*, 2356. [CrossRef]
30. Kıvak, T. Optimization of surface roughness and flank wear using the Taguchi method in milling of Hadfield steel with PVD and CVD coated inserts. *Measurement* **2014**, *50*, 19–28. [CrossRef]
31. *EN 197-1*; Cement—Part 1: Composition, Specifications and Conformity Criteria for Common Cements. Europe Standard: Brussels, Belgium, 2011.
32. *TS EN 196-1*; Methods of Testing Cement—Part 1: Determination of Strength. British Standards Institution: London, UK, 2016.
33. *TS EN 1097-6*; Tests for Mechanical and Physical Properties of Aggregates Đ. British Standards Institution: London, UK, 1996.
34. *ASTM C109*; Standard Test Method for Compressive Strength of Hydraulic Cement Mortars (Using 2-in. or [50-mm] Cube Specimens). ASTM International: West Conshohocken, PA, USA, 2002.
35. *ASTM C1437*; Standard Test Method for Flow of Hydraulic Cement Mortar. ASTM International: West Conshohocken, PA, USA, 2015.
36. Mandal, N.; Doloi, B.; Mondal, B.; Das, R. Optimization of flank wear using Zirconia Toughened Alumina (ZTA) cutting tool: Taguchi method and Regression analysis. *Measurement* **2011**, *44*, 2149–2155. [CrossRef]
37. Assaad, J.J.; Asseily, S.E.; Harb, J. Effect of specific energy consumption on fineness of portland cement incorporating amine or glycol-based grinding aids. *Mater. Struct.* **2009**, *42*, 1077–1087. [CrossRef]
38. Klimpel, R.R.; Manfroy, W. Chemical grinding aids for increasing throughput in the wet grinding of ores. *Ind. Eng. Chem. Process Des. Dev.* **1978**, *17*, 518–523. [CrossRef]
39. Zheng, J.J.; Harris, C.C.; Somasundaran, P. *Role of Chemical Additives in Stirred Media Mill Grinding 5th World Congress of Chemical Engineering*; American Institute of Chemical Engineers: New York, NY, USA, 1996.
40. Nair, P.R.; Paramasivam, R. Effect of grinding aids on the time-flow characteristics of the ground product from a batch ball mill. *Powder Technol.* **1999**, *101*, 31–42. [CrossRef]
41. Vieira, M.G.; Peres, A.E.C. Effect of rheology and dispersion degree on the regrinding of an iron ore concentrate. *J. Mater. Res. Technol.* **2013**, *2*, 332–339. [CrossRef]
42. Altun, O.; Benzer, H.; Toprak, A.; Enderle, U. Utilization of grinding aids in dry horizontal stirred milling. *Powder Technol.* **2015**, *286*, 610–615. [CrossRef]
43. Moothedath, S.K.; Ahluwalia, S.C. Mechanism of action of grinding aids in comminution. *Powder Technol.* **1992**, *71*, 229–237. [CrossRef]
44. Yusupov, T.S.; Kirillova, E.A. Surfactants in fine ore grinding. *J. Min. Sci.* **2010**, *46*, 582–586. [CrossRef]
45. Zhao, J.; Wang, D.; Wang, X.; Liao, S. Characteristics and mechanism of modified triethanolamine as cement grinding aids. *J. Wuhan Univ. Technol.-Mater. Sci. Ed.* **2015**, *30*, 134–141. [CrossRef]

46. Bentz, D.P.; Garboczi, E.J.; Haecker, C.J.; Jensen, O.M. Effects of cement particle size distribution on performance properties of Portland cement-based materials. *Cem. Concr. Res.* **1999**, *29*, 1663–1671. [CrossRef]
47. Ferraris, C.F.; Hackley, V.A.; Avilés, A.I.; Buchanan, C.E. *Analysis of the ASTM Round-Robin Test on Particle Size Distribution of Portland Cement: Phase I*; National Institute of Standards and Technology Report; National Institute of Standards and Technology: Gaithersburg, MD, USA, 2002; Volume 6883.
48. Verwey, E.J.W. Theory of the stability of lyophobic colloids. *J. Phys. Chem.* **1947**, *51*, 631–636. [CrossRef]
49. Maybury, J.; Ho, J.C.M. Shear thickening of cement powder paste–why and how to mitigate? *HKIE Trans.* **2017**, *24*, 193–203. [CrossRef]
50. Gao, X.; Yang, Y.; Deng, H. Utilization of beet molasses as a grinding aid in blended cements. *Constr. Build. Mater.* **2011**, *25*, 3782–3789. [CrossRef]
51. Tuthill, L.H.; Adams, R.F.; Hemme, J.M. Observations in Testing and Use of Water-Reducing Retarders. In *Symposium on Effect of Water-Reducing Admixtures and Set-Retarding Admixtures on Properties of Concrete*; ASTM International: West Conshohocken, PA, USA, 1960.
52. Jumadurdiyev, A.; Ozkul, M.H.; Saglam, A.R.; Parlak, N. The utilization of beet molasses as a retarding and water-reducing admixture for concrete. *Cem. Concr. Res.* **2005**, *35*, 874–882. [CrossRef]

Disclaimer/Publisher's Note: The statements, opinions and data contained in all publications are solely those of the individual author(s) and contributor(s) and not of MDPI and/or the editor(s). MDPI and/or the editor(s) disclaim responsibility for any injury to people or property resulting from any ideas, methods, instructions or products referred to in the content.

materials

MDPI

Article

The Synergistic Effect of Limestone Powder and Rice Husk Ash on the Mechanical Properties of Cement-Based Materials

Jialei Wang [1], Feifei Jiang [2,*], Juan Zhou [2,*] and Zhongyang Mao [3]

[1] School of Civil Engineering and Architecture, NingboTech University, Ningbo 315100, China; wangjl@nit.zju.edu.cn
[2] School of Civil Engineering, Nantong Institute of Technology, Nantong 226000, China
[3] College of Materials Science and Engineering, Nanjing Tech University, Nanjing 211800, China; mzy@njtech.edu.cn
* Correspondence: 999620140019@just.edu.cn (F.J.); zhoujuan198808@163.com (J.Z.)

Abstract: Fully utilizing solid waste as supplementary cementitious materials (SCMs) while ensuring the mechanical properties of cement-based materials is one of the pathways for carbon reduction in the cement industry. Understanding the effects of the two solid wastes-limestone powder (LP) and rice husk ash (RHA) on the mechanical properties of cement-based materials is of great significance for their application in concrete. This study investigates the impact of LP and RHA on the strength of cement mortar at various ages and the microhardness of hardened cement paste. The results suggest that two materials have a certain synergistic effect on the mechanical properties of the cementitious materials. The addition of RHA effectively addresses the issues of slow strength development, insufficient late-stage strength of the cementitious material, and the low strength blended with a large amount of LP, while a suitable amount of LP can promote the strength increase in the cement-RHA system. Based on the comprehensive analysis of compressive strength and microhardness, the optimal solution for achieving high mechanical properties in composite cementitious materials is to use 10% each of LP and RHA, resulting in a 9.5% increase in 28 d strength compared to a pure cement system. The higher the content of LP, the greater the increase caused by 10% RHA in compressive strength of the composite system, which makes the strength growth rate of cementitious material mixed with 10% LP at 3–56 d 62.1%. When the LP content is 20% and 30%, the addition of 10% RHA increases the 28 d strength by 44.8% and 38.8%, respectively, with strength growth rates reaching 109.8% and 151.1% at 3–56 d.

Keywords: limestone powder; rice husk ash; synergistic effect; mechanical properties

1. Introduction

Cement production is one of the main sources of carbon and pollutant gas emissions, with carbon emissions from producing Portland cement estimated at around 0.7–0.9 t/t according to the statistics [1]. Carbon emissions generated by China's cement industry in 2021 was approximately 1.375 billion tons, accounting for 13.5% of the country's total emissions [2]. The reduction of clinker to cement ratio is crucial for decreasing the carbon emissions and achieving low-carbon production [3]. The resource utilization of solid waste is an effective way to reduce carbon emissions in cement production [4], using solid waste with potential pozzolanic activity as SCMs to replace cement. This approach aims to reduce the use of cement clinker from application aspects to production sources in order to control the carbon emissions [5]. However, it is essential to ensure that the main properties such as mechanics of the cement composite materials partially replaced by solid waste are not significantly affected, which raises higher requirements for the selection of solid waste.

Limestone is one of the raw materials for cement production and the major source of carbon emissions from clinker. As a by-product of limestone minerals, LP has been

widely studied as a mineral admixture to replace cement. Although it reduces cement usage from an application perspective, the addition of LP has an adverse impact on the mechanical properties of cement-based materials and their development with age, which has also led to a significant reduction in its utilization rate. The nucleation effect of LP particles promotes the deposition of hydration products, which can accelerate the hydration of cement particles to improve the early strength of cement paste [6]. However, LP does not have pozzolanic activity and the hydration reaction with C_3A in cement clinker is relatively slow. The reduction in cement content caused by dilution effect decreases the amount of hydration products, and excessive amounts of LP negatively impact the late-stage strength of cement-based materials and its development with age [7]. Specifically, adding more than 10% LP can adversely affect the compressive strength of cement paste [8], while exceeding 20% leads to a reduction in strength with the increasing LP content [9]. It is well known that the pore structure is one of the factors that affect the strength of cement-based materials, but the dilution and dissolution behavior of LP can cause the coarsening effect of pores with age [10], which is also the reason for insufficient development of the strength. In order to address the issue and promote the application of LP in cement-based materials, a more reasonable approach is to use other solid-waste materials for system improvement and optimization.

As a type of agricultural solid waste, RHA contains a large amount of active SiO_2 under certain conditions, making it an ideal SCM that seems to be able to mitigate the adverse effects of LP. RHA has the characteristics of high specific surface area and porous structure, which has impacts on the strength of cement paste in various aspects [11,12]. RHA can provide nucleation sites for cement hydration, promote the hydration reaction of cement, and the fine particles can fill the pores in the paste. The pozzolanic reaction consumes $Ca(OH)_2$ (CH) and forms C-S-H gel to further fill the pores and enhance the density of pastes. Additionally, the porous structure facilitates moisture release to promote the further hydration of cement. As a result, the compressive strength and its development of cement-based materials is significantly improved under the physicochemical action of RHA particles [13], along with corresponding increases in tensile and flexural strength [14–16].

The application of LP and RHA in cement-based materials has been studied. Sensale [11] found that the 28 d compressive strength of the 5% LP samples blended with 10%, 15%, 20%, 25%, and 30% RHA, respectively, was the highest compared to other mixtures blended with LP. Sua-iam [17] showed that self-compacting concrete prepared with LP and RHA exhibited higher mechanical properties than the ordinary self-compacting concrete, reaching a strength of 40 MPa at 28 d, an increase of 13%. In a quaternary composite cementitious system, the compressive and flexural strength of 20% fly ash mixed with 10% LP and 10% RHA to replace cement have been improved to varying degrees [18].

However, the application composite system mixed with LP and RHA still has research gaps, and the impact of their synergistic effect on the mechanical properties of the materials has not been clearly expressed. Particularly, the research on their mechanical properties also mainly focuses on the analysis of strength data, lacking studies on the micromechanical properties of the composite system. The role of RHA in enhancing the mechanical properties of composites with high LP content remains unclear, which is crucial for the feasibility of using the composite approach to improve the utilization rate of LP. Therefore, this study aims to improve the low strength and its slow development of the cement-LP system by utilizing the high pozzolanic activity and unique porous structure of RHA. The influence of the interaction between LP and RHA on the mechanical properties of the composite cementitious system was investigated through the strength of mortar and the microhardness of hardened cement paste. The research provides a relevant basis for the feasibility application of using LP and RHA as composite replacements for cement, which can not only improve the comprehensive utilization rate of these two types of solid waste in engineering materials, but can also effectively reduce the high carbon emissions caused by cement application to a certain extent. Therefore, the application of LP and RHA in cementitious materials is of significant importance in engineering.

2. Experimental

2.1. Materials and Mix Proportion

P·I 42.5 Portland cement produced by China United Cement Group Co., Ltd. was used to prepare mortar and paste, with a density of 3.14 g/cm^3, which was marked as P. The LP (produced in Jingmen, China) contained 98.22% $CaCO_3$ with a density of 2.7 g/cm^3, which was marked as L. The preparation of RHA [19,20]: grinding rice husk into powder and soaking it in a 1% dilute hydrochloric acid solution for 1 h to fully acidify the rice husk powder. After pretreatment, the powder was washed and filtered 3 times with clean water, oven-dried, and then heated in a muffle furnace to obtain white RHA, with the combustion program (the calcination needs to be carried out in 3 times) and preparation process shown in Figure 1. After homogenization, the density of RHA was measured at 2.07 g/cm^3, marked as R. The particle size distribution and particle parameters of the powder materials are shown in Figure 2, and the chemical composition of the cement and RHA is listed in Table 1.

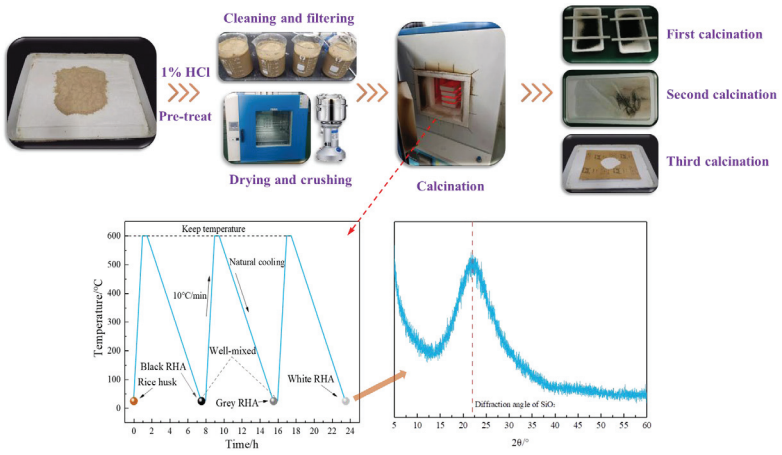

Figure 1. Combustion program and preparation process of RHA.

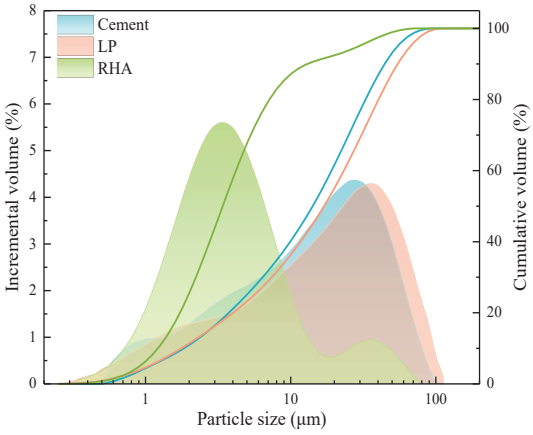

(**a**)

	Mean volume size (μm)	D50 (μm)	Specific surface area (m²/kg)
Cement	19.17	14.16	347
LP	24.57	17.83	417
RHA	6.51	3.56	2380

(**b**)

Figure 2. The (**a**) particle size distribution and (**b**) particle parameters of cement, LP, and RHA.

Table 1. Chemical compositions of the cement and RHA (wt%).

Chemicals	SiO_2	Al_2O_3	Fe_2O_3	CaO	MgO	SO_3	Na_2O_{eq}	Others	F-CaO	LOI
Cement	22.08	4.32	3.43	63.67	2.32	2.62	0.58	—	0.90	2.03
RHA	99.33	0.098	0.047	0.073	0.033	0.083	0.023	0.316	—	—

The fine aggregates were made of quartz sand with a fineness modulus of 2.8, categorized as medium sand in Zone II, with continuous grading. The Sika-3301H type

polycarboxylic superplasticizer was adopted, which was diluted from a stock concentration of 55% to 25% before test. The tap water was used for mixing.

According to Table 1 and Figure 1, the main component of RHA is amorphous SiO_2. The amorphous SiO_2 has high reactivity and can rapidly participate in secondary hydration reaction within cement composite systems, consuming calcium hydroxide and generating more C-S-H gel, which can improve the strength of cement-based materials to some extent. The combustion of organic matter results in a porous powder [21], and its porous structure provides more internal surfaces, which makes the specific surface area (SSA) of RHA much larger than that of cement and LP. In order to confirm the porous structure characteristics of RHA, the hygroscopic properties were tested [22,23]. A certain amount of RHA was spread in a glass petri dish and placed in a constant temperature and humidity chamber to monitor changes in sample mass with time, as shown in Figure 3a. The N_2 adsorption-BJH method was used to obtain the adsorption isotherm of pore volume distribution, with the pore volume distribution illustrated in Figure 3b. Based on the cumulative pore volume per unit mass, the porosity of RHA was 67.04%. Figure 4 shows the microscopic morphological characteristics, which reveals that the particles are polygonal and angular, with pore structures primarily consisting of small pits and holes, exhibiting certain water storage capability. The experimental mix proportions are detailed in Table 2.

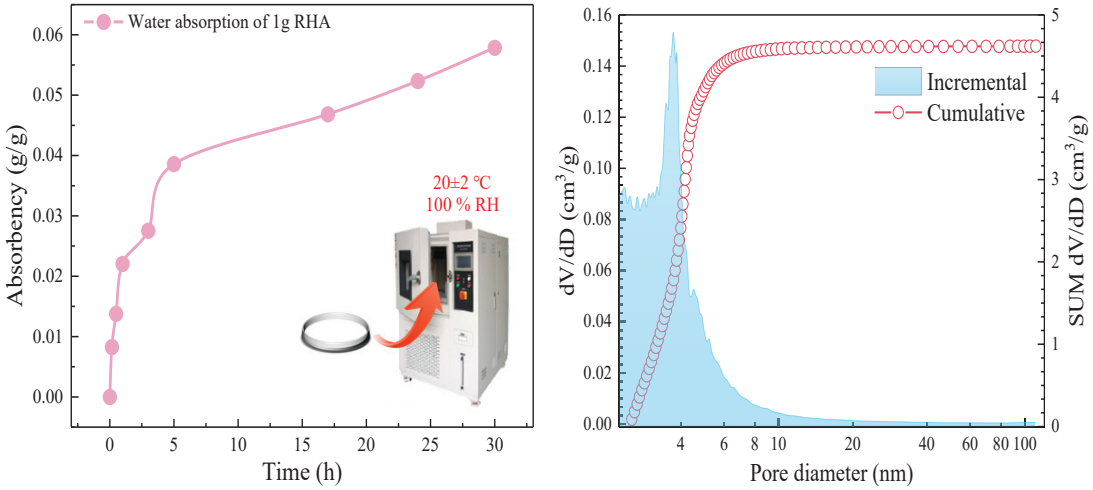

(**a**) Moisture-absorption characteristics (**b**) Pore volume distribution

Figure 3. Characterization of pore structure characteristics of RHA.

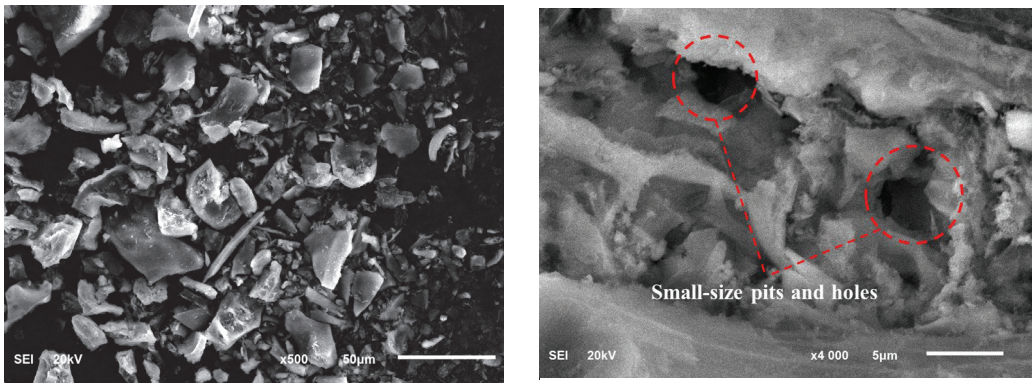

(**a**) (**b**)

Figure 4. SEM images (**a**) ×500 and (**b**) ×4000 of RHA.

Table 2. Mix proportions of cement-LP-RHA composite pastes.

Samples	Cement (wt%)	LP (wt%)	RHA (wt%)	Superplasticizer (wt%)	Sand/Binder	Water/Binder
PC	100	0	0	0	3	0.4
PL10	90	10	0	0	3	0.4
PL20	80	20	0	0	3	0.4
PL30	70	30	0	0	3	0.4
PR5	95	0	5	0.4	3	0.4
PR10	90	0	10	0.4	3	0.4
PR15	85	0	15	0.84	3	0.4
PR20	80	0	20	1.34	3	0.4
PL10R5	85	10	5	0.4	3	0.4
PL10R10	80	10	10	0.4	3	0.4
PL10R15	75	10	15	0.84	3	0.4
PL10R20	70	10	20	1.34	3	0.4
PL20R10	70	20	10	0.4	3	0.4
PL30R10	60	30	10	0.4	3	0.4
PL30R15	55	30	15	0.84	3	0.4
PL30R5	65	30	5	0.4	3	0.4

2.2. Test Methods

2.2.1. Raw Material Performance Tests

Particle Size Distribution (PSD)

The PSD test was conducted using a Malvern-Mastersizer 2000 type laser particle size analyzer produced in Malvern, PA, USA. The refractive index of solid particles was set at 0, and the refractive index of the dispersant was set at 1.33, with opacity ranging from 4% to 8%. The testing range was from 0.02 to 2000 μm. Ethanol was used as the dispersant for the testing of cement, LP, and RHA.

X-Ray Fluorescence (XRF)

XRF analysis was used to determine the types and content of elements in the powder. The sample to be tested was ground using an agate mortar, and an Axios mAX type XRF spectrometer produced by PANalytical B.V. in Almelo, The Netherlands was employed for testing, yielding the elemental mass ratio or the mass ratio of oxides in the material.

N_2 Adsorption Test

Dynamic chromatography was used to measure the nitrogen gas adsorption capacity. Based on the nitrogen isothermal adsorption or desorption curves, the SSA of RHA was obtained. Before conducting the adsorption measurement, the physical adsorbates on the surface of the adsorbent should be removed through "degassing". The RHA powder to be tested was first placed in a U-shaped sample tube, allowing a mixed gas containing a certain proportion of adsorbate to flow through the sample. The adsorption amount of the sample for the adsorbate molecules (N_2) was determined by measuring the change in gas concentration before and after adsorption. By measuring the amount of nitrogen adsorbed by the sample at a nitrogen partial pressure, the nitrogen isothermal adsorption or desorption curve can be plotted, thereby obtaining the SSA or pore size distribution of RHA.

Scanning Electron Microscope (SEM)

A JSM-6700F type SEM produced by JEOL in Tokyo, Japan was used to observe the surface morphology and pore characteristics of RHA powder particles. To prevent the powder from being removed under high vacuum and to enhance the conductivity of the powder particles, gold sputtering treatment was applied to the RHA. The vacuum condition was set to 5×10^{-5} Pa, and the operating voltage was 20 kV.

2.2.2. Strength Test

According to the mix proportions in Table 2, specimens sized 40 mm × 40 mm × 160 mm were prepared. The flexural and compressive strength of the corresponding mortar specimens were tested according to GB/T 17671-2021 [24] "Test Method of Cement Mortar Strength". A DYE-300S flexural and compressive testing machine was used for the tests, with a loading rate of 2.4 kN/s, as shown in Figure 5.

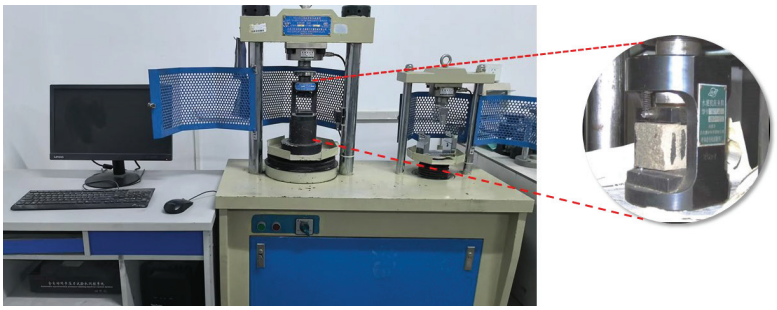

Figure 5. Compressive and flexural strength tests of cement mortar.

2.2.3. Microhardness Test

Based on the mix proportions in Table 2, an equal-proportional cement pastes without sand were prepared. The hardened samples at 28 d were cut into 2 mm thick slices and then broken into block samples of approximately 1–3 cm. Isopropanol was used to terminate hydration for 7 d, after which the samples were vacuum-dried. The dried samples were embedded in epoxy resin, and the epoxy on the testing surfaces was initially pre-ground with 400# sandpaper until samples nearly exposed. This was followed by further grinding with 600# sandpaper until the sample surfaces were fully revealed. Finally, the surfaces were polished to a smooth and reflective state by using 1200# sandpaper. The ground samples were then placed on a polishing machine and polished sequentially with 2.5 μm, 1 μm and 0.5 μm particle sizes of diamond polishing agents. The polished samples were tested using the HMAS-D1000M Vickers microhardness testing system produced by Shanghai Yanrun Optics Technology Co., Ltd., Shanghai, China, applying a load of 0.245 N for 15 s. A 10 × 10 serpentine dot matrix was used for indentation test, with the spacing between each pair of indentations adjusted to 50 μm according to the actual area of the indentation, as shown in Figure 6. The Vickers microhardness values were calculated according to Equation (1).

$$HV = 0.1891 \times \frac{F}{d^2} \quad (1)$$

where HV is the microhardness value of a single indentation, MPa; F is the applied load, and all indentations are uniformly 0.245 N; d is the arithmetic average value of the diagonal of a single indentation, mm.

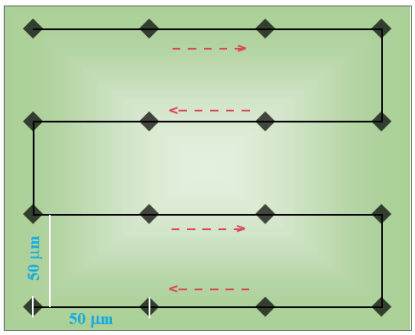

(**a**) Schematic diagram of indentation lattice

Figure 6. *Cont.*

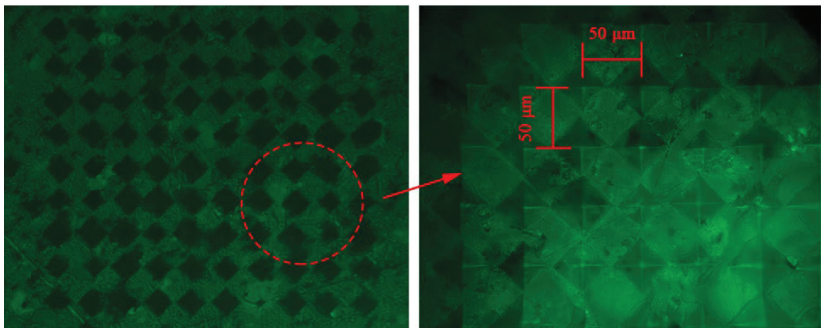

(**b**) Microhardness indentation spacing

Figure 6. Indentation lattice of microhardness.

3. Results and Discussion

3.1. Strength of Composite Cementitious Materials

3.1.1. Improvement of RHA on the Strength of Cement-LP System

Figure 7 shows the variation of compressive and flexural strength of cement mortar with the content of RHA. The effect of RHA on the compressive and flexural strength varies with different hydration ages. As shown in Figure 7a, the compressive strength of cement mortar decreases with RHA at 3 d age. When the age is 7 d, 28 d, and 56 d, 10% RHA significantly improves the compressive strength compared to the pure cement mortar. For 10% and 20% RHA content, the increasing rate in compressive strength accelerates with age, while for 5% RHA, the increase is relatively slow. Figure 7b indicates that 10% RHA also significantly enhances the flexural strength of cement mortar, with a higher content of RHA leading to greater increases with age.

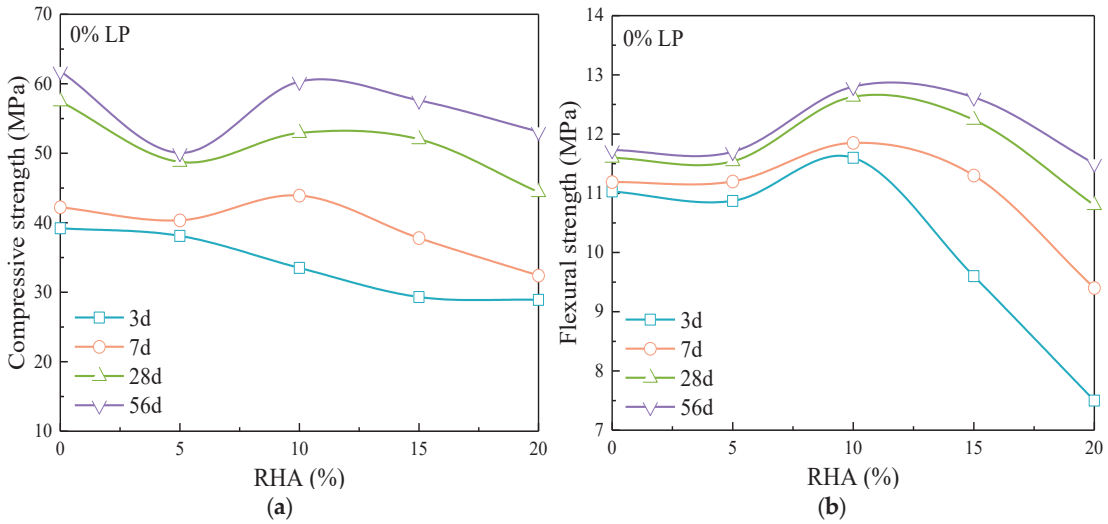

Figure 7. Effect of RHA on (**a**) compressive strength and (**b**) flexural strength of cement mortar.

The addition of the fine particles increases the hydration rate of cement [25]. The average particle size of RHA is much smaller than that of cement and LP, and the pores within the particles provide a larger SSA. RHA can offer the nucleation sites for cement hydration, and the embedded fine particles in the hydration products can better fill the pores of paste. The pozzolanic reaction consumes CH and forms new C-S-H gel, which continues to fill the pores. The porous structure promotes the release of moisture, enhancing the hydration of both cement and RHA, and further improving the density of the mortar [26]. High content of RHA can severely limit the water requirement for early-age cement hydration, significantly reducing the hydration degree. After the paste hardens, the RHA gradually releases water as the humidity changes, which facilitates the formation

of hydration products and fills the pores, thus increases the density. The higher the RHA content, the greater the amount of water released, which more significantly promotes the hydration, resulting in a relatively larger increase in the strength with age.

Figure 8 shows the effect of RHA on the strength of cement-LP mortar. The compressive and flexural strengths of the mortar blended with LP initially increase and then decrease with the content of RHA. The highest mortar strength is achieved with a combination of 10% LP and 10% RHA, resulting in a 9.5% increase in strength at 28 d compared to pure cement mortar. When the age is 7 d, 28 d, and 56 d, 5%, 10% and 15% RHA significantly enhance the strength of the mortar mixed with 10% LP, and 20% RHA increases the late-stage strength growth of the composite mortar, which makes the strength at 28 d and 56 d closer to that of the mortar with 10% LP.

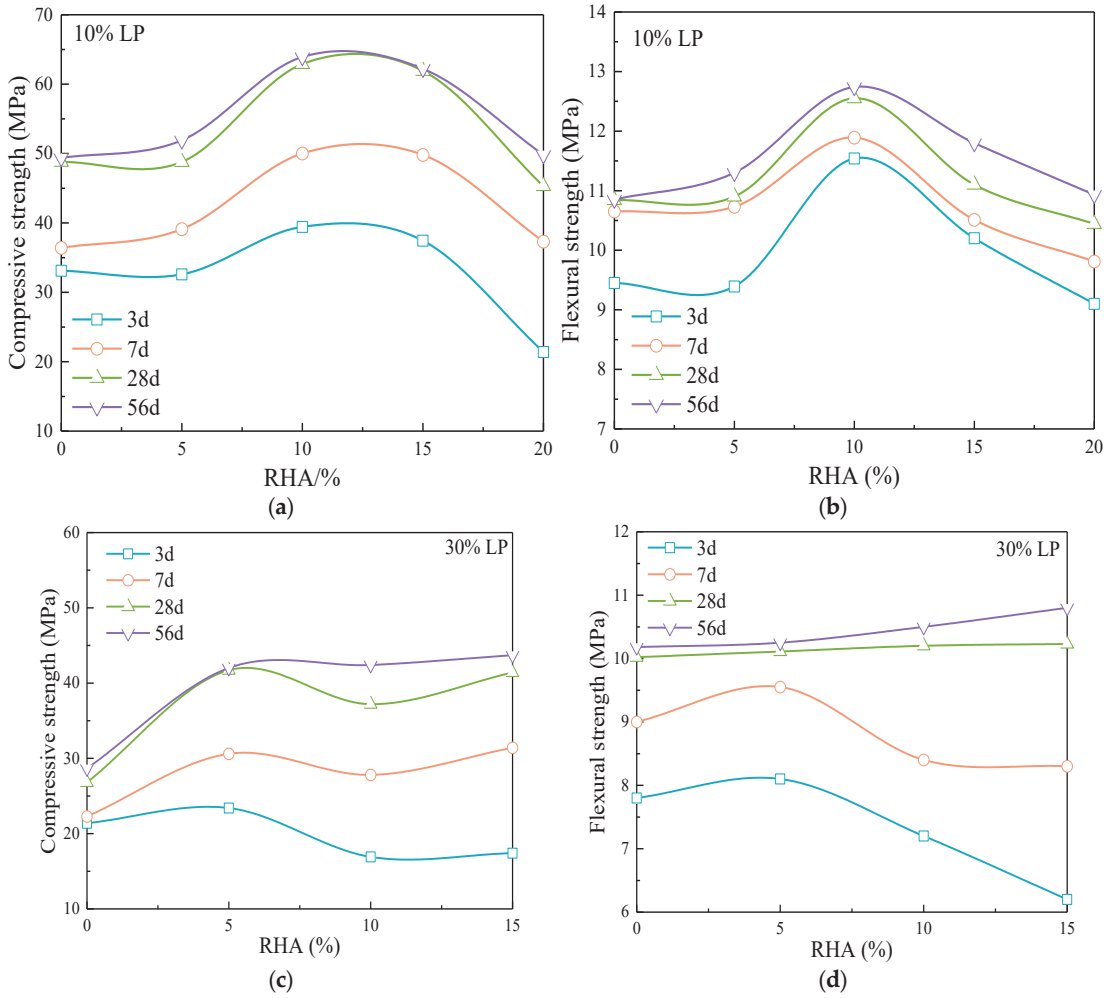

Figure 8. Effect of RHA on (**a**,**c**) compressive strength and (**b**,**d**) flexural strength of cement-LP composite mortar.

Figure 8c,d compare the effect of RHA on the mortar strength when the LP content is 30%. Five percent RHA improves the compressive strength at 3 d age. With the age increases, the higher content of RHA leads to a significant improvement in compressive strength. The higher the content, the more water is released in the late stage, and the more significant the promoting effect on hydration, thereby facilitating the rapid development of later strength.

The flexural strength of the composite mortar mixed with 30% LP exhibits different trends at various ages. The strength initially increases and then decreases with the RHA content at 3 d and 7 d, and it increases with the content at 28 d and 56 d, which indicates that the increased RHA enhances the growth rate of flexural strength with age in the mortar

blended with 30% LP. For mortar with a high LP content, 5% RHA effectively improves the strength at 3 d and 7 d, while 10% and 15% RHA enhance the growth rate of strength with age.

Figure 9 shows the effect of 10% RHA on the compressive strength growth rate of composite systems with different LP contents at 3 d–56 d. The addition of RHA results in higher compressive strength growth rates for the composite mortar compared to the cement-LP system. The improvement in compressive strength is greater with the higher LP content; the growth rate is 62.1% for PL10R10, while PL20R10 and PL30R10 reach growth rates of 109.8% and 151.1%, respectively, indicating a significant increase in compressive strength. This comparative analysis shows that the addition of RHA effectively addresses the issues of slow strength development and insufficient late-stage strength in high LP content systems.

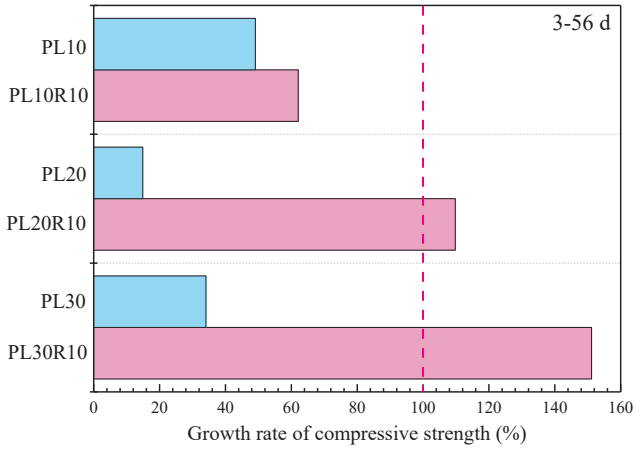

Figure 9. Effect of RHA on compressive strength growth rate of cement-LP mortar.

3.1.2. Effect of LP on Strength of Cement-RHA System

Figure 10 illustrates the changes in compressive strength and flexural strength of cement mortar with varying LP content. The compressive strength of the cement mortar decreases with LP content at all the ages. In the early stages of hydration, the addition of a small amount of LP does not enhance the strength of the cement paste, which differs from the previous studies [27,28]. This is largely due to the significant influence of LP particle size on early strength [29], which is related to the average particle size of LP [30].

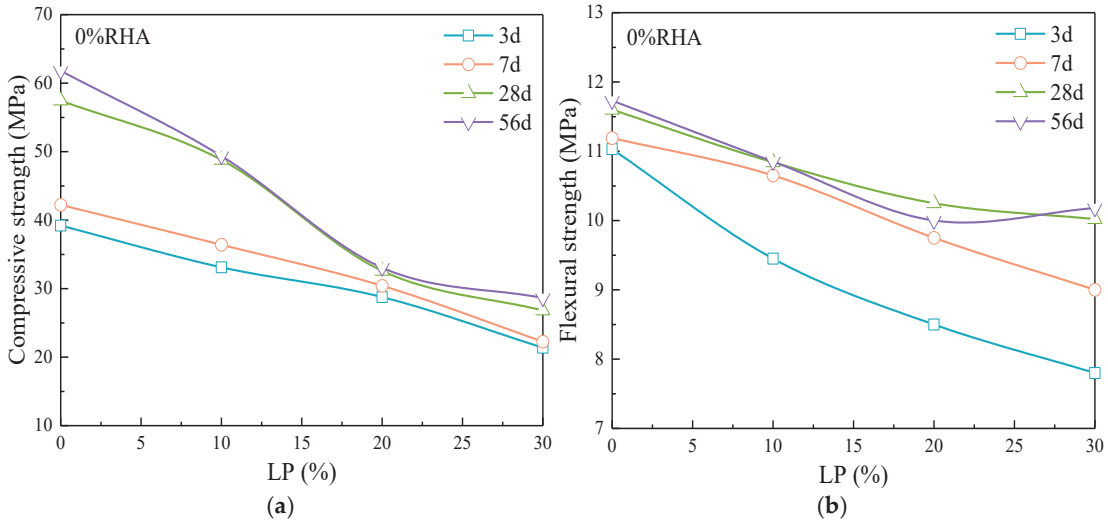

Figure 10. Effect of LP on (**a**) compressive strength and (**b**) flexural strength of cement mortar.

During the initial mixing and plastic state of the cement paste, the nucleation effect of LP allows for effective dispersion and enough hydration of the cement particles. The LP particles embedded in the hydration products also serve as good fillers, forming a favorable particle packing effect that leads to rapid early strength growth of the mortar with the age. However, the average particle size of the LP is 24.57 μm (Figure 2b), which is coarser than that of the cement particles, resulting in a relatively weaker acceleration effect on cement hydration. Thereby, it leads to a decrease in early (3d, 7d) strength of the mortar as the LP content increases. When the LP content is 20% and 30%, the development of strength in the late stage (>7d) is slow, with the strength increase at 7 d–28 d significantly lower compared to the 10% content. Insufficient late-stage strength growth is the major issue in the cement-LP system. The trend of flexural strength variation with LP content is similar to that of the compressive strength, showing rapid growth in the early stage and slow growth in the late stage. However, the flexural strength at 56 d blended with 20% and 30% LP shows an anomalous trend. This is due to the relatively low flexural strength values of the cement mortar, and the higher content of LP leads to a significant reduction in later-stage flexural strength. As a result, certain numerical errors are inevitably present in the lower strength values. Figure 11 shows the effect of LP on the strength of the cement-RHA composite mortar.

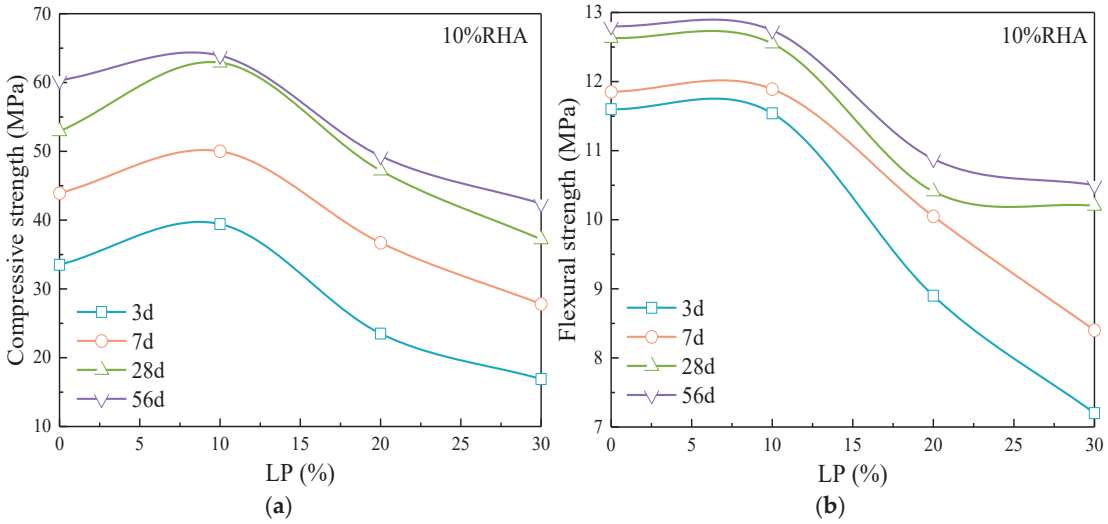

Figure 11. Effect of LP on (**a**) compressive strength and (**b**) flexural strength of cement-RHA mortar.

Due to the extremely low reactivity of LP, the hydration degree of the cementitious materials is significantly reduced. As a result, the strength of mortar blended with a high content of LP is markedly reduced at all the ages. The interaction between LP and RHA has a certain synergistic effect on the hydration of cement. The nucleation effect of RHA can influence the nucleation of hydration products to some extent, and the incorporation of LP can effectively alleviate the issue of insufficient nucleation sites for cement particles. Due to the intense pozzolanic reaction of RHA and the accompanied hydration of cement at an early stage, an appropriate amount of LP mitigates the competitive relationship for nucleation sites between the hydration products of cement and RHA. Both of them can effectively undergo the hydration reactions, which can increase the content of the products and thereby enhances the strength of the mortar. In summary, the cement-LP system exhibits slow strength growth in the late-stages, and excessive LP content can lead to a significant reduction in the strength at all the ages.

3.1.3. Synergistic Effect of LP and RHA

Figure 12 presents the analysis of the synergistic effects of LP and RHA on the compressive strength of the composite cementitious system. The overall trend in compressive

strength at various ages indicates a decrease with the LP content and an increase with the RHA content. For the compressive strength of the composite mortar at 3 d and 56 d, the primary influence factors are the contents of LP and RHA. However, the compressive strength at 7 d and 28 d is greatly affected by the LP content, with strength gradually decreasing as LP content increases.

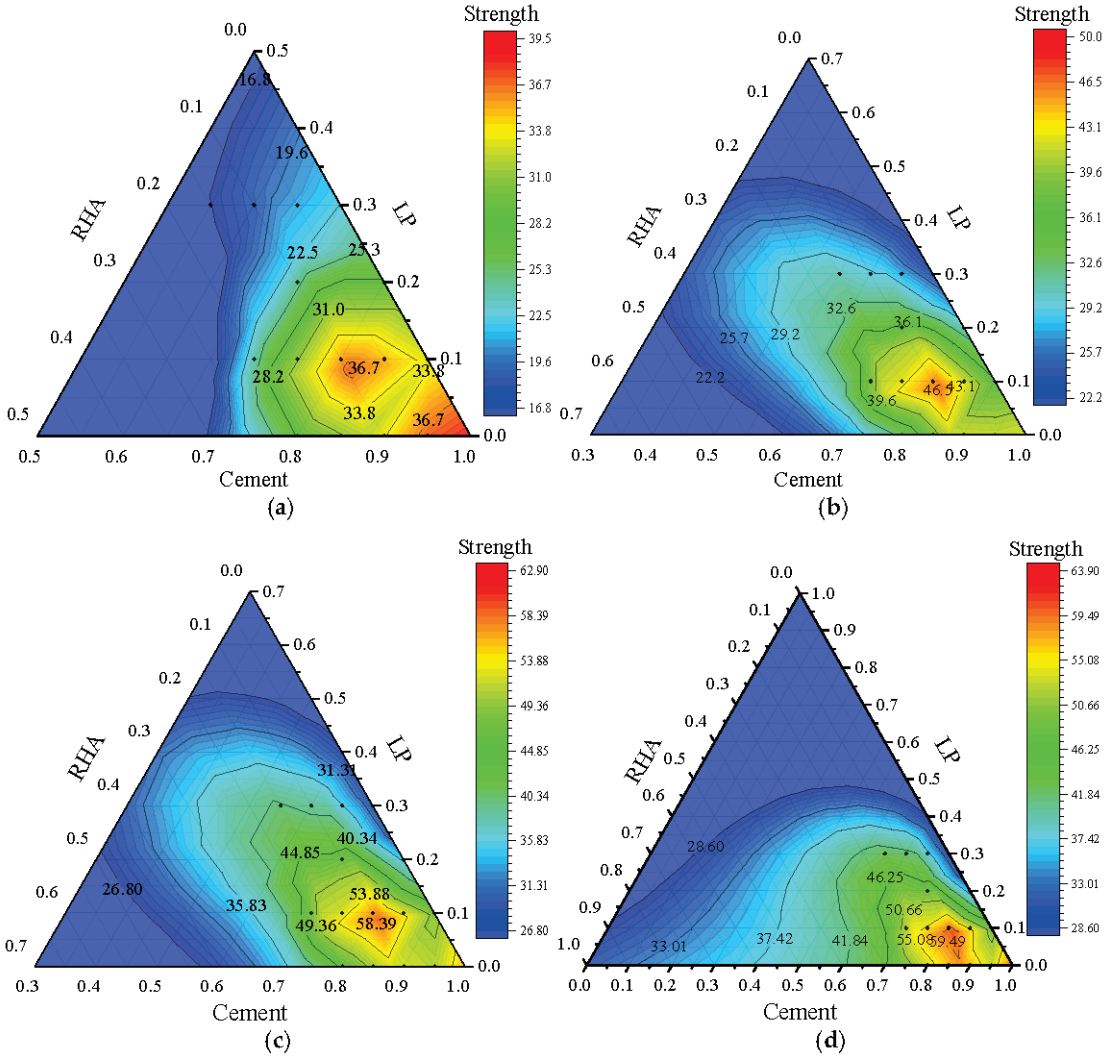

Figure 12. Effect of LP and RHA on compressive strength (**a**) 3 d, (**b**) 7 d, (**c**) 28 d, and (**d**) 56 d in composite system.

At the age of 3 d, 7 d, and 28 d, a peak strength region is observed when the LP content is at 10–20% and the RHA content is at 5–15%. There is an additional peak strength region at 3 d age when both LP and RHA contents are in the range of 0% to 10%. At the age of 56 d, a peak strength region is also observed when the LP content is at 10–20% and the RHA content is at 5–20%. This indicates that an appropriate increase of RHA content significantly enhances the compressive strength of the cement-LP system in the late-stage.

3.2. Micromechanical Properties

The macro-mechanical properties of cement-based materials are closely related to the microstructure. In addition to the pore structure, the load-bearing capacity of hardened cement paste under stress is crucial, which is related to the hardness of the cement paste. Microhardness effectively characterizes the ability of the cement paste to resist the surface-embedding of hard objects. The microhardness of cement stone depends on

the composition and density of the hydration products in the cementitious system. The incorporation of SCMs can change the amount and density of the cement hydration products, thereby affecting the hardness of the cement paste [31,32]. The hydration products of the cementitious system exhibit elastic-plastic characteristics under stress, and their non-uniform distribution at the microscale results in complex and unstable deformation under microstresses, leading to significant data dispersion in microhardness measurements. Therefore, mathematical statistical analysis of the microhardness data is necessary to reduce the substantial errors caused by this dispersion [33]. Due to the high variability in the microhardness test values of the cement paste, some values greater than 200 MPa were excluded. The microhardness testing results of the cement-LP-RHA paste at 28 d of hydration are shown in Figure 13.

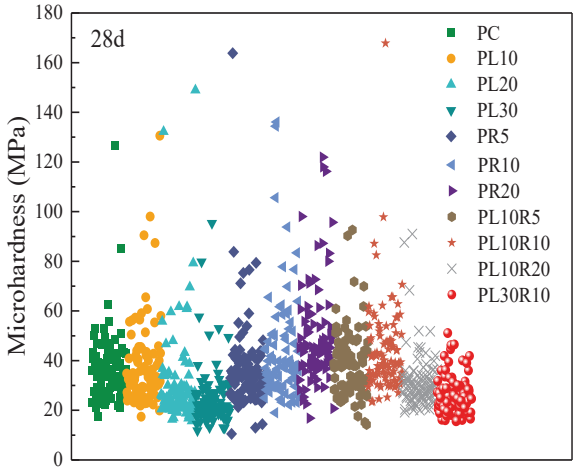

Figure 13. Microhardness of cement-LP-RHA composite paste.

Under the same load, the indentation area at different points varies, reflecting the differences in microhardness. This is primarily due to the differing physical properties of the hydration product at various indentation locations. Although there is significant dispersion in the microhardness test values of the cement paste, the microhardness at the indentation points mainly falls within the range of 10 MPa to 60 MPa. There are fewer hydration products with lower microhardness, and there are fewer unhydrated cement particles with higher hardness values, which indicates that the cement paste has a high degree of hydration.

Figure 14 shows the probability distribution of microhardness. The overall trend in the probability distribution indicates that an increase in LP content reduces the hardness of the cement paste, as shown in Figure 14a,d. Particularly when the content exceeds 10%, the reduction becomes more pronounced. The addition of LP leads to a reduction in cement hydration productsand a looser bridging among the products and the formation of low-density C-S-H gel, which decreases the microhardness of the matrix. An appropriate content of RHA can effectively improve the microhardness, as shown in Figure 14b,c. The pozzolanic reaction of the RHA and its internal curing effect promote the cement hydration, leading to a denser interlayer structure of C-S-H and the formation of high-density C-S-H gel, thereby increasing the microhardness. When the RHA content is too high, it can lead to insufficient tightness in the connections between products, thereby affecting the hardness of the matrix.

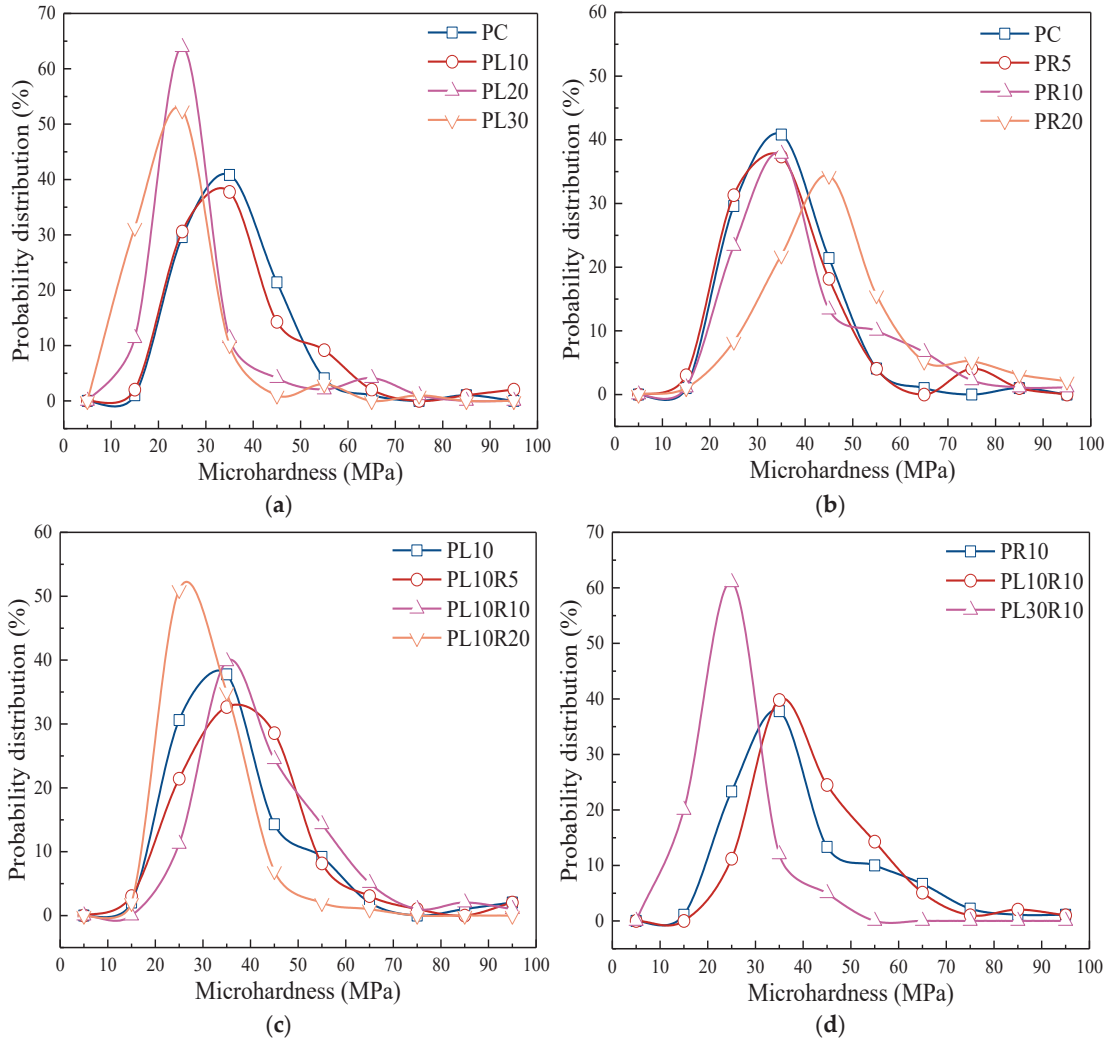

Figure 14. Probability distribution of composite paste microhardness in (**a**) cement-LP, (**b**) cement-RHA and (**c**,**d**) cement-LP-RHA system.

The microhardness at various points within the indentation area shows a concentrated distribution range along with some discrete data points. Based on the theoretical and statistical perspective, when there are enough testing points in the indentation area (100 points in this test), the results should conform to a certain statistical laws. Box plots can display the distribution of the data and identify any outliers, as shown in Figure 15, with statistical parameters listed in Table 3. From the data distribution, the upper and lower quartiles of microhardness values for all the samples range from 18.2 MPa to 58.5 MPa, indicating a wide distribution with many discrete points. The significant dispersion in microhardness test values is primarily due to the heterogeneity of the cement paste, where the distribution of internal hydration product phases is random and uneven. Additionally, the sample preparation process can create certain defects on the indentation surface during grinding. When the diamond indenter of the microhardness tester presses on these defect areas during the pressing process, the defects are flattened first to make them even with the surrounding surface before they can be stabilized. Under the same load, the presence of a certain number of defects and irregular depth distribution leads to a relatively scattered measured microhardness value. However, as shown in the overall data distribution, the microhardness values tend to decrease with the LP content, while they increase with the RHA content.

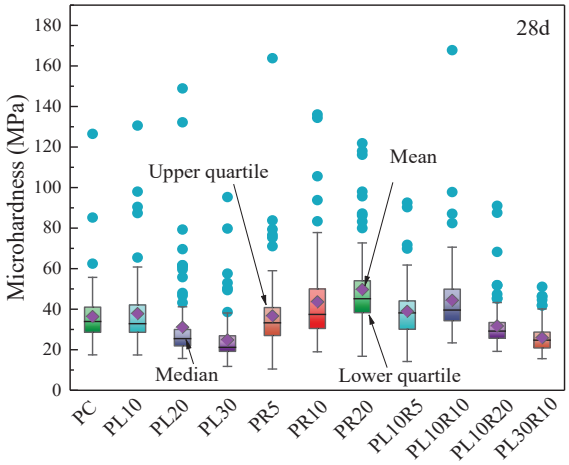

Figure 15. Box-plot of microhardness distribution of hardened cement paste.

Table 3. Statistical results of microhardness (MPa).

Samples	**PC**	**PL10**	**PL20**	**PL30**	**PR5**	**PR10**
Mean	36.31	37.8	31.05	24.82	36.69	43.63
Standard deviation	13.57	16.92	19.81	12.09	18.16	20.96
Maximum	126.50	130.60	148.90	95.30	163.80	136.1
Upper quartile (Q3)	43.00	44.00	34.10	28.60	41.80	52.3
Median	33.90	32.85	25.50	21.20	33.30	37.4
Lower quartile (Q1)	26.80	26.50	21.10	18.20	25.60	29.5
Minimum	17.50	17.40	15.70	11.80	10.50	19
Interquartitle range (IQR)	16.20	17.50	13.00	10.40	16.20	22.8
Range (Max-Min)	109.00	113.20	133.20	83.50	153.30	117.1
Samples	**PR20**	**PL10R5**	**PL10R10**	**PL10R20**	**PL30R10**	—
Mean	49.65	38.94	44.34	31.69	25.86	—
Standard deviation	19.70	13.13	18.32	11.27	7.33	—
Maximum	121.90	92.60	167.8	91.00	51.10	—
Upper quartile (Q3)	58.50	47.40	53.9	35.85	29.85	—
Median	45.15	38.15	39.55	29.20	24.75	—
Lower quartile (Q1)	37.80	29.20	32	25.00	19.95	—
Minimum	16.80	14.20	23.4	19.20	15.60	—
Interquartitle range (IQR)	20.70	18.20	21.9	10.85	9.90	—
Range (Max-Min)	105.10	78.40	144.4	71.80	35.50	—

From the statistical parameters in Table 3, it can be seen that the microhardness of hardened cement paste does not simply follow a normal distribution [34]. The statistical distribution of the microhardness data was examined using Minitab 19.1 software, with the normal, 3-Parameter Lognormal, 3-Parameter Weibull, and 3-Parameter Gamma distributions shown in Figure 16.

In each distribution, the three lines represent the −95%, 100%, and 95% confidence intervals. If data follow a distribution, more points should fall within the −95% to 95% confidence interval region. From Figure 16, it is evident that the microhardness values of the samples are more consistent with the 3-Parameter Lognormal distribution. Minitab provides the statistical value representing the Anderson–Darling statistic, and typically the smaller the AD value, the more likely the data are to follow this distribution. The AD values are shown in Table 4, which further illustrates that the microhardness of the hardened cement paste conforms to the 3-Parameter Lognormal distribution rather than the normal distribution. This result is consistent with previous research findings [35,36].

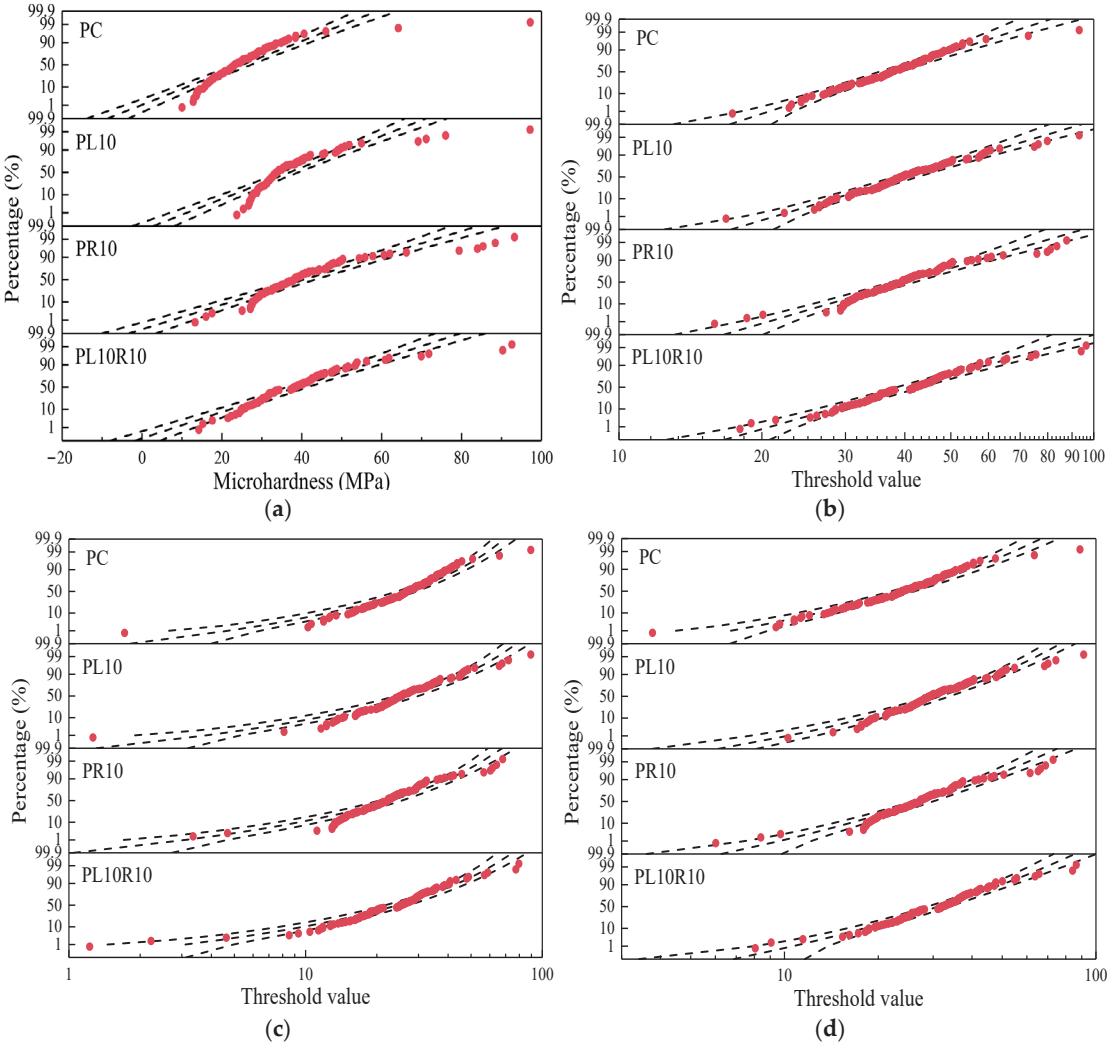

Figure 16. Fitting of microhardness data with different distributions (**a**) normal, (**b**) 3-Parameter Lognormal, (**c**) 3-Parameter Weibull, and (**d**) 3-Parameter Gamma of samples.

Table 4. AD fitting-value of each distribution.

Samples	Normal	3-Parameter Lognormal	3-Parameter Weibull	3-Parameter Gamma
PC	4.206	0.396	1.759	0.642
PL10	6.498	0.566	2.209	1.716
PL20	12.761	1.423	3.898	3.658
PL30	9.387	1.504	3.716	2.899
PR5	4.013	1.366	3.025	1.734
PR10	5.749	0.398	1.591	1.319
PR20	4.462	1.204	2.49	1.594
PL10R5	1.83	0.537	1.282	0.64
PL10R10	5.137	0.274	1.288	0.659
PL10R20	6.9	0.699	1.928	1.268
PL30R10	2.678	0.257	0.493	0.325

Using the goodness of fit test in Minitab, the three parameter values corresponding to the 3-Parameter Lognormal distribution of the sample's microhardness can be obtained: the threshold parameter θ, the location parameter μ, and the scale parameter σ. According to the statistical principles of the lognormal distribution, deconvolution statistical analysis can

be employed to derive the probability density function (PDF) and cumulative distribution function (CDF) of the sample hardness values [37], as shown in Equations (2) and (3).

$$f(u) = \frac{1}{\sigma\sqrt{2\pi}} \exp\left[-\frac{(u-\mu)^2}{2\sigma^2}\right] \tag{2}$$

$$F(u) = \frac{1}{\sigma\sqrt{2\pi}} \int_{-\infty}^{u} \exp\left[-\frac{(u-\mu)^2}{2\sigma^2}\right] du \tag{3}$$

where $f(u)$ represents the PDF of the sample's microhardness values; $F(u)$ is the CDF; μ is the mean of all the test values; σ is the standard deviation of the test values; and u is the microhardness value of a single test point in the sample.

Figure 17 shows the probability density curve of the lognormal distribution of microhardness. Based on the central limit theorem in statistics and the methods for solving the statistical parameters of the lognormal distribution, the mean, median, mode, and the ±95% confidence intervals of the mean corresponding to the 3-Parameter Lognormal distribution are used as statistical parameters for comparison and analysis. The statistical results are presented in Table 5.

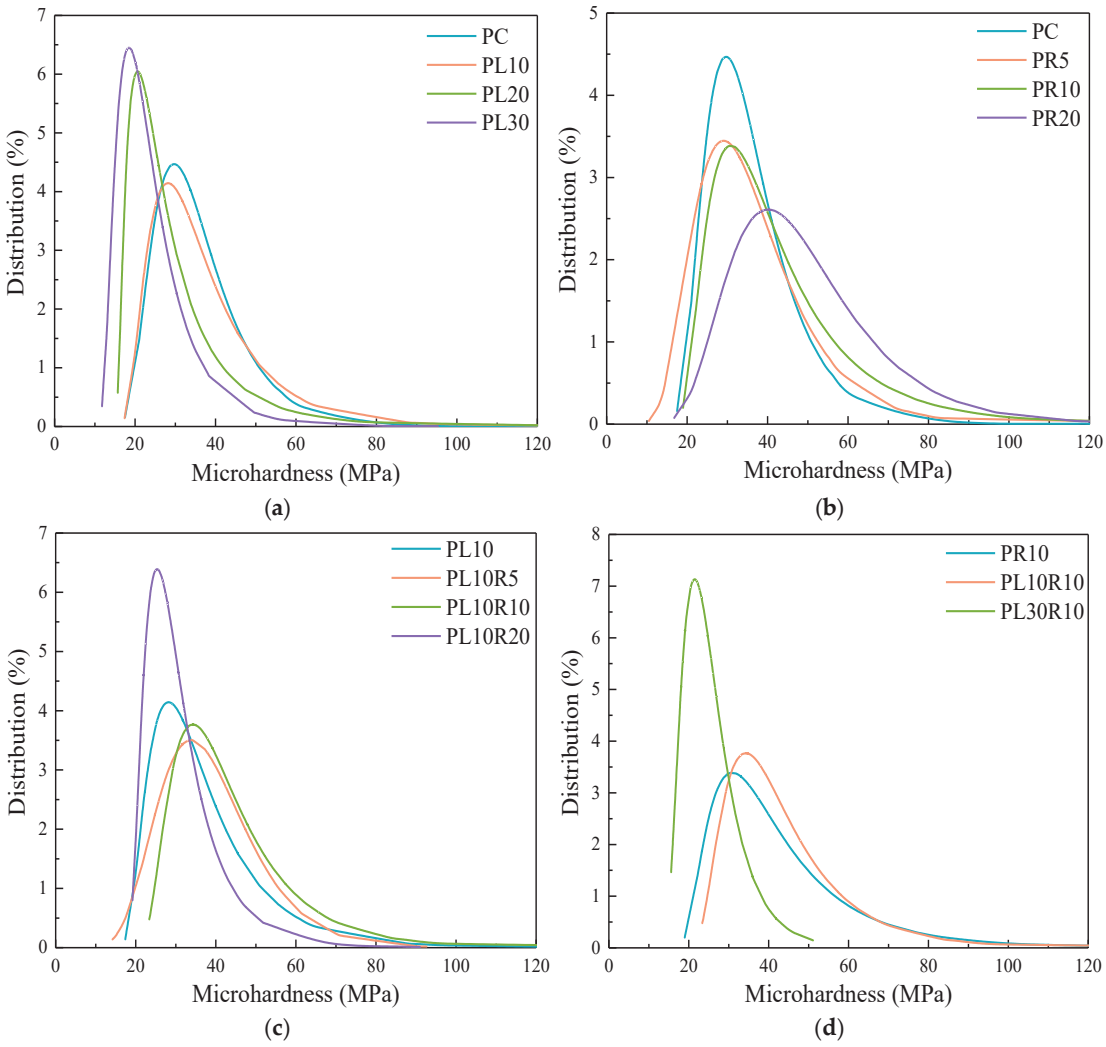

Figure 17. Probability density of 3-Parameter Lognormal distribution of microhardness data in (**a**) cement-LP, (**b**) cement-RHA and (**c**,**d**) cement-LP-RHA system.

Table 5. Statistical parameters of 3-Parameter Lognormal distribution of microhardness data (MPa).

Samples	Hv			
	Mean	Median	Mode	95% Confidence Interval
PC	36.2	33.8	29.7	(34.0, 38.6)
PL10	37.5	33.9	28.2	(34.8, 40.6)
PL20	30.3	26.0	20.6	(27.7, 33.4)
PL30	24.5	22.2	18.5	(22.8, 26.5)
PR5	36.4	33.8	29.1	(33.7, 39.3)
PR10	43.4	38.4	30.9	(39.7, 47.7)
PR20	49.5	46.2	40.2	(46.0, 53.4)
PL10R5	38.9	37.1	33.8	(36.5, 41.5)
PL10R10	44.1	40.3	34.3	(41.2, 47.5)
PL10R20	31.5	29.1	25.4	(29.8, 33.6)
PL30R10	25.9	24.2	21.5	(24.5, 27.4)

The mean and median obtained from the distribution in Table 5 are close to those in Table 3. According to the central limit theorem in statistics, the limiting distribution of any independent random variable follows the normal distribution. In summary, the lognormal distribution can more accurately describe the distribution of microhardness in hardened cement stone. A comparison of the parameters in Table 5 with the compressive strength at the same age (28 d) is shown in Figure 18.

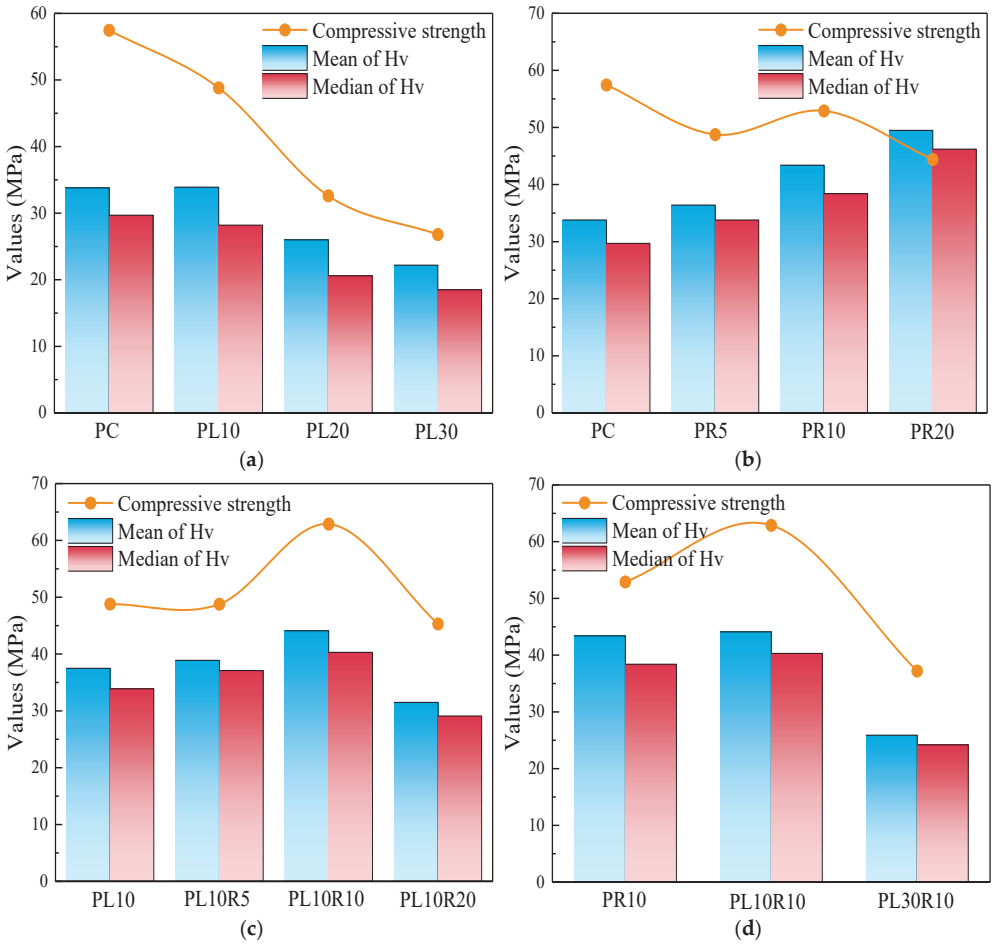

Figure 18. Comparison of compressive strength and statistical parameters of microhardness in (**a**) cement-LP, (**b**) cement-RHA and (**c**,**d**) cement-LP-RHA system.

The compressive strength of cement mortar and the microhardness of cement stone show a high consistency with the varying content of LP, while the effect of RHA on compressive strength and microhardness differs. This is due to the pozzolanic reaction of RHA, which changes the Ca/Si composition of the primary hydration product (C-S-H gel), increasing the density per unit volume of C-S-H and the hardness per unit indentation. The compressive strength is influenced not only by the hardness of the hydration products but also by the pore structure of the paste, leading to some discrepancy with microhardness. As shown in Figure 18, the paste with 10% LP and 10% RHA exhibits superior mechanical property. However, at a higher LP content, there is a significant drop in the mechanical property of the composite cementitious material compared to the sample without LP. It can be seen combining with Figure 9 that at the same LP content, RHA effectively improves the mechanical property of the cementitious material and accelerates the property with the high LP content.

4. Conclusions

(1) Mixing RHA and LP improves the compressive strength of cement-based materials. The highest strength is achieved when both RHA and LP are at 10%, with a 9.5% increase in 28 d strength compared to the pure cement system.

(2) The addition of RHA effectively improves the slow strength development and insufficient late-stage strength of the cement-LP system, as well as the low strength of the cementitious system with high LP content. When the LP content is 20% and 30%, 10% RHA increases the 28 d strength by 44.8% and 38.8%, respectively, and with strength growth rates of 109.8% and 151.1% at 3 d–56 d.

(3) The microhardness data of cement-based materials mixed with either RHA or LP is more consistent with a lognormal distribution. RHA effectively improves the microhardness of composite hardened cement paste. The synergistic effect of the pozzolanic reaction and internal curing water release of RHA, along with the nucleation effect of LP, promotes the hydration of cement, leading to a denser interlayer structure of C-S-H. This results in cement-based materials having relatively high microhardness values.

(4) The synergistic effect of LP and RHA significantly enhances the mechanical properties of the cementitious material. Based on a comprehensive analysis of compressive strength and microhardness, the optimal solution for achieving high mechanical performance in the composite cementitious material is to use 10% substitution to cement for both LP and RHA.

Author Contributions: Conceptualization, J.W.; data curation, J.W.; formal analysis, J.W.; funding acquisition, F.J.; investigation, F.J.; methodology, F.J., J.Z. and Z.M.; project administration, J.Z. and Z.M.; writing—original draft, J.W.; writing—review and editing, Z.M. All authors have read and agreed to the published version of the manuscript.

Funding: This work is supported by the Science and Technology Development Plan of Suzhou (SNG2022015) by Feifei Jiang, Basic Science (Natural Science) Research Project of the Jiangsu Higher Education Institutions (24KJD560004) by Feifei Jiang.

Institutional Review Board Statement: Not applicable.

Informed Consent Statement: Not applicable.

Data Availability Statement: The original contributions presented in the study are included in the article, further inquiries can be directed to the corresponding authors.

Conflicts of Interest: The authors declare no conflicts of any commercial or associative interest in connection with the work submitted.

References

1. Guo, X.L.; Li, Y.X.; Yuan, S.T. Life cycle assessment of cement and its research progress in low environmental load. *J. Build. Mater.* **2023**, *26*, 660–669+677.
2. Liu, X.; Yang, L.; Du, J.; Zhang, H.; Hu, J.; Chen, A.; Lv, W. Carbon and air pollutant emissions forecast of China's cement industry from 2021 to 2035. *Resour. Conserv. Recycl.* **2024**, *204*, 107498. [CrossRef]
3. Guo, X.; Li, Y.; Shi, H.; She, A.; Guo, Y.; Su, Q.; Ren, B.; Liu, Z.; Tao, C. Carbon reduction in cement industry-An indigenized questionnaire on environmental impacts and key parameters of life cycle assessment (LCA) in China. *J. Clean. Prod.* **2023**, *426*, 139022. [CrossRef]
4. Li, Y.X.; Guo, X.L. Coupling evaluation of carbon emissions and strength: Early carbonation curing of cement mortar containing incinerated sewage sludge ash (ISSA). *Constr. Build. Mater.* **2024**, *427*, 136278. [CrossRef]
5. Tao, M.; Lu, D.; Shi, Y.; Wu, C. Utilization and life cycle assessment of low activity solid waste as cementitious materials: A case study of titanium slag and granulated blast furnace slag. *Sci. Total Environ.* **2022**, *849*, 157797. [CrossRef]
6. Li, L.G.; Kwan, A.K.H. Adding limestone fines as cementitious paste replacement to improve tensile strength, stiffness and durability of concrete. *Cem. Concr. Compos.* **2015**, *60*, 17–24. [CrossRef]
7. Tsivilis, S.; Chaniotakis, E.; Badogiannis, E. Study on the parameters affecting the properties of Portland limestone cements. *Cem. Concr. Compos.* **1999**, *21*, 107–116. [CrossRef]
8. Xiao, F.; Cui, H.; Chen, J.; Chen, H.B. Study on high strength concrete containing ultra-fine limestone powder. *Bull. Chin. Ceram. Soc.* **2010**, *29*, 1303–1307.
9. Liu, S.; Yan, P. Influence of limestone powder on filling effect of cement paste and pore structure of sand grout. *J. Chin. Ceram. Soc.* **2008**, *1*, 69–72+77. [CrossRef]
10. He, Z.; Cai, R.; Chen, E.; Tang, S. The investigation of early hydration and pore structure for limestone powder wastes blended cement pastes. *Constr. Build. Mater.* **2019**, *229*, 116923. [CrossRef]
11. Sensale, G.R.; Viacava, I.R. A study on blended Portland cements containing residual rice husk ash and limestone filler. *Constr. Build. Mater.* **2018**, *166*, 873–888. [CrossRef]
12. Zhu, H.; Liang, G.; Xu, J.; Wu, Q.; Zhai, M. Influence of rice husk ash on the waterproof properties of ultrafine fly ash based geopolymer. *Constr. Build. Mater.* **2019**, *208*, 394–401. [CrossRef]
13. Van Tuan, N.; Ye, G.; van Breugel, K.; Fraaij, A.L.A.; Bui, D.D. The study of using rice husk ash to produce ultra high performance concrete. *Constr. Build. Mater.* **2011**, *25*, 2030–2035. [CrossRef]
14. Ahsan, M.B.; Hossain, Z. Supplemental use of rice husk ash (RHA) as a cementitious material in concrete industry. *Constr. Build. Mater.* **2018**, *178*, 1–9. [CrossRef]
15. Zareei, S.A.; Ameri, F.; Dorostkar, F.; Ahmadi, M. Rice husk ash as a partial replacement of cement in high strength concrete containing micro silica: Evaluating durability and mechanical properties. *Case Stud. Constr. Mater.* **2017**, *7*, 73–81. [CrossRef]
16. Kannan, V. Strength and durability performance of self compacting concrete containing self-combusted rice husk ash and metakaolin. *Constr. Build. Mater.* **2018**, *160*, 169–179. [CrossRef]
17. Sua-iam, G.; Sokrai, P.; Makul, N. Novel ternary blends of Type 1 Portland cement, residual rice husk ash, and limestone powder to improve the properties of self-compacting concrete. *Constr. Build. Mater.* **2016**, *125*, 1028–1034. [CrossRef]
18. Kathirvel, P.; Saraswathy, V.; Karthik, S.P. Strength and durability properties of quaternary cement concrete made with fly ash, rice husk ash and limestone powder. *Arab. J. Sci. Eng.* **2013**, *38*, 589–598. [CrossRef]
19. Chen, P. Effect of Pretreatment on Properties of Rice Husk Ash. Master's Thesis, Harbin Institute of Technology, Harbin, China, 2014.
20. Lu, S. Effects of Pretreatment and Calcination Conditions of Rice Husk on the Activity of Rice Husk Ash. Master's Thesis, Shenyang University of Chemical Technology, Shenyang, China, 2019.
21. Bui, D.D. *Rice Husk Ash a Mineral Admixture for High Performance Concrete*; Delft University Press: Delft, The Netherlands, 2001.
22. Kang, S.H.; Hong, S.G.; Moon, J. The use of rice husk ash as reactive filler in ultra-high performance concrete. *Cem. Concr. Res.* **2019**, *115*, 389–400. [CrossRef]
23. Breugel, K.V.; Guang, Y.; Tuan, N.V. Ultra high performance concrete made with rice husk ash for reduced autogenous Shrinkage. In Proceedings of the 4th International FIB Congress: Improving Performance of Concrete Structures, Mumbai, India, 10–14 February 2014.
24. *GB/T 17671-2021*; Test Method of Cement Mortar Strength (ISO method). Standards Press of China: Beijing, China, 2021.
25. Zunino, F.; Scrivener, K.L. The influence of the filler effect on the sulfate requirement of blended cements. *Cem. Concr. Res.* **2019**, *12*, 105918. [CrossRef]
26. Van Tuan, N.; Ye, G.; van Breugel, K.; Guo, Z.; Dai, B.D. Hydration process of rice husk ash and silica fume in cement paste by means of isothermal calorimetry. In Proceedings of the Sixth International Conference on Concrete under Severe Conditions Environment and Loading (CONSEC'10), Yucatan, Mexico, 7–9 June 2010; Volume 2, pp. 1521–1528.
27. Xiang, J.; Liu, L.; Cui, X.; He, Y.; Zheng, G.; Shi, C. Effect of limestone on rheological, shrinkage and mechanical properties of alkali–Activated slag/fly ash grouting materials. *Constr. Build. Mater.* **2018**, *191*, 1285–1292. [CrossRef]
28. Kang, S.H.; Jeong, Y.; Tan, K.H.; Moon, J. High-volume use of limestone in ultra-high performance fiber-reinforced concrete for reducing cement content and autogenous shrinkage. *Constr. Build. Mater.* **2019**, *213*, 292–305. [CrossRef]

29. Kumar, A.; Oey, T.; Kim, S.; Thomas, D.; Badran, S.; Li, J.; Fernandes, F.; Neithalath, N.; Sant, G. Simple methods to estimate the influence of limestone fillers on reaction and property evolution in cementitious materials. *Cem. Concr. Compos.* **2013**, *42*, 20–29. [CrossRef]
30. Bentz, D.P.; Ardani, A.; Barrett, T.; Jones, S.Z.; Lootens, D.; Peltz, M.A.; Sato, T.; Stutzman, P.E.; Tanesi, J.; Weiss, W.J. Multi-scale investigation of the performance of limestone in concrete. *Constr. Build. Mater.* **2015**, *75*, 1–10. [CrossRef]
31. Sato, T.; Beaudoin, J.J. Effect of nano-$CaCO_3$ on hydration of cement containing supplementary cementitious materials. *Adv. Cem. Res.* **2011**, *23*, 33–43. [CrossRef]
32. Erdem, S.; Dawson, A.R.; Thom, N.H. Influence of the micro and nanoscale local mechanical properties of the interfacial transition zone on impact behavior of concrete made with different aggregates. *Cem. Concr. Res.* **2012**, *42*, 447–458. [CrossRef]
33. Jiang, Y.; Dang, Y.; Qian, J.; Li, X.; Shi, X.; Yang, Z. Influence of surface status of hardened cement paste on its microhardness and statistical distribution. *J. Chin. Ceram. Soc.* **2017**, *45*, 212–219.
34. Factor, M.; Roman, I. Vickers microindentation of WC-12%Co thermal spray coating: Part 1: Statistical analysis of microhardness data. *Surf. Coat. Technol.* **2000**, *132*, 181–193. [CrossRef]
35. Xie, Y.; Wang, X.; Long, G.; Ma, C. Quantitative analysis of the influence of subfreezing temperature on the mechanical properties of steam-cured concrete. *Constr. Build. Mater.* **2019**, *206*, 504–511. [CrossRef]
36. Dang, Y.; Shi, X.; Qian, J.; Jiang, Y.; Li, X. Statistical characteristics of microhardness of hardened cement paste. *J. Wuhan Univ. Technol.-Mater. Sci. Ed.* **2018**, *33*, 924–931. [CrossRef]
37. Yang, X.; Liu, J.; Li, H.; Xu, L.; Ren, Q.; Li, L. Effect of triethanolamine hydrochloride on the performance of cement paste. *Constr. Build. Mater.* **2019**, *200*, 218–225. [CrossRef]

Disclaimer/Publisher's Note: The statements, opinions and data contained in all publications are solely those of the individual author(s) and contributor(s) and not of MDPI and/or the editor(s). MDPI and/or the editor(s) disclaim responsibility for any injury to people or property resulting from any ideas, methods, instructions or products referred to in the content.

materials

MDPI

Review

Research Progress and Application Prospects of Plant Fibers in Geopolymer Concrete: A Review

Zijian Li [1], Jinjie Li [1], Weihua Lu [1] and Yongxing Zhang [1,2,*]

[1] School of Civil Engineering, Nanjing Forestry University, Nanjing 210037, China
[2] Jiangsu Provincial Highway Intelligent Detection and Low-Carbon Maintenance Engineering Research Center, Nanjing Forestry University, Nanjing 210037, China
* Correspondence: zhanguongxing81@aliyun.com or yxzhang1@njfu.edu.cn

Abstract: Plant fibers, characterized by their low density, renewable nature, and environmentally friendly characteristics, offer considerable potential as reinforcement materials in geopolymer composites. This review provides a critical and thorough examination of recent developments and emerging trends in plant fiber-reinforced geopolymer concrete (PFRGC). The paper commences by detailing the inherent characteristics of plant fibers and the mechanisms governing their interfacial adhesion with the geopolymer matrix, with specific emphasis on the impact of fiber surface modification on interface properties. The review offers a comprehensive investigation of the mechanical properties of plant fiber-reinforced geopolymer concrete, encompassing compressive strength, tensile strength, and toughness. Additionally, the paper examines the influence of plant fiber integration on the durability of geopolymer concrete, discussing improvements in freeze-thaw resistance, permeability, and carbonation resistance. In conclusion, this review highlights the prevailing challenges in the domain and provides insights into future developments of plant fiber-reinforced geopolymer concrete. An analysis was performed utilizing papers from 2000 to 2025 indexed in prominent databases including Web of Science, Scopus, and ScienceDirect to enhance the review. Integrating plant fibers into developing technologies, such as 3D printing of geo-polymer matrices, signifies a promising avenue for structural applications. It advocates that future research efforts should focus on enhancing fiber modification techniques, exploring novel fiber materials, and doing thorough assessments of long-term performance.

Keywords: geopolymers; plant fibers; mechanical properties; durability

1. Introduction

Under the dual challenges of global climate change and resource shortening, the construction industry, as one of the major areas of resource consumption and carbon emission, is facing unprecedented pressure for transformation. The high energy consumption and large amount of CO_2 emissions in the traditional cement production process have become an important obstacle to sustainable development [1,2]. Against this background, Geopolymer Concrete (GPC), as a new type of low-carbon and environmentally friendly cementitious material system, has received widespread attention due to its significant environmental benefits and excellent engineering performance.

GPC is mainly formed by the hardening of industrial wastes (e.g., fly ash, slag, etc.) rich in activated silica-aluminum through alkali-activated polymerization reaction [3]. Compared with traditional cement concrete, GPC not only exhibits excellent early strength development,

better heat resistance and chemical stability, but also effectively solves the problem of industrial solid waste disposal and realizes the recycling of resources [3,4]. However, similar to traditional cement concrete, GPC has inherent defects such as high brittleness, low tensile strength, and poor impact resistance, which severely limit its application in structures that require high toughness and ductility [4]. Consequently, enhancing the mechanical properties of GPC, particularly its toughness and ductility, has emerged as a critical scientific challenge for facilitating its broader implementation.

Fiber reinforcement technology, as a mature and effective method of concrete modification, can significantly improve the crack resistance, toughness and ductility of composite materials by incorporating fiber materials with high tensile strength into the brittle matrix [5]. Traditional research on fiber-reinforced concrete mainly focuses on steel fibers and synthetic fibers (e.g., polypropylene fibers, carbon fibers, etc.). However, the production process of these synthetic fibers is usually accompanied by high energy consumption and environmental pollution, which contradicts the environmental protection concept of GPC [6]. The concept of sustainable development has become a hotspot for research on plant fibers. With the deepening of the concept of sustainable development, natural, renewable and environmentally friendly plant fibers have gradually become a research hot spot [7].

Plant fibers, including bamboo, hemp, coconut, sisal, and jute, possess diverse sources, affordability, low density, and high specific strength. Notably, their manufacturing and processing methods are characterized by low energy consumption and environmental sustainability [8]. The application of plant fibers to the reinforcement modification of GPC not only enhances the mechanical properties of GPC, but also further enhances its environmental sustainability and realizes the synergistic use of industrial waste and natural renewable resources, which is of great environmental and economic significance.

However, Plant Fiber Reinforced Geopolymer Concrete (PFRGC), as an emerging composite material, still faces many challenges in its performance regulation mechanism and engineering applications. Firstly, the hydrophilicity and porous structure of plant fibers may affect the workability and compactness of concrete; secondly, the stability and durability of plant fibers in high alkaline environments are of concern; furthermore, the interfacial bonding mechanism between the fibers and the geopolymer matrix and its effect on the performance of the composites have not been fully elucidated. The solution of these scientific issues is crucial for the performance optimization and engineering applications of PFRGC.

This review provides a thorough examination of the evolution of PFRGC, aimed at facilitating continued research and practical implementation by scientists, engineers, and practitioners in the discipline. The reviewed literature covers the period from 2000 to 2024 and was obtained from prominent databases including Web of Science, Scopus, and ScienceDirect, utilizing keyword combinations such as “plant fiber”, “natural fiber”, “geopolymer”, “geopolymer concrete”, “mechanical properties”, and “durability”. The review examines the interfacial interactions between plant fibers and the geopolymer matrix, methods for enhancing mechanical performance, and aspects linked to durability. It additionally examines the scientific and technical problems that persist and delineates possible directions for future research. This work aims to elucidate existing knowledge and enhance the design and implementation of PFRGC in engineering contexts by referencing a wide array of publications.

2. Interfacial Bonding Between Plant Fibers and Geopolymer Matrix

The interfacial adhesion between the plant fibers and the geopolymer matrix is essential for the composite’s overall performance. If the interfacial bonding is poor, the fibers

will be easily debonded from the matrix when subjected to force, thus weakening the reinforcing effect of the composites. Thus, it is crucial to comprehensively examine the interfacial bonding performance between plant fibers and the geopolymer matrix, along with its assessment methodology.

The interfacial bonding property is an essential feature of fiber-reinforced composites, directly influencing the effectiveness of reinforcement. In plant fiber-reinforced geopolymer concrete, the qualities of interfacial bonding are especially critical. Compared to inorganic and synthetic fibers, plant fibers have unique properties that complicate their interfacial bonding behavior with the geopolymer matrix.

2.1. Types and Properties of Plant Fibers

Natural plant fiber is a kind of natural composite material with precise hierarchical structure, which can be divided into eight categories according to its source parts and usage characteristics: bast fiber (from the epidermis and phloem of plant stems), leaf fiber (extracted from leaf tissues), herbaceous fiber (obtained from graminaceous plants), seed fiber (obtained from the epidermis of the seed or endocarp), and root fiber (obtained from the root tissues of the plant), Fruit fibers (from the epidermis or endocarp of the fruit), stem core fibers (from the medullary part of the plant stem), and wood pulp fibers (separated from wood by chemical or mechanical processes).

The chemical composition primarily comprises cellulose (35–85%), hemicellulose (10–25%), lignin (5–30%), and trace quantities of organic constituents such as pectin and wax. These components construct a multilevel structural system from molecular to macroscopic scales by precise spatial organization, establishing a distinctive mechanical property transmission process.

From the structural level, the cell walls of plant fibers show a highly organized laminar structure [9]: the outermost layer is the primary wall, the inner one is the secondary wall consisting of S1, S2, and S3 layers, and the center is the lumen. The S2 layer, one of the three layers of the secondary cell wall, is crucial in determining the mechanical properties of natural fibers because of its significant thickness and highly ordered structure. It primarily comprises helically arranged cellulose microfibrils embedded in an amorphous matrix of lignin and hemicellulose, creating a natural fiber-reinforced composite. Cellulose, the principal structural component, consists of linear chains of β-1,4-linked D-glucose units, which constitute the repeating unit of the polymer with the chemical formula $(C_6H_{10}O_5)_n$. These chains consolidate into crystalline microfibrils, whose alignment within the S2 layer determines the tensile strength and rigidity of the fiber.

In this sophisticated structural system, hemicellulose is distributed among cellulose microfibrils in a disordered amorphous state, which provides secondary mechanical support while its hydrophilic character significantly influences the interfacial interactions between the fibers and the geopolymer matrix. Lignin, on the other hand, acts as a natural binder to cement the entire structure into a unified whole, and its complex network of aromatic polymers not only enhances the rigidity and structural stability of the fibers, but also affects the durability of the composites by regulating the water absorption. The bast fibers show a regular longitudinal texture on the surface, the leaf fibers have a helical vascular bundle structure, and the stalk fibers exhibit a porous network structure. This structural diversity stems from the specific assembly of cell wall components during biosynthesis, which directly affects the reinforcement of fibers in composites.

The stability of plant fiber characteristics is substantially affected by environmental variables. As can be seen from the figure, the strength enhancement, water absorption, thermal degradation and biodegradation properties of fibers are all closely related to their component structures and show obvious hierarchical nature: lignin, hemicellulose and

cellulose are involved in these processes sequentially, forming a complex performance response mechanism. The multilayer structure-property relationship serves as a crucial framework for comprehending and enhancing the utilization of plant fibers in geopolymer reinforcement systems.

Considering the fundamental structural attributes and chemical composition of plant fibers, those derived from various organ origins exhibit distinct structural characteristics and performance due to variations in their growth environments and physiological functions. Therefore, a comprehensive analysis of the differences in characteristics among common fiber types is essential from an organ classification perspective. According to the origin of plant organs, the common fiber types and their characteristics are as shown in [Table 1].

Table 1. Physical and mechanical characteristics of frequently documented plant fibers in literature.

Fiber Type	Fiber	Density (g/cm^3)	Tensile Modulus (GPa)	Tensile Strength (MPa)	Elongation (%)	Organ Source Classification	Reference
Seed Fibers	Cotton	1.5–1.6	5.5–12.6	287–597	7.8–8.2	Seed epidermal unicellular fibers	[10]
Bast Fibers	Flax	1.4–1.5	27.6–103	343–2000	1.2–3.3	Primary phloem of flax stem	[10,11]
	Hemp	1.4–1.5	23.5–90	270–900	1–3.5	Cannabis sativa stem phloem	[10]
	Jute	1.3–1.49	8–78	320–800	1–1.8	Jute secondary phloem	[10]
	Ramie	1.0–1.55	24.5–128	400–1000	1.2–4.0	Ramie bast fiber bundle	[10]
	Kenaf	1.4	14.5–53	223–930	1.5–2.7	secondary phloem of red hemp (Jatropha curcas)	[10]
Leaf Fibers	Sisal	1.33–1.5	9.0–38	363–700	2.0–7.0	sisal leaf vascular fiber	[10]
	Abaca	1.5	6.2–20	400–980	1.0–10	Plantago lanceolata leaf sheath fiber bundle	[10]
	Pineapple leaves	0.8–1.6	144–825	180–1627	1.6–14.5	Pineapple Leaf Fiber	[10]
	Banana	1.35	12	500	1.5–9	Banana leaf sheath fiber bundle	[10]
Stalk Fibers	Bamboo	0.6–1.1	11–32	140–800	1.5–9	vascular fibers of bamboo stems	[10]
	Bagasse	1.25	17–27.1	222–290	1.1	Sugar cane stalk fiber	[10]
Fruit Fibers	Oil palm	0.7–1.55	0.5–3.2	80–248	17–25	Oil Palm Husk Fiber Bundle	[10]
	Coconut shell	0.8	3.5	174	25	Coconut fruit husk fiber bundle	[12]

Among the many plant fibers, the bast fiber class shows the most excellent mechanical properties. Flax fiber, for example, has tensile strength up to 1800 MPa, elasticity modulus up to 103 GPa [10,11], which is closely related to its highly oriented cellulose molecular structure. In situ tensile test results show that flax fiber in the force process shows obvious graded damage characteristics; this progressive destruction mechanism is conducive to improving the toughness of the composite material. Leaf fiber class has a high elongation at

break due to its unique helical structure, and exhibits excellent energy absorption capacity under dynamic loading.

The subsequent heatmap displays a normalized comparison of four essential mechanical properties—density, tensile modulus, tensile strength, and elongation at break—across fourteen prevalent plant fibers [Figure 1]. Each statistic was normalized to a range of 0 to 1 to remove unit discrepancies and emphasize relative performance. The deeper hues in the spectrum signify elevated values. This visualization technique has been effective in enabling an intuitive assessment of fiber appropriateness for reinforcing in geopolymer.

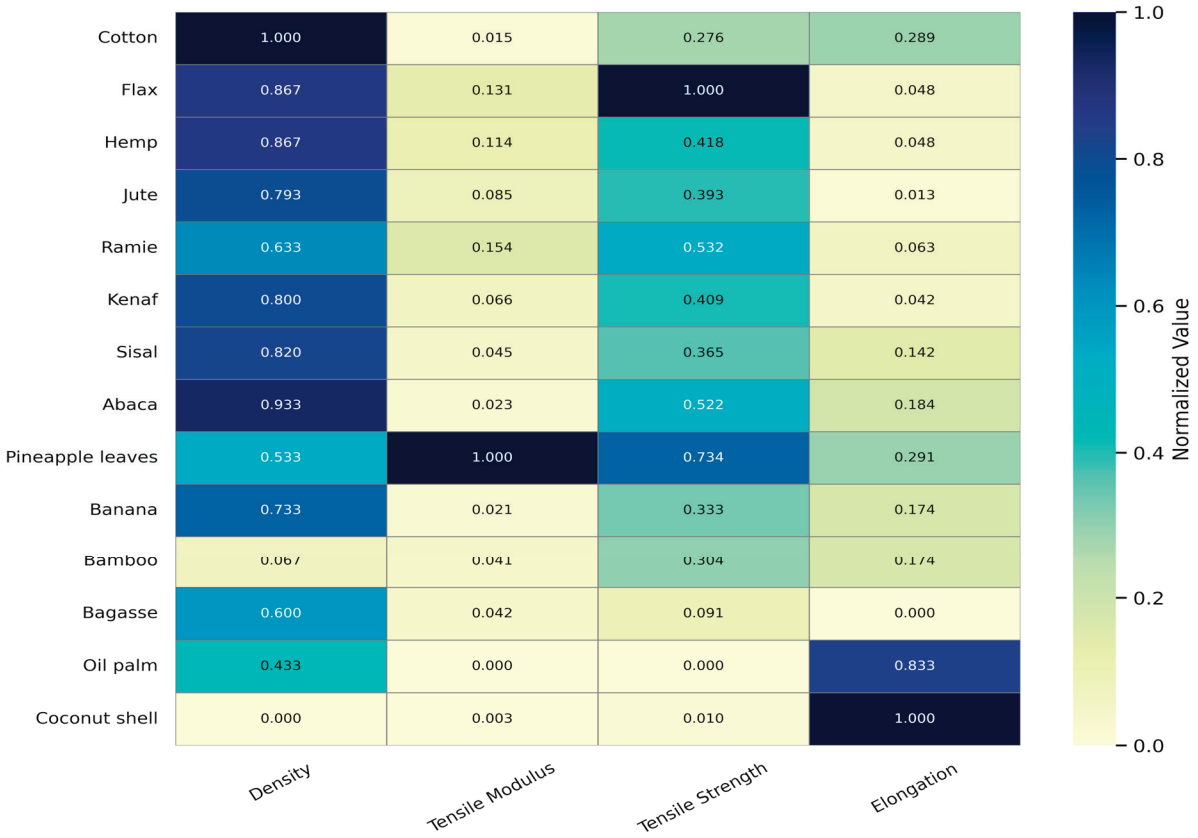

Figure 1. Normalized comparison of key mechanical properties among various plant fibers.

However, the intrinsic properties of plant fibers pose a serious challenge to interfacial stability. The primary problem is the dimensional instability due to the hydrophilic nature of the fibers, a volume change that causes interfacial stress concentration and microscopic crack formation. More critically, Melo Filho et al. [13] revealed two main degradation mechanisms of plant fibers in alkaline environments [Figure 2]: one is the process of mineralization by deposition of calcium hydroxide crystals on the surface of the fibers, which significantly reduces the active cellulose content of the fibers, weakening their reinforcing effect; and the other is the process of hemicellulose and chemical degradation of lignin in an alkaline environment, and this component dissociation process destroys the integrity of the fiber, which in turn affects the long-term stability of interfacial bonding. The molecular chains of cellulose consist of crystalline and amorphous areas, which exhibit reduced stability in alkaline conditions [14].

The morphological attributes of the fibers (e.g., aspect ratio, cross-sectional geometry, surface texture) substantially influence their properties. The degree of processing of plant fibers directly affects their reinforcing capacity in geopolymers. Korniejenko et al. [15] conducted a comprehensive study on the effects of various fiber types and processing stages on the characteristics of fly ash-based geopolymers. The inclusion of unrefined fibers, marked

by a rough texture, presents a difficulty in the mixing process owing to their propensity for uneven dispersion. This may result in the development of stress concentration zones, hence diminishing the composite's overall performance. In contrast, finely treated fibers demonstrate improved distribution and establish stronger interfacial interactions with the matrix, resulting in significant enhancements in flexural and compressive properties.

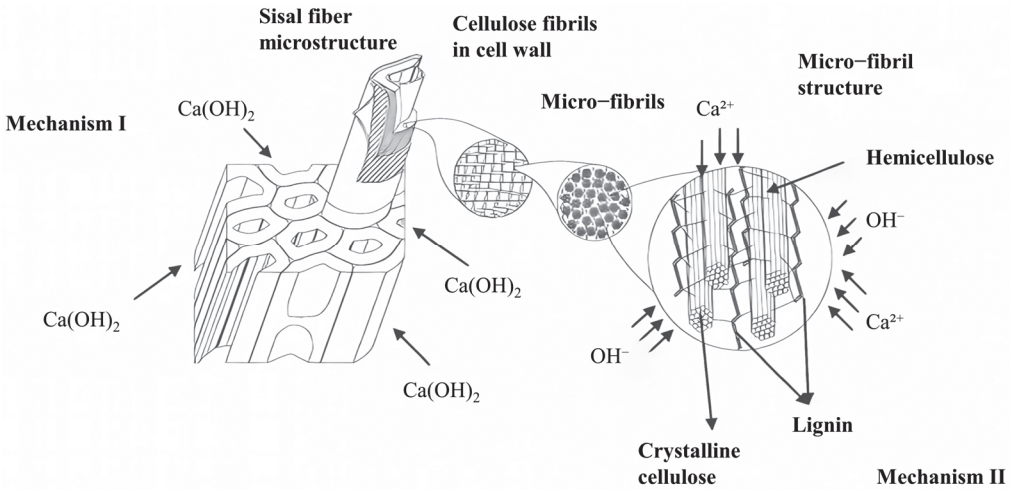

Figure 2. Degradation mechanism of plant fibers proposed [13].

In conclusion, all these factors affect the long-term stability of interfacial bonding, highlighting the need for a systematic modification strategy. Therefore, a systematic modification strategy is required to optimize the fiber-matrix interfacial properties, which will be discussed in detail in the subsequent sections.

2.2. Fiber Surface Treatment

Fiber surface treatment is a prevalent technique employed to enhance adhesion at the fiber-matrix contact. Physically or chemically altering the surface of plant fibers can enhance their surface qualities, hence improving binding strength with the geopolymer matrix.

2.2.1. Alkali Treatment

Alkali treatment is a straightforward and efficient technique for fiber surface modification. Soaking plant fibers in alkaline solutions, such as sodium hydroxide and calcium hydroxide, effectively eliminates waxes, oils, and other surface contaminants, enhances the roughness of the fiber surface, and improves mechanical interlocking. Simultaneously, alkali treatment can partially eliminate lignin and hemicellulose from the cellulose surface, thereby exposing additional cellulose and augmenting the quantity of hydroxyl groups on the fiber surface. This enhancement facilitates chemical reactions with the geopolymer matrix and improves the mechanical properties and durability of the composites [16,17].

Alkali treatment process parameters such as lye concentration, treatment temperature, and time have a significant effect on the modification effect [18,19]. Bast fibers, including jute and flax, are often treated with a 5–8% NaOH solution for 1–4 h at ambient temperature, whereas woody fibers, such as bamboo and rice straw, generally require treatment at 60–80 °C. Excessive alkali treatment can cause hydrolytic destruction of cellulose molecular chains, leading to reduced fiber strength; thus, optimizing the treatment conditions is essential [20].

The enhancement of interfacial characteristics between plant fibers and geopolymer through alkali treatment was evident. Single-fiber pull-out test findings indicated that treatment with 5% NaOH enhanced the interfacial shear strength between fibers and the GPC matrix by a factor of 2.5 [21]. The 5% NaOH-treated fiber-reinforced composites shown

notable improvements in overall performance, with tensile and flexural strengths rising by 8.14% and 7.88%, respectively [22]. Under elevated temperature conditions (100 °C, 1% NaOH, 1 h), the treated date palm fiber composites demonstrated superior mechanical properties, including enhanced impact strength, tensile strength, tensile modulus, and flexural strength, along with improved fiber dispersion within the matrix [23]. In addition, alkali treatment is effective in reducing the degradation rate of plant fibers in alkaline geopolymer environments, improving the durability and dimensional stability of the composites.

Nonetheless, a contradiction exists regarding the alkali treatment technique: whereas the monofilament tensile strength of the treated fibers often diminishes, composites fabricated from these fibers exhibit enhanced mechanical properties [24]. The research performed by Fernandes et al. [25] offers significant insights into the comprehension of this phenomenon. Sisal fibers, despite a decrease in strength from the partial extraction of hemicellulose and lignin, achieved excellent mechanical qualities when included into composites at a concentration of 10 wt%. The essence of this apparent contradiction is in the augmented surface roughness resulting from the alkali treatment, which markedly improves the mechanical interlocking at the fiber-matrix interface [26]. Optimization of surface morphology and improvement of interfacial structure may contribute more to the composite properties than the single fiber strength.

In summary, the alkali treatment method significantly enhances the interfacial compatibility and bonding characteristics between plant fibers and the geopolymer matrix via various physicochemical mechanisms. Nevertheless, the impact of a singular alkali treatment on certain plant fibers may nevertheless exhibit constraints.

2.2.2. Silane Coupling Agent Treatment

Silane coupling agent modification, as a key technology for surface treatment of plant fibers, significantly improves fiber-substrate interfacial properties through molecular bridging mechanisms. The molecular structure of silane coupling agents is usually expressed as R-Si(OR')$_3$, where R represents an organic functional group capable of reacting with plant fibers, and the Si(OR')$_3$ portion is hydrolyzed to form a chemical bond with the geopolymer matrix [27,28].

The molecular mechanism of silane modification includes two key steps, hydrolysis and condensation: silane molecules are first hydrolyzed in aqueous solution to generate Si-OH groups, which subsequently condense with the hydroxyl groups on the fiber surface to form Si-O-C bonds, and at the same time, self-condensation between adjacent Si-OH groups to form a Si-O-Si network structure [28–30]. This silicone crosslinked network not only improves the hydrophobicity of the fibers, but also establishes a stable chemical connection between the organic fibers and the inorganic matrix.

The application effects of different types of silane coupling agents are different. KH570 significantly enhanced the interfacial integrity of the system by dehydration condensation reaction with free water or adsorbed water in the matrix [31]. Wu and Zuo's research [32] showed that in the plant cellulose/waste tire powder composite system, Si69 showed a better interfacial enhancement effect than KH550 at the optimal addition amount. The 5% KH550 treatment can increase the energy absorption capacity of the fiber reinforced system by 13.8% and improve the cracking behavior [33]. According to Zhao et al. [34], KH550 showed the most significant enhancement in both sisal fiber and matrix properties due to its amino functional group, which contributes to superior hydrophobicity, degradation resistance, barrier performance, and interfacial bonding. KH792 ranked second in efficacy, while KH560 and KH570 showed relatively weaker and inconsistent effects. Liu et al. [35] found that KH560, when used as an intermediate agent in nano-SiO_2 surface modification,

facilitated strong adhesion between nanoparticles and fiber surfaces by inducing abundant hydrogen bonds at the interface. Furthermore, nano-SiO_2 could interact with the N-A-S-H gel matrix to form ionic and covalent Si–O–Si bonds, thereby significantly enhancing the interfacial bonding strength.

Silane treatment has a different mechanism of action compared to alkali treatment: alkali treatment improves interfacial bonding mainly by increasing surface roughness and active sites, whereas silane treatment realizes chemical bonding at the molecular scale. The alkali-silane composite modification process has been shown to fully utilize the synergistic effect of the two methods, and Orue and Jauregi et al. [21] showed that pretreatment with a low concentration (2–5%) of NaOH to remove surface waxes and activate hydroxyls, followed by silane treatment, increased the bond strength of the fiber-substrate interface by a factor of 2–3. Similarly, Asim et al. [30] confirmed that a 2% silane solution treatment for 3 h significantly improved the tensile strength and interfacial adhesion of pineapple and jute fibers. SEM, FTIR, and tensile tests confirmed the removal of non-cellulosic components and enhanced compatibility between the fibers and the geopolymer matrix.

2.2.3. Polymer Coating

Polymer cladding, a novel fiber surface modification technology, provides an innovative solution to the durability of fibers in geopolymer environments by constructing a continuous or semi-continuous polymer protective layer on the surface of plant fibers. This surface engineering strategy has been shown to significantly reduce water absorption while forming a flexible transition zone between fibers and the matrix, thereby optimizing interfacial stress distribution. Common cladding materials include epoxy resins, polyurethanes, acrylic resins, and other polymers, the selection of which is primarily based on compatibility with fibers and the matrix, as well as target performance requirements.

Research has demonstrated that the application of fiber surface protection, encompassing methods such as polymer coating and alkali treatment, constitutes a highly efficacious approach to mitigating the degradation of plant fibers within alkaline contexts [36]. The fundamental basis of this protective effect is the construction of a barrier layer that effectively mitigates the erosion of fibers by alkaline media.

Li et al. [37] elucidate the mechanism of action underlying polymer encapsulating technology. The epoxy glue penetrates the fiber lumen to create a reinforcing structure and effectively inhibits crack propagation. The occupation of the lumen space by the hydrophobic epoxy resin markedly enhances the water resistance of the fiber. The experimental findings indicate that this treatment can significantly enhance the mechanical properties of the composites, including tensile strength, bending strength, and impact strength, while efficiently regulating the water absorption rate.

However, the relatively high cost of raw materials and the more complex process have limited its large-scale application to some extent.

2.2.4. Other Surface Treatment Methods

In addition to the aforementioned methods, there are other fiber surface treatment methods, including but not limited to plasma treatment, graft copolymerization, and microwave treatment [38,39]. The combination of multiple treatments often exhibits a synergistic effect, resulting in a modification that is often superior to that of a single treatment. Each of these methods possesses its characteristics, with a different scope of application and effects. Therefore, the selection of an appropriate method must be made according to the specific fiber type and application requirements.

It is important to acknowledge the existence of discrepancies in the mechanisms through which diverse surface treatments influence the performance of fiber-GPC composites. Their

applicability is also closely related to specific fiber types, matrix ratios, and application environments. Alkali treatment remains the most widely used method due to its simplicity, efficiency, and significant effect. Polymer coating and silane coupling agent treatment are dominant in high-performance applications. Emerging technologies, such as plasma treatment and microwave treatment, show promise for development in specific scenarios.

2.3. Geopolymer Matrix Modification Methods

The design of matrix modification is crucial and serves as another important way to improve the performance of fiber-reinforced composites. Optimizing the mixing ratio can enhance the compatibility of the fiber-matrix interface, encompassing precursor composition, alkali-activated ratio, and liquid-solid ratio, among other variables [40]. The Si/Al molar ratio exerts a substantial influence on the structural characteristics of geopolymer networks and the properties that define their interfacial interactions [41].

The durability of fibers can be improved via matrix modification, with volcanic ash materials providing a unique benefit as a cement alternative. The consumption of calcium hydroxide by the matrix pore solution results in the formation of C-S-H/C-A-S-H, leading to a reduction in pH, which in turn mitigates the degradation of plant fibers [42]. Wei and Meyer's research [43] demonstrated that the incorporation of 30% rice husk ash, instead of Portland cement, resulted in a decline of the substrate pH from 13.75 to 12.7. This adjustment effectively mitigated the degradation of sisal fibers. With regard to the optimization of raw material combinations, Gholampour et al. [44]. The study's findings revealed that the ratio of fly ash (FA) to blast furnace slag (GGBS) significantly influenced the strength development and microstructure of GPC. In both the F80G20 and F50G50 ratios, increased GGBS content was shown to facilitate C-S-H gel formation, thus improving concrete densities and strengthening fiber-matrix interface bonding. This conclusion is corroborated by the research conducted by Poletanovic et al. [45]. This finding further corroborates the study's conclusions. Through a comparative analysis of alkali-activated mortars comprising solely fly ash (FA1) and fly ash-slag mixtures (FA2S), it was ascertained that the gels generated by these disparate precursors exerted a substantial influence on the mechanical properties and pore structure of the materials. The incorporation of hemp fibers led to a substantial enhancement in the energy absorption capacity of the alkali-activated materials, a phenomenon that was particularly evident in brittle matrices. Furthermore, the study indicated that the incorporation of fibers exerted a negligible effect on density and water absorption. Nonetheless, it enhanced the compressive strength of the fly ash-based mortar, an effect principally ascribed to the improved interfacial bonding and frictional stress transmission mechanisms.

The optimization of the alkali-activated system is a pivotal factor influencing the performance of plant fiber-reinforced geopolymers. Phoo-ngernkham et al. [46] The Na_2SiO_3/NaOH composite activator was found to significantly improve the densification of the interfacial zone in comparison with single NaOH or KOH systems. This enhancement in performance is attributed chiefly to the additional Si source provided by the soluble silicate, which promotes the formation of a Si-O-Si network structure, optimizes the pore structure characteristics of the matrix, and enhances the mechanical occlusion with the fiber surface.

The type and concentration of alkali activators have been demonstrated to exert a substantial influence on material properties. It has been demonstrated that higher concentrations of sodium hydroxide, while increasing the compressive strength, concomitantly reduce the workability of the material [47]. Regarding activator selection, Sá Ribeiro et al. [48] reported that sodium-based systems exhibit superior performance compared to potassium-based counterparts. In their study, a sodium-metakaolin geopolymer incorporating 20 wt% fine sand and 5 wt% bamboo fibers achieved a 32% higher flexural strength than its

potassium-based equivalent. Toledo Filho et al. [12] determined through immersion experiments that the tensile strength of fibers was entirely diminished after 300 days in a calcium hydroxide solution, whereas the strength of sisal and coir fibers decreased by 72.7% and 60.9%, respectively, in a sodium hydroxide solution. This finding indicates that the pore solution of traditional cementitious materials exerts a more pronounced erosive effect on plant fibers compared to the NaOH-activated alkali-activated system. M. Jegan et al. [49] The study demonstrated that the judicious selection of alkali activators has the potential to enhance the interfacial interaction between the fibers and the geopolymer matrix. Moreover, it was demonstrated that this selection enables the fibers to fulfill both reinforcing and bonding roles in the concrete structure.

The liquid-solid ratio and the curing conditions have been demonstrated to exert a substantial influence on interfacial properties. Silva et al. [50] found that. In the range of observation, the liquid-solid ratio exhibited a decrease from 0.29 to 0.27. There was a significant increase in the compressive strength of the samples. However, Li et al. [51] A substantial body of research has demonstrated that elevated liquid-solid ratios result in a decline in compression and splitting tensile strength. This phenomenon is predominantly ascribed to the augmentation of material porosity and the diminution of interfacial compactness that accompany higher liquid-solid ratios. Furthermore, curing time and temperature have been shown to exert a substantial influence on material properties [50]. The application of heat during curing has been shown to enhance and expedite the dissolution of silica and alumina in precursor materials [52]. Consequently, the density of the material is increased, and the hardening process is accelerated.

Furthermore, nanomineral admixtures have been shown to enhance the microstructure and interfacial properties of the matrix through the microaggregate effect and volcanic ash reaction. Asaedi et al. [53] The research demonstrated that the toughness of the fly ash-based polymer matrix enhanced by roughly 58% as the concentration of silica nanoparticles rose from 1.0 wt% to 2.0 wt%. The improvement in performance is mainly due to the increased density (reduced porosity) resulting from the elevated gel content, which enhances the interfacial bonding between the fibers and the matrix. The synergistic application of multi-component mineral dopants, such as the integration of nano-SiO_2 with nano-Al_2O_3, has been shown to enhance the Si/Al ratio and particle gradation. This combination has demonstrated a significant interfacial increase relative to a single component [54]. The selection and dosage optimization of dopants must include their compatibility with matrix components and their effect on workability.

2.4. Microstructural Characteristics of Interfacial Transition Zones (ITZ)

The Interfacial Transition Zone (ITZ) between plant fibers and the geopolymer matrix is a crucial area influencing the characteristics of composites. The microstructure and characteristics of the plant directly influence the composite's overall performance. This interfacial contact exhibits distinct multi-scale characteristics: At the nanoscale, the plentiful hydroxyl functional groups on the fiber surface establish molecular interfacial connections with the silica-alumina-oxygen complexes in the matrix via covalent and hydrogen bonding. At the micrometer scale, the distinctive morphological characteristics on the fiber surface, such as grooves and pores, offer mechanical occlusion sites to the matrix, thereby improving interfacial anchoring. At the macroscopic scale, the spatial orientation and network structure of the fibers directly influence the efficiency and uniformity of stress transfer within the composites. The scale, spatial orientation distribution, and network structure of fibers directly influence the efficiency and homogeneity of stress transfer in composites.

ITZ formation in geopolymer systems is distinct from the process in conventional cementitious materials and is characterized by unique properties [55]. The surface of plant fibers exhibits partial solubility in hemicellulose and lignin. In an alkaline environment, hemicellulose and lignin on the surface of plant fibers are partially solubilized, creating a distinct "dissolution layer". Simultaneously, the hydroxyl groups on the fiber surface engage in an ion exchange reaction with the silica-alumina-oxygen tetrahedra, facilitating the heterogeneous nucleation of alumino-silicate gels [56].

The interfacial enhancement mechanism is predominantly composed of chemical bonding and physico-mechanical occlusion [57]. The formation of chemical bonds is predominantly facilitated through the establishment of hydrogen, ionic, and covalent bonds (after surface modification) between hydroxyl groups located on the fiber surface and the geopolymer network [29]. In contrast, physical-mechanical occlusion is attributed to factors such as fiber surface roughness, mechanical locking of matrix products, and interfacial stress distribution. The formation of a robust interfacial bond between cellulose and the matrix is crucial for achieving optimal occlusion of the spiny or lamellar structure of the fiber surface with the matrix [58].

The factors that influence interfacial properties encompass environmental factors, such as temperature, humidity, and pH, as well as material factors, including fiber type and morphology, matrix composition, and maintenance conditions [59–62]. Wang et al. [61] has been determined that the proper conditioning temperature and relative humidity are conducive to the development of interfacial structure. Conversely, elevated pH levels (greater than 13) have been observed to potentially induce alkali corrosion of fibers and compromise the long-term stability of the interface [14]. The impact of fiber type and morphology on the formation of interfacial structures has been demonstrated to be significant. For instance, bast fibers, such as those found in flax and jute, have been observed to exhibit superior interfacial bonding properties due to their higher surface roughness [63]. Indeed, as Ye et al. [16], the structural characteristics of the interface between the geopolymer matrix and the all-cellulose fibers were revealed [Figure 3]. The spiny or lamellar structures on the cellulose surface were embedded into the interface of the geopolymer matrix, forming an effective mechanical anchorage point. Good interfacial bonding between cellulose and matrix was still formed in strong alkaline environments, and no obvious cellulose degradation was observed [58].

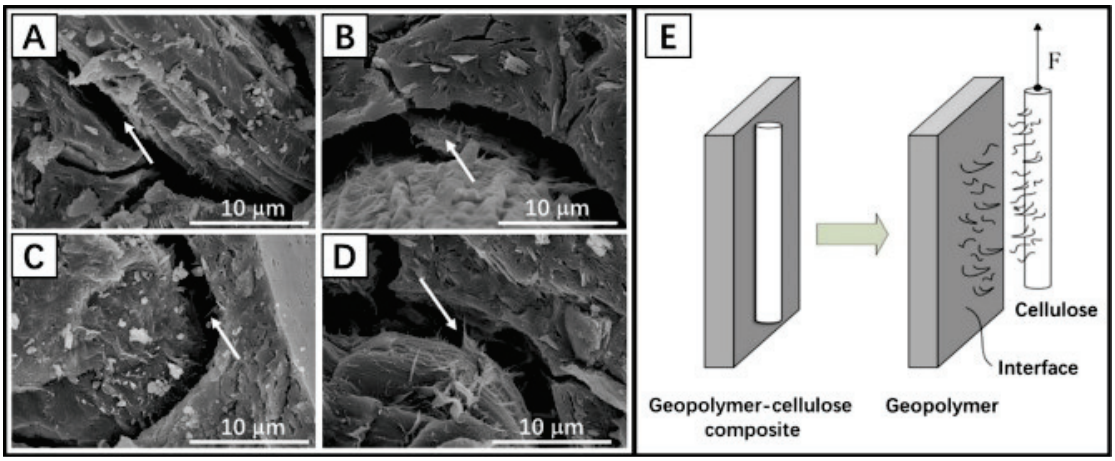

Figure 3. SEM images of the fiber–geopolymer interface (**A**–**D**). Arrows indicate embedded cellulose fiber fragments—mainly sheet- or needle-like—anchored in the matrix after flexural loading. (**E**) Schematic illustration of the bonding mechanism between cellulose fibers and the geopolymer matrix [16].

The microstructural modulation of the interfacial transition zone establishes a microscopic foundation for enhancing the overall performance of the composites. By systematically optimizing the structure of the interfacial zone, the mechanical and durability properties of the composites can be significantly enhanced. The effectiveness of these microstructure modulation strategies must be verified by scientific interfacial bonding performance evaluation methods.

2.5. Methods for Evaluating Interfacial Bonding Properties

The systematic evaluation of interfacial bonding properties is important for understanding the mechanical behavior and optimizing the interface design of fiber-reinforced geopolymer composites (FRGPC). Based on the multiscale characteristics of interfacial interaction, its evaluation system covers macroscopic mechanical properties, microstructural features and their interrelationships to form a complete interface characterization methodology.

The single fiber pull-out test (SFPT) is considered the most representative standard approach. The extensive utilization of it might be ascribed to its significant standardization and data dependability. The principal failure mechanisms for both species have been recognized as fiber fracture and matrix pullout. The failure mechanism of the fiber-matrix interface was methodically assessed, and the interfacial shear strength was measured by meticulously regulating the fiber embedment length (10–25 mm) and the pull-out rate (0.5–2 mm/min). The standard load-displacement curve is segmented into four phases: the linear elastic phase (Step 1, 0–0.2 mm), which indicates initial stiffness and elastic deformation as dictated by Hooke's law; the debonding phase (Step 2, 0.2–0.3mm) The contact begins to deteriorate when the tensile force attains the maximal bonding strength (τ_{bs}). This is succeeded by the fracture propagation phase (Step 3, 0.3–0.5 mm), during which interfacial cracks expedite their growth, bonding strength diminishes, and friction is added. Ultimately, the friction stage (Step 4, >0.5 mm) is attained, wherein the fiber is entirely extracted, and the remaining load-bearing capacity depends exclusively on friction [Figure 4]. The determination of interfacial shear strength is conducted via the examination of curve attributes, as specified in the following formula:

$$\tau = \frac{F}{\pi d L} \tag{1}$$

In this formula, F denotes the maximum pull-out force, which is to be determined through predictive tests. d represents the fiber diameter, and L signifies the effective burial length.

Single-fiber diagonal pull tests were conducted by varying the fiber inclination angle (0–45°) to evaluate the mechanical response of the interface under composite stresses. The most significant increase in interface strength was found at an inclination angle of 15–30°, which is mainly attributed to the contribution of the fiber "wedge effect".

The fiber critical length method is predicated on the Kelly-Tyson model.

$$\tau = \frac{\sigma f \cdot d}{2Lc} \tag{2}$$

In this equation, σ_f is the fiber tensile strength, which is to be determined by predictive tests, d is the fiber diameter, and L_c is the critical length.

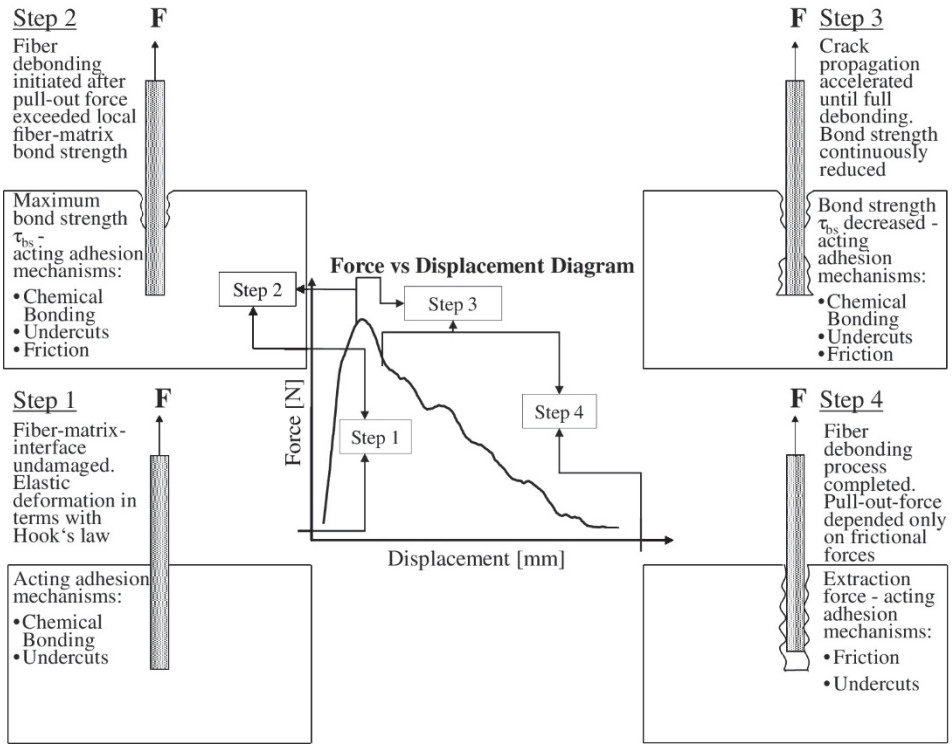

Figure 4. Schematic description of single fiber pull-out test (SFPT) steps [64].

The method involves the use of fibers of varying lengths, which are mixed into the matrix. The statistical distribution of fiber lengths post-fracture is subsequently determined to ascertain the critical length. Fiber breakage occurs when the fiber length exceeds the critical length, and interfacial debonding occurs when it is less than the critical length. A significant advantage of this method is that it enables the simultaneous testing of a large number of fibers, thereby facilitating the acquisition of statistically significant interfacial property data. This method is particularly well-suited for short-fiber-reinforced systems.

Conversely, the three-point bending test appraises the interfacial action from the vantage point of overall performance. The measurement of load-deflection curves enables the determination of critical parameters, including initial cracking strength (σ_{fc}), ultimate strength (σ_u), and toughness index (TI). When these parameters are considered in conjunction with the crack extension mode and fiber bridging behavior, a comprehensive evaluation of the effect of interfacial modification can be performed.

In addition to macroscopic evaluations, microscopic techniques provide critical insight into the interfacial behavior between plant fibers and the geopolymer matrix. High-resolution SEM and EDS analyses have been used extensively to visualize fiber-matrix bonding states, crack propagation patterns, and elemental distributions such as Na, Al, and Si [63,65]. SEM investigations indicate that sisal fibers possess rough, grooved surfaces that facilitate mechanical interlocking, whereas jute fibers exhibit smoother surfaces with less interfacial friction [Figure 5].

Similar to cementitious materials, the interfacial stress transmission between the fibers and the matrix in FRGPC, along with the composite's behavior in the post-peak area, is regulated by three principal mechanisms: (i) Chemical connection between the fibers and the matrix (adhesion), (ii) friction produced when the fibers are extracted from the matrix and traverse inside the channel, and (iii) mechanical resistance offered by the fiber anchorage (hooked or deformed geometry of the fibers) [45,65].

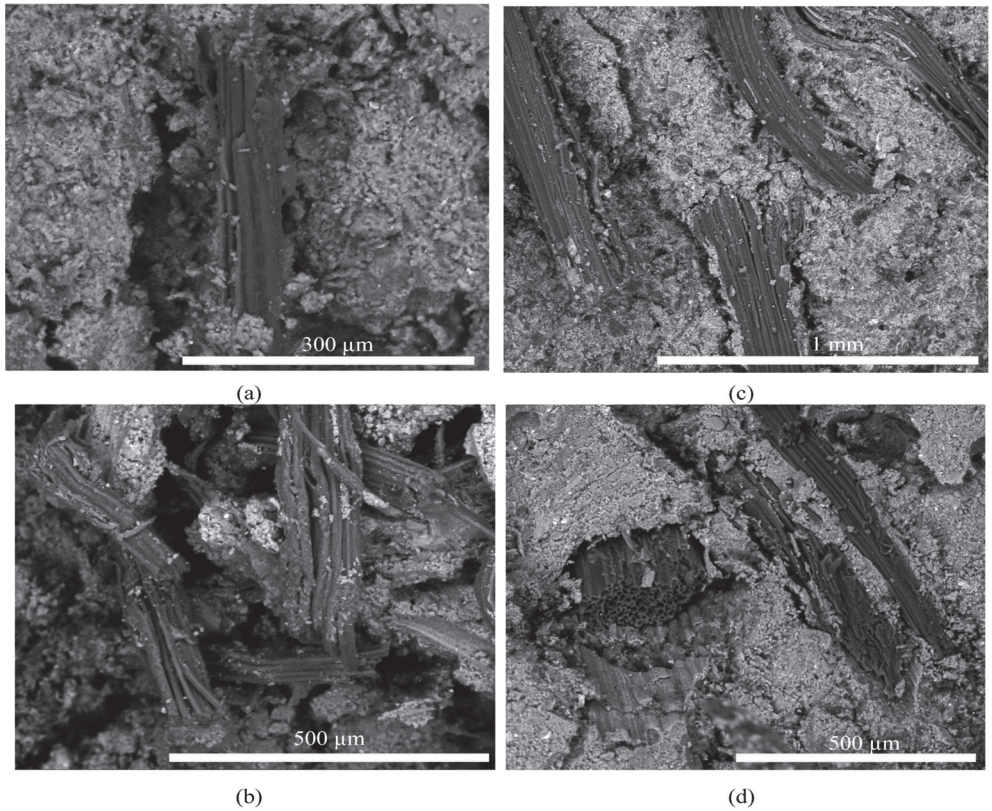

Figure 5. SEM micrographs of broken FRGCs: (**a**) Fiber-matrix bonding in jute-FRGC (2% wt%); (**b**) Failure mechanisms of jute-FRGC (2% wt%); (**c**) Fiber-matrix bonding in sisal-FRGC (3% wt%); (**d**) Failure mechanisms of sisal-FRGC (3% wt%) [63].

Advanced methods such as synchrotron X-ray tomography and digital image correlation (DIC) allow non-destructive 3D interface reconstruction and real-time strain mapping during loading [66,67], providing dynamic insights into damage evolution. At the nanoscale, atomic force microscopy (AFM) and molecular dynamics (MD) simulations provide quantitative evidence of interfacial adhesion and predict mechanisms of bond formation [68–71].

Notwithstanding their benefits, these procedures exhibit disadvantages, such as elevated costs, intricate sample preparation, and an absence of standardized testing protocols. Consequently, additional research is required to develop dependable multiscale evaluation frameworks and in situ methodologies for assessing interfacial performance under prolonged service circumstances.

3. Mechanical Properties of Plant Fiber-Reinforced Geopolymer Concrete

3.1. Compressive Strength

Compressive strength is a crucial measure of the mechanical properties of concrete materials. The effect of fiber admixture on compressive strength is complex, principally determined by elements like fiber type, admixture content, and mixture ratio. The integration of plant fibers, when used in appropriate quantities, has a minimal effect on the compressive strength of geopolymer concrete, potentially resulting in a tiny reduction in certain cases.

The development of compressive strength in plant fiber-reinforced geopolymer concretes significantly differs from that of conventional cementitious composites. The inclusion of fibers at reduced doses ($\leq$1.0 wt%) has demonstrated an enhancement in compressive strength attributed to better crack resistance and densification effects. In contrast, high

dosages (≥1.0 wt%) sometimes lead to a decrease in strength, a fact ascribed to fiber aggregation and heightened matrix porosity [72–74].

It is important to note that the optimal fiber content varies considerably depending on the type of fiber and the characteristics of the matrix. Studies by Alomayri et al. [72] and Korniejenko et al. [74] demonstrated that moderate incorporation (around 0.5–1.0 wt%) of cotton, coconut, and ramie fibers provided notable strength improvement. Conversely, higher levels of incorporation, particularly with bamboo, raffia, and sweet sorghum fibers, have been observed to result in adverse effects, including fiber agglomeration and compromised matrix continuity [44,73,75]. Furthermore, as reported by Ayeni et al. [26], the incorporation of red hemp, coconut, and oil palm fibers beyond a certain threshold consistently led to a decline in compressive performance owing to structural discontinuities and enhanced porosity.

A summary of specific optimal dosages, fiber types, and associated quantitative results is presented in Table 2.

Table 2. Summary of compressive strength results of PFRGCs with different fiber types and dosages.

Fiber Type	Matrix	Fiber Dosage	Length	Compressive Strength Trend	Remarks	Reference
Cotton	FA-based	0.5 wt%	10 mm	↑ 140%	Peak at 0.5 wt%, then ↓ at 0.7–1.0 wt%	[72]
Coconut, Cotton, Sisal, Raffia	FA-based	1.0 wt%	Cotton: 30 mm Others: 3 mm	Coconut ↑ 27%, Cotton ↑ 1 5%, Sisal ↑ 2%, Raffia ↓ 45%	Fiber type affects the trend	[74]
Sweet Sorghum	FA-based	1–3 wt%	≤50 mm	↓ 9–26%	Strength declines with increasing dosage	[75]
Bamboo	MK-based	5 wt%	≤40 mm	↓ 50%	Long fibers at high dosage are detrimental	[73]
Ramie, Coir, Sisal, Jute, Hemp	FA-based	1–2 wt%	≤25 mm	Ramie (1%) highest strength; others are slightly ↓	Ramie shows potential	[44]
Coconut Trunk	FA-based	0–1 g	30–50 mm	Peak at 0.5 g	Highest value 89.44 MPa	[76]
Kenaf, Coconut, Oil Palm	FA-based	0–1 vol%	25 mm	↓ With increasing fiber content	Due to increased porosity	[26]

Note: wt% = weight percentage; vol% = volume percentage; FA = fly ash; MK = metakaolin; ↑ = increase; ↓ = decrease.

The compressive strength of PFRGC demonstrated considerable variety across many experiments, ranging from 20 to 89 MPa. A crucial doping level, generally between 0.5% and 1.0%, has been recognized as a significant determinant affecting the compressive strength of PFRGC. Below this crucial threshold, the addition of a small quantity of fibers has been shown to strengthen the matrix structure, decrease porosity, and boost densification, thereby slightly increasing the compressive strength. Conversely, beyond the critical threshold, the compressive strength generally diminishes, primarily due to the following factors: (1) the strength and stiffness of plant fibers are inferior to that of the GPC matrix, and an excessive quantity of fibers reduces the matrix material's proportion; (2) plant fibers exhibit high absorbency, which interferes with the hydration reaction and hardening

process; and (3) a substantial quantity of fibers tends to agglomerate within the matrix, creating defects and compromising the material's homogeneity and compactness.

3.2. Tensile and Flexural Strength

Unlike compressive strength, plant fibers provide a significant enhancement to the tensile and flexural strength of geopolymer concrete. Essentially a brittle material with high compressive strength but low tensile strength, plant fibers, under their high tensile strength and elongation, can take up tensile stresses when PFRGC is subjected to tensile or flexural stresses, and effectively inhibit crack extension [Figure 6].

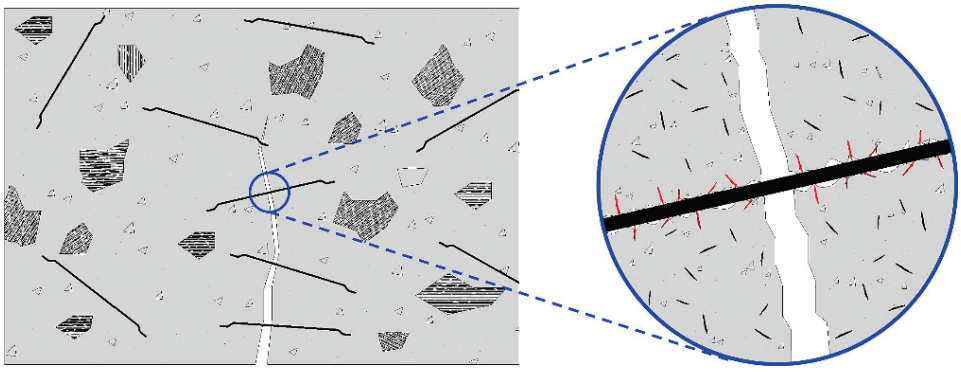

Figure 6. Mechanism of whisker enhancement for macroscopic fiber pull-out friction [77].

The integration of plant fibers has repeatedly demonstrated enhancements in the tensile and flexural properties of geopolymer composites, especially when utilized at moderate levels. Table 3 indicates that fibers including sweet sorghum, pineapple, coconut, and bamboo demonstrate considerable strengthening effects, with optimal enhancements often attained within the range of 0.5–2.0 wt% or vol%. For instance, sweet sorghum and pineapple fibers have demonstrated strength enhancements of up to 36% and nearly 40%, respectively [75,78], while alkali-treated bamboo fibers have been reported to improve flexural strength by more than twofold [79].

However, the advantages of fiber supplementation are not infinite. Excessive fiber content can lead to issues such as inadequate dispersion, fiber aggregation, and heightened porosity, which eventually compromise the mechanical integrity of the matrix [80]. This restriction is notably apparent in research utilizing flax fibers at elevated doses, where anomalously high strength enhancements, such as 1107%, have been documented, yet remain contentious due to concerns about their experimental reproducibility [81].

The reinforcing efficacy of plant fibers is determined not only by their quantity but also by inherent characteristics such as aspect ratio, surface roughness, and chemical compatibility with the binder. The inherently coarse surfaces of bamboo fibers and the enhanced interfacial bonding resulting from alkali treatment of pseudo-banana fibers are pivotal in crack bridging and energy dissipation during tensile and flexural stress [79,82].

Taken together, these findings suggest that maximizing the mechanical performance of plant fiber-reinforced geopolymers requires careful control of fiber dosage, fiber morphology, dispersion uniformity, and interfacial engineering-elements that warrant further attention in both future experimental studies and practical applications.

Table 3. Summary of tensile and flexural strength enhancements in PFRGCs with various plant fiber types and dosages.

Fiber Type	Matrix	Fiber Dosage	Tensile Strength Enhancement	Flexural Strength Enhancement	Remarks	References
Sweet Sorghum	FA-based	2 wt%	↑ 36%	↑ 51%	Optimal at 2 wt%, decline at 3 wt%	[75]
Cotton	FA-based	0–4.1 wt% (Pre-dried)	-	↑ 50% (8 → 12 MPa)	Optimal at 2.1 wt%, decline at 2.8 wt%	[83]
Cotton	FA-based	0–1 wt%	-	↑ 12.5% (10.4 → 11.7 MPa)	Optimal at 0.5 wt%, decline beyond 0.5 wt%	[84]
Pineapple	FA-based	0–0.5 wt% (10–30 mm length)	-	↑ from 6.58 MPa to 9.21 MPa	Optimal at 0.5 wt%, dosage at 30 mm	[78]
Sisal	FA-based	0–1 vol%	↑ 73.6%	↑ 112.9% (3.1 → 6.5 MPa)	Increased strength with content up to 1 vol%	[85]
Coconut	FA-based	0–1 vol%	↑ 15.8%	↑ 106.5% (3.1 → 6.4 MPa)	Increased strength with content up to 1 vol%	[85]
Bamboo	MK-based	1–5 vol%	-	↑ 151% (3.9 → 9.8 MPa)	Optimal enhancement observed at 3 vol%	[79]
Pseudo-banana	FA-based	0.7–2 vol% (5–20 mm length)	↑ 33%	-	Optimal at 1.4 vol%, dosage at 10 mm	[82]
Coconut	FA-based	0–1 vol%	↑ 34.5%	↑ 47.0% (4.11 → 6.04 MPa)	Optimal at 0.75 vol% for flexural	[26]
Kenaf	FA-based	0–1 vol%	↑ 50%	↑ 59.7% (4.93 → 7.87 MPa)	Optimal at 0.75 vol% for flexural	[26]
Oil Palm	FA-based	0–1 vol%	↑ 28.5%	↑ 45.5% (4.02 → 5.85 MPa)	Optimal at 0.75 vol% for flexural	[26]
Flax (questionable)	Halloysite	0–10 wt%	-	↑ 1107% (5.8 → 70.2 MPa)	Results contested	[81]

Note: wt% = weight percentage; vol% = volume percentage; ↑ = increase; → = change from one value to another.

3.3. Toughness and Ductility

Toughness and ductility are critical indicators for evaluating the deformability and energy absorption properties of concrete materials. Plant fiber-reinforced geopolymer concrete (PFRGC) has demonstrated notable advantages in enhancing toughness and ductility.

The enhancement of toughness and ductility in GPC by plant fibers is primarily attributed to their role in bridging and crack control. When cracks emerge in the matrix, the fibers assume the tensile stresses by traversing the cracks, impeding their propagation. Concurrently, the fibers absorb a substantial amount of energy during tensile withdrawal or fracture. Moreover, the incorporation of plant fibers can encourage the refinement and dispersion of cracks, thereby enhancing the material's overall deformation adaptability [86,87].

However, there were significant differences in the enhancement effect of different types of plant fibers on the toughness and ductility of GPC. Chen et al. [75] demonstrated that the post-peak toughness under split tensile loading increased by 1100%, 1600%, and 700%, respectively, when the fly ash-based polymer was reinforced with sweet sorghum fibers (doped with 1%, 2%, and 3% of the mass of the fly ash). A moderate amount of fiber incorporation resulted in a significant improvement in toughness; however, excessive incorporation led to a reduction in this improvement. In a similar study, Alomayri et al. [84] found that the toughness of 10 mm-long cotton fibers reinforced with fly ash-based polymer slurry at 0.5 wt% doping increased by approximately 60% in a three-point bending test. However, an increase in fiber doping to 0.7 wt% and 1.0 wt% resulted in a decrease in toughness due to a reduction in fiber dispersion.

Conversely, hemp fibers have been demonstrated to enhance GPC ductility and energy absorption. Research conducted by Poletanovic et al. [88] substantiated this finding. The en-

ergy absorption capacity of the geopolymer mortar was augmented by approximately 163% with the integration of 1 vol% of hemp fibers (10 mm in length). Following NaOH surface modification, the fiber-matrix interfacial bonding was strengthened, thereby augmenting the energy absorption capacity by approximately 13%. The hemp fiber-reinforced system demonstrates resilience in withstanding high residual loads in a cracked state, thereby enhancing the ductility of the material.

An appropriate increase in fiber doping has been shown to enhance toughness and ductility. However, excessive doping can lead to adverse effects on workability and strength. Furthermore, the contribution of different plant fibers to toughness and ductility varies due to differences in their tensile properties and modulus of elasticity. In general, the selection of plant fibers with high elongation and moderate modulus of elasticity is more conducive to the improvement of ductility [17]. The uniform dispersion and proper orientation of the fibers (particularly perpendicular to the crack propagation direction) can enhance the deformation and energy absorption properties of the material. The uniform dispersion and proper orientation of the fibers (particularly perpendicular to the direction of crack propagation) can optimize their bridging role and further improve the deformation and energy absorption properties of the material [26].

3.4. Impact Resistance Properties

Impact loading, a significant form of dynamic loading, is a common occurrence in the service life of building structures, including but not limited to earthquakes, explosions, impacts, and shocks. The micro-mechanism of the enhanced impact resistance of plant fiber-reinforced GPC can be primarily attributed to three factors: energy absorption, crack control, and stress redistribution. Under the impact load, the plant fiber absorbs the impact energy through its deformation and relative slip at the interface with the matrix. The bridging effect of the fiber effectively inhibits the rapid expansion of cracks and changes the state of stress distribution, thus improving the overall impact resistance of the material [89,90].

In the presence of external forces acting upon a fiber-reinforced geopolymer specimen, a complex stress field is generated internally. The distribution of fibers is of particular significance, as they form a three-dimensional network structure that functions as a bridge during the initiation and expansion of cracks. This results in a substantial increase in the material's energy absorption capacity. Ige Samuel Ayeni et al. [26] The outcomes of the drop impact test ($\varphi 80 \times 160$ mm cylindrical specimen, 4.5 kg drop, 1 mm fall height) based on the ACI 544 (2004) standard demonstrated a substantial enhancement effect of the plant fiber on the impact resistance of GPC. The experimental data indicate a nonlinear relationship between the fiber volume fraction and the impact resistance performance, exhibiting an evident critical volume effect. When the fiber volume percentage was elevated from 0% to 0.75%, the impact strength of specimens reinforced with kenaf, coconut, and oil palm fibers improved by 11.35%, 3.77%, and 2.09%, respectively. Moreover, when the fiber content was elevated to 1.0%, the impact strength showed a pronounced nonlinear enhancement, increasing by 122.11%, 98.33%, and 88.33%, respectively.

The mechanism of this critical volume effect can be attributed to the formation threshold of the fiber three-dimensional network structure. When the fiber content is lower than the critical value, the fiber distribution is relatively dispersed, and it is difficult to form an effective spatial network structure. Conversely, when the fiber content reaches or exceeds the critical value, the fibers begin to form a continuous three-dimensional network, which significantly improves the material's ability to absorb and disperse impact energy. Among the three natural fibers, kenaf fiber exhibits the most pronounced impact enhancement effect, which can be primarily ascribed to its high tensile strength (400–800 MPa) and exceptional interfacial bonding properties.

The Zwick Charpy Impact Tester is a tool used to assess the micro-impact resistance of materials through testing specimens [91]. The Charpy impact strength (σ_i) is calculated by the ratio of the impact energy (E) required to destroy the sample to the sample fracture area (A):

$$\sigma i = E / A$$

The impact strength of fiber-reinforced geopolymer composites is determined by three key factors: the quality of the fiber-matrix interfacial bond, the mechanical properties of the matrix, and the inherent qualities of the fibers [86]. Alomayri et al. [83] A systematic examination was conducted to ascertain the effect of cotton fiber content on the impact strength of geopolymer composites Charpy. The experimental results demonstrated a significant increase in impact strength with an increase in cotton fiber content in the dry composites. Specifically, the addition of 4.5, 6.2, and 8.3 wt% of cotton fibers increased the impact strength from 1.9 kJ/m^2 to 6.2, 8.5, and 13.4 kJ/m^2, respectively, with a maximum enhancement of 605%. This significant enhancement effect is primarily attributed to the increased elongation at break due to the high cellulose content of cotton fibers (approximately 88–96%), which increases the overall elongation at break of the composites and, consequently, the impact strength.

The researchers determined through a comprehensive fracture morphology investigation that, under sudden impact loading, composites lose energy via three principal mechanisms: fiber pullout, fiber fracture, and matrix deformation [92]. The relative contributions of these three mechanisms are contingent upon the strength of the fiber-matrix interfacial bond, the mechanical properties of the fibers themselves, and the deformability of the matrix.

A notable distinction emerges in the impact resistance of GPC when exposed to diverse categories of fibers. In addition to plant fibers, studies that investigate steel fiber reinforcement in GPC offer substantial insights. Rayapudi's study [93] demonstrated that optimized 2% steel fiber-reinforced geopolymer concrete exhibited a 30.19% increase in compressive strength, a 36.67% improvement in splitting tensile strength, and a 75.87% rise in flexural strength, as compared to plain GPC. In GPC slabs with 0.5% to 2% steel fiber content, the initial cracking load increased by 1.25–2.5 times compared to ordinary GPC slabs. These data establish a standard for evaluating the performance of plant fibers in comparison to other types of fibers.

Hybrid fiber systems demonstrate superior impact resistance. Optimal blends of coir and polypropylene fibers are achieved at a total content of 0.3%, exhibiting impact resistance that is up to twice that of single-fiber concrete and up to three times that of standard concrete [94]. This synergistic reinforcement effect is derived from the complementary roles of different types of fibers in terms of scale, stiffness, and interfacial properties. The more rigid fibers primarily control macroscopic crack propagation, while the flexible fibers effectively inhibit microscopic crack sprouting. Collectively, these fibers enhance the overall impact resistance of the material. This finding provides a theoretical foundation for the design of multiscale fiber reinforcement.

In summary, the incorporation of plant fiber reinforcement demonstrated a substantial enhancement in the impact resistance of geopolymer concrete. Through the optimization of fiber type, content, and distribution, the material exhibited an impact strength enhancement ranging from 88% to 605%, accompanied by an increase in the number of first cracking impacts by 1.25 to 2.5 times. The study revealed that distinct fibers exhibited varied reinforcing effects, underscoring the necessity for identifying the optimal fiber content to ensure optimal performance [95].

4. Durability of Plant Fiber-Reinforced Geopolymer Concrete

Durability is a critical index for evaluating the long-term service performance of building materials. The effect of plant fiber incorporation on the durability of GPC is complex and multifaceted, with both positive and possible negative effects. Upon the complete condensation of hydration products, a stabilization of the pH level occurs [96]. This phenomenon is attributed to the provision of conducive conditions that facilitate the durability of plant fibers within the matrix.

4.1. Freeze-Thaw Resistance

The nature of freeze-thaw damage is a cumulative damage process in which the internal stress generated by the phase change and expansion of free water in the material during freezing at low temperatures exceeds the tensile strength threshold of the material, resulting in the development and proliferation of a network of microcracks. In the composition of geopolymers, water is generally present in three states: crystalline water, gel water, and free water [97]. Only the free water within the capillary pore network will crystallize and experience volume expansion as the temperature falls below the freezing point. This expansion is the primary catalyst for frost heave damage.

The influence of plant fibers on the freeze-thaw characteristics of geopolymer composites exhibits a distinct duality. In the low dosage range (volume fraction < 2%), the fibers mainly inhibit the initiation and propagation of microcracks during freeze-thaw cycles through a three-dimensionally distributed bridging network [98], and dissipate part of the frost heave stress through interfacial slip and pull-out processes [99], thereby significantly improving the material's resistance to frost heave damage. Ekiz Barış and Tanaçan's [100] experiments confirmed that the strength retention of a geopolymer with 1.5% banana fiber was approximately 40% superior to that of the control following 300 rigorous freeze-thaw cycles. The microscopic mechanism of this enhancement effect is that the spatial network structure of the fibers creates stress transfer channels, blocking the continuous propagation of cracks during freeze–thaw cycles.

Nevertheless, when the fiber content surpasses a crucial threshold, the freeze-thaw performance diminishes markedly. The internal mechanism of this phenomenon can be attributed to three key factors: Initially, an abundance of fibers results in heightened water absorption of the material, hence augmenting the quantity and distribution range of freezeable water. Second, the agglomeration effect caused by high fiber content destroys the continuity of the matrix and forms high-porosity areas. In particular, the proportion of macropores with a diameter exceeding 200 nm increases, these pores are more likely to undergo destructive expansion during the freezing process; third, the plant fiber experiences structural breakdown due to the combined influence of an alkaline environment and freeze-thaw cycles, resulting in diminished mechanical capabilities and a reduction in the reinforcing effect [101]. Tan et al. [102] systematically investigated the quantitative relationship between the content of rice straw fibers and freeze-thaw damage, determining that 8% represents the ideal fiber content, resulting in the minimal mass loss rate of 0.31% after 50 freeze-thaw cycles. Upon increasing the fiber content to over 12%, the mass loss rate of the material increased sharply to above 0.82%, indicating a significant reduction in freeze-thaw resistance.

Research by Xuan et al. [103] offers significant insights into the correlation between the microstructure of plant fiber-reinforced GPC and its resistance to freeze-thaw cycles. After 25 freeze-thaw cycles, the overall integrity was maintained, with a mass change rate of only 0.1% to 4%, and no macroscopic damage such as surface collapse, missing corners, or obvious cracks. Microscopic investigation revealed that freeze-thaw cycles resulted in

the loosening of the matrix structure surrounding the fibers, leading to the emergence of microcracks at the fiber-matrix interface [Figure 7].

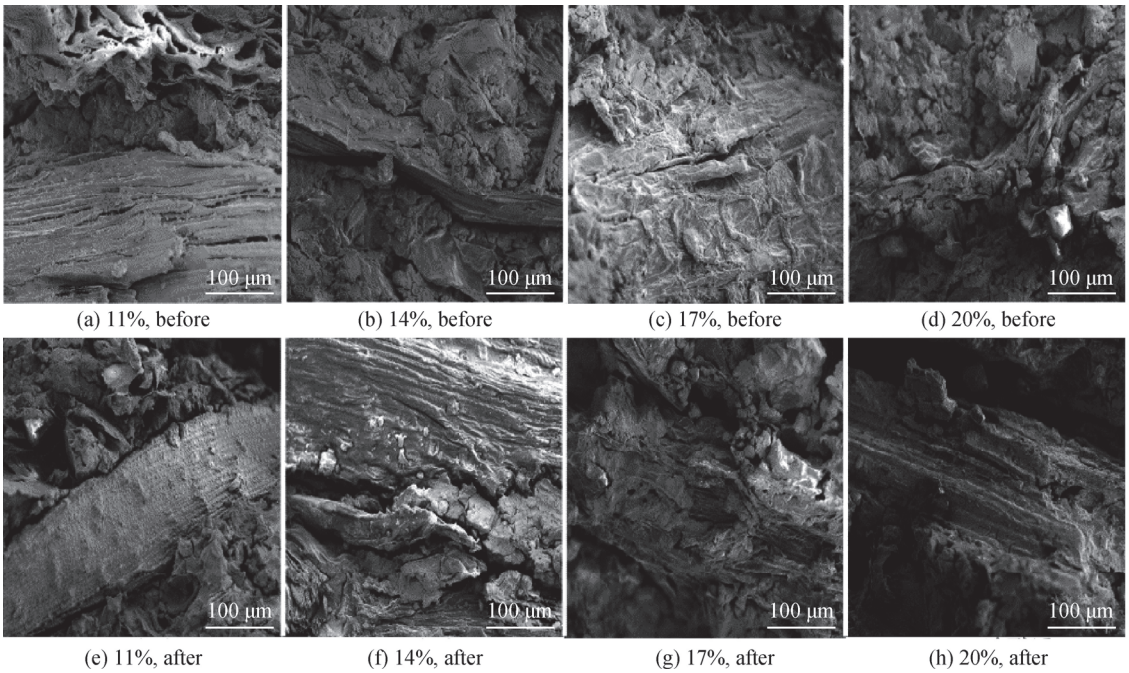

Figure 7. SEM images of geopolymer composites with different fiber content before and after freeze-thaw [103].

Through the examination of the progression of the fiber-matrix interface in a freeze-thaw environment, two technical approaches may be identified to enhance the freeze-thaw performance of plant fibers reinforced with GPC: Hydrophobic alteration of the fiber surface can decrease the water absorption rate and expansion propensity of the fiber, hence mitigating interfacial stress during the freeze-thaw process [104]; on the other hand, The incorporation of active fillers like fly ash can enhance the pore structure of the material, facilitate the development of N-A-S-H gel, occupy the tiny gaps around the fibers, and augment the interfacial bond strength [101]. This fiber-fly ash synergistic system can retain 85–90% of its strength after 100 freeze-thaw cycles, which is significantly better than a single-component system.

The freeze-thaw performance of GPC reinforced with plant fibers demonstrates considerable environmental dependence. Experimental data analysis shows that under moderate freeze-thaw conditions, the bridging of cracks by fibers dominates, and the material exhibits excellent freeze-thaw resistance; however, under extreme freeze-thaw conditions, fiber degradation and interfacial damage accelerate, and the freeze-thaw performance may decrease sharply.

4.2. Permeability Resistance

Permeability resistance is a critical index for evaluating the capacity of concrete to impede the infiltration of water and deleterious substances. It directly correlates with the material's long-term durability in wet and erosive environments. The primary mechanism by which plant fibers enhance the seepage resistance of GPC encompasses two aspects: pore structure regulation and crack control. Adequate fiber incorporation can optimize the pore structure, reduce the proportion of large pores, and limit pore connectivity. Concurrently, the three-dimensional network structure of fibers can effectively impede the creation and propagation of microcracks and diminish the occurrence of through cracks via the bridging effect, thereby reducing the connectivity of infiltration channels.

The hydrophilicity of plant fibers exerts a substantial influence on the impermeability of GPC. Nkwaju et al. [105] ascertained that the water absorption of bagasse fiber-reinforced geopolymer composites exhibited a substantial increase following dry and wet cycling, a phenomenon that was predominantly ascribed to the intrinsic hydrophilicity characteristic of plant fibers. The water-absorbing characteristics of diverse plant fibers exhibited substantial variation. Specifically, ramie fiber-reinforced geopolymers demonstrated the most pronounced increase in water absorption, ranging from 17% to 29% higher than that of the unreinforced samples. Conversely, hemp fiber-reinforced samples had the minimal increase in water absorption, attaining just around 3% more than the unreinforced samples. This mismatch is due to the varying levels of hemicellulose, lignin, and cellulose, which directly affect the hydrophilicity and pore structure of the fibers.

Fiber surface modification treatment has been demonstrated for enhancing fiber-matrix interfacial adhesion and enhancing the impermeability of GPC. Poletanovic et al. [44] have demonstrated that the 9% NaOH-treated hemp fibers exhibited a reduction in fiber absorption of water of approximately 20% and a decrease in mortar porosity of around 26%. This substantial improvement in impermeability was observed in fly ash-based alkali-activated mortar following wet and dry cycling. The alkali treatment has been shown to reduce fiber hydrophilicity and enhance fiber-matrix interfacial bonding by eliminating hemicellulose, pectin, and waxy substances from the fiber surface. In contrast, untreated fibers have been observed to potentially diminish impermeability due to their high water absorption and interfacial defects.

In the context of dry and wet cycling conditions, the bridging effect of plant fibers has been demonstrated to effectively impede microcrack extension and thereby enhance material durability. Yanou et al. [106] observed that geopolymer composites incorporating 3 wt% of bagasse fibers exhibited significantly diminished mass loss and strength reduction compared to unreinforced samples after 20 cycles of dry and wet cycling. Santos et al. [107] research has demonstrated that sisal fiber-reinforced alkali-activated cements demonstrate commendable durability, exhibiting up to 73% flexural strength retention after 10 wet and dry cycles.

The impact of plant fibers on the anti-chlorine ion permeation properties of GPC exhibited clear non-linear characteristics, suggesting the existence of an optimal combination of fiber parameters. The addition of 0.75% volume fraction of kenaf fiber into GPC significantly enhanced its anti-chlorine ion permeation properties. After a 90-day immersion period, the depth of chlorine ion permeation through composites with fibers measuring 20 mm, 30 mm, and 40 mm was reduced by 20.9%, 25%, and 16.36%, respectively. The influence of fiber length on the impermeable performance exhibited clear threshold characteristics. Specifically, the impermeable performance reached its peak at a fiber length of 30 mm, and further increases in fiber length, up to 40 mm, resulted in a 23.7% increase in penetration [108]. This trend followed a typical "first decline and then rise" pattern. This phenomenon is primarily attributable to the propensity of excessively elongated fibers to coalesce, resulting in an augmentation of local porosity and the emergence of infiltration channels.

The combined effect of plant fibers and mineral admixtures has been shown to enhance the seepage resistance of GPC. As Wei et al. [109] have found, the combination of cellulose fibers and fly ash has been demonstrated to enhance the durability of composites under dry and wet cycles of sulfate. Furthermore, the ratio optimization enhances the prevalence of benign pores, including micropores and tiny pores [110]. This synergistic effect is derived from the involvement of fly ash in the geopolymerization reaction, leading to the creation of a gel product that fills a portion of the pores. The fibers simultaneously obstruct the advancement of microcracks.

Nonetheless, the influence of plant fibers on the impermeability of GPC is not consistently advantageous. Gulzar et al. [111] assert, the chloride penetration depth of concrete in a 10% NaCl solution exhibited a 27% increase with the incorporation of 0.5% jute fibers, primarily due to the increased porosity of the composite material resulting from the jute fibers. Nevertheless, this adverse effect can be efficiently mitigated by the addition of high-efficiency water-reducing additives, thereby reducing the depth of chloride ion penetration by approximately 17%. The reduction of the liquid-solid ratio has been shown to effectively diminish the porosity of the composite material, consequently enhancing its permeability resistance [112].

Incorporating sufficient fiber quantities, appropriate fiber lengths, homogeneous distribution, and surface modification has demonstrated that plant fibers improve the resistance to water and chloride ion penetration, as well as the durability of GPC in both wet and dry environments. Conversely, in adverse conditions marked by high fiber content, excessively long fibers, uneven distribution, and untreated hydrophilic fibers, penetration resistance may diminish.

4.3. Carbonation Resistance

Carbonation represents a primary concern in terms of durability for concrete structures during their service life. This phenomenon is the result of complex physicochemical interactions between atmospheric CO_2 and the binder matrix. In conventional Portland cement concrete, carbonation mostly transpires via the reaction between $Ca(OH)_2$ and the calcium silicate hydrate (C-S-H) gel with CO_2, resulting in the formation of calcium carbonate ($CaCO_3$). The carbonation mechanism in geopolymer concrete (GPC) is inherently distinct. In GPC, the process of carbonation primarily entails the interaction of CO_2 with N-A-S-H and C-(A)-S-H gels in the pore solution, leading to the formation of carbonate and bicarbonate compounds, such as Na_2CO_3 and $NaHCO_3$ [113,114]. This process leads to a decrease in the pH of the pore solution and induces gel structure rearrangement and changes in the distribution of pore size. While GPC typically exhibits greater carbonation depth than ordinary Portland cement concrete [115]. The influence of plant fibers on the carbonation resistance of GPC has been minimally addressed in the existing research literature.

Huang et al. [116] conducted a comparative study that revealed that environmental conditions had a substantial impact on the carbonation process of plant fiber-reinforced GPC. The outdoor-exposed samples exhibited the highest degree of carbonization, followed by the indoor samples, while the hermetically stored samples showed the lowest degree of carbonization. This result suggests that ambient humidity and CO_2 concentration are the key factors affecting the carbonation process. The study demonstrated that carbonization has a dual impact on the matrix's durability and the interfacial binding fidelity among the plant fibers and the matrix, hence influencing the composite's overall performance. The external environment inflicted the most significant harm to the geopolymer matrix, plant fibers, and their interfacial adhesion, whereas the fiber strength of the hermetically sealed samples diminished despite the matrix's relative integrity. This finding emphasizes the decisive role of the stability of the interfacial adhesion between plant fibers and the geopolymer matrix regarding anti-carbonation capabilities. Ildiko Merta et al. [117] Systematic studies under accelerated carbonation conditions demonstrated that hemp fibers promoted the precipitation of alkaline and alkaline-earth metal salts in the carbonation reaction by increasing the initial porosity. This resulted in a significant reduction of mortar water uptake (~20%), with a particularly pronounced effect in the fly ash (FA) matrix. The enhancement of the pore structure is advantageous for the material's long-term durability. The carbonation-induced embrittlement of the matrix and fiber/matrix interface compromised the reinforcement provided by the fibers, demonstrating a distinct dual

impact. This effect manifested distinctly across diverse matrix systems: the FA-based mortar demonstrated an improvement of around 40% in compressive strength and 34% in flexural strength attributable to the sufficient carbonation reaction. The embrittlement process resulted in a 7% decrease in energy absorption capability. Conversely, the FA/GBFS (blast furnace slag)-based mortar demonstrated a minimal variation in strength (±10%), due to the decalcification of the high-calcium system and the limited infiltration of CO_2. Furthermore, the elevated fiber dosage, the research indicated that a slight augmentation in fiber content (0.5 vol%) can result in a significant reduction in strength (14–23%). This observation highlights the crucial importance of fiber content in enhancing material characteristics. The results demonstrate that a fiber dose of 0.5 vol% is best for achieving a balance of durability, strength, and energy absorption capability.

The impact of carbonation on the pH of the GPC pore solution is a critical indicator for evaluating the resistance to carbonation. Pouhet and Cyr [118] found that the pH of the pore solution in the geopolymer matrix derived from metakaolin cured in a natural CO_2 environment for 365 days decreased to a lesser extent than that of the ordinary cement matrix, stabilizing at around 10.5. This evidence indicates that GPC can still maintain a certain alkaline environment during long-term carbonation, which is conducive to maintaining the stability of the material. The leaching behavior of sodium carbonate (Na_2CO_3), the main product of carbonation, as a water-soluble substance, exerts a significant impact on the long-term efficacy of the geopolymer.

The beneficial impact of plant fibers on the carbonation resistance of GPC can be attributed to two primary factors. Initially, the three-dimensional network configuration of the fibers retards the rate of carbonation by enhancing microstructural integrity and impeding CO_2 infiltration [119]. Secondly, the crack-mitigating effect of fibers may diminish the initiation and propagation of microcracks during carbonation, hence preserving the structural integrity of the material. In addition, a moderate amount of plant fibers may improve the carbonation resistance through the optimization of the pore architecture of GPC, increasing the material compactness, and reducing the permeability of CO_2. However, under unfavorable conditions (excessive fibers, poor interfacial bonding, harsh environmental conditions), the fibers may increase the material porosity, accelerate the carbonation process, and even lead to performance degradation due to interfacial embrittlement.

4.4. Chemical Resistance

Chemical corrosion resistance is a critical metric for assessing the long-term durability of concrete materials under specific conditions. Under the action of acid rain, sewage, marine environments and other aggressive media, the concrete structure is prone to chemical corrosion, resulting in material expansion and cracking, performance deterioration and even structural damage. Geopolymer concrete (GPC) itself usually has superior chemical corrosion resistance to ordinary silicate cement concrete [120] and the impact of integrating plant fibers on the chemical corrosion resistance of GPC has a complex dual nature.

A systematic investigation of the durability of hemp fiber-reinforced foam concrete in 5% magnesium sulfate ($MgSO_4$) and 5% sodium sulfate (Na_2SO_4) solutions by Osman Gence [101], the results revealed the complex interaction between plant fibers and mineral admixtures in different sulfate environments. In the magnesium sulfate environment, hemp fiber concrete with high fly ash content (50%) performed best with a strength loss of only 4.7%, while concrete with 30% fly ash admixture had the highest loss (23%); in the sodium sulfate environment, hemp fiber concrete with 10% fly ash admixture performed best with a strength loss of only 4.8%. This disparity signifies the ideal proportion of plant fibers to mineral admixtures is highly dependent on the type of erosion medium. In addition, hemp fiber-reinforced concrete showed better sulfate resistance with minimal

loss of flexural strength (9%) at low foam content (50 kg/m^3), which was mainly attributed to lower porosity and higher material compactness. The mechanism is mainly reflected in two aspects: on the one hand, the fibers effectively inhibit the microcrack extension caused by sulfate erosion through bridging, maintaining the structural integrity of the material; on the other hand, the hydrophilicity of the fibers may lead to the absorption of sulfate solution in localized areas and the formation of microcrack origination points under long-term erosion. Mass loss analysis showed that high fly ash content (50%) significantly reduced the solubility loss due to sulfate erosion, while the incorporation of hemp fibers had a very minor impact on mass loss, suggesting that the plant fibers improved the sulfate resistance mainly by influencing the microstructure and crack control of the material.

The nonlinear nature of the influence of plant fibers on the sulfate resistance of GPC was further confirmed by Abbas et al. [108]. The PFRGC exhibited satisfactory sulfate resistance when a moderate amount of kenaf fiber (0.75–1.0%) and short fiber (20–30 mm) was incorporated. However, when the fiber doping was further augmented, the sulfate resistance exhibited a decline due to the escalating porosity resulting from fiber agglomeration. This behavior was ascribed to the moderate quantity of fibers creating a lattice structure inside the geopolymer, thus obstructing the ingress of deleterious particles into the matrix. In contrast, an overabundance of fibers resulted in an irregular distribution, impairing the adhesion of fibers to the matrix, elevating porosity, and diminishing durability. This discovery highlights the necessity of refining fiber properties to enhance the sulfate resistance of GPC.

Zhou et al. [121] discovered that cotton straw powder had a substantial negative impact on the acid resistance of alkali-activated materials (AAM). Following a 14-day exposure to a 2 M hydrochloric acid solution, the compressive strength of the reinforced composites was determined to be 13.5–23.5% diminished compared to that of the original composites. The reduction is mostly due to the high hydrophilicity and inadequate acid stability of the cotton straw powder employed in the composite. The addition of coconut husk fiber has been found to increase the matrix toughness and boost the composite's resistance to acid corrosion [122,123]. This discrepancy is primarily attributable to the elevated lignin content and diminished hydrophilicity of coir fiber, characteristics that confer enhanced stability in acidic environments.

Sá Ribeiro et al. [124] study on kaolin-based polymers reinforced with bamboo fibers demonstrated that the integration of bamboo fibers improved the durability of geopolymer composites (GPC) in sulfuric and hydrochloric acid environments with a concentration of $\leq$15 wt%. The bamboo fibers exhibited a significant improvement in acid resistance through several mechanisms, including crack bridging, microcrack inhibition, and silica gel deposition. The mass loss of the geopolymer matrix rose from 2.7% to 4%. The concentration of sulfuric acid was elevated from 5 wt% to 15 wt%, yielding a 4% rise. The material showed a greater extent of strength deterioration in the H_2SO_4 environment than in the HCl environment. The research determined that bamboo fiber-reinforced geopolymer can be safely applied to building materials exposed to $\leq$15 wt% sulfuric or hydrochloric acid environments, including wastewater systems. However, at high acid concentrations or high fiber doping conditions, bamboo fibers may increase porosity and render the substrate more susceptible to corrosion.

4.5. Drying Shrinkage Behavior

The phenomenon of shrinkage in geopolymers can be classified into three distinct categories: chemical shrinkage, the phenomenon of auto-constriction has been observed, and drying shrinkage. In contrast to Ordinary Portland Cement In contrast to the conventional Portland cement, which undergoes three stages of chemical deformation: shrinkage,

expansion, and subsequent shrinkage [125], drying shrinkage is indicative of the volumetric stability of the material during water loss and the potential risk of cracking. The integration of fibers diminishes the pressures exerted on the matrix, so effectively constraining its drying shrinkage.

The modulation of drying shrinkage properties of geopolymers by plant fibers demonstrates a substantial fiber type dependence. Systematic studies have demonstrated that under identical conditions, ramie, hemp, and bamboo fiber-reinforced geopolymers display diminished drying shrinkage, while jute, coir, and sisal fiber-reinforced geopolymers showed increased drying shrinkage compared to the unreinforced controls [44]. This mismatch can be ascribed to the increased surface roughness of jute, coir, and sisal fibers, which results in augmented porosity within the interfacial region and intensifies capillary water loss. Conversely, the mechanical confinement effect exhibited by ramie, hemp, and bamboo fibers supersedes the impact of their hygroscopic tendencies, thereby effectively curtailing matrix shrinkage.

Alcivar-Bastidas et al. [126] demonstrated that the alkali treatment of abaca fibers has demonstrated to reduce the 28-day drying shrinkage of geopolymer mortar by 13.5%. Moreover, the fiber-reinforced samples have demonstrated superior dimensional stability under wet-dry cycling conditions, thereby confirming the efficacy of the bridging effect of plant fibers in inhibiting microcrack extension. Compared to plant fibers, synthetic fibers like steel and PVA exhibit optimal doping thresholds for controlling geopolymer shrinkage at 1.0% and 0.3%, respectively, beyond which their efficacy reduces [51], the shrinkage exhibited a positive correlation with the water-cement ratio and the curing time.

The mechanism by which plant fibers affect the dry-shrinkage properties of geopolymers exhibits multiscale characteristics. At the microscopic level, Haily et al. found that bio-based fibers produced significantly fewer microscopic defects in the geopolymer matrix than synthetic fibers [127]. The hydrophilicity of plant fibers has a twofold impact on drying shrinkage characteristics. It improves overall hydrophilicity while intensifying drying shrinkage. Conversely, it serves as an internal conservation medium and prevents self-shrinkage [128,129]. This apparent contradiction reflects the complexity of plant fibers affecting drying and shrinkage, which necessitates precise control of fiber properties and matrix ratios to optimize the process.

The process of alkaline hydrolysis of cellulose and hemicellulose has been demonstrated to lead to a decrease in interfacial bond strength and an augmentation in drying shrinkage [130]. Xu et al. [131] has been confirmed that plant fibers can act as stress transfer and energy dissipation mechanisms to reduce crack extension. Maintenance conditions are also a key external factor influencing the dry shrinkage properties of plant fiber-reinforced geopolymers. Amran et al. [132] showed that the interplay between temperature and humidity exerts a synergistic impact on the drying and shrinkage properties of the material. At elevated temperatures, the curing process accelerates the development of strength in the material. However, this increase in strength is accompanied by an exacerbation of water evaporation and shrinkage. This phenomenon can be effectively mitigated by increasing the ambient humidity level to an appropriate extent.

5. Emerging Applications and Future Challenges of Plant Fiber-Reinforced Geopolymer

With the growing demand for green building materials, PFRGC is expanding into several innovative application areas. The introduction of renewable plant fibers into geopolymer systems is not only in line with the concept of a circular economy but also opens up new avenues for the development of lightweight, thermally insulating, and customizable building components. Walbrück et al. [133] researched the application of

miscanthus fibers in geopolymer foams and found a strong bonding between the fibers and the matrix and an irregular pore distribution, which improves the thermal insulation properties. Under the optimal ratio, the thermal conductivity decreased by 55.1%. These properties make it a potential sustainable and environmentally friendly thermal insulation material suitable for walls and cooling systems. Similarly, Novais et al. [134] showed that cork-alkali-activated fly ash multifunctional building materials showed significant results in optimizing thermal conductivity (decreasing up to 67.6%) and excelled in thermal insulation, sound absorption and humidity regulation. In terms of fire resistance, Silva et al. [135] examined a fiber-reinforced lightweight pozzolana-based geopolymer that significantly improved thermal insulation and water absorption. In the fire resistance test, the material can absorb about 65% of the heat from the flame, the temperature on the back side is less than 350 °C, the surface is only slightly discolored, and the shape is stable. It has great application prospects.

Especially in the 3D printing of building materials, the addition of fibers can change the printability, shape retention and interlayer bonding strength of the geopolymer paste [136,137]. In recent years, researchers have attempted to introduce natural plant fibers into the geopolymer system to explore their potential for reinforcement and processing adaptability in 3D printed building materials. Kozub et al. [138] verified the feasibility of fly ash-based geopolymer in 3D printing and demonstrated the potential of cotton fibers to reduce thermal conductivity, but failed to improve mechanical strength. Kong et al. [139] showed that kenaf stalk and straw core can significantly optimize the rheological properties of geopolymer slurries, improve printability and extrusion continuity, while increasing shape retention (thickness retention rate of more than 90%) and interlayer bond strength (compressive strength of 8.39 MPa at 28 days for a three-layer sample). However, fiber agglomeration, increased porosity, and process optimization remain challenges.

Despite the considerable technical potential of PFRGC, several notable challenges remain in current research: (1) inadequate long-term stability of plant fibers in alkaline environments and the absence of effective degradation prevention methods; (2) difficulties in achieving uniform fiber dispersion, particularly at elevated fiber content; (3) a deficiency of quantitative models elucidating the interfacial bonding mechanisms between plant fibers and geopolymer; (4) obstacles in industrial production regarding quality consistency and cost management; and (5) a lack of standardized testing methodologies and design specifications, which constrains engineering applications. The performance deterioration of PFRGC under elevated temperature and humid conditions requires immediate attention.

6. Conclusions

This paper examines the current research related to the interfacial characteristics, mechanical behavior, and durability of plant fiber-reinforced geopolymer concrete and puts forward the following main conclusions based on the analysis:

This critical review employs a systematic literature evaluation method and conducts a comprehensive search of databases such as Web of Science and Science Direct (2000–2025) to provide a thorough understanding of the current state of plant fiber-reinforced geopolymer concrete (PFRGC). This work outlines the current state of research on PFRGC and identifies directions worthy of further investigation. The results suggest that the interfacial bonding between plant fibers and the geopolymer matrix is primarily governed by mechanical interlocking and chemical interactions. Notably, the interfacial transition zone exhibits a gradient structural morphology, reflecting the complexity of the fiber–matrix interface. Experimental evidence indicates that appropriate surface treatment of fibers (particularly via alkali conditioning and silane coupling) can effectively improve interfacial bonding strength. In addition, adjusting the Si/Al ratio and introducing nanomaterials contribute

to the development of a more compact and chemically stable interfacial microstructure. The phase composition and morphology of the interfacial transition zone play a critical role in governing the macroscopic properties of fiber-reinforced geopolymer composites.

Quantitative studies indicate that the influence of plant fibers on the mechanical behavior of geopolymer concrete exhibits a nonlinear pattern. When added at a volume fraction between 0.5% and 1.5%, fibers have been shown to improve flexural strength by 20% to 45% and enhance toughness by 75% to 150%. Nonetheless, a modest decline in compressive strength (typically between 5% and 15%) is often observed. The toughening performance of plant fiber-reinforced geopolymer composites is strongly influenced by the fiber's aspect ratio, geometry, surface chemistry, and dispersion quality within the matrix. These factors collectively determine the efficiency of stress transfer and crack-bridging mechanisms at the fiber–matrix interface.

Long-term durability studies reveal that plant fiber incorporation in geopolymer composites presents a trade-off between improved functional performance and material degradation risks. Properly integrated fibers enhance impermeability, chemical resistance, and dimensional stability by arresting crack propagation and redistributing internal stresses. However, their intrinsic hydrophilicity and chemical instability in alkaline environments can compromise the structural integrity of the composite over time. Addressing this issue requires a combined approach: modifying fiber surfaces to enhance chemical stability and tailoring the matrix composition to ensure interfacial compatibility and resistance to alkaline-induced deterioration.

PFRGC has exhibited considerable benefits in lightweight insulation materials, 3D printed construction, and specialized functional materials (fire resistance, sound absorption, moisture regulation), hence broadening its technological frontiers. Nonetheless, issues including regulated fiber dispersion, interfacial stability, and large-scale manufacturing must be resolved to fully actualize its potential in novel functional applications.

In summary, this paper provides an important scientific basis for understanding the interfacial mechanisms, performance optimization, and application potential of plant fiber-reinforced geopolymer concrete through literature analysis and critical evaluation. As interdisciplinary research continues to deepen, the application of plant fiber-reinforced geopolymer concrete is anticipated to expand to include large-scale implementation in the domains of green building, infrastructure maintenance, and special engineering. This development is expected to provide substantial technical support for the sustainable advancement of the construction industry.

Author Contributions: Conceptualization, Z.L., J.L., W.L. and Y.Z.; validation, J.L. and W.L.; investigation, Z.L. and Y.Z.; data curation, Y.Z.; writing—original draft preparation, Z.L. and J.L.; writing—review and editing, Y.Z.; supervision, Y.Z.; funding acquisition, Y.Z. All authors have read and agreed to the published version of the manuscript.

Funding: This research was funded by the Postgraduate Research and Practice Innovation Program of Jiangsu Province (No. KYCX23_1142).

Institutional Review Board Statement: Not applicable.

Informed Consent Statement: Not applicable.

Data Availability Statement: No new data were created or analyzed in this study. Data sharing is not applicable to this article.

Acknowledgments: During the preparation of this manuscript, the authors used ChatGPT to improve the language and readability. After careful review and editing of the AI-generated content, the authors take full responsibility for the final publication.

Conflicts of Interest: The authors declare no conflict of interest.

Abbreviations

The following abbreviations are used in this manuscript:

GPC	Geopolymer Concrete
PFRGC	Plant Fiber-Reinforced Geopolymer Concrete
FRGC	Fiber-Reinforced Geopolymer Concrete
AAM	Alkali-Activated Materials

References

1. Barbhuiya, S.; Kanavaris, F.; Das, B.B.; Idrees, M. Decarbonising Cement and Concrete Production: Strategies, Challenges and Pathways for Sustainable Development. *J. Build. Eng.* **2024**, *86*, 108861. [CrossRef]
2. International Energy Agency. *Low-Carbon Transition in the Cement Industry*; IEA Technology Roadmaps; OECD: Paris, France, 2018.
3. Amran, Y.H.M.; Alyousef, R.; Alabduljabbar, H.; El-Zeadani, M. Clean Production and Properties of Geopolymer Concrete; A Review. *J. Clean. Prod.* **2020**, *251*, 119679. [CrossRef]
4. Unis Ahmed, H.; Mahmood, L.J.; Muhammad, M.A.; Faraj, R.H.; Qaidi, S.M.A.; Hamah Sor, N.; Mohammed, A.S.; Mohammed, A.A. Geopolymer Concrete as a Cleaner Construction Material: An Overview on Materials and Structural Performances. *Clean. Mater.* **2022**, *5*, 100111. [CrossRef]
5. Pham, K.V.A.; Nguyen, T.K.; Le, T.A.; Han, S.W.; Lee, G.; Lee, K. Assessment of Performance of Fiber Reinforced Geopolymer Composites by Experiment and Simulation Analysis. *Appl. Sci.* **2019**, *9*, 3424. [CrossRef]
6. Karimah, A.; Ridho, M.R.; Munawar, S.S.; Adi, D.S.; Ismadi; Damayanti, R.; Subiyanto, B.; Fatriasari, W.; Fudholi, A. A Review on Natural Fibers for Development of Eco-Friendly Bio-Composite: Characteristics, and Utilizations. *J. Mater. Res. Technol.* **2021**, *13*, 2442–2458. [CrossRef]
7. Manso-Morato, J.; Hurtado-Alonso, N.; Revilla-Cuesta, V.; Skaf, M.; Ortega-López, V. Fiber-Reinforced Concrete and Its Life Cycle Assessment: A Systematic Review. *J. Build. Eng.* **2024**, *94*, 110062. [CrossRef]
8. De Azevedo, A.; Cruz, A.; Marvila, M.; De Oliveira, L.; Monteiro, S.; Vieira, C.; Fediuk, R.; Timokhin, R.; Vatin, N.; Daironas, M. Natural Fibers as an Alternative to Synthetic Fibers in Reinforcement of Geopolymer Matrices: A Comparative Review. *Polymers* **2021**, *13*, 2493. [CrossRef] [PubMed]
9. Shalchian, M.M.; Arabani, M. Application of Plant-Derived Fibers in Soil Reinforcement on Experimental, Numerical, and Case Study Scales: A Review. *Bull. Eng. Geol. Environ.* **2023**, *82*, 19. [CrossRef]
10. Dittenber, D.B.; GangaRao, H.V.S. Critical Review of Recent Publications on Use of Natural Composites in Infrastructure. *Compos. Part A Appl. Sci. Manuf.* **2012**, *43*, 1419–1429. [CrossRef]
11. Bos, H.L.; Van Den Oever, M.J.A.; Peters, O.C.J.J. Tensile and Compressive Properties of Flax Fibres for Natural Fibre Reinforced Composites. *J. Mater. Sci.* **2002**, *37*, 1683–1692. [CrossRef]
12. Tolêdo Filho, R.D.; Scrivener, K.; England, G.L.; Ghavami, K. Durability of Alkali-Sensitive Sisal and Coconut Fibres in Cement Mortar Composites. *Cem. Concr. Compos.* **2000**, *22*, 127–143. [CrossRef]
13. Melo Filho, J.D.A.; Silva, F.D.A.; Toledo Filho, R.D. Degradation Kinetics and Aging Mechanisms on Sisal Fiber Cement Composite Systems. *Cem. Concr. Compos.* **2013**, *40*, 30–39. [CrossRef]
14. Wei, J.; Meyer, C. Degradation Mechanisms of Natural Fiber in the Matrix of Cement Composites. *Cem. Concr. Res.* **2015**, *73*, 1–16. [CrossRef]
15. Korniejenko, K.; Łach, M.; Hebdowska-Krupa, M.; Mikuła, J. The Mechanical Properties of Flax and Hemp Fibres Reinforced Geopolymer Composites. *IOP Conf. Ser. Mater. Sci. Eng.* **2018**, *379*, 012023. [CrossRef]
16. Ye, H.; Zhang, Y.; Yu, Z.; Mu, J. Effects of Cellulose, Hemicellulose, and Lignin on the Morphology and Mechanical Properties of Metakaolin-Based Geopolymer. *Constr. Build. Mater.* **2018**, *173*, 10–16. [CrossRef]
17. Islam, M.R.; Ul Isalm, M.R.; Rashid, M.; Ahammad, F.; Islam, M. Improvements in the Characteristics of Plant Fiber Reinforced Concrete. *Eur. J. Theor. Appl. Sci.* **2024**, *2*, 552–568. [CrossRef] [PubMed]
18. Cai, M.; Takagi, H.; Nakagaito, A.N.; Li, Y.; Waterhouse, G.I.N. Effect of Alkali Treatment on Interfacial Bonding in Abaca Fiber-Reinforced Composites. *Compos. Part A Appl. Sci. Manuf.* **2016**, *90*, 589–597. [CrossRef]
19. Kumar, R.S.; Muralidharan, N.; Sathyamurthy, R. Optimization of Alkali Treatment Process Parameters for Kenaf Fiber: Experiments Design. *J. Nat. Fibers* **2022**, *19*, 4276–4285. [CrossRef]
20. Arsène, M.-A.; Okwo, A.; Bilba, K.; Soboyejo, A.B.O.; Soboyejo, W.O. Chemically and Thermally Treated Vegetable Fibers for Reinforcement of Cement-Based Composites. *Mater. Manuf. Process.* **2007**, *22*, 214–227. [CrossRef]
21. Orue, A.; Jauregi, A.; Unsuain, U.; Labidi, J.; Eceiza, A.; Arbelaiz, A. The Effect of Alkaline and Silane Treatments on Mechanical Properties and Breakage of Sisal Fibers and Poly(Lactic Acid)/Sisal Fiber Composites. *Compos. Part A Appl. Sci. Manuf.* **2016**, *84*, 186–195. [CrossRef]

22. Majhi, S.; Pradhan, S.; Prakash, V.; Acharya, S.K. Influence of Alkali Treatment on the Interfacial Shear Strength of *Agave lechuguilla* Fiber and Its Significance as a Reinforcing Material in Polymer Composites for Mechanical Applications. *Polym. Compos.* **2023**, *44*, 3487–3499. [CrossRef]
23. Oushabi, A.; Sair, S.; Oudrhiri Hassani, F.; Abboud, Y.; Tanane, O.; El Bouari, A. The Effect of Alkali Treatment on Mechanical, Morphological and Thermal Properties of Date Palm Fibers (DPFs): Study of the Interface of DPF–Polyurethane Composite. *South Afr. J. Chem. Eng.* **2017**, *23*, 116–123. [CrossRef]
24. Yan, L.; Chouw, N.; Yuan, X. Improving the Mechanical Properties of Natural Fibre Fabric Reinforced Epoxy Composites by Alkali Treatment. *J. Reinf. Plast. Compos.* **2012**, *31*, 425–437. [CrossRef]
25. Fernandes, E.M.; Mano, J.F.; Reis, R.L. Hybrid Cork–Polymer Composites Containing Sisal Fibre: Morphology, Effect of the Fibre Treatment on the Mechanical Properties and Tensile Failure Prediction. *Compos. Struct.* **2013**, *105*, 153–162. [CrossRef]
26. Ayeni, I.S.; Lim, N.H.A.S.; Samad, M. Engineering Properties of Natural Fibre-Reinforced One-Part Geopolymer Concrete. *Constr. Build. Mater.* **2024**, *456*, 139161. [CrossRef]
27. Abdelmouleh, M.; Boufi, S.; Belgacem, M.N.; Duarte, A.P.; Ben Salah, A.; Gandini, A. Modification of Cellulosic Fibres with Functionalised Silanes: Development of Surface Properties. *Int. J. Adhes. Adhes.* **2004**, *24*, 43–54. [CrossRef]
28. Gao, Y.; Chen, Y.; Gao, J.; Gao, J.; Yang, L.; Zhang, J.; Nan, R.; Cai, M.; Zhang, J. Properties of *Arenga Engleri Becc* Palm Fiber Particles with Silane Coupling Agent KH570 Treatments for Application in Polymer/Cement Composites. *J. Nat. Fibers* **2022**, *19*, 7348–7362. [CrossRef]
29. Zhou, F.; Cheng, G.; Jiang, B. Effect of Silane Treatment on Microstructure of Sisal Fibers. *Appl. Surf. Sci.* **2014**, *292*, 806–812. [CrossRef]
30. Asim, M.; Jawaid, M.; Abdan, K.; Ishak, M.R. Effect of Alkali and Silane Treatments on Mechanical and Fibre-Matrix Bond Strength of Kenaf and Pineapple Leaf Fibres. *J. Bionic Eng.* **2016**, *13*, 426–435. [CrossRef]
31. Feng, Y.; Wang, Q.; Li, L.; Ma, Y.; Li, X. Multiscale Analysis of Silane Coupling Agent Modified Rubber-Fiber Concrete Interfaces. *Mater. Today Commun.* **2023**, *35*, 105960. [CrossRef]
32. Wu, W.; Zuo, H. Used Tire Rubber Powder/Plant Cellulose Composites Treated with Coupling Agent. *Cellulose* **2016**, *23*, 1939–1947. [CrossRef]
33. Liu, T.; Wei, H.; Zhou, A.; Zou, D.; Jian, H. Multiscale Investigation on Tensile Properties of Ultra-High Performance Concrete with Silane Coupling Agent Modified Steel Fibers. *Cem. Concr. Compos.* **2020**, *111*, 103638. [CrossRef]
34. Zhao, L.; Ding, Y.; Li, S.; Song, Y.; Gong, H.; Zhang, Y. Silane Treatment for Sisal Fibers to Improve the Degradation Resistance and Interface with Cement Matrix. *Constr. Build. Mater.* **2024**, *429*, 136435. [CrossRef]
35. Liu, M.; Dai, W.; Li, M.; Jin, W.; Yang, X.; Han, Y.; Huang, M. Mechanism of Interface Performance Enhancement of Nano-SiO_2 Modified Polyvinyl Alcohol Fiber Reinforced Geopolymer Concrete: Experiments, Microscopic Characterization, and Molecular Simulation. *J. Build. Eng.* **2024**, *98*, 111062. [CrossRef]
36. Gapsari, F.; Wijatmiko, I.; Andoko, A.; Diharjo, K.; Mavinkere Rangappa, S.; Siengchin, S. Modification on Fiber from Alkali Treatment and AESO Coating to Enhance UV-Light and Water Absorption Resistance in Kapok Fiber Reinforced Polyester Composites. *J. Nat. Fibers* **2024**, *21*, 2383970. [CrossRef]
37. Li, Y.; Ma, H.; Shen, Y.; Li, Q.; Zheng, Z. Effects of Resin inside Fiber Lumen on the Mechanical Properties of Sisal Fiber Reinforced Composites. *Compos. Sci. Technol.* **2015**, *108*, 32–40. [CrossRef]
38. Adekunle, K.F. Surface Treatments of Natural Fibres—A Review: Part 1. *Open J. Polym. Chem.* **2015**, *05*, 41–46. [CrossRef]
39. Kalia, S.; Kaith, B.S.; Kaur, I. Pretreatments of Natural Fibers and Their Application as Reinforcing Material in Polymer Composites—A Review. *Polym. Eng. Sci* **2009**, *49*, 1253–1272. [CrossRef]
40. Waqas, R.M.; Butt, F.; Zhu, X.; Jiang, T.; Tufail, R.F. A Comprehensive Study on the Factors Affecting the Workability and Mechanical Properties of Ambient Cured Fly Ash and Slag Based Geopolymer Concrete. *Appl. Sci.* **2021**, *11*, 8722. [CrossRef]
41. Wang, H.; Wu, H.; Xing, Z.; Wang, R.; Dai, S. The Effect of Various Si/Al, Na/Al Molar Ratios and Free Water on Micromorphology and Macro-Strength of Metakaolin-Based Geopolymer. *Materials* **2021**, *14*, 3845. [CrossRef]
42. Mohr, B.J.; Biernacki, J.J.; Kurtis, K.E. Supplementary Cementitious Materials for Mitigating Degradation of Kraft Pulp Fiber-Cement Composites. *Cem. Concr. Res.* **2007**, *37*, 1531–1543. [CrossRef]
43. Wei, J.; Meyer, C. Utilization of Rice Husk Ash in Green Natural Fiber-Reinforced Cement Composites: Mitigating Degradation of Sisal Fiber. *Cem. Concr. Res.* **2016**, *81*, 94–111. [CrossRef]
44. Gholampour, A.; Danish, A.; Ozbakkaloglu, T.; Yeon, J.H.; Gencel, O. Mechanical and Durability Properties of Natural Fiber-Reinforced Geopolymers Containing Lead Smelter Slag and Waste Glass Sand. *Constr. Build. Mater.* **2022**, *352*, 129043. [CrossRef]
45. Poletanovic, B.; Dragas, J.; Ignjatovic, I.; Komljenovic, M.; Merta, I. Physical and Mechanical Properties of Hemp Fibre Reinforced Alkali-Activated Fly Ash and Fly Ash/Slag Mortars. *Constr. Build. Mater.* **2020**, *259*, 119677. [CrossRef]
46. Phoo-ngernkham, T.; Maegawa, A.; Mishima, N.; Hatanaka, S.; Chindaprasirt, P. Effects of Sodium Hydroxide and Sodium Silicate Solutions on Compressive and Shear Bond Strengths of FA–GBFS Geopolymer. *Constr. Build. Mater.* **2015**, *91*, 1–8. [CrossRef]

47. Sachet, W.H.; Salman, W.D. Geopolymer Concrete, Mortar, and Paste: A Review. *IOP Conf. Ser. Mater. Sci. Eng.* **2021**, *1076*, 012108. [CrossRef]
48. Sá Ribeiro, M.G.; Miranda, I.P.A.; Kriven, W.M.; Ozer, A.; Sá Ribeiro, R.A. High Strength and Low Water Absorption of Bamboo Fiber-Reinforced Geopolymer Composites. *Constr. Build. Mater.* **2024**, *411*, 134179. [CrossRef]
49. Jegan, M.; Annadurai, R.; Kannan Rajkumar, P.R. A State of the Art on Effect of Alkali Activator, Precursor, and Fibers on Properties of Geopolymer Composites. *Case Stud. Constr. Mater.* **2023**, *18*, e01891. [CrossRef]
50. Silva, G.; Castañeda, D.; Kim, S.; Castañeda, A.; Bertolotti, B.; Ortega-San-Martin, L.; Nakamatsu, J.; Aguilar, R. Analysis of the Production Conditions of Geopolymer Matrices from Natural Pozzolana and Fired Clay Brick Wastes. *Constr. Build. Mater.* **2019**, *215*, 633–643. [CrossRef]
51. Li, H.; Tang, W.; Tan, Y.; Wang, Y.; Guo, B.; Gao, P.; Zhan, B.; Yu, Q. Effect of Short Fibers on Non-Uniform Strain Distribution of Geopolymer Mortar under Dry Conditions. *Constr. Build. Mater.* **2025**, *459*, 139768.
52. Huang, Z.; Wang, Q. The Effect of Temperature on Dissolution Activity of Fly Ash and Metakaolin in Alkaline Conditions. *Cem. Concr. Compos.* **2024**, *146*, 105363. [CrossRef]
53. Assaedi, H.; Shaikh, F.U.A.; Low, I.M. Characterizations of Flax Fabric Reinforced Nanoclay-Geopolymer Composites. *Compos. Part B Eng.* **2016**, *95*, 412–422. [CrossRef]
54. Wang, X.; Zheng, Q.; Dong, S.; Ashour, A.; Han, B. Interfacial Characteristics of Nano-Engineered Concrete Composites. *Constr. Build. Mater.* **2020**, *259*, 119803. [CrossRef]
55. Wang, Y.-S.; Peng, K.-D.; Alrefaei, Y.; Dai, J.-G. The Bond between Geopolymer Repair Mortars and OPC Concrete Substrate: Strength and Microscopic Interactions. *Cem. Concr. Compos.* **2021**, *119*, 103991. [CrossRef]
56. Oriez, V.; Peydecastaing, J.; Pontalier, P.-Y. Lignocellulosic Biomass Mild Alkaline Fractionation and Resulting Extract Purification Processes: Conditions, Yields, and Purities. *Clean Technol.* **2020**, *2*, 91–115. [CrossRef]
57. Rao, J.; Zhou, Y.; Fan, M. Revealing the Interface Structure and Bonding Mechanism of Coupling Agent Treated WPC. *Polymers* **2018**, *10*, 266. [CrossRef]
58. Mourak, A.; Hajjaji, M. Moroccan Heated Clay-Based Geopolymer Reinforced with Date Palm Cellulose: Microstructure Characterization and Mechanical/Physical Properties. *Clay Miner.* **2024**, *59*, 50–62. [CrossRef]
59. Sethi, S.; Ray, B.C. Environmental Effects on Fibre Reinforced Polymeric Composites: Evolving Reasons and Remarks on Interfacial Strength and Stability. *Adv. Colloid Interface Sci.* **2015**, *217*, 43–67. [CrossRef]
60. Rahman, A.S.; Radford, D.W. Evaluation of the Geopolymer/Nanofiber Interfacial Bond Strength and Their Effects on Mode-I Fracture Toughness of Geopolymer Matrix at High Temperature. *Compos. Interfaces* **2017**, *24*, 817–831. [CrossRef]
61. Wang, K.; Lin, B.; Wu, B.; Yao, Y. Repair of Ordinary Concrete Using Basalt Fiber Reinforced Geopolymer: High Temperature Resistance and Micro Structure Evolution of Adhesive Interface. *J. Build. Eng.* **2024**, *97*, 110712. [CrossRef]
62. Yang, Y.; Xiao, Y.; Zhou, W.; Jiskani, I.M.; Luan, B. Strength Analysis of Geopolymer-Rock Interface: Mohr-Coulomb Shear and Interface Transition Zone (ITZ) Nanoindentation Testing. *Constr. Build. Mater.* **2025**, *458*, 139544. [CrossRef]
63. Silva, G.; Kim, S.; Bertolotti, B.; Nakamatsu, J.; Aguilar, R. Optimization of a Reinforced Geopolymer Composite Using Natural Fibers and Construction Wastes. *Constr. Build. Mater.* **2020**, *258*, 119697. [CrossRef]
64. Sigrüner, M.; Muscat, D.; Strübbe, N. Investigation on PULL-OUT Behavior and Interface Critical Parameters of Polymer Fibers Embedded in Concrete and Their Correlation with Particular Fiber Properties. *J. Appl. Polym. Sci.* **2021**, *138*, 50745. [CrossRef]
65. Ferreira, S.R.; Pepe, M.; Martinelli, E.; De Andrade Silva, F.; Toledo Filho, R.D. Influence of Natural Fibers Characteristics on the Interface Mechanics with Cement Based Matrices. *Compos. Part B Eng.* **2018**, *140*, 183–196. [CrossRef]
66. Liu, B.; Hu, X.; Li, Y.; Xiao, T.; Xu, F. Internal Three-Dimensional Strain Evolution of the Failure Process for Short Carbon Fiber Composite through in Situ Synchrotron Radiation X-Ray Computed Tomography. *Carbon* **2020**, *157*, 506–514. [CrossRef]
67. Li, S.; Chen, D.; Lu, Y.; Liu, Z. Fatigue Fracture Characteristics of Normal Concrete and High Ductility Geopolymer Bonding Based on DIC Technique. *Thin-Walled Struct.* **2024**, *196*, 111469. [CrossRef]
68. Leite, F.L.; Herrmann, P.S.P.; Da Róz, A.L.; Ferreira, F.C.; Curvelo, A.A.S.; Mattoso, L.H.C. Investigation of Sisal Fibers by Atomic Force Microscopy: Morphological and Adhesive Characteristics. *J. Nanosci. Nanotech.* **2006**, *6*, 2354–2361. [CrossRef]
69. Liu, W.; Shomali, A.; Zhang, C.; Coasne, B.; Carmeliet, J.; Derome, D. Nanostructure and Interfacial Mechanical Properties of PEG/Cellulose Nanocomposites Studied with Molecular Dynamics. *Carbohydr. Polym.* **2024**, *343*, 122429. [CrossRef] [PubMed]
70. Qin, R.; Li, Y.; Wong, S.Y.; Teo, F.Y.; Yu, Z.; Sun, L.; Zheng, Y. Understanding on the Creep Behavior of Fiber Reinforced Polymer via Fiber/Matrix Interaction. *Constr. Build. Mater.* **2024**, *451*, 138875. [CrossRef]
71. Huang, H.; Luo, J.; Peng, C.; Sun, T.; Deng, T.; Hu, J.; Guzal Anvarovna, K.; Azizbek Davlatali Ugli, N.; Hou, D.; Wei, J.; et al. Interfacial Bond between Modified Micro Carbon Fiber and High-Strength Cement Paste in UHPC: Bond-Slip Tests and Molecular Dynamic Simulation. *Cem. Concr. Compos.* **2023**, *142*, 105168. [CrossRef]
72. Alomayri, T.; Low, I.M. Synthesis and Characterization of Mechanical Properties in Cotton Fiber-Reinforced Geopolymer Composites. *J. Asian Ceram. Soc.* **2013**, *1*, 30–34. [CrossRef]

73. Sá Ribeiro, R.A.; Sá Ribeiro, M.G.; Sankar, K.; Kriven, W.M. Geopolymer-Bamboo Composite—A Novel Sustainable Construction Material. *Constr. Build. Mater.* **2016**, *123*, 501–507. [CrossRef]
74. Korniejenko, K.; Frączek, E.; Pytlak, E.; Adamski, M. Mechanical Properties of Geopolymer Composites Reinforced with Natural Fibers. *Procedia Eng.* **2016**, *151*, 388–393. [CrossRef]
75. Chen, R.; Ahmari, S.; Zhang, L. Utilization of Sweet Sorghum Fiber to Reinforce Fly Ash-Based Geopolymer. *J. Mater. Sci.* **2014**, *49*, 2548–2558. [CrossRef]
76. Amalia, F.; Akifah, N.; Nurfadilla; Subaer. Development of Coconut Trunk Fiber Geopolymer Hybrid Composite for Structural Engineering Materials. *IOP Conf. Ser. Mater. Sci. Eng.* **2017**, *180*, 012014. [CrossRef]
77. Zhao, C.; Wang, Z.; Zhu, Z.; Guo, Q.; Wu, X.; Zhao, R. Research on Different Types of Fiber Reinforced Concrete in Recent Years: An Overview. *Constr. Build. Mater.* **2023**, *365*, 130075. [CrossRef]
78. Zulfiati, R.; Saloma; Idris, Y. Mechanical Properties of Fly Ash-Based Geopolymer with Natural Fiber. *J. Phys. Conf. Ser.* **2019**, *1198*, 082021. [CrossRef]
79. Ayawanna, J.; Poowancum, A. Enhancing Flexural Strength of Metakaolin-Based Geopolymer Reinforced with Different Types of Fibers. *Sustain. Chem. Pharm.* **2024**, *37*, 101439. [CrossRef]
80. Ranjbar, N.; Zhang, M. Fiber-Reinforced Geopolymer Composites: A Review. *Cem. Concr. Compos.* **2020**, *107*, 103498. [CrossRef]
81. Alzeer, M.; MacKenzie, K. Synthesis and Mechanical Properties of Novel Composites of Inorganic Polymers (Geopolymers) with Unidirectional Natural Flax Fibres (*Phormium Tenax*). *Appl. Clay Sci.* **2013**, *75–76*, 148–152. [CrossRef]
82. Addis, L.B.; Sendekie, Z.B.; Habtu, N.G.; Schubert, D.W.; Roether, J.A.; Boccaccini, A.R. False Banana Fiber Reinforced Geopolymer Composite—A Novel Sustainable Material. *Ceram. Int.* **2024**, *50*, 24442–24450. [CrossRef]
83. Alomayri, T.; Shaikh, F.U.A.; Low, I.M. Thermal and Mechanical Properties of Cotton Fabric-Reinforced Geopolymer Composites. *J. Mater. Sci.* **2013**, *48*, 6746–6752. [CrossRef]
84. Alomayri, T.; Shaikh, F.U.A.; Low, I.M. Characterisation of Cotton Fibre-Reinforced Geopolymer Composites. *Compos. Part B Eng.* **2013**, *50*, 1–6. [CrossRef]
85. Wongsa, A.; Kunthawatwong, R.; Naenudon, S.; Sata, V.; Chindaprasirt, P. Natural Fiber Reinforced High Calcium Fly Ash Geopolymer Mortar. *Constr. Build. Mater.* **2020**, *241*, 118143. [CrossRef]
86. Alomayri, T.; Assaedi, H.; Shaikh, F.U.A.; Low, I.M. Effect of Water Absorption on the Mechanical Properties of Cotton Fabric-Reinforced Geopolymer Composites. *J. Asian Ceram. Soc.* **2014**, *2*, 223–230. [CrossRef]
87. Farhan, K.Z.; Johari, M.A.M.; Demirboğa, R. Impact of Fiber Reinforcements on Properties of Geopolymer Composites: A Review. *J. Build. Eng.* **2021**, *44*, 102628. [CrossRef]
88. Poletanovic, B.; Janotka, I.; Janek, M.; Bacuvcik, M.; Merta, I. Influence of the NaOH-Treated Hemp Fibres on the Properties of Fly-Ash Based Alkali-Activated Mortars Prior and after Wet/Dry Cycles. *Constr. Build. Mater.* **2021**, *309*, 125072. [CrossRef]
89. Chen, C.; Zhang, X.; Hao, H. Dynamic Tensile Properties of Geopolymer Concrete and Fibre Reinforced Geopolymer Concrete. *Constr. Build. Mater.* **2023**, *393*, 132159. [CrossRef]
90. Yang, S.; Zhao, R.; Ma, B.; Si, R.; Zeng, X. Mechanical and Fracture Properties of Fly Ash-Based Geopolymer Concrete with Different Fibers. *J. Build. Eng.* **2023**, *63*, 105281. [CrossRef]
91. Low, I.M.; McGrath, M.; Lawrence, D.; Schmidt, P.; Lane, J.; Latella, B.A.; Sim, K.S. Mechanical and Fracture Properties of Cellulose-Fibre-Reinforced Epoxy Laminates. *Compos. Part A Appl. Sci. Manuf.* **2007**, *38*, 963–974. [CrossRef]
92. Wambua, P.; Ivens, J.; Verpoest, I. Natural Fibres: Can They Replace Glass in Fibre Reinforced Plastics? *Compos. Sci. Technol.* **2003**, *63*, 1259–1264. [CrossRef]
93. Rayapudi, S.; Rao, T.C.S. Strength Characteristics and Impact Resistance of Fiber-Reinforced Geopolymer Concrete Elements. In *Low Carbon Materials and Technologies for a Sustainable and Resilient Infrastructure*; Pancharathi, R.K., Leung, K.Y., Chandra, C., Kishen, J.M., Eds.; Lecture Notes in Civil Engineering; Springer Nature: Singapore, 2024; Volume 440, pp. 495–504.
94. Md, B.; Unnikrishnan, S. Mechanical Strength and Impact Resistance of Hybrid Fiber Reinforced Concrete with Coconut and Polypropylene Fibers. *Mater. Today Proc.* **2022**, *65*, 1873–1880. [CrossRef]
95. Wang, W.; Zhang, Y.; Mo, Z.; Chouw, N.; Jayaraman, K.; Xu, Z. A Critical Review on the Properties of Natural Fibre Reinforced Concrete Composites Subjected to Impact Loading. *J. Build. Eng.* **2023**, *77*, 107497. [CrossRef]
96. Santana, H.A.; Andrade Neto, J.S.; Ribeiro, D.V.; Cilla, M.S.; Dias, C.M.R. Accelerated Alkaline Attack of 3D Printing Polymers to Assess Their Durability in Geopolymer-Based Matrices. *J. Mater. Civ. Eng.* **2021**, *33*, 04021327. [CrossRef]
97. Li, F.; Chen, D.; Lu, Y.; Zhang, H.; Li, S. Influence of Mixed Fibers on Fly Ash Based Geopolymer Resistance against Freeze-Thaw Cycles. *J. Non-Cryst. Solids* **2022**, *584*, 121517. [CrossRef]
98. Silva, G.; Kim, S.; Aguilar, R.; Nakamatsu, J. Natural Fibers as Reinforcement Additives for Geopolymers—A Review of Potential Eco-Friendly Applications to the Construction Industry. *Sustain. Mater. Technol.* **2020**, *23*, e00132. [CrossRef]
99. Zhao, N.; Wang, S.; Quan, X.; Xu, F.; Liu, K.; Liu, Y. Behavior of Polyvinyl Alcohol Fiber Reinforced Geopolymer Composites under the Coupled Attack of Sulfate and Freeze-Thaw in a Marine Environment. *Ocean Eng.* **2021**, *238*, 109734. [CrossRef]

100. Bariş, K.E.; Tanaçan, L. Durability behavior of banana fiber-reinforced natural pozzolan geopolymer. *J. Green Build.* **2023**, *18*, 149–168. [CrossRef]
101. Gencel, O.; Yavuz Bayraktar, O.; Kaplan, G.; Benli, A.; Martínez-Barrera, G.; Brostow, W.; Tek, M.; Bodur, B. Characteristics of Hemp Fibre Reinforced Foam Concretes with Fly Ash and Taguchi Optimization. *Constr. Build. Mater.* **2021**, *294*, 123607. [CrossRef]
102. Tan, J.; Huang, Y.; Liu, L.; Yu, S.; Zheng, G. Preparation and Freeze-Thaw Resistance of Geopolymer-Based Natural Plant Fiber Composites. In *Advances in Transdisciplinary Engineering*; Dobrotă, D., Cheng, C., Eds.; IOS Press: Amsterdam, The Netherlands, 2021.
103. Xuan, X.; Tan, J.; Huang, Y.; Xie, M.; Zheng, G. Preparation and Freeze Resistance of Geopolymer-Bagasse Fiber Composites. *Bull. Chin. Ceram. Soc* **2020**, *39*, 532–536. (In Chinese)
104. Sahraei Moghadam, A.; Mirza Goltabar Roshan, A.; Omidinasab, F. Utilization of Agricultural Wastes as Fiber, Binder and Aggregates of Geopolymer Mortars: Application of Taguchi Method for Strength and Durability Optimization. *J. Build. Eng.* **2023**, *75*, 106906. [CrossRef]
105. Nkwaju, R.Y.; Djobo, J.N.Y.; Nouping, J.N.F.; Huisken, P.W.M.; Deutou, J.G.N.; Courard, L. Iron-Rich Laterite-Bagasse Fibers Based Geopolymer Composite: Mechanical, Durability and Insulating Properties. *Appl. Clay Sci.* **2019**, *183*, 105333. [CrossRef]
106. Yanou, R.N.; Kaze, R.C.; Adesina, A.; Nemaleu, J.G.D.; Jiofack, S.B.K.; Djobo, J.N.Y. Performance of Laterite-Based Geopolymers Reinforced with Sugarcane Bagasse Fibers. *Case Stud. Constr. Mater.* **2021**, *15*, e00762. [CrossRef]
107. Batista Dos Santos, G.Z.; Passos De Oliveira, D.; De Almeida Melo Filho, J.; Marques Da Silva, N. Sustainable Geopolymer Composite Reinforced with Sisal Fiber: Durability to Wetting and Drying Cycles. *J. Build. Eng.* **2021**, *43*, 102568. [CrossRef]
108. Noor Abbas, A.-G.; Nora Aznieta Abdul Aziz, F.; Abdan, K.; Azline Mohd Nasir, N.; Fahim Huseien, G. Experimental Study on Durability Properties of Kenaf Fibre-Reinforced Geopolymer Concrete. *Constr. Build. Mater.* **2023**, *396*, 132160. [CrossRef]
109. Wei, Y.; Chai, J.; Qin, Y.; Li, Y.; Xu, Z.; Li, Y.; Ma, Y. Effect of Fly Ash on Mechanical Properties and Microstructure of Cellulose Fiber-Reinforced Concrete under Sulfate Dry–Wet Cycle Attack. *Constr. Build. Mater.* **2021**, *302*, 124207. [CrossRef]
110. Khan, M.; Cao, M.; Chu, S.H.; Ali, M. Properties of Hybrid Steel-Basalt Fiber Reinforced Concrete Exposed to Different Surrounding Conditions. *Constr. Build. Mater.* **2022**, *322*, 126340. [CrossRef]
111. Gulzar, M.A.; Ali, B.; Barakat, O.; Azab, M.; Najemalden, A.M.; Salih Mohammed, A.; Alashker, Y. Influence of Jute Fiber on Tensile, Electrical, and Permeability Characteristics of Slag Concrete: A Better, Cheaper, and Eco-Friendly Substitute for Conventional Concrete. *J. Nat. Fibers* **2023**, *20*, 2170947. [CrossRef]
112. Hadigheh, S.A.; Ke, F.; Fatemi, H. Durability Design Criteria for the Hybrid Carbon Fibre Reinforced Polymer (CFRP)-Reinforced Geopolymer Concrete Bridges. *Structures* **2022**, *35*, 325–339. [CrossRef]
113. Zhang, X.; Long, K.; Liu, W.; Li, L.; Long, W.-J. Carbonation and Chloride Ions' Penetration of Alkali-Activated Materials: A Review. *Molecules* **2020**, *25*, 5074. [CrossRef]
114. Ye, H.; Radlińska, A. Carbonation-Induced Volume Change in Alkali-Activated Slag. *Constr. Build. Mater.* **2017**, *144*, 635–644. [CrossRef]
115. Pasupathy, K.; Sanjayan, J.; Rajeev, P. Evaluation of Alkalinity Changes and Carbonation of Geopolymer Concrete Exposed to Wetting and Drying. *J. Build. Eng.* **2021**, *35*, 102029. [CrossRef]
116. Huang, Y.; Tan, J.; Xuan, X.; Wei, S.; Liu, L.; Yu, S.; Zheng, G. Durability of Plant Fiber Reinforced Alkali Activated Composites. *Constr. Build. Mater.* **2022**, *314*, 125501. [CrossRef]
117. Merta, I.; Poletanovic, B.; Dragas, J.; Carevic, V.; Ignjatovic, I.; Komljenovic, M. The Influence of Accelerated Carbonation on Physical and Mechanical Properties of Hemp-Fibre-Reinforced Alkali-Activated Fly Ash and Fly Ash/Slag Mortars. *Polymers* **2022**, *14*, 1799. [CrossRef]
118. Pouhet, R.; Cyr, M. Alkali–Silica Reaction in Metakaolin-Based Geopolymer Mortar. *Mater. Struct.* **2015**, *48*, 571–583. [CrossRef]
119. Ardanuy, M.; Claramunt, J.; Toledo Filho, R.D. Cellulosic Fiber Reinforced Cement-Based Composites: A Review of Recent Research. *Constr. Build. Mater.* **2015**, *79*, 115–128. [CrossRef]
120. Zhang, B. Durability of Low-Carbon Geopolymer Concrete: A Critical Review. *Sustain. Mater. Technol.* **2024**, *40*, e00882. [CrossRef]
121. Zhou, B.; Wang, L.; Ma, G.; Zhao, X.; Zhao, X. Preparation and Properties of Bio-Geopolymer Composites with Waste Cotton Stalk Materials. *J. Clean. Prod.* **2020**, *245*, 118842. [CrossRef]
122. Lezzerini, M.; Aquino, A.; Pagnotta, S. Acid Resistance of Metakaolin-Based Geopolymers and Geopolymeric Mortars Reinforced with Coconut Fibers. *Fibers* **2024**, *12*, 40. [CrossRef]
123. Thanushan, K.; Sathiparan, N. Mechanical Performance and Durability of Banana Fibre and Coconut Coir Reinforced Cement Stabilized Soil Blocks. *Materialia* **2022**, *21*, 101309. [CrossRef]
124. Sá Ribeiro, M.G.; Sá Ribeiro, M.G.; Keane, P.F.; Sardela, M.R.; Kriven, W.M.; Sá Ribeiro, R.A. Acid Resistance of Metakaolin-Based, Bamboo Fiber Geopolymer Composites. *Constr. Build. Mater.* **2021**, *302*, 124194. [CrossRef]
125. Li, Z.; Zhang, S.; Zuo, Y.; Chen, W.; Ye, G. Chemical Deformation of Metakaolin Based Geopolymer. *Cem. Concr. Res.* **2019**, *120*, 108–118. [CrossRef]

126. Alcivar-Bastidas, S.; Petroche, D.M.; Cornejo, M.H.; Martinez-Echevarria, M.J. Effect of Aging Process on Mechanical Performance of Reinforced Mortar with NaOH Abaca Fibers. *Case Stud. Constr. Mater.* **2024**, *20*, e03122. [CrossRef]
127. Haily, E.; Zari, N.; Bouhfid, R.; Qaiss, A. Natural Fibers as an Alternative to Synthetic Fibers in the Reinforcement of Phosphate Sludge-Based Geopolymer Mortar. *J. Build. Eng.* **2023**, *67*, 105947. [CrossRef]
128. Ranjithkumar, M.G.; Chandrasekaran, P.; Rajeshkumar, G. Characterization of Sustainable Natural Fiber Reinforced Geopolymer Composites. *Polym. Compos.* **2022**, *43*, 3691–3698. [CrossRef]
129. Kawashima, S.; Shah, S.P. Early-Age Autogenous and Drying Shrinkage Behavior of Cellulose Fiber-Reinforced Cementitious Materials. *Cem. Concr. Compos.* **2011**, *33*, 201–208. [CrossRef]
130. Lv, C.; Liu, J. Alkaline Degradation of Plant Fiber Reinforcements in Geopolymer: A Review. *Molecules* **2023**, *28*, 1868. [CrossRef]
131. Xu, S.; Wu, C.; Yue, J.; Xu, Z. Shrinkage and Mechanical Properties of Fibre-Reinforced Blast Furnace Slag-Steel Slag-Based Geopolymer. *Adv. Civ. Eng.* **2022**, *2022*, 8931401. [CrossRef]
132. Amran, M.; Onaizi, A.M.; Makul, N.; Abdelgader, H.S.; Tang, W.C.; Alsulami, B.T.; Alluqmani, A.E.; Gamil, Y. Shrinkage Mitigation in Alkali-Activated Composites: A Comprehensive Insight into the Potential Applications for Sustainable Construction. *Results Eng.* **2023**, *20*, 101452. [CrossRef]
133. Walbrück, K.; Drewler, L.; Witzleben, S.; Stephan, D. Factors Influencing Thermal Conductivity and Compressive Strength of Natural Fiber-Reinforced Geopolymer Foams. *Open Ceram.* **2021**, *5*, 100065. [CrossRef]
134. Novais, R.M.; Carvalheiras, J.; Senff, L.; Lacasta, A.M.; Cantalapiedra, I.R.; Giro-Paloma, J.; Seabra, M.P.; Labrincha, J.A. Multifunctional Cork—Alkali-Activated Fly Ash Composites: A Sustainable Material to Enhance Buildings' Energy and Acoustic Performance. *Energy Build.* **2020**, *210*, 109739. [CrossRef]
135. Silva, G.; Salirrosas, J.; Ruiz, G.; Kim, S.; Nakamatsu, J.; Aguilar, R. Evaluation of Fire, High-Temperature and Water Erosion Resistance of Fiber-Reinforced Lightweight Pozzolana-Based Geopolymer Mortars. *IOP Conf. Ser. Mater. Sci. Eng.* **2019**, *706*, 012016. [CrossRef]
136. Ma, G.; Li, Z.; Wang, L.; Wang, F.; Sanjayan, J. Mechanical Anisotropy of Aligned Fiber Reinforced Composite for Extrusion-Based 3D Printing. *Constr. Build. Mater.* **2019**, *202*, 770–783. [CrossRef]
137. Liu, J.; Lv, C. Properties of 3D-Printed Polymer Fiber-Reinforced Mortars: A Review. *Polymers* **2022**, *14*, 1315. [CrossRef]
138. Kozub, B.; Gądek, S.; Tyliszczak, B.; Wojnar, L.; Korniejenko, K. Leveraging 3D Printing Capability for Geopolymer Composites Based on Fly Ash with Cotton Fibers Addition. *Int. J. Eng. Technol. Innov.* **2024**, *14*, 231–243. [CrossRef]
139. Kong, X.; Dai, L.; Wang, Y.; Qiao, D.; Hou, S.; Wang, S. Influence of Kenaf Stalk on Printability and Performance of 3D Printed Industrial Tailings Based Geopolymer. *Constr. Build. Mater.* **2022**, *315*, 125787. [CrossRef]

Disclaimer/Publisher's Note: The statements, opinions and data contained in all publications are solely those of the individual author(s) and contributor(s) and not of MDPI and/or the editor(s). MDPI and/or the editor(s) disclaim responsibility for any injury to people or property resulting from any ideas, methods, instructions or products referred to in the content.

MDPI AG
Grosspeteranlage 5
4052 Basel
Switzerland
Tel.: +41 61 683 77 34

Materials Editorial Office
E-mail: materials@mdpi.com
www.mdpi.com/journal/materials

Disclaimer/Publisher's Note: The title and front matter of this reprint are at the discretion of the Guest Editor. The publisher is not responsible for their content or any associated concerns. The statements, opinions and data contained in all individual articles are solely those of the individual Editor and contributors and not of MDPI. MDPI disclaims responsibility for any injury to people or property resulting from any ideas, methods, instructions or products referred to in the content.

Academic Open
Access Publishing

mdpi.com

ISBN 978-3-7258-5758-6